Transactions of the ASME

Technical Editor
ARTHUR J. WENNERSTROM
Senior Associate Editor
G. K. SEROVY
Associate Editors
Advanced Energy Systems
S. I. FREEDMAN
Air Pollution Control
H. E. HESKETH
Fuels and Combustion Technologies
R. E. BARRETT
Gas Turbine
S. KUO
Internal Combustion Engine
K. J. SPRINGER
Nuclear Engineering
S. M. CHO
Power
R. W. PORTER

BOARD ON COMMUNICATIONS
Chairman and Vice-President
K. N. REID, JR.

Members-at-Large
W. BEGELL
J. T. COKONIS
W. G. GOTTENBERG
F. LANDIS
J. R. LLOYD
R. E. NICKELL
J. E. ORTLOFF
C. F. PHILLIPS
R. E. REDER
F. W. SCHMIDT

President, L. S. FLETCHER
Executive Director,
PAUL ALLMENDINGER
Treasurer, ROBERT A. BENNETT

PUBLISHING STAFF
Mng. Dir., Publ., J. J. FREY
Dep. Mng. Dir., Pub.,
JOS. SANSONE
Managing Editor,
CORNELIA MONAHAN
Production Editor,
VALERIE WINTERS
Editorial Prod. Asst.,
MARISOL ANDINO

The Journal of Turbomachinery is published quarterly for $100 per year by The American Society of Mechanical Engineers, 345 East 47th Street, New York, NY 10017. Second class postage permission pending at New York, NY and additional mailing offices. POSTMASTER: Send address change to The Journal of Turbomachinery, c/o The AMERICAN SOCIETY OF MECHANICAL ENGINEERS, 22 Law Drive, Box 2300, Fairfield, NJ 07007-2300."
CHANGES OF ADDRESS must be received at Society headquarters seven weeks before they are to be effective. Please send old label and new address.
PRICES: To members, $24.00, annually; to nonmembers, $80.00.
Add $6.00 for postage to countries outside the United States and Canada.
STATEMENT from By-Laws. The Society shall not be responsible for statements or opinions advanced in papers or ... printed in its publications (B 7.1, para. 3).

INDEXED by Engineering Information

Journal of Turbomachinery

Published Quarterly by The American Society of Mechanical Engineers

VOLUME 108 • NUMBER 1 • JULY 1986

TECHNICAL PAPERS

ANNOUNCEMENTS

Journal of Turbomachinery
Formerly Included in the Journal of Engineering for Gas Turbines and Power

Editorial

Welcome to the inaugural issue of the JOURNAL OF TURBOMACHINERY. The JOURNAL OF TURBOMACHINERY is a spinoff from the *Journal of Engineering for Gas Turbines and Power*. It was created to provide the increased publishing capacity necessary to accommodate the increasing number of papers appearing in the field of power generation. This journal will concentrate on compressor and turbine component technology. Judging from the present backlog, the heaviest concentration of papers will be in the area of compressor and turbine aerodynamics, followed by turbine cooling and heat transfer.

The *Journal of Engineering for Gas Turbines and Power* will continue to publish all papers dealing with research, development, and operating experience with complete systems including gas turbines, fossil fuel and nuclear-fired steam power plants, and internal combustion engines. It will also retain all papers on combustion, on system dynamics, most papers on structures and materials topics, and those on control systems and all types of auxiliaries such as fuel systems, pollution control systems, inlet and exhaust systems, etc.

Papers dealing with the fluid mechanics of hydraulic turbines and pumps will continue to appear in the *Journal of Fluids Engineering*.

ARTHUR J. WENNERSTROM
Technical Editor

Spanwise Mixing in Multistage Axial Flow Compressors: Part I—Experimental Investigation

S. J. Gallimore[1]
Rolls-Royce Limited,
Derby, England

N. A. Cumpsty
Whittle Laboratory,
University of Cambridge,
England

Spanwise mixing has been shown to be an essential feature of multistage compressor aerodynamics. The cause of spanwise mixing in multistage axial flow compressors has been investigated directly by using an ethylene tracer gas technique in two low-speed, four-stage machines. The results show that the dominant mechanism is that of turbulent type diffusion and not the radial convection of flow properties as has been previously suggested. The mixing was also found to be substantially uniform in magnitude all the way across the span with levels similar to those found in two-dimensional turbulent wakes.

Introduction

One of the fundamental assumptions that is generally made during the design of a multistage compressor is that the flow remains on axisymmetric stream surfaces as it passes through the machine; this is despite experimental evidence that suggests that substantial amounts of radial or spanwise mixing can take place. This evidence can be found in the calculation of spanwise variations of blade element adiabatic efficiencies in the rear stages of multistage machines from measured total pressure and temperature profiles. These often indicate higher losses at midspan than toward the end walls [1–3], suggesting that the high loss fluid near the walls is being redistributed across the span by radial mixing. The presence of spanwise mixing would also help to explain the existence of the repeating stage condition in multistage machines (although other aspects of this mechanism need investigating also), the flow near the end walls being in a kind of dynamic equilibrium, with end-wall loss generation being balanced by radial spread away from the walls. (This behavior is similar to the existence of the fully developed velocity profile in turbulent pipe flow.)

Adkins and Smith [1] were the first to recognize the potential importance of spanwise mixing and developed an approximate theory for calculating its magnitude and effect on multistage compressor performance. Their model was based on the knowledge that secondary flows have radial velocities associated with them. They calculated spanwise velocities by considering classical secondary flow theory, end-wall boundary layer flow, tip clearance flows, and blade boundary layer cross flows. These radial velocities were assumed to convect the flow properties and so cause their radial redistribution. It is important to recognize that the sources of the apparent mixing postulated by Adkins and Smith are deterministic secondary flows; the mixing is not produced by some random or turbulent diffusion process. Throughflow calculations made using this mixing model showed much improved agreement with experimental results for spanwise distributions of stagnation temperature and pressure compared to those obtained without including the mixing effects.

The work of Adkins and Smith confirmed that spanwise mixing is an important phenomenon in multistage axial compressors but it is not clear that the model of mixing based on radial convection is the correct one for describing this phenomenon. There is no doubt that radial velocities do exist but there is little experimental evidence as to their magnitude in multistage machines or to the amount of mixing they produce. Wagner et al. [4] studied the mixing across an isolated rotor by using a CO_2 tracer gas technique. The gas was injected into the wall boundary layers upstream of the rotor and its concentration measured downstream. Although the rotor exhibited signs of part span stall (and hence large radial velocities on the blade suction surface) at the design flow coefficient, the contours showed little radial distortion and the measured secondary velocities were of the order of 10 percent of the mainstream velocity. They concluded that the radial spread of the gas was much the same as one would expect from a simple thickening of the concentration profiles due to boundary layer growth in an annular duct with no blades present. In earlier work on the same compressor Dring et al. [5] measured total pressure contours in the relative frame of reference at various axial positions downstream of the rotor. They noted that as the flow proceeded downstream the regions of high loss spread out in a way that was primarily a diffusion process, with little sign of convective radial redistribution. These two results, although taken from an isolated rotor, tend to suggest that some kind of diffusion process is dominating the radial mixing, rather than redistribution by deterministic radial flows.

One aspect of the flow that was neglected in the mixing model of Adkins and Smith [1] was that of turbulent or random mixing. The flow through a multistage compressor will

[1] Formerly Whittle Laboratory, University of Cambridge.

Contributed by the Gas Turbine Division of THE AMERICAN SOCIETY OF MECHANICAL ENGINEERS and presented at the 31st International Gas Turbine Conference and Exhibit, Düsseldorf, Federal Republic of Germany, June 8–12, 1986. Manuscript received at ASME Headquarters December 26, 1985. Paper No. 86-GT-20.

inevitably be turbulent due to blade wakes, tip clearance flows, unsteadiness, etc., and if there are random fluctuations in the radial direction they can give rise to turbulent diffusion of flow properties across the span. Schlichting and Das [6] and Kiock [7] have found that the streamwise turbulence intensity well away from the end-wall regions of multistage compressors rises to a level of about 6 percent after five stages. The radial intensities were not measured but the streamwise value gives an indication of its likely level in multistage machines. Lakshminarayana and his co-workers [8–11] have measured radial turbulence intensities of the order of 20 percent in the wakes and end-wall regions downstream of an isolated rotor. They also noted that the radial turbulence level decayed more gradually than both the tangential and streamwise components. These levels should be compared with a typical turbulence intensity perpendicular to the wall of 5 percent in a turbulent flat plate boundary layer. There is clearly a possibility that these high turbulence levels could contribute significantly to spanwise mixing.

This paper reports an experimental investigation aimed at determining directly, by means of a tracer gas technique, the amount of spanwise mixing in multistage axial compressors and the dominant physical mechanism causing it. Attention is restricted to operation at peak efficiency or design conditions and not to the flow near stall where substantial flow separations are most likely. The use of a tracer gas allows estimates to be made of the turbulent species diffusion ϵ. This is related to the eddy viscosity ν by the Schmidt number $\mathrm{Sc}_t = \nu/\epsilon$ and to the eddy thermal conductivity k by the turbulent Lewis number $\mathrm{Le}_t = \rho\epsilon C_p/k$. Experimental evidence suggests that Sc_t and Le_t can be reasonably approximated as unity [12–14] and this equivalence between ϵ, ν, and k will be assumed here throughout. It is perhaps worth pointing out why foreign gas injection is so helpful: It is because the only source of the species is the injection and the spread can be attributed to mixing. For momentum and thermal energy, additions are occurring through the flow as a result of the flow process and contour movements cannot be interpreted solely in terms of ν and k.

The experiments which are reported fully in [15] consisted of the measurement of the mixing in two low-speed four-stage compressors and in a turbulent flat plate boundary layer. The results from the two compressors, however, led to identical conclusions and so, for the sake of brevity, only the experimental results from the larger of the two machines (denoted Compressor A) will be presented here, although the results from the other machine (Compressor B) will be used in the discussion.

Compressor A was built recently and is at the Cranfield Institute of Technology. These tests were squeezed into an early part of the initial testing of the machine. Compressor B was loaned to the Whittle Laboratory by Derby Technical College and has been described elsewhere [16]; the present build was 50 percent reaction with 35 deg stagger and 20 deg camber blades.

The purpose of the experiments in the flat plate boundary layer was to demonstrate that the tracer gas technique gave good estimates of mixing from the measured tracer gas spreads, to provide a direct comparison with the results from the four-stage compressors, and to verify that the injection probes were not seriously perturbing the mixing. The flat plate boundary layer measurements are therefore discussed before those for the compressors.

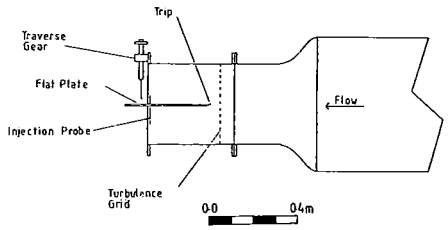

Fig. 1 Schematic diagram of the low-speed wind tunnel

The system used was a slightly modified version of that described by Denton and Usui [17]. A small, but constant, stream of ethylene (about 120 cc/min) was injected into the flow from an injection probe. Ethylene was used as the tracer because it has a molecular weight only 3 percent less than that of air and so minimizes buoyancy effects. The air, contaminated with ethylene, was then sampled downstream at a constant rate through the center hole of a three-hole cobra probe (the side holes being used to align the probe in the mean flow direction). The sample passed to a Flame Ionization Detector unit to give a voltage directly proportional to the amount of ethylene in the sample. Detection of concentrations of only a few parts per million was possible, while peak concentrations of about 1000 ppm were typical in the investigations decribed here.

Boundary Layer Results

A flat plate boundary layer experiment was conducted in a low-speed wind tunnel, the working section of which is shown in Fig. 1. The air flow was provided by a variable speed centrifugal fan, the inlet of which could be throttled. The cylindrical working section was 0.355 m in diameter and 0.380 m long. A flat plate made of epoxy resin, 0.380 m long and 9 mm thick, was fixed horizontally across the diameter of the tunnel, its trailing edge extending 95 mm downstream of the tunnel exit plane. A traverse gear was mounted on the flange at the end of the tunnel allowing area traverses to be made 0.315 m from the flat plate leading edge. A boundary layer trip was fixed to the upper surface leading edge of the plate to ensure a turbulent boundary layer. In addition a turbulence grid, consisting of 1.6-mm-dia bars with a 12.7-mm pitch, could be inserted in a plane 95 mm upstream of the plate leading edge.

The tunnel was run with a mainstream velocity of 30 m/s, similar to the flow velocities found in a stator row of the four-stage compressor. Oil and dye flow visualization on the plate surface showed negligible contraction of the surface streamlines, confirming that the boundary layer was two

Nomenclature

h = blade span
H = shape factor = δ^*/θ
l = turbulent length scale
L_s = axial stage length
P = concentration
ΔP_a = stage static pressure rise
ΔP_i = ideal stage static pressure rise
ΔP_L = loss in stage static pressure rise = $\Delta P_i - \Delta P_a$
q^2 = turbulence velocity scale = $\frac{1}{3}(\overline{u'^2} + \overline{v'^2} + \overline{w'^2})$
r = radial spread = $\{R^2 - z^2\}^{1/2}$
R^2 = $x^2 + y^2 + z^2$
s = blade pitch
Sc_t = turbulent Schmidt number = ν/ϵ
t = blade thickness
u', v', w' = components of turbulent velocity
U_m = mean blade speed
V = flow velocity
x, y, z = rectangular coordinates
δ^* = displacement thickness
ϵ = mixing coefficient
θ = momentum thickness
ν = eddy kinematic viscosity
ρ = density
ϕ = flow coefficient = V_z/U_m
ω = loss coefficient = $\Delta P_L/\rho U_m^2$

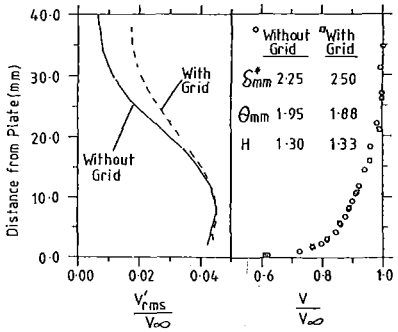

Fig. 2 Boundary layer velocity profiles and turbulence levels

dimensional. The velocity profiles, measured using a three-hole cobra probe, are shown in Fig. 2, for the flow both with and without the turbulence grid in position. The values of shape factor are slightly below the expected level of 1.4 for a zero pressure gradient boundary layer with $Re_\theta = 4000$, indicating a slightly favorable pressure gradient along the plate. This pressure gradient was measured using static pressure tappings on the plate and found to be only one tenth of the value required to produce significant discrepancies from the law of the wall behavior. The radial turbulence intensity was measured by Hart [18] using hot-wire anemometry and his results are also shown in Fig. 2. The turbulence grid increases the free-stream intensity from 0.6 percent to 1.7 percent but does not alter the value near the plate where the boundary layer turbulence generation dominates, the peak intensity being 4.5 percent in this region. These results compare favorably with those reproduced by Schlichting [19] for a similar flow. For the purposes of the mixing experiments described below the measurements therefore showed that the flow could be regarded as a typical two-dimensional boundary layer.

The main difficulty in using the spread of a contaminant as a measure of the mixing in a flow is that the injection probe inevitably disturbs the flow field somewhat and is therefore likely to contribute to the mixing process itself [20, 21]. A development program was therefore undertaken with the aim of producing an injection probe that would fit in the confined space between the blade rows of the compressor while disturbing the flow by a minimum. The final shape decided upon was the crooked probe (Probe B) shown in Fig. 3, which was made of 0.56-mm-dia hypodermic steel tubing. The ethylene is injected parallel to the mean flow direction but offset by 4 mm from the plane of the probe stem so as to avoid most of the effect of the stem wake on the ethylene distribution. The performance of Probe B in the flat plate boundary layer was compared to that of Probe A, which is made of the same tubing, but consists simply of a stem and a downstream trailing arm 35 mm long (rather like a reversed pitot probe). The long length of the tube aligned in the flow direction meant that this probe approximated very closely to the ideal injection case where no disturbance is caused by the injection probe. The ethylene injection rate of 120 cc/min gave an exit velocity of 27 m/s from the probes, assuming uniform outlet flow and no vena contracta, similar to the air flow velocities found in the experiments (about 30 m/s).

Figure 4 shows the ethylene contours measured 65 mm downstream of the injection plane with injection at two distances from the flat plate using both Probes A and B. The contours are presented as percentage values of the peak concentration measured for each particular test. It can clearly be seen that the ethylene spread was greater in the boundary layer than in the free stream because of the higher turbulence intensity there. Increasing turbulence intensity by introducing the turbulence grid also increased the spread in this region as expected. Outside the boundary layer the crooked probe (Probe B) has produced more spread than Probe A, which ap-

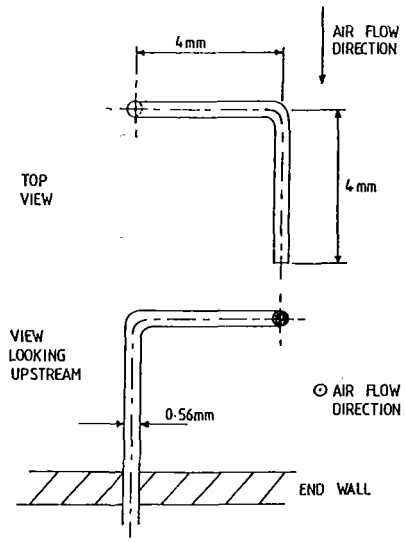

Fig. 3 Ethylene injection Probe B

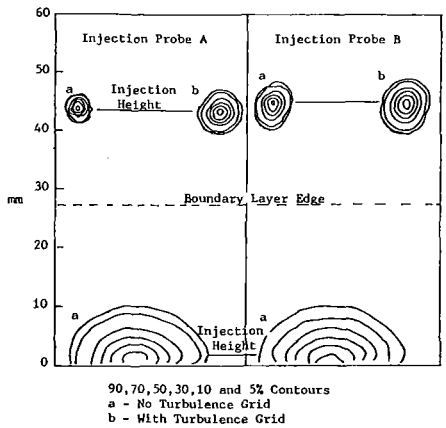

Fig. 4 Ethylene contours in the flat plate boundary layer

proximates to the ideal case. However, the difference in the spread between the two probes was reduced as the turbulence intensity was increased, the ratio of the spread with Probe B to that with Probe A reducing from 1.6 to 1.2. Near the plate, where the turbulence intensity was even greater, the mixing measured with both probes was identical, showing that as the turbulence level increased the crooked injection probe used in the compressor produced spreads that became indistinguishable from the ideal injection case. It will be shown below that the flow in the compressor produced more mixing than the boundary layer flow and so it may be assumed that no error arose from using injection Probe B in that environment. Another point to note is that Probe B did not cause any shift of the peak ethylene concentration point normal to the plate relative to the injection position.

An estimate of the mixing coefficient ϵ that would produce the observed ethylene spreads can be made by assuming that the tracer gas diffuses from a point source in a uniform flow with velocity V_z. Hinze [22] shows that for this case the concentration P obeys the equation

$$P(x, y, z) = \frac{S}{4\pi\epsilon R} \exp[-V_z(R-z)/2\epsilon] \quad (1)$$

where S is the volume flow rate of the source. The peak concentration occurs along the z axis and is given by $P_{peak} = S/4\pi\epsilon z$ from equation (1); equation (1) must therefore be solved for R with $P(x, y, z) = CS/4\pi\epsilon z$. Assuming that $z/R \approx 1$ (which is true to within 2 percent for the data presented here)

Table 1 Four-stage Compressor A rig details

Tip diameter	1.21 m
Hub/tip ratio	0.85
Rotational speed	1000 rpm

Blade details

Twisted, double circular arc, with thickness/chord ratio of 6 percent
Free vortex, zero α_0, high-reaction (85 percent) blading

		Rotor	Stator
No. of blades		59	61
Chord		60.7 mm	60.7 mm
Aspect ratio	midheight	1.5	1.5
Space/chord ratio	midheight	0.988	0.956
Stagger	midheight	53 deg	10 deg
Camber	midheight	23 deg	50 deg
Axial spacing		15 mm	
Tip clearance		0.9 mm	–

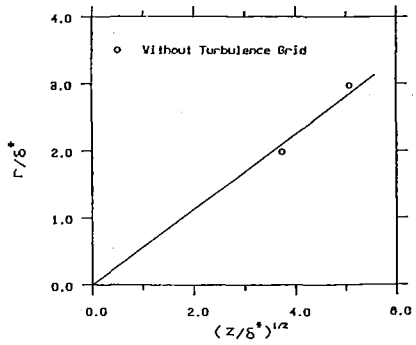

Fig. 5 Ethylene spread in the flat plate boundary layer

$$R = z - \frac{2\epsilon \ln C}{V_z} \tag{2}$$

The spread of the ethylene r in the plane normal to the mean flow direction can now be found by substituting for $R\,(=r^2 + z^2)$ and assuming that $-\epsilon \ln C/V_z << z$ (which is also true for the data presented) to give

$$\frac{r}{L} = \left[-4\,\frac{\epsilon}{V_z L}\,\frac{z}{L}\,\ln C\right]^{1/2} \tag{3}$$

The measurements are presented as contours showing the fraction C of the peak concentration and equation (1) must be adapted to use the data in this form where a nondimensionalizing length scale L has been introduced. Equation (3), which shows that the contours spread as $z^{1/2}$ within the restrictions outlined above, will be used to derive estimates for ϵ from the ethylene data. Although the equation is strictly only true in a uniform flow it will be shown that it gives reasonable estimates of mixing for nonuniform flow in the flat plate boundary layer and it will therefore be used to analyze the ethylene spreads in the four-stage compressor.

Figure 5 shows the spreads of the 5 percent concentration contours measured at two axial locations (30 mm and 60 mm) downstream of injection Probe A positioned 2.5 mm from the flat plate. (Shortage of time prevented the acquisition of data at further axial locations.) The lengths have been nondimensionalized for convenience by the boundary layer displacement thickness with the turbulence grid in place (2.5 mm). The mixing coefficient ϵ was evaluated from the slope of the line using equation (3) assuming that the flow velocity was 0.8 of the free-stream value for this part of the flow. This gave a value of $\epsilon/V_z\delta^* = 2.1 \times 10^{-2}$ where V_z is the free-stream velocity. A check can be made to assess the accuracy of this derived value of mixing by comparing it with values of eddy viscosity ν quoted in the literature. As remarked above this is possible because ϵ and ν are related through the turbulent Schmidt number $\mathrm{Sc}_t = \nu/\epsilon$ and experimental evidence suggests that Sc_t can be sensibly taken as unity for a range of turbulent flows. Schlichting [19] quotes the value of the eddy viscosity in a turbulent flat plate boundary layer as

$$\nu = 0.017\,V_z\delta^*\gamma \tag{4}$$

where γ is the intermittency factor. In the inner 40 percent of the boundary layer $\gamma = 1.0$, denoting fully turbulent flow, giving $\epsilon/V_z\delta^* = 1.7 \times 10^{-2}$, in good agreement with the value deduced above from the ethylene spreads. To summarize: The probe and technique have been shown to work satisfactorily in a turbulent boundary layer and to give estimates of eddy viscosity close to those expected. It was therefore felt that measurements of mixing (and of convected shifts) obtained in compressors would be realistic and reliable.

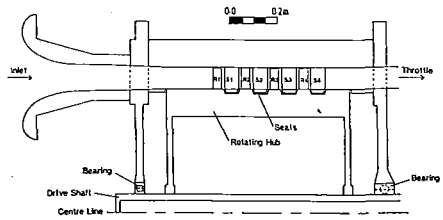

Fig. 6 Overall view of Compressor A

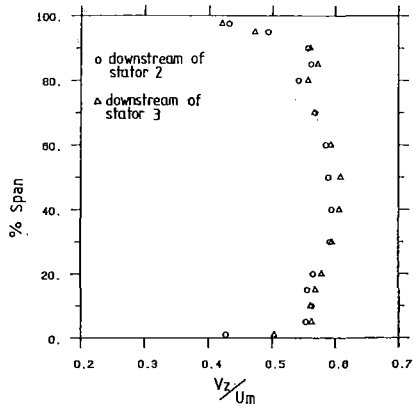

Fig. 7 Compresosr A axial velocity profiles

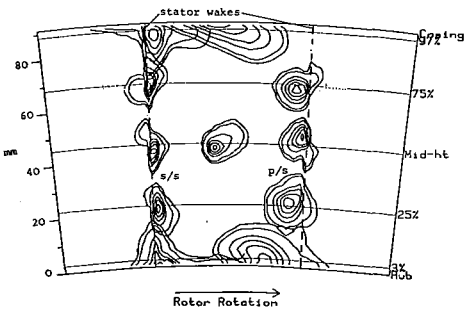

Fig. 8 Compressor A: injection upstream of Stator 3; sampling downstream of Stator 3; 90, 70, 50, 30, 10, and 5 percent contours

Compressor A Results

The low-speed Compressor A, shown schematically in Fig. 6, had four identical stages of zero α_0, free vortex, high reaction blading with shrouded stators, typical of current HP compressor practice. The blading details are given in Table 1. The large scale of the rig allowed blade Reynolds numbers of about 2×10^5 (again typical of current practice) to be achieved at flow velocities of about 30 m/s. Throughout the tests the compressor was operated at its peak efficiency (86 percent) condition with overall $\Delta P_0/\rho U_m^2 = 1.28$ achieved at the design flow

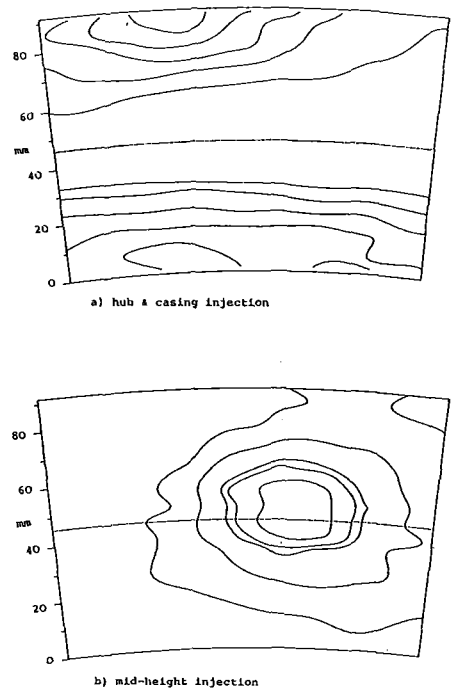

Fig. 9 Compressor A: injection upstream of Rotor 1; sampling downstream of Rotor 4; 90, 70, 50, 30, and 10 percent contours

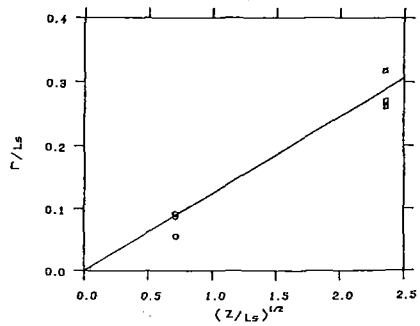

Fig. 10 Ethylene spreads in Compressor A

coefficient of 0.55. Figure 7 shows the axial velocity profiles measured downstream of stators 2 and 3 using a three-hole cobra probe. The profiles suggest that the flow coefficient was somewhat different from 0.55 (the nominal value). This can be explained by circumferential variations in velocity caused by the nonaxisymmetric flow at exit from the stators. Unfortunately this investigation was squeezed into the early testing of Compressor A and there were not sufficient data available to enable circumferential averages to be made. The results presented do show, however, that the third stage has approximately reached the repeating stage condition.

The configuration of the rig traversing rings and probe access points restricted the axial positioning of the ethylene injection and sampling planes such that only two series of tracer gas tests were possible: the first with injection upstream of Stator 3 and sampling downstream of the Stator 3, the second with injection upstream of Rotor 1 and sampling downstream of Rotor 4.

Figure 8 shows the results of eleven separate tracer gas tests conducted across Stator 3 of Compressor A. The ethylene was injected from injection Probe B in a plane 1 mm upstream of the blade leading edge and sampled in a plane 1 mm downstream of the trailing edge. The radial heights of the injection positions are shown on the diagram while the circumferential positions were either at midpassage or just upstream of the leading edge. Where the contour results of two tests overlapped significantly one of the results has been plotted one pitch circumferentially around from its actual test position. Again the contours are percentage values of the peak concentration for that particular test.

The positions of the peak ethylene concentration points for all the tests have not moved far radially from their injection position. The greatest radial displacement occurs either side of the wake at midspan, being 3 mm radially outward on the pressure surface and the same amount radially inward on the suction side. This is over a flow distance of about 65 mm. At 25 percent span from the hub the radial shifts in the wake region are in the same sense as those at midheight but of about half the magnitude; at 75 percent span the radial shifts are now in the opposite direction but of similar magnitude to those at 25 percent span. For injection at midpassage, midheight the ethylene has moved slightly inward from the injection height but this shift is only 1 mm and some of this could be accounted for by positioning error of the injection probe.

In one test ethylene was injected at 3 percent span, near the hub, so as to pass down both sides of the stator and in another test at the same radius injection was at midpassage. The contours are almost symmetric about the blade wake except for the ethylene that has spread toward the pressure side of the passage. This implies some cross-passage boundary layer flow with the fluid being underturned near the hub, because of the high inlet skew at blade inlet. (Yaw angle measurements confirmed that the flow was underturned in this region.) The cross-passage flow causes the ethylene injected at midpassage to appear nearer the pressure side at passage exit; ethylene further from the hub has lagged behind this movement because the cross-passage flow is less in those areas. It should be noted that these stator blades were shrouded.

Near the rotor casing, with injection at 97 percent span, there is some indication of flow overturning, also suggested by yaw angle measurements, with ethylene spreading along the casing away from the blade pressure surface toward the midpassage location. A small distance away from the wall the ethylene has moved in the opposite direction from the midpassage position toward the pressure surface, due to the underturning in this part of the flow.

The contours in Fig. 8 for flow through stator 3 show that the radial shifts of the peak ethylene concentration points were small, indicating that the magnitude of convective radial flows was also small in the blade row. The greatest radial shifts were in the wake region at midheight, but in general it would seem that the ethylene has spread through the blade row by some sort of diffusion process. The overall ethylene spreads were large even for midheight, midpassage injection where the interference of the stators could be expected to be least. This may be seen by comparing the spreads in the compressor with those measured in the flat plate boundary layer over the same flow distance (Fig. 4). In general the spreads in the compressor are about twice those found in the equivalent flow regions near the flat plate, indicating that the compressor flow can be regarded as being highly turbulent, at least more so than the 4 percent intensity measured in the boundary layer.

The effect of this radial mixing on the flow through several stages of the compressor is shown in Fig. 9. For these tests the ethylene was injected at hub, midheight, and casing 250 mm axially upstream of the rotor 1 leading edge using a 1-m length of 0.56-mm-dia hypodermic tubing introduced through the inlet. The ethylene was sampled downstream of rotor 4. The injection could not be made closer to the rotor on the hub because of the rotating hub section and so for comparability the two other tests were also conducted with the same axial injection position. For all the tests the ethylene has spread considerably in the radial direction: from the end walls almost to midheight and with midheight injection almost to the walls.

This shows that the overall effect of spanwise mixing is substantial over 3½ stages with all the flow being affected by diffusion right across the annulus.

An estimate of the mixing coefficient implied by the spreads through the stator and also through 3½ stages can be made using equation (3). The spreads of the 10 percent contours are shown plotted against flow distance in Fig. 10. Both sets of data are nondimensionalized by axial stage length L_s. There is a certain amount of scatter but taking the average slope gives a value of $\epsilon/V_zL_s = 1.8 \times 10^{-3}$. This value can be compared to data in the literature. For example taking the value of ν calculated for the flat plate boundary layer using equation (4) gives a value of $\nu/V_zL_s = 3.2 \times 10^{-4}$. This is lower than that found in the compressor, as expected, because the ethylene spreads were smaller in the boundary layer. Schlichting [19] gives the value of the eddy viscosity in a two-dimensional wake as

$$\nu = 0.047 \times 2 \times b_{1/2} \times V_2$$

where $b_{1/2}$ is the half-wake width at half-depth. A typical value of $b_{1/2}$ would be about one blade thickness giving $\nu/V_zL_s = 2.7 \times 10^{-3}$. This is slightly greater than the value measured in the compressor, showing that the observed mixing is not unreasonably high. Similar calculations using data from Hinze [22] showed that the measured mixing was about twice what would be expected from fully developed pipe flow of similar Reynolds number. It may also be restated here that the experimentally derived mixing levels may be relied upon because injection with Probe B used after Stator 3 becomes indistinguishable from the ideal case as the turbulence level increases and because for injection upstream of Rotor 1 the probe was a long length of small diameter tubing aligned in the flow direction which would not cause significant extra mixing.

Discussion

The experimental evidence from the tracer gas tests conducted across Stator 3 of the four-stage machine showed that there were no large radial shifts of the peak ethylene concentration points, and hence no large radial velocities. However, the ethylene spread substantially in passing through the blade passage, more than in the equivalent tests in the flat plate boundary layer, for all the injection positions. This suggests that the dominant mechanism for spanwise mixing is a random, turbulent type of diffusion process rather than convection by deterministic secondary flows. The magnitude of the mixing that would be caused by the observed radial flows can be quantified by using the observed radial shifts to evaluate the mixing coefficient of Adkins and Smith [1]. If it is assumed that the greatest radial shift observed in the experiments on Compressor A (found either side of the wake at midheight) is caused by a constant radial velocity it implies a radial velocity 0.048 times the throughflow velocity. If it is further assumed that the radial velocity varies linearly across the pitch, that the mixing level is uniform across the span, and that all the blade rows produce the same mixing, the expression for the mixing coefficient derived by Adkins and Smith may be evaluated. Relating their mixing coefficient, which has dimensions of length, to ϵ (dimensions length^2/time) by the throughflow velocity gives $\epsilon/V_zL_s = 5.6 \times 10^{-4}$ based on the observed radial *shifts*. In estimating this value it must be stressed that the maximum observed radial shifts, which occurred in the blade wakes at midheight, were used and it can be seen from the contours in Fig. 8 that the shifts observed elsewhere in the flow were significantly smaller than these. Therefore the calculated value should be regarded as that representing the maximum possible mixing by radial flows, with a more representative value for the whole flow being somewhat less. Despite this the value is only about one third of the amount of mixing deduced from the ethylene *spreads*, showing that the dominant mixing mechanism is a diffusion process.

Table 2 Mixing levels (values of ϵ/V_zL_s)

	Compressor A	Compressor B
Measured ethylene spreads	1.8×10^{-3}	3.8×10^{-3}
Adkins and Smith [1] model		
• based on predicted radial velocities	–	3.9×10^{-3}
• based on observed radial shifts	5.6×10^{-4}	9.7×10^{-4}
Turbulent flat plate		
Boundary layer mixing [19]	3.2×10^{-4}	7.8×10^{-4}
Two-dimensional wake mixing [19]	2.7×10^{-3}	2.7×10^{-3}
Equation (9) for estimating value in multistage compressor	1.6×10^{-3}	2.1×10^{-3}

As mentioned above, tracer gas experiments were also conducted on another smaller four-stage compressor (Compressor B), the same machine as that used by Cumpsty [16]. The contour results have not been presented here because they showed essentially the same information as those already shown (i.e., large amounts of spanwise spread but only small amounts of radial shift). The same estimates of mixing level were made for those results as for those on Compressor A and these are set out in Table 2. In addition the aerodynamic details of the machine were provided to Dr. Smith so that the mixing method described in [1] could be used to calculate the flow. The results of the calculation were kindly made available to the authors by Smith [23] and these showed that the profiles of mean axial velocity had been accurately predicted; also included were the predicted radial velocities upon which the Adkins and Smith mixing model is based. An estimate of the mixing coefficient based on these *predicted* velocities, made in the same way as outlined above, gave a value of $\epsilon/V_zL_s = 3.9 \times 10^{-3}$, very close to the experimental value derived from the ethylene spreads. (This estimation of the mixing level used in the calculation has been confirmed by further communication with Dr. Smith and his colleagues.) However, the maximum radial velocities actually derived from the measured radial shifts of ethylene were about half the predicted velocities giving an estimate for mixing of $\epsilon/V_zL_s = 9.7 \times 10^{-4}$, again some three or four times less than the value derived from the experimentally observed spreads.

It would seem therefore that the experimental evidence from both compressors indicates that the physical model of spanwise mixing based on the radial redistribution of flow properties by deterministic radial flows is inaccurate. The dominant mechanism of spanwise mixing is a random, turbulent type of diffusion process which produces about three or four times the amount of mixing capable of being produced by radial flows. The entire annulus has a level of mixing similar to that found in a turbulent boundary layer or wake, although not necessarily the same turbulent characteristics. This high mixing level will be shown to have a significant influence on the radial distribution of flow properties such as loss and total temperature in Part II of this paper. However even at this stage it is possible to indicate how the recognition that substantial amounts of spanwise mixing exist can alter the interpretation of flow in multistage compressors. A common assumption made in calculations of the throughflow in multistage machines is that the flow can be divided into an inviscid free stream bounded by two annulus wall boundary layers. This is clearly inappropriate if there is continual exchange of momentum and heat radially across the span. The edge of the boundary layers cannot be sensibly defined; Cumpsty [16] pointed out that the extent of the boundary layer measurement on the hub in a four-stage compressor could not be reliably fixed. The presence of spanwise mixing explains this problem, for wherever velocity gradients exist so

too will shear stresses. Spanwise mixing could also be a contributory factor in the setting up and maintaining of the repeating stage condition, the continual radial exchange reducing the accumulation of low total pressure, high total temperature fluid at the end wall which would otherwise increase indefinitely from skin friction, tip clearance flow, and high losses near the endwall.

A Method of Predicting the Mixing Coefficient

With the experimental results presented in this paper constituting the only data available for the levels of eddy viscosity or mixing in multistage compressors any method of predicting these levels will inevitably be somewhat speculative. However, some progress can be made by considering the generation and decay of turbulence in the flow as follows.

Let us consider a repeating stage in a multistage axial compressor where the flow velocities and turbulence levels at exit are identical to those at inlet to the stage. The ethylene tracer gas results show that the radial and circumferential spreads through a single blade row are substantially the same except where end-wall boundary layer cross flows are present. It will therefore be assumed that the turbulence is homogeneous and essentially isotropic. Within the stage turbulence is generated by shear in the blade boundary layers and wakes and in the flow near the end walls. This shear creates a drag force on the flow through the stage which, because the stage is repeating and there is therefore no momentum change across it, must be balanced by a static pressure loss ΔP_L across the stage such that

$$\Delta P_a = \Delta P_i - \Delta P_L$$

where

ΔP_a = actual static pressure rise across the stage
ΔP_i = ideal static pressure rise (i.e., with no loss)

Based on similar work by Owen [24] in analyzing the flow through heat exchangers the amount of turbulence energy generated in the stage is given approximately by

$$\Delta P_L \, V_z \, sh$$

where V_z is the mean axial velocity through the stage, s is the blade pitch, and h is the blade height. If a velocity scale q is defined such that $q^2 = \frac{1}{3}(\overline{u'^2} + \overline{v'^2} + \overline{w'^2})$ the turbulent kinetic energy per unit mass of gas is $(3/2)q^2$ and further, if the typical length scale of the turbulent eddies is l, the rate of dissipation is given approximately by

$$3q^3/2l$$

Hence the rate at which turbulent kinetic energy decays within the stage is $3q^3\rho shL_s/2l$, where L_s is the axial length of the stage. Assuming that the energy decay is balanced by the turbulence generation we can write

$$\Delta P_L V_z = \frac{3}{2} q^3 \rho L_s / l \tag{5}$$

The kinematic eddy viscosity ν, and hence ϵ, can be related to the turbulence level by

$$\nu = Aql \tag{6}$$

where A is a constant.

The scale of turbulence may be assumed to be approximately the blade thickness so that

$$l = 0(t) \tag{7}$$

This is not to suggest that reducing the blade thickness will necessarily result in a smaller value of l but rather to identify a typical length scale of the turbulent eddies. Substituting for q and l in (5), using equations (6) and (7) gives

$$\nu^3 = \frac{2}{3} \frac{\Delta P_L \, V_Z A^3 t^4}{\rho L_s} \tag{8}$$

The velocity is conveniently nondimensionalized by the mean blade speed U_m to give the flow coefficient ϕ. The pressure loss ΔP_L may also be nondimensionalized by ρU_m^2 to give a loss ω; it should be noted that the definition of loss coefficient is usually in terms of relative velocity into the blades and not blade speed but for the very approximate treatment here this distinction is unlikely to be significant. The expression for the eddy viscosity (and hence ϵ), nondimensionalized by stage length and axial velocity is therefore

$$\frac{\epsilon}{V_z L_s} = \frac{At}{L_s} \left[\frac{2\omega (t/L_s)}{3\phi^2} \right]^{1/3} \tag{9}$$

An approximate value of A can be obtained by following the analysis of Savill and Zhou [25] which gives

$$A = \left[\frac{\overline{u'v'}}{q^2} \right]^{1/2} \tag{10}$$

The quantity $\overline{u'v'}/q^2$ has been measured in the turbulent flow near walls and found to be approximately 0.2 [13], which gives A as approximately 0.4.

It must be remembered that the preceding analysis is only very approximate, containing several sweeping assumptions, and a more detailed and complex analysis could probably be made. However, it is thought that until further experimental investigations into the origin of the turbulence in multistage compressors are completed the simple approach presented here gives sufficiently accurate results.

Evaluating equation (9) for the two four-stage compressors used in the experimental investigation gave values of $\epsilon/V_z L_s$ of 1.6×10^{-3} for the larger machine and 2.1×10^{-3} for the smaller one. These are in satisfactory agreement with the experimental results as can be seen from Table 2.

The fact that the correct mixing level can be predicted to within a factor of about two by the simple model confirms the suggestion made earlier that the high values of mixing found in the two compressors are reasonable. It also suggests that the prediction method outlined above may give the correct levels of mixing coefficient (to within better than an order of magnitude) for low-speed multistage machines and perhaps high-speed machines as well, although this must be a tentative conclusion because of the scarcity of experimental data against which to test the method.

Conclusions

The experimental investigation using the tracer gas technique showed that the dominant mechanism causing spanwise mixing in the latter stages of multistage compressors was a random, turbulent-type, diffusion process. The contribution from convection by deterministic radial secondary flows, as has previously been modeled by Adkins and Smith, was small. The levels of mixing were found to be high (about the same as those found in a two-dimensional turbulent wake) and approximately uniform across the whole span. A simple model for predicting the mixing level, based on the balance between the generation and decay of turbulence energy, was developed and shown to give satisfactory results for the two cases where experimental evidence of the mixing level was available.

The high level of mixing well inside multistage compressors helps to explain the existence of the repeating stage condition in such machines, although there are other aspects to this which need explaining also. It also shows that modeling the throughflow as a free stream bounded by two end-wall boundary layers is inappropriate and inaccurate for multistage compressors.

A separate paper will include the effects of mixing (and the consequent shear stresses and heat transfer) in a streamline curvature calculation method for meridional flow. The results and conclusions of that paper may be anticipated to say that with mixing included the predicted radial profiles of total

temperature agree well with measurements for two high-speed compressors examined. With mixing of a realistic magnitude good predictions are obtained with very much larger losses close to the walls and much lower losses away from the walls. Both these trends for loss appear physically appropriate and realistic. It is also true that the results seem fairly insensitive to the magnitude of ϵ and an estimate for ϵ good to one significant figure appears adequate.

Acknowledgments

The authors would particularly like to thank Dr. L. H. Smith of the General Electric Company for providing results from his spanwise mixing calculations and for his most helpful comments. They would also like to thank Mr. C. Freeman and Prof. E. M. Greitzer for their advice and encouragement. The experimental work in Compressor A was carried out at the Cranfield Institute of Technology, Bedford, England and thanks are due to Dr. R. Elder for enabling this to take place. Finally thanks are due to Rolls-Royce Limited for financially supporting the project and allowing the results to be published.

References

1 Adkins, G. G., and Smith, L. H., "Spanwise Mixing in Axial Flow Turbomachines," ASME Paper No. 81-GT-57.

2 Freeman, C., and Dawson, R. E., "Core Compressor Developments for Large Civil Jet Engines," ASME Paper No. 83-Tokyo-IGTC-46.

3 Dransfield, D. C., and Calvert, W. J., "Detailed Flow Measurements in a Four Stage Axial Compressor," ASME Paper No. 76-GT-46.

4 Wagner, J. H., Dring, R. P., and Joslyn, H. D., "Inlet Boundary Layer Effects in an Axial Compressor Rotor: Part II—Throughflow Effects," ASME Paper No. 84-GT-85.

5 Dring, R. P., Joslyn, H. D., and Hardin, L. W., "Experimental Investigations of Compressor Rotor Wakes," AFAPL-TR-79-2107, Wright-Patterson Air Force Base Report, 1979.

6 Schlichting, H., and Das, A., "On the Influence of Turbulence Level on the Aerodynamic Losses of Axial Turbomachines," *Brown Boveri: Flow Research on Blading*, L. S. Dzung, ed., Elsevier, Amsterdam, 1970.

7 Kiock, R., "Turbulence Downstream of Stationary and Rotating Cascades," ASME Paper No. 73-GT-80.

8 Ravindranath, A., and Lakshminarayana, B., "Structure and Decay Characteristics of Turbulence in the Near and Far Wake of a Moderately Loaded Compressor Rotor-Blade," ASME JOURNAL OF ENGINEERING FOR POWER, Vol. 103, Jan. 1981, p. 131.

9 Ravindranath, A., and Lakshminarayana, B., "Rotor Wake Mixing Effects Downstream of a Compressor Rotor," ASME JOURNAL OF ENGINEERING FOR POWER, Vol. 104, Jan. 1982, p. 202.

10 Lakshminarayana, B., and Ravindranath, A., "Interaction of Compressor Rotor Blade Wake With Wall Boundary Layer/Vortex in the End-Wall Region," ASME Paper No. 81-Gr/GT-1.

11 Lakshminarayana, B., Pouagare, M., and Davino, R., "Three Dimensional Flow Field in the Tip Region of a Compressor Rotor Passage—Part II: Turbulence Properties," ASME Paper No. 82-GT-234.

12 Byron-Bird, R., Stewart, W. E., and Lightfoot, E. N., *Transport Phenomena*, Wiley, New York, 1960.

13 Launder, B. E., and Spalding, D. B., *Mathematical Models of Turbulence*, Academic Press, New York, 1972.

14 Eckert, E. R. G., and Drake, R. M., *Analysis of Heat and Mass Transfer*, McGraw-Hill, New York, 1972.

15 Gallimore, S. J., "Spanwise Mixing in Multi-stage Axial Compressors," Ph.D. Dissertation, Cambridge University, 1985.

16 Cumpsty, N. A., "Annulus Wall Boundary Layer Measurements in a Four Stage Compressor," ASME Paper No. 85-GT-62.

17 Denton, J. D., and Usui, S., "Use of a Tracer Gas Technique to Study Mixing in a Low Speed Turbine," ASME Paper No. 81-GT-86.

18 Hart, M., Cambridge University, private communication.

19 Schlichting, H., *Boundary Layer Theory*, 7th ed., McGraw-Hill, New York, 1979.

20 Towle, W. L., and Sherwood, T. K., "Eddy Diffusion Mass Transfer in the Central Portion of a Turbulent Air Stream," *Industrial and Engineering Chemistry*, Vol. 31, No. 4, 1939, p. 457.

21 Moore, J., and Adhye, R. Y., "Injection of Tracer Gas for Studies of Turbulent Mixing," unpublished report, Dept. of Mechanical Engineering, Virginia Polytechnic Institute and State University.

22 Hinze, J. O., *Turbulence* , McGraw-Hill, New York, 1959.

23 Smith L. H., private communication.

24 Owen, P. R., "Buffeting Excitation of Boiler Tube Vibration," *J. Mech. Eng. Sci.*, Vol. 7, No. 4, 1965, p. 431.

25 Saville, A. M., and Zhou, M. D., Appendix B of "Wake/Wake and Wake/Boundary Layer Interactions—Smoke Flow Visualisation and Modelling," *Proceedings of the 2nd Asian Congress of Fluid Mechanics*, Beijing, China, 1983, p. 743.

Spanwise Mixing in Multistage Axial Flow Compressors: Part II—Throughflow Calculations Including Mixing

S. J. Gallimore[1]
Rolls-Royce Limited,
Derby, England

The important influence of spanwise mixing on the flow through multistage axial compressors has been investigated by incorporating the effect into an axisymmetric streamline curvature throughflow program. The mixing was modeled as a turbulent diffusion process based on the experimental observations reported in Part I of this paper, which showed that this was the dominant physical mechanism. The inclusion of the mixing was found to be crucial in accurately predicting spanwise variations of exit total temperature in multistage machines. The effect of mixing on loss distributions inferred from measurements was found to be significant so that upstream loss sources could only be determined from downstream distributions when the effect of mixing was included.

Introduction

Part I of this paper [1] described an experimental investigation aimed at determining directly, by means of a tracer gas technique, the mechanism causing spanwise mixing in multistage compressors. It was found that substantial amounts of spanwise mixing were present all the way across the span and that the dominant mechanism was a random, turbulent diffusion process. The convection of flow properties by deterministic secondary flows, as proposed by Adkins and Smith [2], was found to be comparatively insignificant. The important influence of spanwise mixing on the radial distribution of flow properties such as total temperature in multistage throughflow calculations has already been demonstrated in [2], although it must be stressed again that the physical modeling of the mixing used in that work has been shown by the experiments to be inaccurate. Consequently the new and more correct model of mixing as a turbulent diffusion type process has been incorporated into a streamline curvature throughflow program so that the effects of mixing can be calculated and investigated. This required the use of the axial, radial, and tangential momentum equations and the energy equation to calculate the streamwise changes of stagnation enthalpy, entropy, and tangential momentum caused by the radial diffusion of heat and momentum. The method was then used to calculate the flow through three multistage compressors where the dominant effect of spanwise mixing on the radial variation of loss and total temperature was demonstrated.

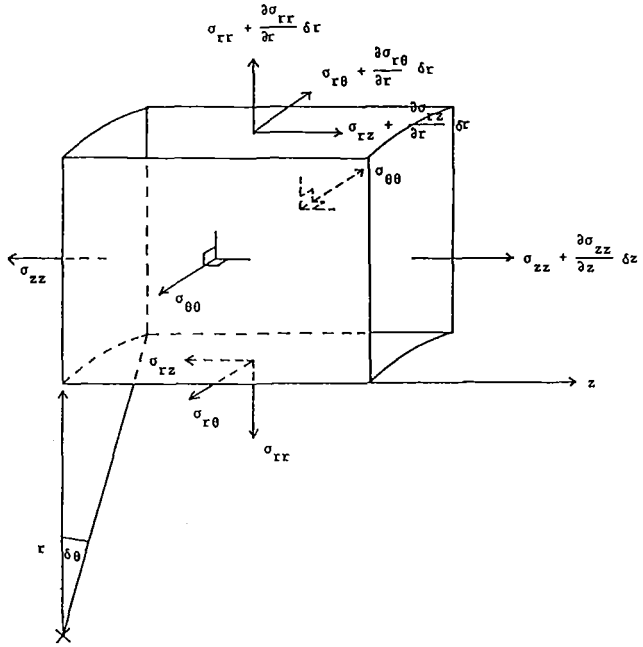

Fig. 1 Stresses on an elemental fluid volume in the *r*, *θ*, *z* coordinate system, with radial mixing

Method and Its Assumptions

The streamline curvature method described below is a modified version of the progam described by Denton [3]. This basic throughflow method assumes that the flow is steady, adiabatic, axisymmetric, and inviscid (i.e., shear stress free). The fluid is a perfect gas and compressible but no allowance is made for supersonic flow (i.e., choking and shocks are precluded). Blade rows are represented by specifying relative

[1] Formerly Whittle Laboratory, University of Cambridge, England

Contributed by the Gas Turbine Division of THE AMERICAN SOCIETY OF MECHANICAL ENGINEERS and presented at the 31st International Gas Turbine Conference and Exhibit, Düsseldorf, Federal Republic of Germany, June 8–12, 1986. Manuscript received at ASME Headquarters December 26, 1985. Paper No. 86-GT-21.

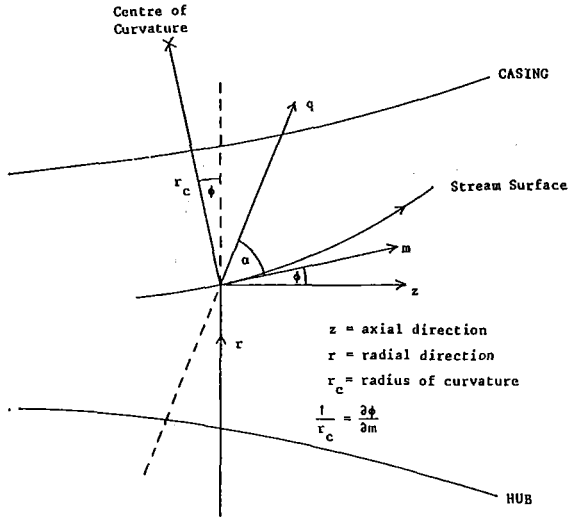

Fig. 2 Streamline curvature coordinate system

flow angles and empirical loss coefficients but the effect of blade thickness is neglected when evaluating the continuity equation for quasi-orthogonals inside a blade row.

The physical processes that are being represented by the mixing model are the radial mixing of momentum and heat by turbulent mixing. It is assumed that these processes can be represented by an eddy viscosity μ_t and an eddy thermal conductivity k_t which are related by the turbulent Prandtl number $\mathrm{Pr}_t = \mu_t C_p/k_t$. The eddy viscosity is related to the mixing coefficient ϵ used in Part I by the turbulent Schmidt number $\mathrm{Sc}_t = \mu_t/\rho\epsilon$. Throughout this paper it is assumed that

$$\mathrm{Pr}_t = \mathrm{Sc}_t = 1.0$$

which was shown to be reasonable in Part I. Laminar or molecular effects are assumed to be negligible; so too are the effects of turbulent mixing in the streamwise direction as a result of the smaller flow property gradients in this direction. The mixing model therefore modifies the adiabatic and inviscid assumptions above, for there is now heat transfer in the radial direction, and the radial transfer of momentum implies the presence of axial and tangential shear stresses. For simplicity in incorporating the model into the streamline curvature method some further restrictions have been adopted. The stream surfaces are assumed to be closely aligned to the machine axis so that radial velocities and their derivatives with position are small. In consequence the program in its present form cannot be used for radial flow machines or axial flow machines with large variations in annulus height or radius but these restrictions could be removed without serious difficulty.

Derivation of the Equations

Consider an element of fluid in the (r, θ, z) cylindrical coordinate system, Fig. 1. These are no shear stresses acting on the tangential facing surfaces because the flow is assumed to be axisymmetric. The shear forces acting on the axial faces are also neglected because it has been assumed that the streamwise gradients are small enough for the effects of turbulent mixing across these faces to be negligible. This leaves two effective shear stresses, implied by the mixing model, acting on the radially inward and outward facing surfaces of the element, σ_{rz} and $\sigma_{r\theta}$. The other stresses acting on the element are the normal stresses. The three momentum equations that govern this fluid element are set out in Appendix 1. Radial mixing implies radial heat transfer and the energy equation for the element, which takes this into account as well as the work done by the effective shear stresses, is given in Appendix 2. These four equations are now manipulated into a form suitable for use in the streamline curvature method.

Figure 2 displays the streamline curvature coordinate system, which immediately shows from the geometry that for steady mean flow $D/Dt = Vm\ \partial/\partial m$. The axial and radial momentum equations are resolved along the quasi-orthogonal and the static pressure written in terms of the stagnation enthalpy and entropy using the second law. If the quasi-orthogonals and the streamlines are nearly at right angles then the shear stresses in the streamwise direction have negligibly small components in the quasi-orthogonal direction. It will also be assumed that the component of blade force acting along the quasi-orthogonal can be neglected leaving the basic streamwise curvature equation the same as that quoted by Denton [3], equation (1) below

$$\underbrace{\frac{\partial}{\partial q}\left(\frac{V_m^2}{2}\right)}_{\mathrm{I}} = \underbrace{\frac{\partial H_0}{\partial q}}_{\mathrm{II}} - \underbrace{\frac{T\partial s}{\partial q}}_{\mathrm{II}} - \underbrace{\frac{1}{2r^2}\frac{\partial}{\partial q}(r^2 V_\theta^2)}_{\mathrm{III}} + \underbrace{\frac{V_m^2}{r_c}\sin\alpha}_{\mathrm{IV}} + \underbrace{V_m\frac{\partial V_m}{\partial m}\cos\alpha}_{\mathrm{V}} \tag{1}$$

Terms IV and V on the right-hand side are evaluated from the streamline slope and curvature and the previous overall flow calculation of V_m, as described by Denton [3]. The remaining terms require the distributions of total enthalpy, entropy, and angular momentum to be known along the quasi-orthogonal. In standard methods with inviscid adiabatic flow these are usually determined by tracing these quantities along streamlines from the quasi-orthogonal immediately upstream. In duct regions all the quantities are conserved along a streamline while in blade rows V_θ can be obtained from V_m and the specified flow directions, stagnation enthalpy can be found by using the Euler work equation, and entropy changes are calculated from specified empirical losses. In the present method, however, the momentum and energy equations are used to evaluate these changes which are affected by the radial turbulent mixing of these quantities between streamlines.

The entropy change along the streamline can be calculated from the energy equation (see Appendix 2)

$$\frac{\partial s}{\partial m} = \frac{1}{r\rho T V_m}\frac{\partial}{\partial r}\left(rk_t\frac{\partial T}{\partial r}\right) + \frac{\Phi}{\rho T V_m} + \frac{\partial s_e}{\partial m} \tag{2}$$

where the last term on the right-hand side represents entropy increases caused by any specified empirical loss coefficients. The tangential momentum equation (Appendix 1) becomes

Nomenclature

r, θ, z = cylindrical coordinate system
r, q, m = streamline curvature coordinate system (Fig. 2)
C_p = specific heat at constant pressure
E_z, E_θ = axial and tangential shear forces
F = blade force density
H_0 = stagnation enthalpy
k_t = eddy thermal conductivity
L_s = axial stage length
p = static pressure
Pr_t = turbulent Prandtl number $= \mu_t C_p/k_t$
Q = heat flux
r_c = radius of curvature (Fig. 2)
s = entropy
Sc_t = turbulent Schmidt number $= \mu_t/\rho\epsilon$
T = static temperature
V = flow velocity
ϵ = mixing coefficient (eddy diffusion)
μ_t = eddy viscosity
ρ = density
σ_{zz}, etc. = shear stresses (Fig. 1)
Φ = dissipation function

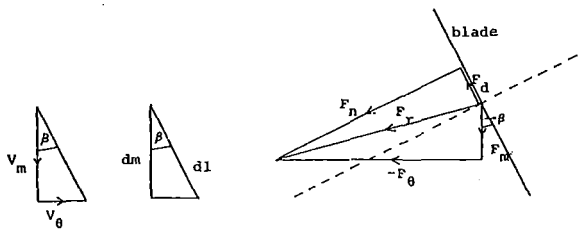

Fig. 3 Body forces acting in a stator blade row

$$V_m \frac{\partial V_\theta}{\partial m} + \frac{V_m V_\theta \sin \phi}{r} = \frac{F_\theta + E_\theta}{\rho}$$

by substituting for D/Dt and V_r where F_θ is the tangential blade force and E_θ the tangential shear force as defined in the Appendix. This can be further rearranged using $\sin \phi = \partial r/\partial m$ to give

$$\frac{1}{2r^2} \frac{\partial}{\partial m}(r^2 V_\theta^2) = \frac{V_\theta}{V_m}\left(\frac{F_\theta + E_\theta}{\rho}\right) \tag{3}$$

allowing the tangential momentum change to be calculated along the streamline. Finally the momentum equation along the streamline can be derived by considering the streamwise components of the radial and axial momentum equations (Appendix 1) which can be expressed to give the stagnation enthalpy change

$$\frac{\partial H_0}{\partial m} = \frac{T \partial s}{\partial m} + \frac{1}{2r^2} \frac{\partial}{\partial m}(r^2 V^2) + \frac{F_m}{\rho} + \frac{E_z}{\rho} \cos \phi \tag{4}$$

Evaluating the Equations

Equations (2)–(4) allow the changes in entropy, tangential momentum, and stagnation enthalpy along streamlines to be calculated. The procedure is as follows. The radial derivatives of velocity and temperature required to evaluate E_z, E_θ, Φ, and the heat transfer term can be found by using a second-order finite-difference scheme on the values calculated in the previous overall iteration. The energy equation can now be solved, with any entropy increases due to empirical loss coefficients ∂s_e included, to give the total entropy change. The change in tangential momentum is likewise calculated from equation (3). This change is the result of two tangential forces, the blade force deduced from the specified relative flow angle in blade rows, and an additional force caused by the tangential shear stress. As a consequence of the effect of shear stress the calculated flow angle will differ slightly from that specified in blade rows. An alternative way of interpreting this is to regard the specified flow angle as that which would be achieved if there were no mixing (and hence no shear stress). The stagnation enthalpy change can now be found from equation (4) provided that a value for the meridional blade force F_m is known. In the present method this can be obtained in a straightforward way because the blade rows are being simply modeled by the blade forces they impose. We consider a blade row with specified empirical loss that implies that the blade imposes two forces on the flow, a normal one F_n, and a drag or dissipative force F_d acting in the flow direction (Fig. 3). The drag force is related to the specified loss by

$$F_d = \rho T \frac{ds_e}{dl} \tag{5}$$

the relationship that Horlock [4] demonstrated was required in order for the loss model to be consistent with the assumption of inviscid and adiabatic flow. The geometry gives the following expression for the meridional blade force

$$F_m = F_\theta \tan \beta - \frac{F_d}{\cos \beta} \tag{6}$$

which can now be evaluated.

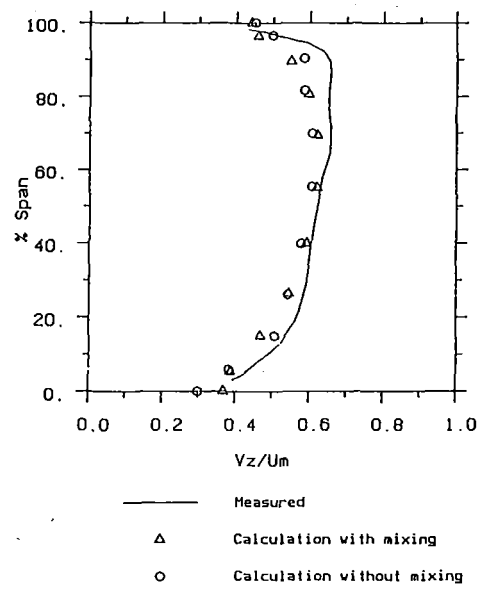

Fig. 4 Axial velocity profiles downstream of four-stage compressor Rotor 3

The equations above have been written in the absolute frame of reference but there is no need for a different formulation for rotors provided that β is there taken as the relative flow angle.

The end-wall conditions are particularly simple because there is no mixing across the solid boundaries and the shear stresses are set to zero there, which also implies that Φ is zero. This is clearly a gross simplification which has to be compensated for by a raised level of losses; future work should remove this limitation. It is also assumed that the end walls are adiabatic. A more detailed description of the derivation and evaluation of the equations is given in [12].

Four-Stage Compressor

One of the most important effects of spanwise mixing in multistage compressors is the redistribution of losses across the span, with the result that a loss distribution measured downstream of a stage does not accurately represent the variation of loss generation. This can have a marked effect on the conclusions drawn from analysis of experimental test data as the following example demonstrates.

The investigation was made on the low-speed four-stage research compressor described by Cumpsty [5] and also used in part of the experimental investigation described in Part I of this paper, where it is designated Compressor B. Firstly the streamline curvature program was used to analyze the compressor performance with the mixing set at zero (i.e., a standard analysis). The rotor and stator relative flow angles measured during the experimental investigation of Cumpsty [5] were used as inputs to the program. The procedure was to run the program including empirical losses so that the measured overall pressure rise was achieved at the nominal design flow coefficient of 0.55 and the calculated velocity profiles downstream of each of the four rotors were in good agreement with the measured values. To achieve this the spanwise distributions of rotor and stator loss coefficients were adjusted. The specified rotor loss distributions were assumed to be identical for all four rotors; the stator loss distributions were also assumed to be the same for each row and equal to the radially inverted rotor distribution (the blades being of 50 percent reaction with cantilevered stators).

The analysis was then repeated but with a conservative value of the measured level of mixing found in the experimental investigation using the tracer gas technique, giving a Reynolds number based on axial velocity, axial stage length and ϵ of

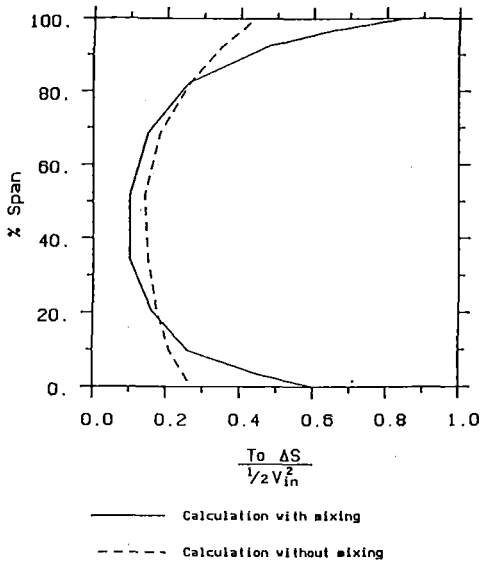

Fig. 5 Variation of rotor loss coefficient with span for four-stage compressor

340. The mixing level was assumed to be uniform throughout the machine with both the turbulent Prandtl and Schmidt numbers set at unity. Again the spanwise variation in loss coefficient was adjusted to give a satisfactory prediction of axial velocity. Figure 4 shows the agreement obtained between the measured axial velocity profile downstream of Rotor 3 and the two calculated profiles. Some of the discrepancy between the measurements and the calculated values can be ascribed to the flow coefficient being slightly greater than 0.55 during the tests. However, the agreement between the two calculated results is good and sufficiently close to the measurements to indicate that a satisfactory solution was achieved in each case. Similar results were obtained downstream of the other rotors.

Running the calculation with and without mixing required very different loss distributions to be specified to achieve the agreement with experimental data and the rotor loss coefficient profiles required in each case are shown in Fig. 5. The generally high levels of loss coefficient required are due to the low measured adiabatic efficiency of the machine (71 percent). As expected the loss distribution used in the calculation without mixing is much flatter than the profile required when mixing is included; in the latter case the loss at the end walls is about twice what one would deduce from a standard, nonmixing analysis. The loss at midheight required for the mixing calculation is about 60 percent of that used in the nonmixing calculation.

This result has important implications for the design of multistage compressors. Faced with the loss distribution for the no-mixing case in Fig. 5 the designer might conclude that the losses are fairly uniformly distributed across the span and that the main attack on them should be via the profile loss. With the loss distribution obtained for the case with mixing an entirely different conclusion is reached. If the end-wall regions are arbitrarily defined as being the 20 percent of span adjacent to the hub and the same amount at the outer casing about 70 percent of the losses are there and only about 20 percent is attributable to the blade profile loss. It is immediately clear that the effort should be aimed at reducing the very high losses near the end walls, particularly in the tip region where the peak is some eight times greater than that found at midheight.

This illustrates the importance of the end-wall regions in dominating the loss generation in multistage compressors. Although reasonably flat loss distributions can be deduced from measurements in multistage machines (or even in some cases lower losses at the end walls than at midspan, as discussed in Part I and in [2, 6]) these results are highly misleading and divert attention away from the important regions of loss creation, the end-wall regions. This was recognized as far back as 1939 by Constant [7] who stated that as long as total head loss coefficients measured in cascades were reasonably low (not above 0.04) their magnitude was only of secondary importance because in a compressor the bulk of the loss is due to "end-effects, tip losses, boundary layer thickening on the casing and rotor surfaces, and to the effects of one row of blades on the next." Much the same conclusion was drawn in 1977 by Wisler et al. [8] who identified the end-wall regions as the area in which there was the greatest potential for efficiency improvements. The results of the calculations just presented emphasize this point yet again.

Two Three-Stage Compressors

The experimental investigation reported in Part I was conducted on two low-speed compressors. In the following section it is assumed that the results from this low-speed research are applicable to higher-speed machines. This is thought to be reasonable because the physical mechanisms causing turbulent diffusion and convective radial flows (and hence their relative contributions to spanwise mixing) are not compressible by nature, with compressibility having only a second-order effect. The same is true of the loss mechanisms near the end walls. Therefore provided that shock waves are absent, which is true for all except for perhaps the front few rotors of a high-speed machine, low-speed compressors are believed to model adequately the behavior of high-speed multistage machines. It is also believed that the mixing mechanism is substantially the same in both cases.

In the previous section it was illustrated how spanwise mixing (which causes effective axial and tangential shear stresses and radial heat transfer) affects the radial distribution of losses in multistage compressors. Realistic blade row loss distributions were shown to be considerably steeper than those deduced from experimental measurements, with much higher values at the end walls than at midspan. However, if these steep loss distributions are used to calculate the throughflow in a multistage machine with a standard streamline curvature method (i.e., one that does not include the effects of spanwise mixing) the predicted temperature profiles in the latter stages are found to give temperature differences between the flow near the end walls and the midspan that are too large. Two examples are now presented that demonstrate how including mixing in the throughflow calculation can overcome this problem.

References [9] and [10] document the design and testing of two three-stage Pratt and Whitney research compressors differing primarily only in aspect ratio. The hub-to-tip ratio was 0.915 and both designs were of 52 percent reaction with rotor relative inlet Mach numbers of around 0.4. The machine designated 3S1 had an average aspect ratio of 0.81 while compressor 3S2 had an aspect ratio of 1.22. Included in the reports is the detailed output from the design throughflow analysis for both compressors, in particular the blade loss coefficient distributions and relative exit air angles assumed in the design are provided. The loss distributions used in the design were obtained from a cascade correlation system which had been previously adjusted to give good agreement with data from three multistage machines with similar loading, work, and flow coefficients. It was shown in the reports that these adjusted losses tended to give slightly flatter total temperature profiles than those measured in the three machines. An example of the loss coefficients derived for the design of 3S1 and 3S2 compressors is given in Fig. 6, the losses for all the blade rows being essentially the same. It can be seen that adjusting the loss correlation system to agree with multistage data has resulted in reasonably flat profiles, with the loss at the end walls being about twice that at midheight. This compares with

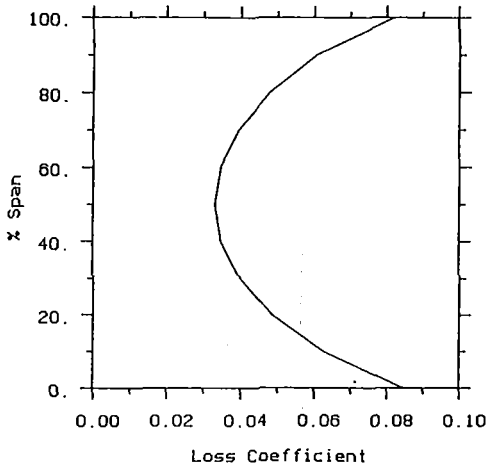

Fig. 6 Specified Rotor 2 loss coefficient from lower aspect ratio compressor 3S1

the loss distribution used in the mixing calculation for the four-stage compressor just described where the losses at the end walls were at least six times the midspan loss. It might be expected that using flattish loss distributions in the design calculation without mixing would produce reasonable agreement with experimental results, without excessive temperature rises near the walls, but this is not the case.

The design loss coefficients and flow angles were used in the present method together with the measured inlet flow profiles. The program was run for each of the two compressors both without mixing and assuming uniform mixing. The mixing levels were calculated from equation (9) of Part I [1] using the measured overall machine performance and with turbulent Schmidt and Prandtl numbers of unity. The Reynolds numbers based on mixing level, velocity, and stage length were 272 for compressor 3S1 and 228 for 3S2.

The calculated exit total temperature profiles are compared to the test data in Figs. 7 and 8. The calculated temperature rises are some 10 percent greater than those measured and it is thought that the main reason for this discrepancy is that the effect of blockage was not taken into account in the present calculations. However, these differences in absolute levels are unimportant in this demonstration of the effect of radial mixing on the spanwise distribution of flow properties, where it is the shape of the distributions that is of interest. Consequently the results have been plotted as variations from the mean value of each distribution. The total temperature profiles calculated for the two compressors show the much improved agreement between the calculation and experiment when mixing is included; the overestimation of the total temperature rise at the end walls has been much reduced to realistic levels. At this point it should be remembered that the specified loss coefficient profiles were comparatively flat, having been adjusted by the designers to give reasonable agreement with multistage data. Despite this, however, the calculations without mixing have still overestimated the wall temperatures by a significant amount everywhere except near the hub of the 3S2 compressor.

The present results bear a remarkable similarity to those presented by Adkins and Smith [2] for their calculation method applied to the same compressors. Nevertheless it remains the assertion of this work that the physical model of the method of Adkins and Smith is invalid for the reasons explained in Part I.

Discussion

The results of the calculations presented here have demonstrated the important effect of spanwise mixing on the

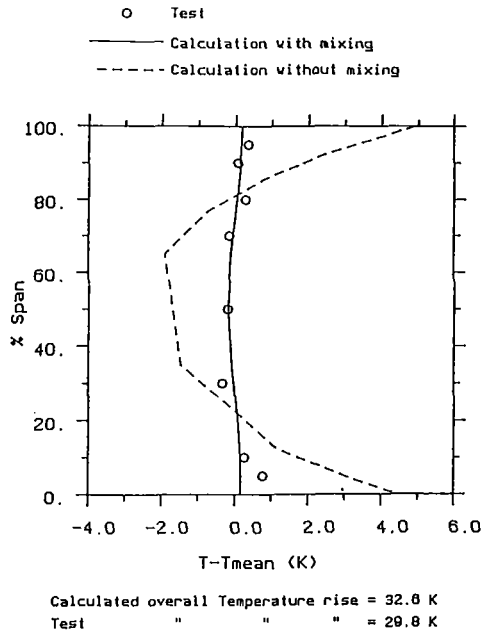

Fig. 7 Exit total temperature profiles from lower aspect ratio compressor 3S1

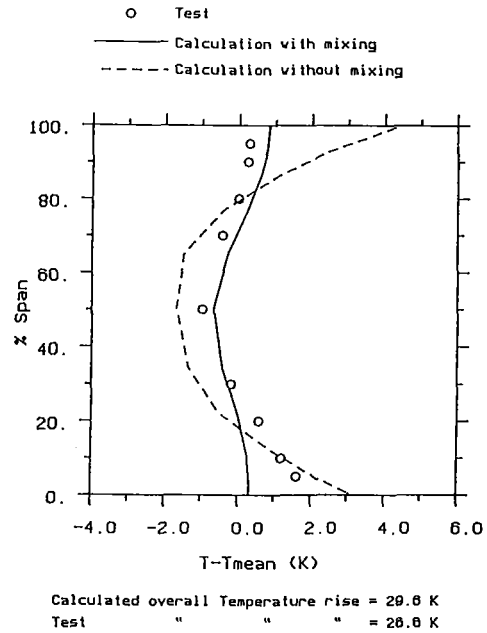

Fig. 8 Exit total temperature profiles from higher aspect ratio compressor 3S2

radial distributions of loss and total temperature in multistage axial compressors.

The spanwise redistribution of loss by mixing was shown to reduce the apparent end-wall loss for a blade row to only about half the actual loss near the end walls, while at the same time increasing the apparent profile loss by some 50 percent from the more realistic value. This may well have diverted attention away from the high loss generating regions of the flow field near the end walls. The mixing is an irreversible process which means that the actual loss distribution that produced the measured profile cannot be determined where mixing is significant (such as deep in a multistage compressor) even if the mixing level is known. However, more realistic loss distributions can be postulated (Fig. 5) which emphasize the large proportion of the overall loss that is produced at the end walls.

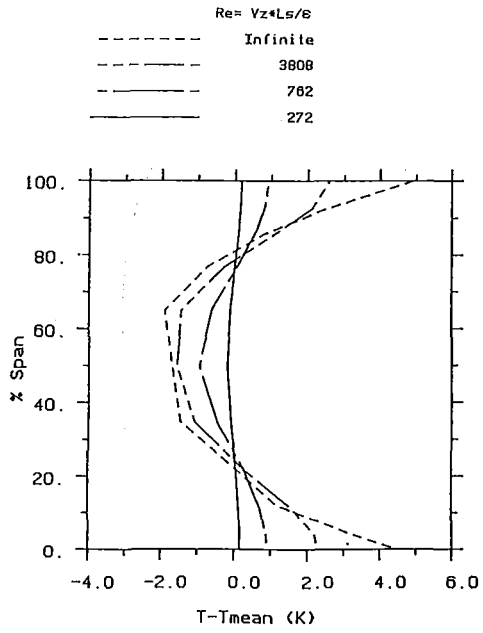

Fig. 9 Effect of mixing level on calculated exit total temperature profiles for lower aspect ratio compressor 3S1

The results from the two three-stage compressors demonstrated that spanwise mixing effects must be included in throughflow calculations for multistage machines if realistic total temperature distributions are to be predicted. Neglecting mixing leads to excessive end-wall temperatures even if an artificially uniform loss distribution is assumed. An interesting fact that emerged from the calculations was that the absolute level of mixing used in the calculations was not critical. Figure 9 shows the calculated exit total temperature profiles from the 3S1 compressor obtained with mixing levels varying from zero to the value believed to be physically correct, obtained from equation (9) of Part I, and used for the results in Fig. 7. It is clear that a Reynolds number $V_z L_s/\epsilon$ of 3808 (which represents only 7 percent of the largest mixing level) has reduced the end-wall temperature significantly while a Reynolds number of 762 (representing 36 percent of the greatest mixing) has produced a temperature profile that has been flattened sufficiently to be considered reasonably close to the experimental result. This helps explain why the present method and that of Adkins and Smith [2] produce such similar results despite the radical difference of the models used to represent the mixing process: Including a reasonable amount of mixing will improve the calculation considerably. Adkins and Smith also vary the level of mixing radially, which seems inappropriate, but the insensitivity to the mixing level shows why this does not matter. Again it should be stated that the experimental evidence presented in Part I indicates that the simple model of spanwise mixing as a random, turbulent type of diffusion process is more correct physically than the complex mechanism of radial convection by deterministic secondary flows used by Adkins and Smith.

Including mixing in throughflow calculations may lead to improved predictions of the spanwise variation in flow angle and hence incidence; the incidence depends both upon the specified loss profiles and the amount of mixing. By specifying more realistic, steeper loss distributions, as is now possible when mixing is included in the calculations, better estimates of incidence variations across the span should be produced. The losses themselves depend on the incidence and a major cause of the high losses near the walls is the high local incidence. It is hoped that eventually the losses can be predicted from the incidence. The interaction between the losses, mixing, and the resulting incidences is currently being investigated.

One of the most surprising effects that has been observed in multistage machines is the existence of the repeating stage condition where velocity profiles entering and leaving a stage are very similar [11]. This condition is highly beneficial, because velocity and flow angle variations deep in multistage machines do not continue to deteriorate, but as yet there is no reasonable explanation of how it is set up and maintained by the flow. Having found that radial mixing has a large influence on the radial distribution of flow properties in a compressor it is reasonable to suggest that spanwise mixing plays an important part in this process. The large amounts of loss generated on the end walls are spread out across the annulus so that the radial gradient of loss is reduced, hence reducing the velocity profile gradient. This is analogous to the production of fully developed pipe flow where the end-wall loss generation is balanced by the continuous spread of loss toward the center of the pipe. Spanwise mixing therefore plays an important part in allowing the rear stages of multistage compressors to perform adequately. Of course the mixing process is irreversible and so creates a certain amount of loss itself. An estimate of this effect can be obtained from the calculations performed in the two three-stage compressors just presented. The overall efficiency of the lower aspect ratio compressor, 3S1, was derived using identical loss inputs both when mixing was neglected and when mixing was included in the calculation. The efficiency was based on the mass-averaged quantities at inlet and exit from the compressor. Including mixing in the calculation caused an adiabatic efficiency drop of 0.4 percent from the value of 91.2 percent calculated when no mixing was present. This is not a great penalty when it is considered how much mixing helps the performance of the latter stages of multistage machines: By reducing the fall in axial velocity near the walls and thereby reducing local incidence onto the blades some check is produced on the deterioration in blade performance near the walls.

Conclusions

Spanwise mixing redistributes losses across the span, in particular reducing the apparent losses near the end walls by spreading it toward midheight. Incorporating the effects of spanwise mixing in a streamline curvature throughflow method by modeling the mixing as a turbulent diffusion process has allowed the effect of this phenomenon on the flow through multistage compressors to be investigated. This allows more realistic spanwise variations of loss coefficient to be specified for blade rows, with the loss concentrated much nearer the end walls than is usually possible with standard throughflow calculations without mixing. This concentrates attention on the end-wall regions where the bulk of the losses in axial compressors are generated. It also reconciles the low losses measured in cascades, which would suggest stage efficiencies in the high 90's, with the much lower stage efficiencies which are measured in machines.

Calculations of the flow through two three-stage compressors showed that it was necessary to include the effects of spanwise mixing in order to predict the correct radial variation of total temperature at compressor exit. The agreement between the experimental data and the predictions for these two cases was found to be similar to that obtained by Adkins and Smith [2] using their radial convection model of mixing, rather than the model of turbulent diffusion based on the experimental evidence of Part I.

All the calculations showed the significant effects spanwise mixing has on the flow in multistage machines and hence the need to include mixing in the design process at an early stage. As mentioned in Part I the division of the flow into a free stream bounded by two annulus wall boundary layers is not valid where spanwise mixing is present. It is also thought that spanwise mixing plays an important part in setting up and

maintaining the repeating stage condition and therefore has a beneficial effect on the performance of stages deep in multistage machines.

Acknowledgments

The author would like to thank Dr. N. A. Cumpsty for supervising this work and Dr. T. P. Hynes and Dr. J. B. Young of the Whittle Laboratory for their helpful suggestions. Thanks are also due to Mr. C. Freeman of Rolls-Royce Limited and Professor E. M. Greitzer of the Massachusetts Institute of Technology for their contributions. Finally, the author would like to thank Rolls-Royce Limited for financially supporting this work and allowing the results to be published.

References

1 Gallimore, S. J., and Cumpsty, N. A., "Spanwise Mixing in Multistage Axial Flow Compressors: Part I—Experimental Investigation," ASME JOURNAL OF TURBOMACHINERY, this issue.

2 Adkins, G. G., and Smith, L. H., "Spanwise Mixing in Axial Flow Turbomachines," ASME Paper No. 67-FE-16.

3 Denton, J. D., "Throughflow Calculations for Transonic Axial Flow Turbines," ASME JOURNAL OF ENGINEERING FOR POWER, Vol. 100, Apr. 1978, p. 212.

4 Horlock, J. H., "On Entropy Production in Adiabatic Flow in Turbomachines," ASME Paper No. 85-GT-62.

5 Cumpsty, N. A., "Annulus Wall Boundary Layer Measurements in a Four Stage Compressor," ASME JOURNAL OF ENGINEERING FOR GAS TURBINES AND POWER, Vol. 108, No. 1, Jan. 1986, pp. 2-6.

6 Freeman, C., and Dawson, R. E., "Core Compressor Developments for Large Civil Jet Engines," ASME Paper No. 83-Tokyo-IGTC-46.

7 Constant, H., "Performance of Cascades of Aerofoils," Note E3696, Royal Aircraft Establishment, June 1939.

8 Wisler, D. C., Koch, C. C., and Smith, L. H., "Preliminary Design Study of Advanced Multi-Stage Axial Flow Core Compressors," NASA CR 135133, Feb. 1977.

9 Burdsall, E. A., Canal, E., Jr., and Lyons, K. A., "Core Compressor Exit Stage Study—Part I: Aerodynamic and Mechanical Design," NASA CR 159714, Sept. 1979.

10 Behlke, R. F., Burdsall, E. C., Canal, E., Jr., and Korn, N. D., "Core Compressor Exit Stage Study—Part II: Final Report," NASA CR 159812, Oct. 1979.

11 Smith, L. H., "Casing Boundary Layers in Multi-Stage Axial Flow Compressors," *Brown Boveri: Flow Research on Blading*, L. S. Dzung, ed., Elsevier, Amsterdam, 1970.

12 Gallimore, S. J., Ph.D. Dissertation, University of Cambridge, 1985.

APPENDIX 1

Momentum Equations

The two effective shear stresses, implied by the mixing model, acting on the radially inward and outward-facing surfaces of the fluid element (Fig. 1) can be related to the velocity gradients by

$$\sigma_{r\theta} = \mu_t \left[\frac{\partial V_\theta}{\partial r} - \frac{V_\theta}{r} \right] \tag{A1.1}$$

$$\sigma_{rz} = \mu_t \left[\frac{\partial V_z}{\partial r} \right] \tag{A1.2}$$

This assumes that the flow is axisymmetric, that changes in V_r with position are small and that changes in the axial direction are comparatively small. Using the same assumptions it may be shown that the normal stresses are related only to the static pressure

$$\sigma_{rr} = \sigma_{\theta\theta} = \sigma_{zz} = -p \tag{A1.3}$$

Denoting the substantive derivative as D/Dt, using equations (A1.1)-(A1.3), and representing body force densities as F the three momentum equations can be written for a compressible fluid with variable μ_t as

r direction
$$\rho \left(\frac{DV_r}{Dt} - \frac{V_\theta^2}{r} \right) = F_r - \frac{\partial p}{\partial r} \tag{A1.4}$$

θ direction
$$\rho \left(\frac{DV_\theta}{Dt} - \frac{V_r V_\theta}{r} \right) = F_\theta + E_\theta \tag{A1.5}$$

z direction
$$\left(\frac{DV_z}{Dt} \right) = F_z - \frac{\partial p}{\partial z} + E_z \tag{A1.6}$$

where

$$E_\theta = \frac{\partial}{\partial r} \left(\mu_t \left[\frac{\partial V_\theta}{\partial r} - \frac{V_\theta}{r} \right] \right) + \frac{2\mu_t}{r} \left[\frac{\partial V_\theta}{\partial r} - \frac{V_\theta}{r} \right] \tag{A1.7}$$

$$E_z = \frac{1}{r} \frac{\partial}{\partial r} \left[\mu_t r \frac{\partial V_z}{\partial r} \right] \tag{A1.8}$$

APPENDIX 2

Energy Equation

The energy equation can be written in terms of the specific entropy thus

$$\rho T \frac{Ds}{Dt} = \frac{DQ}{Dt} + \Phi \tag{A2.1}$$

The heat added per unit volume can only come from radial transfer, according to the present mixing model, and is related to the radial temperature gradient by

$$\frac{DQ}{Dt} = \frac{1}{r} \frac{\partial}{\partial r} \left(r k_t \frac{\partial T}{\partial r} \right) \tag{A2.2}$$

The dissipation function Φ is related to the velocity gradients by

$$\Phi = \mu_t \left[\left(\frac{\partial V_z}{\partial r} \right)^2 + \left(\frac{\partial V_\theta}{\partial r} - \frac{V_\theta}{r} \right)^2 \right] \tag{A2.3}$$

within the assumptions of the mixing model.

Through-Flow Analysis of a Multistage Compressor: Part I—Aerodynamic Input

R. P. Dring
Manager.

H. D. Joslyn
Research Engineer.

Gas Turbine Technology,
United Technologies Research Center,
East Hartford, CT 06108

Through-flow theory is at the heart of turbomachinery aerodynamic design in that it provides the incidence and Mach number distributions that are ultimately used to define the rotor and stator airfoil contours. The assumption of axisymmetry plays a major role in the formulation of the theory and the consequences of this assumption have historically necessitated the introduction of "blockage" to account for the nonaxisymmetries in the flow. The present paper provides an assessment of these assumptions and of through-flow theory in general by making detailed comparisons between computed and measured results for a two-stage axial compressor. Part I focuses on the experimental benchmark data base and on how these data were used to fully define all of the aerodynamic input required by a through-flow analysis.

Introduction

The aerodynamic analysis of the compression system is one of the most challenging aspects of every new or up-rated gas turbine design. The basic aerodynamic mechanisms playing important roles in the compressor include: compressibility, unsteadiness, three dimensionality, and viscous effects such as boundary layer transition and separation. Although highly sophisticated full Navier–Stokes solution algorithms are beginning to appear which have the potential to attack these flows in full generality, the basis of many contemporary design systems is a series of analyses which treat the flow as a sequence of two-dimensional calculations [1–4]. Because of their speed and efficiency these two-dimensional calculations will continue to play a significant role in multistage compressor aerodynamic design. For this reason there is a great incentive to conduct an assessment of these analyses which will guide the compressor analyst as to the interpretation of the results of these calculations and as to how these calculations can be employed most reliably in the design of new configurations and in the analysis of compressor rig data. The objective of the present paper is to provide such an assessment of through-flow theory.

The assessment was conducted using a unique benchmark data base to provide all of the aerodynamic input data required by the calculation. The benchmark data base consists of detailed measurements in the rotating and stationary frames of reference on the second-stage rotor and stator of a large-scale two-stage axial compressor with a hub/tip ratio of 0.8 and airfoil aspect ratios of 1.5 (see [5–7]). These references contain detailed descriptions of the type of multielement pneumatic probes used and of the measurement uncertainty. Sufficient detailed data are available to provide all of the required aerodynamic input for the calculation. In addition, sufficient data are also available to provide an in-depth and detailed assessment of the computed results.

The three dimensionality of the flow in axial turbomachinery arises not only from the geometry but also from the viscous and inviscid flow mechanisms present in the rotating and stationary frames of reference. An example of the complex nature of the flow in a multistage compressor is shown in Figs. 1 and 2 (from [5, 6]). These data were taken downstream of the second-stage rotor and stator at the nominal design flow coefficient ($\Phi = 0.51$). The total pressure contours clearly show the strong three-dimensional effects of tip leakage and hub corner stall. The need for comparisons of the compressor aerodynamic analytical design calculations with this type of benchmark experimental data, especially for multistage configurations, has been recognized for some time [8, 9].

The through-flow analysis of Habashi and Youngson [2, 3] has been selected for the assessment. This is a practical finite element procedure which is well documented in the literature. It is a fast calculation with great geometric flexibility. It has been demonstrated [2] to be in excellent agreement with the more historical streamline curvature method. All of the aerodynamic inputs required by the calculation are available in the data base. This includes a fullspan row-by-row description of the loss, deviation and blockage [7]. The computed results are also directly comparable with the data base. These comparisons include fullspan distributions of axial velocity, static pressure, flow angle, and absolute and relative total pressure [7].

The benchmark data base is unique in that it contains spanwise distributions of blockage calculated directly from the flow field and not deduced indirectly. Of the two types of blockage referred to in the literature [8, 9], endwall blockage and two-dimensional blockage, only the latter is relevant in the present study due to the fact that the fullspan measured data explicitly account for endwall blockage, and due to the

Contributed by the Gas Turbine Division of THE AMERICAN SOCIETY OF MECHANICAL ENGINEERS and presented at the 31st International Gas Turbine Conference and Exhibit, Düsseldorf, Federal Republic of Germany, June 8–12, 1986. Manuscript received at ASME Headquarters December 26, 1985. Paper No. 86-GT-13.

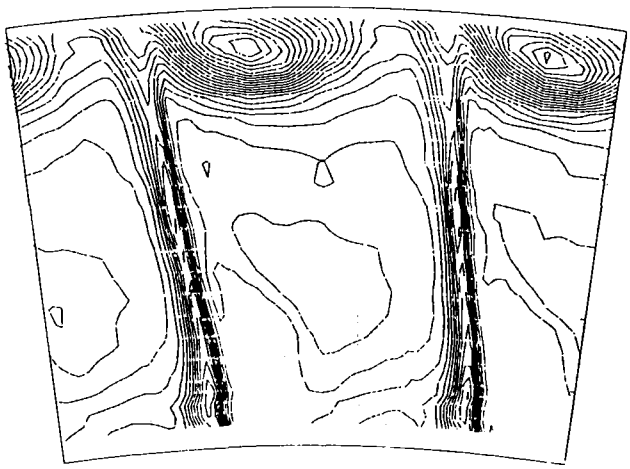

Fig. 1 Second-stage rotor exit rotary total pressure contours; ΔC_{PT} = 0.025, (cl/B) = 0.041, Φ = 0.51

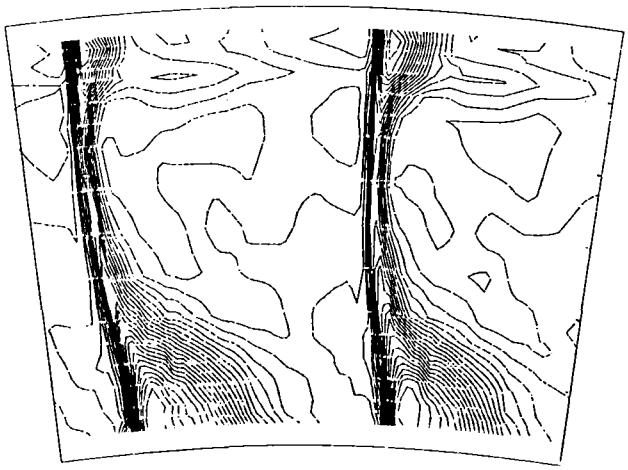

Fig. 2 Second-stage stator exit total pressure contours; ΔC_{PT} = 0.025, (cl/B) = 0.041, Φ = 0.51

fact that these measured distributions will be used directly in the calculation. Two-dimensional blockage is due to the fact that the analysis is axisymmetric and the flow is not (see, for example, Figs. 1 and 2). This departure from axisymmetry is the basis of the calculated blockage distributions [10].

A fundamental question to be answered relates to the importance of an accurate description of blockage. The impact of the details of the blockage distribution needs to be established. It will be determined what errors are incurred in the computed velocity triangles when only the magnitude is known, i.e., the span average, as is the case when blockage is inferred from mass flow and flow path static pressures. It will be determined how well the flow path static pressures are predicted when the measured distributions of blockage are used in the calculation. It will also be determined how the blockage distribution impacts the incident flow angle on a downstream blade row. Finally, the extent to which the blockage due to an upstream blade row needs to be allowed to decay toward zero in a downstream blade row will be established.

Discussion

Theory. The "through-flow" analysis in compressor design is a two-dimensional axisymmetric calculation describing the spanwise variation of the flow at various streamwise locations both within and between the airfoil rows from the inlet of the compressor to its discharge. The actual flow is only axisymmetric in some circumferentially averaged sense and for thermodynamic reasons this average is generally considered to be a mass average (as opposed to an area or density average). Formal derivations of the radial equilibrium equation in terms of circumferentially area-averaged quantities are presented in [11–16]. These derivations result in terms containing circumferentially area and/or density-averaged quantities, e.g., $\bar{C}$, $\bar{T}$, $\bar{I}$, $\bar{s}$, as well as terms involving averages of products of circumferentially varying quantities, e.g., $\overline{C_r'^2}$, $\overline{C_r' C_x'}$, $\overline{C_\theta'^2}$. It has been demonstrated [11–17] that although these "fluctuation" terms are generally small they can be significant in the endwall regions. At present, however, few (if any) practical design calculations actually include these fluctuation terms. Instead, they treat the flow as if it were truly axisymmetric and account for nonaxisymmetric effects through the expedient of a "blockage factor." It is this approximate formulation of the through-flow (or radial equilibrium) equation which will be evaluated in the present assessment. The additional approximation will be made that the radial components of airfoil pressure and frictional forces are negligible. The governing equation can then be written as follows [2, 13–15]

$$C_x\left[\frac{\partial C_r}{\partial x}-\frac{\partial C_x}{\partial r}\right]-\frac{W_\theta}{r}\frac{\partial (rC_\theta)}{\partial r}=T\frac{\partial s}{\partial r}-\frac{\partial I}{\partial r} \qquad (1)$$

Nomenclature

B = airfoil true chord
B_x = airfoil axial chord
C = absolute flow speed
C' = circumferential variation in C
C_P = pressure coefficient $= (P-P_{\mathrm{TOA}})/Q_{Um}$
C_x = axial component of velocity
cl = rotor tip clearance
I = rothalpy
$\bar{K}$ = blockage factor
$\dot{m}$ = mass flow
P = pressure
Q_{Um} = dynamic pressure based on midspan wheel speed $= \frac{1}{2}\rho U_m^2$
Q = incident dynamic pressure
r = radial distance
s = entropy
T = temperature
U_m = wheel speed at midspan
W = relative flow speed
x = axial distance
α = absolute yaw angle (from axial)
β = relative yaw angle (from axial)
θ = circumferential coordinate
Θ = flow yaw angle (from axial)
ρ = fluid density
τ = cascade pitch
ϕ = flow pitch angle (from axial)
Φ = flow coefficient $= (C_x/U_m)$
ψ = stream function

Subscripts

m = midspan
S = static
T = total
0 = compressor inlet station
1, . . . , 5 = compressor axial stations
A = absolute frame of reference
R = rotating frame of reference
x = axial
r = radial
θ = tangential

Superscripts

$-a$, (A) = pitchwise area average
$-m$, (M) = pitchwise mass average

By defining a stream function

$$C_x = \frac{\dot{m}}{2\pi\rho r\bar{K}} \frac{\partial\psi}{\partial r} \tag{2}$$

$$C_r = \frac{-\dot{m}}{2\pi\rho r\bar{K}} \frac{\partial\psi}{\partial x} \tag{3}$$

equation (1) can be written as

$$\frac{\partial}{\partial r}\left(\frac{1}{\rho r\bar{K}} \frac{\partial\psi}{\partial r}\right) + \frac{\partial}{\partial x}\left(\frac{1}{\rho r\bar{K}} \frac{\partial\psi}{\partial x}\right) = \frac{-1}{C_x}\left[\frac{W_\theta}{r} \frac{\partial(rC_\theta)}{\partial r} + T\frac{\partial s}{\partial r} - \frac{\partial I}{\partial r}\right]\frac{2\pi}{\dot{m}} \tag{4}$$

The boundary conditions are

on the hub, $\psi = 0$

on the shroud, $\psi = 1$

at the inlet, $\frac{\partial\psi}{\partial n} = 0$

at the exit, $\frac{\partial\psi}{\partial n} = 0$

where n is the outward normal.

It is important to realize that this formulation is exact only when the flow is axisymmetric and the blockage factor $\bar{K}$ is unity. When this is the case area and mass averages will be equal. In actual compressors, however, the flow is not axisymmetric, especially near the endwall regions (e.g., Figs. 1 and 2). The objective of the present assessment is to determine how well this approximate formulation can predict the flow in an actual compressor where three dimensionality of the flow is a major consideration. It will be demonstrated that the accuracy of the predictions is strongly dependent on the specification of the aerodynamic blockage distribution.

A similar assessment of through-flow theory has been presented [17] where detailed data taken on a single-stage rotor were used as a basis of comparison. This study indicated that while overall agreement between measured and computed results was excellent, there were local discrepancies present in the immediate vicinity of regions of high blockage.

Benchmark Data Sets. The benchmark data sets being used in the present assessment [7] were acquired in a large-scale low-speed two-stage compressor. The test matrix included two values of second rotor tip clearance and three values of flow coefficient. The present assessment will be limited to the case with the compressor operating at its nominal design flow coefficient, $\Phi = 0.51$. The two stages were identical except that the first rotor was staggered closed 3 deg so that the second stage would be the more heavily loaded of the two. At the low speeds at which the compressor was operated compressibility effects were small. The Mach number of midspan wheel speed was typically 0.14. In spite of this, however, the small changes in air density were accounted for both in the data reduction as well as in the through-flow analysis.

Aerodynamic Input

Loss. The spanwise distribution of total pressure loss across each airfoil row was determined by taking the difference between the mass-averaged absolute (or relative) total pressures at the stator (or rotor) inlet and exit. This difference was taken at a fixed radius and it was used in the analysis in a consistent manner, i.e., as the difference at a fixed radius. Loss was not taken along stream lines since their locations are not known a priori. As shown in [5] and elsewhere, loss may appear to be locally negative (i.e., an apparent total pressure rise) due to radial transport of the flow in and between wakes. Loss may also appear to be negative due to radial displacement of stream surfaces. This latter case can only occur, however, where there are radial gradients in total pressure. Although the loss was based on measurements at traverse planes (Stations 3, 4, and 5, Fig. 3) some distance upstream of the airfoil leading edge and some distance downstream of the trailing edge, in the present assessment the loss was assumed to increase linearly from zero at the airfoil leading edge to the measured value at its trailing edge.

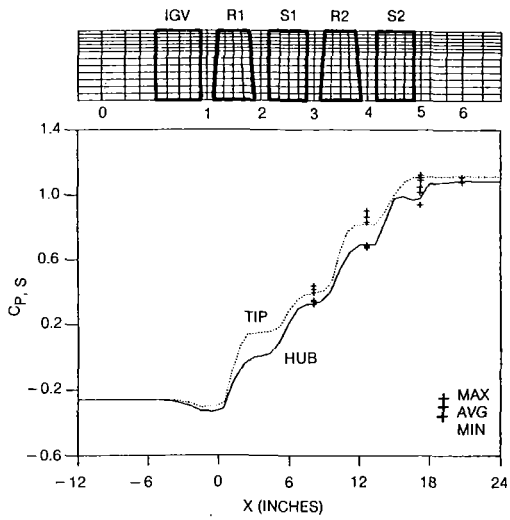

Fig. 3 Two-stage compressor hub and tip static pressure; (*c*/*B*) = 0.041, Φ = 0.51

Exit Flow Angle. The spanwise distributions of airfoil exit flow angle were taken from the mass-averaged yaw angles. These flow angles were measured some distance downstream of the trailing edges (Stations 3, 4, and 5, Fig. 3), yet they were input to the analysis at the trailing edge plane. For this reason small adjustments were made to the input exit flow angle distributions in order to obtain more precise agreement between the measured and computed results at the downstream measurement planes. The maximum adjustment was 0.4 deg at the second stator trailing edge plane at the hub. Turning within each airfoil row was distributed linearly from the leading edge to the trailing edge. The option existed to employ either the leading edge flow angle or the leading edge metal angle as the initial value for the linear distribution of turning; however, for this low-speed comparison the choice had no major effect on the computed results except within the airfoil row. For this reason the leading edge flow angle will be used in this assessment.

Blockage. The spanwise distributions of blockage were taken directly from the measured values. Recall that blockage in the present context is what has been referred to as "tangential" blockage and not "endwall" blockage [9]. The blockage distributions are intended to account for the departure of the actual flow field from axisymmetry as assumed in the through-flow analysis. The blockage relates the results computed in the through-flow analysis (usually presumed to represent circumferentially mass-averaged quantities) to the mass flow (which is related to the area-averaged axial velocity). At each streamwise station and at each radius the circumferentially area-averaged axial velocity ($\bar{C}_x{}^a$) may be related to the axial velocity computed by the through-flow analysis from mass-averaged quantities ($\bar{C}_x{}^{PT}$) by the blockage factor $\bar{K}$ as follows (for incompressible flow) [10]

$$\bar{K} = (\bar{C}_x{}^a/\bar{C}_x{}^{PT}) = f(r) \tag{6}$$

where (for flow in the absolute frame)

$$\bar{C}_x{}^{PT} = \sqrt{2(\bar{P}_T{}^m - \bar{P}_S{}^m)/\rho}\cos\bar{\theta}^m \cos\bar{\phi}^m \tag{7}$$

or, based purely on velocity

$$\bar{C}_x{}^{PT} = \sqrt{\overline{C^{2}}^{m}} \cos \bar{\theta}^{m} \cos \bar{\phi}^{m} \quad (8)$$

In the present study data were not available to describe the streamwise decay of blockage. Hence its decay with downstream distance was based on single-stage rotor data [7, 17] which were acquired at several locations downstream of the rotor trailing edge. Further discussion of blockage is available in [7, 10, 17].

Additional Aerodynamic Input Considerations. A number of rather subjective judgments were required in order to fully define the aerodynamic input to the through-flow analysis, some of which have already been mentioned. For example both the blockage and loss input at the airfoil trailing edge plane were in fact measured a short distance downstream ($\Delta X/B_x = 18$ to 26 percent, Fig. 3). The local loss does not change dramatically with axial distance and hence the impact of applying the measured value at the trailing edge plane is slight. The same cannot be said for blockage. A survey of single-stage rotor blockage data [7, 17] indicated that blockage decayed roughly with the inverse of axial distance downstream of the airfoil, i.e., $(1-\bar{K}) \propto \Delta X^{-1}$. It is reasonable to expect large variations in blockage immediately downstream of the airfoil trailing edge. The data presented in [7, 10, 17] clearly demonstrate this. In the present assessment, for lack of data directly on the airfoil trailing edge plane, the blockage distribution there was made the same as that at the nearest downstream traverse plane. The potential impact of this assumption will be examined as part of the sensitivity analysis in Part II of this paper. However, it can be said in advance that for this low-speed comparison the major impact was localized to the trailing edge plane and that it did not have any major effect on the comparison between measured and computed results at the traverse planes.

The question was considered as to whether the decaying aerodynamic blockage from an upstream airfoil row should be added to the mechanical blockage of a downstream row in multistage configurations. Since the aerodynamic blockage has decayed ($\propto \Delta X^{-1}$, [7, 17]) to such a low level by the time it reached the 25 percent chord location of the downstream airfoil it was neglected at all but the leading edge plane. At the leading edge plane the aerodynamic blockage was significant since the mechanical blockage was zero. At the 25 percent chord location the aerodynamic blockage was negligible relative to the 9 to 13 percent level of mechanical blockage. This approximation may become threadbare at off-design (near stall) conditions where blockage levels are generally much higher [6].

Some aerodynamic blockage was added to the airfoil mechanical blockage at the 75 percent chord location near the hub and the tip in order to simulate the effects within the airfoil rows of hub corner stall and rotor tip leakage. This was found to be necessary in order to suppress static pressure excursions within the airfoil row. These excursions occurred due to the high mechanical blockage at the 50 percent chord locations and the high aerodynamic blockage at the trailing edge planes. The low mechanical blockage between these two locations, i.e., and the 75 percent chord location, caused a static pressure excursion. This excursion could be eliminated by fairing in aerodynamic blockage near the hub and tip to produce a smooth transition from the mechanical blockage profile at 50 percent chord to the aerodynamic blockage profile at the trailing edge.

Analytical Simulation Procedure. The flow path geometry, required airfoil geometry, and airfoil mechanical blockage were input directly from the mechanical design of the compressor ([7], Tables 2, 3, and 4). The inlet guide vane was given the design value of a spanwise constant 25 deg of turning and for the sake of simplicity, no loss. Since no aerodynamic data were available at the first rotor trailing edge its loss, deviation, and blockage were initially based on data from the second

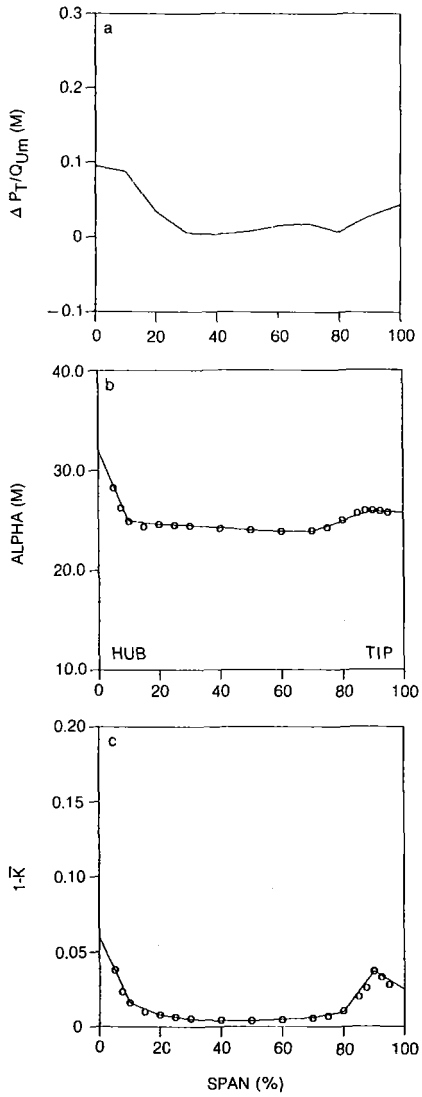

Fig. 4 First stator exit, Station 3; (*cl/B*) = 0.041, Φ = 0.51

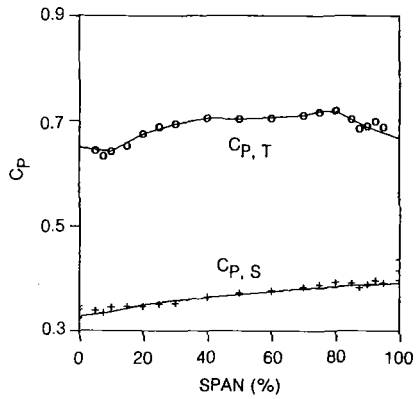

Fig. 5 First-stage stator exit (Station 3); (*cl/B*) = 0.041, Φ = 0.51

rotor from the test with the small tip clearance (the first rotor having the same small tip clearance, $cl/B = 0.007$). The first-stage rotor exit flow angles were increased by 3 deg to account for the 3 deg closure relative to the second rotor.

The first stator deviation and blockage were taken directly from the measured values ([7], Table 6). Without measured data at the first stator inlet, total pressure loss for the first stator was based on the second stator loss for the test with the small rotor tip clearance.

The loss, deviation, and blockage for the second-stage rotor

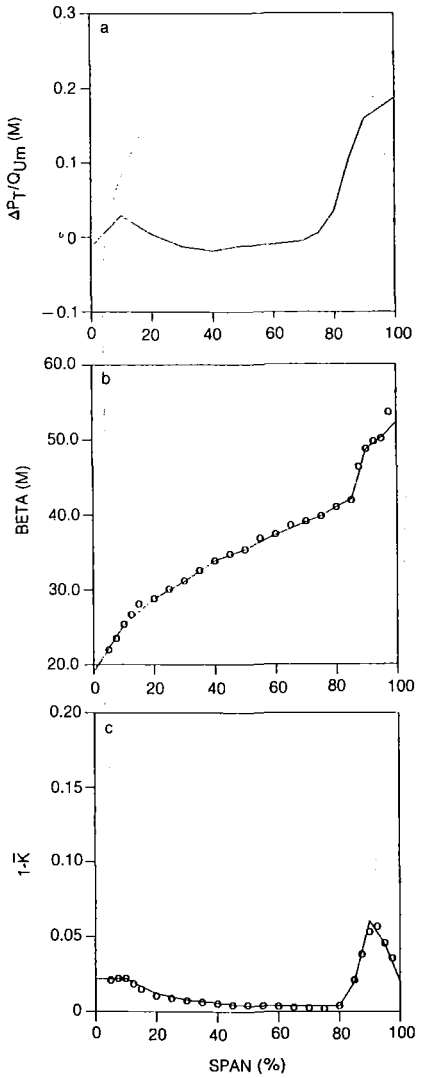

Fig. 6 Second rotor exit (Station 4); (cl/B) = 0.041, Φ = 0.51

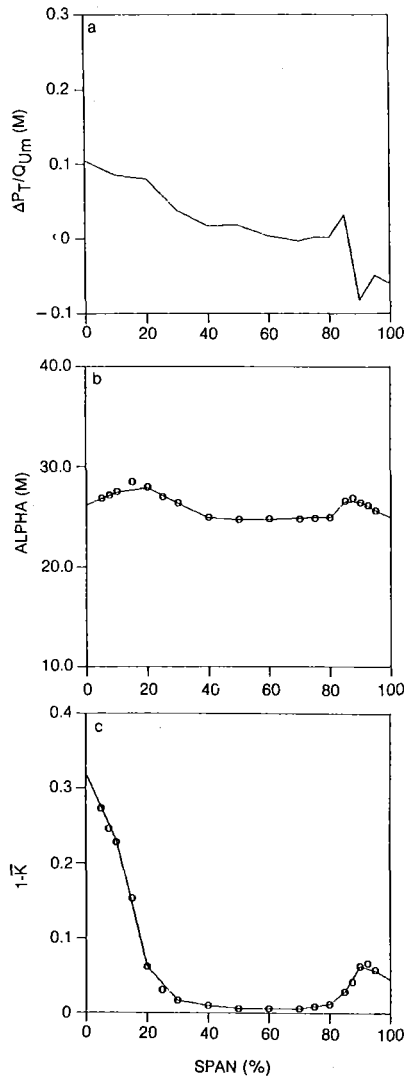

Fig. 7 Second-stage stator exit (Station 5); (cl/B) = 0.041, Φ = 0.51

and stator were taken directly from the measured data ([7], Tables 6, 7, and 8). Blockage at planes downstream of the second stator exit traverse plane (Station 5) were diminished according to (ΔX^{-1}) and set to zero ($1-\bar{K}$ = 0) at the downstream location where the exit static pressures were measured (Stations 6, Fig. 3).

The loss and deviation of the first rotor were then adjusted to obtain rough agreement between the computed and the measured total pressure at the first stator exit traverse plane (Station 3). At this point the first stator losses were adjusted slightly to give a nearly exact match between the measured and computed total pressure profiles at the first stator exit traverse plane (Station 3). By this process, both analytically and experimentally the first stage simply served to provide an initial condition for the highly documented second stage, i.e., close agreement between the measured and computed spanwise distributions of absolute total pressure and absolute yaw angle at Station 3 (Fig. 3). The agreement between all other parameters at this plane and at the downstream planes (Stations 4, 5, and 6) will serve as the basis of this assessment.

Aerodynamic Input Data. A summary is presented in Figs. 4–7 of the aerodynamic input data. This comparison is made at the nominal design flow coefficient (Φ = 0.51) and at the larger of the two second-stage rotor tip clearances tested (cl/B = 0.041).

The computational grid of the finite element solution for this case is shown at the top of Fig. 3. There are four elements in each airfoil row and two between adjacent rows. The stations between adjacent rows correspond to the traverse planes (Stations 1–5). The grid has radial divisions of 10 percent span out to 70 percent span and 5 percent divisions from there to the tip. The refined grid near the tip was required in order to accurately describe the strong gradients that occur due to rotor tip leakage.

The input to the through-flow analysis at the first stage stator exit (Station 3) is shown in Fig. 4. Spanwise distributions of loss, deviation, and blockage are shown. The loss is from the first stator leading edge to the trailing edge plane but the flow angle and blockage plotted are for the downstream traverse plane at Station 3. The blockage profiles at the trailing edge and at Station 3 were made identical and the angle distributions at the two locations differ only slightly. The measured data (symbols) as well as the actual distributions used in the calculation (curve) are both shown. Recall that the first stator loss profile was adjusted to provide agreement between the measured and computed distributions of absolute total pressure at Station 3. This agreement is shown in Fig. 5 along with the measured and computed static pressure distributions which are also in excellent agreement. The average static pressures measured on the hub and tip at this station are plotted at 0 and 100 percent span.

The input to the through-flow analysis at the second-stage rotor exit (Station 4) is shown in Fig. 6. Here again the spanwise distributions of the measured data as well as the actual

profiles used in the calculation are shown for loss, deviation, and blockage at Station 4, downstream of the second rotor trailing edge. The large rotor tip clearance ($cl/B = 0.041$) has caused significant regions of locally high loss, deviation, and blockage. It is these distributions which necessitated the refined radial grid from 70 to 100 percent span (Fig. 3).

The input to the through-flow analysis at the second-stage stator exit (Station 5) is shown in Fig. 7. Here again, the measured and computed distributions are shown for Station 5 downstream of the second stator trailing edge. The large negative loss region at the tip is due to radial redistribution of the flow caused by the large rotor tip clearance in the upstream row (Fig. 1). The large value of blockage near the hub is caused by the severe corner stall present in this region (Fig. 2 and [5]).

Figure 3 shows the computed variation of the static pressure along the annulus hub and tip (plotted in line with the grid above). The measured data are indicated by symbols showing the maximum, average, and minimum static pressures measured on blade-to-blade arrays of static pressure taps on the annulus at Stations 3–6. In general the agreement between the computed and measured flow path static pressures is excellent. In most cases the computed value is within the measured maximum/minimum range and close to the average. The major exception is at the second rotor exit (Station 4) at the tip where the measured average is greater than the computed value by 0.04 (i.e., 4 percent of $\frac{1}{2}\rho U_m^2$). The discrepancy is due to the large rotor tip clearance ($cl/B = 0.041$) as will be demonstrated in Part II of this paper. The relatively large difference between the maximum and minimum static pressures at most locations is a good indication of the critical importance of determining a good average value from measured data. If velocity triangles had been inferred using the through-flow analysis to match the measured flow path static pressures, significantly different results would have been produced depending on where the measured values were in the range between maximum and minimum.

Conclusions

Aerodynamic blockage from an upstream airfoil row decayed sufficiently rapidly that it was small relative to the mechanical blockage of the downstream row and could be neglected at all but the leading edge station.

It is essential to obtain an accurate pitchwise average of the hub and tip static pressures for comparison with a throughflow analysis. The circumferential variation can be a large fraction of the hub-to-tip difference (Fig. 3).

The objective of Part I of this paper was to provide a thorough description of the aerodynamic input used in this assessment of through-flow theory so that Part II could focus on the comparison of the measured and computed results.

Acknowledgments

The authors are indebted to Mr. Gordon Youngson (PW–Canada) for his assistance with the through-flow analysis. The two-stage compressor data were acquired under funding from the Pratt and Whitney Engineering Division of UTC. The software required to produce the various graphic outputs presented in this paper were all developed under UTC Corporate funding. This assessment of through-flow theory was carried out under Navy funding under the direction of Dr. Raymond Shreeve, Contract No. N00014-84-C-0354.

References

1 Wu, C. H., "A General Theory of Three-Dimensional Flow in Subsonic and Supersonic Turbomachines of Axial-, Radial- and Mixed Flow Type," NACA TN 2604, 1952.

2 Habashi, W. G., and Youngson, G. C., "A Transonic Quasi 3-D Analysis for Gas Turbine Engines Including Split-Flow Capability for Turbines," *Int. J. for Num. Meth. in Fluids*, Vol. 3, 1983, pp. 1–21.

3 Habashi, W. G., "Numerical Methods for Turbomachinery," in: *Recent Advances in Numerical Methods in Fluids*, Chap. 8, C. Taylor and K. Morgan, eds., Pineridge Press, 1980.

4 Caspar, J. E., Hobbs, D. E., and Davis, R. L., "Calculation of Two-Dimensional Potential Cascade Flow Using Finite Area Methods," *AIAA Journal*, Vol. 18, No. 1, Jan. 1980, pp. 103–109.

5 Dring, R. P., Joslyn, H. D., and Wagner, J. H., "Compressor Rotor Aerodynamics," *Viscous Effects in Turbomachines*, AGARD-CP-351, Copenhagen, Denmark, June 1–3, 1983, Paper No. 24.

6 Joslyn, H. D., and Dring, R. P., "Axial Compressor Stator Aerodynamics," ASME JOURNAL OF ENGINEERING FOR GAS TURBINES AND POWER, Vol. 107, Apr. 1985, pp. 485–493.

7 Dring, R. P., and Joslyn, H. D., "An Assessment of Single- And Multi-stage Compressor Flow Modeling, Part I: Design Conditions," Final Report for Naval Air Systems Command Contract No. N00014-84-C-0354, July 1985.

8 *AGARD Conference Proceedings No. 195 on Through-Flow Calculations in Axial Turbomachinery*, 47th Meeting of AGARD/PEP, AGARD-CP-195, May 20–21, 1976.

9 AGARD Advisory Report No. 175, Propulsion and Energetics Panel Working Group 12 on Through-Flow Calculations in Axial Turbomachines, AGARD-AR-175, Oct. 1981.

10 Dring, R. P., "Blockage in Axial Compressors," ASME JOURNAL OF ENGINEERING FOR GAS TURBINES AND POWER, Vol. 106, July 1984, pp. 712–714.

11 Ruden, P., "Investigation of Single-Stage Axial Fans," NACA TM 1062, 1944.

12 Smith, L. H., "The Radial Equilibrium Equation of Turbomachinery," ASME JOURNAL OF ENGINEERING FOR POWER, Vol. 88, No. 1, 1966.

13 Hirsch, C., "Unsteady Contributions to Steady Radial Equilibrium Flow Equations," AGARD Conference on Unsteady Phenomena in Turbomachinery, CP-177, No. 13, 1975.

14 Hirsch, C., and Warzee, G., "A Finite Element Method for Through Flow Calculations in Turbomachines," ASME *Journal of Fluids Engineering*, Sept. 1976, p. 403–421.

15 Hirsch, C., and Warzee, G., "An Integrated Quasi-3D Finite Element Calculation Program for Turbomachinery Flows," ASME JOURNAL OF ENGINEERING FOR POWER, Jan. 1979, pp. 141–148.

16 Sehra, A. K., and Kerrebrock, J. L., "The Effect of Blade-to-Blade Flow Variations on the Mean Flow-Field of a Transonic Compressor," AIAA 12th Fluid and Plasma Dynamic Conf., July 1979, Paper No. 79-1515.

17 Dring, R. P., and Joslyn, H. D., "Through-Flow Modeling of Axial Turbomachinery," ASME JOURNAL OF ENGINEERING FOR GAS TURBINES AND POWER, Vol. 108, Apr. 1986, pp. 246–253.

Through-Flow Analysis of a Multistage Compressor: Part II—Analytical-Experimental Comparisons

R. P. Dring
Manager.

H. D. Joslyn
Research Engineer.

Gas Turbine Technology,
United Technologies Research Center,
East Hartford, CT 06108

Through-flow theory is at the heart of turbomachinery aerodynamic design in that it provides the incidence and Mach number distributions that are ultimately used to define the rotor and stator airfoil contours. The assumption of axisymmetry plays a major role in the formulation of the theory and the consequences of this assumption have historically necessitated the introduction of "blockage" to account for the nonaxisymmetries in the flow. The present paper provides an assessment of these assumptions and of through-flow theory in general by making detailed comparisons between computed and measured results for a two-stage axial compressor. Part II focuses on the computed results, particularly the excellent agreement with the measured data that can be obtained, and their sensitivity to various simplifying assumptions.

Introduction

The aerodynamic analysis of the compression system is one of the most challenging aspects of every new or up-rated gas turbine design. The basic aerodynamic mechanisms playing important roles in the compressor include: compressibility, unsteadiness, three dimensionality, and viscous effects such as boundary layer transition and separation. Although highly sophisticated full Navier–Stokes solution algorithms are beginning to appear which have the potential to attack these flows in full generality, the basis of many contemporary design systems is a series of calculations which treat the flow as a sequence of two-dimensional calculations [1–4]. Because of their speed and efficiency these two-dimensional calculations will continue to play a significant role in multistage compressor aerodynamic design. For this reason there is a great incentive to conduct an assessment of these analyses which will guide the compressor analyst as to the interpretation of the results of these calculations and as to how these calculations can be employed most reliably in the design of new configurations and in the analysis of compressor rig data. The objective of the present paper is to provide such an assessment of the through-flow theory.

The objective of Part I of this paper [5] was to provide a thorough description of the aerodynamic input used in this assessment. This included a discussion of how the row-by-row description of airfoil total pressure loss, deviation, and blockage were defined from the benchmark data base and how they were used in the analysis. The objective of Part II of this paper is to provide a detailed comparison of the measured and computed results and to examine the sensitivity of the computed results to various simplifying assumptions. The comparisons between the measured and computed results will include hub and tip static pressures as well as spanwise distributions of the flow speed and direction, and absolute and relative total and static pressures. It will be shown that while excellent agreement can be achieved between the measured and computed results, this agreement is strongly dependent on using not only the correct level of blockage, but also the correct spanwise distribution.

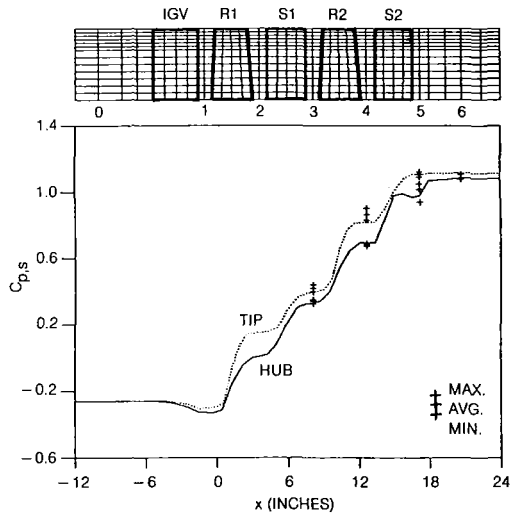

Fig. 1 Hub and tip static pressures; $(cl/B) = 0.041$, $\Phi = 0.51$

Contributed by the Gas Turbine Division of THE AMERICAN SOCIETY OF MECHANICAL ENGINEERS and presented at the 31st International Gas Turbine Conference and Exhibit, Düsseldorf, Federal Republic of Germany, June 8–12, 1986. Manuscript received at ASME Headquarters December 26, 1985. Paper No. 86-GT-14.

Discussion

For the sake of completeness, Fig. 3 of Part I is duplicated here as Fig. 1. In addition to showing the finite element grid and the airfoil and measurement plane locations, this figure shows the measured and computed static pressures along the annulus hub and tip. The symbol indicating the measured data illustrates the maximum, average, and minimum static pressures as measured on dense blade-to-blade arrays of static pressure taps on the annulus hub and tip at Stations 3–6. The relatively large difference between the maximum and minimum static pressures at most locations is a good indication of the need for care in determining a good average value from measured data.

The computed hub and tip static pressures show a generally increasing trend across each airfoil row. There is a weak local minimum in the hub static pressure at the second stator trailing edge where the local blockage is very high ($1-\bar{K}=0.32$, see [5], Fig. 7*c*). This behavior is similar to the low hub static pressure predicted at the trailing edge of the single-stage rotor of [6, 7] where the local blockage was also very high ($1-\bar{K}=0.39$). In general, the agreement between the computed and measured results is excellent. At most locations the computed value is within the measured maximum/minimum range and close to the average. The only exception to this is at the second rotor exit (Station 4) at the tip where the average measured value is greater than the computed value by 0.04 (i.e., 4 percent of Q_{U_m}). It will be demonstrated later that this difference is due to the large rotor tip clearance (4.1 percent chord). This generally good agreement suggests that the rationale for determining blockage [5, 8] is reasonable.

From this point on, this assessment will focus on comparing spanwise distributions of various measured and computed quantities in the absolute and rotating frames of reference at the three traverse planes (3, 4, and 5). At various points both area and mass-averaged measured data will be used for comparison. The difference between these two averages is important since an axisymmetric through-flow analysis is usually considered to be a prediction of mass-averaged quantities.

The area-averaged axial velocity ($C_x \cdot \bar{K}$), relative yaw angle, and absolute and relative flow speed profiles at the first stator exit traverse plane (Station 3) are shown in Fig. 2. The measured and computed axial velocity are in excellent agreement except very near the tip. The computed relative yaw angle (BETA) is within one degree of the measured profile. The absolute and relative flow speeds are also in excellent agreement with the measured data. In the absolute flow speed plot where two symbols are plotted the circle (o) is the mass average (M) and the cross (+) is the area average (A). For the relative speed the two averages are virtually identical.

Figure 3 shows the measured and computed velocities and absolute yaw angle (ALPHA) at the second rotor exit traverse

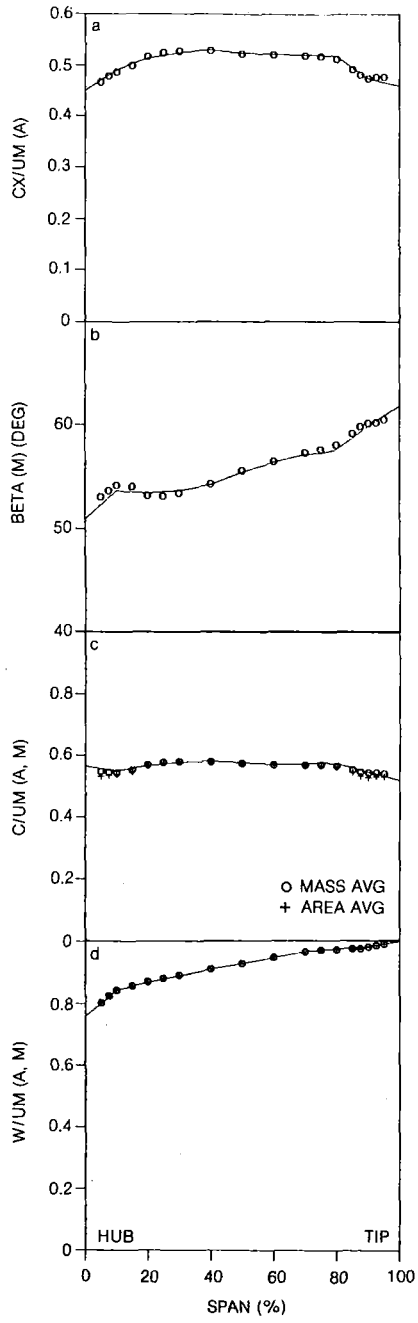

Fig. 2 First-stage stator exit (Station 3); (cl/B) = 0.041, Φ = 0.51

Nomenclature

B = airfoil true chord
B_x = airfoil axial chord
C = absolute flow speed
C_P = pressure coefficient = $(P-P_{T0A})/Q_{U_m}$
C_x = axial component of velocity
cl = rotor tip clearance
D_f = NASA diffusion factor
$\bar{K}$ = blockage factor
P = pressure
Q_{U_m} = dynamic pressure based on midspan wheel speed $= \frac{1}{2}\rho U_m^2$
Q = incident dynamic pressure
r = radial distance
U_m = wheel speed at midspan
W = relative flow speed
x = axial distance
α = absolute yaw angle (from axial)
β = relative yaw angle (from axial)
θ = flow yaw angle (from axial)
Φ = flow coefficient = C_x/U_m
ρ = fluid density

Subscripts

m = midspan
S = static
T = totals
0 = compressor inlet station
1, . . . ,5 = compressor axial stations
A = absolute frame of reference
R = rotating frame of reference
x = axial
r = radial
θ = tangential

Superscripts

$-a, (A)$ = pitchwise area average
$-m, (M)$ = pitchwise mass average

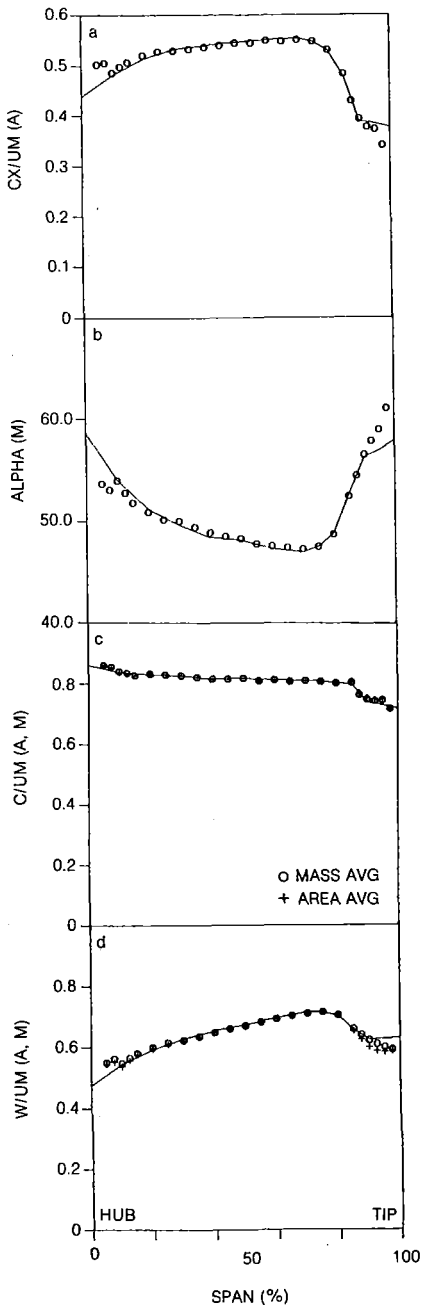

Fig. 3 Second-stage rotor exit (Station 4); $(cl/B) = 0.041$, $\Phi = 0.051$

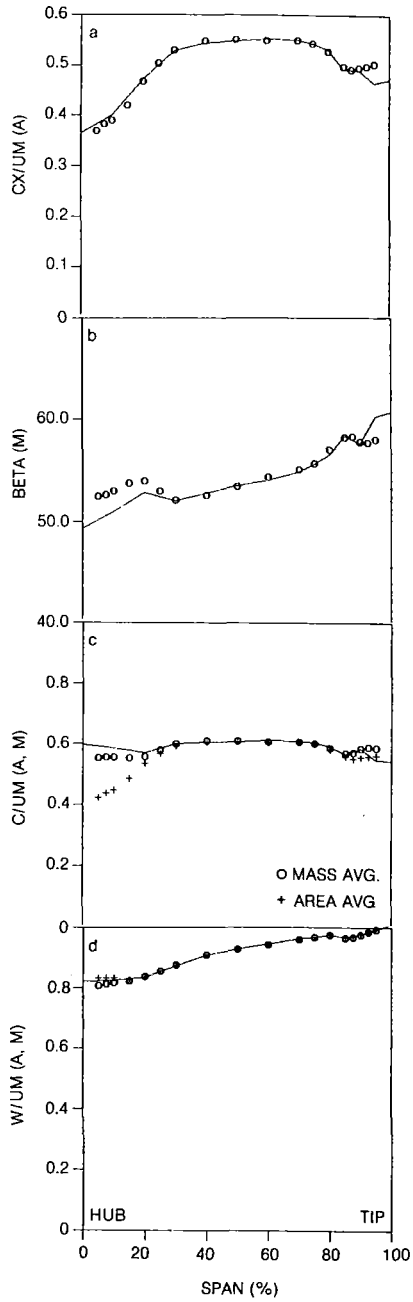

Fig. 4 Second-stage stator exit (Station 5); $(cl/B) = 0.041$, $\Phi = 0.51$

plane (Station 4). The axial velocity is well predicted except very close to the hub and tip. There is a significant difference between the measured and computed absolute yaw angles from 90 percent span to the tip. This difference could be reduced by locally increasing the rotor loss but such an increase cannot be justified with the measured rotor loss distribution ([5], Fig. 6*a*). The agreement between the measured and computed absolute yaw angles at the tip could also be improved by increasing the rotor exit relative yaw. This also might seem attractive in light of the data point at 97.5 percent span in Fig. 6(*b*) of [5]. It was demonstrated, however, that a 4 deg increase in relative yaw at 100 percent span resulted in an increase of only 1 deg in absolute yaw which is quite small in comparison to the discrepancy in Fig. 3(*b*). In addition this 4 deg increase in relative yaw angle caused a reduction in absolute flow speed (*C/UM*) of 0.04 and a drop of 0.06 in the absolute total pressure coefficient at the tip. Both of these changes would have degraded the agreement between the measured and computed results (see Figs. 3*c* and 5*d*). For these reasons, and because of general uncertainty about the accuracy of the data point at 97.5 percent span due to the close proximity of the rotating frame probe and the stationary case surface, the rotor exit relative yaw angle profile was chosen as shown in Fig. 6(*b*) of [5].

The absolute and relative flow speeds are in excellent agreement with the computed results except for the regions very close to the hub and tip. Where two symbols are shown for the relative flow speed the circle (o) is the mass-averaged flow speed and the cross (+) is the area average. The two averages are virtually identical for the absolute flow speed.

The flow speeds and relative yaw angle at the second stator exit traverse plane (Station 5) are shown in Fig. 4. The axial velocity is well predicted except for very close to the tip. The relative yaw is also well predicted except in the hub region where significant differences exist between the measured and computed results ($\approx$2 deg). The computed absolute flow

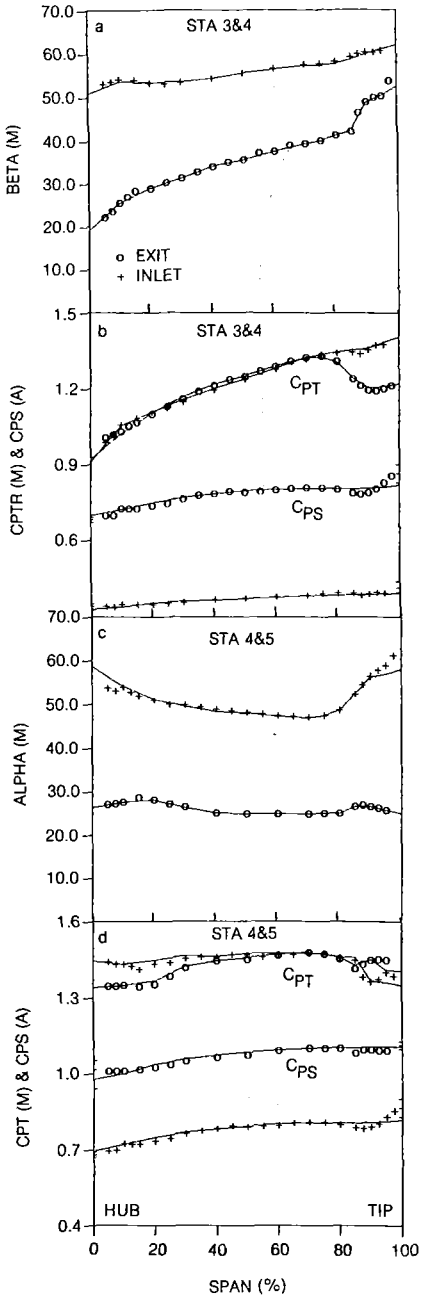

Fig. 5 Second rotor and stator inlet and exit conditions; (cl/B) = 0.041, Φ = 0.51

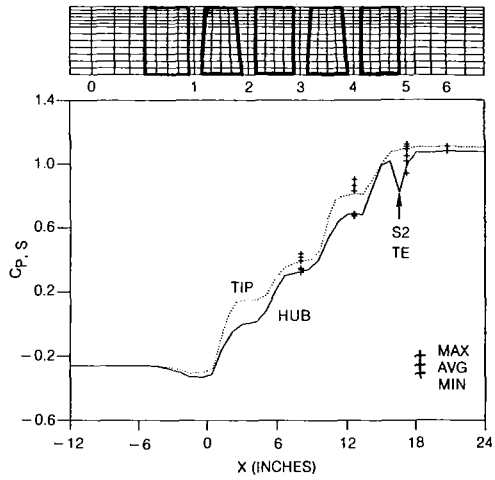

Fig. 6 Case A: trailing edge blockage increased 1.5 ×; (cl/B) = 0.041, Φ = 0.51

speed is in good agreement with the measured mass averages (o). The area-averaged flow speed (+) is significantly below the prediction due to the high blockage in this region. The mass and area-averaged relative flow speeds are much closer in magnitude and in excellent agreement with the computed values.

The inlet and exit relative flow angles as well as the inlet and exit relative total and static pressures for the second rotor are shown in Figs. 5(*a*) and 5(*b*). Similar absolute frame quantities for the second stator are shown in Figs. 5(*c*) and 5(*d*). Recall that the exit angle profiles are part of the input data and for this reason these curves essentially lie on the measured data. As mentioned above the computed inlet angles are in excellent agreement with the measured values except at the stator tip where a significant difference exists. For the case with the smaller second rotor tip clearance ($cl/B = 0.007$) the agreement between the measured and computed second stator inlet absolute flow angles is excellent from hub to tip. This indicates that the disagreement at the tip with the large clearance is attributable to the locally high values and rapid spanwise gradients of loss, deviation, and blockage for this case ([5], Fig. 6).

Because the rotor and stator losses are input the difference between the inlet (+) and exit (o) total pressures in Fig. 5(*b*) and 5(*d*) are identical with the measured values. Thus, the assessment of the prediction is based on how well the inlet relative and absolute total pressure profiles are predicted. The agreement between the measured and computed results is in general agreement. (Recall the regions of negative loss near midspan on the rotor and near the tip of the stator.) The static pressure profiles are in general well predicted as to level and trend. The most notable exception is at the rotor exit/stator inlet (Station 4) where the data indicate a local minimum in the static pressure between 85 and 90 percent span which is only weakly suggested by the computed result. Several points are worth mentioning with regard to this static pressure minimum within the flow: (1) It was not present for the case with reduced tip clearance (Fig. 13). (2) It has been observed downstream of a single-stage rotor ([9], Fig. 2) where, for reasons not related to tip leakage, there was a high loss region at the tip ([10], Fig. 16). (3) It has been observed that low static pressure is often associated with regions of high total pressure loss downstream of compressor airfoil rows ([9], conclusions 1 and 2).

Looking back over this assessment of through-flow theory (Figs. 1–5) one is led to the conclusion that, given the "proper input," there is every expectation that an accurate prediction will result. The assessment represents a particularly challenging demonstration of the robust nature of through-flow theory because of the strongly three-dimensional flow mechanisms that were present in the data base due to the large rotor tip clearance [11] and due to the large region of hub corner stall on the second stator [12] (see [5], Figs. 1 and 2). The key is proper input and the least well understood part of the input is the blockage. It is noteworthy, however, that the description of blockage used in this assessment ([5], equations 6, 7, and 8, and [8]) has resulted in what is believed by the authors to be the first accurate prediction of static pressure based purely upon measured data.

In the absence of such proper input one needs to know the impact of using less detailed or less accurate information. Other questions arise as to the impact of the fineness of the finite element grid, or the impact of some of the subjective judgments made about the input (e.g., making the trailing edge plane blockage equal to the downstream traverse plane blockage). These and other questions are addressed in the following paragraphs.

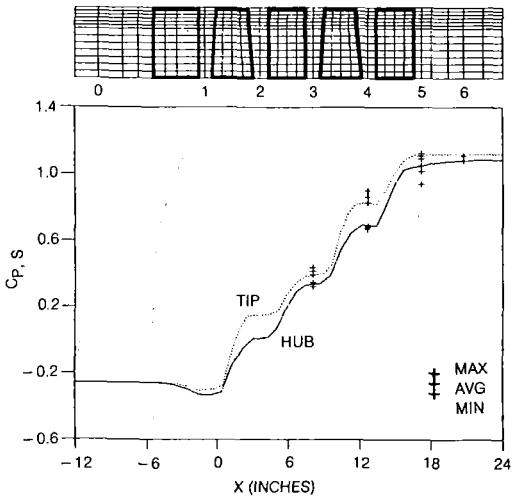

Fig. 7 Case B: aero blockage $\neq f$(span); $(cl/B) = 0.041$, $\Phi = 0.51$

A number of calculations have been carried out to demonstrate the sensitivity of the computed results to specific details of the input data and to the computational mesh. The computed results from the comparison with measured data in the previous section will serve as the base case against which the sensitivities will be determined. Sensitivity will be determined for five example cases in the following three areas: (1) aerodynamic blockage, (2) mechanical blockage, and (3) computational mesh.

Case A: Blockage at the Trailing Edge Planes. Aerodynamic blockage data were only available at the traverse planes (Stations 3, 4, and 5) and yet aerodynamic blockage had to also be specified at the airfoil trailing edge planes. In spite of the fact that it is known that blockage decays rapidly with distance downstream of an airfoil [8], for lack of better information the trailing edge blockage distributions were made equal to those at the traverse planes downstream. In order to demonstrate the sensitivity of the computed results to this approximation, Case A was run with the trailing edge blockages increased arbitrarily by 50 percent (1.5×). Since these blockage increases affected the flow angles at the traverse planes, the trailing edge deviations were adjusted in order to restore the agreement between the measured and computed exit flow angles at the traverse planes. The resulting flow path static pressure distribution is shown in Fig. 6. When compared with the base case (Fig. 1) the results are virtually identical except at the second stator trailing edge (*S2/TE*) where a strong local low pressure spike is present at the hub ($\Delta C_{PS} = 0.12$). The effects on the computed results at the traverse and leading edge planes were minimal, the change in static pressure (ΔC_{PS}) being typically less than 0.01 and the change in incidence being a small fraction of one degree. Although the equation governing the through-flow analysis ([5], equation (4)) is elliptical the effects of changing blockage are very localized in extent axially (for this low-speed comparison). The converse would have been painful.

Case B: Spanwise Constant Aerodynamic Blockage. Distributions of aerodynamic blockage input at the traverse planes (and at the trailing edge planes) vary strongly with span ([5], Figs. 4*c*, 6*c*, and 7*c*). Since historically spanwise distributions of blockage have not been available to the analyst it would be of value to know the magnitude of the errors incurred by simply using a constant value of blockage across the span. This was investigated by taking the spanwise mass-averaged aerodynamic blockage at the trailing edge, traverse, and leading edge planes from the base case and substituting these constant values from hub to tip at each axial station. At

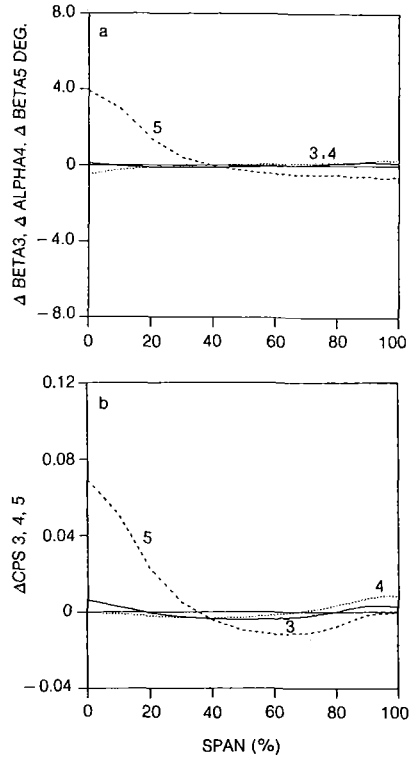

Fig. 8 Case B: aero blockage $\neq f$(span); $(cl/B) = 0.041$, $\Phi = 0.51$

the first stator trailing edge and at Station 3 a constant blockage of 1.3 percent ($\bar{K} = 0.987$) was used instead of the measured distribution ([5], Fig. 4*c*). At the second rotor exit and at Station 4 a constant value of 1.3 percent was used in place of the measured profile ([5], Fig. 6*c*). At the second stator exit and at Station 5 a constant value of 4.8 percent was used in place of the measured profile which reached a maximum value of 32 percent at the hub ([5], Fig. 7*c*). The resulting flow path static pressure distribution is shown in Fig. 7. In addition, Fig. 8 shows how this case differs from the base case in terms of the spanwise distributions of static pressure and incidence at the three traverse planes. The changes plotted represent Case B values minus the base case values. At the first stator and second rotor exits (Stations 3 and 4) the differences are minimal. This is due to the fact that the maximum local blockage at these planes was low (approximately 6 percent, [5], Figs. 4*c* and 6*c*). At the second stator trailing edge (Station 5) the impact of a constant blockage is significant at the hub. This sensitivity is due to the fact that the maximum local blockage at the hub at this plane was very high (32 percent, [5], Fig. 7*c*). At this location the constant blockage has increased the local static pressure ΔC_{PS} by 0.07, or 17 percent of the stator exit dynamic pressure, and it has increased the relative flow angle (incidence on a downstream rotor) by 4 deg. The conclusion here is that using the correct spanwise distribution of blockage is important in correctly predicting the flow. For this case there is a local 1 deg error in incidence for every 7 percent error in local blockage. From this comparison it is clear that the computed flows are sensitive to the spanwise distribution of aerodynamic blockage. The sensitivity to the level of blockage will be considered in Case D.

Case C: Impact of Mechanial Blockage. In this case the sensitivity of the computed results to mechanical blockage was assessed by setting the blockage (aerodynamic and mechanical) to zero ($\bar{K} = 1$) at the three axial stations within each airfoil row. The maximum values of the mechanical blockage were at the 25 percent chord locations and they were in the vicinity of 9 to 13 percent. Eliminating mechanical blockage at the intra-airfoil stations only had significant im-

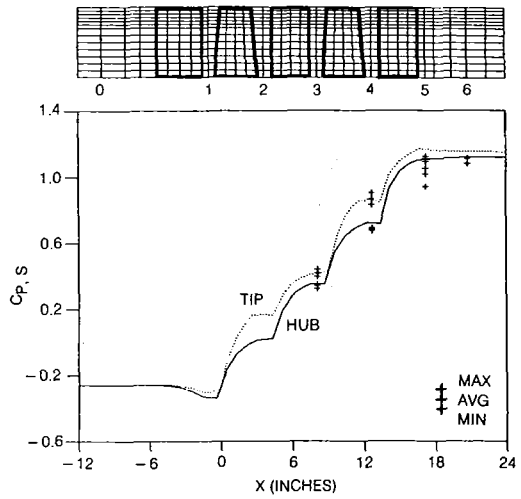

Fig. 9 Case D: no aerodynamic or mechanical blockage; (c/B) = 0.041, $\Phi = 0.51$

pact at these stations and not at stations between rows. The impact at the leading edge, trailing edge, and traverse locations was very small (for this low-speed comparison). At the traverse planes the static pressure profiles ΔC_{PS} varied by less than 0.01 and the incidence to downstream rows varied by less than 1/2 deg.

Case D: No Aerodynamic or Mechanical Blockage. As an assessment of a worst case condition in terms of blockage a calculation was carried out without any aerodynamic or mechanical blockage ($\bar{K} = 1$). Since the impact of eliminating blockage within the airfoil rows was negligible, as demonstrated in Case C, the major impact of the present case will be in eliminating all aerodynamic blockage (at the trailing edge, traverse, and leading edge planes). The computed flow path static pressure distribution is shown in Fig. 9. Comparison of these results with the base case (Fig. 1) shows that the elimination of blockage has had a major impact, especially at the second stator trailing edge where the measured aerodynamic blockage had been large (32 percent at the hub). The computed spanwise distributions of the second rotor and stator, inlet and exit, total and static pressures are compared with the measured distributions in Figs. 10(*a*) and 10(*b*). In addition, the differences between this prediction and the base case prediction of the spanwise distributions of the incidence on downstream airfoils and static pressure are shown in Figs. 10(*c*) and 10(*d*). The absence of blockage has caused significant errors in the total and static pressures. At the first stator exit traverse plane (Station 3) Fig. 10(*d*) shows that the static pressure error ΔC_{PS} is typically 0.02 and that at the second rotor exit traverse plane (Station 4) it is typically 0.03. At the second stator exit traverse plane (Station 5) the static pressure error is typically 0.06 and it rises to 0.13 at the hub. These errors correspond to 15 and 32 percent, respectively, of the second stator exit dynamic pressure. At this plane the computed incidence for a downstream rotor (Fig. 10*c*) would be in error by typically 2 deg and by 6 deg at the hub. The positive incidence error indicates a rotor relative inlet angle which is 6 deg too high.

By comparing Case D (with no blockage) to Case B (with constant aerodynamic blockage) it is possible to isolate the effect of the level of aerodynamic blockage from the effect of the spanwise distribution of aerodynamic blockage. (Recall that mechanical blockage only had a significant impact within the airfoil rows.) Comparing Figs. 8(*a*) and 8(*b*) (Case B) with Figs. 10(*c*) and 10(*d*) (Case D) indicates that the spanwise distribution of aerodynamic blockage has a significant impact on the spanwise distributions of static pressure and incidence and that the level of aerodynamic blockage has a significant

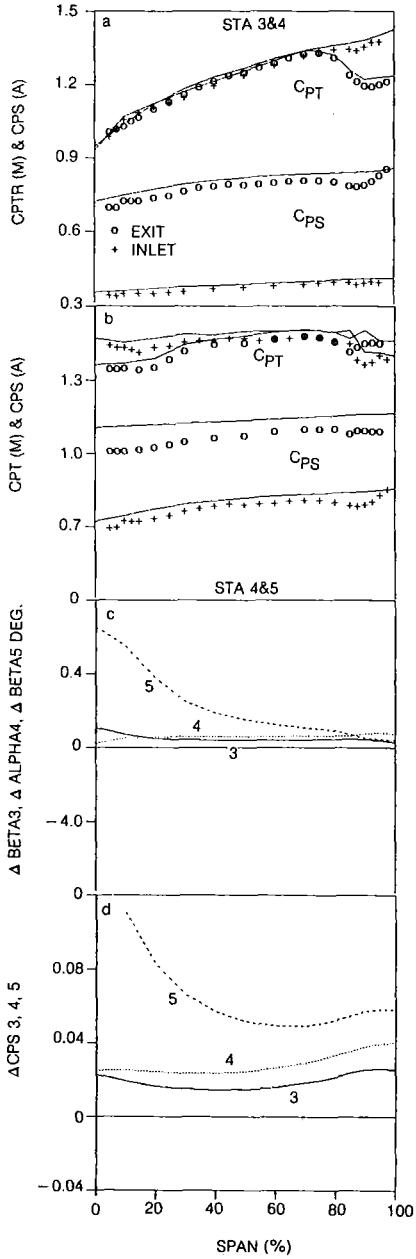

Fig. 10 Case D: no aerodynamic or mechanical blockage; (c/B) = 0.041, $\Phi = 0.51$

impact on the levels of static pressure and incidence. The differences between Cases B and D and the base case are very similar in spanwise variation but they are significantly different in level.

The conclusion from these comparisons and from Case B is that an adequate modeling of the levels and spanwise distributions of aerodynamic blockage is necessary for an accurate prediction of the total and static pressure distributions as well as for an accurate prediction of incidence.

Case E: Coarse Axial Grid. Given the insensitivity of the computed results to conditions within the airfoil rows (i.e., aerodynamic and mechanical blockage), and in the interest of minimizing the amount of input required, a calculation was carried out with a coarse axial mesh. This mesh had axial planes only at the airfoil leading and trailing edge locations (Fig. 11). It should be pointed out that the finite element scheme contains node points at the midpoint of each element side. Therefore, in spite of the fact that there are mesh planes only at the leading and trailing edge planes, there are node

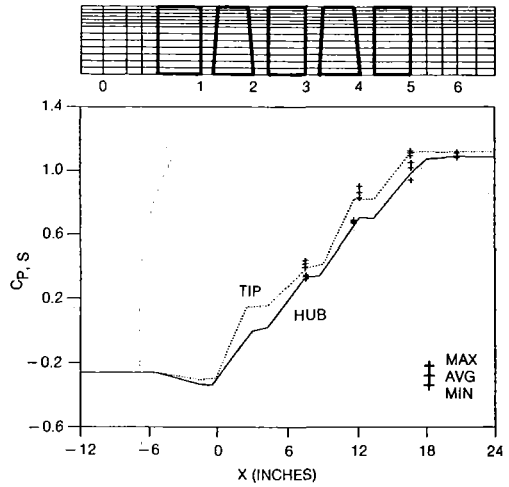

Fig. 11 Case E: coarse axial grid (*LE* and *TE* stations only); (cl/B) = 0.041, $\Phi = 0.51$

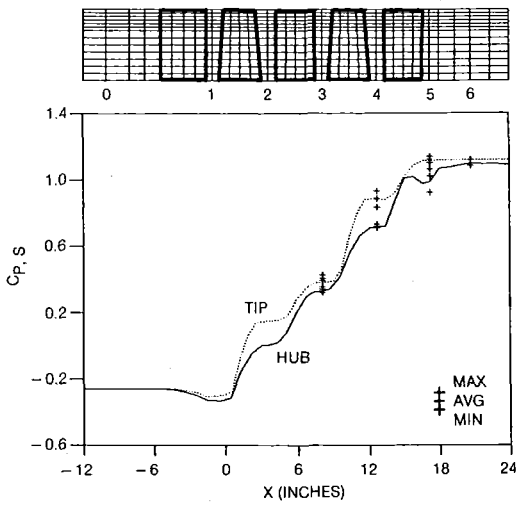

Fig. 12 Hub and tip static pressures; (cl/B) = 0.007, $\Phi = 0.51$

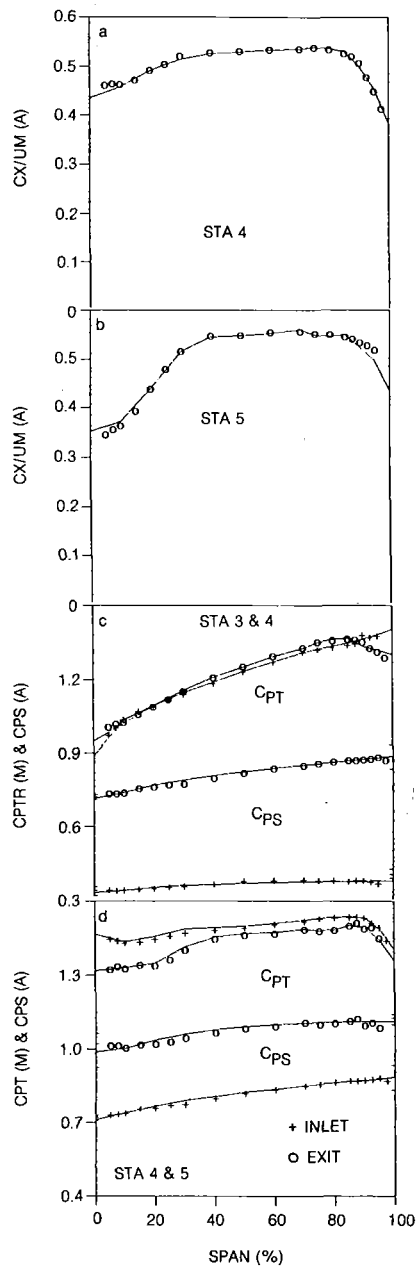

Fig. 13 Second rotor and stator inlet and exit conditions; (cl/B) = 0.007, $\Phi = 0.51$

points at the midchord of each airfoil. Since even the traverse planes downstream of each airfoil row were deleted, the measured data were compared with the computed results at the trailing edge planes. Aside from the coarse grid, all other aerodynamic and geometric input was identical with the base case. The resulting flow path static pressure distribution is shown in Fig. 11. It can be seen by comparing these results with those of the base case (Fig. 1) that aside from the lack of resolution within the airfoil rows coarsening the axial grid had negligible impact on the computed results. At the trailing edge planes the change in the spanwise distribution of static pressure ΔC_{PS} was less than 0.01 and the change in incidence to downstream rows was less than 1/2 deg. A calculation was also made which retained the traverse planes in the calculation. The results were virtually identical to the case described here without them. The conclusion reached in this comparison is that for the through-flow method of [2, 3] the bare minimum grid (leading and trailing edge stations) is sufficient to produce an accurate calculation (at least for low-speed flows).

Small Rotor Tip Clearance (cl/B) = 0.007. A second set of data had been acquired on the two-stage compressor with the second-stage rotor running at a tip clearance which was much smaller than that which existed in the previous comparisons ($cl/B = 0.007$ versus 0.041). The relevance to the present assessment is that this reduced tip clearance produced a rotor exit flow field in which the three-dimensional effects and the general distortion of the flow field were greatly reduced relative to the large clearance case. For this reason it is to be expected that the through-flow calculation will predict the measured flows even more accurately than for the large clearance case.

The computational grid and the computed flow path hub and tip static pressures for the small tip clearance case are shown in Fig. 12 along with the measured static pressures at Stations 3–6. The major difference between these results and those for the large clearance case (Fig. 1) occurs at the tip between the second stage rotor and stator (Station 4). The measured data are slightly different from the large clearance case but the major difference is that the predicted static

pressure at the tip is in excellent agreement with the average measured static pressure. All other differences are small relative to this change.

Comparisons of a more detailed nature are shown in Fig. 13. The spanwise distribution of axial velocity at the second rotor exit (Station 4) shown in Fig. 13(*a*) can be compared with a similar figure for the large clearance case, Fig. 3(*a*). Reducing the rotor tip clearance has had a major effect in increasing the axial velocity from the 80 percent span location out to the tip. Whereas for the large clearance case the axial velocity profile at the tip was predicted reasonably well, for the small clearance case agreement was virtually exact. Similar results were also obtained for the absolute flow angle profile. Whereas for the large clearance case there was a large increase in flow angle from 80 percent span to the tip which was well predicted out to 90 percent but not well predicted from there to the tip (Fig. 3*b*), for the small clearance case the magnitude of the flow angle increase was lower by approximately 50 percent and it was predicted almost exactly by the through-flow analysis.

The axial velocity profile for the small clearance case at the second stator exit (Station 5), Fig. 13(*b*), can be compared with similar results for the large-clearance case in Fig. 4(*a*). Here again, reducing the tip clearance has produced a smoother spanwise profile. However, even for the small clearance case there is still a significant difference between the measured and computed results between 90 percent span and the tip.

The spanwise distributions of inlet and exit, total and static pressures for the second-stage rotor and stator are shown in Figs. 13(*c*) and 13(*d*). These results for the small-clearance case can be compared with the large-clearance case in Figs. 5(*b*) and 5(*d*). As expected the agreement between measured and computed results for the small-clearance case is significantly better than for the large-clearance case. The major differences in total pressure between the two cases is in the tip region where reducing the tip clearance markedly reduced the loss in relative total pressure across the rotor. The negative loss region at the stator tip with the large clearance (Fig. 5*d*) has become a region of positive loss with the small clearance (Fig. 13*d*). Recall that the negative loss had been attributed to a radial redistribution of the flow as it passed through the stator passage due to strongly three-dimensional flow at the rotor tip.

The last major difference between the large and small rotor tip clearance cases is in the static pressure profiles downstream of the second rotor at Station 4 (Figs. 5*b* and 5*d* and Figs. 13*c* and 13*d*). The oscillation in the measured static pressure between 80 percent span and the tip for the large-clearance case has completely disappeared for the small-clearance case. For the large-clearance case this oscillation was faintly suggested by the prediction but generally speaking it was not predicted. For the small-clearance case the agreement between the measured and computed results was excellent.

Finally, some measure of caution must be exercised in the interpretation of the through-flow analysis results presented here. Since this comparison has been for low-speed flow some of the observations made in this discussion may not be valid for high-speed flows. In particular, the insensitivity of the computed results to trailing edge blockage, airfoil mechanical blockage, and grid coarseness may be valid only for low-speed flows. The results of [13] indicate that high-speed flows are sensitive to some of these variables. For example, in the analysis of a high-through-flow compressor stage, a change of 3 deg in rotor hub incidence occurred when the through-flow analysis grid was changed from having no calculation stations within the blade row (i.e., only leading and trailing edge stations, [13], Fig. 111, p. 97) to having 5 intrarow stations (i.e., every 20 percent chord, [13], Fig. 121, p. 102). A similar observation is made in [14].

Conclusions

An assessment of through-flow theory has been carried out by comparing the predictions of a modern finite element through-flow analysis [2, 3] with a benchmark data base acquired on a low-speed two-stage axial compressor. The benchmark data base was used to supply the aerodynamic input required by the analysis including loss, deviation, and blockage. The following conclusions were drawn:

1 It is essential to obtain an accurate pitchwise average of the hub and tip static pressures for comparison with a through-flow analysis. The circumferential variation can be a large fraction of the hub-to-tip difference (Fig. 1).

2 Given proper input, there is every expectation that an accurate prediction will result (Figs. 1–5).

3 The description of tangential aerodynamic blockage used in this assessment (from [8]) has produced an accurate prediction of most aspects of the flow field.

4 Computed results at locations between adjacent airfoil rows are mainly dependent on the blockage profile at those locations and only weakly dependent on the trailing edge plane blockage profile immediately upstream (Figs. 1 and 6).

5 Airfoil mechanical blockage only had a significant impact at stations within the airfoil row and not at stations between adjacent airfoil rows.

6 The computed results are strongly dependent on the spanwise distribution of aerodynamic blockage. It was demonstrated that using the correct level of blockage but the wrong distribution (i.e., a constant) produced significant errors in both static pressure and incidence (Fig. 8).

7 The spanwise distribution of aerodynamic blockage has a significant impact on the spanwise distributions of static pressure and incidence and the level of aerodynamic blockage has a significant impact on their levels (Figs. 8 and 10).

8 The minimum streamwise grid density (leading and trailing stations only) is sufficient to produce an accurate calculation with the through-flow analysis used in this assessment [2, 3] (Fig. 11).

9 The measured and computed results were in closer agreement for the case with the small rotor tip clearance than for the large clearance (Figs. 1 and 12). This is to be expected due to the more strongly three-dimensional nature of the flow with the large rotor tip clearance.

Acknowledgments

The authors are indebted to Mr. Gorden Youngson (PW–Canada) for his assistance with the through-flow analysis. The two-stage compressor data were acquired under funding from the Pratt and Whitney Engineering Division of UTC. The software required to produce the various graphic outputs presented in this paper were all developed under UTC Corporate funding. This assessment of through–flow theory was carried out under Navy funding under the direction of Dr. Raymond Shreeve, Contract No. N00014-84-C-0354.

References

1 Wu, C. H., "A General Theory of Three-Dimensional Flow in Subsonic and Supersonic Turbomachines of Axial-, Radial- and Mixed Flow Type," NACA TN 2604, 1952.

2 Habashi, W. G., and Youngson, G. C., "A Transonic Quasi 3-D Analysis for Gas Turbine Engines Including Split-Flow Capability for Turbofans," *Int. J. for Num. Meth. in Fluids*, Vol. 3, 1983, pp. 1–21.

3 Habashi, W. G., "Numerical Methods for Turbomachinery," in: *Recent Advances in Numerical Methods in Fluids*, Chap. 8, C. Taylor and K. Morgan, eds., Pineridge Press, 1980.

4 Caspar, J. E., Hobbs, D. E., and Davis, R. L., "Calculation of Two-Dimensional Potential Cascade Flow Using Finite Area Methods," *AIAA Journal*, Vol. 18, No. 1, Jan. 1980, pp. 103–109.

5 Dring, R. P., and Joslyn, H. D., "Through-Flow Analysis of a Multistage Compressor: Part I—Aerodynamic Input," ASME Paper No. 86-GT-13.

6 Dring, R. P., and Joslyn, H. D., "Through-Flow Modeling of Axial Turbomachinery," ASME JOURNAL OF ENGINEERING FOR GAS TURBINES AND POWER, Vol. 108, Apr. 1986, pp. 246-253.

7 Dring, R. P., and Joslyn, H. D., "An Assessment of Single- and Multistage Compressor Flow Modeling, Part I: Design Conditions," Final report for Naval Air Systems Command Contract No. N00014-84-C-0354, July 1985.

8 Dring, R. P., "Blockage in Axial Compressors," ASME JOURNAL OF ENGINEERING FOR GAS TURBINES AND POWER, Vol. 106, July 1984, pp. 712-714.

9 Wagner, J. H., Dring, R. P., and Joslyn, H. D., "Inlet Boundary Layer Effects in an Axial Compressor Rotor: Part II—Through-Flow Effects," ASME JOURNAL OF ENGINEERING FOR GAS TURBINES AND POWER, Vol. 107, Apr. 1985, pp. 381-386.

10 Dring, R. P., Joslyn, H. D., and Hardin, L. W., "An Investigation of Compressor Rotor Aerodynamics," ASME JOURNAL OF ENGINEERING FOR POWER, Vol. 104, Jan. 1982, pp. 84-96.

11 Dring, R. P., Joslyn, H. D., and Wagner, J. H., "Compressor Rotor Aerodynamics," *Viscous Effects in Turbomachines*, AGARD-CP-351, Copenhagen, Denmark, June 1-3, 1983, Paper No. 24.

12 Joslyn, H. D., and Dring, R. P., "Axial Compressor Stator Aerodynamics," ASME JOURNAL OF ENGINEERING FOR GAS TURBINES AND POWER, Vol. 107, Apr. 1985, pp. 485-493.

13 Wennerstrom, A. J., Law, C. H., and Buzzell, W. A., "Investigation of a 1500 ft/sec, Transonic, High-Through-Flow, Single Stage Axial Flow Compressor With Low Hub/Tip Ratio," AFAPL-TR-76-92, Air Force Aero Propulsion Laboratory, Wright-Patterson Air Force Base, OH 45433, 1976.

14 Calvert, W. J., and Ginder, R. B., "A Quasi-Three Dimensional Calculation System for the Flow Within Transonic Compressor Blade Rows," ASME Paper No. 85-GT-22.

The Development of a Second Generation of Controlled Diffusion Airfoils for Multistage Compressors

R. F. Behlke
Project Engineer.
Commercial Engineering,
Pratt & Whitney,
United Technologies Corporation,
East Hartford, CT 06108

The evolution of Controlled Diffusion Airfoils[1] is traced from inception of the theoretical design model to demonstration of significant performance gains at engine operating conditions in a multistage compressor rig. The proven aerodynamic benefits and versatility of first-generation Controlled Diffusion Airfoil blade elements are extended to the endwall flow region using an Integrated Core/Endwall Vortex design model to produce a new full-span optimized second-generation Controlled Diffusion design. Highlighted are the essential roles of extensive cascade, low-speed, large-scale, and high Mach number compressor rig testing in developing and substantiating the second-generation Controlled Diffusion technology resulting in a 1.5 percent increase in efficiency and 30 percent increase in surge-free operation relative to first-generation Controlled Diffusion Airfoils.

Introduction

The demand for lower fuel consumption and reduced cost of modern gas turbine engines has led to a requirement for both increased efficiency and higher aerodynamic loading capability in compressors. The application of the first generation of nonstandard airfoils, designated "Controlled Diffusion Airfoils," in the seventies was a major contribution to demonstrated increases in compressor performance (Fig. 1). Commercial engine compressors with Controlled Diffusion Airfoils were improved by 2 percent in polytropic efficiency and 60 percent in pressure rise per airfoil by the early eighties. The NASA/Pratt & Whitney Energy Efficiency Engine compressor demonstrated the ability to push the improvement in pressure rise per airfoil to 150 percent of the standard airfoil technology of the seventies while improving efficiency by 1 percent. Controlled Diffusion Airfoil (CDA) technology produced benefits beyond the flowpath, rotational speed, and configuration changes by increasing both efficiency and airfoil pressure loading; it was instrumental in bringing the compressor state-of-the-art performance above 90 percent polytropic efficiency. Controlled Diffusion Airfoil technology also produced significant reductions in the airfoil count of the PW2037 and PW4000 commercial engines. As this paper will show, further gains in efficiency and surge margin are attainable with a new generation of Controlled Diffusion Airfoils.

These airfoil technical advances were built on the foundation of a modern two-dimensional compressible potential flow code combined with improved boundary layer codes providing the capability to design sections which minimize boundary layer growth and prevent boundary layer separation. When applied to the multistage core compressor environment, however, the ability of these modern airfoil sections to meet their peak aerodynamic potential is limited by the three-dimensional effects imposed by the endwall environment. Secondary flow patterns are caused by (1) cross channel, pressure-gradient induced vortices, (2) tip clearance loss in rotors, (3) cavity loss in stators, and (4) general endwall friction [1]. These patterns modify the flowfield so drastically that their effects must be accurately modeled and reflected in the design geometry to achieve peak performance. This is especially true in the middle and rear stages of

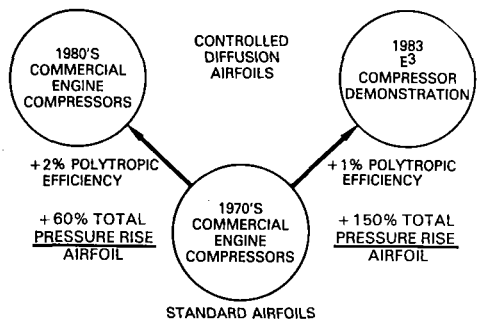

Fig. 1 First-generation controlled diffusion airfoil efficiency and loading contributions

[1] "Controlled Diffusion" is the trade name given by Pratt & Whitney to a simplified procedure for specifying the geometry of high-performance, custom-designed airfoil sections disclosed under U.S. Patent No. 4,431,376.

Contributed by the Gas Turbine Division and presented at the 1985 Beijing International Gas Turbine Symposium and Exposition, Beijing, People's Republic of China, September 1–7, 1985. Manuscript received at ASME Headquarters May 6, 1985. Paper No. 85-IGT-9.

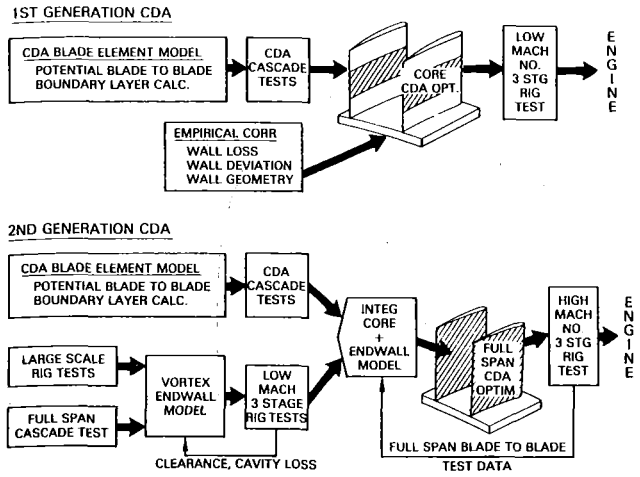

Fig. 2 Second-generation CDA design-development approach extends CDA technology to the endwalls

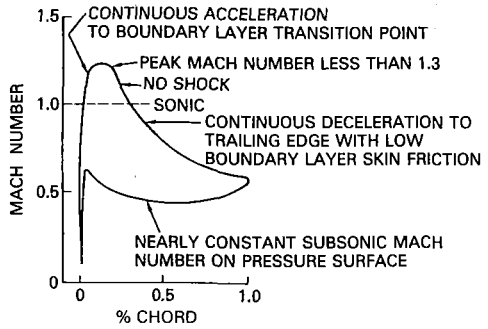

Fig. 3 First-generation CDA design criteria are adapted to the endwalls in the second-generation approach

multistage compressors where higher hub/tip ratios, lower aspect ratio, and a highly developed endwall boundary layer produce endwall efficiency penalties on the order of 5.0 percentage points. That is, about 50 percent of the total inefficiency is caused by endwall effects.

Further advances in the state of the art of multistage compressor design require a design approach that extends the refined CDA blading philosophy into the endwall region for optimized full-span performance. This paper traces the development of such a design system and its use in originating a new family of advanced compressor airfoils – second-generation Controlled Diffusion Airfoils developed for future models of modern engines. The evolution of second-generation Controlled Diffusion Airfoils (CDA-II) is followed from analytical model to performance demonstration to show the critical roles and relationship of cascade, large scale, and low Mach number compressor rigs in the development of this new technology.

Design and Development Approach

The design and development of high-speed multistage compressors is one of the most demanding technical challenges in engineering today. It is a multidimensional problem. A complex three-dimensional flowfield exists in each blade row. The multiplicity of blade rows, their aerodynamic interaction, and the desire to have all rows reach peak performance simultaneously are added dimensions. The challenge of finding and developing new technology in this atmosphere requires a sophisticated approach which accurately models the physics of these complex aerodynamic interactions.

The first-generation CDA design approach concentrated on the optimization of airfoil sections in the core, or the region of the span little affected by wall effects, using extensive cascade testing to substantiate modeling of the blade-to-blade potential flowfield and boundary layer. The endwall regions whose extent and aerodynamics were defined by simple empirical correlations were treated as boundary conditions to the core. Endwall blading was treated as an extension of the core blading modified only in metal angle based on a boundary layer approximation. The substantiation of this first-generation approach occurred in full multistage rigs in the NASA Energy Efficient Engine program and in rigs and engines of commercial engine programs.

The design-development approach presented here for second-generation Controlled Diffusion Airfoils combines an aerodynamic model with cascade, low and high Mach number rig testing to extend the proven benefits and versatility of Controlled Diffusion blade elements into the endwall region. The elements of this second-generation CDA approach are presented in flow chart form in Fig. 2 to show their relationship among themselves and to the first-generation CDA design foundation on which this approach is built. The core and endwall CDA blading elements utilizing both profile shape and angle interact through the integrated flowfield model to optimize full-span performance. The cascade, large-scale, low and high Mach number compressor rigs provide detailed flowfield and blade element data feedback to develop and substantiate aerodynamic models for wall friction, tip clearance, and cavity effects. These rigs form a comprehensively instrumented and controlled environment, which provides great accuracy in isolating and understanding aerodynamic effects. They are building blocks in the formulation and substantiation of the model leading to overall verification and feedback in high Mach number rig testing. The High Mach Number Closed Loop Compressor Test facility reproduces the engine environment to provide final verification that the technology is immediately usable under engine conditions without the necessity of transformation for Mach number and Reynolds number effects. The formulation of each of these elements and their role in the development and successful demonstration of the second-generation controlled diffusion design are discussed below.

Basic Controlled Diffusion Airfoil Foundation

The success of first-generation Controlled Diffusion Airfoils in producing increased efficiency and loading capability of subsonic and transonic airfoils in modern compressors resulted from extensive theoretical analysis and cascade testing extending back to 1974. The significant milestones in the development of this technology are presented in detail by Weingold and Hobbs [2]. The Controlled Diffusion Airfoil design criteria resulting from this technology are illustrated in Fig. 3. The major features of these criteria are (1) continuous suction surface Mach number acceleration to boundary layer transition, (2) peak Mach number less than 1.3, and (3) diffusion rate controlled to prevent separation and minimize skin friction.

Cascade test results presented in [2] confirmed that airfoil sections designed to these criteria could operate at higher Mach numbers with less loss penalty than standard airfoils and with up to 25 percent greater incidence range at a given loss. These benefits have undoubtedly contributed greatly to their success in multistage compressors where matching of the many airfoil rows, stagewise and spanwise, is a major problem. The cascade testing of these initial CDA sections also provided feedback on the accuracy of the aero codes and design criteria. An example of the agreement of design code surface Mach number prediction versus Mach number derived from test surface static pressure measurements is given in Fig. 4; the data show excellent agreement for a highly loaded 1.0 solidity section tested in both a cascade tunnel and at 50 percent span of a single stage stator. Figure 4 also reveals in its smooth monotonic closure of suction and pressure surface

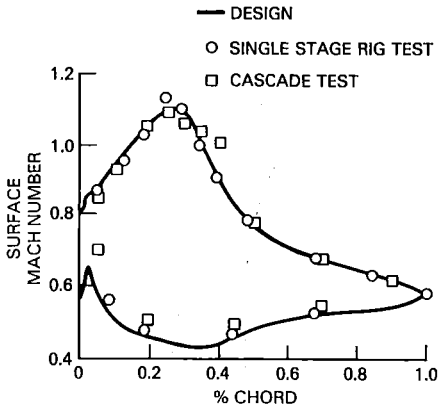

Fig. 4 Cascade and single-stage rig airfoil surface static pressure measurements verify the CDA blade element design system

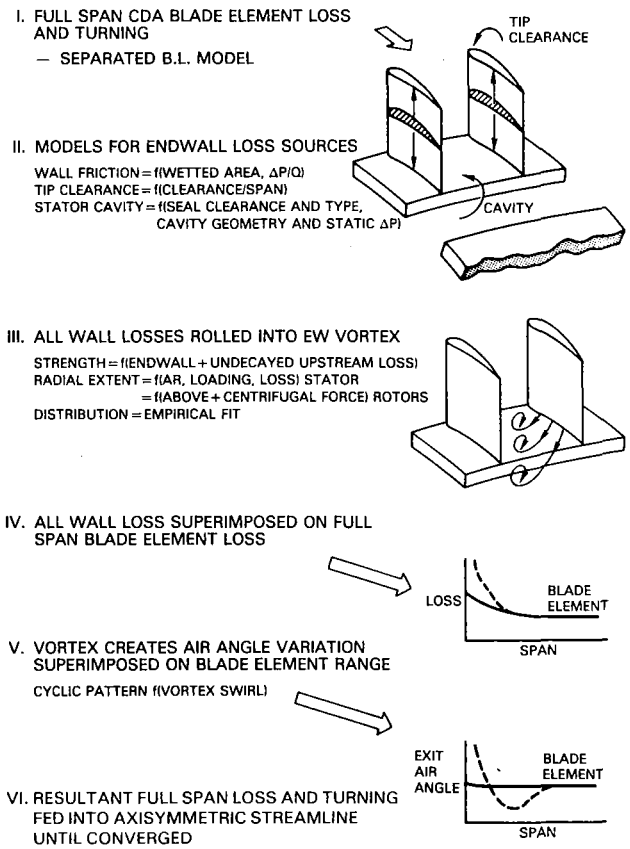

Fig. 5 Integrated core/endwall aerodynamic model used in the second-generation CDA designs

Mach numbers at the trailing edge that the design goal was met: elimination of separation by control of diffusion rate through scheduling of profile thickness and angle. The second-generation CDA approach retains this basic CDA foundation but adapts it to the endwall environment.

Extension of Basic CDA Philosophy to the Endwalls

Formulation of the Integrated Core/Endwall Aerodynamic Model. The foundation of the second-generation CDA design is the formulation of an analytical design model which accurately represents the physics of the multidimensional flowfield and its interaction with airfoil blade element geometry. The major elements of this integrated core/endwall aerodynamic model are presented in Fig. 5. This design model combines a two-dimensional, potential blade element solution with compressible boundary layer calculation from wall to wall; subroutines calculate loss and deviation when the airfoil boundary layer is separated, as often occurs near walls. Superimposed on this base are vortices which wrap up endwall loss sources including wall friction, tip clearance, shroud cavity, and undecayed upstream effects. The resultant spanwise loss and turning distributions are fed into an axisymmetric streamline program which integrates their effect on the flow field through radial equilibrium and continuity solutions.

The interaction of the CDA-designed endwall airfoil sections with the aerodynamics imposed by the endwall flowfield provide the necessary ingredients for optimizing the endwall airfoil shapes and inlet and exit angles. This provides design capability to reduce endwall loss and increase endwall loading capability for increased surge margin. An equally important feature of this system is the feedback of loss and turning from the CDA endwall airfoil sections to the endwall flowfield aerodynamic model to more accurately set the endwall blockage and boundary conditions on the two-dimensional core. This improved evaluation of interaction of core and endwall permits optimization of each for maximum overall performance. A more complete discussion of the formulation of this design system and its substantiation by cascade, large-scale, low and high Mach number rig testing follows.

Substantiation of the Vortex Aerodynamic Model in Stators. It has been shown in Fig. 4 that the CDA blade element model is effective in representing unseparated two-dimensional cascade and stator core sections. The extension of CDA blade elements to the endwalls, however, requires an analytical model capable of handling severely stalled and often separated sections. Accurate modeling of separated airfoil loss and turning is needed to provide a vehicle for determining the best section shape and angle for optimum endwall performance. A separated loss and turning model was developed for second-generation Controlled Diffusion Airfoils using two-dimensional cascade test data and added to the basic boundary layer calculation. This model relates the loss and turning of a separated cascade to the Mach number and boundary layer properties at the calculated point of separation from the potential flow/boundary layer solution. Loss is calculated for a mixing process at the separated Mach number; deviation has been modeled as a function of separation point, potential unseparated turning and cascade geometry.

A basic source of endwall loss in stators and all configurations is frictional drag. In the Integrated Core/Endwall Aero Model, friction is considered to be due to boundary layer growth resulting from the pressure gradient impressed on the endwall by the airfoil cascade. It is modeled as a function of loading ($\Delta P/Q$), Reynolds number, and cascade geometry, and integrated from blade to blade along the wall with analytical modifications for airfoil boundary layer separation and removal of fluid by the vortex. This is one of the loss sources wrapped up into the endwall vortex.

The accuracy of the model in predicting the full span loss and turning of a stator is shown in Figs. 6(*a*) and 6(*b*) for a highly loaded 65/CA cascade in which total pressure and angle measurements were taken from wall to wall. The blade element and friction elements of the model calculated loss are shown at the top of Fig. 6(*a*) while the blade element and endwall vortex ingredients of turning are presented below. The presence of underturning due to the vortex is shown in both the model prediction and the data. The ability of the blade element model to predict pressure rise of both unseparated core sections and separated endwall sections is shown in Fig. 6(*b*).

The strength of the endwall vortex in stators is increased beyond that of the above example by virtue of shroud cavity

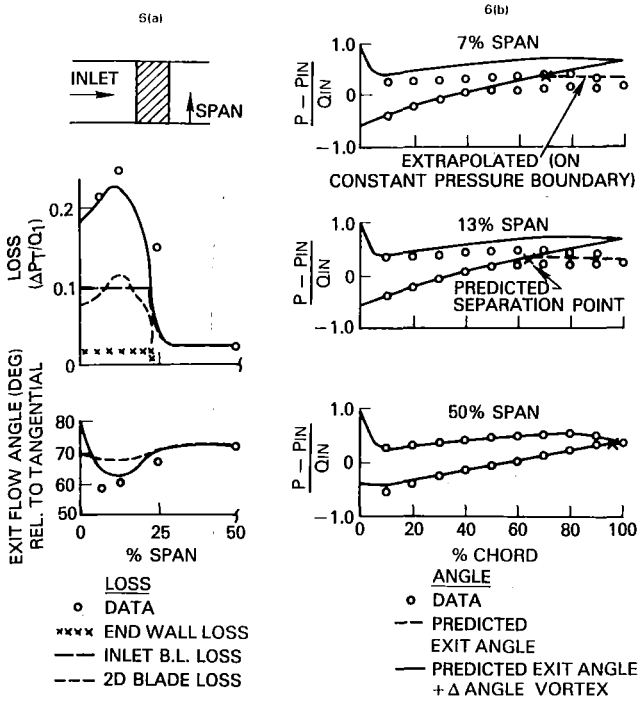

Fig. 6 Aerodynamic model matches test airfoil surface static pressure, loss, and turning at midstream and endwalls of a 65/CA stator cascade with 40 deg of camber

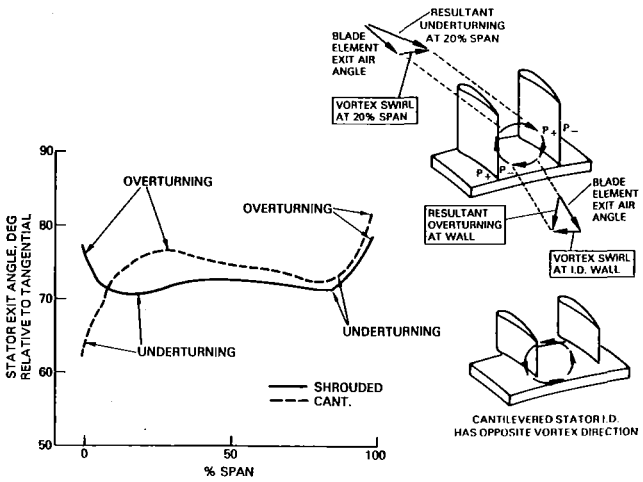

Fig. 7 Low Mach number, three-stage rig testing shows the influence of stator construction on vortex-induced endwall overturning and underturning

or cantilevered stator clearance loss. The flowfield modeling assumes that these wall losses, tip clearance, and stator cavity losses are rolled up into a vortex which cleans the endwall region of low-momentum fluid. These losses are redistributed in the vortex and are seen as an unrecoverable solid body swirl velocity superimposed on the freestream velocity. The direction and magnitude of the vortex vary according to the driving source. A tip clearance vortex is opposite in direction to the tip wall vortex with the stronger of the two setting the resultant direction. Cantilevered stator root losses are derived from a correlation of loss versus tip clearance/span while stator cavity losses have been modeled as a function of pressure rise, seal tip clearance, and cavity geometry. Both of these correlations were based on low-speed, three-stage compressor rig testing to relate performance changes to specific geometric variations. The pressure gradient of a shrouded stator root produces a vortex opposite in rotation to that of a cantilevered stator which is driven by the tip clearance flow.

These modeling concepts were graphically illustrated by back-to-back cantilevered and shrouded stator tests in the low Mach number three-stage rig shown in Fig. 7. Cantilevered and shrouded inner wall angle measurements underturned and overturned, respectively, in opposite directions, and the outer wall showed overturning for both stator constructions. The physics of the vortex model reflect the spanwise turning effects due to stator construction, as shown in these data.

Substantiation of Vortex Model in Rotors. Vortex strength and radial extent in rotors are driven by the same physical forces as in stators, but one must consider the addition of centrifugal force in the determination of radial extent. Rotor tips are modeled similar to the free ends of cantilevered stators where the sign of the clearance flow vortex is opposite to that of the solid wall. Rotor roots are geometrically similar to stator outer shrouds, but one must add a centrifugal stretching effect caused by the dragging of endwall particles up to wheel speed U by wall friction and the resultant lack of equilibrium due to high centrifugal force and low axial momentum. Rotor tips are not assumed to experience these forces, since the outer wall is not rotating and acts as a constraint to radial flow. In addition, tip leakage flow acts against swirl causing a reduction in centrifugal force.

Modeling of the rotor root vortex stretching concept was substantiated with the use of a large-scale rotating compressor rig. This rig employs its 5-ft diameter and slow rotational speed to make detailed surveys of exit total pressure and angle in the rotating reference frame of the rotor. Coupled with rotor surface static pressure measurements and flow visualization techniques, these surveys provided the ability to assess the location and strength of the vortex and determine its impact on blade element performance thus contributing to two parts of the model. This rig has been run in both isolated rotor and two stage versions. Test results for a 6-in. chord, aspect ratio of 1.0 isolated rotor with hub/tip of 0.85 [3, 4] were used in the development of the rotor model. Figure 8 compares the model-predicted blade element pressure coefficient with test-measured values on the rotor pressure and suction surfaces of this rig. Predicted values are in close agreement with suction surface measured values across most of the span; this provides an accurate basis for calculating loss and turning. The more stalled-looking test distributions on the root sections are not duplicated exactly by the model, but the overall pressure rise is closely matched. The model is calibrated to produce correct overall pressure rise and loss, permitting the optimization of endwall sections.

The lack of a viscous interaction between the potential flow and boundary layer calculations and the circumferential averaging of inlet and exit boundary conditions are compensating approximations in this approach which tend to facilitate the calibration of overall properties. An exact three-dimensional solution with viscous effects would be more desirable, but it would add significant complexity and is beyond current computational capability in multistage compressors. The simplified modeling presented here produces the correct overall result; it will be shown to provide an excellent basis for developing improved endwall performance technology.

A final substantiation of the analytical model using the Large Scale rig data was the comparison of the model's integration of core and endwall loss and turning with measured values. The measured spanwise total pressure loss curve and measured rotor relative exit air angle in Fig. 9 agree closely with predicted values. The large tip loss and underturning of this blade reflect its large tip clearance of 2.2 percent span. It is also evident in the test root loss that centrifugal stretching

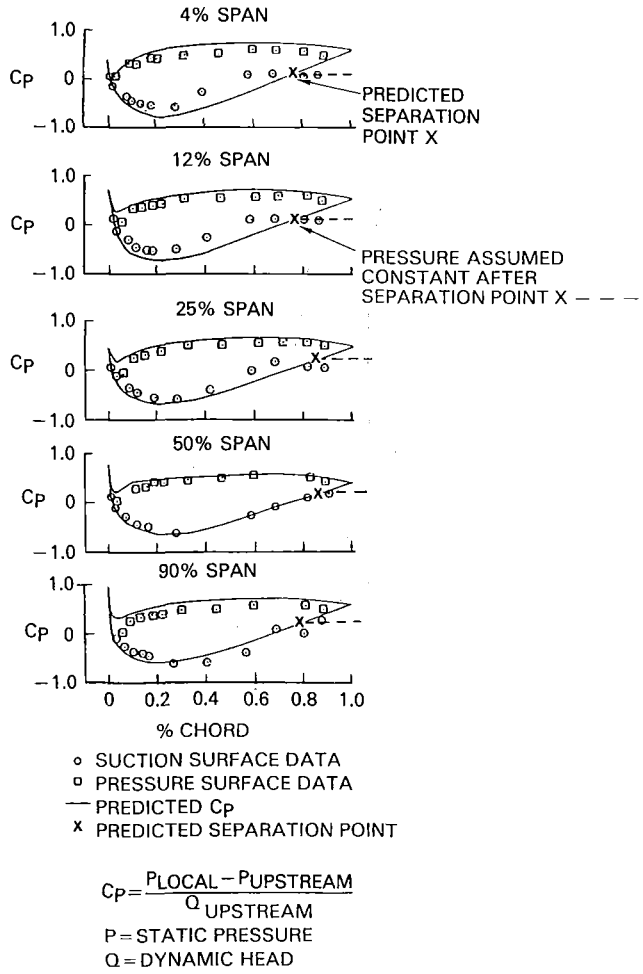

Fig. 8 Surface static pressure measurements in the rotating frame of the Large-Scale rig confirm the aerodynamic model to within 4 percent span of the wall

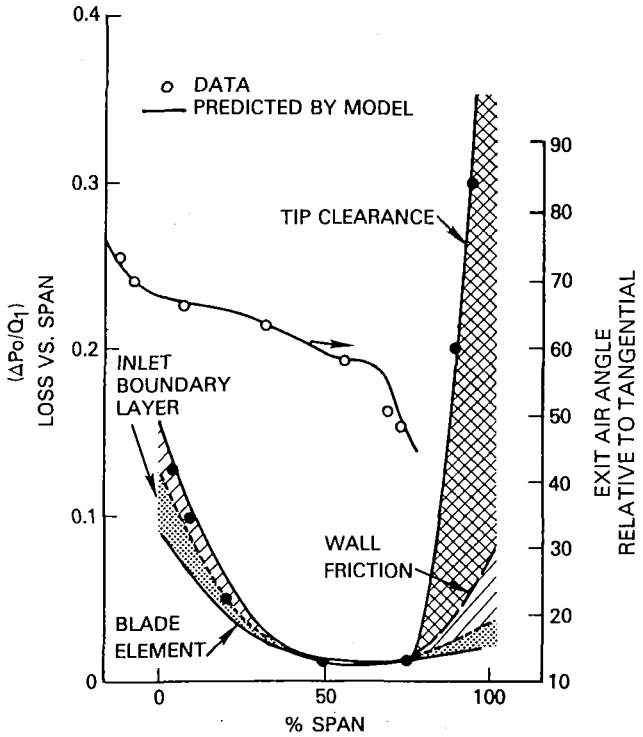

Fig. 9 Large-Scale rig loss and angle measurements confirmed the integrated Core/Endwall model predictions in the rotating frame

out of the loss to 50 percent of span is well represented by the model. Without this centrifugal stretching parameter the predicted endwall loss would have extended only to 25 percent of span and underestimated the loss at that span.

Substantiation of Multistage Effects Using Low-Speed Rigs. The previous sections were concerned with the development and substantiation of individual elements of the analytical model which are present in isolated blade rows. This section addresses the need to model differences in the flow field caused by linking these blade rows in a multistage compressor.

The added element occurring in the prediction of multistage performance is the necessity to translate aerodynamic conditions from upstream to downstream blade rows. In this relatively short axial interval, wakes decay, vorticity dissipates, spanwise profiles are mixed, and a change in reference frame occurs. These phenomena are treated in the Integrated Core/Endwall model by two devices: the spanwise profiles and a retained vorticity parameter. Blade row discharge blade element total pressure, total temperature, and angle profiles are transferred at constant angular momentum along streamlines to the downstream row leading edge. It is assumed that, in the core region of the span, wakes are dissipated before reaching the following row's leading edge. In the endwall region, however, the upstream vorticity and wakes were found to strengthen the downstream row's vortex based on studies of differences between isolated rotors and several multistage compressors. This incomplete mixing process was found to follow a logarithmic function of axial gap between rows, upstream chord, airfoil circumferential spacing, and the strength of the loss source. The analytical model with this downstream decay feature was employed to predict multistage rigs of differing axial gaps, blading geometry, and endwall defects to test and develop its predictive capability. Two pairs of these prediction examples will be presented here.

Low Mach number, three-stage rig tests were chosen to illustrate the model's predictive ability for a multistage rig with close axial gapping (16 percent of chord) and strong endwall effects by virtue of its low aspect ratio (1.0). The low Mach number, three-stage rig has been used to assess a large number of aerodynamic and geometric parameters including flowpath, airfoil tip clearance, and cavity variations.

The three-stage rig has the capability to independently vary rotor and stator stagger to optimize matching at different loading levels. Leading-edge and overall total pressure and temperature pole rake instrumentation as well as extensive wall static pressure measurements in a controlled environment make this rig a valuable developmental tool. It is employed to assess overall performance and stage matching; more importantly, it is capable of assessing spanwise profile differences as parameters are varied to evaluate endwall health. A comparison of the model-predicted total pressure and total temperature profiles versus test values for the third stator leading edge of a baseline build of this rig in Fig. 10 shows good overall agreement in shape. The large pressure defect below 50 percent span in the test data is also well represented by the model, reflecting a strong vortex due to the low aspect ratio which feeds downstream as a result of the close axial gaps. A test in this same rig of a 5-deg closed restagger of the blading also provided an opportunity to assess the model's ability to predict performance differences due to geometry changes. Comparison of exit spanwise profiles and overall performance for these two rigs to model-predicted values are given in Fig. 11. As in the internal leading-edge data comparisons the spanwise character of the profiles is represented closely. The overall performance difference resulting from the increased loading at reduced stagger is also closely predicted.

Data published in [5, 6] by General Electric from a large-

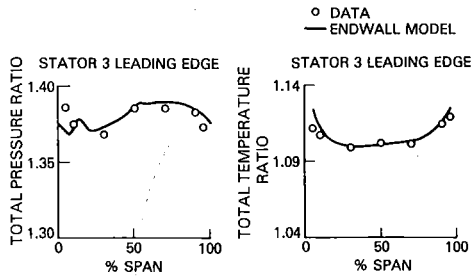

Fig. 10 Integrated Core/Endwall model predicts spanwise profiles of the low Mach number, three-stage rig, illustrating its multistage capability

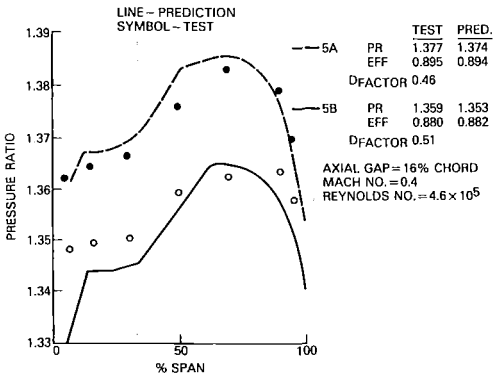

Fig. 11 Integrated Core/Endwall model matched spanwise profiles and overall performance differences of the low Mach number, three-stage rig at two loading levels

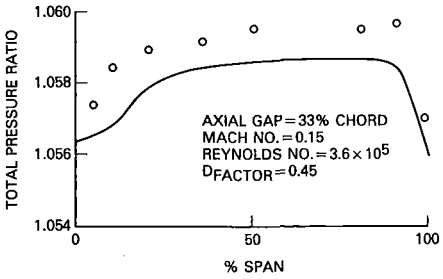

Fig. 12 Aerodynamic model matches the exit pressure profile of the G.E. large-scale four-stage rig [5]

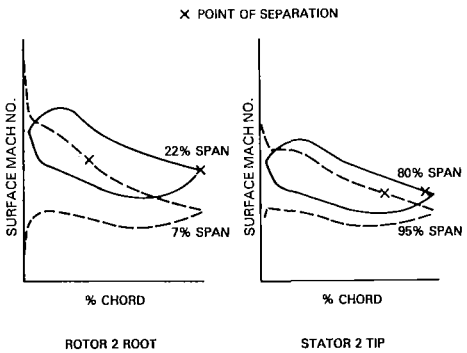

Fig. 13 Analysis of the first-generation CDA baseline design with the integrated Core/Endwall model showed severely separated wall sections and unseparated core sections

scale four-stage rig also provided an opportunity to test the model's ability to predict performance for a more widely spaced (33 percent chord) and higher aspect ratio (1.2) rig. As might be expected, the endwall pressure fall-off shown in Fig. 12 is not as pronounced as that of the lower aspect ratio more closely spaced three-stage rig previously discussed. The Integrated Core/Endwall model captures the essence of this

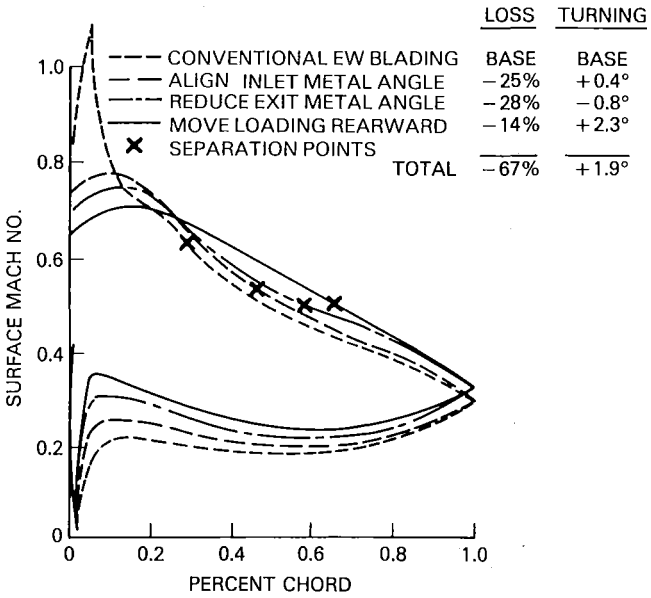

Fig. 14 Second-generation CDA endwall geometry changes were predicted to produce significant improvements in loss and turning by reducing separation of first-generation CDA's

fuller profile in the comparison in Fig. 12, although the innermost pressure reading falls off more than predicted. It is noteworthy that the model predicted the overall test efficiency gain of 0.3 percent when the stators of this rig were twisted closed at the endwalls by 8.0 deg. The predicted efficiency gain was primarily within 20 percent of the endwalls where the twists occurred and where the major differences in test pressure profiles occurred.

Design of Second-Generation Controlled Diffusion Airfoils. The previous sections have shown that the elements of the Integrated Core/Endwall aerodynamic model represent the physics of the endwall and core flowfields and their interaction with one another. The design philosophy of the first-generation Controlled Diffusion Airfoils is to apply high diffusion in the forward section of the airfoil chord where the boundary layer is thin and decrease the rate of diffusion aft according to the boundary layer health to prevent separation. This provided a decided benefit over previous standard airfoil series most of which had 10–15 percent of their chord separated. The same philosophy was extended from the core into the endwall region with only general recognition of the different nature of its flowfield.

The Integrated Core/Endwall model used in the analysis mode showed that the endwall blading of the first-generation CDA design, which had demonstrated 1980s state-of-the-art spanwise average efficiency, was at stalled incidence with severely separated boundary layers. As illustrated in Fig. 13, the wall sections were analyzed to have excessive suction surface leading edge overspeed and resultant early separation compared to typical core sections. This separation occurred at both walls despite leading and trailing edge overcambers developed through years of testing and based on empirical data and simplified wall boundary layer modeling. It is also doubtful that the core blading of this design was operating at full capacity due to the change in the radial flowfield caused by the stalled endwall, although empirical blockage factors derived from test checkouts could account for much of it in this highly developed compressor. However, design studies conducted with the Integrated Core/Endwall Model revealed several blade angle and shape changes to improve endwall and overall performance. Model results for one representative endwall section are presented in Fig. 14 to illustrate the

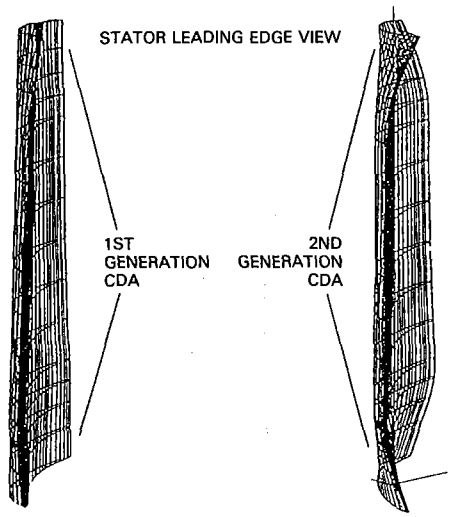

Fig. 15 The radially stacked sections of the second-generation CDA design reveal significantly more skewing of metal angle in the endwall region compared to first-generation CDA's

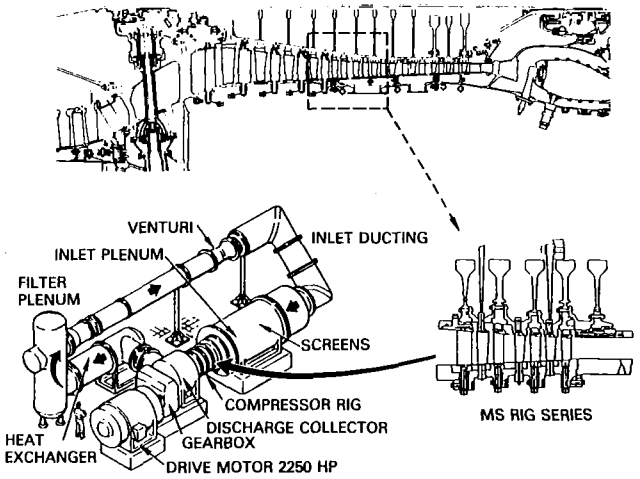

Fig. 16 Middle stages of a modern, commercial HPC were duplicated and tested at engine size, Reynolds number, and Mach number in a modern, closed-loop facility to establish a realistic baseline

benefits of endwall geometry changes. The most influential change was to match leading edge blade angle in the endwall region to prevent the suction surface overspeed.

The aerodynamic model predicted that aligning the leading-edge metal angle would delay boundary layer separation 15 percent further aft on the blade chord and result in a 25 percent predicted reduction in loss of this typical rotor root endwall section. The model indicated the reduction in loss and a 0.4-deg increase in turning were derived by eliminating suction surface overspeed and rapid recompression, as shown in Fig. 14, producing a healthier boundary layer.

The increase in turning and reduction in loss by aligning leading-edge incidence leads to the prospect of reducing work in the endwall sections. Trailing-edge metal angles can be reduced while still meeting the original design pressure ratio because of the more efficient sections. Studies showed that reducing the camber to reduce exit air angle only 0.8 deg resulted in a 28 percent reduction in total pressure loss cumulative with the leading-edge alignment benefit.

One of the major objectives of the second-generation CDA design was to exploit the potential of CDA section shape in improving endwall performance. Analysis showed that aft loading of the endwall sections by increasing the camber rate of the rear while reducing that of the front part of the airfoil chord resulted in a further 14 percent reduction in loss, 5 percent movement aft of the separation point, and a 2.3 deg increase in section turning.

The improvement in separation point and loss by moving diffusion aft was beneficial due to the high degree of separation in the endwall region. Core airfoil sections with 10 to 15 percent of their chord separated can be made unseparated by moving diffusion forward, but an endwall section with 30 percent or more of its chord separated cannot sustain enough front loading to eliminate separation. In this environment, the amount of separation was predicted to be reduced by *unloading* the front part of the airfoil resulting in a net predicted benefit in loss and turning. Since the benefit of the aft loading concept depended on the degree of separation, it was applied after employing the improved incidence and reduced work and was still predicted to improve loss and turning.

The cumulative total benefits of these three endwall geometry innovations tabulated in Fig. 14 is a 67 percent predicted reduction in loss and 1.9-deg increase in turning for this typical section near the inner endwall. The amount of recambering of leading and trailing-edge angles and the section shape modifications varied depending on the airfoil row and spanwise position, due to the differing friction vortex strengths and extents of each section location. The mass-flow averaged, full-span, overall three-stage benefit of these endwall geometries when combined with the integrated core design was predicted to be approximately 1 percent in efficiency at 1.85 pressure ratio. The reduction in required work in the endwalls and the more efficient endwall sections also reduced aerodynamic loading in the endwalls, potentially improving surge margin. The more stable state of the boundary layer on these endwall sections should delay their aerodynamic breakdown as often occurs when the compressor is throttled up the speedline. Analysis of the improved endwall sections showed a 0.15 average reduction in diffusion factor and a reduced sensitivity to stalling incidence equivalent to 6 percent surge margin.

It is interesting to note that Wisler [5] showed similar endwall geometry trends for improved performance based on low-speed model testing. His geometry modifications were derived from direct analysis of test results, however, rather than a flow field model, and were applied differently. In Wisler's work, geometry twist gradients were applied only to stators in response to their separated pressure distributions, and aft-loaded sections were concluded to be beneficial only at rotor tips due to the tip leakage effect on surface pressure distribution; both concepts were found to be beneficial at all wall sections in the CDA-II studies discussed here.

A sample second-generation CDA stator stacked airfoil view from this rig design is presented in Fig. 15. Note the impression of a twisted closed endwall given by the leading-edge alignment and reduction in work of the endwall sections. Although this CDA-II design is derived from a significantly more sophisticated model and analysis than previous designs, it is still partially empirical: a simplified approach to a very complex problem. In short, it is in need of test substantiation and development under realistic engine conditions.

High Mach Number Multistage Rig Demonstration of Second-Generation CDA Benefits

Comparative First-Generation CDA Baseline Tests. The final objectives in the development of new technology are the demonstration of its benefits and its rapid assimilation into production engines. These objectives were met for the second-generation CDA geometry by demonstrating its performance in a high Mach number multistage rig test back to back with a first-generation CDA baseline. The closed-circuit compressor test facility (Fig. 16) was designed specifically for this purpose by providing the capability to test full-size engine hardware at

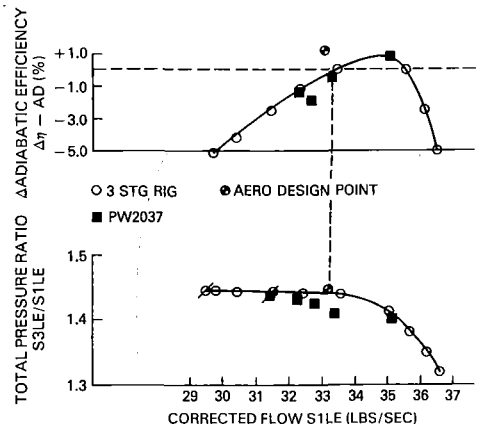

Fig. 17 Overall characteristics of the commercial engine HPC middle stages tested in the closed-circuit test facility matched interstage instrumentation results from full-rig testing

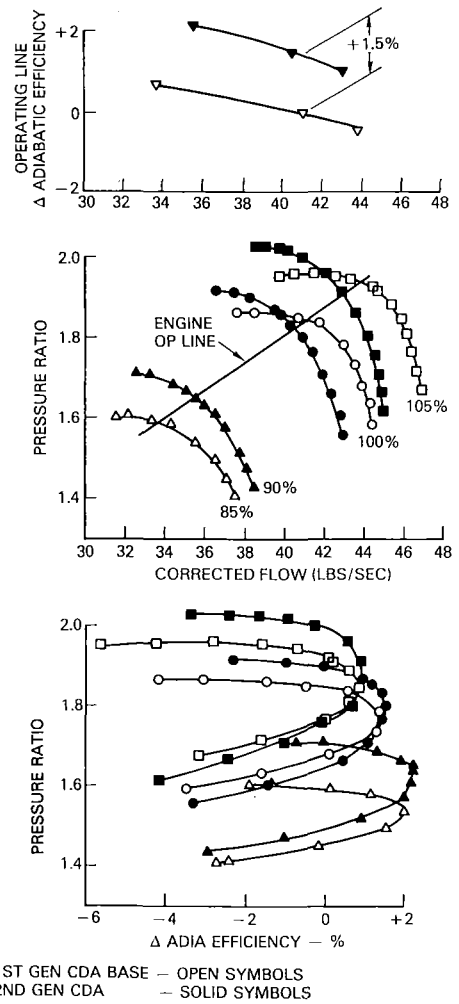

Fig. 18 Second-generation Controlled Diffusion Airfoils increased operating line efficiency by 1.5 percent with 8 percent increased surge margin

engine levels of Mach number and Reynolds number. In this modern facility a heat exchanger is utilized to control rig inlet temperature while inlet pressure is boosted by an outside pressure source to vary Reynolds number. The 2250 hp motor permits testing in the size range of engine compressors using three stages to establish the multistage effects, but maintains a sizable cost advantage over testing the full compressor.

The middle three stages of the PW2037 commercial engine high-pressure compressor were duplicated in exacting

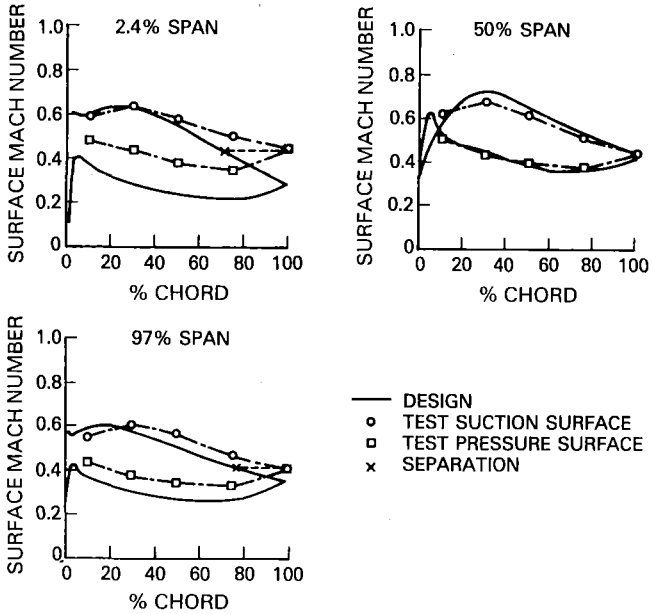

Fig. 19 High Mach number, three-stage test airfoil surface static pressure measurements match second-generation airfoil design intent

aerodynamic detail, as shown in Fig. 16, to establish a realistic modern baseline for the development of second-generation Controlled Diffusion Airfoils. This rig has adjustable rotor and stator capability for aero development, but it has maintained the airfoil, flowpath, tip clearance, and cavity dimensions of the original engine stages. A comparison of the closed-loop baseline rig test characteristics with those of the equivalent PW2037 stages taken from an engine development high compressor test is presented in Fig. 17.

The middle-stage group was tested with an inlet screen and inlet preswirl vanes to duplicate inlet boundary conditions from the engine. The close agreement of pressure and efficiency characteristic shapes attests to the care taken to duplicate engine geometry and operating environment. This middle-stage group rig is, therefore, a viable baseline for assessing the benefits of the second-generation Controlled Diffusion Airfoils.

High Mach Number Rig Testing of Second-Generation CDA Benefits. The test evaluation of second-generation Controlled Diffusion Airfoils at engine operating conditions in the high Mach number three-stage rig was both a performance success and a verification of the design-development system used. The as-designed CDA-II geometry produced a 1.5 percent increase in operating line efficiency and 8 percent increased surge margin relative to the CDA-I baseline as shown in the compressor map of Fig. 18. The CDA-II speed line was notably more vertical than that of the baseline indicating that the endwalls were less stalled and able to sustain higher loading with less loss. The goal of matching the combined core and endwall at peak performance on the operating line was achieved; this resulted in a 1.5 percent efficiency gain on the operating line, where it will have the greatest impact on engine performance. A subsequent test in this rig revealed that efficiency and surge margin gains were substantially retained when the small flow deficit of the CDA-II in Fig. 18 was eliminated by adding camber to the endwall region. This improvement has been designed into future models of commercial engines.

Although the performance improvements produced in High Mach Number Rig testing are of great value to the engines which can immediately absorb them, the feedback of data into the design-development system is of equal importance to

future engines. Comparison of Mach number derived from airfoil surface static pressure measurements in Fig. 19 provides a direct comparison of the modeled aerodynamics to test.

Predicted vane suction and pressure surface Mach numbers are reasonably good matches of the test shape and excellent matches of the overall diffusion at the inner wall, midspan, and outer wall sections. Predicted midspan Mach number distribution is nearly identical to the test and confirms the design intent of eliminating separation by diffusing smoothly to the trailing edge. The wall section predicted Mach number shapes are not as perfect matches of test as at midspan, but follow shape reasonably well and match overall diffusion at the predicted separation point. A closer match of shape would be possible as previously discussed, if the viscous solution were recycled through the potential field calculation and iterated to a final solution. The fact that the overall performance of the CDA-II geometry designed with this model was successful suggests that this procedure is a reasonable basis for design.

Concluding Remarks

The successful demonstration of second-generation CDA geometry at engine conditions has shown that the extension of CDA technology to the endwalls using an Integrated Core/Endwall aerodynamic model is an effective approach to developing new technology in multistage compressors. The 1.5 percent increase in operating line efficiency and 8 percent gain in surge margin confirms the overall design-development system of cascade, low and high Mach number rigs which supported this design model. These significant performance gains represent a new plateau of technology which must be exploited for maximum advantage to forthcoming engine multistage compressors. The improved surge margin of 8 percent is a 30 percent increase in surge-free operating capability, which can be used to push to higher lift/drag airfoils resulting in either fewer airfoils or greater pressure ratio per stage. Employing three-dimensional Euler multigrid/Navier-Stokes improved flowfield definitions translated from fan experience into multistages, these high lift/drag principles can be transformed into the compact, high-performance compressors needed for future high-thrust/weight fuel efficient engines. These future generations of Controlled Diffusion Airfoils have the potential of improving multistage compressor efficiency an additional 1 to 2 percentage points with surge margins at least as good as present-day compressors.

Acknowledgments

The work described in this paper was accomplished by design, development, and test groups at Pratt & Whitney and the United Technologies Research Center. The success of this research is attributed to their spirit of cooperation and team effort.

References

1 Adkins, G. G., Jr., and Smith, L. H., Jr., "Spanwise Mixing in Axial-Flow Turbomachines," ASME JOURNAL OF ENGINEERING FOR POWER, Vol. 104, Jan. 1982.

2 Hobbs, D. E., and Weingold, H. D., "Development of Controlled Diffusion Airfoils for Multistage Compressor Application," ASME JOURNAL OF ENGINEERING FOR GAS TURBINES AND POWER, Vol. 106, No. 2, Apr. 1984, pp. 271–278.

3 Wagner, J. H., Dring, R. P., and Joslyn, H. D., "Inlet Boundary Layer Effects in an Axial Compressor Rotor: Part I—Blade-to-Blade Effects," ASME JOURNAL OF ENGINEERING FOR GAS TURBINES AND POWER, Vol. 107, No. 2, Apr. 1985, pp. 374–380.

4 Wagner, J. H., Dring, R. P., and Joslyn, H. D., "Inlet Boundary Layer Effects in an Axial Compressor Rotor: Part II—Throughflow Effects," ASME JOURNAL OF ENGINEERING FOR GAS TURBINES AND POWER, Vol. 107, No. 2, Apr. 1985, pp. 381–386.

5 Wisler, D. C., "Loss Reduction in Axial Flow Compressors Through Low-Speed Model Testing," ASME JOURNAL OF ENGINEERING FOR GAS TURBINES AND POWER, Vol. 107, No. 2, Apr. 1985, pp. 354–363.

6 Wisler, D. C., "Blading Design," Vol. I, NASA CR-135391, Dec. 1977; "Core Compressor Exit Stage Study," Vol. IV, NASA CR-159499, Apr. 1981.

future engines. Comparison of Mach number derived from airfoil surface static pressure measurements in Fig. 19 provides a direct comparison of the modeled aerodynamics to test.

Predicted vane suction and pressure surface Mach numbers are reasonably good matches of the test shape and excellent matches of the overall diffusion at the inner wall, midspan, and outer wall sections. Predicted midspan Mach number distribution is nearly identical to the test and confirms the design intent of eliminating separation by diffusing smoothly to the trailing edge. The wall section predicted Mach number shapes are not as perfect matches of test as at midspan, but follow shape reasonably well and match overall diffusion at the predicted separation point. A closer match of shape would be possible as previously discussed, if the viscous solution were recycled through the potential field calculation and iterated to a final solution. The fact that the overall performance of the CDA-II geometry designed with this model was successful suggests that this procedure is a reasonable basis for design.

Concluding Remarks

The successful demonstration of second-generation CDA geometry at engine conditions has shown that the extension of CDA technology to the endwalls using an Integrated Core/Endwall aerodynamic model is an effective approach to developing new technology in multistage compressors. The 1.5 percent increase in operating line efficiency and 8 percent gain in surge margin confirms the overall design-development system of cascade, low and high Mach number rigs which supported this design model. These significant performance gains represent a new plateau of technology which must be exploited for maximum advantage to forthcoming engine multistage compressors. The improved surge margin of 8 percent is a 30 percent increase in surge-free operating capability, which can be used to push to higher lift/drag airfoils resulting in either fewer airfoils or greater pressure ratio per stage. Employing three-dimensional Euler multigrid/Navier-Stokes improved flowfield definitions translated from fan experience into multistages, these high lift/drag principles can be transformed into the compact, high-performance compressors needed for future high-thrust/weight fuel efficient engines. These future generations of Controlled Diffusion Airfoils have the potential of improving multistage compressor efficiency an additional 1 to 2 percentage points with surge margins at least as good as present-day compressors.

Acknowledgments

The work described in this paper was accomplished by design, development, and test groups at Pratt & Whitney and the United Technologies Research Center. The success of this research is attributed to their spirit of cooperation and team effort.

References

1 Adkins, G. G., Jr., and Smith, L. H., Jr., "Spanwise Mixing in Axial-Flow Turbomachines," ASME JOURNAL OF ENGINEERING FOR POWER, Vol. 104, Jan. 1982.

2 Hobbs, D. E., and Weingold, H. D., "Development of Controlled Diffusion Airfoils for Multistage Compressor Application," ASME JOURNAL OF ENGINEERING FOR GAS TURBINES AND POWER, Vol. 106, No. 2, Apr. 1984, pp. 271–278.

3 Wagner, J. H., Dring, R. P., and Joslyn, H. D., "Inlet Boundary Layer Effects in an Axial Compressor Rotor: Part I—Blade-to-Blade Effects," ASME JOURNAL OF ENGINEERING FOR GAS TURBINES AND POWER, Vol. 107, No. 2, Apr. 1985, pp. 374–380.

4 Wagner, J. H., Dring, R. P., and Joslyn, H. D., "Inlet Boundary Layer Effects in an Axial Compressor Rotor: Part II—Throughflow Effects," ASME JOURNAL OF ENGINEERING FOR GAS TURBINES AND POWER, Vol. 107, No. 2, Apr. 1985, pp. 381–386.

5 Wisler, D. C., "Loss Reduction in Axial Flow Compressors Through Low-Speed Model Testing," ASME JOURNAL OF ENGINEERING FOR GAS TURBINES AND POWER, Vol. 107, No. 2, Apr. 1985, pp. 354–363.

6 Wisler, D. C., "Blading Design," Vol. I, NASA CR-135391, Dec. 1977; "Core Compressor Exit Stage Study," Vol. IV, NASA CR-159499, Apr. 1981.

DISCUSSION

I. G. Rice, P.E[2]

It is true that considerable progress has been made during the past few years with axial flow compressors in the area of greater efficiency and higher pressure rise per stage, wherein better three-dimensional-flow computer programs have been developed. The NASA E^3 program funded by the U.S. Government has, as their author states, been very successful.

Reference is made to Fig. 15 of the paper. The leading and trailing edges of the second-generation CDA rotating blades seem to resemble the Rolls-Royce compressor blade "end-bend" shape developed for the RB211-535 E4 engine, and in this regard the effect of endwall region flow distortion has been previously known and dealt with. If Rolls-Royce has presented any technical papers on this subject, such papers should be included by the author in the reference list. The effect of CDA on the final tip and root shape is admittedly another situation, however.

There also appears to be a similarity between the CDA shape and Whitcomb's (NASA) supercritical airfoil shape (U.S. Patent No. 3,952,971). Both airfoils work in a similar manner by subduing the shock wave; but the CDA, when operating in a cascade, lets the supersonic velocity down much closer to the leading edge. The author might comment on the similarities and differences.

[2]Consultant, Spring, TX 77373; Fellow ASME

Before World War II it was the gas turbine industrial arena that brought forward the axial flow compressor – notably Brown-Boveri of Switzerland. After WWII the aircraft Research and Development for jets took the lead with the second-generation jets; and now the third generation is presently emerging. Industrial gas turbine manufacturers in turn have applied the jet engine developments to industrial prime movers. There is a need to expedite this new E^3 technology for industrial use. The aircraft manufacturers can help in this regard.

We are on the threshold of being able to make a 38 to 42-cycle pressure ratio gas turbine to operate at continuous combustor outlet temperatures of 2400°F (1316°C). Such turbines are directly applicable to the new fan jets, ducted and unducted, that operate as simple cycle mechanical drive machines. The key to such future gas turbines lies in the axial flow compressor and the contribution being made through CDA and end-bend innovations. Such gas turbines can be adapted to reheat for industrial power plants to obtain very high combined cycle efficiencies.

The challenge lies in applying innovations such as reheat and steam blade cooling using third-generation high-pressure ratio jet engines where the market is somewhat limited in terms of numbers of units compared to aircraft use. The industrial market must, by necessity, rely on jet R & D as there is very little, if any, industrial U.S. Government funding taking place. More rapid cross pollination is not only needed, but it is

obligatory. The U.S. must compete effectively with Japan in the industrial world market.

Author's Closure

The author wishes to thank Mr. Rice for his comments on this paper. It is true that pictures of the Rolls-Royce RB211-535E4 airfoils appearing in aviation periodicals have a similarity to the second-generation Controlled Diffusion Airfoil presented in Fig. 15. It is nearly impossible, however, to discern from a pictorial comparison whether the skewed endwall appearance reflects predominant leading edge "end bend," trailing edge end bend, or both because of the strong influence that stacking axis selection has on airfoil shape. Development end bends are not new. They have been used in commercial compressors since the late 1950s. The intent of the subject paper was to show that end bends can be effectively designed using a full-span aerodynamic model and to demonstrate the effectiveness of this approach in a realistic test. Rolls-Royce, however, has not published a technical document in the open literature describing the aerodynamic philosophy or design execution of their airfoils nor have they presented test data to substantiate the performance benefits of their geometry. The lack of these facts makes it impossible to provide a meaningful comparison.

In regard to Mr. Rice's request for a comparison of Controlled Diffusion Airfoil aerodynamics to the Whitcomb airfoil, the paper by Weingold and Hobbs [2] gives a good accounting of the evolution of high Mach number Controlled Diffusion Cascade Airfoils from the supercritical isolated airfoil principles.

Finally, the author agrees with Mr. Rice's closing comment that these advanced generations of compressor airfoils are fundamental building blocks for the high overall pressure ratio high performance engines of the future. The demonstrated increase in surge margin can be used to produce greater pressure ratio per stage to produce greater overall pressure ratio at high efficiency without causing excessive axial length or airfoil count.

Comparison of Calculated and Experimental Cascade Performance for Controlled-Diffusion Compressor Stator Blading

N. L. Sanger
NASA Lewis Research Center,
Cleveland, OH 44135

R. P. Shreeve
Naval Postgraduate School,
Turbomachinery Laboratory,
Monterey, CA 93940

The midspan section of a previously reported controlled-diffusion compressor stator has been experimentally evaluated in cascade. Measurements were taken over a range of incidence angles for blade chord Reynolds numbers from 470,000 to 690,000. Blade chord length was 12.7 cm, aspect ratio was 2.0, and solidity was 1.67. Measurements included conventional cascade performance parameters as well as blade surface pressures. Computations were made for the inviscid flow field, surface boundary layers, and loss for several of the blade inlet angle conditions, and compared against corresponding data.

Introduction

In a paper presented at a recent International Gas Turbine Conference, the design of a controlled diffusion compressor stator using an automated design procedure based on numerical optimization was described [1]. The controlled-diffusion stator was a redesign of the first stage stator of the NASA two-stage fan [2]. The original design was highly successful, demonstrating a first stage peak abiabatic efficiency of 87 percent, and a radial distribution of loss across the stator which was remarkably low. The purpose of the redesign was to develop and demonstrate the feasibility of an automated design process using numerical optimization methods. Although significant performance improvement from an already excellent stator design was not expected, at least equivalent performance was expected. In addition, the redesigned stator was intended to provide a research vehicle for the new controlled-diffusion class of blading.

As described in [1], the controlled-diffusion stator was designed using a series of computational analysis methods coupled by a numerical optimization procedure. The blade shapes were specified by a geometry code extracted from the NASA throughflow compressor design program [3]. Blade section mean lines and thickness distributions were described by several polynomial curves. The potential flow about each two-dimensional blade section was calculated by the TSONIC code developed by Katsanis [4]. Surface boundary layers were calculated using the McNally BLAYER code [5], and the optimization procedure used to couple all of the aerodynamic and geometric codes together was the COPES/CONMIN code [6, 7].

The midspan section of the blade has been built and tested

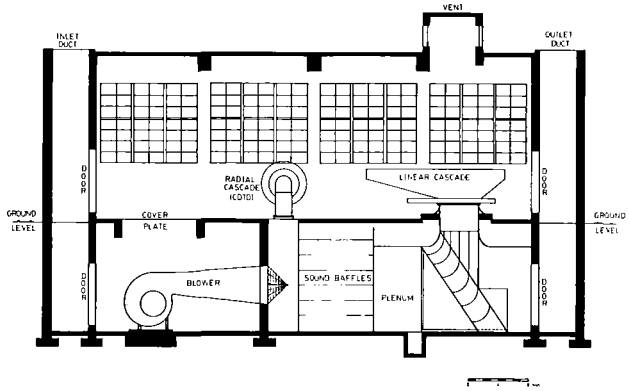

Fig. 1 Cascade wind tunnel test facility

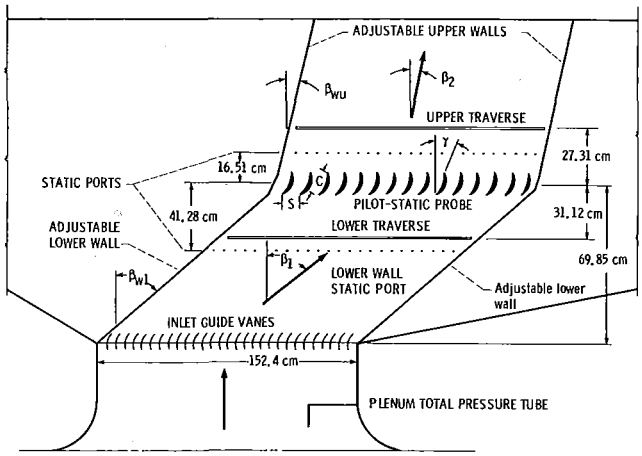

Fig. 2 Test section instrumentation and physical dimensions

Contributed by the Gas Turbine Division of THE AMERICAN SOCIETY OF MECHANICAL ENGINEERS and presented at the 31st International Gas Turbine Conference and Exhibit, Düsseldorf, Federal Republic of Germany, June 8–12, 1986. Manuscript received at ASME Headquarters January 8, 1986. Paper No. 86-GT-35.

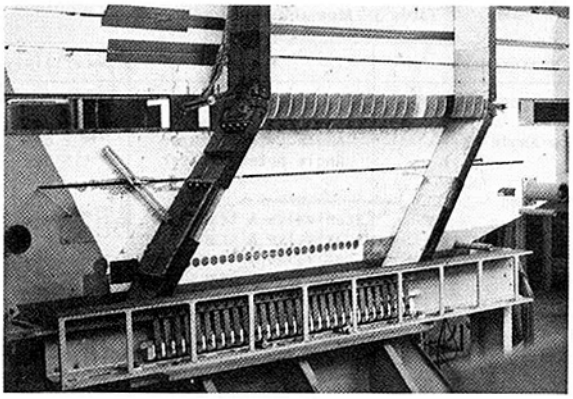

Fig. 3 Cascade test section with front wall removed

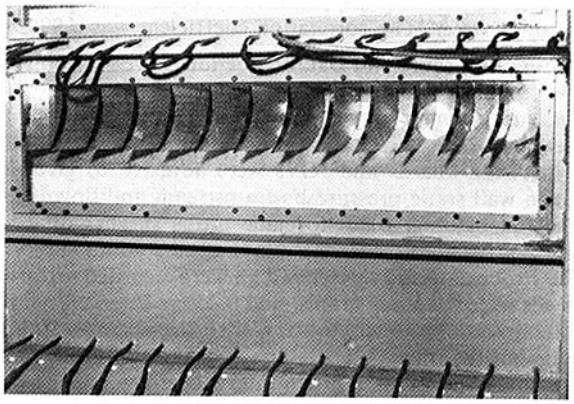

Fig. 4 View of test blading through plexiglas window

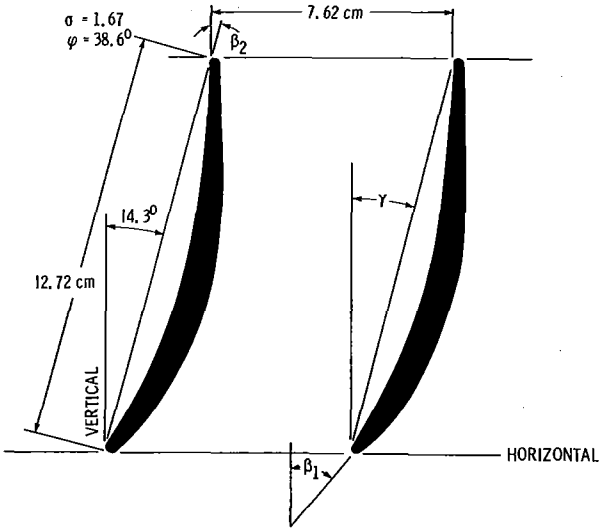

Fig. 5 Cascade geometry

in a cascade windtunnel at the Naval Postgraduate School. Although inlet Mach numbers (0.2) in this subsonic tunnel are less than the design level (0.68), experiments can be conducted at realistic Reynolds numbers (500,000 to 700,000) on relatively large-scale blading (12.7-cm chord), on which detailed surface pressures can be obtained. Furthermore, since the computational codes used to design the blading were quasi-three-dimensional and steady state, it is of interest to obtain experimental data in a similar flow environment, as well as in the real, unsteady, fully three-dimensional environment of the compressor stage. The data obtained in cascade provide an excellent opportunity to assess the accuracy of the flow codes not only at the design point, but also at off-design conditions. In this report, data obtained over the full range of incidence angle (including flow visualization data) are compared against the calculated results from several flow codes.

Experimental Program

Description of the Test Facility. The arrangement of the cascade wind-tunnel facility is shown in Fig. 1. The tunnel is supplied by a 700 hp blower in the basement of the building through an arrangement of sound baffles and turning vanes. The air enters the tunnel through two, two-dimensional bellmouth contractions in series which produce a 152.4 by 25.4 cm (60 by 10 in.) section just above floor level. The 25.4-cm width is maintained between heavy side walls, between which an adjustable test section is formed as shown in Fig. 2. The blades of the test cascade are mounted in a rack which can be moved along the (fixed) back wall. The front wall is readily removed by overhead crane to give access to test section and instrumentation (Fig. 3). The air angle into the test cascade is governed by the setting of the adjustable lower end walls and the 59 inlet guide (or turning) vanes. The adjustable upper (exit) end walls are individually adjusted during operation to angles required to produce uniform static pressure at the wall in the blade-to-blade direction. Static pressure taps are provided at 5.08-cm intervals in the blade-to-blade direction at vertical (axial) distances of 41.28 cm upstream and 16.51 cm downstream of the center of the test blades. Spanwise and blade-to-blade probe traverses are provided at 31.12 cm vertically upstream and 27.31 cm vertically downstream of the same reference. Plexiglas windows in the removable wall at the test blading facilitate the use of flow visualization techniques (Fig. 4).

Unusual features of the facility are the large scale, the large number of test blades (20, at 7.62 cm spacing), and the technique for controlling inlet air angle. Considerable facility development and test experience [8–13] preceded the present test program. Upstream flow uniformity, periodicity, and steadiness, and acceptable axial velocity-density values without resort to boundary layer suction, were achieved as a result of the initial design features and subsequent experimen-

Nomenclature

AVDR = axial velocity-density ratio (equation (1))
C_p = surface pressure coefficient (equation (8))
Cr = local-to-reference pressure (equation (4))
c = blade chord
i = incidence angle (air angle–blade metal angle)
k = local-to-reference mass flux (equation (3))
P = total pressure
p = static pressure
q = dynamic pressure
Re = Reynolds number based on chord
s = blade spacing
V = velocity
x/c = fraction of chord
β = air angle
γ = stagger angle (Fig. 5)
ρ = density
σ = blade solidity
ϕ = blade camber angle
$\bar{\omega}$ = loss coefficient (equation (2))
$\bar{}$ = mass-averaged value

Subscripts

1 = inlet plane
2 = outlet plane
ref = reference conditions
t = stagnation conditions

Table 1 Blade and cascade geometry

Camber, deg	41.09
Max thickness, percent chord	7.0
Leading edge radius, percent chord	0.9
Trailing edge radius, percent chord	1.26
Solidity	1.67
Stagger angle, deg	14.27
Cascade aspect ratio	2.0
Chord, cm	12.7
Blade Spacing, cm	7.62

Table 2

1. Flow survey probes	
Upstream traverse	United Sensor DA-125 5-Sensor cylindrical pneumatic probe
Downstream traverse	United Sensor DC-125-24-F-22-CD 5-Sensor pneumatic cone probe
2. Wall Static Pressure Taps	5.08 cm intervals in blade-to-blade direction on fixed wall upstream and downstream of test blades
3. Blade Surface Pressure Taps	39 taps on center blade, 6 taps (at selected corresponding locations) on 2 adjacent blades
4. *Tunnel Reference* Measurements	
Plenum	Impact pressure tube Thermocouple Sensor
Cascade Inlet	Fixed Prandtl probe Central Wall Static Tap
5. Flow Visualization	
China clay	One blade (5th from center)
Tufts	One blade and side wall

tal programs. Turbulence intensity, measured across five turning vane pitches at blade midheight, was 2 percent.

Test Blade. The blade shape is represented in cascade in Fig. 5. The meanline is represented by two segments, each described by polynomial curves. A symmetric thickness distribution is built on the meanline. This thickness is made up of a front segment and a rear segment, each represented by a separate polynomial. The polynomial coefficients were arrived at through an optimization process described in [1]. A summary of the section geometrical properties is given in Table 1.

Instrumentation and Data Acquisition. The instrumentation is summarized in Table 2. The flow survey probes were calibrated using Zebner's surface approximation method [15] with computer programs given in [16].

A Hewlett-Packard HP3052 Data Acquisition system incorporating an HP9845A desktop computer and NPS/TPL HG-78K Scanivalve Controller were used to acquire pressure and temperature data. Flow survey probes, and tunnel reference pressures were connected to one 48-port Scanivalve and blade surface pressures and reference readings to another. Measurement uncertainties are given in Table 3. Tunnel wall statics were displayed and observed on a 50-tube water manometer.

The china clay technique was used as described in [13]. Surface patterns were recorded in color using a movie camera, and transition and separation distances were scaled from projected frames. The observations made with china clay were first "calibrated" by applications of the technique to both a sharp and a rounded leading edge flat plate model set into the cascade in place of the test blading [13].

Turbulence intensity measurements were taken with a four micron tungsten wire. The wire was calibrated using King's

Table 3 Measurement uncertainty

Measurement	Method	Uncertainty
Probe position	Linear potentiometer	±0.02 cm
Flow angle (β_1)	Angle potentiometer	±.2 deg
(β_2)	Angle potentiometer	±.5 deg
Pressures		
Plenum	Scanivalve & transducer	±.05 cm water
Wall static	Scanivalve & transducer	±.05 cm water
Blade surface	Scanivalve & transducer	±.05 cm water
Probe	Scanivalve & transducer	±.05 cm water
Flow field	Calibrated probe	
Stagnation pressure		±.05 cm water
Static pressure		±.2 cm water
Velocity		±.5 percent

Law over 14 points from a tunnel dynamic pressure of 0 to 39.4 cm of water. The correlation coefficient was 0.995.

Testing Procedure and Data Reduction. Seven inlet air flow angles from 24 to 46 deg were selected and set in turn. At each angle setting similar procedures were followed. With the tunnel set to the desired inlet dynamic pressure (either 33 or 20 cm of water) tail boards and IGVs were adjusted to give near-uniform wall static pressure both upstream and downstream of the test blading. Blade-to-blade probe surveys were then conducted over four adjacent blade spaces about the center blade. Probe data and reference data were recorded at 0.64-cm intervals over the outer spaces, and 0.25-cm intervals over the central spaces. The lower probe trailed the upper by 3.84 cm throughout the traverse procedure. A spanwise probe survey was then conducted at 1.27-cm intervals at the upper station with the probe located at about 2.5 cm from the suction side of the center blade. The survey procedure was repeated with the lower probe at approximately 2.5 cm from the pressure tube of the central blade. The blade surface pressures and reference data were then recorded with tunnel reference data.

China clay observations were made for similar settings of the cascade at a dynamic pressure of approximately 9.3 cm of water. The somewhat reduced velocity was necessary since higher velocities give too rapid a drying rate, and difficulty in recording and interpreting the drying patterns. Blade static pressure distributions were recorded when china clay observations were made. These data could be compared with data already recorded at two high Reynolds numbers.

In the reduction of the probe survey data, after reduction to velocity, pressure, and flow angle at each point, the data were referenced to quantities derived from the tunnel plenum to atmospheric pressure (driving potential). As shown in [9, 10], this permits integration of the measurements over the blade-to-blade displacement to obtain the axial velocity-density ratio (AVDR) and loss coefficient such that small variations in supply conditions during the survey have little effect. The AVDR was calculated using the definition.

$$\text{AVDR} = \frac{\int_0^s \rho_2 V_2 \cos \beta_2 ds_2}{\int_0^s \rho_1 V_1 \cos \beta_1 ds_1} \tag{1}$$

and the loss coefficient using the definition

$$\bar{\omega} = \frac{\bar{P}_{t1} - \bar{P}_{t2}}{\bar{P}_{t1} - P_1} \tag{2}$$

where bars denote mass-averaged values.

Defining local-to-reference mass flux as

$$k = \frac{\rho V \cos \beta}{\rho_{\text{ref}} V_{\text{ref}}} \tag{3}$$

and local-to-reference pressure as

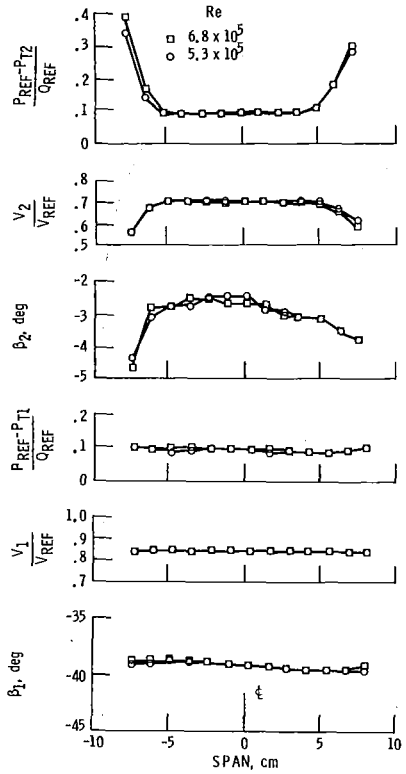

Fig. 6 Measured inlet and outlet flow field in the spanwise direction at design inlet angle

$$Cr = \frac{P}{P_{\text{ref}}} \tag{4}$$

then equations (1) and (2) become, respectively,

$$\text{AVDR} = \frac{\int_0^s k_2 ds_2}{\int_0^s k_1 ds_1} \tag{5}$$

and

$$\bar{\omega} = \frac{\int_0^s k_1 Cr_{t1} ds - \frac{1}{\text{AVDR}} \int_0^s k_2 Cr_{t2} ds}{\int_0^s k_1 Cr_{t1} ds - \int_0^s k_1 Cr_1 ds} \tag{6}$$

which is, equivalently,

$$\bar{\omega} = \frac{\bar{Cr}_{t1} - \left(\frac{1}{\text{AVDR}}\right) \bar{Cr}_{t2}}{\bar{Cr}_{t1} - \bar{Cr}_1}$$

Probe data were reduced using equations (3) to (6), using overlapping quadratic interpolation to carry out the numerical integrations to obtain AVDR and loss coefficient.

Surface pressures were reduced to pressure coefficients using the definition

$$Cp = \frac{p - p_1}{\frac{1}{2} \rho_1 V_1^2} \tag{8}$$

To verify accuracy, the reference upstream conditions were derived in three different ways, namely: as the mass average of the blade-to-blade probe surveys; from the ensemble average of stagnation pressure readings and derived static pressure values during blade-to-blade probe surveys; and as derived from the fixed Prandtl probe measurements.

Calculation Methods

Inviscid Flow Solution. The inviscid flow about the blade section in the two-dimensional, blade-to-blade plane has been calculated by two methods: the method described by Katsanis, TSONIC [4], and the panel method developed by McFarland [17]. The TSONIC program solves the stream function equation by finite difference techniques for the subsonic, compressible flow regime. It is necessary to specify as input the fluid properties, inlet total temperature and density, weight flow, blade geometry, inlet and outlet flow angle, finite difference mesh, and a meridional distribution of streamtube height. In the work presented herein, a linear distribution of streamtube height was utilized so as to match the measured axial velocity-density ratio.

Because the nature of the equations dictates that the solution be of the boundary value type, the outlet flow angle must be specified on the downstream boundary. In these calculations, measured exit angle was used.

The TSONIC code uses a uniform mesh and, therefore, mesh packing in regions where more definition is desired is not permitted. To better define the calculated flow properties in the leading edge region, McFarland's panel code [17] was used. The code is a surface singularity method which solves the inviscid, irrotational, compressible blade-to-blade flow equations on a surface of revolution. Streamsheet thickness can be incorporated as a function of meridional distance. The governing equations are linearized by approximating compressibility effects, and solved using an integral technique (panel method). Up to 98 panel elements are possible. Computational time for a typical case is under 4 CPU seconds on an IBM 3033 computer. The method is limited to subsonic flow and is less accurate for low-solidity blade rows. The same input data set used for TSONIC can be used for the panel code. Because of user freedom to distribute panel elements, excellent definition in the leading edge region can be obtained.

Boundary Layer and Loss Calculations. Blade surface boundary layers were calculated using the program developed by McNally [5]. In addition to the surface velocities, required input includes upstream flow conditions, fluid properties, and blade surface geometry. Among the outputs provided by the program are the conventional integral thicknesses, form factors, wall friction coefficient, and momentum thickness Reynolds number.

The program uses integral methods to solve the two-dimensional, compressible laminar and turbulent boundary layer equations in an arbitrary pressure gradient. Cohen and Reshotko's method [18] is used for the laminar boundary layer, transition is predicted by the Schlichting–Ulrich–Granville method [19], and Sasman and Cresci's method [20] is used for the turbulent boundary layer.

A boundary layer which is initially laminar may proceed through normal transition to a turbulent boundary layer, or it may undergo some form of laminar separation before becoming turbulent. To provide flexibility for analyzing this behavior, several program options are available to the user. The calculations may proceed from a laminar boundary layer through transition to a turbulent boundary layer. However, if laminar separation is predicted before transition, the turbulent calculations may be started by specifying a factor by which the last calculated value of momentum thickness is multiplied (this factor is commonly chosen to be 1.0 to satisfy conservation of momentum). This new momentum thickness and a value for form factor used on the last calculated momentum thickness Reynolds number are used as initial values for the turbulent calculations. In no case is an initial turbulent boundary layer allowed which has a momentum thickness Reynolds number less than 320 [21]. Laminar separation is predicted when skin friction becomes zero. Prediction of turbulent separation is inexact. A separation criterion common to compressor blade

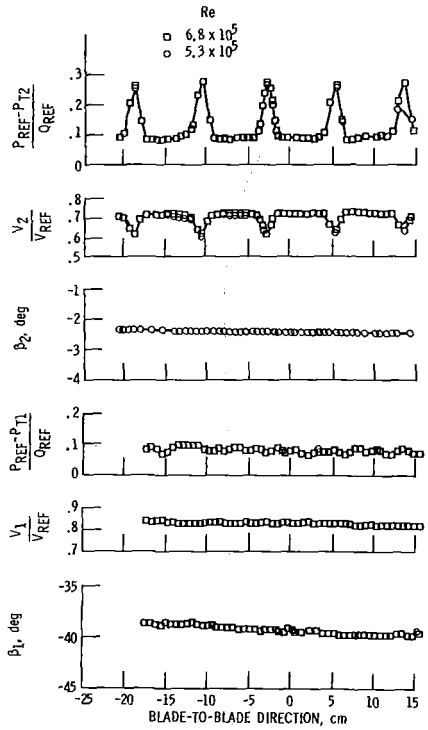

Fig. 7 Measured cascade inlet and outlet flow field in blade-to-blade direction at design inlet angle

analyses which use integral boundary layer methods is the incompressible form factor *Hi*. Values of 1.8 to 2.6 have been proposed and used in the past [22]. In this report, critical values will be inferred from comparisons with data.

Total pressure loss coefficients were calculated using Stewart's method [23]. Required input includes upstream flow conditions, fluid properties, displacement and momentum thickness at the trailing edge, blade spacing, trailing edge thickness, and exit velocity and flow angle. There is no satisfactory method for calculating loss when the boundary layer is separated, and a combination of analytic art and empiricism is generally used. In this report, for off-design cases where turbulent separation occurs, the displacement and momentum thicknesses at the location of critical form factor are assumed to remain constant to the blade trailing edge. These values are then used in the loss calculations from that point. Expected accuracy diminishes as incidence angle increases or decreases siginificantly from the design point.

Results and Discussion

Experimental Observations. Since the cascade facility is somewhat unconventional, the quality of the flow is discussed before results are presented.

Flow Quality. Data were obtained at inlet air angles ranging from 25 to 46 deg. Care was taken at each setting to verify that the inlet pressure and velocity and the outlet pressure were acceptably uniform, and that two-dimensional flow conditions with streamline contraction prevailed to the downstream measurement plane. Surveys of upstream and downstream flow for all test conditions are documented in detail in [14]. In Figs. 6 and 7 are shown, for illustration, the results of spanwise and blade-to-blade probe surveys, respectively, at the design air-inlet angle of 39 deg. In Fig. 6 it can be seen that the flow remains nearly uniform over the center 40 percent of the blade.

In Fig. 7, showing the blade-to-blade conditions, the variation which appears almost as noise on the inlet stagnation pressure profile is what remains of the wakes produced by the

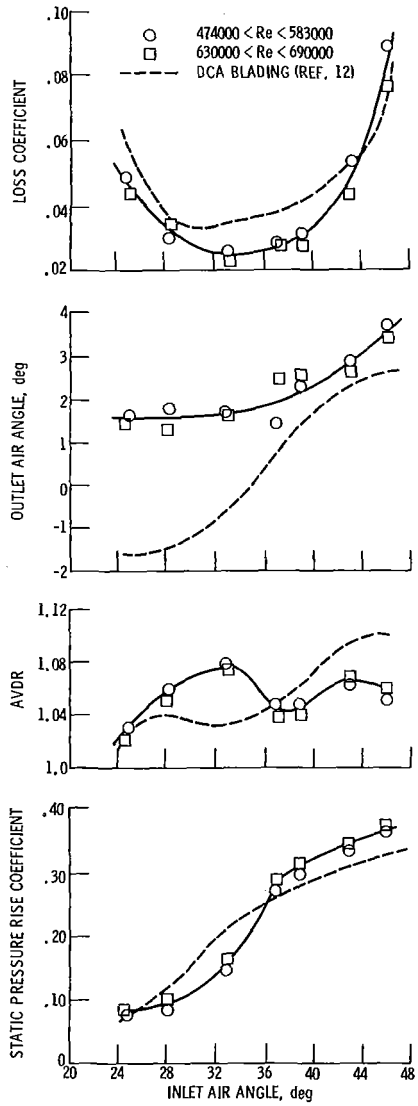

Fig. 8 Cascade performance from probe survey data

turning vanes. The peak-to-peak variation seen in Fig. 7 is about ±1.4 percent of the reference dynamic pressure, or ±1.1 percent of the cascade inlet dynamic pressure. Thus, the inlet velocity was uniform to within 1.2 percent, and these small variations were accounted for by mass averaging in evaluating both AVDR and losses. The inlet flow angle was uniform to within 0.5 deg over the central four blade passages which were surveyed.

In viewing the downstream flow distributions in Fig. 7, it should be noted that data were taken at close intervals (0.25 cm) for integration over one blade passage, and over coarse intervals (0.62 cm) for the other three. All data points are shown connected by straight lines. The minor departure from strictly repetitive conditions seen in the first (left-hand) blade interval was observed in all data sets. Integration to obtain blading performance was therefore carried out over the third blade interval. Periodicity within the blade passages was verified using corresponding pressure taps on three instrumented blades.

The quality of the test conditions did not change significantly except to the two extreme angles tested. At the lowest air angle (25 deg), the inlet uniformity decreased fractionally as a result of operating the inlet turning vanes considerably off design, while the physical separation of the wakes was increased because of the less oblique wall angle. At the highest angle (46 deg), the uniform core of the spanwise profile was

reduced from 40 to 20 percent of span as a result of increased wall and passage viscous effects associated with increased loading.

Overall Performance. The results obtained for the cascade performance based on survey probe measurements are shown in Fig. 8. Also shown for comparison are the corresponding curves for data obtained by Himes [12] for the equivalent cascade of DCA blades. Some differences are noted. First, the loss coefficient for the controlled-diffusion blade was measured to be less than that for the DCA blade at the design point, and over the useful range of air inlet angle. The data for loss coefficient were well behaved and showed no discernible effect on Reynolds number, except (perhaps) at the highest air inlet angles.

There were measurable differences in behavior at air inlet angles less than design. The outlet air angle did not change significantly for the DCA blade, and ranged from 1/2 to 3 deg greater than measured for the CD blade. Larger values of AVDR were also measured, although at angles approaching and exceeding the design value, the AVDR was measured to be lower than for the DCA cascade.

The AVDR is largely a consequence of the behavior of the end-wall boundary layers in passing through the cascade, and the reason for the high value of 33 deg inlet air angle is not clear. However, a much reduced static pressure rise was also registered, and this was confirmed by manometer readings of the distributions of wall static pressures. In fact, the pressure rise across the cascade dropped very abruptly with reduced air inlet angle, the drop being associated with the detection of leading edge separation on the pressure side of the blade. Subsequent examination of all the information obtained in the

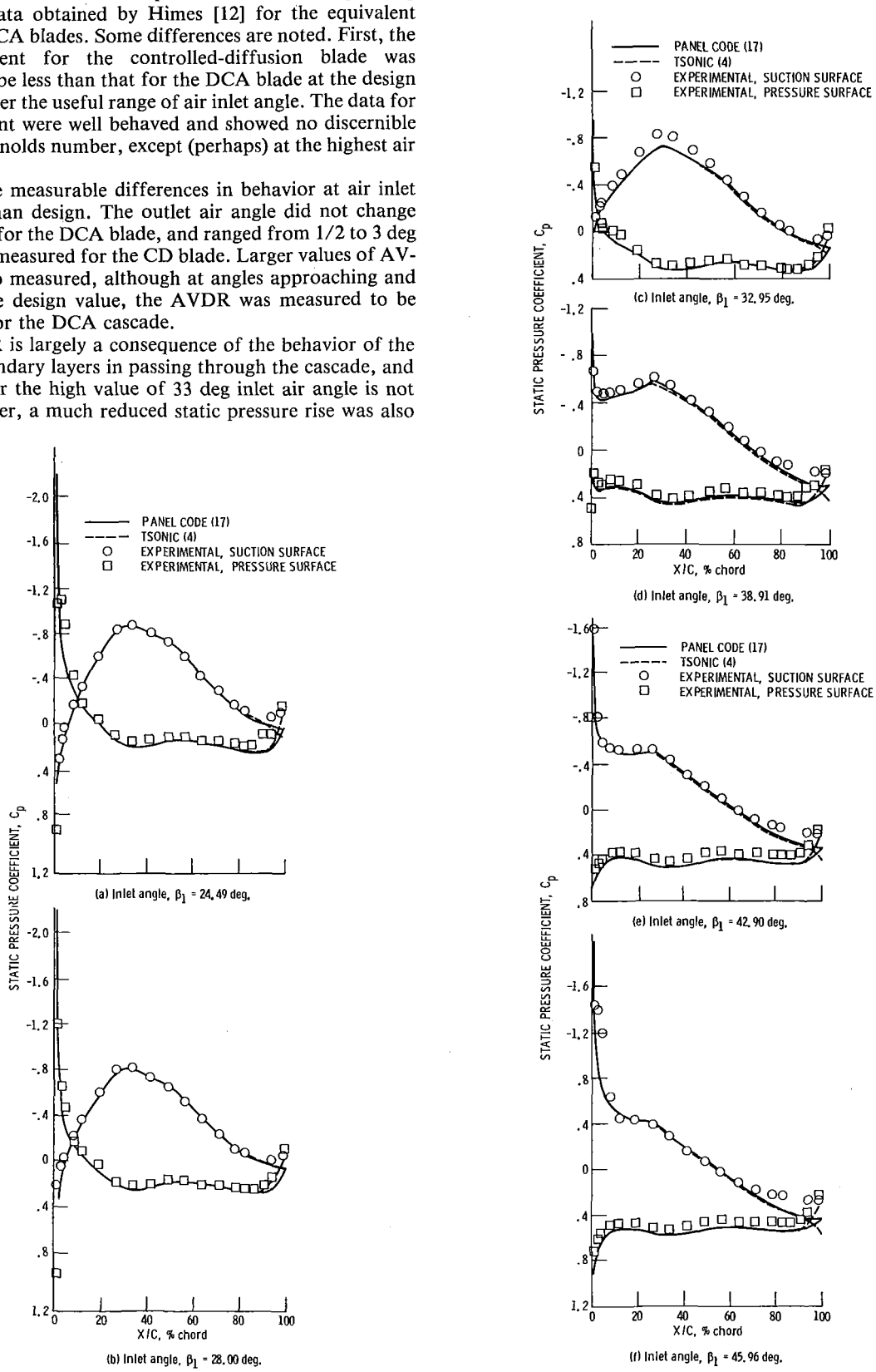

Fig. 9 Comparison of experimental and calculated surface pressure coefficient

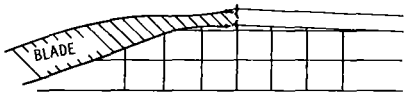

(a) Construction of effective wake.

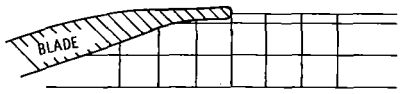

(b) Original trailing edge model (ref. 9).

Fig. 10 Mass flow injection model: TSONIC program

tests pointed to a need to obtain more information in the range of inlet flow angles between 30 and 36 deg.

Vortex Shedding. During testing at the three lowest air inlet angles, pure, highly audible tones were heard as the tunnel was brought up to the required test conditions. The tones occurred at discrete settings of the plenum pressure, and the frequency increased (1080, 1960, 2380, 3080 Hz) as the inlet velocity at which it occurred increased (approximately 30, 34.5, 42, 48.5, 56 m(s). Vortex shedding in the blunt blade wake was suspected when the Strouhal number based on trailing edge thickness was found to be 0.17 (when the tones occurred). An experiment was conducted to verify this explanation. The bluntness was removed by taping metal shim-stock to produce sharp trailing edges on all blades. The tones then did not occur. The removal of the shim-stock from one blade resulted in the reoccurrence of tones, but very faintly.

Vortex shedding in turbomachinery blade wakes has been observed or suspected in several turbomachinery research experiments [24–28]. However, the occurrence in the present case was particularly graphic because the frequencies were in the audible range and, despite the tunnel background noise level, some had the clarity of pure organ tones.

In high-speed compressors and turbines, these resonant frequencies can be over 100 kHz and therefore too high to be detected by other than the highest response transducers (see [28], for example). The issue of vortex shedding must be raised when attempting to obtain comparisons of data with analyses which aim at the correct modeling of the flow. Whether any special treatment of the trailing edge flow is required when vortex shedding occurs, compared to when it does not, requires that a more detailed study be conducted than was possible in the present series of tests.

Comparison of Calculated and Experimental Results. Inviscid flow computations, presented as static pressure coefficient versus percent of chord, are compared with experiment in Fig. 9. The solid line represents panel code calculations and the dashed line represents TSONIC results.

There is very little difference between TSONIC and panel code calculations, except in the trailing edge region. Even there, the differences are minor and are due to differences in the way each code models the trailing edge. No inviscid code will calculate the flow accurately near the trailing edge of a blade row because real, viscous effects are the most prominent in that region. For blades with round trailing edges, and particularly for the present case with a blade having a relatively large trailing edge diameter, the Kutta condition does not truly apply. Some artifice must be used, and code developers employ different methods.

In TSONIC, Katsanis has used a mass injection or wake simulation model [1] sketched in Fig. 10. Tangents are formed at the intersection of the trailing edge circle and the blade surface, and extended to the vertical line which forms a tangent with the trailing edge circle (Fig. 10). The "wake" is then extended downstream with an orientation determined by the downstream whirl boundary condition. Pressure is allowed to

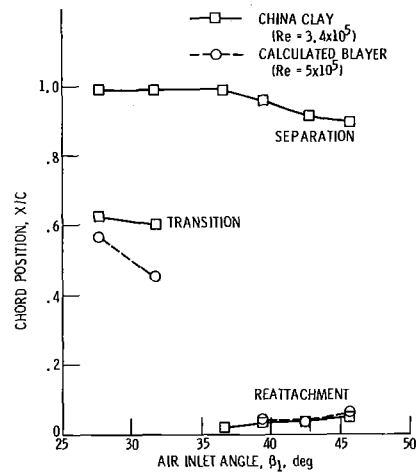

Fig. 11 Comparison of boundary layer behavior between china clay experiments and calculations using experimental surface pressure distributions; suction surface

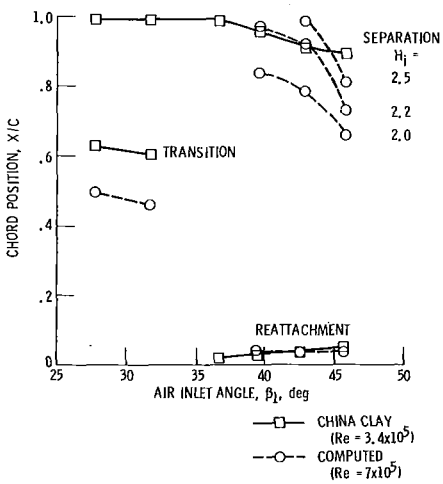

Fig. 12 Comparison of boundary layer behavior between china clay experiments and calculations using calculated surface pressure distributions; suction surface

vary across the simulated wake. This modeling removes the trailing edge circle and the attendant accelerations and decelerations associated with curvature. The user may vary exit angle until "closure" of the pressure distribution occurs at the trailing edge to simulate a Kutta condition, or the user may specify an exit angle (such as an experimentally measured angle) and accept the crossing of suction and pressure surface pressures near the trailing edge, as in the present calculations.

McFarland sets the downstream static pressure by continuity considerations. He then forces the surface pressures on both surfaces to meet this pressure at the trailing edge by an interpolation process involving the last three panel elements on each surface. To achieve satisfactory results in the trailing edge region, it was found necessary in these calculations to use all 98 panel elements, and to pack points in the trailing edge (FTE set equal to 1.05).

Both methods are artificial. But inviscid flow, in itself, is artificial, and comparisons will always differ from the real flow in regions where viscous effects are strong.

Experimental measurements are generally in good agreement with both methods of calculation. Viscous effects near the trailing edge begin to appear (as a divergence between calculation and measurement) at the design point (Betal = 38.91) and increase as incidence increases. The last pressure tap on each surface is in a region of curvature and reflects the

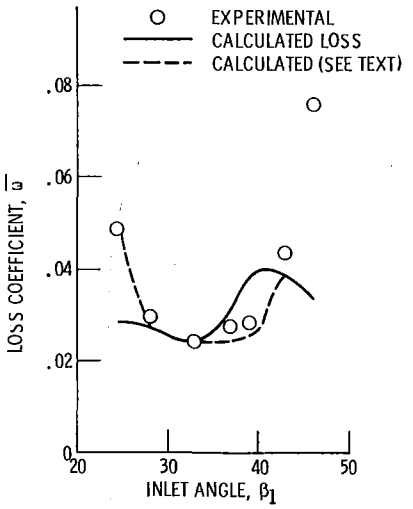

Fig. 13 Calculated loss (Stewart's model) compared with experimental measurements

decreased pressure (increased velocity) there, particularly at lower inlet angles where suction surface boundary layers are relatively thin. Corresponding trailing edge accelerations do not appear in the calculations because the trailing edge has been modeled to remove them.

Measured pressures compare very well with the calculations in the leading edge region. Because of mesh limitations, TSONIC did not pick up any leading edge acceleration/decelerations upstream of 3 percent chord, and therefore was quite limited in boundary layer calculations. The panel code provided quite adequate resolution. A point of concern to code users has always been the calculated leading edge pressure spikes, and they are evident here even at the design point (Betal = 38.91). The excursions can be large and are mathematically consistent. How much of such an excursion is actually felt by the real flow will determine the nature of the boundary layer behavior. It appears from the measured data that the flow does experience a large proportion of the calculated leading edge velocity diffusion.

Two principal boundary layer calculations were made, one set using data from low Reynolds number tests to compare against flow visualization experiments performed at low Reynolds number (340,000), and one set using calculated pressure distributions corresponding to higher Reynolds number tests (670,000). The latter results were used to calculate loss coefficient to compare against measured loss.

China clay flow visualization experiments were run on the suction surface of the blade over the full range of incidence angles, but at a low Reynolds number to accommodate drying times of the solvent. The results are presented in Fig. 11. The axial position at which laminar separation-turbulent reattachment, transition, and turbulent separation occur is plotted against the inlet flow angle condition. The figure shows the existence of a laminar boundary layer to about 60 percent of chord at the two lowest flow angles. As incidence angle was increased, an abrupt change occurred and a laminar separation with turbulent reatttachment was produced very near the leading edge (2 to 5 percent chord) at all of the higher inlet angles.

The boundary layer calculations were made using experimental surface pressures as input, and results are also plotted on Fig. 11. In all cases, laminar separation with turbulent reattachment was predicted, rather than pure transition. The calculated laminar separation point is reasonably close to experiment for Betal = 28.00, but disagrees by about 15 percent chord at Betal = 32.87. The calculated trends appear to be more valid because as incidence angle is increased, the adverse pressure gradient on the suction surface becomes steeper. Since laminar separation is strongly influenced by pressure gradient, earlier separation would be expected at Betal = 32.87. At the higher inlet angles there is good agreement between experiment and calculation. The adverse gradient near the leading edge is very steep and produces almost immediate laminar separation. Due to the magnitude of the adverse pressure gradient in most cases, and the Reynolds number levels, the laminar separation bubbles are presumed to be short.

The experimental static pressure distributions already reflect turbulent separation, i.e., reduced adverse pressure gradients in the separated region near the trailing edge. Using these reduced gradients as input to a boundary layer calculation is not likely to result in prediction of turbulent separation, and did not for these calculations. It should also be noted that the experimental turbulent separation locations shown in Fig. 11 for Betal = 28, 32, and 36 deg are more likely to be a localized drying phenomenon than a separation.

Boundary layer calculations on both surfaces were conducted for the highest Reynolds number case over the full range of incidence angles using calculated surface pressures as input. The calculated laminar and turbulent separation locations are shown in Fig. 12, using the china clay results as reference. Predicted laminar separation locations occur earlier for both Betal = 28 and 32.87, but agree with china clay results at the higher inlet angles. Turbulent separation is not predicted for the two lower inlet angles, but is predicted for all inlet angles 38 deg and greater. Assuming separation to occur at critical incompressible form factors of 2.0, 2.2, and 2.5, the corresponding locations are plotted as percent chord in Fig. 12. The best correlation with flow visualization data is given by $Hi = 2.2$. For the step adverse gradient at Betal = 45.96, a flow visualization separation location of 90 percent chord does not appear to be consistent. The 73 percent chord value, corresponding to $Hi = 2.2$, agrees better with the flattening of the pressure distribution shown in Fig. 9(*f*).

Total pressure loss coefficients were calculated using Stewart's method [23], and are compared with experimentally measured values in Fig. 13. Attempting to calculate loss at off-design conditions using an integral boundary layer method and a one-dimensional loss model is a dubious enterprise. The calculations obviously break down at the two extremes of inlet angle (solid line). But agreement is remarkably good at the other incidence angles. For cases in which turbulent separation is predicted, the values of displacement and momentum thickness corresponding to $Hi = 2.2$ were assumed to remain constant to the trailing edge of the blade where the loss model was applied.

One notable point of disagreement is at the design inlet angle of 38.91. A recalculation of the boundary layer beginning at about 4 percent of chord beginning with a laminar boundary layer produces loss predictions in agreement with measurements (dashed line, Fig. 9*d*). To accomplish this it would be necessary for the boundary layer to have relaminarized in the reacceleration region between 4 and 25 percent of chord (Fig. 9*d*). Although there is no evidence of this from the china clay experiments, this appears to be the only way the measured loss values could be reconciled with computations.

The boundary layer calculations for the lowest inlet angle (24.49) were particularly troublesome on the pressure surface due to the excessively steep adverse pressure gradient. Laminar separation followed by turbulent separation was predicted. The boundary layer calculations can be continued through modestly high form factors, and values of displacement and momentum thickness were obtained at the trailing edge. However, with such a steep pressure gradient, turbulent separation would not be unexpected, and due to the much relaxed pressure gradient at 30 percent of chord, turbulent

reattachment could be envisioned. Using this speculative approach, a loss coefficient comparable to experimental measurements was achieved by reattaching the turbulent boundary layer at 30 percent chord with a displacement and momentum thickness equivalent to a fourfold increase over values at predicted turbulent separation (dashed line, Fig. 13). Using such methods to predict loads at far off-design conditions is clearly speculative. More sophisticated modeling is required or, at least, an extensive data base is necessary to permit consistent empirical enhancement.

Summary of Results

The midspan section of a controlled diffusion stator was tested in a two-dimensional cascade. Measurements over a wide range of incidence angles were obtained. A quite acceptable minimum loss coefficient level of 0.0241 was measured, a value lower than that measured on the reference double circular arc blade. Operating range was slightly better than for the DCA blade.

Measurements of surface pressure compare well against results computed by the TSONIC and panel codes over the full incidence angle range. Integral boundary layer calculations using the McNally code showed generally good agreement with flow visualization data when measured surface pressures were used as input. When computed inviscid surface pressures were used as input, laminar separation was predicted with less accuracy. Correlations between computed boundary layers and flow visualization data produced a critical incompressible form factor value for turbulent separation of 2.2 for this set of data. Loss calculations using the Stewart loss model provided remarkably good agreement except, as expected, at the extremes of the incidence angle range.

Acknowledgments

The authors would like to acknowledge the assistance of Eric McFarland for his aid with the panel code, and Allan McGuire of The Naval Postgraduate School for his efforts in obtaining the china clay and other data. The experimental program was funded by NASA Lewis Research Center, and partially by Navel Air Systems Command, Code 310E.

References

1 Sanger, N. L., "The Use of Optimization Techniques to Design Controlled-Diffusion Compressor Blading," ASME JOURNAL OF ENGINEERING FOR POWER, Vol. 105, Apr. 1983, pp. 256–264.

2 Urasek, D. C., Gorrell, W. T., and Cunnan, W. S., "Performance of Two-Stage Fan Having Low-Aspect-Ratio, First Stage Rotor Blading," NASA TP-1493, Aug . 1979.

3 Crouse, J. E., and Gorrell, W. T., "Computer Program for Aerodynamic and Blading Design for Multistage Axial-Flow Compressors," NASA TP-1946, Dec. 1981.

4 Katsanis, T., "Fortran Program for Calculating Transonic Velocities on a Blade-to-Blade Stream Surface of a Turbomachine," NASA TN D-5427, 1969.

5 McNally, W. D., "Fortran Program for Calculating Compressible Laminar and Turbulent Boundary Layers in Arbitrary Pressure Gradients," NASA TN D-5681, 1970.

6 Vanderplaats, G. N., "CONMIN: a Fortran Program for Constrained Function Minimization, User's Manual," NASA TM X-62282, 1973.

7 Vanderplaats, G. N., "COPES: a Fortran Control Program for Engineering Synthesis," Naval Postgraduate School, 1980.

8 Moebius, R. C., "Analysis and Testing to Improve the Flow From the Plenum of a Subsonic Cascade Wind Tunnel," M.S. thesis, Naval Postgraduate School, Monterey, CA, 1980.

9 Duval, D. A., "Evaluation of a Subsonic Cascade Wind Tunnel for Compressor Blade Testing," M.S. thesis, Naval Postgraduate School, Monterey, CA, 1980.

10 Cina, F. S., "Subsonic Cascade Wind Tunnel Tests Using a Compressor Configuration of DCA Blades," M.S. thesis, Naval Postgraduate School, Monterey, CA, 1981.

11 Molloy, W. D., "Preliminary Measurements and Code Calculations of Flow Through a Cascade of DCA Blading at a Solidity of 1.67," M.S. thesis, Naval Postgraduate School, Monterey, CA, 1982.

12 Himes, S. J., "Report of Tests of a Compressor Configuration of DCA Blading," M.S. thesis, Naval Postgraduate School, Monterey, CA, 1983.

13 McGuire, A. G., "Determination of Boundary Layer Transition and Separation on Compressor Blades in a Large Subsonic Cascade," M.S. thesis, Naval Postgraduate School, Monterey, CA, 1983.

14 Koyuncu, Y., "Report of Tests of a Compressor Configuration of CD Blading," M.S. thesis, Naval Postgraduate School, Monterey, CA, 1984.

15 Zebner, H., "Procedure and Computer Program for Approximation of Data (With Application to Multiple Sensor Probes)," Naval Postgraduate School Contractor Report, NPS67-80-001CR, Monterey, CA, 1980.

16 Neuhoff, F., "Computer Software for the Calibration of Pneumatic and Temperature Probes," Turbopropulsion Laboratory Technical Note 82-03, Naval Postgraduate School, Monterey, CA, 1982.

17 McFarland, E. R., "A Rapid Blade-To-Blade Solution for Use in Turbomachinery Design," ASME JOURNAL OF ENGINEERING FOR GAS TURBINES AND POWER, Vol. 106, No. 2, Apr. 1984, pp. 376–382.

18 Cohen, C. B., and Reshotko, E., "The Compressible Laminar Boundary Layer With Heat Transfer and Arbitrary Pressure Gradient," NACA TR-1294, 1956.

19 Schlichting H., "Origin of Turbulence II," in: *Boundary Layer Theory*, 7th ed., McGraw-Hill, New York, 1979, pp. 489–554.

20 Sasman, P. K., and Cresci, R. J., "Compressible Turbulent Boundary Layer With Pressure Gradient and Heat Transfer," *AIAA Journal*, Vol. 4, No. 1, Jan. 1966, pp. 19–25.

21 Preston, J. H., "The Minimum Reynolds Number for a Turbulent Boundary Layer and the Selection of a Transition Device," *Journal of Fluid Mechanics*, Vol. 4, No. 1, Jan. 1958, pp. 373–384.

22 Von Doenhoff, A. E., and Tetervin, N., "Determination of General Relations for the Behavior of Turbulent Boundary Layers," NACA Wartime Report L-382, 1943.

23 Stewart, W. L., "Analysis of Two-Dimensional Compressible-Flow Loss Characteristics Downstream of Turbomachine Blade Rows in Terms of Basic Boundary-Layer Characteristics," NACA TN 3515, July 1955.

24 Heinemann, H. J., and Butefisch, K. A., "Determination of the Vortex Shedding Frequency of Cascades With Different Trailing Edge Thicknesses," AGARD-CP277, 1977.

25 Heinemann, H. J., Lawaczeck, O., and Butefisch, K. A., "von Karman Vortices and Their Frequency Determination in the Wakes of Profiles in the Sub- and Transonic Regimes," *IUTAM Symposium Transonicum II*, Springer Verlag, Berlin/Heidelberg/New York, 1976. pp. 75–82.

26 Ng, W. F., and Epstein, A. H., "Unsteady Losses in Transonic Compressors," ASME JOURNAL OF ENGINEERING FOR GAS TURBINES AND POWER, Vol. 107, Apr. 1985, pp. 345–353.

27 Hathaway, M. D., Gerts, J., Epstein, A., and Strazisar, A. J., "Rotor Wake Characteristics of a Transonic Axial Flow Fan," AIAA-85-1133, presented at the AIAA/SAE/ASME/ASEF 21sat Joint Propulsion Conference, Monterey, CA, July 8–10, 1985.

28 Neuhoff, F., Shreeve, R. P., and Fottner, L., "Evaluation of the Blade-to-Blade Flow From a High Speed Compressor Rotor," ASME Paper No. 86-GT-117.

Study of Three-Dimensional Viscous Flows in an Axial Compressor Cascade Including Tip Leakage Effects Using a SIMPLE-Based Algorithm

M. Pouagare
Assistant Professor,
Department of Mechanical Engineering
and Materials Science,
Duke University,
Durham, NC

R. A. Delaney
Supervisor,
Computational Fluid Mechanics,
Allison Gas Turbine Division,
General Motors Corporation,
Indianapolis, IN

A multisweep space-marching solver based on a modified version of the SIMPLE algorithm was employed to study the three-dimensional flow field through a linear cascade. Three cases were tested: one with moderate loading, one with high loading, and one with high loading and tip clearance. The results of the numerical simulation were compared with available experimental measurements, and the agreement between the two was found satisfactory. The numerical simulation provided insight into several important endwall flow phenomena such as the interaction between the leakage and passage vortices, the interaction between the leakage vortex and the wake, the effect of leakage flow and loading on losses and secondary kinetic energy, the suction side corner separation, and the blowing of this separation by the leakage flow.

Introduction

A multisweep space-marching code called IMPACT [1] has been developed at Allison Gas Turbine Division and has been successfully tested for the flow through centrifugal impellers [2]. The purpose of this study is twofold: (1) to evaluate the applicability of IMPACT in axial compressor blade passages; and (2) to use IMPACT to gain a better insight into the complex three-dimensional flow phenomena occurring in the endwall region of the compressor blade passages.

The flow through the endwall region of a compressor blade passage is highly three dimensional with strong secondary flows that form the passage and leakage vortices. It is not clear how these vortices interact, how the loading affects these vortices, what trajectories these vortices follow, how the loss distribution correlates with the location of these vortices, and how the leakage flow interacts with the suction side corner separation [3].

Experimental cascade studies have shown that a saddle point of separation exists near the leading edge and that a horseshoe vortex trails around the blades [4]. The corresponding phenomena in compressor cascades have yet to be investigated. Similarly, the variation of loss, secondary kinetic energy distributions with loading, and the effect that the leakage flow has on these distributions have not been studied in detail.

The pioneering work of Moore et al. [5], Hah [6], Briley and McDonald [7], Walitt [8], and others has shown that a considerable understanding of the three-dimensional viscous flows in turbomachines can be gained through numerical simulation of the flow.

The IMPACT code is used to study the three-dimensional flow through a linear compressor cascade for which experimental data are available. This provides a check on the applicability of the code to axial compressor blade passages and also provides detailed information on the flow phenomena occurring in the endwall region of a compressor cascade. This detailed information is very difficult or impossible to obtain experimentally.

Governing Equations

The IMPACT code can be run in either the compressible or incompressible mode and the coordinate system can be rotating or stationary. In this study, the code was run in the incompressible mode and the coordinate system was stationary. The flow is governed by the steady time-averaged continuity and momentum equations

$$\frac{\partial}{\partial x_j} u_j = 0 \tag{1}$$

$$\frac{\partial}{\partial x_j}(u_i u_j) = \frac{1}{\rho}\frac{\partial p}{\partial x_i} + \frac{\partial}{\partial x_j}\left([\nu + \nu_t]\left[\frac{\partial u_i}{\partial x_j} + \frac{\partial u_j}{\partial x_i}\right]\right) \tag{2}$$

The k–ϵ turbulence model [9] is used to find the eddy viscosity

$$\nu_t = C\mu\, k^2/\epsilon \tag{3}$$

Contributed by the Gas Turbine Division of The American Society of Mechanical Engineers and presented at the 31st International Gas Turbine Conference and Exhibit, Düsseldorf, Federal Republic of Germany, June 8–12, 1986. Manuscript received at ASME Headquarters January 17, 1986. Paper No. 86-GT-84.

Table 1 Geometry and flow conditions for the cascade experiments

Parameter	Test A	Test B	Test C
		Geometry	
Profile	–	NACA 65-12-A_{10}-10	–
Stagger (λ)	–	30 deg	–
Space-to-chord ratio (S/C)	–	0.8	–
Span-to-chord ratio ($2H/C$)	–	2.1	–
Gap-to-chord ratio (t/C)	0	0	0.011
		Flow conditions	
Inlet flow angle (β_1)	48.3 deg	56.2 deg	55.5 deg
Outlet flow angle (β_2)	20.9 deg	24.4 deg	24.6 deg
Reynolds number (Re)	4.05×10^5	4.28×10^5	4.26×10^5

where $C\mu$ is a constant, k the turbulence kinetic energy, and ϵ the turbulence energy dissipation rate. The turbulence quantities k and ϵ are found from their respective transport equations

$$\frac{\partial}{\partial x_i}(u_i k) = \frac{\partial}{\partial x_i}([\nu_t/\sigma_k][\partial k/\partial x_i]) + P - \epsilon + G_c \tag{4}$$

$$\frac{\partial}{\partial x_i}(u_i \epsilon) = \frac{\partial}{\partial x_i}([\nu_t/\sigma_\epsilon][\partial \epsilon/\partial x_i]) + \frac{\epsilon}{k}(C_1 P - C_2 \epsilon + G_c) \tag{5}$$

where P is the rate of production of k and G_c is a term that accounts for the streamline curvature effects on turbulence and is a function of the local streamline curvature, shear stress, and velocity [2]. The empirical constants C_μ, C_1, C_2, σ_k, σ_ϵ are set to the following values: $C_\mu = 0.09$; $C_1 = 1.47$; $C_2 = 1.92$; $\sigma_k = 1.0$; and $\sigma_\epsilon = 1.3$. The wall function method [10] is used to minimize the number of grid points needed near solid surfaces.

Equations (1), (2), (4), and (5) are transformed to an arbitrary curvilinear coordinate system in ξ, η, ζ where ξ is the coordinate approximately aligned with the primary flow direction and η, ζ are the coordinates in the transverse plane. Invoking the parabolic flow approximation, the diffusion terms in the ξ direction are dropped.

Numerical Algorithm

The details of the numerical algorithm are given in [1] and, therefore, only a brief description will be given here. The numerical algorithm is similar to the semi-implicit pressure linked equation (SIMPLE) [11] algorithm and is based on the multisweep space-marching procedure originally devised by Pratap and Spalding [12] and later generalized to arbitrary curvilinear coordinates by Rhie [1]. The solution is marched in the primary flow direction starting from prescribed conditions on an inlet plane. The algorithm employs a finite-volume integration method for the momentum and turbulent transport equations. These equations are solved in the transverse plane using the alternating direction implicit (ADI) method. The method uses the pressure-correction procedure to enforce local and global mass conservation during a marching sweep. After each forward marching sweep, a three-dimensional elliptic pressure-correction equation is solved to get a new estimate for the pressure field. When reverse flow occurs, the FLARE approximation is used according to which convective terms in the ξ direction are neglected.

Experimental Setup

Papailiou et al. [13] performed a series of tests in a linear compressor cascade. Three of those tests are used in this study for comparison with the numerical predictions. Table 1 shows the geometry of the cascade and the flow conditions for

Nomenclature

ADI = alternating direction implicit
C = chord length
CPU = central processing unit
C_p = pressure coefficient = $(p-p_1)/(\frac{1}{2}\rho V_1^2)$
$\bar{C}_{p0}$ = passage and mass-averaged total pressure loss coefficient
C_x = axial chord length
H = half-span height
k = turbulent kinetic energy
$\bar{K}$ = passage and mass-averaged secondary kinetic energy
p = pressure
p_0 = total pressure
p_{01}^* = total pressure at midspan upstream of the cascade
Re = Reynolds number = $V_1 C/\nu$
s, n = streamwise and normal coordinates (streamwise direction is parallel to the local velocity direction at midspan)
SIMPLE = semi-implicit pressure linked equation
ss, ps = suction surface, pressure surface
t = tip clearance height
u_i = velocity component in the i direction
u_x, u_y, u_z = velocity components in the x, y, and z directions (normalized by V_1)
U_z = velocity component in the z direction normalized by V
U_s = streamwise velocity normalized by the local V
U_n = normal velocity normalized by the local V
u_n = normal velocity normalized by V_1
V = velocity magnitude at midspan
x, y, z = Cartesian coordinates
β = flow angle measured from the axial direction
ϵ = turbulent kinetic energy dissipation rate
λ = stagger angle
ν = kinematic viscosity
ν_t = eddy viscosity
ξ, η, ζ = curvilinear coordinates
ρ = density

Subscripts

1 = upstream of the cascade
2 = downstream of the cascade
p = pressure side
s = suction side

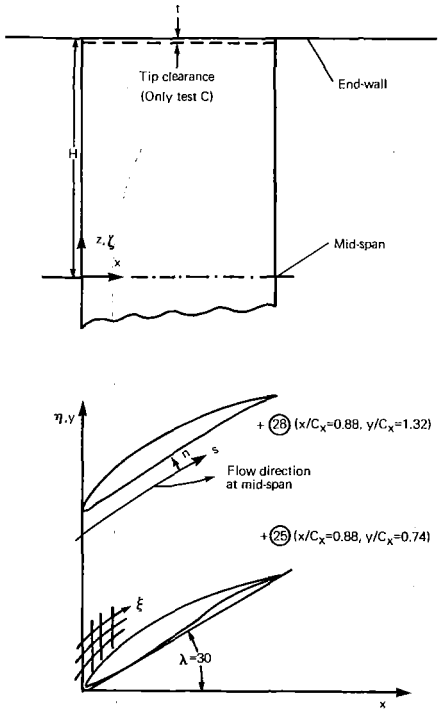

Fig. 1 Cascade geometry and coordinate systems

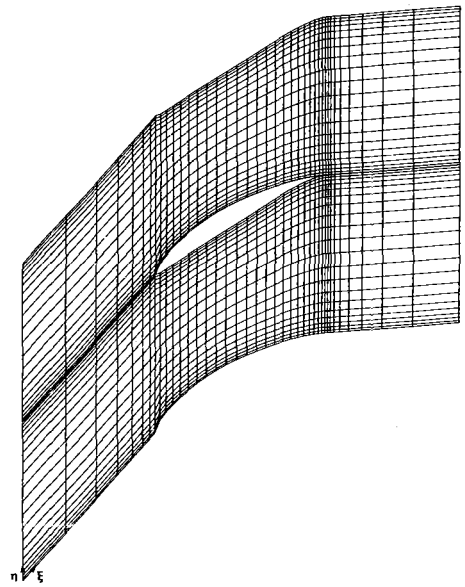

Fig. 2 Grid in the ξ–η plane outside the tip clearance

the three tests: Test A is a case with moderate loading; test B is a case with high loading; and test C is a case with loading approximately the same as test B but with a clearance at the end of the blades ($t/c = 0.011$).

The experiments were performed with a thick inlet boundary layer. The inlet boundary layer thickness was equal to 60 percent of the half-span height and it was approximately the same for the three tests. Figure 1 shows the cascade and the coordinate system.

Computational Grid

A body-fitted grid is used to represent the cascade geometry. The grid consists of 21 × 21 × 40 nodes in the blade-to-blade, spanwise, and streamwise directions, respectively. The grid in the ξ–η plane is shown in Fig. 2. In tests A and B, the grid in the η–ζ plane is everywhere orthogonal with

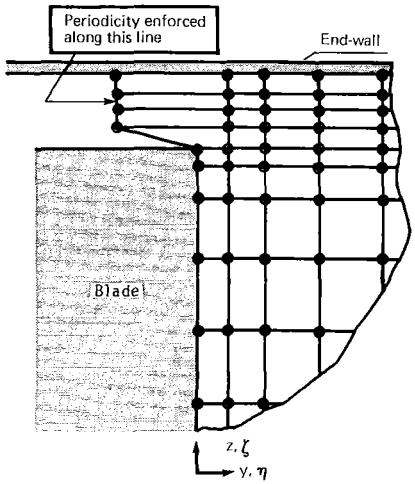

Fig. 3 Details of the grid inside the tip clearance (figure not to scale)

the grid points clustered near the endwall, the leading edge, and the trailing edge. In test C, the grid is modified to model the tip clearance. Figure 3 shows the details of the grid inside and near the tip clearance. Five nodes are located between the blade tip and the endwall. The nodes inside the tip clearance are equally spaced.

Boundary Conditions

In the inlet plane, the three velocity components, the pressure, the turbulent kinetic energy, and the turbulent kinetic energy dissipation rate were specified. The inlet plane was located at $x/C_x = -0.66$. At that location, the flow was collateral and uniform in the y direction. The inlet velocity profiles employed in the numerical simulation were obtained from the experimental data through interpolation. The pressure was taken as uniform in the inlet plane. The only experimental information on turbulence upstream of the cascade was that the level of turbulence intensity was 0.5 percent. Based on this information and on Klebanoff's data [14], an inlet turbulent kinetic energy distribution was assumed. The turbulent kinetic energy dissipation rate at the inlet plane was estimated from k and an assumed turbulence length scale.

No slip boundary conditions were used on the blade surface and the endwall. Wall functions were used for the turbulent quantities on solid surfaces [10]. Periodic conditions were enforced along the boundaries upstream, downstream, and inside the tip clearance.

The flow was symmetric about the midspan plane and, therefore, the solution was carried out only in the upper half domain between midspan and endwall. A symmetry boundary condition was applied at the midspan location: $u_z = 0$, and derivatives with respect to z of all other variables equal to zero.

Analysis of Results and Comparison With Data

The IMPACT code was run for the three tests listed in Table 1. Each run took approximately 250 global iterations to converge. On an IBM 3084, the central processing unit (CPU) time per grid point per iteration was 2.5×10^{-3} s and on a CRAY 1S was 0.42×10^{-3} s.

Blade Pressure Distribution. Figure 4 shows the predicted and measured blade pressure distributions C_p at midspan as well as the predicted C_p at a spanwise location very close to the endwall. The predictions on the pressure side at midspan agree with the experimental data in the three tests. There are some discrepancies between the predicted and measured values at midspan on the suction side, especially in the leading-edge region. This is attributed to the inadequate grid resolution in that region. The flow goes through rapid changes near the

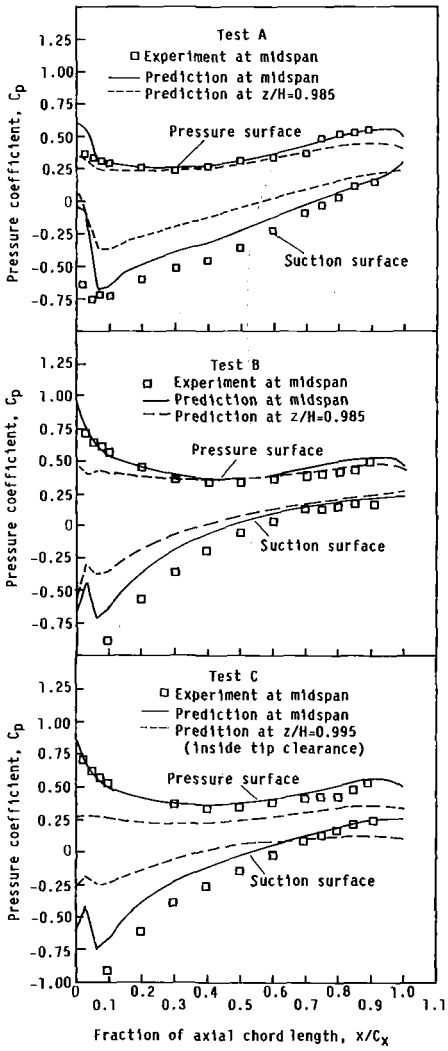

Fig. 4 Blade pressure distribution

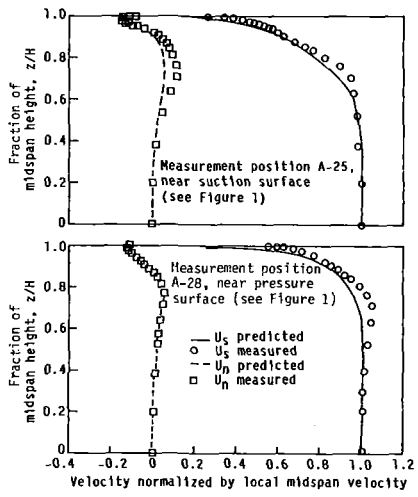

Fig. 5 Streamwise and normal velocity profiles (test A)

leading edge and a denser grid is needed to accurately capture these changes.

The predicted C_p distributions near the endwalls for tests A and B indicate that the loading is less than at midspan. In test C, the predicted C_p distributions show an even larger spanwise loading variation. Note that the pressures used to find C_p at

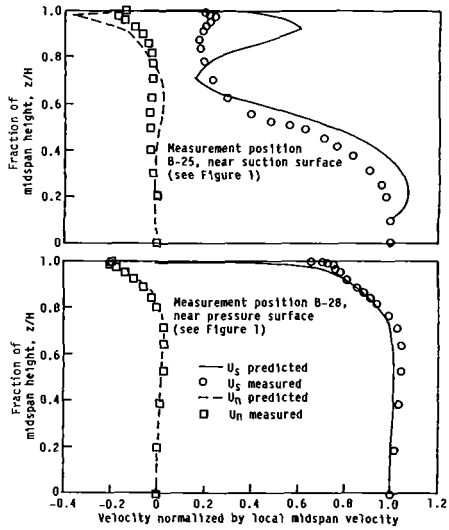

Fig. 6 Streamwise and normal velocity profiles (test B)

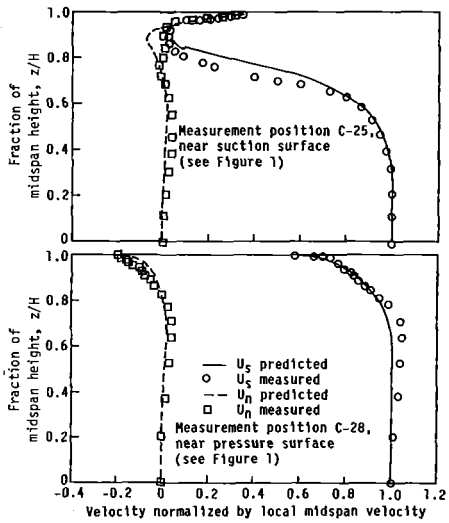

Fig. 7 Streamwise and normal velocity profiles (test C)

$z/H = 0.995$ for test C are the values at one grid point away from the periodic boundaries.

Streamwise and Normal Velocity Profiles. The streamwise direction is defined as the direction parallel to the flow direction at the midspan location. The streamwise velocity U_s is defined as the velocity component parallel to the streamwise direction and normalized by the velocity at midspan. The normal velocity U_n is defined as the velocity component normal to the streamwise direction nondimensionalized by the velocity at midspan. By definition, $U_s = 1$ and $U_n = 0$ at midspan. The normal velocity U_n is considered positive when it causes underturning (see Fig. 1). Papailiou et al. [13] measured U_s and U_n at 18 locations upstream and inside the cascade. The predictions agreed with the measured profiles at most locations for all three tests. The most difficult to predict locations are location 25 (closest to the trailing edge near the suction surface) and location 28 (closest to the trailing edge near the pressure surface). These two locations are shown in Fig. 1. The predicted and measured profiles at locations 25 and 28 are shown in Figs. 5–7. The predictions for test A agree well with the measurements at both locations. Both U_s and U_n profiles have the expected shape.

At location 28, the predictions for tests B and C (Figs. 6 and 7) agree with the measurements. Qualitatively, both U_s and U_n at location 28 look more or less the same for all three tests.

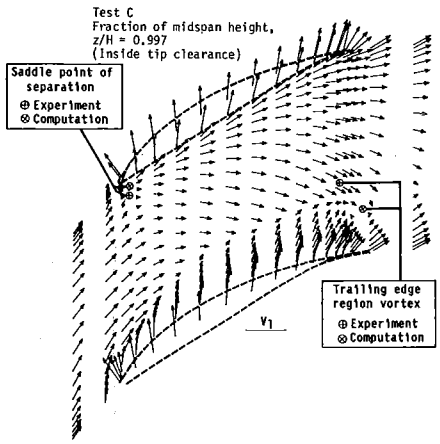

Fig. 8 Velocity vectors in the blade-to-blade plane at $z/H = 0.997$ (test C)

Fig. 9 Flow visualization on the endwall (test C)

This indicates that the tip leakage flow does not affect the flow in the vicinity of location 28. Examining the velocity profiles at many other locations (not shown here), it is concluded that the tip leakage flow affects the flow significantly only in the vicinity of the suction side. This will become clear in the following section where the velocity vectors in the blade-to-blade plane are shown. At location 28, the maximum absolute value of U_n near the endwall is larger for tests B and C (approximately 0.2) than for test A (approximately 0.15). This is because the flow is turned more in tests B and C than in test A.

At location 25, the predictions for test B do not agree with the measurements near the endwall. Qualitatively, however, the profiles show similar trends. Note in particular that a maximum in the U_s profiles occurs near the endwall in both the predictions and the measurements. This location is where the poorest agreement exists between the measured and predicted values. At all other locations, the agreement was very good.

In test C, the numerical simulation predicted the effect of the leakage flow on the streamwise and normal velocity profiles at location 25. The normal velocity U_n is positive near the endwall, which is a direct result of the leakage flow. Also, the shape of the streamwise velocity profile near the endwall in test C is different from that in test B, again a direct result of the leakage flow.

Flow Characteristics in the Blade-to-Blade Plane. Plots of the velocity vectors in the blade-to-blade plane are useful in understanding the basic phenomena that take place in the flow through a cascade. The plots help to visualize the flow.

Figure 8 shows the velocity vectors for test C at $z/H = 0.997$, the location inside the tip clearance that is closest to the endwall. Figure 9 (taken from [15]) shows the experimental flow visualization on the endwall. In both figures, the flow can be seen going from the pressure to the suction surfaces of the blades. Figure 8 also shows that the leakage flow starts from the leading-edge location. Away from the suction and pressure side regions, the familiar overturning of the flow can be seen.

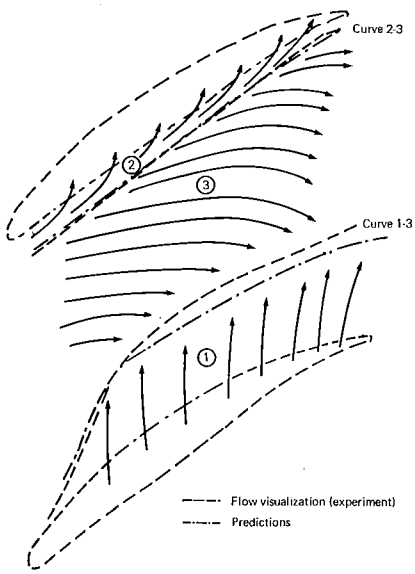

Fig. 10 Qualitative behavior of the flow near the endwall in the presence of tip clearance

Three flow regions can be identified near the endwall (see Fig. 10): (1) the region near the suction side where the leakage flow dominates, (2) the region near the pressure side that supplies the flow that goes through the tip clearance, and (3) the region that is away from the blade surfaces and is overturned. Region 1 is separated from region 3 by a well-defined curve (curve 1-3 in Fig. 10). This curve can be clearly identified in both Figs. 8 and 9 and is the line along which the main flow meets the leakage flow. Region 2 is separated from region 3 by curve 2-3 (see Fig. 10). Again, this curve can be identified in both Figs. 8 and 9 (though not as clearly as curve 1-3) and is the line along which the flow that is going through the tip clearance departs from the main flow direction. In Fig. 10, the predicted curves 1-3 and 2-3 compare well with the curves obtained from the flow visualization. In the trailing-edge region, the tangential extents of regions 1 and 2 are approximately 35 and 6 percent of the blade spacing, respectively.

Also shown in Figs. 8 and 9, the saddle point of separation can be identified near the leading edge. Unlike turbine cascades, no horseshoe vortex was detected trailing around the blades. In the trailing-edge region, a vortex with its axis normal to the blade-to-blade plane can be seen in both Figs. 8 and 9. A possible explanation for the formation of this vortex is as follows: The leakage flow loses its strength in the trailing-edge region and the main flow manages to penetrate the leakage flow region. During this penetration, the main flow loses most of its momentum and, therefore, as soon as it gets into the leakage flow region, it is turned back (by the leakage flow). This sets up a vortex. This argument is supported by the fact that the center of this vortex is on curve 1-3 that separates the leakage flow region from the main flow region. In Fig. 8, the computed saddle point of separation and trailing-edge region vortex location are compared with those experimentally determined from the flow visualization.

Passage and Leakage Vortices. Figure 11 shows the secondary velocity vectors in the y–z plane at $x/C_x = 0.967$ for test B. The secondary velocity vectors are defined as follows

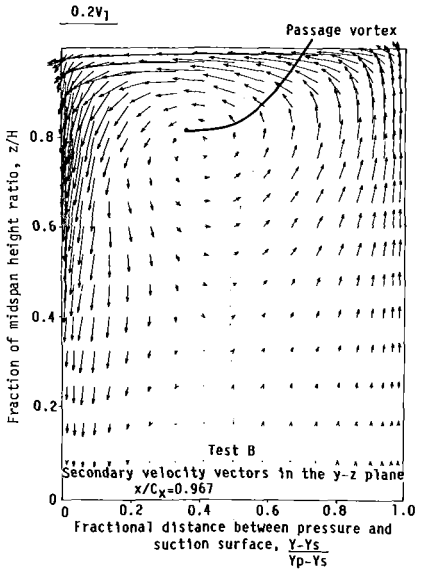

Fig. 11 Secondary velocity vectors in the y-z plane at $x/C_x = 0.967$ (test B)

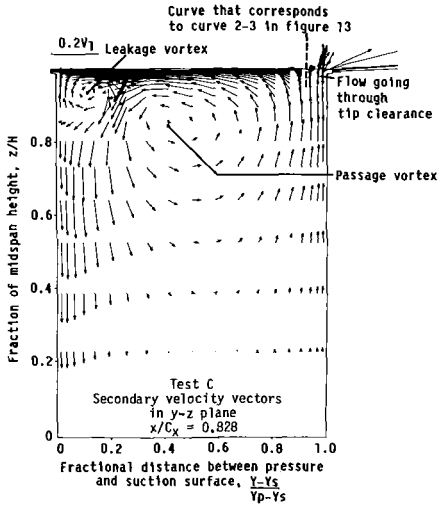

Fig. 12 Secondary velocity vectors in the y-z plane at $x/C_x = 0.828$ (test C)

$$\mathbf{U}_{sec} = \mathbf{U}_n + \mathbf{U}_z \tag{6}$$

The familiar passage vortex can be identified.

Figure 12 shows the secondary velocity vectors in the y-z plane at $x/C_x = 0.828$ for test C. Two contrarotating vortices, namely the passage and the leakage vortices, can be clearly identified. Figure 12 and others at different axial locations not shown here indicate that inside the blade passage the leakage and passage vortices coexist without considerable mixing. This is similar to the findings of Hansen et al. [16] who performed extensive visualization studies of leakage and secondary flows in cascades. Beyond the trailing edge, there is a strong interaction between the leakage vortex and the wake that results in a rapid dissipation of the leakage vortex. The dissipation of the passage vortex is much slower.

Figures 13 and 14 show the trajectories of the center of the leakage and passage vortices in the x-z and x-y plane, respectively. A comparison of the trajectory of the passage vortex for tests A and B shows that for test B the passage vortex is closer to the suction side and farther away from the endwall than for test A. This is because in test B the turning is higher and the passage vortex stronger than in test A. Comparing the trajectories of the passage vortex for tests B and C (which have the same turning), it is concluded that the leakage vortex has only a minor effect on the trajectory of the passage vortex.

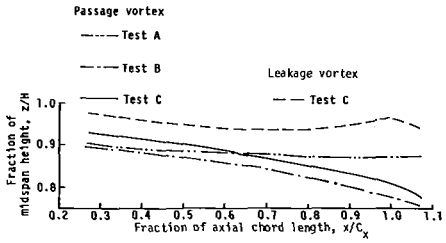

Fig. 13 Trajectories of passage and leakage vortices in the x-z plane

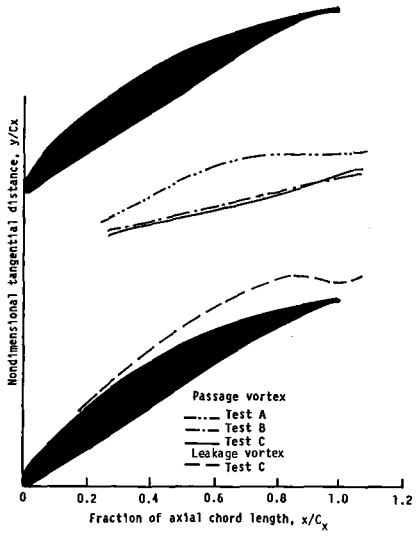

Fig. 14 Trajectories of passage and leakage vortices in the x-y plane

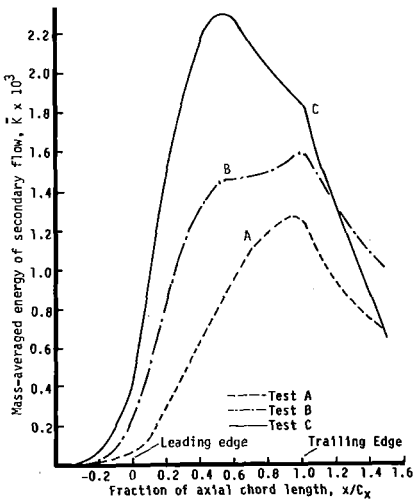

Fig. 15 Passage and mass-averaged secondary kinetic energy

The trajectory of the leakage vortex is close to the suction side and the endwall. Near the trailing edge, the leakage vortex follows a rather peculiar trajectory. This is perhaps due to the influence of the trailing-edge region vortex (see Figs. 8 and 9) or simply because the leakage flow has lost its strength in the trailing-edge region and has started to move closer to the suction side and the endwall. Beyond the trailing edge, the leakage vortex started moving away from the endwall again, probably pulled down by the passage vortex.

Figure 15 shows the variation of the axial direction of the passage and mass-averaged kinetic energy of the secondary flow $\bar{K}$ that is defined as follows:

Table 2 Values of $\bar{C}_{p0}$

Parameter	Test A	Test B	Test C
x/C_x			
1.0	0.136	0.180	0.179
1.666	0.150	0.219	0.232

$$\bar{K} = \frac{\frac{1}{2}\int_0^H \int_{y_s}^{y_p} u_x(u_n^2 + u_z^2)dydz}{\int_0^H \int_{y_s}^{y_p} u_x dydz} \quad (7)$$

In test B, $\bar{K}$ is higher than in test A as expected due to the larger turning (loading) of test B. In tests A and B, $\bar{K}$ increases continuously from the leading edge to the trailing edge. Beyond the trailing edge, $\bar{K}$ decreases due to the dissipation of the passage vortex. In test C, the value of $\bar{K}$ is much higher than in test B because of the leakage vortex. Also, $\bar{K}$ does not peak at the trailing edge location as in tests A and B but it peaks close to the midchord location where the leakage flow is strongest. However, beyond the peak point, $\bar{K}$ decreases much faster in test C than in tests A and B. This is because of the higher dissipation that occurs in test C due to the presence of both the passage and the leakage vortex as well as the presence of the trailing-edge region vortex.

Loss Distribution. The passage and mass-averaged total pressure loss coefficient is defined as follows

$$\bar{C}_{p0} = \frac{\int_0^H \int_{y_s}^{y_p} u_x \frac{p_{01}^* - p_0}{0.5\rho V_1^2} dydz}{\int_0^H \int_{y_s}^{y_p} u_x dydz}$$

Table 2 lists the values of $\bar{C}_{p0}$ at the trailing-edge location and at two thirds of the chord downstream of the trailing edge.

The losses in test B are higher than the losses in test A by 32 percent at the trailing edge and by 46 percent at $x/C_x = 1.666$. The losses in tests B and C are almost the same at the trailing-edge location, which indicates that the increase in losses due to the leakage flow has been balanced by a reduction in losses due to the blowing of the suction side corner separation. However, beyond the trailing edge, the losses in test C increase faster than in test B, and at $x/C_x = 1.666$ the losses in test C are 6 percent higher than the losses in test B. This is because of the additional mixing losses occurring from the interaction between leakage vortex and wake. The secondary velocity vectors in the y–z plane showed that the leakage vortex has almost disappeared at $x/C_x = 1.666$.

Figures 16 and 17 show the total pressure loss contours $\bar{C}_{p0}$ in the y–z plane at $x/C_x = 1.0$ for tests B and C, respectively. In test B, the maximum width in the y direction of the region with $0.667 \leq \bar{C}_{p0} \leq 1.0$ occurs away from the endwall at the location where separation is maximum. In test C, the same region ($0.667 \leq \bar{C}_{p0} \leq 1.0$) increases in width in the y direction near the endwall and decreases away from the endwall. The increase near the endwall is due to the presence of the leakage vortex and the interaction between leakage flow and main flow. The decrease away from the endwall is due to the reduction in separation resulting from leakage blowing.

Note that there is no correlation between passage vortex location and high loss region. This conclusion is similar to the findings of investigators studying three-dimensional flows in turbine cascades (e.g., see [17]).

Closing Remarks and Conclusions

The present study proved that the IMPACT code can provide relatively accurate predictions of the turbulent three-dimensional endwall flow through compressor blade passages with and without tip clearance. More importantly, the present study improved the understanding of or reinforced earlier-made assumptions on compressor endwall flow phenomena. The most important conclusions are as follows:

- The passage vortex moves closer to the suction side and away from the endwall when loading is increased.

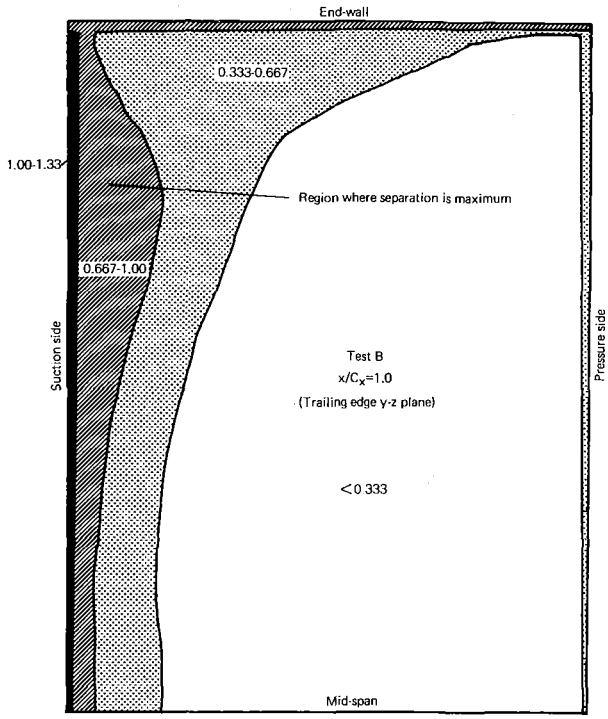

Fig. 16 Contours of total pressure loss coefficient $\bar{C}_{p0}$ at $x/C_x = 1$ (test B)

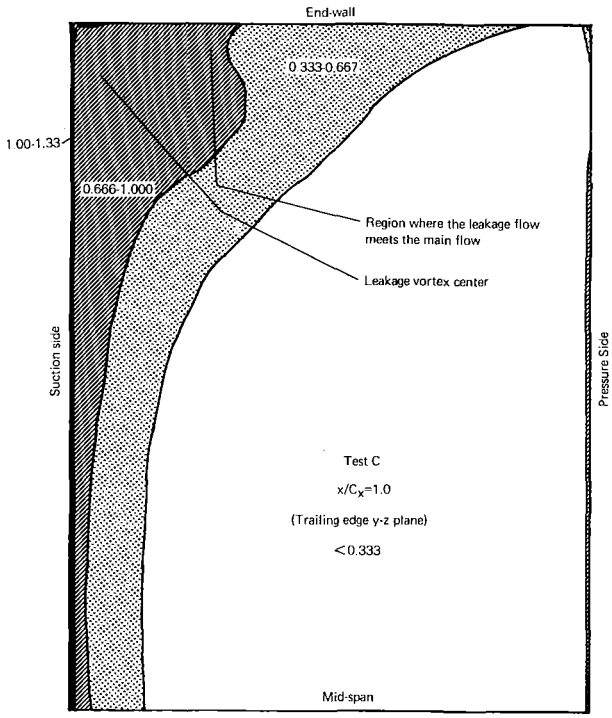

Fig. 17 Contours of total pressure loss coefficient $\bar{C}_{p0}$ at $x/C_x = 1$ (test C)

• The presence of the tip clearance affects a significant part of the flow in the suction side region, whereas it affects only a small part in the pressure side region.

• The leakage vortex has only marginal effect on the passage vortex trajectory.

• The leakage and passage vortex do not mix significantly.

• Immediately downstream of the trailing edge, an intense interaction between leakage vortex and wake takes place resulting in rapid dissipation of the leakage vortex and a rapid increase in losses.

• The passage vortex dissipation is much slower than the leakage vortex dissipation.

• When there is a tip clearance, the flow near the endwall is divided into three regions: (1) leakage flow region (near the suction side), (2) a region that supplies the flow that goes through the tip clearance (near the pressure side), and (3) overturned main flow region. Two distinct curves divide region 1 from 3 and region 2 from 3. This understanding can contribute to the development of tip leakage flow models that can be used by designers of axial flow compressor blade passages.

• A vortex exists in the trailing-edge region with an axis normal to the blade-to-blade plane.

• The leakage flow blows out the suction side corner separation near the endwall.

• When tip leakage is absent, the secondary kinetic energy reaches its maximum in the trailing-edge region. When tip leakage is present, the maximum secondary kinetic energy occurs near the midchord location.

• The losses inside the passage are more or less the same with and without tip clearance (for constant loading). However, at the exit of the passage, the losses are higher with tip clearance than without.

• The center of the passage vortex has no correlation with the high loss region.

• As in turbines, a saddle point of separation exists near the leading edge. However, unlike turbines, no horseshoe vortex was detected trailing around the leading edge.

Acknowledgments

The authors wish to thank Allison Gas Turbine Division, General Motors Corporation, for permitting the publication of this paper. All the computations were carried out at Allison in Indianapolis, Indiana, where M. Pouagare was employed for the summer of 1985.

References

1 Rhie, C. M., "Basic Calibration of a Partially-Parabolic Procedure Aimed at Centrifugal Impeller Analysis," *AIAA 21st Aerospace Sciences Meeting*, Reno, NV, 1983, AIAA Paper No. 83-0260.

2 Rhie, C. M., Delaney, R. A., and McKain, T. F., "Three-Dimensional Viscous Flow Analysis for Centrifugal Impellers," *AIAA/SAE/ASME 20th Joint Propulsion Conference*, Cincinnati, OH, 1984, AIAA Paper No. 84-1296.

3 Lakshminarayana, B., and Horlock, J. H., "Leakage and Secondary Flows in Compressor Cascades," ARC R&M Paper No. 3483, 1967.

4 Langston, L. S., Nice, M. L., and Hooper, R. M., "Three-Dimensional Flow Within a Turbine Cascade Passage," ASME JOURNAL OF ENGINEERING FOR POWER, Vol. 99, Jan. 1977, pp. 21-28.

5 Moore, J., Moore, J. G., and Timmis, P. H., "Performance Evaluation of Centrifugal Compressor Impellers Using Three-Dimensional Viscous Flow Calculation," ASME JOURNAL OF ENGINEERING FOR GAS TURBINES AND POWER, Vol. 106, Apr. 1984, pp. 475-481.

6 Hah, C., "A Navier-Stokes Analysis of Three-Dimensional Flow Inside Turbine Blade Rows at Design and Off-Design Conditions," ASME JOURNAL OF ENGINEERING FOR GAS TURBINES AND POWER, Vol. 106, Apr. 1984, pp. 421-429.

7 Briley, W. R., and McDonald, H., "Analysis and Computation of Viscous Subsonic Primary and Secondary Flows," 4th AIAA CFD Conference, Williamsburg, VA, 1979, AIAA Paper No. 79-1453.

8 Walitt, L., "Calculation of the 3-D Viscous Flow at the Endwall Leading Edge Region of an Axial Annular Turbine Cascade," NASA CR 168275, 1984.

9 Jones, W. P., and Launder, B. E., "The Prediction of Laminarization With a Two-Equation Model of Turbulence," *International Journal of Heat and Mass Transfer*, 1972, pp. 304-314.

10 Launder, B. E., and Spalding, D. B., "The Numerical Calculation of Turbulent Flows," *Computer Methods in Applied Mechanics and Engineering*, Vol. 3, 1974, pp. 269-289.

11 Patankar, S. V., *Numerical Heat Transfer and Fluid Flow*, Hemisphere, Washington, DC, 1980.

12 Pratap, V. S., and Spalding, D. B., "Fluid Flow and Heat Transfer in Three-Dimensional Duct Flows," *International Journal of Heat and Mass Transfer*, Vol. 19, 1976.

13 Papailiou, K., Flot, R., and Mathieu, J., "Secondary Flows in Compressor Bladings," ASME Paper No. 76-GT-57.

14 Klebanoff, P. S., "Characteristics of Turbulence in a Boundary Layer With Zero Pressure Gradient," NACA Report No. 1247, 1955.

15 Flot, R., and Papailiou, K., "Couches Limites et Effects d'Extrêmités dans les Turbomachines," *METRAFLU*, Contract DRME 73/373, 1975.

16 Hansen, A. G., Herzig, H. Z., and Costello, G. R., "A Visualization Study of Secondary Flows in Cascades," NACA TN No. 2947, 1953.

17 Sieverding, C. H., "Recent Progress in the Understanding of Basic Aspects of Secondary Flows in Turbine Blade Passages," ASME JOURNAL OF ENGINEERING FOR GAS TURBINES AND POWER, Vol. 107, No. 2, Apr. 1985, pp. 248-257.

On the Application of a Linearized Unsteady Potential-Flow Analysis to Fan-Tip Cascades

W. J. Usab, Jr.

J. M. Verdon

United Technologies Research Center,
East Hartford, CT 06108

A linearized potential flow analysis, which accounts for the effects of nonuniform steady flow phenomena on the unsteady response to prescribed blade motions, has been applied to five two-dimensional cascade configurations. These include a flat-plate cascade and three cascades which are representative of the tip sections of current fan designs. Here the blades are closely spaced, highly staggered, and operate at low mean incidence. The fifth configuration is a NASA Lewis cascade of symmetric biconvex airfoils for which experimental measurements are available. Numerical solutions are presented that clearly illustrate the effects and importance of blade geometry and mean blade loading on the linearized unsteady response at high subsonic inlet Mach number and high blade-vibrational frequency. In addition, a good qualitative agreement is shown between the analytical predictions and experimental measurements for the cascade of symmetric biconvex airfoils. Finally, recommendations on the research needed to extend the range of application of linearized unsteady aerodynamic analyses are provided.

Introduction

The severe flow conditions imposed on modern fans operating at off-design positive incidence conditions make the possibility of flutter an ever-present concern. The flow in the fan-tip regions of these designs is of particular interest since the blades in this region have thin, slightly cambered profiles that are closely spaced and highly staggered. These features when combined with transonic mean flow conditions and high mean incidence enhance the likelihood of an aeroelastic instability. The aeroelastician is then faced with the task of determining the flutter boundaries for such designs. It is usually sufficient to consider the stability of the design with respect to infinitesimal unsteady excitations, and for this purpose a linearized unsteady aerodynamic theory is appropriate.

Until recently the unsteady aerodynamic models used for turbomachinery aeroelastic design predictions were essentially based on classical linearized theory, where the unsteady flow is regarded as a small-amplitude fluctuation relative to a uniform mean flow. With this assumption the unsteady aerodynamic problem reduces to one of determining an unsteady solution for flow over a cascade of flat plates operating at zero mean incidence relative to a uniform stream. Although classical formulations are computationally very efficient, they apply only to purely subsonic or purely supersonic flows and they do not account for interactions between steady and unsteady disturbances. Therefore, they fail to properly account for the effects of blade geometry, mean blade loading, and shock discontinuities on the unsteady response. To overcome these limitations, linearized unsteady aerodynamic formulations have been developed recently which include the foregoing effects by regarding the unsteady flow as a small-amplitude harmonic fluctuation about a fully nonuniform steady flow [1–6]. While still in the development stage, these new formulations promise to provide the next generation of tools for fan flutter analysis.

The present work involves the application of one of these new approaches [1, 5, 6], to two-dimensional cascades which are representative of the outer-span sections of modern fan rotor. The unsteady solution is constructed in two steps. First, the nonlinear full-potential analysis, described in [7, 8], is used to provide a detailed definition of the mean or steady flow through the cascade. This analysis has been applied extensively in the design of compressor and turbine stages. The application of this code to the analysis of flows in high-speed fan stages, particularly at the conditions at which subsonic/transonic positive-incidence flutter is of serious concern, has been much more limited. Consequently, the present code, and probably all current inviscid flow solvers, are limited in the range of flow conditions for which fan-cascade solutions can be determined. In the second step, the linearized potential flow analysis of [1, 5, 6] is applied to predict the unsteady flow perturbation relative to the mean flow solution for a prescribed mode and frequency of blade motion. This subsonic/transonic analysis has been developed to investigate the importance of blade geometry and mean pressure rise (or fall) across the blade row on the unsteady response to blade vibrations. It also includes the effects of shock discontinuities and their motions in the prediction of unsteady airloads; however, only continuous solutions are reported here.

As previously stated the geometric configuration and off-design flow conditions present in the fan rotor tip region im-

Contributed by the Gas Turbine Division of THE AMERICAN SOCIETY OF MECHANICAL ENGINEERS and presented at the 31st International Gas Turbine Conference and Exhibit, Düsseldorf, Federal Republic of Germany, June 8–12, 1986. Manuscript received at ASME Headquarters January 17, 1986. Paper No. 86-GT-87.

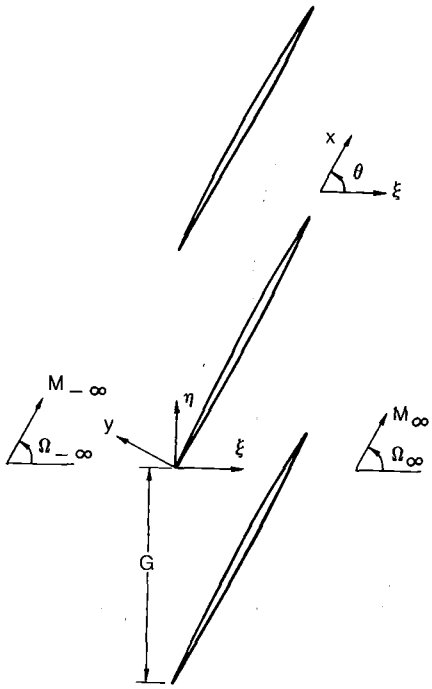

Fig. 1 Two-dimensional fan-tip cascade

pose severe requirements on a numerical prediction scheme. In the present effort the foregoing steady and linearized unsteady potential-flow analyses have been applied to three two-dimensional cascade configurations which are representative of the outer span stations of current fan designs. These configurations were constructed to include the important geometric characteristics; the blades are thin, highly staggered, and closely spaced. However, since the existing steady analysis does not apply readily to thin blades with rounded edges of high curvature and/or blades operating at high mean incidence, some modifications to the leading-edge geometry definition and the mean-flow conditions were necessary to make the analytical results possible. These should be viewed as limitations of the current steady solution procedures and not the general unsteady formulation. To illustrate the importance of thickness and loading in the first three cases, corresponding solutions for a cascade of unloaded flat plates are also presented. A fifth configuration, the NASA Lewis cascade of symmetric biconvex airfoils, has been included in this study because of the availability of experimental data [9] for comparison. Our purpose in choosing each of these cases is threefold: to demonstrate the application of a linearized unsteady analysis to fan configurations, to determine the improvements required before such an analysis can be used in a positive-incidence flutter prediction system, and finally, to provide some analytical results for a basic configuration for comparison with other approaches. It is the authors' view that the present results are indicative of the current application limits of steady and linearized unsteady potential-flow analyses.

Governing Equations

Consider isentropic and irrotational flow of a perfect gas through a two-dimensional cascade of vibrating airfoils (see Fig. 1). The blades are undergoing identical harmonic motions at a frequency ω, but with a constant phase angle σ between the motions of adjacent blades. It is assumed that the flow remains attached to the blade surfaces and that the blade motion is the only source of unsteady excitation.

As a result of the foregoing assumptions the flow through the cascade is governed by the mass conservation law, expressed here in terms of the unsteady velocity potential $\tilde{\Phi}(\mathbf{X}, t)$

$$\frac{\partial \tilde{\rho}}{\partial t} + \nabla \cdot (\tilde{\rho}\ \nabla\ \tilde{\Phi}) = 0 \tag{1}$$

and the compressible Bernoulli equation

$$\tilde{\rho}^{(\gamma-1)} = (\gamma M^2_{-\infty} \tilde{P}/2)^{(\gamma-1)/\gamma} = (M_{-\infty} \tilde{A})^2$$
$$= 1 - (\gamma-1) M^2_{-\infty} [\tilde{\Phi}_t + ((\nabla \tilde{\Phi})^2 - 1)/2]. \tag{2}$$

Here γ is the specific heat ratio of the fluid, M is the Mach number of the undisturbed or steady flow, $\tilde{P}$ is the fluid pressure, $\tilde{A}$ is the speed of sound propagation, and the subscript $-\infty$ refers to the upstream free-stream condition. It should be noted that in the present discussion all physical quantities are dimensionless. Lengths have been scaled with respect to blade chord, time with respect to the ratio of blade chord to upstream free-stream speed, and density and pressure with respect to the upstream free-stream density and dynamic pressure, respectively. In addition to equations (1) and (2), the flow must be tangential to the moving blade surfaces and acoustic energy must either attenuate or propagate away from or parallel to the blade row in the far field. Finally, we also require that the mass and tangential momentum be conserved across any shocks that might be present and that pressure and the normal component of the fluid velocity be continuous across the vortex-sheet unsteady wakes which emanate from the blade trailing edges and extend downstream.

Equations (1) and (2) along with the equations based on the foregoing conditions at blade, shock, and wake surfaces and in the far field are sufficient to determine the unsteady flow. However, the computing resources required by this nonlinear time-dependent unsteady aerodynamic formulation limit its usefulness for turbomachinery aeroelastic investigations. Instead, a small-unsteady-disturbance assumption is usually invoked. This assumption permits an efficient approximate description of the unsteady flow which is suitable for aeroelastic applications.

Thus, following the approach used in [5, 6], we assume that the blades are undergoing small-amplitude (i.e., of $O(\epsilon) \ll 1$) unsteady motions and expand the flow variables in asymptotic series in ϵ; e.g.,

$$\tilde{\Phi}(\mathbf{X}, t) = \phi_0(\mathbf{X}) + \epsilon\, \phi_1(\mathbf{X}, t) + \ldots$$
$$= \Phi(\mathbf{X}) + \tilde{\phi}(\mathbf{X}, t) + \ldots \tag{3}$$

Here, $\Phi(\mathbf{X})$ is the zeroth-order or steady-flow potential, $\tilde{\phi}(\mathbf{X}, t) = \mathrm{Re}\{\phi(\mathbf{X}) e^{i\omega t}\}$ is the first-order (in ϵ) unsteady perturbation potential produced by harmonic blade motions, and Re { } denotes the real part of { }. In addition to (3), Taylor series expansions are used to refer the information on moving blade, shock, and wake surfaces to the respective mean positions of these surfaces. After substituting these expansions into the full governing equations, equating terms of like power in ϵ, and neglecting terms of higher than first order in ϵ, time-independent nonlinear and linear variable-coefficient boundary-value problems are obtained, respectively, for the zeroth- and first-order flows.

The field equations governing the steady (zeroth-order) flow are the same as those obtained from equations (1) and (2) after replacing the time-dependent variables $\tilde{\rho}(\mathbf{X}, t)$ and $\tilde{\Phi}(\mathbf{X}, t)$ by their zeroth-order or steady-flow counterparts $\rho(\mathbf{X})$ and $\Phi(\mathbf{X})$ and setting temporal derivative terms equal to zero. The resulting equations, when combined with prescribed uniform flow conditions at the inflow boundary, and a Kutta condition at blade trailing edges, describe the steady background flow through the stationary cascade.

The differential equation governing the first-order or linearized unsteady flow, i.e.,

$$A^2 \nabla^2 \phi = \frac{D_S^2 \phi}{Dt^2} + (\gamma-1) \nabla^2 \Phi \frac{D_S \phi}{Dt} + \nabla(\nabla\Phi)^2 \cdot \nabla\phi/2 \tag{4}$$

follows from the mass conservation law (1), Bernoulli's equation (2), the isentropic relations, and the asymptotic expansions for the flow variables. Here $A = \gamma P/\bar{\rho}$ is the speed of sound propagation in the steady background flow, $D_S/Dt = i\omega + \nabla\Phi\cdot\nabla$ is a mean flow convection derivative operator, and $\phi(\mathbf{X})$ is the complex amplitude of the linearized unsteady potential. Solutions to equation (4) are subject to both boundary conditions at the mean positions of the blade, shock, and wake surfaces and requirements on the behavior of the unsteady disturbances far upstream and downstream from the blade row. Shock and wake (i.e., the steady downstream stagnation streamlines) mean positions are determined from the steady solution. The unsteady surface and far-field conditions are given explicitly in [5, 6] and will not be repeated here.

The preceding aerodynamic formulation for determining the unsteady flow through a cascade of airfoils undergoing small-amplitude harmonic oscillations requires the solution of a nonlinear boundry-value problem for the zeroth-order or steady flow, followed by the solution of a linear variable-coefficient boundary-value problem for the first-order or linearized unsteady flow. Both of these problems are time independent. Moreover, because of the cascade geometry and the assumed form of the blade motion, the steady and linearized unsteady flows must exhibit blade-to-blade periodicity. Thus, for example

$$p(\mathbf{X} + mG\mathbf{e}_\eta) = P(\mathbf{X}) \tag{5}$$

and

$$p(\mathbf{X} + mG\mathbf{e}_\eta) = p(\mathbf{X})e^{im\sigma} \tag{6}$$

where $P(\mathbf{X})$ is the steady pressure, $p(\mathbf{X})$ is the complex amplitude of the linearized unsteady pressure, $m = 0, \pm 1, \pm 2, \ldots$ is a blade number index, G is the blade spacing, and $\mathbf{e}_\eta$ is a unit vector in the "circumferential" or η direction (see Fig. 1).

Conditions (5) and (6) allow a numerical resolution of the steady and the linearized unsteady flow equations to be restricted to a single extended blade-passage region of the cascade. Although the unsteady solution is dependent on the steady solution, the numerical procedures used to solve the two equation sets can be independent of each other. The numerical approximations used in the present study are described briefly below.

Numerical Solution Schemes

The steady or mean flow solutions, reported herein, were determined using the two-dimensional transonic finite area potential flow solution scheme described in [7, 8]. In this method the integral form of the continuity equation is approximated in the physical plane over polygons constructed through the triangularization of the computational mesh. The flow is assumed known and uniform upstream and downstream of the cascade. For blades with sharp trailing edges one downstream flow condition may be replaced by imposing a Kutta condition at the blade trailing edge. For transonic flows, artificial compressibility is introduced in supersonic regions to stabilize the solution scheme and to capture shocks.

The unsteady differential equation (4) must be solved subject to boundary or jump conditions at mean positions of the blade, wake, and shock surfaces. The blade mean positions are prescribed and the mean positions of wake (i.e., the downstream stagnation streamlines) and shock surfaces are determined by the steady flow solution. Discrete approximations to the linear unsteady equation and boundary conditions are formulated using an implicit, least-squares, interpolation procedure [5, 10] which is applicable on arbitrary computational meshes. In this approach the linear differential operator is approximated for subsonic flow as a nine-point centered difference star at internal points and as a nine-point one-sided difference star at all boundary points. In transonic applications one must distinguish between regions of subsonic flow where the unsteady differential equation is elliptic and supersonic flow where it is hyperbolic. This change in equation type, which depends on the mean-flow Mach number, is handled with local type-dependent differencing. In the present scheme the differential operator is first split into two parts: an operator consisting of terms contributing to the second partial derivative of ϕ in the local streamwise direction and a second operator consisting of the remaining terms in the unsteady differential equation. The difference approximation to the first operator is then determined based on the local steady Mach number (i.e., central in subsonic regions and upwind in supersonic regions), while the latter operator is approximated with the standard central difference star. Once the appropriate difference star has been chosen the difference weights within the star are determined through a weighted least-squares procedure (see [5]). For all of the cases considered in this paper, both the steady and the unsteady solutions were determined on a sheared H-type "cascade" mesh (see Fig. 2*a* of [6]).

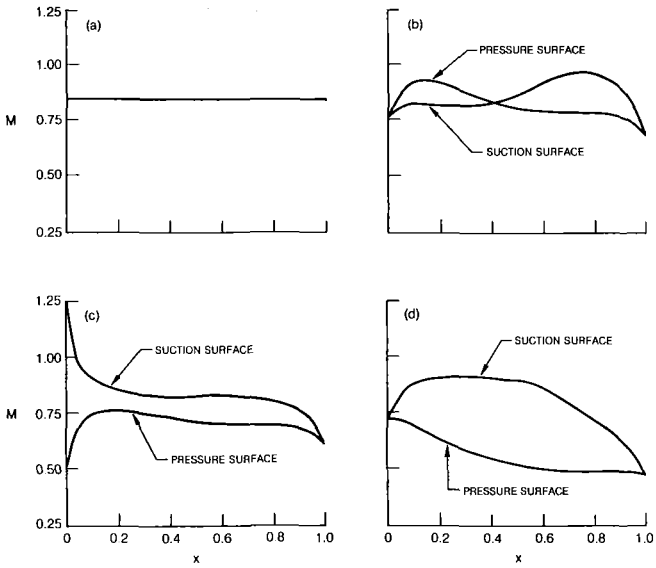

Fig. 2 Steady surface Mach number distributions: (*a*) unloaded flat-plate blades; (*b*) sharp-edged blades at zero incidence; (c) sharp-edged blades at small positive incidence; (*d*) cambered blades at zero incidence

Numerical Solutions

Two different classes of two-dimensional cascades will be considered. The first is a set of four configurations, three of which are representative of the tip sections found in current fan designs, while the fourth is a cascade of flat-plate blades. The solutions for this first set are important in that they demonstrate the importance of blade thickness, mean incidence, and mean blade loading on the unsteady response of closely spaced, highly staggered blades operating at high subsonic inlet Mach number. In addition these solutions represent a first step toward understanding off-design flutter in fans. In generating these solutions the areas which will require additional development of the present model have been identified. The foregoing solutions are then followed by a presentation of selected results for a NASA Lewis flutter cascade. This second class of cascades serves as an important test case for which both the cascade geometry and flow conditions have been clearly defined and some experimental data are currently available [9]. This case has been considered in the hope that it may become a baseline case for comparison with other analyses and future experimental investigations.

Fan-Tip Cascades. The first set is composed of the following two-dimensional configurations: (*a*) a cascade of unload-

Table 1 Reference-blade surface coordinates for cascade *b*

x	y_{upper}	y_{lower}	x	y_{upper}	y_{lower}
0.0000	0.0000	0.0000	0.5161	0.0195	-0.0141
0.0023	0.0001	-0.0002	0.5484	0.0207	-0.0137
0.0099	0.0005	-0.0007	0.5886	0.0215	-0.0133
0.0198	0.0011	-0.0015	0.6129	0.0220	-0.0129
0.0323	0.0017	-0.0024	0.6452	0.0221	-0.0124
0.0495	0.0025	-0.0036	0.6774	0.0220	-0.0118
0.0645	0.0032	-0.0046	0.7097	0.0215	-0.0111
0.0793	0.0039	-0.0056	0.7419	0.0207	-0.0104
0.0968	0.0046	-0.0066	0.7742	0.0195	-0.0096
0.1290	0.0056	-0.0082	0.8065	0.0181	-0.0087
0.1613	0.0065	-0.0094	0.8387	0.0162	-0.0078
0.1935	0.0074	-0.0105	0.8710	0.0141	-0.0067
0.2258	0.0084	-0.0114	0.9032	0.0115	-0.0053
0.2581	0.0094	-0.0123	0.9214	0.0097	-0.0044
0.2903	0.0105	-0.0130	0.9355	0.0081	-0.0037
0.3226	0.0116	-0.0136	0.9536	0.0060	-0.0027
0.3548	0.0127	-0.0141	0.9677	0.0043	-0.0019
0.3871	0.0140	-0.0144	0.9784	0.0029	-0.0013
0.4194	0.0153	-0.0146	0.9956	0.0007	-0.0002
0.4516	0.0166	-0.0146	1.0000	0.0000	0.0000
0.4839	0.0180	-0.0145			

Table 2 Mean inlet and exit conditions

Cascade	$M_{-\infty}$	$\Omega_{-\infty}$(deg)	M_{∞}	Ω_{∞}(deg)
a	0.85	59.75	0.85	59.75
b	0.82	61.3	0.77	60.6
c	0.85	63.0	0.68	60.5
d	0.85	64.8	0.51	56.3

ed flat-plate blades; (*b*) a cascade of sharp-edged blades operating at "zero" mean incidence; (*c*) the same cascade as (*b*) operating at a small positive incidence; and (*d*) a cascade of blades which were constructed by superimposing the blade profile of cases (*b*) and (*c*) on a circular arc camber line having a maximum height of 0.03 at midchord. In case (*d*) the blades also operate at zero mean incidence. Here the term zero mean incidence is defined as the flow incidence at which there is no steady loading at the blade leading edges. The surface coordinates for the reference blade geometry, cascade *b* or *c*, are given in Table 1. This blade profile is typical of that found in the tip region of modern fan-rotor designs, with the following exception. In the vicinity of the leading and trailing edges where the actual blades have small edge radii the present blades have been closed in wedge-shaped edges. This modification has been made to simplify the numerical definition of the blades and to eliminate a geometric feature of the blades which can not be adequately resolved using an H-type cascade mesh. In each case the cascade stagger angle θ is 59.75 deg and the gap/chord ratio G is 0.746 (see Fig. 1).

The predicted steady surface Mach number distributions for the four cascades are shown in Fig. 2. These results were determined using the steady potential flow analysis of [7, 8]. In each case the inlet Mach number was prescribed and a Kutta condition was imposed at blade trailing edges. In addition, the inlet flow angle was prescribed for case (*c*) but a zero incidence condition was imposed in cases (*a*), (*b*), and (*d*). The resulting inlet and exit flow conditions for the example configurations are listed in Table 2, where $M_{-\infty}$ and $\Omega_{-\infty}$ denote the inlet Mach number and flow angle, respectively, and $M_{+\infty}$ and $\Omega_{+\infty}$ refer to the corresponding exit properties. Our original intent was to prescribe the same inlet Mach number for all cases, but we found that for an inlet Mach number of 0.85 a supersonic region extended across the entire blade passage in case (*b*). At the present time the steady and unsteady analyses apply only to flow in which a local supersonic region occurs adjacent to each blade. Therefore we lowered the inlet Mach number in case (*b*) to 0.82. Further, our purpose in studying the cambered blades (case *d*) was to examine the effects of high mean blade loading on unsteady response.

The surface Mach number distributions shown in Figs. 2(*a-d*) correspond to the unloaded flat-plate cascade (M = constant), the two-dimensional cascade of Table 2 operating at $M_{-\infty} = 0.82$ and zero incidence, the same cascade operating at $M_{-\infty} = 0.85$ and at small positive incidence, and finally a cascade of similar (i.e., the same thickness distribution) but highly cambered blades operating at $M_{-\infty} = 0.85$ and at zero incidence, respectively. The predicted steady flows are entirely subsonic for the cascades operating at zero incidence, but for the blade operating at small positive incidence the predicted steady flow is supersonic along the suction surface of each blade in the immediate vicinity of the leading edge. It should be noted that the detailed flow behavior near the leading edge of a thin blade operating at small but nonzero incidence is extremely complicated, but the impact of this detailed behavior on global unsteady response quantities, and hence on aerodynamic stability may not be critical, at least for attached flow. Therefore, in the present study we have essentially avoided a detailed treatment of leading-edge phenomena by considering sharp-edged blade profiles and determining steady and unsteady solutions on relatively coarse cascade-type meshes.

It is clear from studying the mean-flow Mach number distributions presented in Fig. 2, which are representative of current potential flow solution capabilities, that we are still some distance from the actual flow conditions encountered in fans operating at off design. The areas which will require significant future development to the steady potential flow solver include the ability to calculate transonic flows where the supersonic region spans the entire blade passage and to provide a correct or at least an adequate model for the flow in the leading edge region for blades operating at high incidence (up to 10 deg or more). While some may question the validity of an inviscid flow model under conditions in which viscous effects will play an important role, the ability to model only major flow features with such an analysis should be sufficient to study the unsteady blade response.

Unsteady response predictions for the above cascades have been determined for blades undergoing harmoinc single-degree-of-freedom torsional vibrations about midchord. The angular displacement $\tilde{\alpha}(t)$ of the mth blade, which is assumed to be positive in the counterclockwise direction, is given by

$$\tilde{\alpha}_m(t) = \mathrm{Re}\{\alpha e^{i(\omega t + m\sigma)}\}, \qquad m = 0, \pm 1, \pm 2, \ldots, \tag{7}$$

where m is the blade number index and α is the complex amplitude of the reference blade displacement. After expanding the pressure $\tilde{P}$ in the manner indicated by equation (3) and using Taylor series expansions to refer information to the moving blade surface, it follows from the steady and unsteady Bernoulli relations that the first harmonic component of the pressure acting at a moving blade surface is given by

$$p_{\mathcal{B}} = \left[-2(M_{-\infty} A)^{\frac{2}{\gamma - 1}} \frac{D_S \phi}{Dt} + (\boldsymbol{\alpha} \times \mathbf{R}_p) \cdot \nabla P \right]_{\mathcal{B}} \tag{8}$$

The unsteady aerodynamic moment, i.e.

$$\tilde{c}_{M_m}(t) = \mathrm{Re}\{c_M e^{i(\omega t + m\sigma)}\}, \qquad m = 0, \pm 1, \pm 2, \ldots, \tag{9}$$

is the important global response parameter for torsional blade

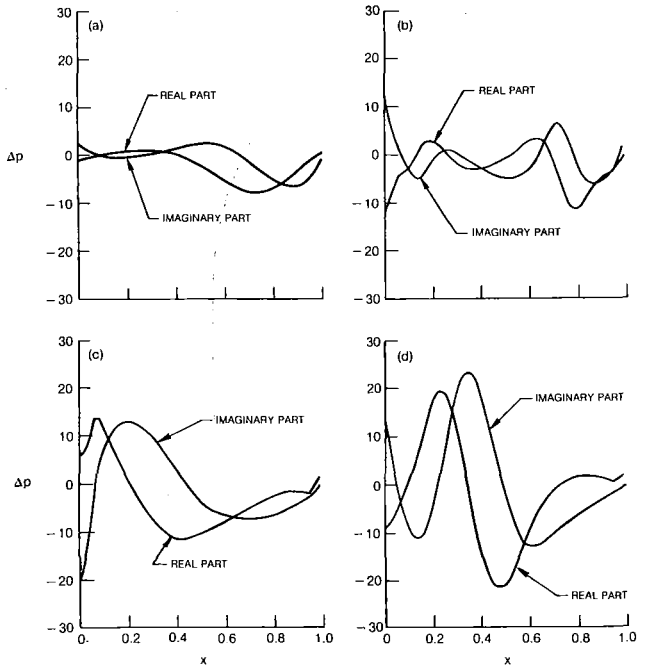

Fig. 3 Unsteady pressure difference distributions due to in-phase ($\sigma = 0$ deg) torsional blade vibrations: (*a*) unloaded flat-plate blades; (*b*) sharp-edged blades at zero incidence; (*c*) sharp-edged blades at small positive incidence; (*d*) cambered blades at zero incidence

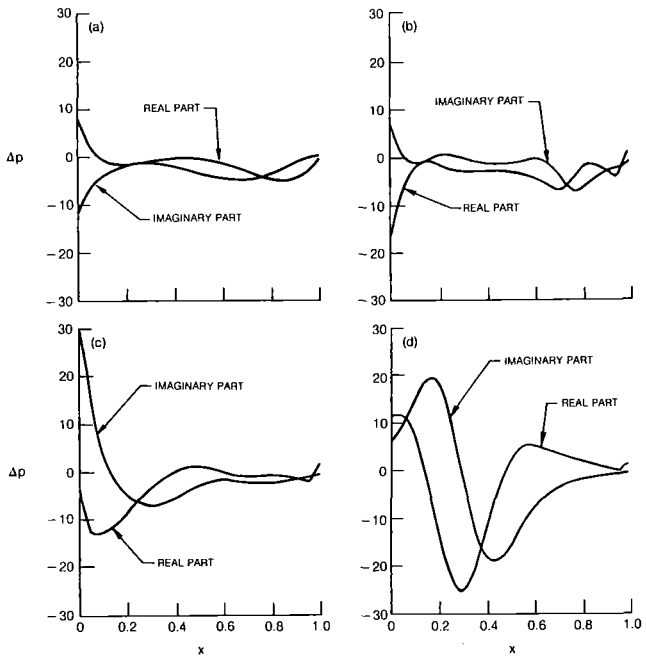

Fig. 4 Unsteady pressure difference distributions due to torsional vibrations at $\sigma = 60$ deg: (*a*) unloaded flat-plate blades; (*b*) sharp-edged blades at zero incidence; (*c*) sharp-edged blades at small positive incidence; (*d*) cambered blades at zero incidence

motions and is also taken as positive in the counterclockwise direction. Here

$$c_M = \oint_{\mathfrak{B}} p_{\mathfrak{B}}(\mathbf{R}_p \cdot d\tau) \tag{10}$$

is the complex amplitude of the unsteady moment acting on the reference blade, $p_{\mathfrak{B}}$ is the complex amplitude of the unsteady pressure acting at the instantaneous position of this blade surface $\mathfrak{B}$, $\mathbf{R}_p$ is a position vector extending from the torsional axis of the reference blade to points on its surface and $d\tau$ is a differential vector tangent to the reference blade surface and directed in the counterclockwise direction. The

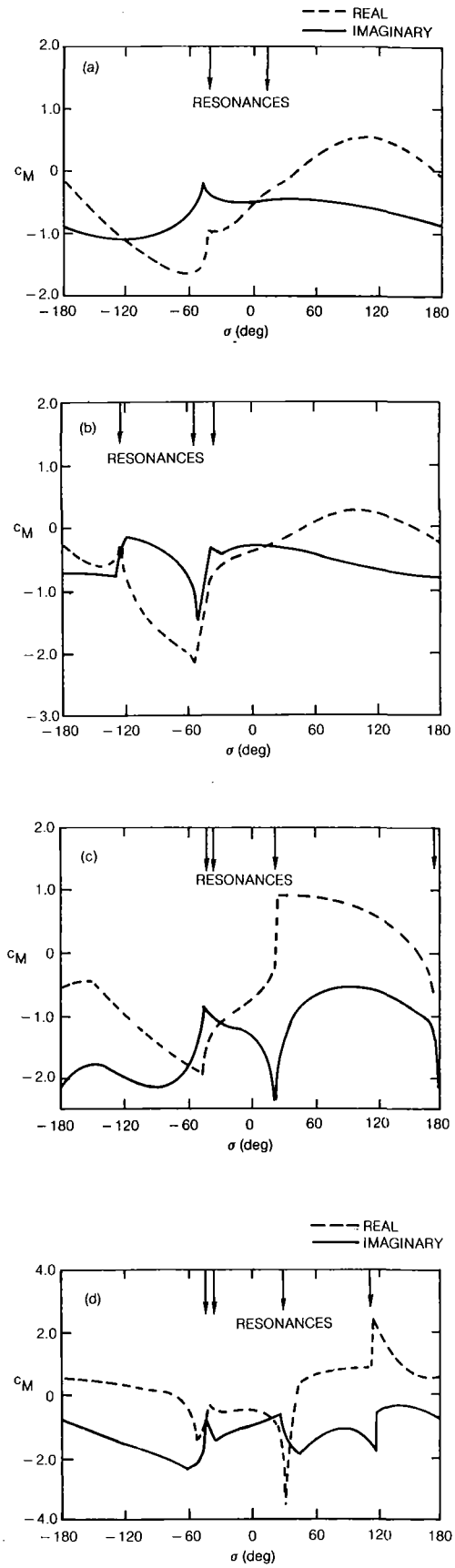

Fig. 5 Unsteady moments due to torsional vibrations: (*a*) unloaded flat-plate blades; (*b*) sharp-edged blades at zero incidence; (*c*) sharp-edged blades at small positive incidence; (*d*) cambered blades at zero incidence

Table 3 Unsteady far-field behavior

Cascade	Phase Angle Range (degrees)	Type of Blade Motion Sub- or Superresonant	Propagating Waves (Upstream, Downstream)
a	[-180, -38.8)	Superresonant	(1, 1)
	(-38.8, 15.1)	Superresonant	(2, 2)
	(15.1, 180]	Superresonant	(1, 1)
b	[-180, -125.5)	Superresonant	(1, 1)
	(-125.5, -53.4)	Superresonant	(1, 0)
	(-53.4, -38.2)	Subresonant	(0, 0)
	(-38.2, -37.2)	Superresonant	(0, 1)
	(-37.2, 180]	Superresonant	(1, 1)
c	[-180, -40.4)	Superresonant	(1, 0)
	(-40.4, -37.8)	Superresonant	(1, 1)
	(-37.8, 24.7)	Superresonant	(2, 1)
	(24.7, 178.3)	Superresonant	(1, 1)
	(178.3, 180]	Superresonant	(1, 0)
d	[-180, -44.1)	Superresonant	(1, 0)
	(-44.1, -37.4)	Superresonant	(1, 1)
	(-37.4, 29.6)	Superresonant	(2, 1)
	(29.6, 113.0)	Superresonant	(1, 1)
	(113.0, 180]	Superresonant	(1, 0)

stability of single-degree-of-freedom torsional vibration is determined by the component of the moment which is out-of-phase with the blade displacement. Thus if we take α to be a real quantity, the stability of the pure torsional blade motion is governed by the imaginary part of c_M, i.e., if $Im\{c_M\}$ is less than zero, the airstream tends to suppress the motion and this motion is stable according to linearized theory.

The unsteady solutions reported here were determined using a sheared H-type mesh consisting of 152 circumferential (ξ = constant) lines uniformly spaced from one axial chord upstream to one axial chord downstream of the blade row and 37 evenly spaced axial lines. This extremely fine mesh spacing (2 percent of chord in the streamwise and circumferential directions) is necessary to resolve the high wave number (spatial frequency) unsteady phenomena resulting from high-frequency blade motions at high subsonic Mach number. Predictions for unsteady pressure difference distributions, i.e.,

$$\Delta p(x) = p_{@-}(x) - p_{@+}(x), \qquad 0 \le x \le 1, \qquad (11)$$

and for unsteady aerodynamic moments are presented in Figs. 3–5 for blades undergoing unit-amplitude (α = 1, 0) torsional vibrations at a reduced frequency ω equal to 1.75. In equation (11) Δp is the complex amplitude of the unsteady pressure acting on the reference blade, the subscripts − and + refer to the lower (pressure) and upper (suction) surfaces of this blade, and x measures the distance along the chord from the blade leading edge. The pressure-difference distributions shown in Fig. 3 are for in-phase torsional vibrations while those in Fig. 4 are for vibrations in which the motion of a given blade leads that of the adjacent blade below by 60 deg. The moment curves in Fig. 5 cover the entire interblade phase angle range, i.e., $-180 \le \sigma \le 180$ deg.

The unsteady aerodynamic response to the blade motion depends, to a a large extent, upon the far-field behavior of the acoustic waves generated by the blade motion. This behavior depends, in turn, on the mean inlet and exit flow conditions (i.e., Mach number and flow angle), the blade spacing, and the frequency and interblade phase angle of the blade motion. The latter can be classified as subresonant if all acoustic waves attenuate with increasing axial distance ($|\xi| \to \infty$) from the blade row or as superresonant if at least one such wave persists in the upstream or downstream far-field and propagates away from the blade row. Resonances occur at the boundaries between various regions. At resonance at least one wave persists far upstream or downstream and carries energy only in the circumferential or η direction (Fig. 1). The classification of the various motions for the example configurations is summarized in Table 3. This information helps to explain the differences between the unsteady pressure-difference distributions at σ = 0 deg (Fig. 3) and σ = 60 deg (Fig. 4) for configurations *a*, *c*, and *d*, as well as the different trends observed by the unsteady moment curves (Fig. 5) over different ranges of interblade phase angle.

Several noteworthy features of the pressure difference distributions shown in Figs. 3 and 4 are the "waviness" of the curves, the abrupt changes in the pressure difference distributions near the trailing edge for cascade (*b*) and near the leading and trailing edges for cascade (*c*), and the relatively large unsteady pressure differences which act on the more highly loaded, cambered blades of example (*d*). The waviness of the pressure difference distributions is due primarily to the high blade-vibration frequency (ω = 1.75) considered. The abrupt changes in Re(Δp) near blade edges is due to inviscid stagnation phenomena which is partially, but not accurately, picked up by the steady solution. It is possible to eliminate the unrealistic inviscid stagnation phenomena at blade trailing edges by artificially extending the blade profile into a cusped trailing-edge section (see [4]). Such a procedure represents, at least approximately, an attempt to model the effects of fluid viscosity which tend to eliminate strong adverse mean pressure gradients immediately upstream of an airfoil trailing edge. Finally, the large-amplitude out-of-phase pressure differences acting on highly cambered blades and upstream of midchord tend to produce large clockwise or stabilizing out-of-phase moments, particularly at σ = 60 deg. The specific reasons for this behavior are not clear, but the cambered blades are more heavily loaded and operate at a much lower exit Mach number than those of the other configurations. The moment curves depicted in Fig. 5 indicate that the torsional blade motions of each cascade are stable (i.e., $Im\ (c_M) < 0$) for ω = 1.75.

NASA Lewis Flutter Cascade. The NASA Lewis flutter cascade consists of nine uncambered or symmetric biconvex airfoils which are driven simultaneously to provide a 1.2 deg amplitude pitching motion about midchord. The cascade has a stagger angle θ of 53 deg and a gap/chord ratio G of 0.767 (see Fig. 1). The symmetric biconvex airfoils have a thickness/chord ratio of 0.0761 and a radius of curvature/chord ratio for both the upper (suction) and lower (pressure) surfaces of 3.60. The experimental airfoils close in rounded leading and trailing edge sections with radius/chord ratio of 0.000033. Tests were performed at an inlet Mach number of 0.65 and an inlet flow angle of 53 deg in an attempt to simulate an unloaded and shock-free mean-flow condition. Tests were also performed at an inlet Mach number of 0.8 and an inlet flow angle of 60 deg in order to observe the surface-pressure response when an oscillating shock occurs near the leading edge of each airfoil. The unsteady experimental response data for torsional vibrations about midchord at interblade phase angles of −90 deg and 90 deg and vibration frequencies of 200 Hz and 500 Hz (i.e., reduced frequencies based on experimental blade chord of ω = 0.422 and 1.106 for $M_{-\infty}$ = 0.65, and ω = 0.366 and 0.916 for $M_{-\infty}$ = 0.8) are given in [9]. Both

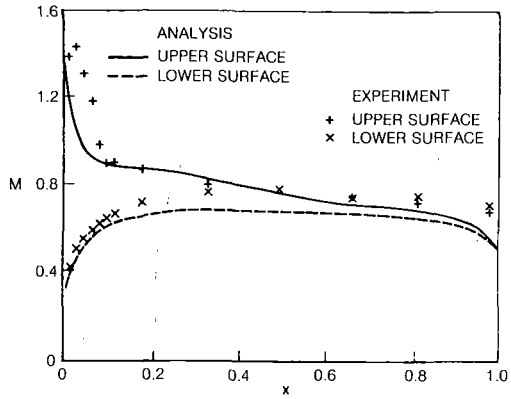

Fig. 6 Steady surface Mach number distributions for the NASA Lewis cascade; $M_{-\infty} = 0.8$, $\Omega_{-\infty} = 60$ deg

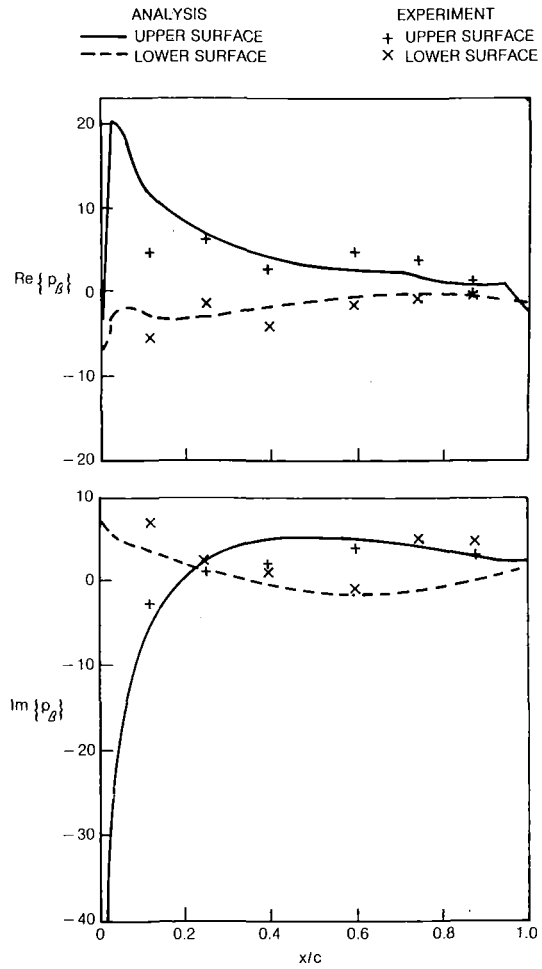

Fig. 7 Unsteady surface-pressure coefficient for the NASA Lewis cascade; $M_{-\infty} = 0.8$, $\Omega_{-\infty} = 60$ deg, $\omega = 0.916$, $\sigma = -90$ deg

cases have been studied in detail in [11], but only selected results for the latter case will be presented here.

Analytical results for the NASA Lewis cascade are depicted, along with the measurements of [9], in Figs. 6–8. The blades used in the analytical study are extended versions of those used in the experiment. That is, sharp-edged biconvex blades having the same surface radius and the same thickness at midchord as those used in the experiment were employed, but the upper and lower surfaces of the blades used in the analysis were extended to close in wedge-shaped leading and trailing edges. As a result the blades used in the analysis are 4 percent longer than those used in the experiment. This modification

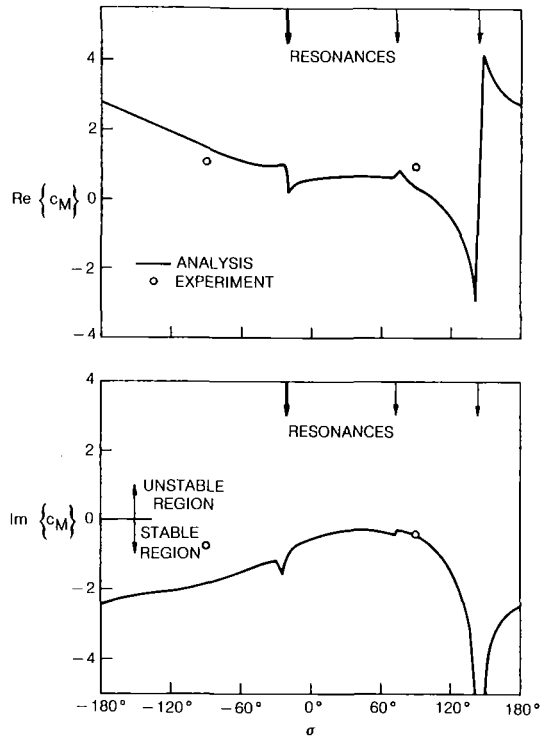

Fig. 8 Unsteady moment due to torsion about midchord for the NASA Lewis cascade; $M_{-\infty} = 0.8$, $\Omega_{-\infty} = 60$ deg, $\omega = 0.916$

was introduced to simplify analytical considerations at blade edges. All other experimental parameters have been retained in the analytical study. It is particularly important to note that the reduced frequency has been defined in terms of the experimental blade chord rather than the analytic blade chord to keep the blade-vibration frequency the same in both the experiment and analysis. The steady full-potential analysis [7, 8] was used to determine the high inlet Mach number ($M_{-\infty} = 0.8$), high mean incidence ($\sigma = 60$ deg) mean-flow solution shown in Fig. 6. In this case the analytical predictions in the vicinity of the blade leading edge are questionable because the steady and unsteady flow behavior in the vicinity of a sharp leading edge at incidence cannot be predicted adequately. Indeed, unless a relatively coarse computational grid is employed near the leading edge of a blade, the iterative solution procedure for the steady full-potential equation will diverge. It is therefore not possible to predict the unsteady effects associated with certain phenomena observed in the experiment [9], e.g., leading-edge lambda-type shocks and flow separations downstream of these shocks, using the current inviscid steady and unsteady codes. In view of these limitations the correlation between the predicted and measured surface Mach number distributions, shown in Fig. 6, is encouraging.

The predicted and measured unsteady surface-pressure coefficients for torsional vibrations about midchord at a reduced frequency of 0.916 and phase angle of -90 deg are shown in Fig. 7. This figure illustrates the level of qualitative agreement between analysis and experiment found for most of the cases for which experimental data were available. Large differences do exist over the forward part of the blade suction surface where the leading edge flow and shock detail are not being correctly resolved by the steady mean-flow analysis. In addition, as might be expected, significant differences between the analytical and experimental unsteady pressure distributions were found (see [11]) when the blade motion was close to a resonance condition. Figure 8 shows the real and imaginary components of the unsteady moment coefficient as a function of the interblade phase angle. Once again there is reasonable agreement with the experimental data. We note, however, that

the experimental moment coefficients were estimated from unsteady pressure-response data available at only six points on each blade surface (suction and pressure). Hence, the experimental estimates for the unsteady moment coefficients may not be too reliable.

Future Research Recommendations

The foregoing results pertain to essentially subsonic mean flow. As part of the present study we also attempted to examine the unsteady response of cascades (*b*) and (*d*) operating under transonic conditions; i.e., at a sufficiently high subsonic inlet Mach number such that a local supersonic region would occur along the suction surface of each blade. It was found that there is a strong need for further development of steady mean-flow analyses (both the present one and those currently available in the literature) if we plan to move toward the positive incidence flutter problem. In particular, there are two types of transonic flow common in fan-tip cascade geometries which are very difficult to resolve. The first type results when the inflow Mach number is raised at low incidence. Under such conditions the flow in the blade passage very quickly reaches the point at which a supersonic region spans the entire passage. While subsonic flow with a local supersonic region and supersonic flow with a local subsonic region are both commonly solved using standard full-potential analyses, when the local supersonic (or subsonic) region spans the complete passage, a solution is much more difficult to obtain. Under such conditions the mass flow is determined not only through the inflow/outflow boundary conditions but by the passage throat dimensions. When solving the full potential equation under these conditions, there is a conflict between the mathematical boundary conditions required to solve the full potential equation (i.e., Dirichlet, Neumann, or some combination of the two around the complete computational boundary) and the physical boundary conditions which actually determine the flow (total conditions upstream and static pressure downstream). There have been some new approaches to this problem, see for example [12], but additional work is still necessary.

The second type of transonic flow occurs when the blades are operating at high mean incidence. It is much more difficult to determine an inviscid steady solution under these flow conditions than for the low incidence case. Even if a numerical solution is possible the solution is questionable on physical grounds, since viscous phenomena will play an important role in the determination of these flows. Hopefully it will be possible to provide a rational procedure for the calculation of the steady mean flow at high incidence using the methods of viscid/inviscid interaction theory, but this will require a long-range research effort requiring some breakthroughs in theoretical formulation and numerical modeling. For near-term design applications it may be possible to introduce a simple separation model into the present analysis such as one developed by Chi [13] for use in classical linearized formulations.

In addition to the steady flow analysis, there exist a number of fundamental questions about the unsteady analysis which must be addressed. The combination of high-frequency blade vibrations and high inflow Mach numbers places severe requirements on the density of the meshes needed to resolve the unsteady phenomena. These mesh requirements were studied to a limited degree with the fan-tip cascade cases, and these cases illustrate the mesh density necessary to resolve the unsteady phenomena. These meshes are much finer than those commonly used in previous studies. As higher and higher frequencies are considered, the mesh requirements will have to be addressed.

In addition, the present unsteady analysis should be modified to remove the spurious behavior predicted at blade leading and trailing edges. For thin blades a detailed resolution of the local inviscid behavior associated with flow stagnation is very difficult to achieve and, in fact, such a detailed resolution is not even appropriate at blade trailing edges since viscous effects eliminate the inviscid stagnation point. In the present study a deliberate attempt has been made to ignore such local behavior by restricting consideration to sharp-edged blades operating at low incidence and determining inviscid solutions only on cascade meshes. Although it appears that local inviscid behavior has been successfully eliminated from the prediction of mean or steady flow properties (see Fig. 2), such behavior is partially retained in the prediction of unsteady properties (see Figs. 3 and 4). The reason for this is that the relevant steady flow properties depend only on the first partial derivatives of the steady potential, while unsteady properties depend also on the second partial derivatives of this potential, and local inviscid stagnation phenomena have not been completely removed from the prediction of these second derivatives. Thus simple methods for smoothing the second derivatives of the steady potential near blade edges should be devised.

Concluding Remarks

Existing full-potential and linearized potential flow analyses have been applied to the prediction of the steady and unsteady flows through two-dimensional fan-tip cascades. This effort represents an ambitious application of existing numerical analyses and computer codes to highly staggered cascades of thin, closely spaced blades vibrating at high frequency. Numerical results have been reported for four configurations each having a stagger angle of 59.75 deg and a gap/chord ratio of 0.746. The first configuration, an unloaded flat-plate cascade, has been included to provide a basis for interpreting and comparing unsteady response predictions. The second (*b*) and third (*c*) configurations consisted of sharp-edged blades whose thickness and camber distributions are typical of those found in the fan rotor tip region. In case (*b*) the inlet flow angle was determined by prescribing a zero incidence condition, while in case (*c*) the blades operated at small positive incidence. Finally, the fourth configuration (*d*), which consisted of highly cambered blades having the same thickness distributions as those in (*b*) and (*c*), was selected to illustrate partially the effects of mean blade loading on unsteady response. Comparison of these cases with the flat-plate cascade (*a*) clearly illustrates the importance of incidence and blade loading on the resulting unsteady response at high subsonic inlet Mach number and blade-vibration frequency.

As a result of this study it is recommended that further research be conducted to improve the numerical resolution of steady transonic phenomena and high-frequency unsteady phenomena for fan-type cascades. In addition, the possibility of developing a rational approach for introducing viscous effects into the theoretical prediction of unsteady response phenomena for cascades operating at high mean incidence should be investigated.

Acknowledgments

This research was sponsored by the Air Force Systems Command under Contract F33515-79-C-2087 and by the NASA Lewis Research Center under Contract NAS3-23696. This support, and the experimental data and assistance in its interpretation provided by D. R. Boldman, are gratefully acknowledged.

References

1 Verdon, J. M., and Caspar, J. R., "Subsonic Flow Past an Oscillating Cascade With Finite Mean Flow Deflection," *AIAA Journal*, Vol. 18, 1980.

2 Whitehead, D. S., and Grant, R. J., "Force and Moment Coefficients for

High Deflection Cascades," in: *Proc. 2nd Intl. Symp. on Aeroelasticity in Turbomachines*, P. Suter, ed., 1981, pp. 85–127.

3 Caruthers, J. E., "Aerodynamic Analysis of Cascaded Airfoils in Unsteady Rotational Flow," in: *Proc. 2nd Intl. Symp. on Aeroelasticity on Turbomachines*, P. Suter, ed., 1981, pp. 31–61.

4 Whitehead, D. S., "The Calculation of Steady and Unsteady Transonic Flow in Cascades," Cambridge University Engineering Department Report, CUED/A-Turbo/TR 118, 1982.

5 Verdon, J. M., and Caspar, J. R., "Development of an Unsteady Aerodynamic Analysis for Finite-Deflection Subsonic Cascades," *AIAA Journal*, Vol. 20, No. 9, Sept. 1982, pp. 1259–1267.

6 Verdon, J. M., and Caspar, J. R., "A Linearized Unsteady Aerodynamic Analysis for Transonic Cascades," *Journal of Fluid Mechanics*, Vol. 149, Dec. 1984, pp. 403–429.

7 Caspar, J. R., Hobbs, D. E., and Davis, R. L., "Calculation of Two-Dimensional Potential Cascade Flow Using Finite Area Methods," *AIAA Journal*, Vol. 18, Jan. 1980, pp. 103–109.

8 Caspar, J. R., "Unconditionally Stable Calculation of Transonic Potential Flow Through Cascades Using an Adaptive Mesh for Shock Capture," ASME JOURNAL OF ENGINEERING FOR POWER, Vol. 105, No. 3, July 1983, pp. 504–513.

9 Shaw, L. M., Boldman, D. R., Buggele, A. E., and Buffman, D. J., "Unsteady Pressure Measurements on a Biconvex Airfoil in a Transonic Oscillating Cascade," ASME Paper No. 85-GT-212.

10 Caspar, J. R., and Verdon, J. M., "Numerical Treatment of Unsteady Subsonic Flow Past an Oscillation Cascade," *AIAA Journal*, Vol. 19, No. 12, Dec. 1981, pp. 1531–1539.

11 Verdon, J. M., and Usab, W. J., Jr., "Application of a Linearized Unsteady Aerodynamic Analysis to Standard Cascade Configurations," NASA Contractor Report 3940, Jan. 1986.

12 Habashi, W. G., Hafez, M. M., and Kotiuga, P. L., "Computation of Choked and Supersonic Turbomachinery Flows by a Modified Potential Method," *AIAA Journal*, Vol. 23, No. 2, Feb. 1985, pp. 214–221.

13 Chi, M. R., "Unsteady Aerodynamics in Stalled Cascade and Stall Flutter Prediction," ASME Century 2 Aerospace Conference, Paper No. 80-C2/Aero-1, 1980.

Computation of Inviscid Incompressible Flow Using the Primitive Variable Formulation

S. Abdallah

H. G. Smith[1]

Applied Research Laboratory,
The Pennsylvania State University,
State College, PA 16804

The primitive variable formulation originally developed for the incompressible Navier–Stokes equations is applied for the solution of the incompressible Euler equations. The unsteady momentum equation is solved for the velocity field and the continuity equation is satisfied indirectly in a Poisson-type equation for the pressure (divergence of the momentum equation). Solutions for the pressure Poisson equation with derivative boundary conditions exist only if a compatibility condition is satisfied (Green's theorem). This condition is not automatically satisfied on nonstaggered grids. A new method for the solution of the pressure equation with derivative boundary conditions on a nonstaggered grid [25] is used here for the calculation of the pressure. Three-dimensional solutions for the inviscid rotational flow in a 90 deg curved duct are obtained on a very fine mesh (17 × 17 × 29). The use of a fine grid mesh allows for the accurate prediction of the development of the secondary flow. The computed results are in good agreement with the experimental data of Joy [15].

Introduction

Background. Secondary flow motion is defined as the motion of a fluid in planes perpendicular to the primary flow direction and is associated with streamwise vorticity. A large streamwise vorticity can be generated by the deflection of initially sheared primary flow in a curved passage. Briley and McDonald [1] observed that streamwise vorticity on the order of 50 percent of the transverse vorticity is generated by a flow deflection of merely 15 deg. The authors observed streamwise vorticity on the order of 140 percent of the inlet transverse vorticity in a square duct after 60 deg of turning.

There are four major effects that secondary flow has on turbomachinery components. Secondary flow can: transfer low-energy fluid to regions or surfaces of decelerating flow where boundary layer separation can occur; extract kinetic energy from the primary flow which is eventually lost through viscous dissipation; and affect the efficiency of the machine by influencing successive blade row angles of attack [2]. Kreskovsky et al. [3] noted that secondary flow can remove the wall boundary layer fluid and replace it with mainstream flow thus affecting wall heat transfer.

The generation of streamwise vorticity in turbomachinery and cascades occurs mostly due to the curvature effect on an initially sheared flow. In the early 1950s, fluid dynamicists began to derive analytical methods to predict the development of secondary flow. Squire and Winter [4] developed an equation for the generation of streamwise vorticity in an inviscid fluid. Hawthorne [5] developed a more general expression for the secondary flow vorticity. Horlock and Lakshminarayana provide an extensive review of the secondary flow problem in [6]. By the early 1970s, fluid dynamicists turned their efforts to numerical predictions of the development of secondary flow. Inviscid flow solutions for the secondary flow problem require three-dimensional solutions of Euler equations. A brief description of these techniques is given in the following sections.

Quasi-Three-Dimensional Methods. Quasi-three-dimensional solutions are synthesized from two-dimensional flow solutions on intersecting families of stream sheets of variable thicknesses. Wu [7] developed a general theory to obtain the three-dimensional solutions using the S_1 (blade-to-blade) and S_2 (meridional) relative stream surfaces. Katsanis [8, 9], Marsh [10], and Wilkinson [11] and many others developed computer programs to calculate solutions on the S_1 and S_2 surfaces using Wu's method. Wang et al. [12] developed an S_1–S_2 iterative scheme to solve for the three-dimensional rotational flow. This type of analysis may only be applicable for cases with mild vorticity in passages with relatively small curvature. For large secondary flow, the S_1 and S_2 stream surfaces become highly twisted because of the developed streamwise vorticity. The surfaces may even be doubled back over themselves as Katsanis and McFarland pointed out in their discussion of [12]. An early attempt was made by Fagan [13] to adopt the S_1 and S_2 method to highly rotational flow by using coordinates that rotate with the stream surfaces. This attempt was not successful.

Few methods have been developed to solve the secondary flow problem on fixed non-stream surfaces. Stuart and

[1]Present Address: General Dynamics Corporation, Fort Worth Division, Fort Worth, TX, U.S.A.

Contributed by the Gas Turbine Division of THE AMERICAN SOCIETY OF MECHANICAL ENGINEERS and presented at the 31st International Gas Turbine Conference and Exhibit, Düsseldorf, Federal Republic of Germany, June 8–12, 1986. Manuscript received at ASME Headquarters January 27, 1986. Paper No. 86-GT-141.

Hetherington [14] employed the streamline curvature method to obtain quasi-three-dimensional solutions on two sets of fixed surfaces in curved ducts. They compared their numerical results with Joy's [15] experimental data successfully. The same problem was computed using the streamlike function formulation of Abdallah and Hamed [16]. In this method, three-dimensional solutions are obtained on three sets of fixed non-stream surfaces. Hamed and Liu [17] used the same method to calculate the compressible secondary flow in an accelerating elbow with 90 deg of turning.

There are a number of nonprimitive variable methods that are applicable for the inviscid secondary flow solutions such as the methods of Lacor and Hirsh [18] and Abdallah and Hamed [19].

The Artificial Compressibility Method. In the artificial compressibility method, first suggested by Chorin [20], a time derivative of the pressure divided by a large factor is added to the continuity equation. The addition of the time-derivative term to the continuity allows the use of standard compressible flow techniques for the incompressible equations. Choi and Merkle [21] investigated the stability and convergence characteristics of this system of equations using the implicit algorithm. Their study was done for both the compressible and incompressible flow equations. They recommended that the factor of the time derivative term in the continuity equation be chosen near the free-stream velocity to speed convergence of the numerical solution. Rizzi and Eriksson [22] examined the same system of equations in the incompressible form and arrived at similar conclusions.

The Pressure Poisson Equation Method. The pressure Poisson equation method was first developed by Harlow and Welch in 1965 [23] for the solution of the incompressible Navier–Stokes equations. In their formulation, the unsteady momentum equation is solved for the velocity field by marching in time. The pressure is calculated from a Poisson-type equation derived from the divergence of the momentum equation. The pressure equation replaces the continuity equation in the Navier–Stokes equations. Continuity is satisfied indirectly through the solution of the pressure equation at each grid point in the flow field. It is important to mention here that boundary conditions for the pressure which are obtained from the momentum equation are of the Neumann type. Solutions for the Poisson equation with Neumann boundary conditions require the satisfaction of a compatibility condition resulting from Green's theorem. Failure to satisfy this condition leads to nonconvergent iterative solutions [24]. While the compatibility condition is not automatically satisfied on regular (nonstaggered) finite-difference grids it is satisfied for staggered grids. Although solutions using this technique are obtained for two- and three-dimensional problems on staggered grids, use of staggered grids for three-dimensional problems is very complex. To the best of the author's knowledge, the pressure Poisson equation formulation has never been adopted using staggered or nonstaggered grids for inviscid flow calculations before.

The Present Approach. In the present study, we adopted to the inviscid flow problem the primitive variable formulation [23] detailed in the above section. As in the viscous flow solutions, the unsteady momentum equations are solved for the velocity components by a time-marching procedure. Also, the continuity equation is satisfied indirectly in the pressure Poisson equation. Boundary conditions for the pressure are of the Neumann type. The only difference between the inviscid and viscous flow versions of the primitive variable formulation is in the boundary conditions for the pressure and the velocity.

The major difficulty in this analysis, as pointed out before for the viscous flow analysis, is in the solution of the pressure Poisson equation on regular (nonstaggered) grids. A new technique developed by Abdallah [25] for the solution of the Poisson equation with Neumann conditions which satisfies the compatibility condition on nonstaggered grids is used in the present study.

In this primitive variable formulation, the continuity equation is satisfied indirectly through the solution of the pressure Poisson equation at each grid point. Since the pressure equation is solved in the interior grid points, continuity is enforced only at the interior points. The continuity equation cannot be satisfied at the boundaries since the pressure equation is not solved there. In the present inviscid flow analysis, the momentum equations are solved at the solid boundaries to calculate the slip velocities. The Neumann boundary conditions for the pressure are modified in order to satisfy the continuity equation at the boundaries.

The primitive variable method has three major advantages over the classical nonprimitive solvers of the incompressible Euler equations: (1) The method is very efficient because the number of governing equations is four compared with six in other nonprimitive solvers [24]; (2) the boundary conditions in this method are simple (no-flux) compared with the complex

Nomenclature

A, B, C = finite difference coefficients, equation (10)
D = dilatation, equation (5*b*)
dS = surface increment
H = duct height
L = number of grid points in z direction
M = number of grid points in θ direction
N = number of grid points in r direction
P = static pressure
R_i = radius of duct inner wall, Fig. (1)
R_o = radius of duct outer wall, Fig. (1)
r = radial coordinate
u = radial velocity component
v = through-flow velocity component
v_i = inlet through-flow velocity
w = vertical velocity component
z = vertical coordinate
α = dummy variable, equation (14)
θ = through-flow coordinate
θ_e = duct turning angle
σ = right-hand side, equation (5)
$d\tau$ = control volume increment
Δr = grid spacing in radial direction
Δt = integration step size (time step)
Δz = grid spacing in vertical direction
$\Delta\theta$ = grid spacing in through-flow direction

Subscripts

e, w, n, s, u, d = control volume boundary points, Fig. (1*a*)
(i, j, k) = finite difference grid node points in (θ, r, z) directions
n = denotes a normal derivative
t = denotes a time derivative
r, z, θ = denote a derivative in corresponding direction

Superscripts

n = denotes time level t
$n+1$ = denotes time level $t + \Delta t$

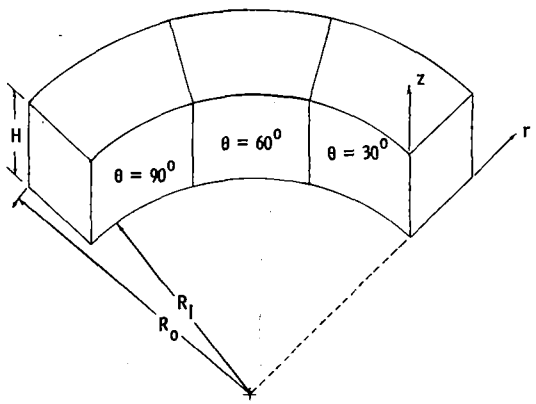

Fig. 1 Duct geometry

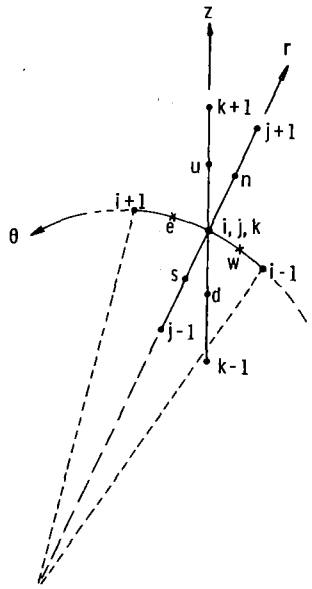

Fig. 1(a) Finite-difference grid

boundary conditions of the other nonprimitive solvers [24]; and (3) the method is applicable for two and three dimensions, and steady and unsteady problems without major modifications.

Application of the method for the solution of secondary flow in a curved duct is presented. Numerical results are obtained and compared with the experimental data of Joy [15].

Mathematical Formulation

The governing equations for incompressible inviscid flow are written in cylindrical polar coordinates r, θ, and z for the curved duct shown in Fig. 1.

Continuity equation:

$$\frac{1}{r}(ru)_r+\frac{1}{r}v_\theta+w_z=0 \tag{1}$$

Momentum equations:

$$u_t+uu_r+\frac{v}{r}u_\theta+wu_z-\frac{v^2}{r}=-P_r \tag{2}$$

$$v_t+uv_r+\frac{v}{r}v_\theta+wv_z+\frac{uv}{r}=-\frac{1}{r}P_\theta \tag{3}$$

$$w_t+uw_r+\frac{v}{r}w_\theta+ww_z=-P_z \tag{4}$$

where u, v, and w are the velocity components in the r, θ, and z directions, respectively, P is the static pressure, and t is the time. The static pressure P in the above equations is calculated from a Poisson-type equation.

Pressure Equation. The pressure equation is derived from the divergence of the momentum equation

$$\frac{1}{r}(rP_r)_r+\frac{1}{r^2}P_{\theta\theta}+P_{zz}=\sigma \tag{5}$$

where

$$-\sigma=\frac{1}{r}(ruu_r+vu_\theta+rwu_z-v^2)_r+\frac{1}{r}\left(uv_r+\frac{v}{r}v_\theta+wv_z+\frac{uv}{r}\right)_\theta+\left(uw_r+\frac{v}{r}w_\theta+ww_z\right)_z+D_t \tag{5a}$$

and

$$D=\frac{1}{r}(ru)_r+\frac{1}{r}v_\theta+w_z \tag{5b}$$

The unsteady term in equation (5*a*) is approximated by

$$D_t=\frac{D^{n+1}-D^n}{\Delta t} \tag{5c}$$

where n and $n+1$ refer to time levels t and $t+\Delta t$, respectively.

The governing equations (1) to (5) for the variables u, v, w, and P are not independent. The continuity equation (1) is eliminated from the system of equations, and it is directly enforced in the pressure equation (5) by setting $D = 0$. However, this leads to nonlinear instabilities in the momentum equations. The term D^n in equation (5*c*) is retained to eliminate these instabilities [23, 24].

Equations (2), (3), and (4) are solved for the velocity components u, v, and w, respectively. Equation (5) is then solved for the pressure P.

Boundary Conditions. Boundary conditions for the momentum equations (2), (3), and (4) are obtained from the no-flux condition at the solid boundaries. With reference to Fig. 1,

$$u=0 \quad \text{at } r=R_i, \quad R_o \tag{6a}$$

$$w=0 \quad \text{at } z=0, \quad H \tag{6b}$$

$$u=w=0 \text{ and } v=v_i \quad \text{at } \theta=0 \tag{6c}$$

$$u_\theta=w_\theta=v_\theta=0 \quad \text{at } \theta=\theta_e \tag{6d}$$

Boundary conditions at the exit station $\theta = \theta_e$ are obtained from the assumption that far downstream, there is a uniform swirling flow pattern, repeated at all subsequent planes of cross section [13, 14, 16]. This is physically acceptable since the secondary velocity in inviscid flows is developed due to the curvature effect. Thus, the fluid leaving the exit station will continue to rotate with the same exit vorticity in a straight path.

Boundary conditions for the pressure Poisson equation (5) are obtained from the steady form of the momentum equations (2), (3), and (4). The time derivative terms in the boundary conditions are important if the unsteady case is considered.

$$-P_r=uu_r+\frac{v}{r}u_\theta+wu_z-\frac{v^2}{r} \quad \text{at } r=R_i, \quad R_o \tag{7a}$$

$$-P_z=uw_r+\frac{v}{r}w_\theta+ww_z \quad \text{at } z=0, \quad H \tag{7b}$$

$$-\frac{1}{r}P_\theta=\frac{v}{r}v_\theta \quad \text{at } \theta=0 \tag{7c}$$

$$-\frac{1}{r}P_\theta=uv_r+wv_z+\frac{uv}{r} \quad \text{at } \theta=\theta_e \tag{7d}$$

The above boundary conditions for the pressure are of the Neumann (derivative) type. Solutions for the Poisson equation (5) with the Neumann boundary conditions (7) exist only if the following compatibility condition (Green's theorem) is satisfied:

$$\iiint \sigma \, d\tau = \iint P_n dS \tag{8}$$

where $d\tau$ is the volume increment, dS is the surface increment, and n is the outward normal to the surface S.

For the duct geometry shown in Fig. 1, equation (8) becomes

$$\iiint \sigma \, r dr \, d\theta \, dz = \iint P_r \, r d\theta \, dz + \iint P_z \, r dr \, d\theta + \iint \frac{1}{r} P_\theta \, dr \, dz \tag{9}$$

This condition is not automatically satisfied on nonstaggered finite difference grids. Failure to satisfy this condition leads to nonconvergent iterative solutions [24]. The compatibility condition is automatically satisfied on staggered grids because: (1) the calculation of the pressure at the center of the finite-difference control volume and the velocity components at the center of the control volume surfaces preserves the conservative property of the compatibility condition, and (2) the Neumann boundary conditions are applied at one-half grid spacing away from the boundaries. As will be seen later in the analysis, the present method satisfies the above two conditions on nonstaggered grids. The method is outlined here for inviscid flow solutions and interested readers are referred to [25] for the viscous case.

Consistent Finite-Difference Approximation for the Pressure Equation. The method reported in [25] consists of two steps when applied to inviscid flow analysis:

1 Write the pressure Poisson equation in a divergence form, equation (5).

2 Boundary conditions for the pressure should be evaluated at one-half grid spacing away from the boundaries for consistency with the divergence form of equation (5).

The above procedure satisfies the compatibility condition equation (8) on nonstaggered grids.

Finite-Difference Approximation for Equation (5). Referring to Fig. 1(*a*), equation (5) is approximated at the grid point (i, j, k), which corresponds to (θ, r, z) directions, by using central second-order accurate formulas as follows:

$$r_{i,j,k}[(rP_r + A)_n - (rP_r + A)_s] + \frac{\Delta r}{\Delta \theta}[(P_\theta + B)_e - (P_\theta + B)_w] + r_{i,j,k}^2[(P_z + C)_u - (P_z + C)_d] = r_{i,j,k}^2 \frac{\Delta r}{\Delta t} D_{i,j,k}^n \tag{10}$$

where

$$A = ruu_r + vu_\theta + rwu_z - v^2 \tag{10a}$$

$$B = ruv_r + vv_\theta + rwv_z + uv \tag{10b}$$

$$C = uw_r + \frac{v}{r} w_\theta + ww_z \tag{10c}$$

and Δr, $\Delta \theta$, and Δz are the grid spacing in the r, θ, and z directions, respectively. Equal grid increments in the r and z directions are considered here.

The flux components P_r, P_θ, and P_z are approximated using central second-order accurate formulas at the location e, w, n, s, u, and d which correspond to $(i+1/2, j, k)$, $(i-1/2, j, k)$, $(i, j+1/2, k)$, $(i, j-1/2, k)$, $(i, j, k+1/2)$, and $(i, j, k-1/2)$, respectively, as follows

$$P_r\Big|_n = (P_{i,j+1,k} - P_{i,j,k})/\Delta r \tag{11a}$$

$$P_r\Big|_s = (P_{i,j,k} - P_{i,j-1,k})/\Delta r \tag{11b}$$

$$P_\theta\Big|_e = (P_{i+1,j,k} - P_{i,j,k})/\Delta \theta \tag{11c}$$

$$P_\theta\Big|_w = (P_{i,j,k} - P_{i-1,j,k})/\Delta \theta \tag{11d}$$

$$P_z\Big|_u = (P_{i,j,k+1} - P_{i,j,k})/\Delta z \tag{11e}$$

$$P_z\Big|_d = (P_{i,j,k} - P_{i,j,k-1})/\Delta z \tag{11f}$$

By substituting equation (11) in equation (10), one obtains

$$-P_{i,j,k}\left(\frac{r_0(r_n + r_s)}{\Delta r} + \frac{2\Delta r}{\Delta \theta^2} + \frac{2r_0^2}{\Delta z}\right) + P_{i,j+1,k}\left(\frac{r_0 r_n}{\Delta r}\right) + P_{i,j-1,k}\left(\frac{r_0 r_s}{\Delta r}\right) + P_{i+1,j,k}\left(\frac{\Delta r}{\Delta \theta^2}\right) + P_{i-1,j,k}\left(\frac{\Delta r}{\Delta \theta^2}\right) + P_{i,j,k+1}\left(\frac{r_0^2}{\Delta z}\right) + P_{i,j,k-1}\left(\frac{r_0^2}{\Delta z}\right) = -r_0(A_n - A_s) - \frac{\Delta r}{\Delta \theta}(B_e - B_w) - r_0^2(C_u - C_d) + r_0^2 \frac{\Delta r}{\Delta t} D_{i,j,k}^n \tag{12}$$

where $r_0 = r_{i,j,k}$.

The parameters A, B, and C at the locations e, w, n, s, u, and d are calculated as follows

$$A_n = \frac{r_n u_n}{\Delta r}(u_{i,j+1,k} - u_{i,j,k}) + \frac{v_n}{4\Delta \theta}(u_{i+1,j+1,k} + u_{i+1,j,k} - u_{i-1,j+1,k} - u_{i-1,j,k}) + \frac{r_n w_n}{4\Delta z}(u_{i,j,k+1} + u_{i,j+1,k+1} - u_{i,j,k-1} - u_{i,j+1,k-1}) - v_n^2 \tag{13a}$$

$$B_e = \frac{r_e u_e}{4\Delta r}(v_{i,j+1,k} + v_{i+1,j+1,k} - v_{i,j-1,k} - v_{i+1,j-1,k}) + \frac{v_e}{\Delta \theta}(v_{i+1,j,k} - v_{i,j,k}) + \frac{r_e w_e}{4\Delta z}(v_{i,j,k+1} + v_{i+1,j,k+1} - v_{i,j,k-1} - v_{i+1,j,k-1}) + u_e v_e \tag{13b}$$

$$C_u = \frac{u_u}{4\Delta r}(w_{i,j+1,k+1} + w_{i,j+1,k} - w_{i,j-1,k+1} - w_{i,j-1,k}) + \frac{v_u}{4r_u \Delta \theta}(w_{i+1,j,k+1} + w_{i+1,j,k} - w_{i-1,j,k+1} - w_{i-1,j,k}) + \frac{w_u}{\Delta z}(w_{i,j,k+1} - w_{i,j,k}) \tag{13c}$$

Expressions similar to the above parameters can be obtained for A_s, B_w, and C_d by using the same procedure.

The parameters at n, s, e, w, u, and d in equations (12) and

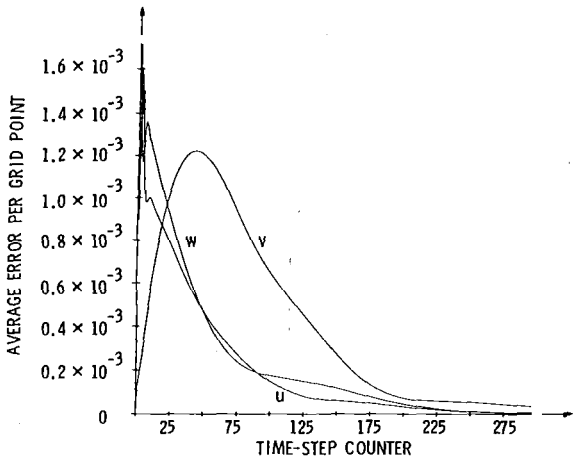

Fig. 2 Error for the velocity components u, v, and w

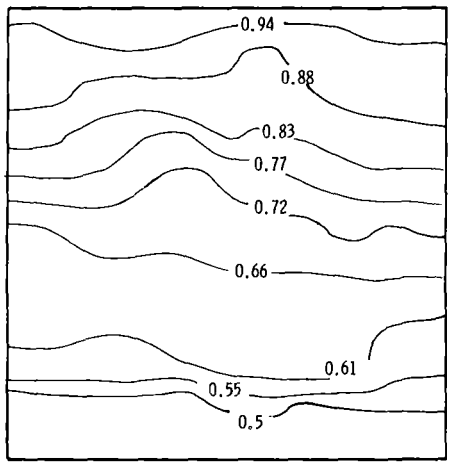

Fig. 3 Inlet velocity profile, experimental data of Joy [15]

(13) are calculated from their values at the grid locations by averaging for example

$$\alpha_n = \frac{\alpha_{i,j+1,k} + \alpha_{i,j,k}}{2} \tag{14a}$$

$$\alpha_e = \frac{\alpha_{i+1,j,k} + \alpha_{i,j,k}}{2} \tag{14b}$$

$$\alpha_u = \frac{\alpha_{i,j,k+1} + \alpha_{i,j,k}}{2} \tag{14c}$$

where α is r, u, v, or w.

Finite Difference Approximation for Boundary Conditions Equation (7). With reference to Fig. 1(a), equation (7) is approximated at one-half grid spacing away from the boundaries using second-order accurate central finite-difference formulas.

$$(P_{i,2,k} - P_{i,1,k})/\Delta r = -(A/r)_{i,3/2,k} \tag{15a}$$

$$(P_{i,N-1,k} - P_{i,N,k})/\Delta r = (A/r)_{i,N-1/2,k} \tag{15b}$$

$$(P_{i,j,2} - P_{i,j,1})/\Delta z = -C_{i,j,3/2} \tag{15c}$$

$$(P_{i,j,L-1} - P_{i,j,L})/\Delta z = C_{i,j,L1/2} \tag{15d}$$

$$(P_{2,j,k} - P_{1,j,k})/\Delta\theta = -B_{3/2,j,k} \tag{15e}$$

$$(P_{M-1,j,k} - P_{M,j,k})/\Delta\theta = B_{M-1/2,j,k} \tag{15f}$$

where M, N, and L are the number of grid points in θ, r, and z directions, respectively.

The summation of the left- and right-hand members (L.H.M. and R.H.M., respectively) of equations (12) and (15) for all the grid points (i, j, k) can be interpreted as the divergence theorem in discrete form [26].

$$\text{L.H.M.} = 0$$

$$\text{R.H.M.} = 0$$

This proves that the compatibility condition equation (8) is exactly satisfied on nonstaggered grids.

Results and Discussion

Numerical solutions for the governing equations (2), (3), and (4) at the interior grid points are obtained for the velocity components using Lax's scheme [27]. These equations are also solved at the solid boundaries to calculate the slip velocities. The pressure Poisson equation (5) is solved at the interior points using the successive overrelaxation method. Since the continuity equation is enforced through the solution of the pressure equation, high residuals D result at the boundaries. The Neumann boundary conditions for the pressure are modified to enforce the continuity equation at the solid boundaries.

Computations are carried out in a curved duct of square cross section (Fig. 1) to facilitate comparison with Joy's [15] experimental data. Joy measured flow properties in a 90 deg curved duct (constant mean radius of 38.1 cm) with a rectangular cross section (12.7 × 25.4 cm). The flow in the duct was shear flow of air at 15°C and a Reynolds number of approximately 10^5.

The flow was symmetrical about the horizontal center plane of the duct. To take advantage of the symmetry, computations in this study are carried out in only one half of the duct.

A very fine grid mesh was used (17 × 17 grid nodes in 29 cross-sectional planes) to accurately capture the details of secondary flow. Execution time was 17 min on an IBM 3033 to converge to an average tolerance of 10^{-8} at a grid point for the velocity components. The average error in the velocity component u, for example, is defined as

$$\sum_{i=1}^{M}\sum_{j=1}^{N}\sum_{k=1}^{L}(u^{n+1} - u^n)_{i,j,k}$$

divided by the total number of grid points ($N \times M \times L$ = 8381 grid points). The pressure equation does not need to be solved to full convergence at each time step if only the steady state solution is desired. In this analysis, 11 iterations for the pressure are allowed at each time step. The authors did not attempt to optimize any of the parameters that affect convergence such as the time-marching step size, the successive overrelaxation factor, and the number of iterations allowed for the pressure equation at each time step. A plot of the average error for each velocity component versus time step is shown in Fig. 2. This plot represents a typical behavior of the error in all cases computed using (9 × 9), (11 × 11), and (15 × 15) grid nodes in 29 cross-sectional planes.

Comparison With Experimental Data. The experimental data from the lower half of Joy's [15] duct are used for comparison because the data are smoother there. Figure 3 shows the normalized inlet velocity gradient measured by Joy in the lower half of the duct (zero turning). Unfortunately, Joy's data are incomplete since he did not provide measurements of the tangential (in-plane) velocity components in the inlet section. Following Stuart and Hetherington [14] the in-plane inlet velocity field is taken as zero. The experimental inlet velocity data are also highly irregular and smoothing of the through-flow velocity profile has been done by all researchers who studied this problem [13, 14, 16]. A linear variation in the inlet primary velocity (0.2 to 1.0) is used here to obtain the numerical solutions.

Joy presented total pressure contours expressed in units of

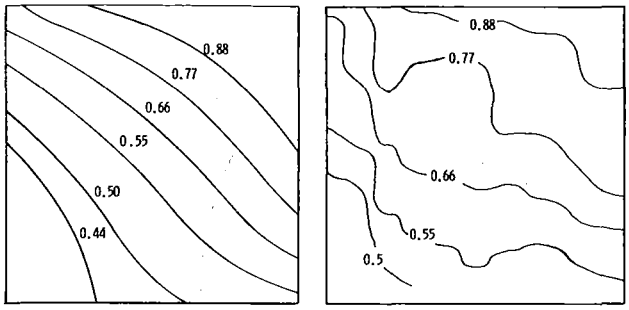

Fig. 4(a) Fig. 4(b)

Fig. 4 Velocity contours at θ = 30 deg: (a) computed results; (b) experimental data of Joy [15]

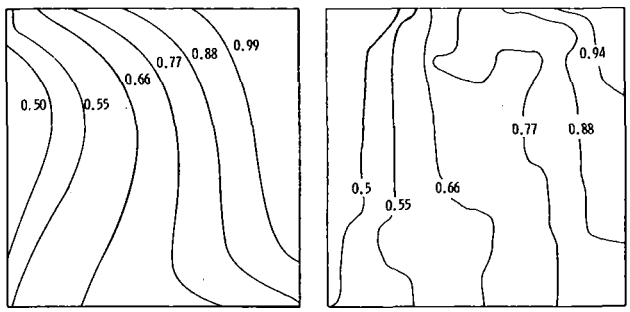

Fig. 5(a) Fig. 5(b)

Fig. 5 Velocity contours at θ = 60 deg: (a) computed results; (b) experimental data of Joy [15]

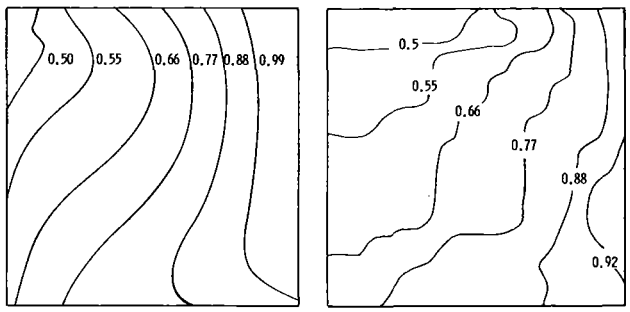

Fig. 6(a) Fig. 6(b)

Fig. 6 Velocity contours at θ = 90 deg: (a) computed results; (b) experimental data of Joy [15]

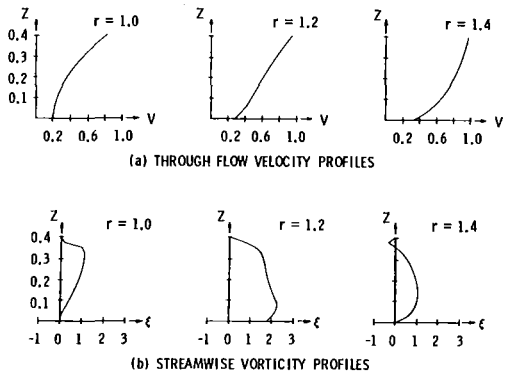

Fig. 7 Velocity and vorticity profiles at θ = 30 deg

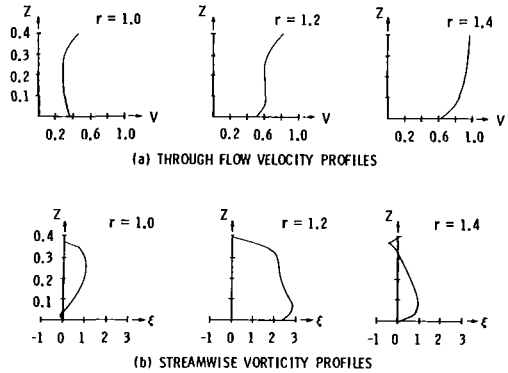

Fig. 8 Velocity and vorticity profiles at θ = 60 deg

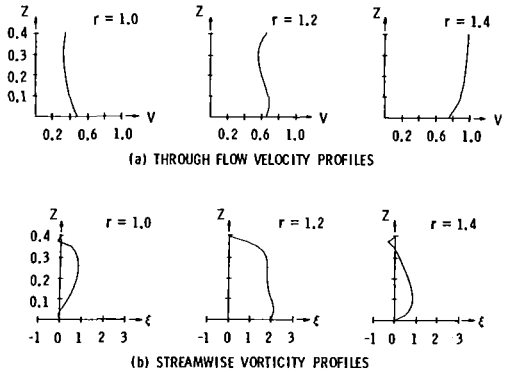

Fig. 9 Velocity and vorticity profiles at θ = 90 deg

velocity with zero static pressure ($\sqrt{2P_T}$) on cross-sectional planes located at 30, 60, and 90 deg of turning, respectively. The numerical prediction of the rotation of the contours is in good agreement with the experimental data except at 60 deg of turning. This discrepancy between the experimental data and the computed results is detected in all numerical solutions of this problem. Previous investigators [13, 14] have speculated about boundary layer separation near the duct centerline in the experimental measurements [15]. It is interesting to note that there is a strong similarity between the present results and the results of Abdallah and Hamed [16] using the streamlike function formulation.

Streamwise Velocity and Vorticity Profiles. Figures 7, 8, and 9 show streamwise velocity and vorticity profiles along vertical lines in the duct cross-sectional planes. It can be seen from these figures that the developed streamwise vorticity is tending to make the through-flow velocity uniform along vertical planes. This behavior was also detected in the viscous flow calculations of [28]. The present results based on inviscid flow assumptions indicate that the streamwise vorticity is responsible for making the through-flow velocity almost uniform along vertical planes.

Static Pressure Contours in Cross-Sectional Planes. Computed static pressure contours are presented at 0, 30, 60, and 90 deg in Fig. 10. These contours show that the static pressure is not constant over the duct cross-sectional planes, not even at the inlet section.

Joy [15] did not present static pressure measurements and so comparison with experimental data cannot be made. However, the contours at all locations exhibit the same trends that were predicted by Abdallah and Hamed [16] for the same duct using the streamlike function formulation. The secondary flow has the most effect on static pressure contours near the inner wall of the duct where the low energy flow region is located (see Figs. 4–6).

Streamwise Vorticity and Secondary Flow Rotation. Figures 11, 12, and 13 present the three-dimensional streamwise vorticity contour plots with the corresponding secondary flow velocity vectors for 30, 60, and 90 deg of turning, respectively. The increase in streamwise vorticity to its maximum at about

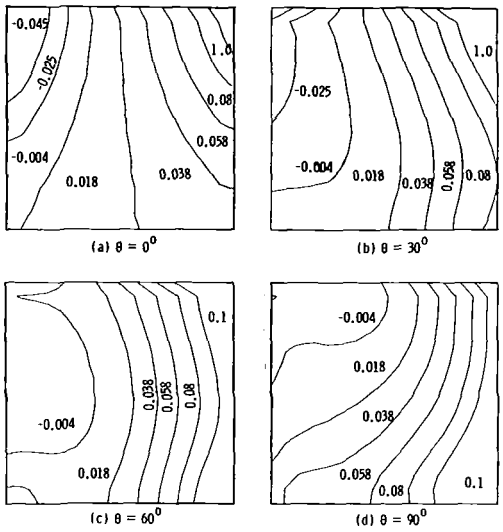

Fig. 10 Static pressure contours

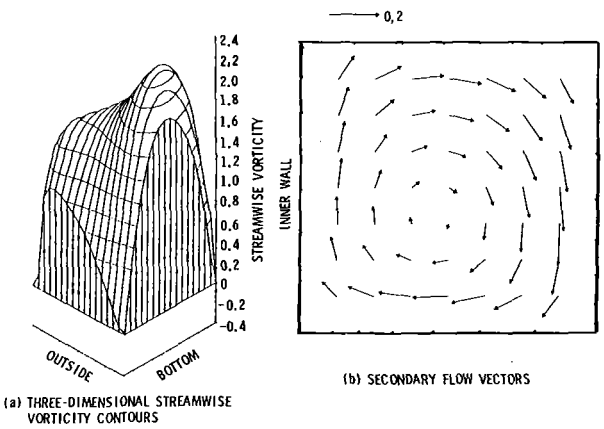

Fig. 11 Vorticity and secondary flow at θ = 30 deg

60 deg and its subsequent decrease is clearly shown. The location of maximum vorticity is near the bottom wall and is seen to move toward the inner wall as the flow moves downstream. The center of secondary flow rotation is located near the center of the duct and moves upward and toward the outer wall as the flow moves downstream. The center of secondary flow rotation and the center of maximum vorticity are not coincident due to the effect of through-flow velocity on secondary flow development.

Wall Total Pressure Contours. Figure 14 shows a three-dimensional view of the duct with total pressure contours on the duct walls. One can see that the low-energy fluid at the bottom in the duct inlet moves to the inner wall and finally to the top corner at the duct exit. The low-energy fluid that moves to the duct inner wall can cause separation at the duct center plane as speculated by all researchers who studied this problem [13, 14].

Conclusions

The primitive variable formulation, originally developed for the solution of Navier–Stokes equations, is adapted to the solution of the Euler equations on nonstaggered grids. The compatibility condition of the pressure Poisson equation is exactly satisfied on nonstaggered grids using a two step procedure. First, write the pressure Poisson equation in a divergence form. Second, the boundary conditions for the pressure should be applied at one-half grid spacing away from the boundaries for consistency with the divergence form.

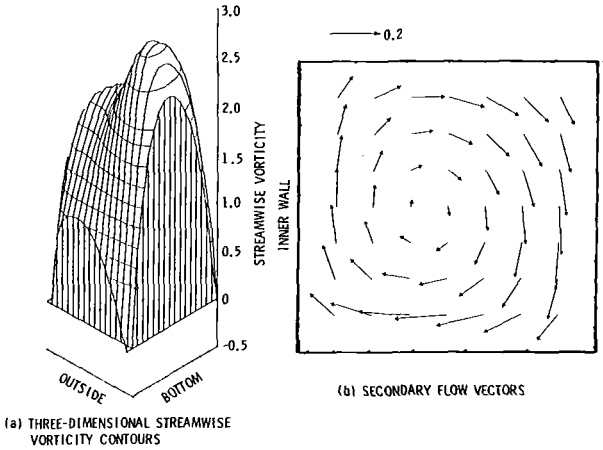

Fig. 12 Vorticity and secondary flow at θ = 60 deg

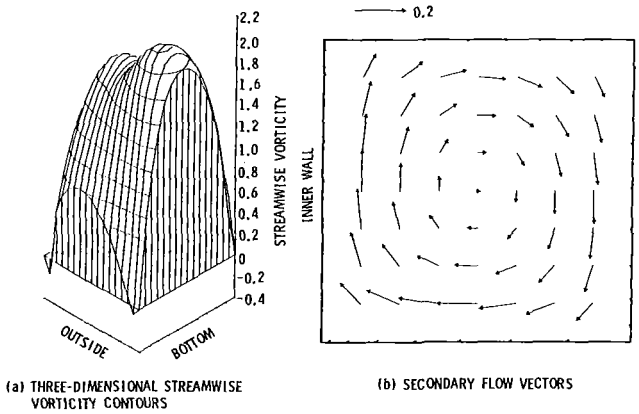

Fig. 13 Vorticity and secondary flow at θ = 90 deg

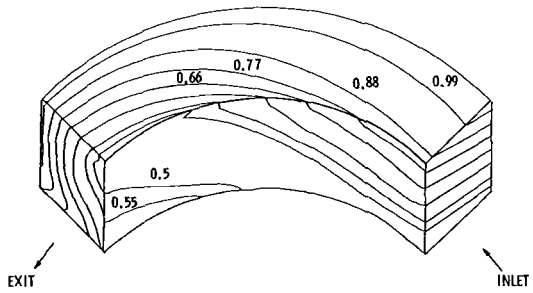

Fig. 14 Total pressure contours

The primitive variable approach is applied to calculate the three-dimensional rotational flow in a curved duct. The computed results are in good agreement with the experimental data of [26].

Acknowledgments

This research was supported by E/F funding at the Applied Research Laboratory, The Pennsylvania State University.

References

1 Briley, W. R., and McDonald, H., "Three-Dimensional Viscous Flows With Large Secondary Velocity," *Journal of Fluid Mechanics*, Vol. 144, 1984, pp. 47–77.

2 Stanitz, J. D., Osborn, W. M., and Mizisin, J., "An Experimental Investigation of Secondary Flow in an Accelerating, Rectangular Elbow With 90° of Turning," NACA Technical Note, TN-3015, 1953.

3 Kreskovsky, J. P., Briley, W. R., and McDonald, H., "Prediction of Laminar and Turbulent Primary and Secondary Flows in Strongly Curved Ducts," NASA Contractor Report CR-3388, 1981.

4 Squire, H. B., and Winter, K. G., "The Secondary Flow in a Cascade of Airfoils in a Nonuniform Stream," *Journal of Aeronautical Sciences*, Vol. 18, 1951, pp. 247–274.

5 Hawthorne, W. R., "Secondary Circulation in Fluid Flow," *Proceedings of the Royal Society A*, Vol. 206, 1951, p. 374.

6 Horlock, J. H., and Lakshminarayana, B., "Secondary Flows: Theory, Experiment, and Application in Turbomachinery Aerodynamics," *Annual Review of Fluid Mechanics*, Vol. 5, 1973, pp. 247–280.

7 Wu, C. H., "A General Theory of Three-Dimensional Flow in Subsonic and Supersonic Turbomachines of Axial-, Radial-, and Mixed-Flow Types," NACA Technical Note, TN-2604, 1952.

8 Katsanis, T., "Computer Program for Calculating Velocities and Streamlines on a Blade-to-Blade Stream Surface of a Turbomachine," NASA Technical Note, TND-4525, 1968.

9 Katsanis, T., "Revised Fortran Program for Calculating Velocities and Streamlines on the Hub-Shroud Midchannel Stream Surface of an Axial-, Radial-, or Mixed-Flow Turbomachine or Annual Duct. I: User's Manual," NASA Technical Note, TND-8430, 1977.

10 Marsh, H., "A Digital Computer Program for the Through Flow Fluid Mechanics in an Arbitrary Turbomachine Using a Matrix Method," Aeronautical Research Council R&M No. 3509, 1966.

11 Wilkinson, D. H., "Calculation of Blade-to-Blade Flow in a Turbomachine by Streamline Curvature," Aeronautical Research Council R&M No. 3704, 1972.

12 Wang, Q., Zhu, G., and Wu, C. H., "Quasi-Three-Dimensional and Full Three-Dimensional Rotational Flow Calculations in Turbomachines," ASME JOURNAL OF ENGINEERING FOR GAS TURBINES AND POWER, Vol. 107, 1985, pp. 277–285.

13 Fagan, J. R., "Three Dimensional Subsonic Duct Flow Analysis," Detroit Diesel Allison, Division of General Motors Corp., No. EDR7451, 1972.

14 Stuart, A. R., and Hetherington, R., "The Solution of Three-Variable Duct-Flow Equations," NASA SP-304, *Fluid Mechanics, Acoustics and Design of Turbomachinery*, Part I, 1974, pp. 135–153.

15 Joy, W., "Experimental Investigation of Shear Flow in Rectangular Bends," M.S. Thesis, Massachusetts Institute of Technology, 1950.

16 Abdallah, S., and Hamed, A., "The Elliptic Solution of the Secondary Flow Problem," ASME JOURNAL OF ENGINEERING FOR POWER, Vol. 105, 1983, pp. 530–535.

17 Hamed, A., and Liu, C., "Three-Dimensional Rotational Compressible Flow Solution in Variable Area Channels," AIAA Paper No. 83-0259, 1983.

18 Lacor, C., and Hirsch, Ch., "Rotational Flow Calculations in Three Dimensional Blade Passages," ASME Paper No. 82-GT-316, 1982.

19 Abdallah, S., and Hamed, A., "Inviscid Solution for the Secondary Flow in Curved Ducts," *AIAA Journal*, Vol. 19, 1981, pp. 993–999.

20 Chorin, A. J., "A Numerical Method for Solving Incompressible Viscous Flow Problems," *Journal of Computational Physics*, Vol. 2, 1967, pp. 12–26.

21 Choi, D., and Merkle, C. L., "Application of Time-Iterative Schemes to Incompressible Flow," AIAA Paper No. 84-1638, 1984.

22 Rizzi, A., and Eriksson, L., "Computation of Inviscid Incompressible Flow With Rotation," *Journal of Fluid Mechanics*, Vol. 153, 1985, pp. 275–312.

23 Harlow, F. H., and Welch, J. E., "Numerical Calculation of Time-Dependent Viscous Incompressible Flow of Fluid With Free Surface," *Physics of Fluids*, Vol. 8, No. 12, 1965, pp. 2182–2189.

24 Roache, P. J., *Computational Fluid Dynamics*, Hermosa Publishers, Albuquerque, NM, 1972.

25 Abdallah, S., "Part I: Numerical Solutions for the Pressure Poisson Equation With Neumann Boundary Conditions Using a Non-staggered Grid," submitted to *Journal of Computational Physics*, 1985.

26 Alfrink, B. J., "On the Neumann Problem for the Pressure in a Navier–Stokes Model," *Numerical Methods in Laminar and Turbulent Flow*, C. Taylor and B. A. Schrefler, eds., Pineridge Press, Swansea, U.K., 1981, pp. 389–412.

27 Lax, P. D., "Weak Solutions of Nonlinear Hyperbolic Equations and Their Numerical Computation," *Communications on Pure and Applied Mathematics*, Vol. 7, 1954, pp. 159–193.

28 Schwab, J. R., and Povinelli, L. A., "Comparison of Secondary Flows Predicted by a Viscous Code and an Inviscid Code With Experimental Data for a Turning Duct," *Computation of Internal Flows: Methods and Applications*, ASME, New York, 1984, pp. 29–36.

Performance of Axial Compressor With Nonuniform Exit Static Pressure

H. Kodama
Research and Development Department,
Aeroengine and Space Operations,
Ishikawajima-Harima Heavy Industries,
Tokyo, Japan

An analytical model has been developed to predict the performance of axial compressors with an exit static pressure perturbation. The model uses a two-dimensional compressible semi-actuator disk model. This method can be applied to the compressor with known circumferential variation in exit static pressure which is measured or predicted by an analytical method. The analytical results are found to be in good agreement with experiments carried out on two transonic fans.

Introduction

The performance of axial flow fans and compressors is affected by the circumferential variation in exit static pressure produced by the downstream thick struts or other components, if the distortion is not sufficiently attenuated. Because the rotors are subjected to an unsteady flow field, not only is the rotor performance degraded, but also both total pressure and total temperature distortions are formed by the circumferentially varied rotor work, and subsequently harm downstream components. The potential field due to downstream struts also produces large cyclic stresses to the rotor [1] and interaction tone noise [2].

There have been only a few investigations which treated the interaction of axial compressors with downstream perturbation. Mazzawy [3] developed the nonlinear flow model for the prediction of compressor performance in which the exit static pressure variation could be imposed as the downstream boundary condition. This model essentially depends on a complicated flow model, so that it may be difficult to gain some insight into the effect of a circumferential variation in exit static pressure on the compressor performance. Therefore an analytic model should be needed.

The semi-actuator disk model by small perturbation theory has been often applied as an analytic model to the analysis of the cascade with circumferential distortions [4, 5, 6]. This model has the advantage of treating the effect of wave transmission through rotor rows. But there appears to be no previous work which uses this model for performance predictions with downstream static pressure perturbations.

In this paper, a two-dimensional compressible semi-actuator disk model with exit static pressure perturbations is presented, and the validity of the theory is demonstrated by comparing the theoretical results with experimental data.

Formulation

The semi-actuator disk model assumes that the circumferential wavelength of disturbances is much larger than the blade spacing. This makes it possible to treat the flow in the cascade as one-dimensional channel flow, since the variations of flow quantities in the direction normal to a chord are quite small. In the present model, for simplicity, the cascade is assumed to be composed of flat plate airfoils. Further, flow deviation at the cascade exit is neglected and the Kutta condition is assumed. Hence the flow turning occurs suddenly at the leading edge plane of the cascade. It should be emphasized that this flow turning is not required to be small. It is also assumed that the streamline contraction and the total pressure losses occur there.

The coordinate systems for each flow field are shown in Fig. 1.

The Flow Field Outside the Cascade. The governing equations for an ideal, inviscid, isentropic (but not homoentropic) compressible fluid with no body forces can be linearized if it is assumed that the perturbation quantities are small compared to the mean quantities. The resultant equations in a rotor fixed coordinate system are

Continuity

$$\frac{\partial \rho}{\partial t}+U\frac{\partial \rho}{\partial x}+V\frac{\partial \rho}{\partial y}+\rho_0\left(\frac{\partial u}{\partial x}+\frac{\partial v}{\partial y}\right)=0 \qquad (1)$$

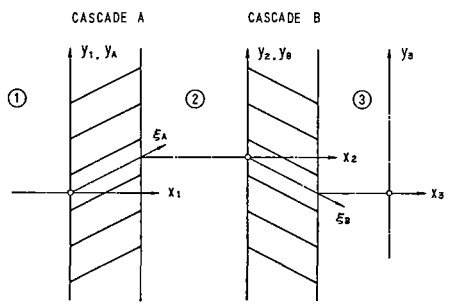

Fig. 1 Coordinate system

Contributed by the Gas Turbine Division and presented at the 1985 Beijing International Gas Turbine Symposium and Exposition, Beijing, People's Republic of China, September 1–7, 1985. Manuscript received at ASME Headquarters May 13, 1985. Paper No. 85-IGT-43.

Momentum

$$\rho_0 \frac{\partial u}{\partial t} + \rho_0 U \frac{\partial u}{\partial x} + \rho_0 V \frac{\partial u}{\partial y} = -\frac{\partial p}{\partial x} \tag{2}$$

$$\rho_0 \frac{\partial v}{\partial t} + \rho_0 U \frac{\partial v}{\partial x} + \rho_0 V \frac{\partial v}{\partial y} = -\frac{\partial p}{\partial y} \tag{3}$$

Energy

$$\frac{\partial}{\partial t}\left(\frac{p}{p_0} - \kappa\frac{\rho}{\rho_0}\right) + U\frac{\partial}{\partial x}\left(\frac{p}{p_0} - \kappa\frac{\rho}{\rho_0}\right) + V\frac{\partial}{\partial y}\left(\frac{p}{p_0} - \kappa\frac{\rho}{\rho_0}\right) = 0 \tag{4}$$

The perturbations in pressure, density, and velocity are assumed to be of the wave forms

$$f = F_n \exp(\lambda x)\exp(i\omega t + iky) \tag{5}$$

where

$$\omega = -kV_s \tag{6}$$

$$k = \frac{2\pi n}{L} \tag{7}$$

and the sign of V_s is taken in the opposite direction of y. Substitution of the assumed solutions from equation (5) into (1)–(4) yields the following expressions.

$$\frac{p}{p_0} = \{C_1\exp(\lambda_1 x) + C_2\exp(\lambda_2 x)\}\exp(i\omega t + iky) \tag{8}$$

$$\frac{u}{a_0} = \left\{ -\frac{1}{\kappa}\frac{\frac{\lambda_1}{k}}{\mathrm{M}_x\left(\frac{\lambda_1}{k}\right) + i(\mathrm{M}_y - \mathrm{M}_s)} C_1\exp(\lambda_1 x) - \frac{1}{\kappa}\frac{\frac{\lambda_2}{k}}{\mathrm{M}_x\left(\frac{\lambda_2}{k}\right) + i(\mathrm{M}_y - \mathrm{M}_s)} C_2\exp(\lambda_2 x) + i\frac{1}{2\pi n}\frac{1}{\left(\frac{\lambda_3}{k}\right)^2 - 1} R\exp(\lambda_3 x)\right\}\exp(i\omega t + iky) \tag{9}$$

$$\frac{v}{a_0} = \left\{ -\frac{1}{\kappa}\frac{i}{\mathrm{M}_x\left(\frac{\lambda_1}{k}\right) + i(\mathrm{M}_y - \mathrm{M}_s)} C_1\exp(\lambda_1 x) - \frac{1}{\kappa}\frac{i}{\mathrm{M}_x\left(\frac{\lambda_2}{k}\right) + i(\mathrm{M}_y - \mathrm{M}_s)} C_2\exp(\lambda_2 x) - \frac{1}{2\pi n}\frac{\frac{\lambda_3}{k}}{\left(\frac{\lambda_3}{k}\right)^2 - 1} R\exp(\lambda_3 x)\right\}\exp(i\omega t + iky) \tag{10}$$

$$\frac{\rho}{\rho_0} = \{C_1\exp(\lambda_1 x) + C_2\exp(\lambda_2 x) - S\exp(\lambda_4 x)\} \times \exp(i\omega t + iky) \tag{11}$$

where

$$a_0 = \sqrt{\frac{\kappa p_0}{\rho_0}}$$

and

$$\mathrm{M}_x = \frac{U}{a_0}, \qquad \mathrm{M}_y = \frac{V}{a_0}, \qquad \mathrm{M}_s = \frac{V_s}{a_0}$$

In these equations, eigenvalues of perturbation quantities λ are given by

Nomenclature

a_0 = velocity of sound
C_1, C_2 = complex coefficient of the pressure perturbation outside cascade
C_p = static pressure coefficient
C = airfoil chord
D_1, D_2 = complex coefficient of perturbations within cascade
E = complex coefficient of entropy perturbation within cascade
h = stream tube height (see Fig. 2)
i = $\sqrt{-1}$
k = parameter defined by equation (7)
L = periodic length scale of cascade
M = Mach number of mean flow
M_s = Mach number of rotor rotation
n = circumferential harmonic number
P_T = total pressure
P_0, P = mean and perturbation components of static pressure
Pr = static pressure ratio across the leading edge plane
R = complex coefficient of the vortex perturbation outside cascade
r = coordinate in radial direction
S = complex coefficient of the entropy perturbation outside cascade
s = cascade spacing (see Fig. 2)
T_T = total temperature
t = time
U, V = x, y components of mean velocity
u, v = x, y components of velocity perturbation
V_s = velocity of rotor rotation
W = ξ component of mean velocity
w = ξ component of velocity perturbation
X = coordinate in axial direction
y = coordinate in circumferential direction
β = angle of inlet air flow
θ = stagger angle
κ = ratio of specific heats
λ = eigenvalues of perturbation quantities
ξ = coordinate in chordwise direction
ρ_0, ρ = mean and perturbation components of density
ω = disturbance circular frequency
$\bar{\omega}$ = total pressure loss coefficient

Subscripts and Superscripts

0 = mean component of flow quantity
c = flow quantity within cascade
d = just downstream of trailing edge plane
u = just upstream of leading edge plane
x = x component
y = y component
ξ = ξ component
$'$ = mean value plus perturbation

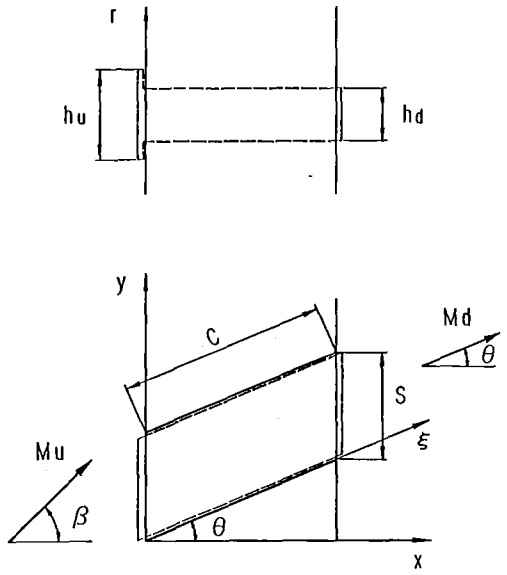

Fig. 2 Control volume

$$\lambda_2^1 = \frac{k}{1-M_x^2}\{iM_x(M_y - M_s) \pm \sqrt{1-M_x^2-(M_y-M_s)^2}\} \quad (12)$$

$$\lambda_3 = \lambda_4 = -ik\frac{M_y - M_s}{M_x} \quad (13)$$

As seen from equations (8-13), there are four waves in the flow field. Two of them are pressure waves which are related to the irrotational field. One attenuates in the upsteam direction (λ_1) and the other in the downstream direction (λ_2), if the subsonic compressor is assumed. It is easily found from equation (12) that a circumferentially higher harmonic perturbation attenuates rapidly. The vorticity wave (λ_3) and the entropy wave (λ_4) have the forms which are convected downstream by the free stream. Therefore the downstream distortions which affect the upstream compressor take the wave form of λ_1.

The expressions for the perturbation quantities in a stationary coordinate system are deduced from those in a rotor fixed coordinate system by letting the rotor speed V_s go to zero.

The Flow Field Inside the Cascade. Since the flow in the cascade is treated as one-dimensional channel flow, the linearized equations are given by

Continuity

$$\frac{\partial \rho_c}{\partial t} + W\frac{\partial \rho_c}{\partial \xi} + \rho_0 \frac{\partial w_c}{\partial \xi} = 0 \quad (14)$$

Momentum

$$\frac{\partial w_c}{\partial t} + W\frac{\partial w_c}{\partial \xi} = -\frac{1}{\rho_0}\frac{\partial p_c}{\partial \xi} \quad (15)$$

Energy

$$\frac{\partial}{\partial t}\left(\frac{p_c}{p_0} - \kappa\frac{\rho_c}{\rho_0}\right) + W\frac{\partial}{\partial \xi}\left(\frac{p_c}{p_0} - \kappa\frac{\rho_c}{\rho_0}\right) = 0 \quad (16)$$

Assuming the wave form in the cascade is

$$g = G\exp(\lambda\xi)\exp(i\omega t) \quad (17)$$

we obtain the perturbation quantities as follows.

$$\frac{p_c}{p_0} = \{D_1\exp(\lambda_5\xi) + D_2\exp(\lambda_6\xi)\}\exp(i\omega t) \quad (18)$$

$$\frac{w_c}{a_0} = \frac{1}{\kappa}\{D_1\exp(\lambda_5\xi) - D_2\exp(\lambda_6\xi)\}\exp(i\omega t) \quad (19)$$

$$\frac{\rho_c}{\rho_0} = \frac{1}{\kappa}\{D_1\exp(\lambda_5\xi) + D_2\exp(\lambda_6\xi) - E\exp(\lambda_7\xi)\} \times \exp(i\omega t) \quad (20)$$

where

$$\lambda_5 = ik\frac{M_s}{1+M_\xi} \quad (21)$$

$$\lambda_6 = -ik\frac{M_s}{1-M_\xi} \quad (22)$$

$$\lambda_7 = ik\frac{M_s}{M_\xi} \quad (23)$$

The pressure wave λ_5 travels in the flow direction. On the other hand, the pressure wave λ_6 is transmitted from downstream to upstream. The entropy wave λ_7 is convected downstream by the free stream in the form of the density perturbation.

In the case of a stator, no wave exists in the chordwise direction. The perturbation quantities can be expressed as

$$\frac{p_c}{p_0} = D_1 \quad (24)$$

$$\frac{w_c}{a_0} = -\frac{1}{\kappa M_\xi}D_1 + \frac{1}{M_\xi}D_2 \quad (25)$$

$$\frac{\rho_c}{\rho_0} = \frac{1}{\kappa}(D_1 - E) \quad (26)$$

Thus we have four unknowns (C_1, C_2, R, S) in the flow field outside the cascade and three unknowns (D_1, D_2, E) in the cascade, since the mean quantities are known.

Boundary Condition. Figure 2 shows the control volume of the mathematical model. The flow fields inside and outside (upstream and downstream) of the control volume have to be matched. Then the boundary conditions are

- Conservation of mass for a control volume
- Conservation of energy for a control volume
- Change of total pressure loss at the leading edge plane
- Smooth continuation of pressure, density, and two velocity components at the trailing edge plane

In the present model, the variation of total pressure loss can be considered assuming that the total pressure loss coefficient is a function of cascade geometry, upstream Mach number, upstream flow angle, and static pressure ratio across the leading edge plane. The resultant equations for the perturbation quantities are shown in the Appendix.

Here we have seven boundary conditions for one cascade. If the compressor has N blade rows, there are $N+1$ flow fields outside the cascades, then the number of unknowns becomes $(7N+4)$. On the other hand, the number of constraint equations for cascades is $7N$. So, in order to determine all perturbation quantities, we have to set four boundary conditions in the upstream and downstream flow fields of the compressor. One of them should be the downstream static pressure perturbation. Consequently the $(7N+4)$ simultaneous equations are obtained.

The analysis has been carried out for a circumferentially pure harmonic perturbation. But, because of the linearized nature of the solution, any arbitrary perturbation profile may be handled as the summation of its harmonic components.

Comparison Between Theory and Experiment

A comparison between theory and experiment has been performed for two single-stage transonic fans. Both of them are the rig test fans for high bypass ratio turbofan engines,

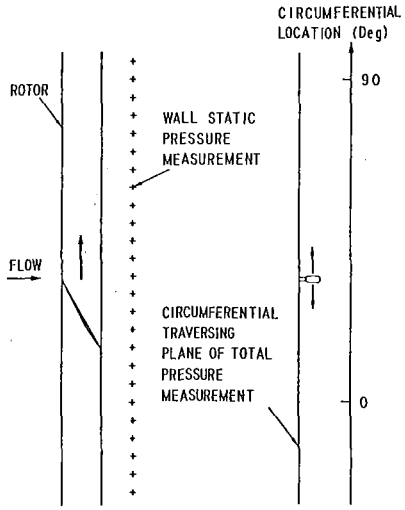

Fig. 3 Schematic of test fan 1

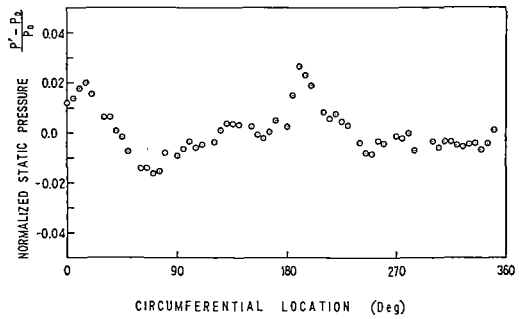

Fig. 4 Measured static pressure perturbation behind rotor in test fan 1

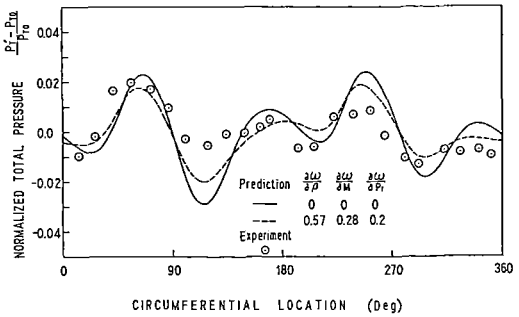

Fig. 5 Predicted and measured circumferential total pressure behind rotor in test fan 1

and have the thick struts downstream which simulate the nacelle pylon or structural struts in the engines.

The experiments have been performed with uniform inlet conditions. Also the rig structural struts were located far upstream of the test fans. Therefore, it could be assumed that, in the upstream field, there was no perturbation which affected the fan performance. Thus the upstream boundary conditions for both cases are

$$\frac{P'_T - P_{T0}}{P_{T0}} = 0 \tag{27}$$

$$\frac{T'_T - T_{T0}}{T_{T0}} = 0 \tag{28}$$

$$C_2 = 0 \tag{29}$$

The expressions for total pressure and total temperature perturbations are shown in the Appendix.

Test Fan I. The experiment was performed at design rotor

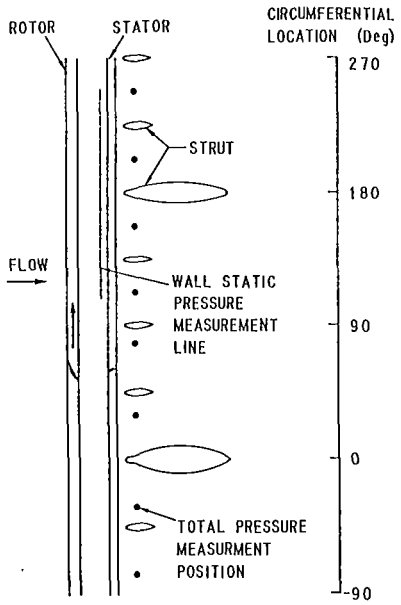

Fig. 6 Schematic of test fan 2

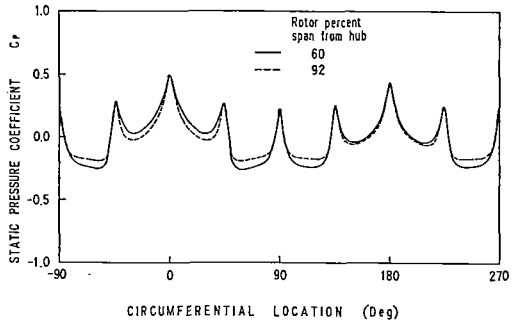

Fig. 7 Predicted static pressure perturbation due to downstream struts in test fan 2 (incompressible solution)

speed. As a result of the interaction between the rotor and downstream potential fields, the circumferential distribution of wall static pressure shown in Fig. 4 was measured behind the fan rotor (see Fig. 3). This wall static pressure distribution was used as the downstream boundary condition in the analysis of this case. It should be noted that the measured wall static pressure was considered to include two pressure waves, that is wave λ_1 and λ_2. The total pressure distributions behind the fan rotor were compared between the theoretical results and experiment. The comparison was made at 80 percent rotor span from the hub. At this section, the mean relative Mach number at rotor inlet was 1.34 and the mean rotor total pressure ratio was 1.9. The results are shown in Fig. 5. In this figure, two predictions are compared, one with the total pressure loss variation included and the other neglected. The slopes of the total pressure loss coefficients were estimated from the rotor performance map and the assumed shock model. A better agreement was obtained, when the total pressure loss variation was considered.

Test Fan 2. The fan performance was affected by the eight struts including two fat struts with different thicknesses shown in Fig. 6. In this case, the static pressure perturbation due to the downstream struts was obtained from a potential flow solution. First, the incompressible static pressure coefficient $C_{p_{\text{incomp}}}$ in front of the struts was calculated by the singularity superposition method, and the results are shown in Fig. 7. In this calculation, the mean flow quantities at the stator exit were used as the upstream condition. It should be noted that this implied the assumption that the potential flow

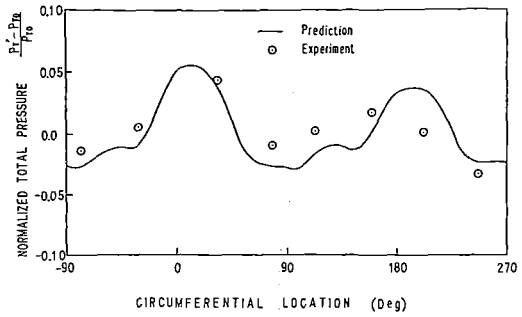

Fig. 8 Predicted and measured circumferential total pressure behind stator in test fan 2 (60 percent rotor span)

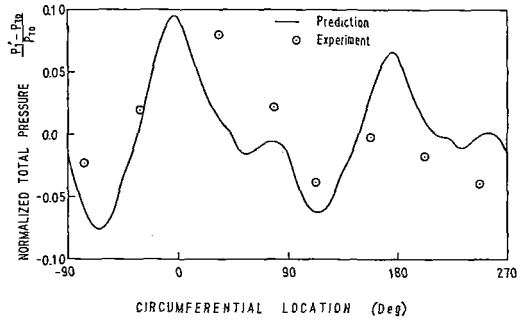

Fig. 9 Predicted and measured circumferential total pressure behind stator in test fan 2 (92 percent rotor span)

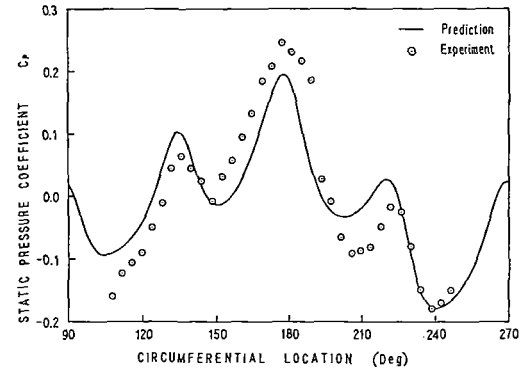

Fig. 10 Predicted and measured circumferential wall static pressure in front of stator

field due to the struts was not affected by the upstream rotor and stator. Then the compressible static pressure coefficient $C_{p_{\text{comp}}}$ was obtained by the Prandtl-Glauert transformation

$$C_{p_{\text{comp}}} = \frac{C_{p_{\text{incomp}}}}{\sqrt{1-\mathrm{M}^2}}$$

This static pressure perturbation was regarded as the pressure wave λ_1 which attenuates in the upstream direction. The experiment was performed at 90 percent rotor speed, and the comparisons between theory and experiment were made at two radial sections, 60 percent and 92 percent rotor span from the hub. At these sections, the mean relative Mach numbers at rotor inlet were respectively 1.18 and 1.42, and the mean stage total pressure ratios were 1.60 and 1.63. The total pressure loss variations were neglected in the predictions. The total pressure perturbations at the stator exit are compared in Figs. 8 and 9. Although the level of the downstream static pressure perturbation at 60 percent rotor span was essentially the same as at 92 rotor span, the predicted total pressure perturbation showed a smaller peak-to-peak variation in magnitude. The experimental results showed a similar difference in a total pressure perturbation level between the two radial sections. In Fig. 10, the wall static pressure distribution measured in front of the stator row is compared with the theoretical results at 92 percent rotor span. It is considered that one of the reasons for the differences between experiment and theory is the viscous effect in the stator row.

Conclusions

An analysis has been developed to predict the performance of compressors with downstream static pressure perturbations. The method is based on the use of a two-dimensional compressible semi-actuator disk model. The analysis has been verified by experimental data taken in two transonic fans. The predictions of the theoretical model were found to be in good agreement with the experimental results. It is expected that the present model can be used to predict the unsteady aerodynamic forces on the rotors which have downstream static pressure perturbations. These predicted forces can be used in aeroelastic calculations and noise estimations.

References

1 Yokoi, S., Nagano, S., and Kakehi, Y., "Reduction of Strut Induced Rotor Blade Vibration With the Modified Stator Setting Angles," *International Symposium on Airbreathing Engines*, 5th edn., Bangalore, India, Feb. 1981, pp. 61-1 to 61-7.

2 Woodward, R. P., and Balombin, J. R., "Tone Generation by Rotor-Downstream Strut Interaction," *Journal of Aircraft*, Vol. 21, Feb. 1984, pp. 135-142.

3 Mazzawy, R. S., "Multiple Segment Parallel Compressor Model for Circumferential Flow Distortion," in: *Unsteady Phenomena in Turbomachinery*, AGARD-CP-177, 1976.

4 Tanida, Y., "Inlet Distortion and Blade Vibration in Turbomachinery," *International Symposium on Airbreathing Engines*, 2nd edn., Sheffield, Mar. 1974.

5 Savell, C. T., and Wells, W. R., "Rotor Design to Attenuate Flow Distortion: Part 1—A Semiactuator Disk Analysis," ASME JOURNAL OF ENGINEERING FOR POWER, Vol. 97, Jan. 1975.

6 Seidel, B. S., Matwey, M. D., and Adamczyk, J. J., "Inlet Flow Distortion in Turbomachinery," ASME JOURNAL OF ENGINEERING FOR POWER, Vol. 102, Oct. 1980.

APPENDIX

The relations for perturbation quantities are

Mass

$$i\omega c\bar{\rho}_c \frac{h_d}{h_u}\cos\theta + (\rho_{0d}u_d + \rho_d W_d \cos\theta)\frac{h_d}{h_u} - (\rho_{0u}u_u + \rho_u W_u \cos\beta) = 0 \tag{A1}$$

Energy

$$\frac{i\omega c}{\rho_{0d}W_d}\frac{\bar{p}_c - a_{0d}^2\bar{\rho}_c}{\kappa-1} + i\omega c\bar{w}_c + \frac{a_d^2}{\kappa-1}\left(\frac{p_d}{p_{0d}} - \frac{\rho_d}{\rho_{0d}}\right) + W_d(u_d\cos\theta + v_d\sin\theta) - \frac{a_u^2}{\kappa-1}\left(\frac{p_u}{p_{0u}} - \frac{\rho_u}{\rho_{0u}}\right) - W_u(u_u\cos\beta + v_u\sin\beta) = 0 \tag{A2}$$

where

$$(\bar{\ }) = \frac{1}{c}\int_0^c (\ )\,d\xi$$

Total pressure loss

$$\left\{\frac{\partial\tilde{\omega}}{\partial\beta_u}\frac{1}{W_u}(v_u\cos\beta_u - u_u\sin\beta_u) + \frac{\partial\tilde{\omega}}{\partial \mathrm{M}_u}\frac{1}{a_u}(u_u\cos\beta_u + v_u\sin\beta_u) + \frac{\partial\tilde{\omega}}{\partial Pr}\frac{p_{0d}}{p_{0u}}\left(\frac{p_c(0)}{p_{0d}} - \frac{p_u}{p_{0u}}\right)\right\} p_{0u}\left(C_u^{\frac{\kappa}{\kappa-1}} - 1\right)$$

$$+\tilde{\omega}\left\{C_u^{\frac{1}{\kappa-1}}\frac{\kappa p_{0u}\mathrm{M}_u^2}{2}\left(\frac{\rho_u}{\rho_{0u}}-\frac{p_u}{p_{0u}}\right)+C_u^{\frac{1}{\kappa-1}}\frac{\kappa p_{0u}\mathrm{M}_u}{a_u}(u_u\cos\beta_u\right.$$

$$\left.+v_u\sin\beta_u)+p_u\left(C_u^{\frac{\kappa}{\kappa-1}}-1\right)\right\}$$

$$=p_uC_u^{\frac{\kappa}{\kappa-1}}-p_c(0)C_d^{\frac{\kappa}{\kappa-1}}+C_u^{\frac{1}{\kappa-1}}\frac{\kappa p_{0u}\mathrm{M}_u^2}{2}\left(\frac{\rho_u}{\rho_{0u}}-\frac{p_u}{p_{0u}}\right)$$

$$-C_d^{\frac{1}{\kappa-1}}\frac{\kappa p_{0d}\mathrm{M}_d^2}{2}\left(\frac{\rho_c(0)}{\rho_{0d}}-\frac{p_c(0)}{p_{0d}}\right)-C_d^{\frac{1}{\kappa-1}}\frac{\kappa P_{0d}\mathrm{M}_d}{a_{0d}}w_c(0)$$

$$+C_u^{\frac{1}{\kappa-1}}\frac{\kappa p_{0u}\mathrm{M}_u}{a_{0u}}(u_u\cos\beta_u+v_u\sin\beta_u) \tag{A3}$$

where

$$C_u=1+\frac{\kappa-1}{2}\mathrm{M}_u^2,\qquad C_d=1+\frac{\kappa-1}{2}\mathrm{M}_d^2$$

Exit condition

$$p_c(c)=p_d \tag{A4}$$

$$\rho_c(c)=\rho_d \tag{A5}$$

$$w_c(c)\cos\theta=u_d \tag{A6}$$

$$w_c(c)\sin\theta=v_d \tag{A7}$$

Total pressure and total temperature perturbations are

$$\frac{P_T'-P_{T0}}{P_{T0}}=\left(1-\frac{1}{2}\frac{\kappa M^2}{C_0}\right)\frac{p}{p_0}+\frac{1}{2}\frac{\kappa\mathrm{M}^2}{C_0}\frac{\rho}{\rho_0}$$

$$+\frac{\kappa}{C_0}\left(\frac{u}{a_0}\mathrm{M}_x+\frac{v}{a_0}\mathrm{M}_y\right) \tag{A8}$$

$$\frac{T_T'-T_{T0}}{T_{T0}}=\frac{1}{C_0}\left(\frac{p}{p_0}-\frac{\rho}{\rho_0}\right)+\frac{\kappa-1}{C_0}\left(\frac{u}{a_0}\mathrm{M}_x+\frac{v}{a_0}\mathrm{M}_y\right) \tag{A9}$$

where

$$C_0=1+\frac{\kappa-1}{2}\mathrm{M}^2$$

Predictive Surge Control and Optimization for a Centrifugal Compressor

D. Patlovany
Rohm and Haas Texas, Inc.,
Houston, TX

A. B. Focke
Boyce Engineering International, Inc.
Houston, TX

This paper details the installation of a retrofit supervisory control system on a large air compressor for the purpose of minimizing energy costs and protecting the compressor from surge. The paper discusses how an accurate prediction of the compressor's stable operating region can be calculated to develop a compressor performance "map" and how this map can then be used to cut energy consumption by the compressor driver. The compressor is protected from surging by a "predictive" control method. Instead of waiting for the compressor to surge, and then reacting, the system calculates when surge is about to occur and takes action to avoid a surge event before it occurs. The installation of a control system of this type can result in a substantial dollar savings in energy costs, while guaranteeing that a compressor will be protected from any damage from a severe surge event. This system has been installed in our plant and proven in practice. The paper details the installation of this system and its results.

Introduction

In the constantly changing environment of today's petrochemical industry, new processes are being started up, and the old ones they replace being shut down on an almost continuous basis. Because of these changes, and the high cost of new construction, many large turbines and compressors are pushed into service at load conditions far from their original design. In some cases, the machines may be undersized for their new roles, but in others, they may be grossly oversized. This paper documents an energy optimization project for a large centrifugal compressor built in 1966 that is now supplying air to a process that consumes less air than the surge flow of the compressor.

The compressor in question is a single-shaft, six-stage air compressor with two stages of intercooling, driven by a 17,000 hp gas turbine as shown in Fig. 1. The compressor was originally designed to compress 66,000 scfm of air at a discharge pressure of 100 psig and a rotating speed of 4760 rpm.

From 1966 to 1978, this compressor did exactly that with high reliability and low maintenance. In 1978, the process requirements changed to 30,000 scfm at only 90 psig. A quick look at the manufacturer's performance curves of this compressor as shown in Figs. 2–5 shows that 30,000 scfm is well below the stable operating region of the compressor at all temperatures, and that the lowest speeds at which the compressor could be run in its stable region were 4280 rpm at an inlet temperature of 40°F and 4400 rpm at an inlet temperature of 95°F. The reader should note that the family of curves supplied by the manufacturer differ only in the first-stage inlet temperature. The intercooler outlet temperatures are assumed constant, which may not reflect actual conditions. Figure 6 shows how the surge line is shifted at various ambient conditions.

Fearing a surge event that could cause serious damage to the compressor, the operators conservatively ran the compressor at 4400 rpm on a cold day and as high at 4550 on a hot day. At times, the compressor was compressing as much as 60,000 scfm of air, while the process was only using 30,000 scfm. The rest of the compressed air was simply being vented for the exclusive purpose of preventing the machine from surging.

This vented air required a considerable amount of horsepower to compress, which meant higher fuel costs for the gas turbine. This project was undertaken to decrease the amount of air being vented to a minimum, reducing fuel costs without endangering the reliability of the compressor.

Project Objectives

The main objective of this project was to run the compressor at the slowest speed required to maintain a discharge pressure of 90 psig, and maintain an air flow through the compressor equal to 105 percent of the predicted surge volume at that pressure. Assuming that the starting point for this project is a compressor speed of 4550 rpm, a discharge pressure of 90 psig and a discharge flow of 59,000 scfm, a review of compressor performance curves (for simplicity, all further references to the compressor performance curves will be at an inlet temperature of 95°F) shows that the compressor uses 12,600 hp to compress air at these conditions. The predicted surge point of the compressor at 90 psig is 39,000 scfm, and 105 percent of that is 41,000 scfm. At this point in the perfor-

Contributed by the Gas Turbine Division of THE AMERICAN SOCIETY OF MECHANICAL ENGINEERS and presented at the 31st International Gas Turbine Conference and Exhibit, Düsseldorf, Federal Republic of Germany, June 8–12, 1986. Manuscript received at ASME Headquarters January 30, 1986. Paper No. 86-GT-147.

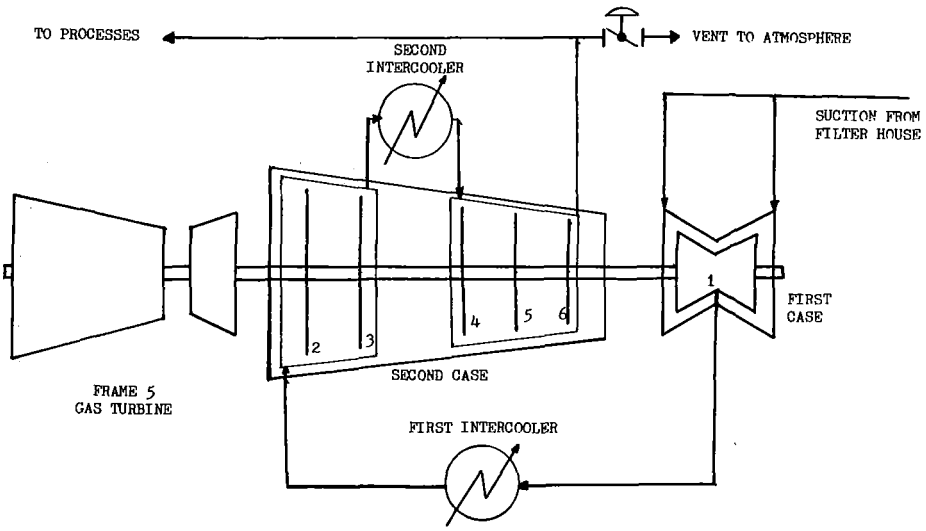

Fig. 1 Turbine/compressor layout

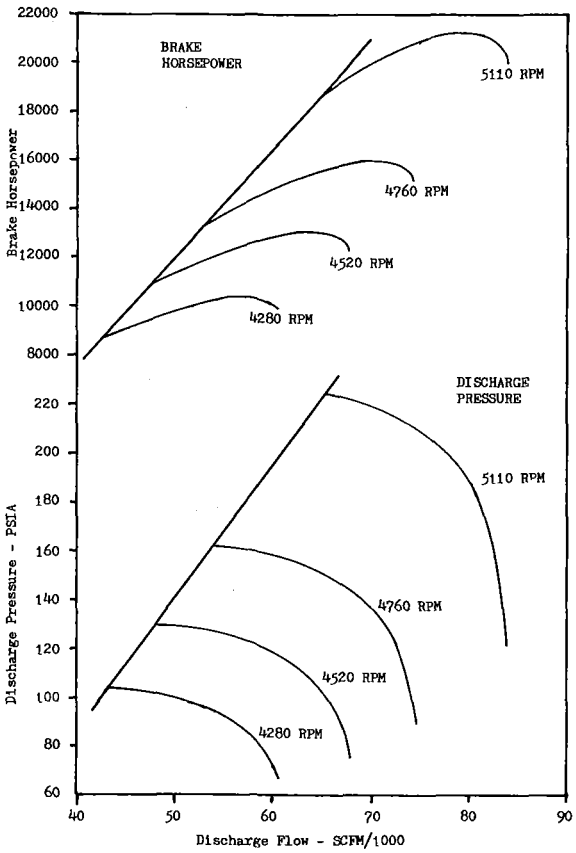

Fig. 2 Manufacturer's compressor performance curves based on an inlet temperature of 40°F and intercooling to 105°F

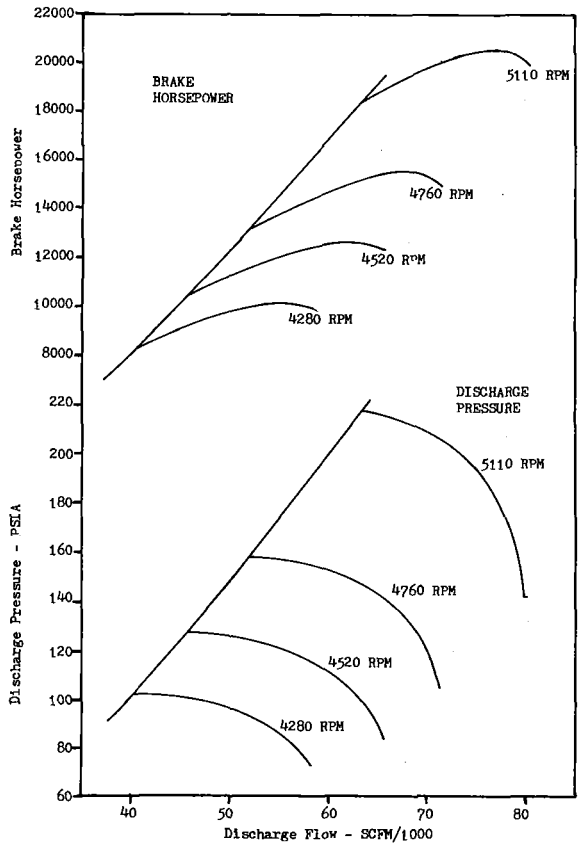

Fig. 3 Manufacturer's compressor performance curves based on an inlet temperature of 60°F and intercooling to 105°F

mance curves, the compressor speed is 4350 rpm and the power consumption is 9000 hp. To give the reader an idea as to the potential savings, a 3000 hp cutback can make a gas turbine with a fuel cost of about $4/million Btu and an efficiency of eighteen percent use about $1.4 million less in fuel over a year's time.

Surge Prediction

To operate a compressor as close as possible to its surge line, the surge line must be determined with extreme accuracy. Before describing how the surge line of this particular compressor was "mapped," a discussion on surge should be pursued, which is provided below.

Surge is generally known as the lower limit of stable operation for a compressor. Specifically, surge in a compressor occurs when a compressor wheel is unable to overcome the resistance of the system to air flowing through the compressor. Resistance to air flow is attributable to a combination of rotor and stator energy losses [1]. Rotor losses include inducer incidence angle losses, diffusion blading losses, skin friction losses due to shear forces in the boundary layers, clearance losses, and recirculating losses.

Stator losses include skin friction losses in the diffuser and

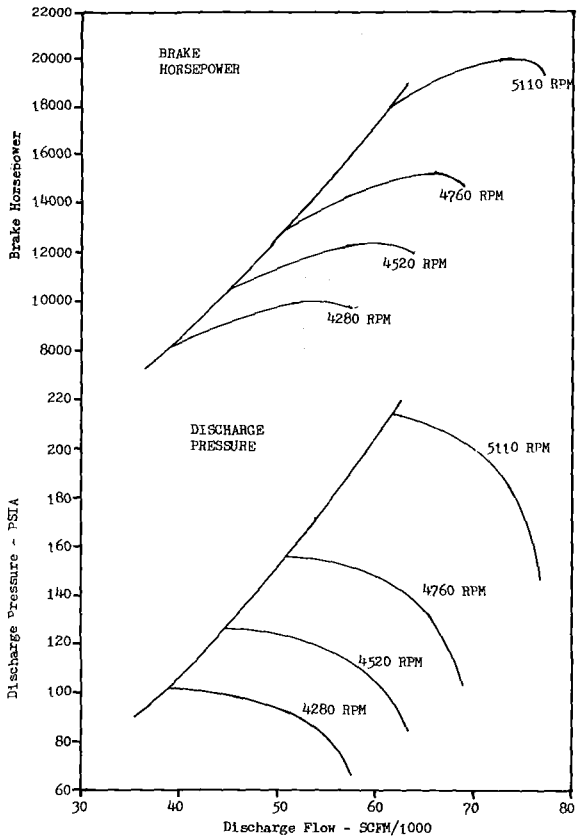

Fig. 4 Manufacturer's compressor performance curves based on an inlet temperature of 80°F and intercooling to 105°F

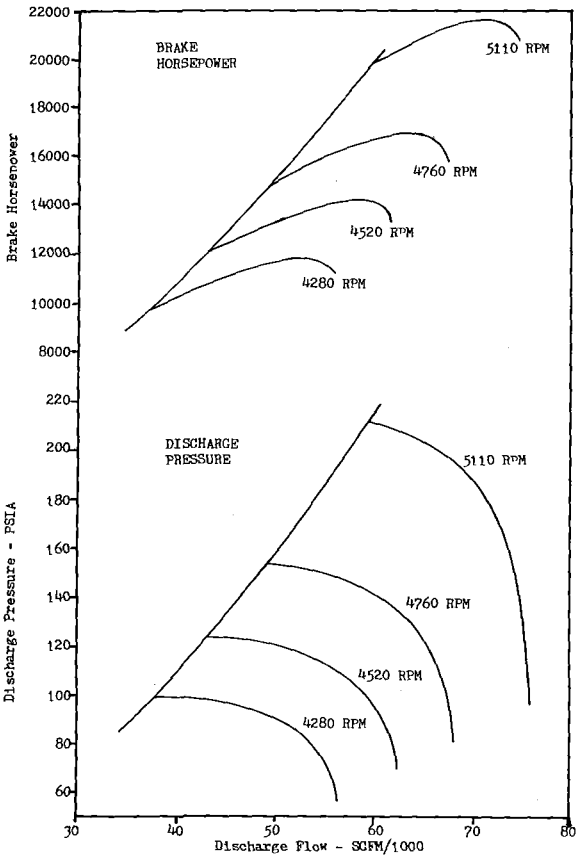

Fig. 5 Manufacturer's compressor performance curves based on an inlet temperature of 95°F and intercooling to 105°F

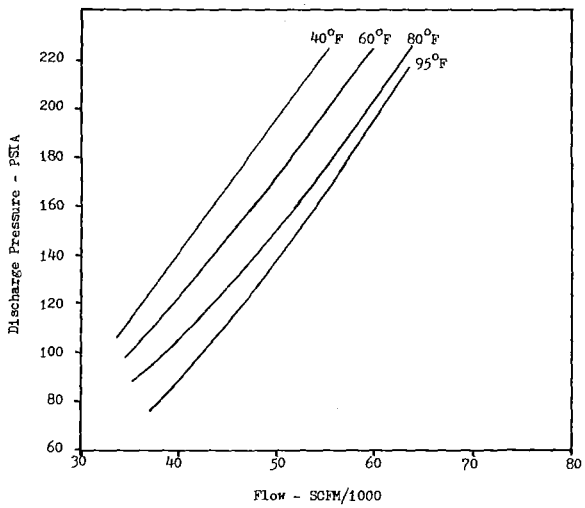

Fig. 6 Shift of surge line with temperature

wake mixing losses caused by the "wake" of an impeller blade as it moves into a radial vaneless space. All of these losses rob energy from the air flow. As the air flow decreases, portions of the compressor will stall, and if the stall is sufficient strength, the compressor will surge.

For a given compressor speed and flow rate, the higher the fluid velocity through the machine, then the higher the rotor and stator energy losses. A simple analogy is an automobile moving at 70 mph and traveling 100 miles that loses considerably more energy through aerodynamic drag than an automobile covering the same distance at 40 mph.

This fact applies to compressors, in that multistage compressors frequently have more than one stage with the same wheel design. Ideally, each successive stage of a compressor should have smaller passages so that as pressure increases across each stage, flow velocity is not reduced. Because compressors are not built to ideal design conditions in each stage, high-pressure stages of similar design to low-pressure stages suffer lower stator and rotor energy losses, and therefore, are generally more stable than the low-pressure stages.

Intercooling also tends to move a higher pressure stage into a more stable operating region, but because the fluid flow must move out of the compressor case through a heat exchanger and back into the compressor case, system design configuration could actually cause a high-pressure stage to be less stable than a lower-pressure stage of similar design.

Compressor surge prediction, therefore, must be conducted in a stage-by-stage analysis to take into account wheel designs, intercooling, and piping configuration to determine exactly which stage of the compressor will surge at the highest flow rate. The stage that surges with the highest flow rate is the limiting factor on how close the entire compressor can be run to its surge line.

The compressor documented in this paper is a six-stage machine with a flow-balanced first-stage impeller, intercooling after the first stage, an unshrouded second-stage impeller, a shrouded third-stage impeller, intercooling after the third stage, and shrouded fourth, fifth, and sixth-stage impellers of identical design to the third stage. Surge line prediction on a stage-by-stage basis on a machine such as this cannot be done by simply running the machine at varying discharge pressures and suction temperatures and decreasing speeds and thereby flow, until a surge event is recorded. This can only create a surge "map" of the machine as a whole, and is liable to inaccuracies because the onset of surge in a single stage of a compressor is rarely noticeable audibly, and only becomes so when its instability causes the rest of the machine to surge.

A decision was made to conduct performance tests of the compressor. These tests would obtain data on the three sec-

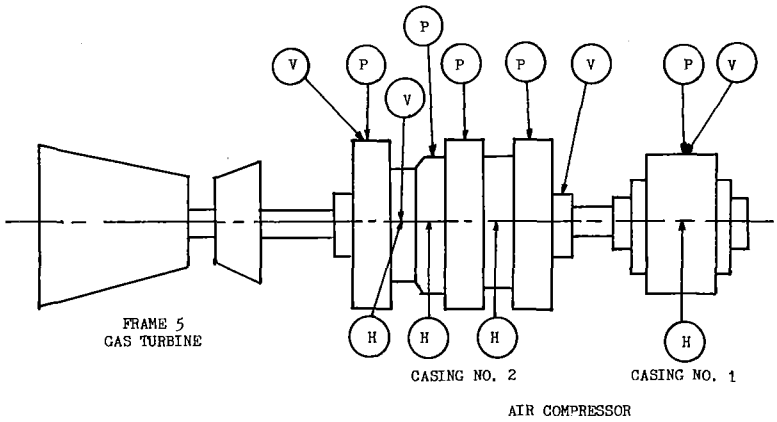

Fig. 7 Locations of data collection points: H = accelerometers in horizontal plane; V = accelerometers in vertical plane; P = dynamic pressure transducer mounted on casing bleed tap

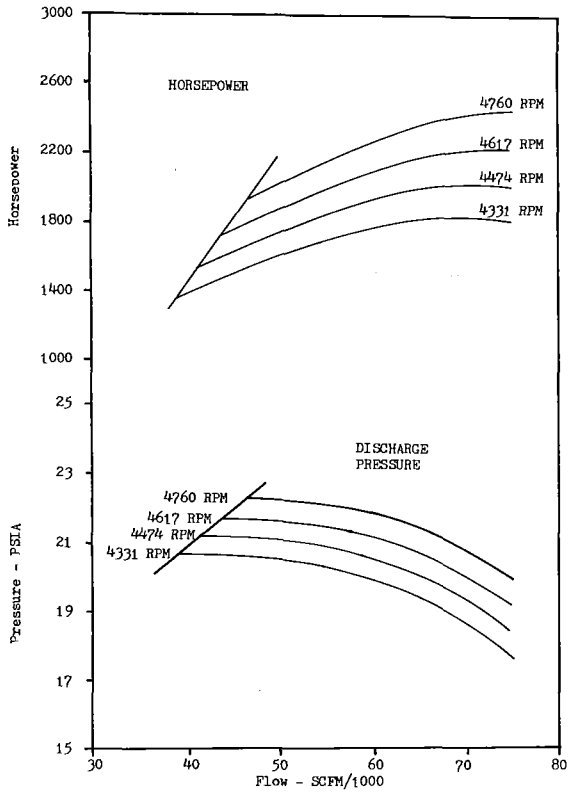

Fig. 8 First-stage performance curves at an ambient temperature of 95°F

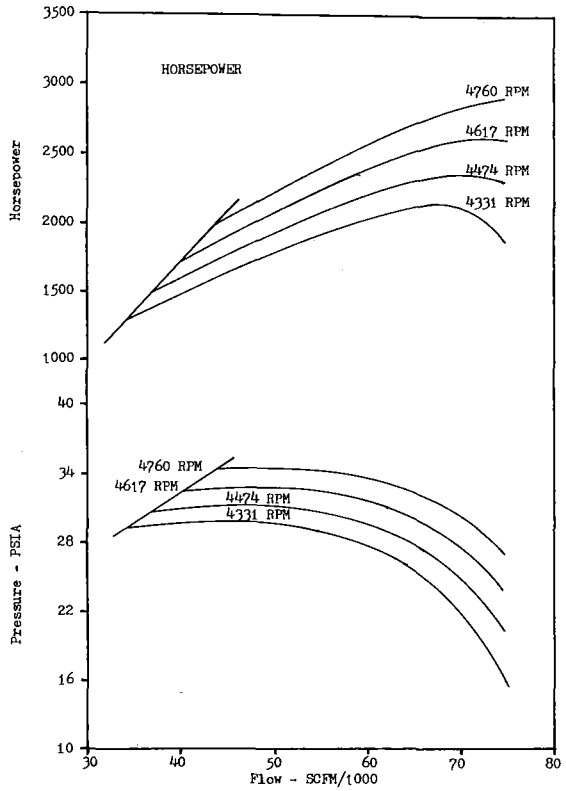

Fig. 9 Second-stage performance curves at an ambient temperature of 95°F

tions. These data can then be used to check the accuracy of the stage-by-stage surge line predictions which make up each section. Information required for an analysis program in the prediction of compressor performance includes physical dimensions of rotors and diffusers, dynamic pressure and case vibrational data, and flow and speed data.

The analysis software, using a complex and unique algorithm of the Navier–Stokes equation [2], uses this information to compute the performance and surge point for the compressor using a detailed aerodynamic solution of each stage.

A solution of inlet and exit velocity triangles is performed for calculation of Euler head and discharge pressure. Head losses in the impeller (rotor losses) are calculated and an impeller efficiency is computed. The impeller efficiency is used in an iteration on the velocity triangles to calculate real conditions versus ideal conditions. Knowing the impeller discharge pressure, velocities through the diffuser are computed and head losses are then used to calculate a diffuser efficiency, overall stage efficiency, and stage exit pressure.

Surge points are then calculated by generating a velocity profile for flow through the impeller and surge is said to occur when the velocities indicate separation of flow from the wall: a stall. The surge point is calculated in a dimensionless parameter, which can then be related back to any flow, pressure, speed, or temperature conditions. Detailed performance "maps" and surge line predictions can be generated and printed out for easy reference. The inaccuracy of the final solution is estimated to be less than 2 percent.

Data on the subject compressor of this paper were collected by mounting dynamic pressure transducers on bleed taps of each stage, and by mounting accelerometers on the compressor case in both the horizontal and vertical planes as shown in Fig. 7. Data were recorded at two machine speeds,

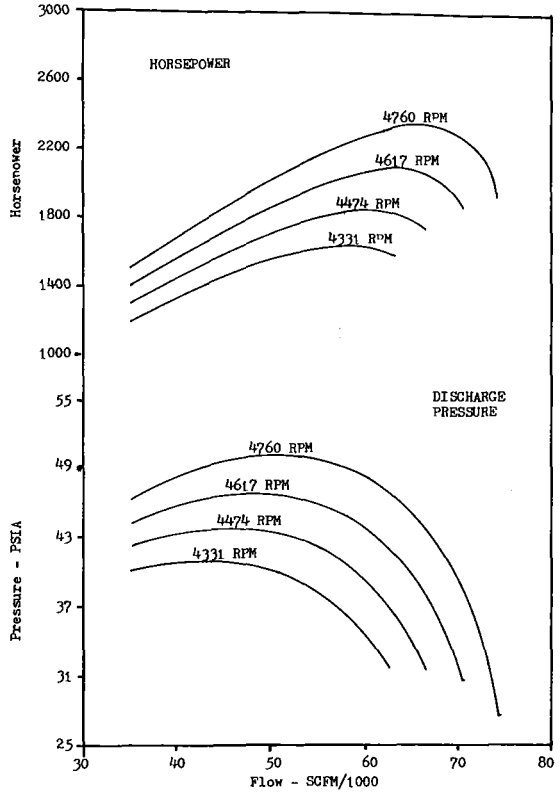

Fig. 10 Third-stage performance curves at an ambient temperature of 95°F

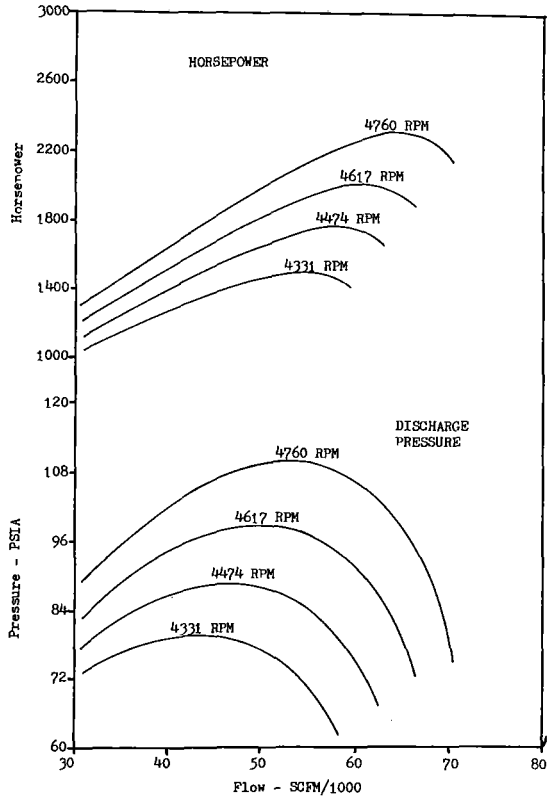

Fig. 12 Fifth-stage performance curves at an ambient temperature of 95°F

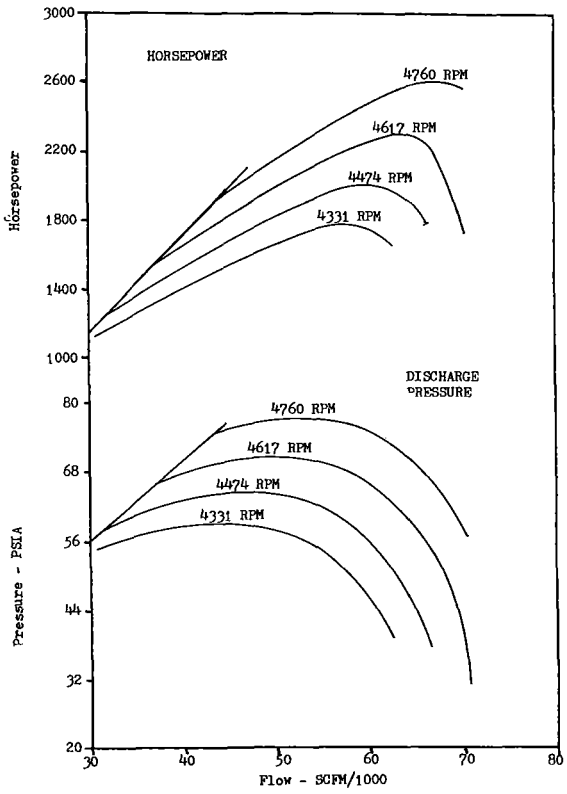

Fig. 11 Fourth-stage performance curves at an ambient temperature of 95°F

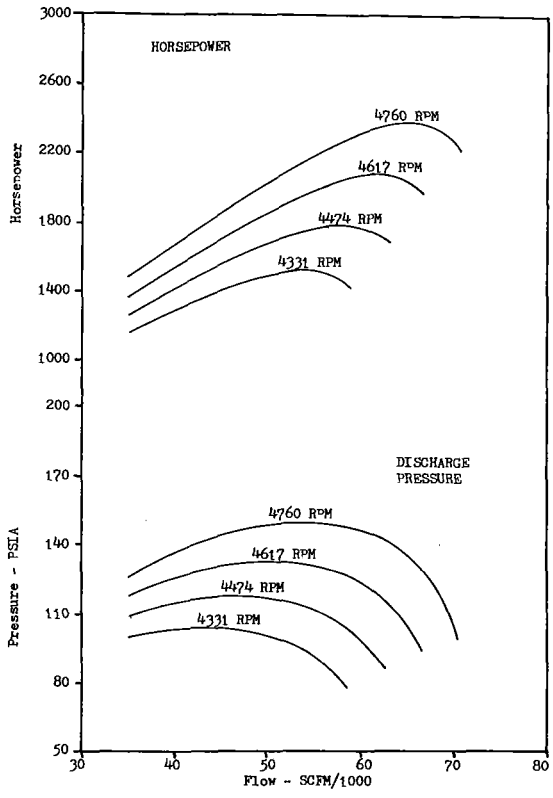

Fig. 13 Sixth-stage performance curves at an ambient temperature of 95°F

4410 and 4520 rpm, using an eight-track AM/FM recorder. Compressor speed, air flow, and temperatures were recorded manually from the control instrumentation in normal use on the machine. Diffuser and rotor dimensions were collected while the compressor was disassembled for annual maintenance.

Test Results

The results of the analysis program are plotted in Figs. 8–13. All six flow/pressure/speed graphics are displayed over the same flow range. Examination shows the first stage to be the stage with the highest surge flow at 39,000 scfm at 4331 rpm. The second stage is next, with a surge flow of roughly 34,000 scfm. The fourth stage is the next closest to surge at 4331 rpm with a surge flow of 31,000 scfm. The third, fifth, and sixth stages have a predicted surge flow so low that it cannot be plotted on the scale of 30,000 to 80,000 scfm.

With the air path configuration of the compressor as it existed, with an air vent at the discharge of the entire compressor, the air flow rate through the compressor at 105 percent of volumetric surge was 41,000 scfm at a discharge pressure of 90 psig which generally agreed with the manufacturer supplied curves. Referring to Fig. 1, the reader may note that the three stages closest to the surge point of the compressor, the first, second, and fourth stages, are all in a position where their suction air comes from outside the compressor case. By dividing the compressor into sections, with the first section being the first stage, the second section being the two stages between the two intercoolers, and the third section being the last three stages of the compressor, a trend can be discovered whereby each successive compressor section has a lower surge flow.

If the first section was limited to a minimum flow of 41,000 scfm, why should the second and third sections be required to compress 41,000 scfm when their surge limits are below 34,000 scfm, and the process requirement is only 30,000 scfm?

Excess air compressed in each section of the compressor is horsepower wasted. If air could be vented off in a controlled manner between the sections of the compressor, each section of the compressor could be run independently at the lowest flowrate required to prevent it from surging. The original goal of this project was to reduce the flow of air through the entire compressor to 105 percent of the volumetric flow rate of the predicted surge point. By taking the effort to carefully study the compressor on a stage-by-stage basis, the opportunity was discovered to reduce flow through successive sections of the compressor for an additional 900 horsepower savings.

The compressor air path was modified by adding a vent valve at the discharge of the first stage of the compressor before the air entered the first intercooler. The control valve and associated piping were sized for a maximum air flow of 8000 scfm at a first-stage discharge pressure of 6 psig. The added valve is shown in Fig. 14 as CV 1. At flowrates near the surge points, a centrifugal compressor can deliver a fairly wide flow range without greatly affecting discharge pressure, so varying the flow of the first stage of this compressor would have very little effect on the operation of the latter stages.

Control System Update

The existing controls on the compressor were all field-mounted, large case pneumatics. The compressor discharge vent valve was controlled by a system using a pressure controller with an override flow controller. The flow controller was always kept at a setpoint known to be well away from the surge flow at any ambient conditions. Operators were required to manually adjust the speed of the turbine to keep the flow controller from overriding the pressure controller and causing the discharge pressure to droop. The vent valve was a 10-in. Fisher V-ball with a stroking time of roughly 45 s to 1 min.

The turbine speed control systems consisted of a mechanical governor linked mechanically to the starter steam turbine throttle valve and pneumatically to the gas turbine throttle valve. These controls were very susceptible to dirty or wet instrument air, and the governor became unstable below 4400 rpm.

The existing compressor and turbine controls were not capable of accepting the implementation of a sophisticated surge control algorithm requiring extremely fine control movements and quick responses. Any new control system would have to be as reliable as the old systems because unwanted shutdowns would cause expensive process upsets.

With these thoughts in mind, separate digital control systems were installed for turbine speed control and compressor surge control. The turbine speed control system chosen was a Tri-Sen TS-500 dual processor controller. The dual processor gave complete control backup so that in case one of the controllers failed, the turbine would continue to run on the second controller. The TS-500 provided complete start-up sequencing for the gas turbine and was very easy to interface with an external surge controller using analog signals.

The surge controller chosen was a Boyce Engineering

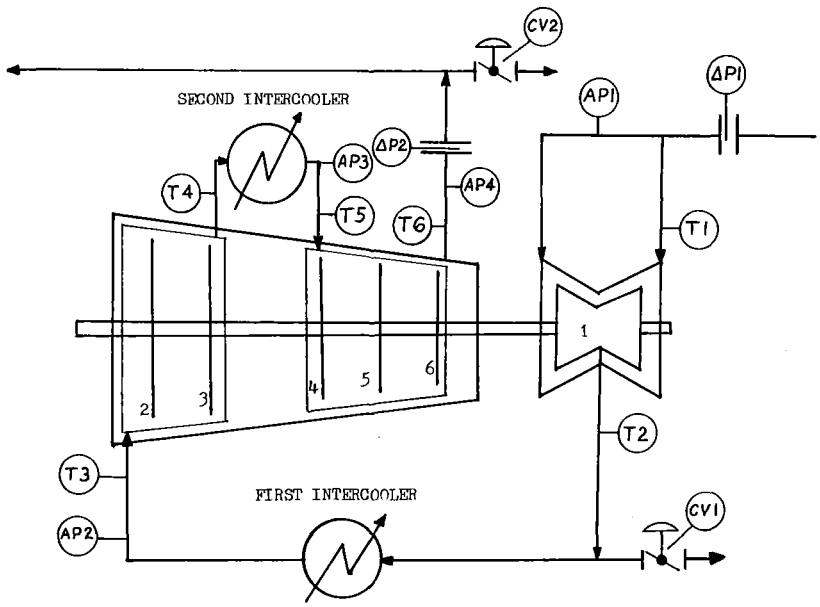

Fig. 14 Transmitter and control valve locations: AP = absolute pressure transmitter; P = differential pressure (flow) transmitter, T = temperature transmitter (RTD); CV = control valve

SURGE+ system, which was designed around a Texas Instrument PM-550 programmable logic controller. The PM-550 is capable of handling both ladder logic and relatively sophisticated math control functions. The ladder logic is capable of updating outputs at well over 50 times per second while the math portion operates at an independent rate. This is achieved by the PM-550 dual processor arrangement which allows one processor to do integer functions, while the other does floating point math. The pacing of programming calculations and surge avoidance control responses could therefore be done in ladder logic, and an extremely quick response time was achieved.

New electronic field transmitters were required in addition to replacing existing pneumatic discharge pressure and flow transmitters. A flowmeter was installed in the suction piping. Four absolute pressure transmitters were installed at the suction of each compressor section and at the discharge of the third compressor section. Six RTD elements were installed in the piping as close as possible to the compressor cases at the inlets and outlets of all three compressor sections. The RTDs are of the direct insertion type, with no thermowells being used for quick temperature measurement response time. Figure 14 is a compressor layout drawing showing the location of these transmitters.

The compressor is controlled by three control loops in the PM-550 analog controlware. Using the dimensionless surge point parameter developed by the software, and the flow, pressure, and temperature information, the surge controller calculates a percentage of surge flow for all six stages of the compressor. This number is the process variable for the surge control loops.

The surge flow number for the first stage is used by the number one control loop to modulate the vent valve at the discharge of the first stage. The lowest surge flow number of all six stages is used as the setpoint of the number two control loop to modulate the vent valve at the compressor discharge. The degree to which the number one wheel is included in the selection process is dependent upon the remaining authority of the first-stage vent valve.

A third loop is the discharge pressure control. The first and second control loops are actually flow controls, maintaining flow through the compressor by opening and closing the two air vents. The third loop controls pressure by varying the compressor speed.

If process needs are below the surge point of the compressor, the control valves vent off just enough air to maintain an air flow of 105 percent of predicted surge volume. If process needs go above 105 percent of the predicted surge volume, the vent valves close fully, and the only control required is to maintain pressure with speed changes.

Herein lies the sophistication of this control system. The surge point of the compressor shifts considerably with small changes in ambient pressure and temperature. As this occurs, the predicted surge volume calculated from the dimensionless surge number also changes, so as atmospheric conditions change, the surge controller always keeps the compressor operating at 105 percent of the predicted surge flow at that given time; hence the term "predictive surge control."

With this control system, the compressor can be operated extremely close to its surge limit because the exact surge limits are known at any given time. Previous compressor surge control systems available on the open market have used pressure versus flow curves, then applied a "safety factor" to draw a control line away from the predicted surge lines [2]. The safety factor can be inaccurate since it is not responsive to interstage changes. Because of these inaccuracies of the safety line, the closest these control systems have been able to run to the surge line and guarantee no surge events is around 113–115 percent of volumetric surge.

The ladder logic portion of the controller is used to protect the compressor from surging when the analog control loops respond too slowly to cutbacks in process air consumption due to plant upsets. Two separate levels of events can cause the surge controller to take "surge avoidance" action. If the ladder logic calculates an air flow equal to or less than 100 percent of the predicted surge flow for over one-tenth of a second, a surge avoidance is triggered. Also, if an actual surge event is detected, the ladder logic will initiate a surge avoidance reaction.

An actual surge event is detected in three ways: (*a*) by detecting a sudden drop in discharge flow, (*b*) by detecting a sudden increase in inlet pressure of any compressor section, or (*c*) by detecting a sudden increase in inlet temperature for any of the compressor sections. Any of these three incidences indicate that surge is already occurring and that surge avoidance must be taken immediately. Surge avoidance action itself is simply ramping the vent valves open to increase air flow and boosting compressor speed so as not to greatly affect the discharge pressure. If a surge event is recognized, the controller raises the predicted surge flow by one percent. This gives the controller the ability to learn and adapt as the machine ages.

As stated earlier, the compressor discharge vent valve had a stroking time of over 45 s. To improve this slow response time, a volume booster was installed between the positioner and the diaphragm. The booster reduced the stroking time to 4 s, which for this particular installation was found to be faster than necessary.

Before installing the surge controller on the compressor, a complete computerized model of the compressor was developed to test the control response. Using the speed output signals as an input to the compressor model, and by manually entering suction temperature and pressure conditions, the model calculated the flow, temperature, and pressure variables at each transmitter location (see Fig. 14). These variables were then converted to analog signals and input into the surge controller. The controller now had a "live" compressor to control. Although actual response times of the real compressor could not be simulated exactly, the simulator was an invaluable tool for developing surge avoidance response and for developing tuning parameters for the initial startup.

Startup

Startup sequencing for the entire turbine compressor train is performed by the electronic speed governor. The control function includes flow and pressure controls for ease of operation when placing the compressor into process service, and because the surge controller is not a redundant controller. Once the compressor is in the run mode, the speed controller closes a contact input to the surge controller which gives the surge controller "permission" to take over control of the compressor. The surge controller monitors the turbine speed and the output signal to the discharge vent control valve so that transfer of control is "bumpless."

When the surge controller start button is depressed, the surge controller closes a contact input to the speed controller. This causes the speed controller to begin accepting a speed setpoint from the surge controller and hands control of the discharge vent valve to the surge controller. The surge controller slowly ramps the vent valve closed until the flow through any one of the compressor stages reaches 105 percent of the predicted surge flow volume.

The surge controller opens the first-stage vent valve when the machine reaches minimum speed. This action steps the first wheel back approximately 20 percent. Once the last five compressor stages are optimized by the discharge vent valve, the surge controller starts to close the first-stage vent valve. When flow through the first stage has been reduced to 105 percent of surge flow, the compressor has been reduced to its

most efficient point, only venting air required to keep the compressor from surging.

Startup of this control system took place in December 1984. Because considerable effort had been spent with the control system on the computer simulator, very few problems were encountered. One unexpected problem uncovered during the testing of the surge avoidance logic was that a valve stroking time of 4 s was too fast. Upon taking a surge avoidance reaction, if the vent valves ramped open too quickly, the speed controller could not accelerate the turbine fast enough to keep the compressor discharge pressure from drooping. A pressure drop could cause process upsets downstream, so the valve stroking speed was decreased to 16 s. The predictive surge avoidance reaction is so quick that the control valves are being opened before the compressor can begin surge, and slowing the valve stroking speed allows the turbine to maintain discharge pressure as the flow increases. By tuning the surge avoidance response to the entire system of piping, a response was developed which could handle a complete shutoff of process air flow in less than 15 s without allowing the discharge pressure to vary more than 1 psi.

Purposefully lowering the turbine speed and making the compressor surge at various discharge pressures has proved the computer-generated performance curves to be so accurate that they have been accepted as actual compressor performance curves.

Results

The original goals of the project were to cut energy costs of running a centrifugal compressor that was supplying process air at a flow rate well below its stable operating region, and to protect it from any damage due to an unwanted surge event.

The manufacture's performance curves indicated that a reduction of 3600 hp could be achieved by decreasing air flow through the entire compressor to 105 percent of the predicted surge flow. A detailed performance analysis of the compressor revealed the manufacture's curves to be optimistic, and that a savings of only 3200 hp could be achieved by reducing total flow to 105 percent of surge flow. However, the detailed analysis also revealed the opportunity to save an additional 900 hp by venting 6000 scfm at the discharge of the first stage. Theoretically, the compressor energy consumption could be reduced by 4100 hp, or about $1.9 million in fuel costs in one year.

During installation of the surge controller, the original process air flowmeter was found to be reading incorrectly because it was still calibrated for a discharge pressure of 100 psig. Because the entire surge prediction was based upon this flowmeter, the actual energy savings available were substantially reduced. In practice, the surge controller was able to reduce the energy consumption of the compressor train by 2300 hp by reducing the air flow to 105 percent of the total machine surge flow, but the full 900 hp savings were realized by installing the first-stage vent valve and venting 6000 scfm. Operating the compressor in this manner resulted in an actual energy savings of 3200 hp, resulting in an annual fuel savings of about $1.5 million.

The surge protection of the controller is designed to handle a total loss of process air consumption in 15 s. On two occasions in February 1985, power failures caused the process air consumption to drop from 30,000 scfm to nothing in less than 5 s. The compressor stayed on-line without surging and a pressure swing of less than 2 psi was recorded. Losses of individual downstream processes usually result in an 8000 scfm reduction in process air consumption, and the surge controller is able to protect the compressor from surging. On these occasions, the pressure bobbles less than 1/2 psi, so the remaining processes on-line are never affected by the process upsets.

Conclusions

Centrifugal compressors operating at load conditions well below their design points are required to vent or recycle considerable amounts of compressed gas to prevent them from surging. Large fuel savings can be realized by operating these compressors as close as possible to their predicted surge limit.

To determine whether a compressor is being run at the lowest possible speed and flow without endangering its health due to surging, a detailed performance map of the compressor should be generated. A set of performance maps should be organized on a stage-by-stage basis to take into account the different inlet conditions of each stage due to intercooling, site piping configurations, and rotor design limitations.

When detailed performance maps have been generated a predictive surge control system can be implemented to control the compressor at flow rates extremely close to its surge limit. A predictive surge controller is able to calculate the "live surge limit" for each wheel of the compressor for all possible limit, interstage, and outlet conditions so that the control setpoint never enters the compressor's unstable operating region. This precise calculation also allows for much quicker response to load swings so that no surge cycle is experienced, even when the compressor is rapidly and completely unloaded.

The complexity of a predictive surge controller's calculations also creates the opportunity for large energy savings with the selective use of interstage venting or recycling. Unloading latter compressor stages that do not require the flow rates of previous stages for surge protection saves energy because a portion of the compressor's inlet air flow is not compressed to the full discharge pressure.

References

1 Boyce, M. P., *Gas Turbine Engineering Handbook*, Gulf Publishing Company, 1982.

2 Boyce, M. P., Trevillion, W. L., and Brown, M. L., *Advanced Research Programs in Turbomachinery*, Proceedings of the Fifth Turbomachinery Symposium, Texas A&M University, 1976, pp. 31–44.

3 Boyce, M. P., Bohannan, W. R., Brown, R. N., Gaston, J. R., Meher-Homji, C. B., Meier, R. H., and Pobanz, N. E., *Tutorial Session on Practical Approach to Surge and Surge Control Systems*, Proceedings of the Twelfth Turbomachinery Symposium, Texas A&M University, 1983, pp. 145–173.

Heat-Flux Measurements for the Rotor of a Full-Stage Turbine: Part I—Time-Averaged Results

M. G. Dunn
Calspan–UB Research Center,
Buffalo, NY 14225

This paper describes time-averaged heat-flux distributions obtained for the blade of a Garrett TFE 731-2 hp full-stage rotating turbine. Blade measurements were obtained both with and without injection. The injected gas was supplied from a separate reservoir and was directed into the turbine gas path via nozzle guide vane (NGV) pressure surface slots located at approximately 63 percent of the wetted distance. Blade heat-flux measurements were performed for two different injection gas temperatures, $T_c/T_0 = 0.53$ and $T_c/T_0 = 0.82$. A shock tube is used as a short-duration source of heated air to which the turbine is subjected and thin-film gages are used to obtain the heat-flux measurements. Results are presented along the blade in the flow direction at 10, 50, and 90 percent span for both the pressure and suction surfaces. A sufficient number of measurements were obtained to also present spanwise distributions. At approximately the 50 percent span location, two contoured inserts containing closely spaced gages were installed in the blade so that the leading-edge region distribution could be resolved in detail. The blade results are compared with predictions obtained using a flat-plate technique and with predictions obtained using a version of STAN 5. The results suggest that: (1) The suction surface laminar flat-plate prediction is in reasonable agreement with the data from the stagnation point up to approximately 10 percent of the wetted distance. Beyond 10 percent, the laminar prediction falls far below the data and the turbulent flat-plate prediction falls above the data by about 60 percent. The laminar portion of the STAN 5 prediction as configured for the present calculation does not provide good comparison with the data. However, the turbulent flat-plate boundary-layer portion of STAN 5 does provide reasonably good comparison with the data. On the pressure surface, the turbulent flat-plate prediction is in good agreement with the data, but the laminar flat-plate and the STAN 5 predictions fall far low. (2) The influence of upstream NGV injection is to significantly increase the local blade heat flux in the immediate vicinity of the leading edge; i.e., up to 20 percent wetted distance on the suction surface and up to 10 percent on the pressure surface. (3) The effect on local heat flux of increasing the coolant-gas temperature was generally less than 10 percent.

Introduction

The interaction between the rotor blade and the flow exiting the vane row is an important consideration to the designers of gas turbine engines. Since most modern gas turbines have vane cooling, it is also important to investigate the influence of cooling-gas injection on the local blade heat-flux values. In general, it is difficult to obtain detailed blade measurements under conditions that duplicate the turbine stage flow function, pressure ratio, temperature ratio, Mach number distribution, and corrected speed. With the added complication of coolant-gas injection, one will find very few applicable blade data in the open literature. The experimental technique used to obtain the results reported here uses a shock tube to generate a short-duration source of heated air and fast-response, thin-film thermometers to measure the surface-temperature histories at prescribed locations on the blade surface. Heat-flux rates are then inferred from the temperature histories, using standard data reduction procedures.

Previous results of this measurement program were reported as they became available [1–9]. Reference [6] reported blade heat-flux data for the Garrett TFE 731-2 hp rotor, but since that work was published the blades were re-instrumented and the surface coverage for the measurements reported in the current paper is significantly more complete. Some of the same instrumentation locations were utilized and the earlier results are consistent with those reported here. Reference [7] reported the results of a measurement program for which cooling gas was injected through the NGV slots, but the emphasis of the measurements reported in [7] was on the

Contributed by the Gas Turbine Division of THE AMERICAN SOCIETY OF MECHANICAL ENGINEERS and presented at the 31st International Gas Turbine Conference and Exhibit, Düsseldorf, Federal Republic of Germany, June 8–12, 1986. Manuscript received at ASME Headquarters January 13, 1986. Paper No. 86-GT-77.

influence of cooling gas on the vane heat-flux distribution. Thus rotor data were not reported in [7]. The instrumented vanes described in [7] were installed for the current program and the data from these gages were recorded but will not be described here. The discussion presented in this paper will be confined to the steady-state heat-flux distributions on the blade, both without and with upstream NGV cooling gas injection. A detailed description of the analysis technique and typical time-resolved heat-flux data obtained for this turbine rotor under the same experimental conditions reported here is given in Part II of this paper.

Experimental Apparatus

A schematic of the experimental apparatus, the operation of this device, and the technique used to obtain the desired experimental conditions are described in [6] and will not be repeated here. It suffices to note that the measurements are performed using a full-stage rotating turbine operating in a flow environment described in the next paragraph.

The shock-tunnel facility provides a clean, uniform, and well-known gas-dynamic condition at the inlet to the NGV. The experimental technique will duplicate the design flow function ($\dot{W}\sqrt{\theta}/\delta$), the ratio of wall temperature to total temperature (T_w/T_0), the design rotor speed, the design tip/shroud clearance, the design stator-rotor spacing, the ratio of coolant to total temperature (T_c/T_0), and the incoming turbulence intensity. The intent of the experiment is to have the flow conditions sufficiently well known and enough parameters duplicated so that the measured heat-flux distributions can be used to validate and improve confidence in the accuracy of full-stage design data and predictive techniques under development. Several different types of measurements must be obtained in order to provide this information. The primary measurement is heat-flux which is obtained using platinum thin-film gages. The substrate onto which these gages are painted can be made in many sizes and shapes, depending upon the particular portion of the turbine stage for which one is interested in obtaining data; i.e., the button gage, the leading-edge gage, contoured strip gages, or stagnation-point gages. Static pressure, rotor speed, and tip clearance are other parameters that are both routinely measured and duplicated in these experiments.

The air coolant gas was supplied from an independent reservoir and was injected through the NGV pressure surface slots at a temperature of either 530 R or 820 R at a weight-flow rate equal to approximately 2 percent of the turbine flow rate. A photograph of the vane slot configuration is shown in Fig. 12 of [7]. The coolant gas was supplied to the 360 deg annular NGV row via a manifold that surrounded the vane coolant supply holes. The procedure was to open a fast-acting valve located between the reservoir and the manifold just prior (on the order of 50-100 ms) to the arrival of the model test-gas flow in order to establish the coolant-gas weight flow, $\dot{W}_c$. The magnitude of $\dot{W}_c$ was maintained by the flow control

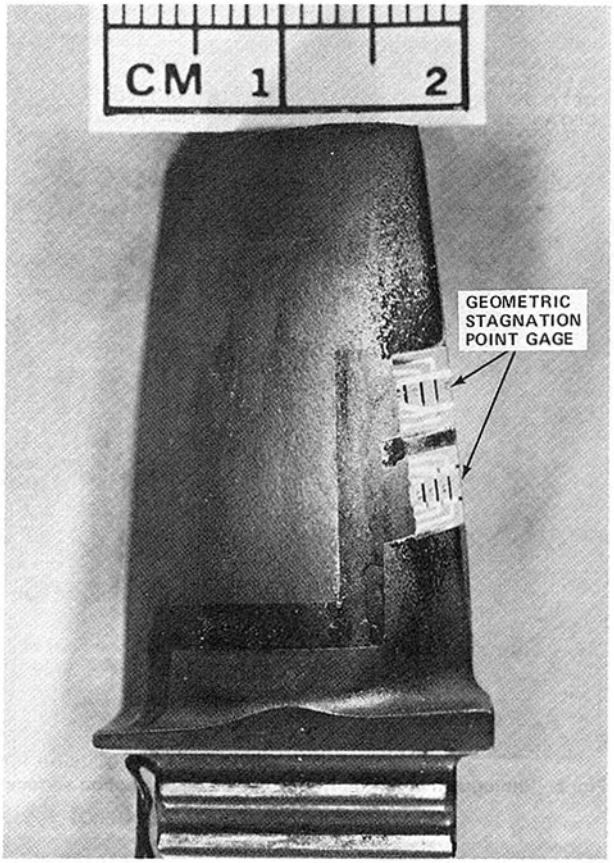

Fig. 1 Photograph of contoured leading-edge inserts for rotor blade

orifice (all flow control orifices used here were standard ASME design) located between the valve and the vane coolant inlet holes. Care is taken to maintain the reservoir pressure at a sufficiently high value so that when the test flow is established in the model, and thus the pressure level existing at the slot is transmitted to the feed system plenum, the pressure ratio across the orifice is sufficient to maintain a choked orifice. The weight flow of coolant gas can then be estimated from the geometry and the coolant reservoir conditions. The pressure history downstream of the orifice is measured in the manifold feeding the vane inlet holes and a typical pressure history is given in [7]. A rubber gasket is used to provide a gas–metal interface seal between the manifold and the vanes.

In the case of the elevated T_c, the reservoir containing the coolant air was heated to 870 R over a period of several hours at a pressure of 250 psig. However, the flow channel through which the heated injection gas flows was at 530 R and it should be anticipated that the injected gas temperature at the slot will be lower than the 870 R reservoir value. The temperature

Nomenclature

A = NGV inlet area
Flow Function = $\dot{W}\sqrt{\theta}/\delta$
h = heat transfer coefficient
H_0 = total enthalpy
$H_w(T)$ = wall enthalpy
k = thermal conductivity
N_{corr} = corrected rotor speed $= N_{phy}/\sqrt{\theta}$
N_{phy} = physical rotor speed
Pr = Prandtl number
$\dot{q}(T)$ = heat flux corrected for variable thermal properties of the Pyrex substrate
$\dot{q}(T_w)$ = cold-wall heat flux
S = distance measured along surface
S_T = distance measured along surface from leading edge of trailing edge
St = Stanton number
T_w = initial wall temperature
T = local temperature of thin-film gage evaluated as a function of time
ΔT = measured surface-temperature rise of Pyrex substrate
T_c = coolant-gas temperature at injection location
T_0 = total temperature
$\dot{W}$ = weight flow through turbine
$\dot{W}_c$ = coolant weight flow
δ = $P_{T,in}/14.696$
θ = $T_0/518$ R

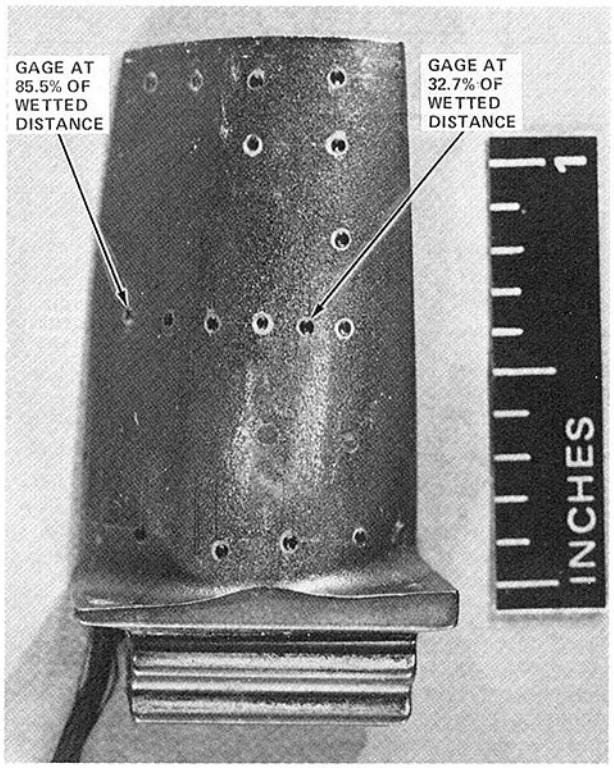

Fig. 2 Photograph of button-type gages on blade suction surface

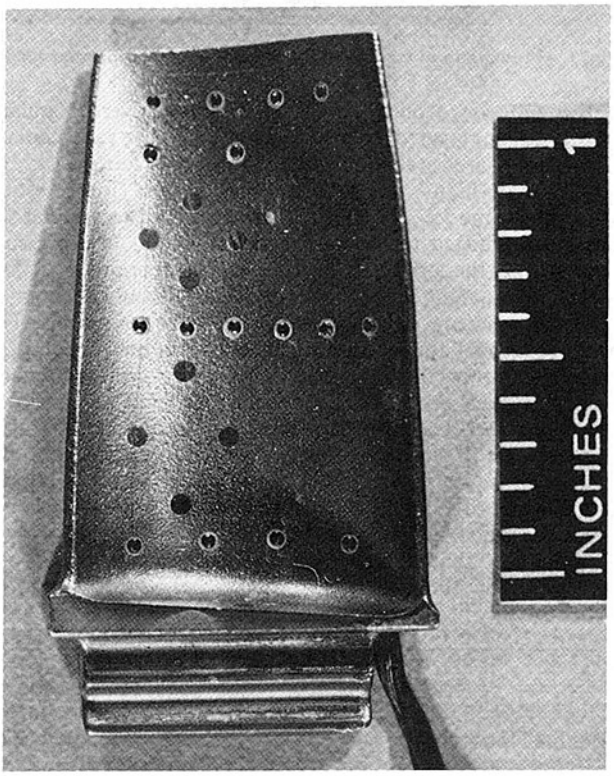

Fig. 3 Photograph of button-type gages on blade pressure surface

decrease as a result of heat loss in flowing from the reservoir to the slot was calculated to be 50 R giving an estimated injection gas temperature at the slot of 820 R.

A photograph of a typical button-type heat-flux gage used in this work was taken through a Leitz microscope and is shown in [6]. The thin-film gages are made of platinum (~ 50 to 100 Å thick) and are painted on a pyrex substrate

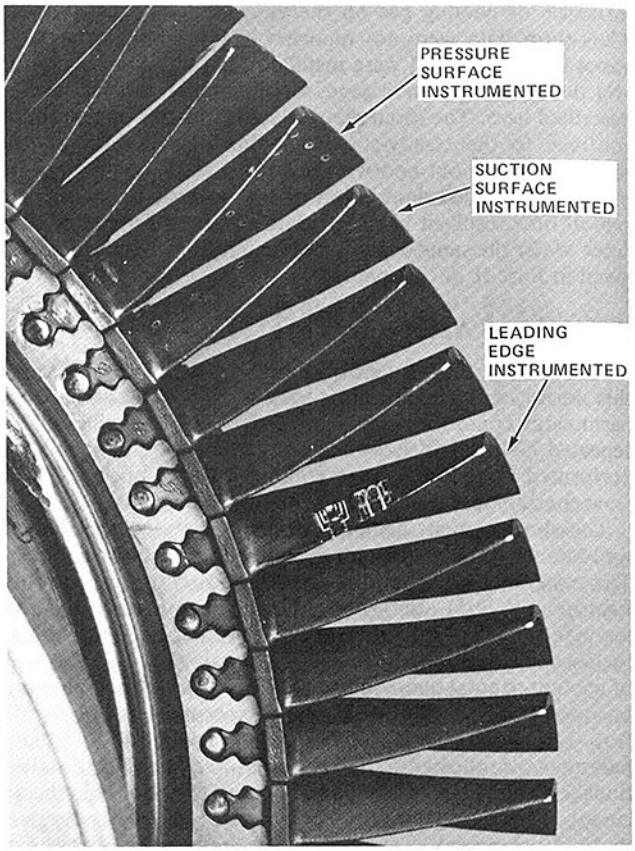

Fig. 4 Photograph of instrumented blades installed in rotor disc

9.7×10^{-4}m (0.04 in.) in diameter in the form of a strip approximately 1.0×10^{-4}m (0.004 in.) wide by about 5.1×10^{-4}m (0.02 in.) long. In building these gages, the intent is to obtain a gage with a room temperature resistance on the order of 50 to 100Ω. The thickness of the pyrex substrate depends upon the gage location. Those gages located in the NGV trailing edge and near the rotor blade trailing edge are approximately 3.8×10^{-4}m (0.015 in.) thick, but gages at other locations are 7.1×10^{-4}m (0.03 in.) thick. The response time of these heat transfer elements can be shown to be on the order of 10^{-8} s. A coating of magnesium fluoride (~ 1200 Å thick) is vapor deposited over the gage to protect the platinum element against abrasion.

Both the button-type gages and the contoured leading-edge inserts were installed on the rotor blades and used to perform the measurements reported in this paper. Figure 1 is a photograph of two contoured leading-edge inserts used on the rotor blade. The upper insert has one gage at the geometric stagnation point and three gages spaced at intervals of approximately 0.001 m (0.040 in.) on the pressure surface while the lower insert has one gage at the geometric stagnation point and three gages at approximately 0.001-m (0.040-in.) intervals on the suction surface. Figure 2 is a photograph of the suction surface button-type gage instrumentation illustrating detailed gage density at the 10, 50, and 90 percent span locations, with an additional two gages at the 81 percent and a single gage at the 65 percent span locations. Except for the leading-edge region, the small button-type gages were used on the blade because of the interest in very local measurements that can be used in time-resolving events taking place during wake and passage cutting. Figure 3 is a photograph of the blade pressure-surface instrumentation illustrating the measurement pattern at approximately 10, 50, and 90 percent of span, with an additional two gages at the 81 percent span location. One additional blade was instrumented on the suction surface at the 50 percent span location and was separated from the

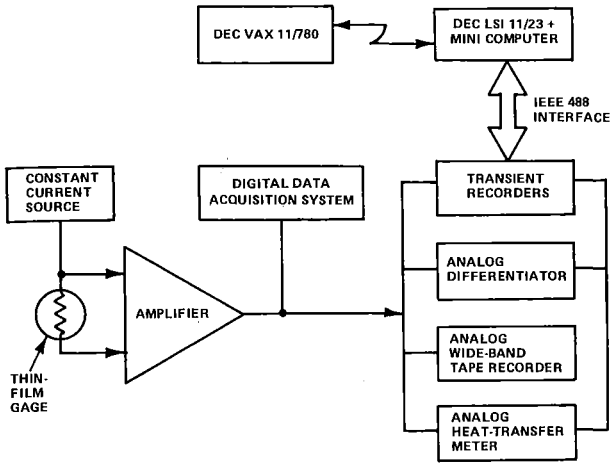

Fig. 5 Schematic of on-line data recording system for short-duration facility

blades described above by two blades. Figure 4 is a photograph of the instrumented blades installed in the rotor disc in the configuration for which they were run. The gage lead wires are routed down the opposite side of the disc into a hollow shaft and then to the slip-ring unit.

A schematic of the on-line data recording system used to obtain the data reported in Part I and Part II of this paper is given in Fig. 5. A detailed description of this system is given in [8] and will not be repeated here. It suffices to comment that the data described in Part I relied on the digital data acquisition system and the data reported in Part II relied on the entire right-hand portion of the schematic diagram as described in [8].

Experimental Conditions

Table 1 gives the experimental conditions and measured parameters for the results presented in this paper. These conditions are very close to those obtained for the results presented in [6, 7]. Therefore, the flat-plate and STAN 5 predictions previously published in [6] are reproduced here to compare with the experimental results.

Experimental Results

The Stanton number used here for the blades is based on conditions at the NGV inlet and was evaluated using the relationship

$$\mathrm{St}_{\mathrm{inlet}} = \frac{q(t)}{(\dot{W}/A)(H_0 - H_w(T))} \tag{1}$$

It is illustrated in [11] that the Stanton number defined in equation (1) is equivalent to the cold-wall Stanton number. Thus, the cold-wall heat flux $q(T_w)$ can be calculated from the results presented herein by multiplying the Stanton number by $(\dot{W}/A)(H_0 - H_w(T_w))$. The mean and the standard deviation of the Stanton number have been computed for each heat-flux gage using the expression:

$$\mathrm{St}_{\mathrm{mean}} = \frac{1}{N}\sum_{i=1}^{n}(\mathrm{St})_i \tag{2}$$

$$\mathrm{St}_{\substack{\mathrm{standard}\\ \mathrm{deviation}}} = \left[\frac{1}{N}\sum_{i=1}^{n}(\mathrm{St}_i - \mathrm{St}_{\mathrm{mean}})^2\right]^{0.5} \tag{3}$$

On all of the data plots presented here, the symbol will represent the mean value of the Stanton number given by equation (2) and the bar will represent the standard deviation given by equation (3). If the bar does not appear along with the symbol, then the standard deviation falls within the symbol unless otherwise noted.

Table 1 Test conditions and parameters

Reflected-shock pressure	7.43×10^3 kPa	(1078 psia)
Reflected-shock temperature	559.4 K	(1007 R)
NGV inlet total temperature	559.4 K	(1007 R)
Static pressure at NGV inlet	6.79×10^2 kPa	(98.5 psia)
Static pressure downstream of rotor	3.56×10^2 kPa	(51.7 psia)
Area on which Stanton number is based	3.17×10^{-2} m^2	(0.34 ft^2)
Weight flow without coolant	9.31 kg/s	(20.5 lb/s)
Weight flow with coolant	9.45 kg/s	(20.8 lb/s)
Corrected rotor speed	100 percent	–
Turbulence intensity upstream of NGV	~5.5 percent	–
Reflected-shock enthalpy	5.6×10^5 J/kgm	(240.98 Btu/lb)
Wall enthalpy at 530 R	2.96×10^5 J/kgm	(127.30 Btu/lb)
T_wT_0	0.53	

Blade Results Without Injection

Figure 6 is a sketch of the turbine stage giving the measured wall static pressures upstream of the NGV and downstream of the rotor for the experiments described herein. In addition, the static pressure at the slot location (63% wetted distance) was measured using a pressure gage located in the coolant supply plenum. This pressure was approximately the same, with or without injection. The pressure downstream of the rotor was measured at the hub and at the tip walls and then further down in the exit channel. Unless otherwise noted, the rotor was operated at approximately 100 percent corrected speed. The weight flow with injection was calculated using the measured pressure in the same manner as the weight flow without injection and was found to be approximately 2 percent greater. The coolant supply calculation which is believed to be reasonably accurate for this purpose gave a value of 2.3 percent for the $T_c = 530$ R case and 1.8 percent for the $T_c = 820$ R case.

Typical pressure records for the reflected-shock reservoir and for a location on the model hub surface at 0.016 m upstream of the NGV inlet are shown in Fig. 7. The time of shock reflection from the endwall is noted on Fig. 7(*a*) and the magnitude of the uniform pressure pulse is on the order of 7.6×10^3 kPa (1100 psia). The time required to establish uniform flow in the turbine model is illustrated on Fig. 7(*b*) as is the duration of the test period. The test-time duration is sufficient to collect blade data over approximately six revolutions of the rotor.

Figure 8 presents the Stanton number distribution as a function of wetted surface distance at three spanwise locations, 10 percent (near the hub), 50 percent, and 90 percent (near the tip). The extent of the leading-edge inserts is noted on Fig. 8. The heat-flux gages on these inserts are closely spaced, being on the order of 4 percent of wetted distance apart. A measurement at the geometric stagnation point was obtained for each of the two inserts. The inserts are located within approximately ±4 percent of the 50 percent span location, but sufficiently close to be considered representative of the 50 percent line for this particular turbine.

The geometric stagnation-point values are shown on Fig. 8

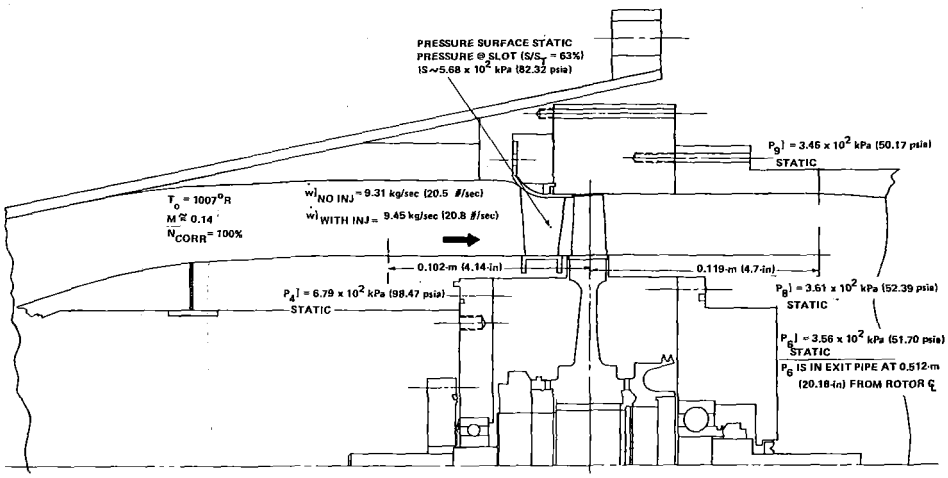

Fig. 6 Sketch of stage and associated flow field parameters

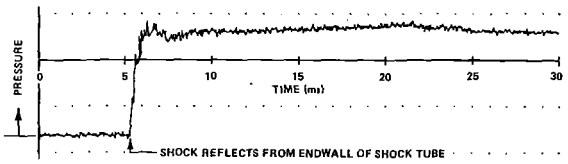

Fig. 7(*a*) Reflected-shock pressure measurement

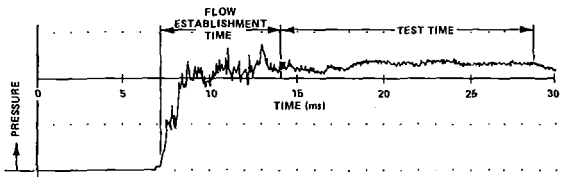

Fig. 7(*b*) Static pressure on model at ~0.102 m upstream of NGV

Fig. 7 Typical shock tube reflected-shock pressure measurement and corresponding static pressure on turbine model upstream of NGV

to be in excellent agreement with each other. Also shown are the previously mentioned flat-plate and STAN 5 predictions for the 50 percent span location from [6]. In this calculation, the local properties and the Stanton number were evaluated at the proper relative temperature. Calculations were also performed for 10 and 90 percent span, but they give Stanton numbers within 10 percent of the midspan result and thus will not be presented. The STAN 5 calculation shown here used a transition Reynolds number of $Re_\theta = 200$ and a complete description of this calculation is given in [6]. The measured suction side Stanton number drops rapidly over the first 10 percent of wetted distance and appears to approximate the laminar flat-plate and STAN 5 predictions. However, at about 10 percent of wetted distance, the trend of the data is to flatten, followed by a relatively small increase and then a further decay with increasing distance. Attention should be called to two data points appearing at about 23 percent wetted distance which are nearly identical. The gages are located on blades separated by several passages and illustrate the uniformity of the flow through the rotor from passage to passage. The turbulent flat-plate calculation overpredicts the data by about 60 percent over the entire suction surface while the STAN 5 prediction is very low for the initial 40 percent of wetted distance but then comes into reasonable agreement once transition occurs and the assumed boundary layer becomes turbulent. Further, the suction surface results illustrate that beyond 50 percent wetted distance, the Stanton number is significantly greater (approximately 40 percent) at the 90 percent span location (solid symbol) than the corresponding values at either 10 or 50 percent. This is also consistent with previous measurements [6] and is felt to be the result of tip leakage flow interacting with flow over the suction surface. As noted above, the flat-plate predictions at the 90 percent span location were on the order of 10 percent greater than the midspan values and cannot explain the observed 40 percent value. The values at 10 and 50 percent are in reasonably good agreement with each other and this is in quantitative agreement with the flat-plate prediction. Detailed time-resolved shroud pressure histories are available as are the shroud and tip heat-flux values. These data are currently being used to estimate the tip region flow and may soon offer a confirmation of the influence of tip leakage at the 90 percent span location.

The pressure surface data shown on Fig. 8 illustrate that the Stanton number falls extremely rapidly over the initial 5 percent of wetted distance to a relatively uniform level. The turbulent flat-plate and the STAN 5 predictions taken from [6] are included on this plot. Both the laminar flat-plate and the STAN 5 predictions fall far below the data. The turbulent flat-plate prediction provides a reasonable approximation to the data over most of the pressure surface. Only in the vicinity of 40 percent wetted distance is there a significant difference among the spanwise results, illustrating a 30 percent difference between 10 and 90 percent with the 50 percent value falling in between and also illustrating at the 50 percent spanwise, 45 percent wetted distance a relatively large standard deviation. Our experience with these rotating turbine measurements suggests that a large standard deviation usually indicates a local sensitivity to incidence angle, blade geometry, boundary-layer state, etc. The data presented in Fig. 8 represent a compilation of many separate runs obtained at approximately the same rotor speed. It is difficult to reproduce the speed to better than ±1 percent. Therefore, locations on the blade surface that are sensitive to the influence of incidence angle can generally be identified by relatively large standard deviations. By running off-design speed data, which has also been performed as part of this work, the influence of the changed incidence angle can be seen.

An analysis is currently being completed that improves significantly the correlation between the experimental data presented here and the prediction. Several factors have been changed which account for the improved correlation that is being achieved. They are as follows: (*a*) The technique used to obtain the blade pressure loadings used in the predictions presented here (obtained using a streamline curvature method [12]) has been replaced with MERIDL [13] and TSONIC [14] and (*b*) the innards of the STAN 5 boundary-layer code used

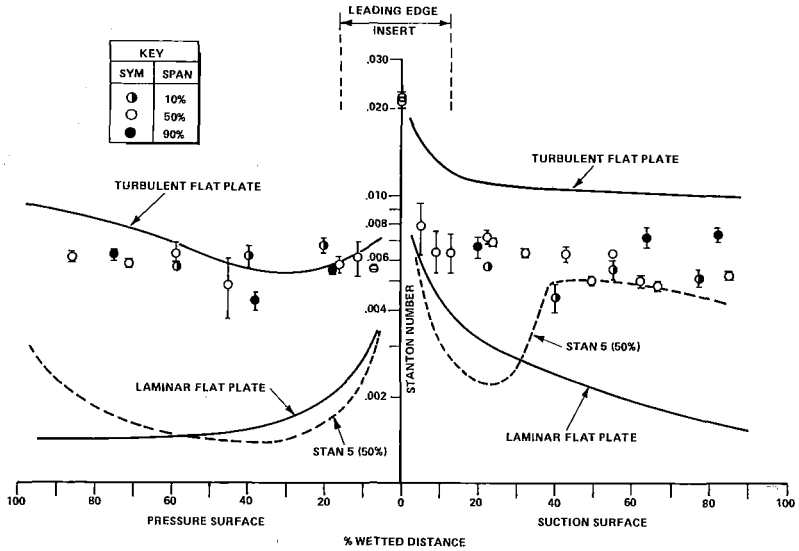

Fig. 8 Inlet Stanton number distribution on blade without injection

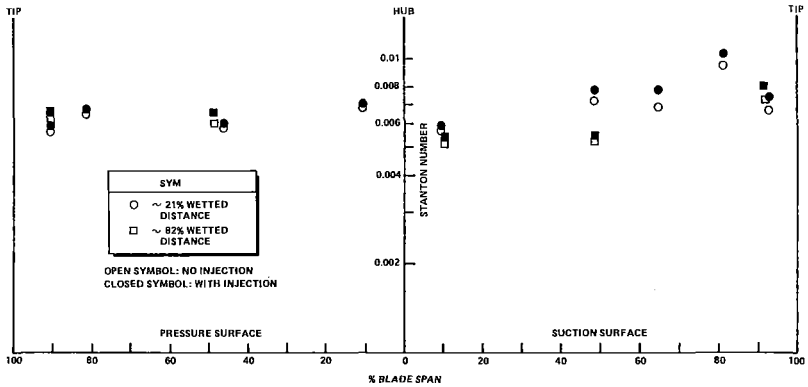

Fig. 9 Spanwise distribution of Stanton number of blade

to obtain the predictions presented in this paper [15] have been replaced with a different leading-edge model and with an improved modeling of the turbulence field which incorporates the kinetic-energy-dissipation model of turbulence.

Figure 9 presents the spanwise distributions of Stanton number both without (open symbol) and with (closed symbol) injection for the suction and pressure surfaces at approximately 21 and 82 percent wetted distance. In order to simplify this figure, only the $T_c/T_0 = 0.53$ result is plotted. Subsequent figures will give the appropriate comparison to illustrate the influence of injected-gas temperature on the local Stanton number. The heat-flux gage distribution was such that more detail could be provided at 21 than at 82 percent. The general trend on the suction surface at the 21 percent location is for the Stanton number to increase from the hub region toward the tip with a peak value occurring near 81 percent span. The magnitude of this peak Stanton number is about 32 percent greater than the midspan value. A similar trend was observed further along the blade surface at the 82 percent wetted distance. The trend of the suction side data is for the Stanton number at span locations nearer the tip to be larger than the midspan values and for locations nearer the hub to be lower than the midspan values. The 81 percent span location is sufficiently removed from the tip region that it is doubtful that this peak can be blamed completely on tip-flow leakage, but an interaction between the tip leakage and suction surface flow is probable. As illustrated by the closed symbols on Fig. 9, the results obtained with injection have the same general pattern as the no-injection data, but the effect of the injected cooling gas is to increase the local Stanton number (or heat flux) by an amount dependent upon the specific location, with the largest influence observed nearer the tip region on the suction surface.

On the pressure surface side of the blade, the spanwise Stanton number distribution illustrates an inverse trend in that the values are larger near the hub region and decrease toward the tip. The magnitude of the hub-region value is on the order of 16 percent greater than the corresponding midspan value, which is significantly smaller than the 40 percent variation observed for the suction surface in going from the midspan to the tip region. It is noted that the magnitude of the local influence of injection on the pressure surface result is generally less than that observed on the suction surface.

Blade Results With Injection

As previously described, the coolant gas was supplied by a separate reservoir and was injected into the flow path through NGV pressure surface coolant slots. Measurements were performed for two different coolant gas (air) temperatures (530 R and 820 R). Oscilloscope records illustrating the pressure histories recorded in the coolant gas plenum downstream of the orifice and the pressure measured just upstream of the NGV inlet were given in [7]. The magnitude of the pressure determined by the pressure transducer located in the coolant supply plenum can be used to estimate the gas path static pressure at the slot location. This has been done and the result is in good agreement with a previously reported calculation [4].

Figure 10 presents a comparison between the Stanton

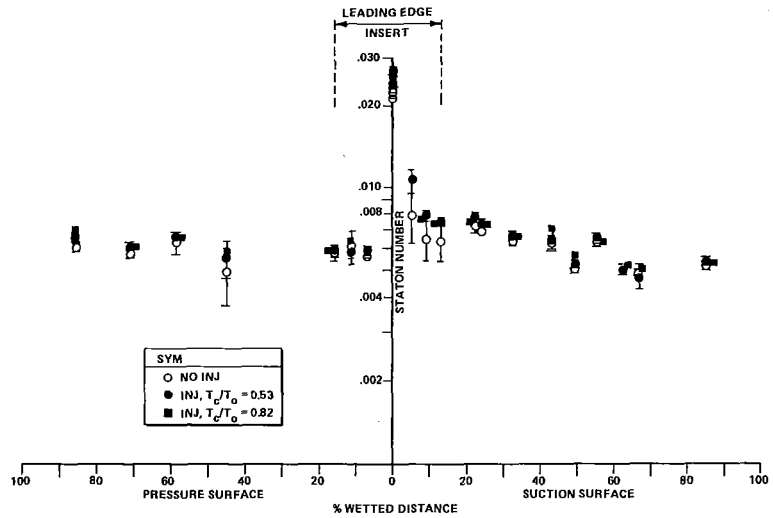

Fig. 10 Comparison between inlet Stanton number without injection and inlet Stanton number with injection at midspan

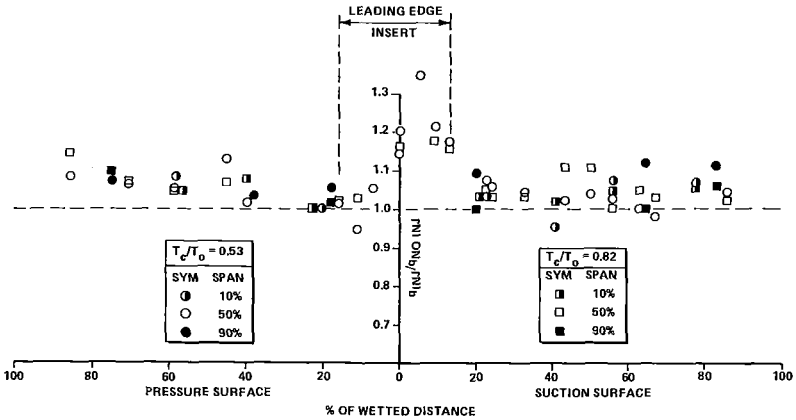

Fig. 11 Ratio of local heat flux with injection to local heat flux without injection for blade surface

numbers without injection and the corresponding values with injection at the 50 percent span location for both temperature ratios, 0.53 and 0.82. The injection results are in general close to each other with the exception of the 90 percent span location on the suction surface. In several cases the symbols have been slightly displaced for illustrative purposes, but the data were actually taken at the same location. By comparison with the no-injection data, the greatest influence of injection appears at the geometric stagnation point and on the suction surface over the initial 20 percent wetted distance. For the remainder of the suction surface and over most of the pressure surface the result of upstream injection is a relatively small increase in local Stanton number. The Stanton numbers presented in Fig. 10 and those for the 10 and 90 percent locations were used to compute the ratio $q_{inj}/q_{no\text{-}inj}$ and this ratio is plotted in Fig. 11 as a function of wetted distance for all three spanwise locations. This plot illustrates that the stagnation point heat-flux value with injection increases by about 18 percent, while the heat-flux value with injection at 5 percent of the suction surface increases by 35 percent and the values at 9 and 13 percent increased by 20 and 18 percent, respectively. At the remaining 10 and 50 percent spanwise locations on the suction surface, with-injection heat-flux values were generally within 5 percent of the no-injection values. At the 90 percent span location beyond 50 percent wetted distance on the suction surface, the with-injection heat-flux values were approximately 10 percent greater than the no-injection values. With the exception of the data point at 45 percent wetted distance, the pressure surface values of heat flux with injection were on the order of 2 to 8 percent greater than the corresponding no-injection values. It is important to note that the results presented in Fig. 11 are not suggesting a shift in the location of the stagnation point because the measured peak heat-flux values are still associated with the gages located at the geometric stagnation point both with and without injection as demonstrated by the Stanton number results presented in Fig. 10. However, it is suggested that injection causes a significant flow disturbance in the vicinity of 5 percent wetted distance on the suction surface that results in significant increases in the local heat-flux values over the initial 20 percent of the suction surface. One can speculate on the nature of this flow disturbance but it is difficult to be definitive at this time.

As noted above, the with-injection Stanton number distributions for both temperature ratios are compared to the without-injection distribution on Fig. 10 and the ratio of heat-flux values for the two temperature ratios is presented on Fig. 11. The desire was to obtain injection data at $T_c/T_0 = 1.0$ for comparison with the 0.53 result, but constraints on the existing injection gas reservoir plumbing would permit a maximum of 0.82. Figure 10 illustrates that the coolant gas temperature has a relatively small influence on the with-injection Stanton number distribution. This can be seen in a little more detail on Fig. 11 where the ratio of heat flux with injection to the heat flux without injection is plotted on a linear plot instead of a logarithmic plot for the various blade positions. The largest differences between the results of the

two temperature ratios were not more than 10 percent and these were observed at the 90 percent span location over most of the suction surface where the 0.82 result was found to be lower than the 0.53 result. However, at the two blade measurements in the vicinity of 40 to 50 percent wetted distance on the suction surface, the results at midspan suggest a reversal of this trend with the heat-flux value for the 0.82 temperature ratio being larger than that observed for the 0.53 measurements. For the remaining locations on the blade surface, the influence of injection-gas temperature appears to be reasonably small.

Conclusions

Detailed measurements of local heat flux on the blade of the Garrett TFE 731-2 hp rotating turbine have been obtained at realistic flow conditions. Results have been presented on the blade, both without and with upstream injection of coolant gas. A comparison is presented between the experimental results and flat-plate and STAN 5 predictions. Over both surfaces of the blade in the absence of upstream injection, reasonable agreement can be demonstrated between the data and one or more of the predictions. That is, the laminar flat-plate prediction for the suction surface is in reasonable agreement with the data up to approximately 10 percent of wetted distance. Beyond 10 percent, the laminar prediction falls far below the data and the turbulent flat-plate prediction falls above the data. On the pressure surface, the turbulent flat-plate prediction is in good agreement with the data but both the laminar flat-plate and the STAN 5 predictions fall far below the data. However, neither of the predictive techniques does a good job of predicting the results over the entire surface. The effect of upstream injection is to cause large increases in the local heat-flux values at the blade geometric stagnation point and over the initial 20 percent wetted distance of the blade suction surface. At other locations, injection results in a small increase in local heat-flux values on the order of 2 to 8 percent. The influence of injection gas temperature ratio is generally small over most of the blade surface.

Acknowledgments

The author would like to thank G. Lukis, M. Urso, R. L. Orszulak, N. J. Kay, and S. J. Sweet of Calspan for their dedicated efforts during the course of this work.

This work was supported by the National Aeronautics and Space Administration, Lewis Research Center, Cleveland, Ohio, under support of Grant NAG 3-469 and Grant NAG 3-581.

References

1 Dunn, M. G., and Stoddard, F. J., "Application of Shock-Tube Technology to the Measurement of Heat Transfer Rate to Gas Turbine Components," 11th International Symposium on Shock Tubes and Waves, July 1977.

2 Dunn, M. G., and Stoddard, F. J., "Measurement of Heat Transfer Rate to a Gas Turbine Stator," ASME JOURNAL OF ENGINEERING FOR POWER, Vol. 101, No. 2, Apr. 1979.

3 Dunn, M. G., and Hause, A., "Measurement of Heat Flux and Pressure in a Turbine Stage," ASME JOURNAL OF ENGINEERING FOR POWER, Vol. 104, No. 1, Jan. 1982.

4 Winstanley, D. K., Booth, T. C., and Dunn, M. G., "The Predictability of Turbine Vane Convection Heat Transfer," AIAA/SAE/ASME 17th Joint Propulsion Conference, Colorado Springs, CO, July 27–30, 1981, Paper No. AIAA-81-1435.

5 Dunn, M. G., and Holt, J. L., "Turbine Stage Heat Flux Measurements," AIAA/ASME 18th Joint Propulsion Conference, Cleveland, OH, June 21–23, 1982, Paper No. 82-1289.

6 Dunn, M. G., Rae, W. J., and Holt, J. L., "Measurement and Analysis of Heat-Flux Data in a Turbine Stage: Part I: Description of Experimental Apparatus and Data Analysis: Part II: Discussion of Results and Comparison With Predictions," ASME JOURNAL OF ENGINEERING FOR GAS TURBINES AND POWER, Vol. 106, Jan. 1984, pp. 229-240.

7 Dunn, M. G., "Turbine Heat Flux Measurements: Influence of Slot Injection on Vane Trailing Edge Heat Transfer and Influence of Rotor on Vane Heat Transfer," ASME JOURNAL OF ENGINEERING FOR GAS TURBINES AND POWER, Vol. 107, Jan. 1985, pp. 76–83.

8 Dunn, M. G., Lukis, G., Urso, M., Heimenz, R. J., Orszulak, R., and Kay, N. J., "Instrumentation for Gas Turbine Research in Short-Duration Facilities," Aerospace Congress and Exposition, Long Beach, CA, Oct. 15–18, 1984, Paper No. 841504.

9 Dunn, M. G., "Heat-Flux Measurements and Analysis for a Rotating Turbine Stage," *Proceedings of the 65th Symposium of the Propulsion and Energetics Panel of AGARD on Heat Transfer and Cooling in Gas Turbines*, Bergen, Norway, May 6–10, 1985.

10 Dunn, M. G., George, W. K., Rae, W. J., Woodward, S. H., Moller, J. C., and Seymour, P. J., "Heat-Flux Measurements for the Rotor of a Full-Stage Turbine: Part II, Description of Analysis Technique and Typical Time-Resolved Measurements," 31st ASME Gas Turbine Conf., Dusseldorf, West Germany, June 8–12, 1986, Paper No. 86-GT-78.

11 Dunn, M. G., Martin, H. L., and Stanek, M. J., "Heat Flux and Pressure Measurements and Comparisons With Prediction for a Low Aspect Ratio Turbine Stage," 31st ASME Gas Turbine Conf., Dusseldorf, West Germany, June 8–12, 1986, Paper No. 86-GT-79.

12 Wysong, R. R., et al., "Turbine Design System," AFAPL-TR-78-92, Nov. 1978.

13 Katsanis, T., and McNally, W. D., "Revised Fortran Program for Calculating Velocities and Streamlines on the Hub-Shroud Midchannel Stream Surface of an Axial-, Radial- or Mixed-Flow Turbomachine or Annular Duct. Vol. I – User's Manual," NASA TN D-8430, 1977.

14 Katsanis, T., "Fortran Program for Calculating Transonic Velocities on a Blade-to-Blade Stream Surface of a Turbomachine," NASA TN-D-5427, 1969.

15 Gaugler, R. E., "Some Modifications to, the Operating Experiences With, the Two-Dimensional Finite-Difference, Boundary-Layer Code, STAN 5," ASME Paper No. 81-GT-89.

Heat-Flux Measurements for the Rotor of a Full-Stage Turbine: Part II—Description of Analysis Technique and Typical Time-Resolved Measurements

M. G. Dunn
W. K. George
W. J. Rae
S. H. Woodward
J. C. Moller
P. J. Seymour

Calspan-UB Research Center,
Buffalo, NY 14225

This paper presents a detailed description of an analysis technique and an application of this technique to obtain time-resolved heat flux for the blade of a Garrett TFE 731-2 hp full-stage rotating turbine. A shock tube is used as a short-duration source of heated air and platinum thin-film gages are used to obtain the heat-flux measurements. To obtain the heat-flux values from the thin-film gage temperature histories, a finite-difference procedure has been used to solve the heat equation, with variable thermal properties. The data acquisition and the data analysis procedures are described in detail and then their application is illustrated for three midspan locations on the blade. The selected locations are the geometric stagnation point, 32.7 percent wetted distance on the suction surface, and 85.5 percent wetted distance on the suction surface. For these measurements, the turbine was operating at the design flow function and very near 100 percent corrected speed. The vane–blade axial spacing was consistent with the engine operating configuration. The results demonstrate that the magnitude of the heat-flux fluctuation resulting from the vane–blade interaction is large by comparison with the time-averaged heat flux at all locations investigated. The magnitude of the fluctuation is greatest in the stagnation region and decreases with increasing wetted distance along the surface. A Fourier analysis by FFT of a portion of the heat-flux record illustrates that the dominant frequencies occur at the wake-cutting frequency and its harmonics.

Introduction

One of the basic turbomachinery problems that remains of interest concerns the unsteady flow environment generated as a result of rotating blades cutting through nozzle guide vane (NGV) wakes and the resulting influence of this unsteadiness on the blade surface-pressure and heat-flux distributions, on the inner blade-row gas-dynamic parameters, on the state of the boundary layer, and on the stage efficiency. Significant fluctuations in the local heat flux are important from a material fatigue or life cycle point of view. The specific component addressed in this paper is the turbine, but an early paper by Kerrebrock and Mikolajczak [1] addressing a similar problem for the compressor is very helpful in describing the essential physical processes that occur. Lakshminarayana et al. [2–4] have reported the results of several measurement programs designed to measure the boundary-layer and turbulence characteristics inside turbomachinery rotor passages using a large-scale slowly rotating rig as the test bed and hot-wire anemometry as the prime diagnostic. Dring et al. [5–7] have utilized a large-scale rotating rig which can be made to look like either a compressor or a turbine and with this facility they have performed many different types of measurements in the rotating frame including blade surface heat transfer and static pressure, total-pressure surveys and flow visualization. In [7], Dring et al. present the detailed results of a rotor–stator interaction study that included time-resolved thin-film gage data obtained on the blade. The authors demonstrate a strong unsteadiness near the blade leading edge that occurred at stator passing frequency. The magnitude of this fluctuation decreased with increasing distance away from the leading edge. They also found regions of large random fluctuation due to the turbulence in the stator wake that was superimposed on the periodic fluctuation.

Hodson [8–10] has utilized several different facilities to obtain measurements of wake-generated unsteadiness in the rotor passages and to perform measurements of boundary-layer transition and flow separation. In [9], detailed measurements of the unsteadiness contained in the rotor in-

Contributed by the Gas Turbine Division of THE AMERICAN SOCIETY OF MECHANICAL ENGINEERS and presented at the 31st International Gas Turbine Conference and Exhibit, Düsseldorf, Federal Republic of Germany, June 8–12, 1986. Manuscript received at ASME Headquarters January 13, 1986. Paper No. 86-GT-78.

flow are presented which illustrate the change in incidence angle and the change in turbulence associated with the stator wakes. The author does not present heat-flux data, but it is felt that both the change in incidence angle and the increased turbulence will influence the local blade heat transfer. Binder et al. [11] have looked at the influence of NGV wakes on the unsteady rotor flow using a laser velocimeter system. They illustrate very high turbuence levels associated with the stator wakes. The influence of this turbulence on the blade heat-flux level is not addressed. Doorly et al. [12, 13] have used a short-duration facility and a system of rotating bars to study the effects of shock waves and wakes shed by the NGV row on the turbine rotor flow field and surface heat-flux distribution. The authors have used thin-film heat flux gages to measure the magnitude of the heat-flux fluctuation experienced by a rotor blade in passing through the simulated wake. In [12] the authors present very nice Schlieren photographs illustrating the structure of the bar wake and its subsequent passage through the cascade. The technique is ideal for providing an environment in which detailed understanding of the flow phenomena associated with vane/blade interactions can be obtained.

The purpose of this paper is to present a detailed description of an analysis technique used to deduce time-resolved heat-flux data from thin-film heat-flux gages mounted on the rotor of a full-stage rotating turbine (Garrett TFE 731-2 hp). The long-range intent in this work is to spatially resolve the local heat flux to as small an area as possible and to perform these local measurements from the blade geometric stagnation point to near the blade trailing edge and to obtain the measurements in as realistic a turbine environment as is possible. Although a great deal of these data have been obtained as part of this program, it was felt that prior to presenting detailed time-resolved heat-flux data for the entire blade surface that have been obtained from such a complicated experiment, a thorough explanation of the data reduction procedures was in order. It should be kept in mind during this discussion that actual engine components (NGVs and blades) are used and they are not polished to a mirror finish. However, the heat transfer instrumentation is installed under a microscope and there is no surface discontinuity at the junction between the instrumentation and the component. The experimental technique being used is the short-duration, shock-tunnel approach, in which fast-response, thin-film thermometers are used to measure the surface temperature histories at prescribed locations on the blade. Instantaneous heat-flux rates can then be deduced from these temperature-time histories using a technique described herein. The shock-tunnel technique allows one to use actual turbine hardware and to operate it at the design flow function and at 100 percent corrected speed. Because of the high wake cutting frequency (approx. 13,000 wakes/s) and the short-duration (~ 20 to 30 ms) nature of this experimental technique, many new data-analysis techniques had to be developed in order to achieve the objectives. The rotor data of interest have been obtained and analyzed successfully using techniques that have not previously been applied to this problem and thus have not previously been published in this context.

The specific topics that will be addressed in this paper are: (*a*) description of the experimental technique, the heat-flux gage instrumentation, and the data recording procedure; (*b*) description of the analysis technique used to deduce the instantaneous heat-flux values from the gage surface-temperature histories; (*c*) description of the fast-Fourier transform analysis and associated data handling techniques that are used to obtain time-resolved data; and (*d*) application of the techniques that have been developed using rotor blade data obtained for a full-stage rotating turbine.

Experimental Apparatus

The experimental apparatus used in this measurement program is described in detail in Part I of this paper and will not be repeated here. That portion of the apparatus and instrumentation new to this work will be described.

For the rotor speeds used here, a blade traverses a vane exit passage in approximately 75 μs. However, the blade traverses a vane wake in a significantly shorter time, on the order of 5 to 10 μs. In order to resolve vane wake cutting data and to avoid aliasing, it is important to be able to sample the thin-film gage output at a sampling rate of at least twice the highest frequency present in the signal (100 kHz in this experiment, requiring 200 kHz minimum sampling rate). In addition, one needs a minimum of 10 bit resolution and as much storage per channel as possible. Two different transient recorders, a Data Laboratories 2000 series and a Physical Data 515A, were used. Both of these were eight channel units with 4K words/channel storage capability and each channel could be sampled at a rate in the 200 kHz to 2 MHz range. Several other features of these units are particularly useful for obtaining time-resolved heat-flux data for a turbine stage: (*a*) The dual time base capability allows one to sample the early portion of a heat-flux gage history at a low sampling rate and then at a predetermined time to switch to a much higher sampling rate, (*b*) the multiple channel data stored in the recorder can be simultaneously displayed on an oscilloscope and photographed, (*c*) the stored data can be transferred to an on-line minicomputer (DEC LSI 11/23 plus) for additional analysis, printing, and plotting, and (*d*) the stored data can be transferred to tape and analyzed at a later date. A Sangamo Sabre III FM tape recorder with an 80 kHz bandwidth is normally used to record an additional 13 channels of high-frequency thin-film data. The majority of the data analysis is performed on a DEC VAX 11/780. A schematic of the on-line data recording system is given in Part I.

Data Processing

The voltage output history from the thin-film gages and associated follower circuits shows typically a rapid rise in level ($\sim t^{1/2}$) with superimposed fluctuations. As noted earlier, a major objective of the present work has been to resolve quantitatively the time-dependent part of the heat transfer. Even though this part is generally greater than 10 percent of the time-averaged heat transfer rate, it is only a small fraction (typically 5 percent) of the temperature signal from the gages. Therefore, to resolve these fluctuations, it has been found necessary to revise some of the data-reduction procedures that have been used in the past.

The thin-film gage voltage output can be recorded digitally, or it can first be passed through an analog network [16, 17]. Both the analog and digital implementations have problems when applied to the gas turbine flow environment, especially when the heat-flux fluctuations are of interest. When either

Nomenclature

C = specific heat
f = frequency, Hz
$j = \sqrt{-1}$
k = thermal conductivity
n = quantization error
S = spectrum
t = time
T = temperature
x = distance normal to gage surface
α = thermal diffusivity = $k/\rho C$
η, τ = see equation (16)
ρ = density
ϕ = see equation (15)
ω = radian frequency
$\hat{(\ )}$ = denotes Fourier transform

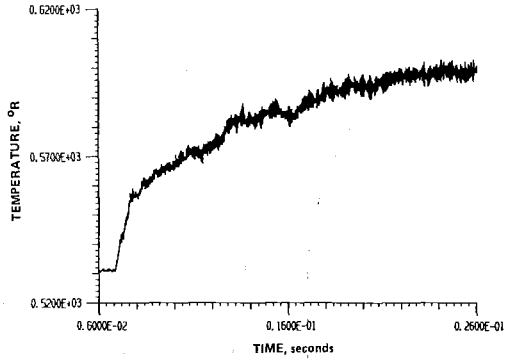

Fig. 1(*a*) Surface temperature history at 32.7 percent wetted distance on blade suction surface

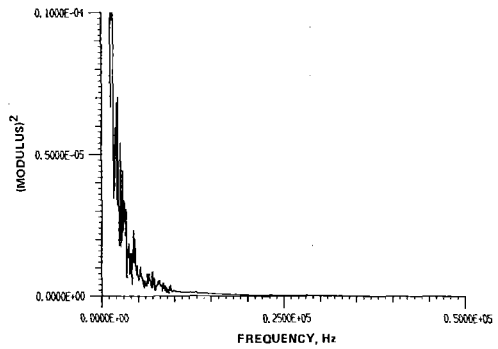

Fig. 1(*b*) Modulus of Fourier transform of temperature history given in Fig. 1(*a*)

temperature or analog outputs are sampled digitally, the subsequent analysis is limited by the quantization errors inherent in the A/D process. An additional problem arises from the fact that analog or Q-meter techniques depend on the assumption of the constant thermal properties of the substrate, an assumption not valid in the current environment. While computational algorithms can be devised which include variable thermal properties, numerical errors arising from the occurrence of a high-frequency skin depth preclude the use of such algorithms for the determination of fluctuating heat-flux values at frequencies approaching the sampling rate used here.

As part of this effort, a new approach to the problem has been developed. Surface temperature and its first derivative have been sampled digitally. From these a composite signal has been constructed which minimizes the effects of the quantization errors on the fluctuating signals. This composite temperature signal is then analyzed by a combination of numerical and Fourier transform techniques to yield a composite time-dependent heat-flux value. This high-fidelity signal is then available for subsequent analysis as will be described.

Quantization Errors. Quantization errors arise from the discretization of an analog signal. Whereas all values within a given range are possible for an analog signal, only those particular values corresponding to integral multiples of the step size are possible for a digitally sampled signal. Values of the signal between these discrete levels are simply placed into the nearest level. The sampled signal can thus be represented as the sum of the original signal and a random quantization error or noise.

The quantization noise can be modeled as being uncorrelated at different times and as having a uniform probability of being between $\pm\Delta/2$ where Δ is the step size of the A/D. (The step size can be determined by dividing the range of the A/D, say R, by the number of levels available. In our case the A/D was 10 bits so the number of levels was $2^{10} = 1024$, thus $\Delta = R/1024$.)

Figure 1(*a*) shows a typical surface temperature record from a thin-film gage on the suction surface of the blade (see Part I). The rapid rise in temperature signals the arrival of the test-gas flow and thus the initiation of the experiment. If this were the only phenomenon present, then heating the substrate would cause the surface temperature to rise as $T \sim t^{1/2}$ corresponding to a constant heat flux [19, 22]. As previously noted, it is this temperature rise over the course of the experiment which necessitates accounting for the variable thermal properties of the substrate on which the gage is painted.

The passage of the blade through the NGV wakes and the presence of turbulence and secondary flows in the NGV passage flow give rise to the fluctuations which are superimposed on the temperature history. If the unsteady heat-flux value is to be examined, it is these temperature fluctuations which must be faithfully translated into an unsteady heat-flux signal. Unfortunately, because the A/D converter must capture the entire range of temperature (since the instantaneous heat flux represents an integral over the temperature history), the fluctuating signal is discretized into only a small portion of the total voltage level available. As a consequence, *the unsteady signal of interest is likely to be buried in the quantization noise and the unsteady heat flux calculated from it will be primarily noise.*

The situation can best be illustrated by looking at the constant properties solution to the one-dimensional heat transfer equation

$$\rho C \frac{\partial \mathrm{T}}{\partial t} = \frac{\partial}{\partial x}\left(k \frac{\partial T}{\partial x}\right) \tag{1}$$

subject to the surface boundary condition

$$q_w = -k \frac{\partial T}{\partial x}\Big|_{x=0} \tag{2}$$

The objective is to relate the temperature at the surface to the heat flux there.

Let $\hat{q}_w(f)$ and $\hat{T}_w(f)$ be the Fourier-transformed heat flux and surface temperature defined by

$$\hat{q}_w(f) = \int_{-\infty}^{+\infty} e^{-j2\pi ft} q_w(t)\,dt \tag{3}$$

and

$$\hat{T}_w(f) = \int_{-\infty}^{+\infty} e^{-j2\pi ft} T_w(t)\,dt \tag{4}$$

Then it is straightforward to show that

$$\hat{q}_w(f) = \sqrt{j2\pi \mathrm{f}}\,\sqrt{\rho C k}\;\hat{T}_w(f) \tag{5}$$

or

$$|\hat{q}_w(f)| = \sqrt{\rho C k}\,\sqrt{\pi f}\;|\hat{T}_w(f)| \tag{6}$$

and

$$\angle\,\hat{q}_w(f) = \angle\,\hat{T}_w(f) + \frac{\pi}{4} \tag{7}$$

where $\angle$ denotes the "phase angle of." Thus the modulus of the transform of the heat flux is proportional to the square root of the frequency times the modulus of the temperature, while the phase of the heat flux is the phase of the temperature shifted by +45 deg.

The exact manner in which quantization errors affect the calculation of heat flux from a quantized temperature will be the subject of a subsequent paper. The problem can be illustrated, however, by a simple example. Suppose that the unsteady heat flux due to a wake crossing corresponds to a square wave. Then the even harmonics are exactly zero, and the odd harmonics are related to the amplitude of the fundamental by $A_n/A_1 = 1/n$, where $(n-1)$ is the order of the

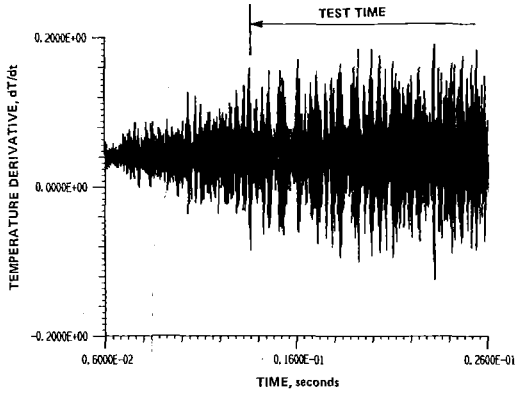

Fig. 2(a) Temperature derivative signal at 32.7 percent wetted distance of blade suction surface

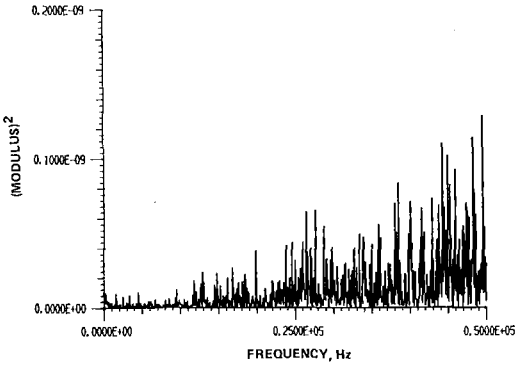

Fig. 2(b) Modulus of Fourier transform on temperature derivative given in Fig. 2(a)

harmonic. If the amplitude of the fundamental of the surface temperature sensed by the gage is B_1, then it follows from equation (6) that the odd harmonics are given by $B_n/B_1 = 1/n \cdot \sqrt{n}$. Thus if $B_1 \simeq 3$ R (as in Fig. 1), $B_3 \sim 0.55$ R, and $B_5 \leq 0.28$ R. If (as in Fig. 1), the range of the A/D is set to correspond to approximately 0 to 102.4 R and the number of bits of resolution is 10 corresponding to 1024 levels, the quantizing step size is 0.1 R. Thus the directly recorded temperature will have its harmonics largely obscured by the quantizing error. Because the effect of the quantization noise on the Fourier transform of the signal is random, the harmonics will be impossible to discern without substantial averaging of many independent experiments.

Figure 1(*b*) show the modulus squared of the Fourier transform of the temperature trace shown in Fig. 1(*a*). Clearly evident is the low-frequency portion of the signal associated with the overall rise in level. Not at all evident are the fundamental and harmonics of the wake crossing frequency which are buried in the random quantization noise (which is below the threshold of the plotter sensitivity). Since the fluctuating heat flux is proportional to the inverse transform of this signal multiplied by the square root of frequency and since the higher the frequency the weaker the Fourier components of the signal, the quantization noise dominates the calculated heat-flux transform as the frequency increases.

The statistics of the quantization noise can easily be computed if its probability density is known. Usually the quantization error is assumed to have a uniform probability of being between $\pm\Delta/2$. It follows that the mean square quantization error is $\Delta^2/12$. Most important for our application is that the spectrum of the quantization noise is white, that is, it is the same at all frequencies. Thus, if S_n is noise spectrum as a function of the frequency f

$$S_n(f) = \begin{cases} (\Delta^2/12f_s & , \quad f<f_s \\ (\quad 0 & , \quad f>f_s \end{cases} \tag{8}$$

where f_s is the sampling rate. The spectrum S_n is calculated as

$$S_n(f) = \frac{1}{T}\,\overline{|\hat{u}_n(f)|^2} \tag{9}$$

where T is the length in time of each individual record, $\hat{u}(f)$ is the Fourier transform of the noise for the record, and the overbar indicates that many realizations are averaged together.

In the data-analysis portions of this paper, plots of the modulus of the Fourier transform of signal plus noise are presented. It is important to note that although equations (8) and (9) imply that the mean square value of the Fourier transform of the noise is the same at all frequencies, transforms of individual records (unaveraged) will vary randomly from one frequency to another. Thus spurious peaks can appear in individual records which have no physical significance (certainly this is the case in Figs. 10–12). Nonetheless, it is clear from equation (8) that these random excursions are minimized by either decreasing the step size (less range or more bits) or by increasing the sampling rate.

The randomness of individual records is a characteristic of all random signals (such as turbulence) and is not unique to quantization noise. This randomness only disappears as successive independent records are averaged together. Thus care must be taken in inferring frequency content from individual records, and it should not be done unless there is a good physical reason to suspect that a particular frequency represents a nonrandom event. Such will be the case for the blade crossing harmonics identified later.

It is clear from the above that if fluctuating heat-flux rates are to be analyzed it is necessary to raise the fluctuating signal above the quantization noise *before* digitization. The analog Q-meter[1] accomplishes this by effectively multiplying the transform of the temperature by $\sqrt{j2\pi}\,f$ *before recording* so that the spectrum of the quantization noise (as it affects the heat flux) is now white instead of increasing linearly with frequency as in the directly recorded case. Another alternative that was used in this investigation is to differentiate the temperature before digitizing so that the transform of the digitized signal is $j2\pi f$ times that of the temperature. In this case the noise spectrum of the computed heat-flux signal will *roll off* linearly with frequency, thereby allowing even weaker signals to be captured at the higher frequencies.

Figure 2(*a*) shows the unsteady temperature derivative signal corresponding to Fig. 1(*a*). Gone is the rapid rise (since the low-frequency part of the signal has been buried in the noise by the multiplication of its transform by $j2\pi f$) while present in abundance are the high-frequency fluctuations which have been selectively and progressively amplified. In effect, the part of the signal corresponding to the unsteady flow has been spread over the entire range of the A/D so that the quantization errors are relatively much less. Figure 2(*b*) shows the Fourier transform of the derivative signal which clearly indicates how the higher frequencies have been raised above the quantization noise level.

Composite Temperature. While taking the derivative raises the fluctuations above the noise, it buries in the noise the overall temperature rise from which the varying thermal properties must be computed. In order to simultaneously capture both the overall rise and the unsteady characteristics with minimum quantization error, a hybrid scheme has been

[1] It was discovered in the course of this investigation that the Q-meters in common use [17], including ours, do not maintain the phase relation demanded by equation (7) over any of the frequency range of interest in this experiment (10 to 100 kHz). Therefore, the results obtained using the device are not reported here.

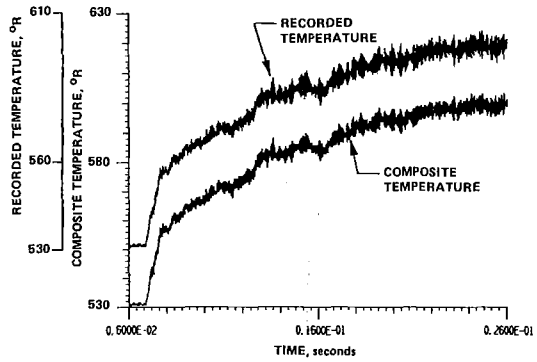

Fig. 3(*a*) Comparison between temperature history as recorded and composite temperature history at 32.7 percent wetted distance on blade suction surface

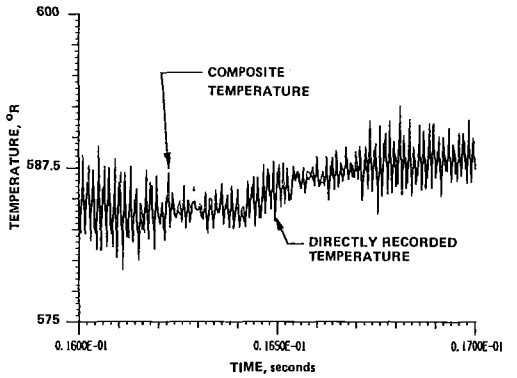

Fig. 3(*b*) Comparison between directly recorded temperature and composite temperature in time interval 16 to 17 ms

adopted which involves splicing two different signals in Fourier space. This is accomplished by simultaneously recording both the temperature and its derivative on separate channels. The recorded data are then Fourier transformed using a FFT alogrithm.

A minor complication arises from the fact that the records are of finite length. As a consequence, the transforms are not of the temperature and its derivative, but rather of the products of these functions with the time window $w(t)$ given by

$$w(t)=\begin{cases}1, & 0<t<t_1\\ 0, & \text{otherwise}\end{cases} \tag{10}$$

where t_1 is the record length. Thus

$$\hat{T}(f)=\int_{-\infty}^{+\infty} e^{-j2\pi ft}T(t)\quad w(t)dt \tag{11}$$

and

$$\hat{\dot{T}}(f)=\int_{-\infty}^{+\infty} e^{-j2\pi ft}\dot{T}(t)\quad w(t)dt \tag{12}$$

It is well known that if a signal of infinite length is sampled at a rate faster than twice the highest frequency present in the signal, the signal can be completely reconstructed [18] (this is the so-called Nyquist criterion). Moreover, the transforms of the signal and its first derivative differ by only a factor of $j2\pi f$. In our case, however, because of the window function which truncates the record, this is not true, even if the Nyquist criterion is satisfied. It is, however, straightforward to show for these finite length signals that the finite transforms of the recorded temperature and its derivative are related by

$$\hat{T}(f)=\frac{1}{j2\pi f}\{\hat{\dot{T}}(f)-[T(0)e^{j2\pi ft_1}-T(t_1)e^{-j2\pi ft_1}]\} \tag{13}$$

The term in brackets arises from the presence of the window function in the Fourier transform.

The composite temperature as a function of time has been assembled by carrying out the Fourier transform (using a FFT algorithm) on the composite transform defined by

$$\hat{T}_{\text{comp}}(f)=\begin{cases}\hat{T}(f), & f<f_1\\ \dfrac{1}{j2\pi f}[\hat{\dot{T}}(f)-(T(0)e^{j2\pi ft_1}-T(t_1)e^{-j2\pi ft_1})], & f>f_1\end{cases} \tag{14}$$

The frequency f_1 corresponds to the unity-gain frequency of the diffentiator and is chosen to be less than the primary wake crossing frequency, but greater than the frequencies comprising the overall temperature rise. In the experiments reported here, f_1 was approximately 10 kHz.

Figure 3 shows a comparison between the directly recorded temperature and the composite temperature computed from the inverse Fourier transform of equation (14). All subsequent references in the remainder of this paper to the temperature field and all calculations of heat flux presented will use the composite temperature field.

Variable Thermal Properties. The influence of variable substrate thermal properties on the deduced heat-flux value has been understood for a long time [19, 20], but until recently it has not been accounted for in data-reduction procedures [15]. The primary physical effect is an increase in the thermal conductivity of the substrate; thus a given heat-flux value produces a lower rise in surface temperature than would be produced by a substrate whose properties remain fixed at their pretest values. Conversely, the heat-flux value inferred from a given surface-temperature history is larger when variable thermal properties are accounted for. The error made by the constant-property model can be on the order of 5–15 percent [15], and is therefore not tolerable for the accuracy desired in the present work.

Consequently, the constant-property data-reduction procedures [19, 21, 16, 22] have been replaced in the present work by a finite-difference solution of equation (1), where it is convenient to employ the Kirchhoff transformation [23]

$$\phi\int_{T_{\text{ref}}}^{T}\frac{k}{k_{\text{ref}}}dT;\qquad \frac{\partial\phi}{\partial t}=\alpha\frac{\partial^2\phi}{\partial x^2} \tag{15}$$

In this equation $\alpha = k/\rho C$ is the temperature-dependent thermal diffusivity.

High-Frequency Fluctuation of Surface Temperature. For the problem of interest here, one must also be concerned with the high-frequency temperature fluctuations very near the gage surface. In [15], numerical solutions of equation (15) were reported, based on a Crank–Nicholson finite-difference procedure. The actual equation solved was a transformed version of equation (15), in which the x coordinate was scaled by the thermal penetration depth

$$t=\tau,\qquad \eta=x/2\sqrt{\alpha_{\text{ref}}\,t} \tag{16}$$

In these variables, equation (15) is

$$\frac{\alpha}{\alpha_{\text{ref}}}\frac{\partial^2\phi}{\partial\eta^2}+\frac{2\eta\partial\phi}{\partial\eta}=4\tau\frac{\partial\phi}{\partial\tau} \tag{17}$$

This formulation has the advantage that the spatial scale is uniform in time. Numerical solutions using a fixed step size $\Delta\eta$ can then be found, for given values of ϕ at the surface, and for $\phi\to 0$ when η is on the order of 3 to 5.

The above coordinate transformation is based on the assumption that the thermal penetration depth $\sqrt{\alpha t}$ is the significant length scale in the problem. Analytic solutions for the constant-property case reveal that this is the proper scale for a step-function time variation of the surface heat transfer.

However, when the heat transfer rate contains a part that fluctuates with frequency ω, a second scale enters the problem, namely $\sqrt{\alpha/\omega}$, which is properly called the skin depth and is independent of time. The classical solution for a sinusoidal surface-temperature variation [23]

$$\Delta T_{\text{surface}}(t) = A \cos \omega t$$

contains an early-time transient plus the solution:

$$\Delta T(x, t) = A \exp\{-x\sqrt{\omega/2\alpha}\} \cos\{\omega t - x\sqrt{\omega/2\alpha}\} \qquad (18)$$

Thus the high-frequency portion of the surface-temperature rise has a very shallow penetration, and care must be taken in the numerical work to resolve this thin layer properly. Solutions of equation (17) which use a fixed step size in the η-direction will have a small value of Δx at early time, and a large one at late time. It has been found that for the blade-passing frequencies of interest here this procedure loses accuracy at late time. Accordingly, a revised procedure has been adopted, as described in the next paragraph.

Implicit numerical procedures for solving equation (17) work best when the step-size ratio

$$r \equiv \alpha \Delta t/(\Delta x)^2$$

is in the range 0.25 to 0.5. It happens that this criterion can be met for the test conditions of interest here. The sampling interval Δt is taken, on the basis of the Nyquist criterion, to be inversely proportional to the highest frequency of interest

$$\Delta t \sim 1/\omega$$

The spatial step size Δx must be small enough to resolve the skin depth; thus

$$\Delta x \sim \sqrt{\alpha/\omega}$$

Thus a constant value of the step-size ratio r will satisfy both of these criteria.[2]

The finite-difference algorithm used is the simple implicit one:

$$\frac{\phi(i, j+1) - \phi(i, j)}{t_{j+1} - t_j} = \alpha(x_i, t_j) \times \frac{\phi(i+1, j+1) - 2\phi(i, j+1) + \phi(i-1, j+1)}{(\Delta x)^2} \qquad (19)$$

This equation was solved on a grid of variable size: At every time step, the boundary condition of zero temperature rise was enforced at a depth of $5\sqrt{\alpha_{\text{ref}} t}$. The heat transfer rate was found from a second-order-accurate expression for the derivative at the surface. As noted in (24), this algorithm is capable of following a rapidly fluctuating temperature more accurately than its Crank–Nicholson counterpart. However, numerical checks for a constant-property test case reveal that it does introduce a phase shift into the inferred heat transfer rate, and that accurate results require a time-step size small enough to give approximately 30 data points per cycle. (The test case used a heat-transfer rate consisting of a step function followed by a pure sine wave. The corresponding surface-temperature history contains a square root of time, plus a Fresnel-integral term that rapidly approaches a sine wave shifted by 45 deg.) In practice, because of memory limitations, the number of samples per cycle actually available from the A/D is usually much less then the 30 required; thus the numerical treatment decribed above is suitable only for the low-frequency portions of the recorded signal.

Practical Scheme. It is evident from the above that there is little hope of calculating by numerical techniques the heat-flux fluctuations at frequencies approaching the rate at which the data have been sampled. While it is theoretically possible for an infinitely long record (if the Nyquist criterion is satisfied) to upward decimate the data to as fine a time grid as desired, this is not true for a finite time record. Therefore, in principle, *no numerical technique will be able to produce a heat-flux history with the bandwidth of the originally recorded temperature signal.* If a sufficiently fast A/D with sufficient storage capacity were available, the problem could be easily solved by sampling the data at a much higher rate than needed. Unfortunately, the storage limitations of our hardware (4K/channel), the bandwidth of the experimental signals of interest (80–100 kHz), and the length of the test (20–30 ms), preclude this option. Fortunately, the nature of the signal itself provides an alternative.

It has already been pointed out that the temperature (and heat flux) events can be characterized by two different time scales: a slow time variation corresponding to the overall temperature rise, and a fast time variation corresponding to the gas dynamics associated with the rotating turbine. In fact, this dual nature of the signals has already been exploited in designing a recording scheme and in devising a computational grid. It will again be exploited here.

The scheme which has been adopted is based on the fact that it is the overall rise in temperature, or the *slow* process, which is primarily responsible for the variation in the thermal properties of the gage. The turbine gas dynamics, or *fast* process, is merely riding on the slow process. (Note that this would *not* be the case were the fluctuations due to the turbine of the same order of magnitude as the overall rise.)

It has already been shown that the frequency content of the overall rise is at frequencies substantially below the primary wake crossing rate in our experiments. Therefore, two new temperature signals can be created from the composite temperature defined earlier—a low-passed temperature, $T_{LP}(t)$, containing the slow process, and a high-passed temperature, $T_{HP}(t)$, containing the fast process. The heat flux associated with the low-passed temperature can then be analyzed by the variable property numerical technique described above, while the high-passed signal can be analyzed by applying the constant properties solution locally in time as described below.

The high- and low-passed temperature signals must be created by filtering the composite signal at any frequency below the wake crossing frequency subject to the following constraints:

(*i*) The low-passed signal must faithfully capture the overall rise, especially near the beginning of the experiment.

(*ii*) The sum of the high- and low-passed signals must equal the original temperature signal.

(*iii*) The filters must not introduce spurious oscillations or phase shifts in the time-series data.

Condition (*ii*) can be satisfied by any pair of linear filters. Condition (*iii*) eliminates the simple splitting in Fourier space used to develop the composite temperature since merely discarding the information above a given frequency corresponds to multiplying by a box-car window in frequency with the result that the low-passed signal oscillates badly in the time domain. Condition (*i*) can be determined by trial and error.

In our experiments, numerical RC-type filters were utilized with the following frequency response functions:

$$H_{LP}(f) = \frac{1}{1 + jf/f_2} \qquad (20)$$

$$H_{HP}(f) = \frac{jf/f_2}{1 + jf/f_2} \qquad (21)$$

A cutoff frequency f_2 of 2.5 kHz (about 1/5 the wake cross-

[2] The authors are grateful to Prof. Dale B. Taulbee, SUNY Buffalo, for calling attention to this fact and for suggesting use of the simple implicit method.

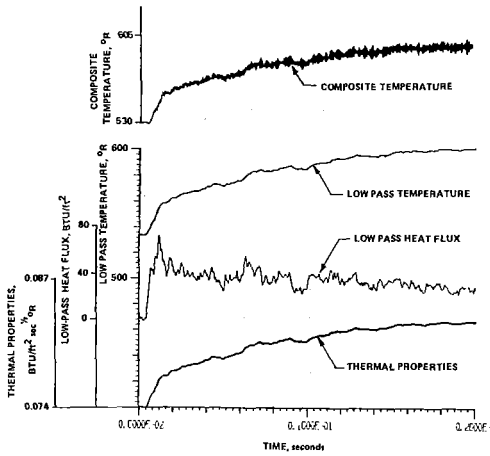

Fig. 4 History of the composite temperature, low-pass temperature, the low-pass heat flux and the value of the variable thermal properties for 32.7 percent wetted distance on blade suction surface

ing rate) was found to adequately capture the initial rise (see Fig. 4).

The Fourier transforms of the low- and high-passed temperature signals are given by

$$\hat{T}_{LP}(f) = \hat{T}_{\text{comp}}(f)\, H_{LP}(f) \tag{22}$$

$$\hat{T}_{HP}(f) = \hat{T}_{\text{comp}}(f)\, H_{HP}(f) \tag{23}$$

The low-passed transformed composite temperature was then inverse transformed to yield $T_{LP}(t)$. This in turn was used as input to the variable properties numerical code described earlier to determine the low-passed heat-flux signal.

Figure 4 illustrates the composite and the low-passed temperature signals, and the heat flux and thermal properties history generated from the latter. Since the data were low-pass filtered at 2.5 kHz and sampled at 200 kHz, approximately 40 points/cycle were available to the numerical code at the frequency of the filter—well above any reasonable numerical requirements.

The heat flux from the high-passed temperature signal was computed directly from its Fourier transform using equation (5). Thus

$$\frac{1}{\sqrt{\rho Ck}}\,\hat{q}_{HP}(f) = \sqrt{j2\pi f}\;\hat{T}_{HP}(f) \tag{24}$$

from which the time-dependent high-passed heat flux (divided by $\sqrt{\rho Ck}$) can be obtained by inverse transformation. The actual time-dependent heat flux is computed by multiplying each time value so obtained by the local value of $\sqrt{\rho Ck}$ determined from $T_{LP}(t)$. This procedure can be formally justified by a two time scale expansion of equation (1). This technique has been utilized to obtain the results presented in the following section of the paper.

Discussion of Results. A description of the experimental conditions used in this work and a detailed discussion of the time-averaged heat-flux distributions for the blade surface is given in Part I of this paper. By way of a brief review, the flow conditions at the inlet to the NGV were: total temperature = 1000 R, static pressure = 98.5 psia, weight flow = 20.5 lb/s, turbulence intensity = 5.5 percent, and model wall temperature = 530 R. The turbine operates at 100 percent corrected speed with a rotor/stator axial spacing of 0.18 stator chord and a tip clearance of approximately 1.16 percent of blade height. The TFE 731 vane row operates with a throat Mach number on the order of 0.85. Therefore, the rotor gas dynamics should not be influenced by the presence of significant shock waves.

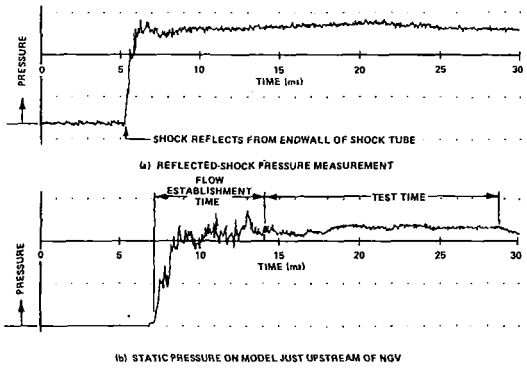

Fig. 5 Typical shock tube reflected-shock pressure measurement and corresponding static pressure on turbine model upstream of NGV

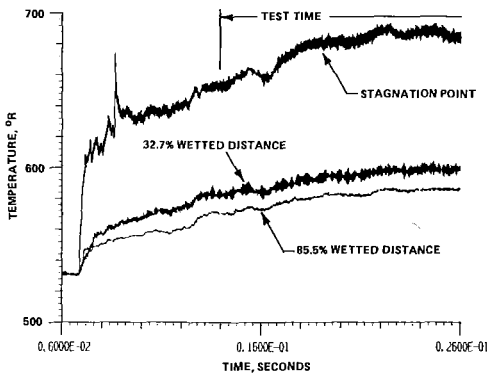

Fig. 6 Composite temperature history at stagnation point, 32.7 percent wetted distance, and 85.5 percent wetted distance on blade suction surface

Previous publications [25, 26] have presented oscilloscope records and detailed discussions of pressure histories obtained at various locations within the model. However, a brief review of pressure records relevant to the heat-flux measurements described in this paper is appropriate. Figure 5 presents a typical shock tube reflected-shock pressure measurement and the corresponding static pressure on the bullet nose just upstream of the NGV row. The time at which the shock reflects from the shock tube endwall is noted on Fig. 5(*a*). As illustrated on Fig. 5(*a*), the pressure history of the reflected-shock reservoir that is supplying the air flow for the turbine model is very uniform for a substantial period of time. Figure 5(*b*) presents the corresponding static pressure obtained just upstream of the stator. The period of flow establishment is followed by the period of relatively uniform pressure called the test time. The results presented in Part I are the time-averaged heat-flux distributon over the test time shown in Fig. 5(*b*) while the results presented in this paper are obtained only up to about the 26 ms location on Fig. 5(*b*). In order to obtain the time-resolved data, the transient recorders discussed earlier must be used. These recorders have the disadvantage of limited storage (4K words/channel) but they have the advantages of high sampling rates and a dual time base. This dual time base can be used to sample the pretest base line and the flow establishment period at a relatively low frequency and then at a predetermined time, to initiate high-frequency sampling. Another alternative is to delay the initiation of sampling by a predetermined time selected on the basis of Fig. 5(*b*). Either of these techniques provides samples at constant time. However, an external clock driven by a shaft encoder has also been used in this work to sample at constant phase. Several shaft encoders were used in this work providing 1, 6, 41, 82, 500, and 1000 pulses per revolution. It is not possible

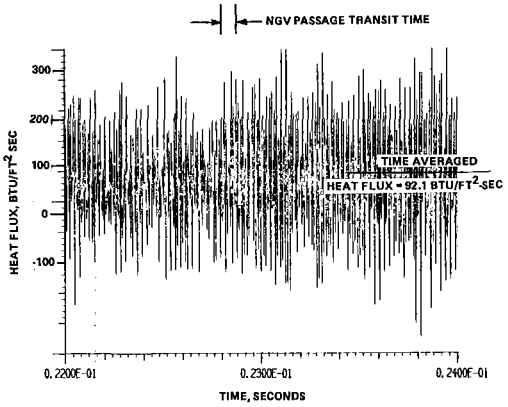

Fig. 7 Time-resolved heat-flux history at blade geometric stagnation point

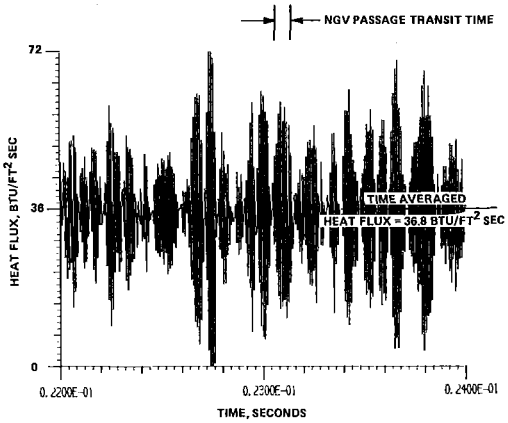

Fig. 8 Time-resolved heat-flux history at 32.7 percent wetted distance on blade suction surface

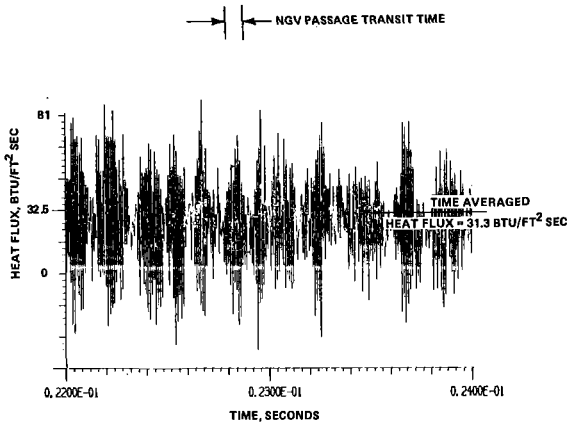

Fig. 9 Time-resolved heat-flux history at 85.5 percent wetted distance on blade suction surface

to discuss both data sets in this paper so the discussion will be confined to the data sampled at constant time.

Figure 6 presents the composite temperature histories for the geometric stagnation point, 32.7 percent wetted distance, and 85.5 percent wetted distance on the blade suction surface. The time at which uniform flow is established is denoted in Fig. 6. The maximum substrate temperature rise occurs in the stagnation region and it is in this region that the influence of variable thermal properties of the substrate becomes most important.

Figures 7–9 are the time-resolved heat-flux histories for the locations noted above computed in the manner described

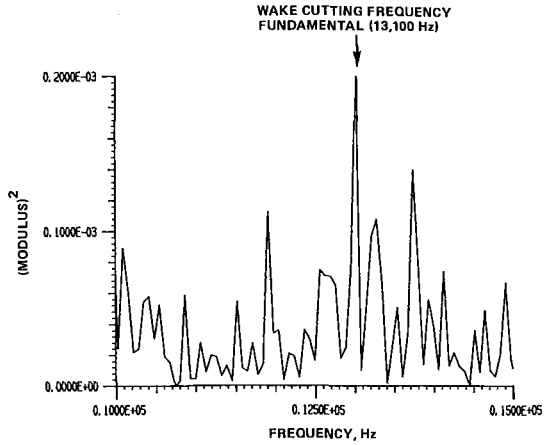

Fig. 10(*a*) Modulus of Fourier transform of heat-flux history for blade geometric stagnation point

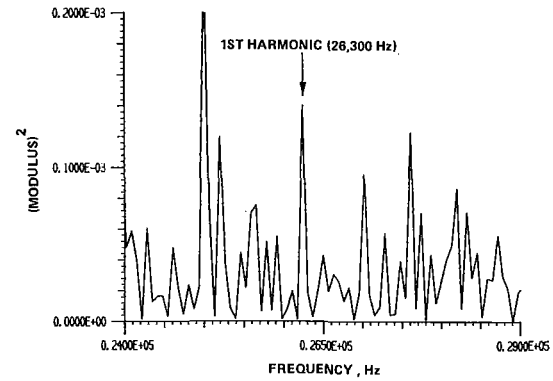

Fig. 10(*b*) Modulus of Fourier transform of heat-flux history for geometric stagnation point

earlier, for the time interval 22 to 24 ms. The time-averaged heat-flux value that is obtained from a separate data recording system and sampled at 20 kHz per channel is also shown on each of these plots. Figure 7 illustrates substantial fluctuations in the heat-flux value in the stagnation region. The magnitude of the fluctuation is time dependent as would be anticipated and a Fourier spectrum of the frequency content will be presented later in the paper. Moving back on the blade to the 32.7 percent location, the pattern of the heat-flux history is different as illustrated by Fig. 8. However, relative to the time-averaged heat-flux, the magnitude of the fluctuations is still significant at this location. Again, the value of the time-averaged heat flux is shown for comparison purposes. Figure 9 presents the heat-flux time history recorded near the trailing edge of the blade. The pattern at this location is similar to that observed elsewhere. Relative to the time-averaged heat flux, the fluctuations are significant even near the trailing edge of the blade.

The burst-like behavior observed in Figs. 7–9 is felt to be related to the period of the blade crossing the NGV exit passages. The characteristic time for the blade to traverse a single passage is denoted on each of the figures. In addition, the fluctuations of the calculated heat flux can be observed to go negative. The same features were observed when the temperature signal was directly input to a high-frequency Q-meter [17], and cannot, therefore, be readily attributed to the analysis. Thus it must either represent a phenomenon in the flow or be the effect of electronic noise.

Obviously, the heat-flux results given in Figs. 7–9 need to be analyzed further to determine whether or not the observed fluctuations are related to wake cutting. Figures 10–12 present the modulus squared of the Fourier transform, over a signifi-

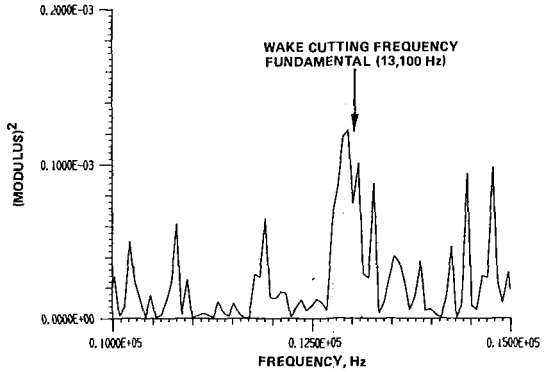

Fig. 11(*a*) Modulus of Fourier transform of heat-flux history for 32.7 percent wetted distance on blade suction surface

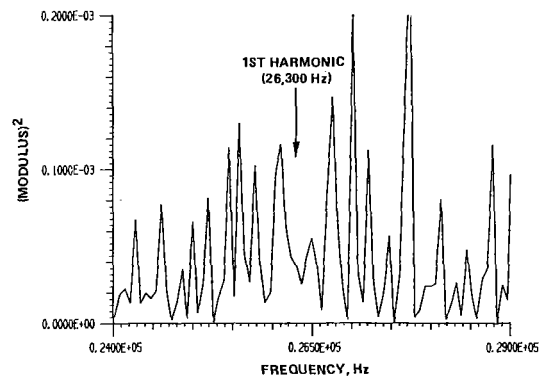

Fig. 11(*b*) Modulus of Fourier transform of heat-flux history for 32.7 percent wetted distance on blade suction surface

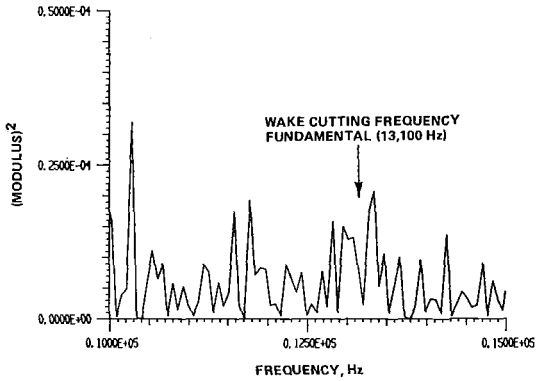

Fig. 12(*a*) Modulus of Fourier transform of heat-flux history for 85.5 percent wetted distance on blade suction surface

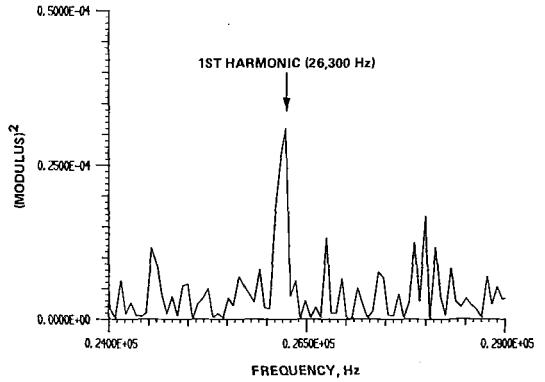

Fig. 12(*b*) Modulus of Fourier transform of heat-flux history for 85.5 percent wetted distance on blade suction surface

cant portion of the test time, of the heat-flux histories for the stagnation point, 32.7 percent, and 85.5 percent wetted distance, respectively. During this time period, the flow does work on the turbine, causing it to accelerate slightly. This acceleration has the effect of broadening the energy peaks associated with wake cutting. The frequency spectrum[3] is presented over a range of 10 to 15 kHz and 24 to 29 kHz. The previously mentioned shaft encoders were used to determine that the rotor speed at the 22 to 24 ms time interval was on the order of 19,200 rpm. For this turbine, there are 41 nozzle guide vanes and 78 rotor blades giving a fundamental wake cutting frequency of 13,100 Hz. Both the fundamental and the first harmonic are noted on Figs. 10–12.

The results for the stagnation region given on Figs. 10(*a*) and 10(*b*) demonstrate a sharp peak at the fundamental wake cutting frequency and two other rather broad peaks, of smaller magnitude, in the immediate vicinity. These later peaks suggest that there is significant energy content in the frequency range around the fundamental wake cutting frequency. The first harmonic peak at 26,300 Hz is shown on Fig. 10(*b*) as well as a relatively strong second peak at 25,000 Hz. At this time, it is not clear just what causes the 25 kHz peak.

Figures 11(*a*) and 11(*b*) present similar frequency spectra for 32.7 percent wetted distance on the suction surface. At this location, the FFT analysis suggests that the frequency content in the neighborhood of the fundamental has broadened, but is still very much related to wake cutting. The first harmonic at 26,300 Hz is very near a peak at 26,100 Hz and the previously observed peak at 25,000 Hz is reduced.

Figures 12(*a*) and 12(*b*) illustrate what one observes by moving farther along the surface toward the trailing edge. The frequency spectrum has a significant peak in the vicinity of the fundamental wake cutting frequency, but it is not as pronounced as at locations closer to the leading edge. The first harmonic, however, is very pronounced and stands out above all of the higher frequency content.

The results presented in Figs. 10–12 illustrate the presence of wake cutting in the heat-flux data. However, these frequency spectra also suggest that wake cutting is not the only important factor influencing blade heat transfer since there appears to be significant energy contained in other portions of the frequency domain.

Conclusions

A description of an analysis technique and its application using typical data for time-resolved heat-flux measurements on the blade of a full-stage rotating turbine has been presented. The magnitude of the fluctuation is largest over the forward portion of the blade and decreases as the trailing edge is approached. However, relative to the time-averaged heat-flux values at this downstream location, the magnitude of the fluctuations is significant. An FFT analysis of the time-resolved heat flux demonstrates the presence of peaks at the fundamental and first harmonic of the wake cutting frequency. The frequency spectra also demonstrate the presence of energy at frequencies other than wake cutting.

Acknowledgments

The research reported in this paper was supported by the National Aeronautics and Space Administration, Lewis Research Center, Cleveland, Ohio, under Grant No. NAG 3-469 and Grant No. NAG 3-581.

[3] The term "spectrum" is loosely used here to indicate the modulus squared of the Fourier transform of the record and no averaging is implied.

References

1 Kerrebrock, J. L., and Mikolajczak, A. A., "Intra-stator Transport of Rotor Wakes and Its Effect on Compressor Performance," ASME JOURNAL OF ENGINEERING FOR POWER, Oct. 1970, pp. 359–368.

2 Gorton, C. A., and Lakshminarayana, B., "A Method of Measuring the Three-Dimensional Mean Flow and Turbulence Quantities Inside a Rotating Turbomachinery Passage," ASME JOURNAL OF ENGINEERING FOR POWER, Apr. 1976, pp. 137–146.

3 Amand, A. K., and Lakshminarayana, B., "An Experimental Study of Three-Dimensional Turbulent Boundary Layer and Turbulence Characteristics Inside a Turbomachinery Passage," ASME Paper No. 78-GT-114.

4 Lakshminarayana, B., Govindan, T. R., and Reynolds, B., "Effects of Rotation and Blade Incidence on Properties of Turbomachinery Rotor Wake," *AIAA Journal*, Vol. 20, No. 2, Feb. 1982, pp. 245–253.

5 Dring, R. P., and Joslyn, H. D., "Measurement of Turbine Rotor Blade Flows," ASME JOURNAL OF ENGINEERING FOR POWER, Apr. 1981, pp. 400–405.

6 Dring, R. P., Blair, M. F., and Joslyn, H. D., "An Experimental Investigation of Film Cooling on a Turbine Rotor Blade," ASME JOURNAL OF ENGINEERING FOR POWER, Jan. 1980, pp. 81–87.

7 Dring, R. P., Joslyn, H. D., Hardin, L. W., and Wagner, J. H., "Turbine Rotor-Stator Interaction," ASME JOURNAL OF ENGINEERING FOR POWER, Oct. 1982, pp. 729–742.

8 Hodson, H. P., "Boundary Layer and Loss Measurements on the Rotor of an Axial-Flow Turbine," ASME Paper No. 83-GT-4.

9 Hodson, H. P., "Measurements of Wake-Generated Unsteadiness in the Rotor Passages of Axial Flow Turbine," ASME Paper No. 84-GT-189.

10 Hodson, H. P., "Boundary-Layer Transition and Separation Near the Leading Edge of a High-Speed Turbine Blade," ASME Paper No. 84-GT-179.

11 Binder, A., Forster, W., Kruse, H., and Rogge, H., "An Experimental Investigation Into the Effect of Wakes on the Unsteady Turbine Rotor Flow," ASME Paper No. 84-GT-178.

12 Doorly, D. J., and Oldfield, M. L. G., "Simulation of the Effects of Shock Wave Passing on a Turbine Rotor Blade," ASME Paper No. 85-GT-112.

13 Doorly, D. J., Oldfield, M. L. G., and Scrivener, C. T. J., "Wake-Passing in a Turbine Rotor Cascade," *Heat Transfer and Cooling in Gas Turbines*, AGARD Conf. preprint No. 390, Bergen, Norway, May 6–10, 1985.

14 Dunn, M. G., and Holt, J. L., "Turbine Stage Heat Flux Measurements," AIAA/ASME 18th Joint Propulsion Conference, Cleveland, OH, June 21–23, 1982, Paper No. 82-1289.

15 Dunn, M. G., Rae, W. J., and Holt, J. L., "Measurement and Analysis of Heat-Flux Data in a Turbine Stage: Part I: Description of Experimental Apparatus and Data Analysis; Part II: Discussion of Results and Comparison With Predictions," ASME JOURNAL OF ENGINEERING FOR POWER, Vol. 106, Jan. 1984, pp. 229–240.

16 Skinner, G. T., "Analog Network to Convert Surface Temperature to Heat Flux," *Journal of the American Rocket Society*, June 1960, pp. 569–570.

17 Oldfield, M. L. G., Burd, H. J., and Doe, N. G., "Design of Wide-Bandwidth Analogue Circuits for Heat Transfer Instrumentation in Transient Tunnels," Oxford Univ., O.U.E.L. Report No. 1382/81.

18 Jenkins, G. M., and Watts, D. G., *Spectral Analysis and Its Application*, Holden-Day, San Francisco, 1968.

19 Vidal, R. J., "Model Instrumentation Techniques for Heat Transfer and Force Measurements in a Hypersonic Shock Tunnel," Cornell Aeronautical Laboratory Report M. AD-917-A-1, Feb. 1956.

20 Miller, C. G., "Comparison of Thin-Film Resistance Heat-Transfer Gages With Thin-Skin Transient Calorimeter Gages in Conventional Hypersonic Wind Tunnels," NASA TM 83197, 1981.

21 Cook, W. J., and Felderman, E. J., "Reduction of Data From Thin-Film Heat-Transfer Gages: A Concise Numerical Technique," *AIAA Journal*, Apr. 1966, pp. 561–562.

22 Schultz, D. L., and Jones, T. V., "Heat-Transfer Measurements in Short Duration Hypersonic Facilities," AGARDograph No. 165, Feb. 1973.

23 Carslaw, H. S., and Jaeger, J. C., *Conduction of Heat in Solids*, 2nd ed., Section 2.16, Clarendon Press, 1960.

24 Richtmeyer, R. C., and Morton, K. W., *Difference Methods for Initial Value Problems*, 2nd ed., Wiley, New York, 1967, Chap. 8.

25 Dunn, M. G., and Stoddard, F. J., "Application of Shock-Tube Technology to the Measurement of Heat-Transfer Rate to Gas Turbine Components," 11th International Symposium on Shock Tubes and Waves, July 1977.

26 Dunn, M. G., and Hause, A., "Measurement of Heat Flux and Pressure in a Turbine Stage," ASME JOURNAL OF ENGINEERING FOR POWER, Vol. 104, No. 1, Jan. 1982.

Heat-Flux and Pressure Measurements and Comparison With Prediction for a Low-Aspect-Ratio Turbine Stage

M. G. Dunn
Calspan Advanced Technology Center,
Buffalo, NY 14225

Capt. H. L. Martin

M. J. Stanek

Aero Propulsion Laboratory,
Wright-Patterson
Air Force Base, OH 45433

This paper describes the detailed measurement of heat-flux distributions for the nozzle guide vane (NGV) airfoil, the NGV hub and tip endwalls, and the blade for the Garrett low-aspect-ratio turbine (LART) stage. A shock tube was used to generate a short-duration source of heated air and thin-film gages were used to obtain detailed heat-flux measurements. In addition to the heat-flux measurements, surface-pressure measurements were obtained on the vane pressure and suction surfaces and on the hub and tip endwalls. These pressure measurements are shown to compare favorably with those taken at the same locations but in a long-run time facility. The time-averaged heat-flux data were obtained by sampling the gage signals at a frequency of 20 kHz/channel and then averaging the output over the test time of the experiment. The results are presented as a function of location within the stage and are compared with the results of a local flat-plate prediction technique.

Introduction

The current interest in increasing the thrust-to-weight ratio of future gas turbine engines requires that the turbine inlet temperatures of these machines be increased significantly over current values. Increased inlet temperature implies increased heat load and a corresponding need for rapid advances in materials and cooling capability for the hot-section portion of the machine. For design reasons, it is important to improve the current state-of-the-art predictability of these hot-section heat loads so that the thermal design can be conservative, but to a reasonable and acceptable level. It is therefore important to obtain an experimental data base under known conditions for as realistic a gas-dynamic environment as possible and then to compare these data with the results of current design-system prediction techniques. The results described in this paper represent a step toward obtaining the data base. The major emphasis has been placed on obtaining accurate measurements of heat-flux distributions for a modern low-aspect-ratio high-pressure turbine stage at known laboratory conditions. The results of the time-averaged measurements have been compared with the results of a local flat-plate prediction technique. More sophisticated techniques are currently being used to correlate these data.

The measurement technique utilizes the short-duration shock-tunnel approach in which fast-response, thin-film thermometers are used to measure the surface temperature histories at prescribed positions on the various component parts. Heat-flux values are then inferred from these temperature histories, using standard data-reduction techniques. With the shock-tunnel approach, one can simultaneously duplicate the turbine design point flow function, the corrected speed, the stage pressure ratio, and the wall to total temperature ratio. Because of the limited flow duration (on the order of 20 ms) and the clean nature of the flow environment, the instrumentation life is relatively long.

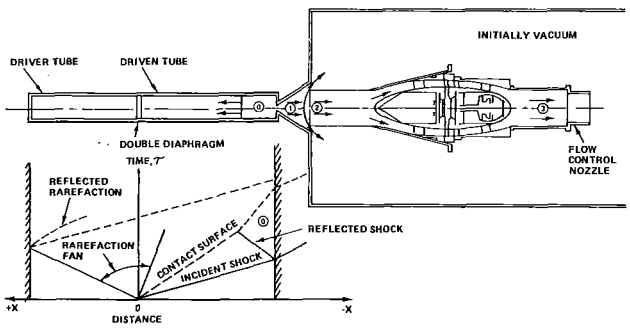

Fig. 1 Schematic of experimental apparatus

The results reported here are part of a more extensive program for which detailed measurements have been performed for two turbines. The first of these is the Garrett Turbine Engine Company TFE 731-2 high-pressure turbine stage with an aspect ratio of approximately 1.5 and the results have been reported in [1–11]. The second turbine stage for which measurements have been obtained and are reported here is the Air Force/Garrett low-aspect-ratio (LART) turbine which has an aspect ratio of approximately 1.0.

Contributed by the Gas Turbine Division of THE AMERICAN SOCIETY OF MECHANICAL ENGINEERS and presented at the 31st International Gas Turbine Conference and Exhibit, Düsseldorf, Federal Republic of Germany, June 8–12, 1986. Manuscript received at ASME Headquarters January 13, 1986. Paper No. 86-GT-79.

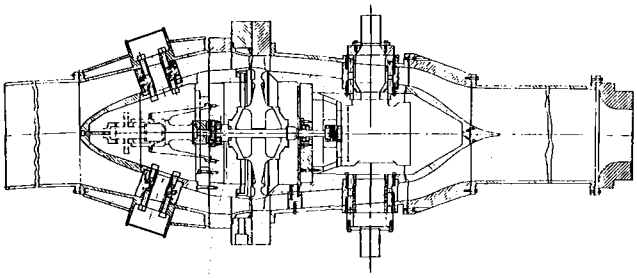

Fig. 2 Sketch of turbine model

The intent of the work described in this paper was to perform detailed heat-flux measurements with gages spaced relatively close together, at distances on the order of 2.5×10^{-3}m (0.100 in.) over the meanline region of the vane and blade. In the leading-edge region, the spacing was decreased by a factor of more than two so that the stagnation-region distribution could be resolved. Several additional heat-flux measurements were obtained on the NGV endwalls, the blade tip, and the blade platform. Along with the heat-flux measurements, surface-pressure measurements were obtained simultaneously at selected locations on the NGV for comparison with the Garrett steady-stage rig results and for comparison with the results of a three-dimensional flow prediction performed using [12, 13].

Experimental Apparatus

The experimental apparatus sketched in Fig. 1 consists of a 0.20-m (8-in.) i.d. helium-driven shock tube with a 12.2-m (40-ft) long driver tube and a 15.2-m (50-ft) long driven tube, as a short-duration source of heated air, supplying the test-section device mounted near the exit of the primary shock-tunnel nozzle. The receiver tank is initially evacuated to a pressure of approximately 1 torr in order to minimize the initial resistance of the turbine wheel and to improve the flow-establishment characteristics of the model. A more complete description of this facility is given in [11] and will not be repeated here. The test-section device housing the LART stage is sketched in Fig. 2 and consists of a forward transition section with a circular opening facing the supersonic primary nozzle flow. This transition section is followed by a 360-annular passage containing the LART IIB NGV row which has 24 vanes, the LART IIA rotor with 50 blades, and an exit passage. A contoured nozzle is located at the end of the exit passage and is used to establish the pressure ratio across the turbine state. It is an iterative process to set this pressure ratio usually requiring two or three runs. The forward bullet nose houses a 100-channel slip ring unit. This is a high-speed, low-noise unit having a maximum noise level of 25 μvolts for any individual ring. Experience with this unit has always resulted in the noise level being substantially below the maximum level. The aft bullet nose houses an air-driven motor that is used to accelerate the turbine from rest to the desired design speed just prior to initiation of the experiment and prior to the arrival of the test-gas flow. The lead wires are routed from the blades onto the disc where they are attached to terminal strips, banded to the disc, and covered with an epoxy cement. They are then routed to the forward portion of the hollow drive shaft and then onto the slip ring connector plug.

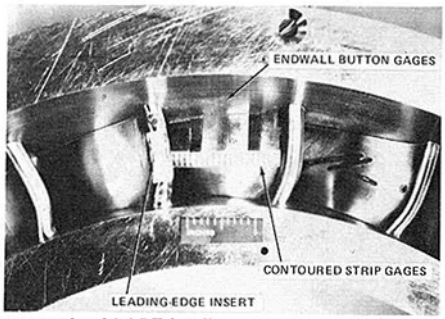

Fig. 3 Photograph of LART leading-edge insert and pressure surface instrumentation

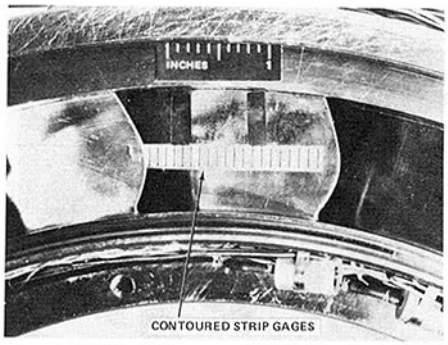

Fig. 4 Photograph of heat-flux gage distribution for LART NGV suction surface

The heat-flux gage instrumentation used in this program consisted of button-type gages on the rotor tip, the rotor pressure surface, the rotor suction surface, the rotor platform, the NGV hub endwall, and the NGV tip endwall. A photograph of the button gage is shown in [11] and a description of the construction technique is given in [8]. In addition to the button gages, new instrumentation consisting of surface contoured substrate sections onto which thin-film gages were then painted was introduced for this measurement program in the inlet vane leading edge, the vane pressure-surface, the vane suction-surface, and the rotor leading-edge regions.

The LART instrumentation concentrated on the meanline

Nomenclature

A = NGV inlet area
Flow Function = $\dot{W}\sqrt{\theta}/\delta$
H_0 = total enthalpy evaluated at T_0
$H_w(T)$ = wall enthalpy evaluated at the local wall temperature
k = thermal conductivity
N_{corr} = corrected rotor speed = $N_{phy}/\sqrt{\theta}$
N_{phy} = physical rotor speed
Pr = Prandtl number
$\dot{q}(T)$ = heat flux corrected for variable thermal properties of the Pyrex substrate
$\dot{q}_{cw}$ = cold wall heat flux
S = distance measured along surface
S_T = total distance measured along surface from leading edge of trailing edge
St = Stanton number
T = local temperature of thin-film gage evaluated as a function of time
T_w = initial wall temperature
ΔT = measured surface temperature rise of Pyrex substrate
T_0 = total temperature
$\dot{W}$ = weight flow
δ = $P_{T,in}/14.696$ psia
θ = $T_0/518$ R

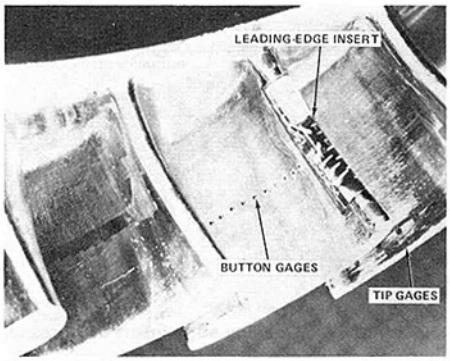

Fig. 5 Photograph of LART rotor leading-edge insert and pressure surface instrumentation

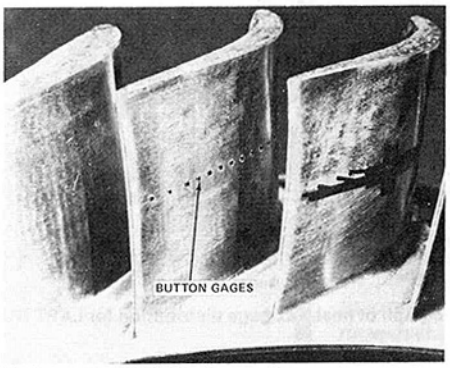

Fig. 6 Photograph of LART rotor suction-surface instrumentation

portion of the vane and the blade and on the tip endwall region. Figure 3 is a photograph of the contoured leading-edge insert and of the contoured pressure-surface insert for the LART nozzle guide vane. In the leading-edge region, the gages are painted on an insert that has been contoured to the airfoil geometry. The technique used to construct this insert is described in [8]. The gages on this insert are spaced approximately 1.0×10^{-3} m (0.040 in.) apart starting at the geometric stagnation point and continuing around both the pressure and suction sides of the insert. The contoured pressure-surface insert, also shown on Fig. 3, contains thin-film gages that have been painted at intervals of approximately 2.5×10^{-3} m (0.100 in.) from the termination of the leading-edge insert to the trailing edge of the vane. An arrow points to one of the tip endwall button gages located to the left of the pressure surface insert.

Figure 4 is a photograph of the NGV suction surface heat-flux gage distribution. For this region, a Pyrex strip was contoured to the airfoil geometry and then the thin-film gages were painted on the insert at intervals of approximately 2.5×10^{-3} m (0.100 in.) starting near the termination of the leading-edge insert and continuing to a location near the trailing edge.

Figures 5 and 6 are photographs of the LART blade leading-edge insert and the button gage pattern on both the pressure and suction surfaces. The spacing between gages used for the blade instrumentation was very similar to that used for the NGV airfoil. The button gages located in the tip of the blade to the right of the insert in Fig. 5 are located with the call out. There were ten gages located in the tip region of this blade.

At the same time that the heat-flux distributions were being obtained, surface-pressure measurements were also obtained at selected locations on the NGV portion of the stage. A more detailed description of how the pressure measurement was performed is given later in the paper. In addition, the static pressure upstream of the NGV and downstream of the rotor was also measured.

Table 1 Experimental conditions

	Column I Initial Values Based on Data and Calculation	Column II Design Conditions	Column III Operating Point Deduced by Garrett from Calspan Measurements
Physical weight flow, lb_m/sec	28.0		27.33
Inlet area used in Stanton Number, ft^2	0.64		
Flow function	6.65	6.39	6.49
Total temperature @ NGV inlet, ^oR	1001		
Total pressure @ NGV inlet, psia	86.5		
Mach number @ NGV inlet	0.14		
Wall temperature of stage, ^oR	531		
Wall enthalpy, Btu/lb_m	127.3		
Inlet total enthalpy, Btu/lb_m	241		
Total pressure ratio across stage	3.2	3.09	3.75
Reynolds number @ NGV inlet	2.7×10^5		
Reynolds number @ NGV exit	3×10^6		
$V/V_{CR}]_{exit}$		0.555	0.686
α_{exit}, deg		-17.8	-27.5
$\Delta H/\Theta$, Btu/lb_m		31.6	35.0
$N/\sqrt{\Theta}$, RPM	10,227	10,408	10,227

Experimental Conditions

Static pressure measurements across the stage are taken in order to be able to arrive at a flow function setting that approximates the turbine-stage design point. In order to duplicate the design-point value, one must iterate between the experiment and the design code. However, this process is not always possible to do in an efficient way because of prior commitments on the part of one or both of the parties involved, making it necessary to set an approximate operating point and then to determine the more precise value at a later time. This technique was used for the measurements reported here and is the explanation for the third column of Table 1. The first column gives the values determined while the measurements were being performed. The inlet area, the wall temperature, the static pressure at the NGV inlet, the static pressure ratio across the stage (both hub and tip), and the total temperature are measured values. The total pressure ratio across the stage is calculated from the static pressures assuming a negligible influence of swirl. The weight flow is calculated from the design NGV throat area, the measured total temperature, and the total pressure upstream of the vane. The inlet Mach number, the Reynolds number, the flow function, and the inlet total enthalpy are calculated from measured conditions. The rotor speed is continuously measured.

The second column of Table 1 gives the design-point conditions for the turbine stage provided by the stage manufacturer. Upon completion of the measurements, the values given in column 1 and additional static pressure data were supplied to the Garrett Turbine Engine Company and they in turn

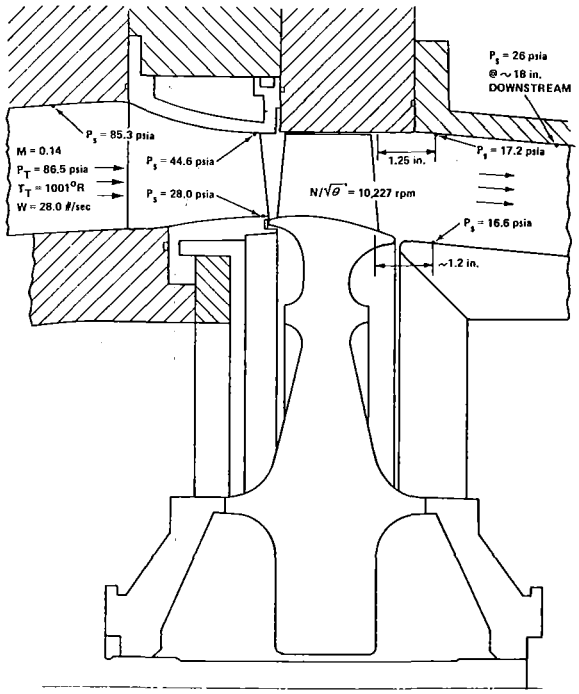

Fig. 7 Sketch of LART stage

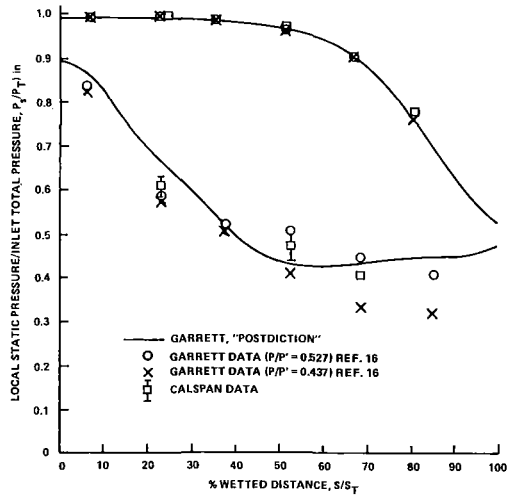

Fig. 8 Pressure distribution for LART IIB NGV meanline

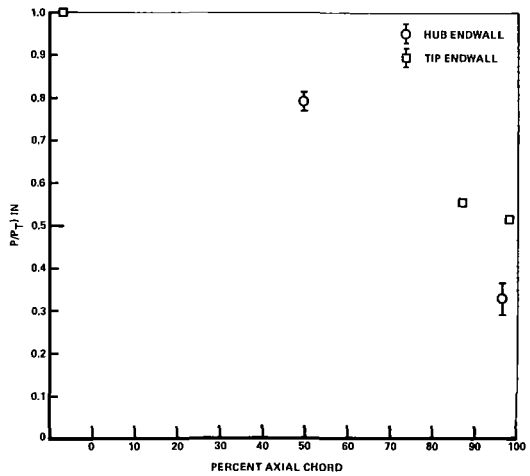

Fig. 9 Measured pressure on LART NGV tip and hub endwall at midendwall location

calculated the operating point condition given in column 3 of Table 1.

Experimental Results and Predictions

The experimental results given here are presented in the form of a Stanton number based on conditions at the NGV inlet which is evaluated using the relationship

$$\mathrm{St}_{\mathrm{Inlet}} = \frac{\dot{q}(T)}{(\dot{W}/A)(H_0 - H_w(T))} \tag{1}$$

In equation (1), H_0 is the real gas enthalpy determined from [14], $\dot{q}(T)$ is the heat flux evaluated for each thin-film gage accounting for the variable thermal properties of the substrate, $H_w(T)$ is the real-gas wall enthalpy evaluated for each gage at the wall temperature corresponding to $\dot{q}(T)$, $\dot{W}$ is the turbine weight flow, T is the thin-film gage temperature evaluated as a function of time at the sampling frequency, and A is a characteristic area (NGV inlet) of the turbine which is a constant value and is given in Table 1. The Stanton number written in equation (1) is commonly referred to as the equivalent cold-wall Stanton number. On all of the data plots presented here, the symbol will represent the mean value of the Stanton number and the bar will represent the standard deviation. If the bar does not appear on the plot, then the standard deviation falls within the symbol unless otherwise noted.

The LART IIB stator used in this work had previously been used at Garrett and came with static pressure taps on the hub and tip end walls and on the vane meanline. The taps are approximately 6.0×10^{-4} m (0.027 in.) in diameter and are connected to an external piezoelectric pressure gage via hypodermic tubing. For the purposes of the short-duration measurements reported here, the tubing was cut off to the minimum possible length and the transducers were placed as close to the tap locations as possible. The pressure transducers used were either PCB piezoelectric Model 112M37 or Model 113M12 with a resonant frequency in the range of 250 kHz. Although the hypodermic tubing significantly reduces the frequency response of the system, the gage output reaches steady state after a few milliseconds which is sufficiently rapid to obtain pressure data on the time scale of the experiment.

Figure 7 is a sketch of the LART stage configuration giving physical locations for the static pressure measurements. The stage is assembled so that the vane/blade spacing and the tip/shroud clearance are consistent with the values used in the engine assembly. On the left of Fig. 7 the inlet Mach number, total pressure, total temperature, and weight flow are tabulated. The static pressure values measured on the hub and tip endwall near the vane exit are given in the center of the sketch. The static pressure values measured just downstream of the rotor exit on the hub and tip endwall are also given as is the static pressure measured far downstream near the flow control nozzle. This latter pressure can be used along with the known geometry of the flow control nozzle to verify the calculated weight flow.

Upon completion of the measurement program, Garrett personnel ran their version of the three-dimensional flow Denton code [12, 13] to obtain the vane and blade pressure loading on the basis of the measured parameters given on Fig. 7, and granted permission to use the result here [15]. Figure 8 presents a comparison among the NGV meanline pressure distribution measured in the Garrett long run-time facility [16], that measured in the Calspan short-duration facility, and the result of the Denton calculation noted above. This particular version of the Denton code has a cusp in the leading-edge region and closure in this region is difficult to obtain. At the trailing edge, closure is better but still not complete.

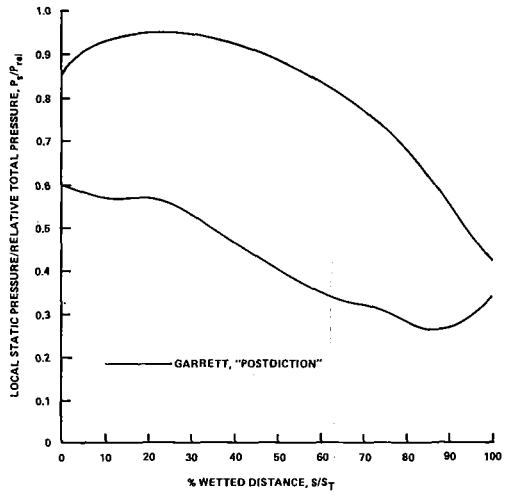

Fig. 10 Pressure distribution for LART IIA rotor meanline

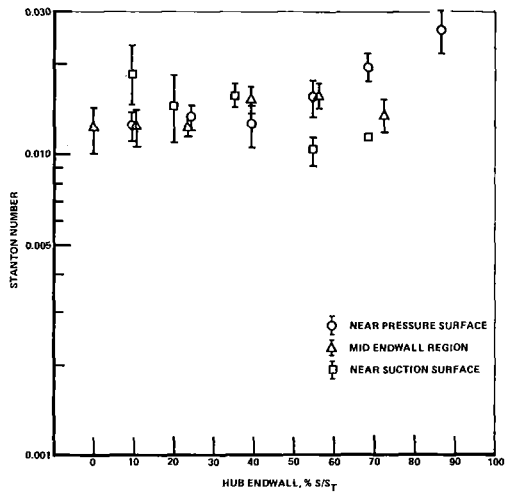

Fig. 12 Stanton number distribution for LART NGV hub endwall

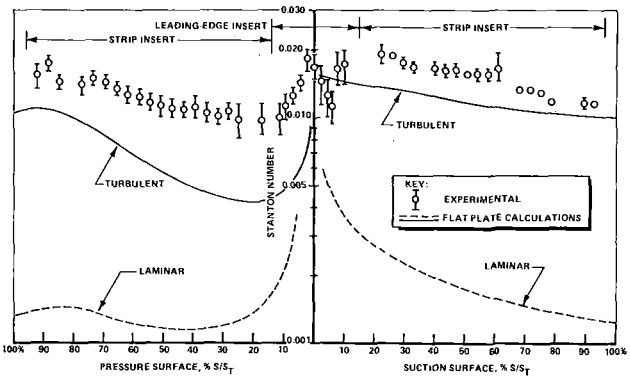

Fig. 11 Stanton number distribution for LART NGV meanline

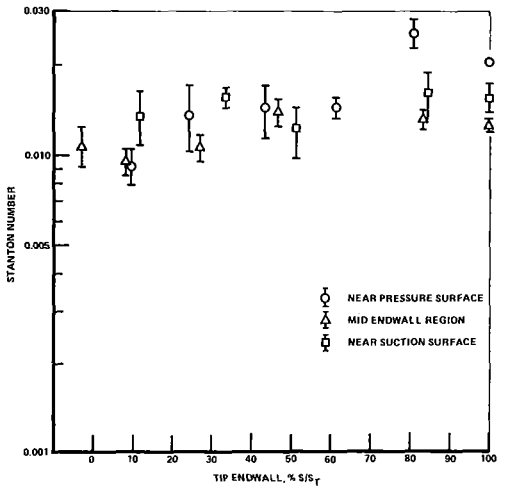

Fig. 13 Stanton number distribution for LART NGV tip endwall

However, for the purposes of this comparison and for input to the relatively crude flat-plate calculations to be performed, the calculation is satisfactory. The Garrett pressure distributions were measured for two values of pressure ratio, 0.527 and 0.437. The Calspan measurements were performed at a condition closer to the 0.527 case. On the pressure surface, the agreement among the steady-state data, the short-duration data, and the calculation is excellent. On the suction surface, the agreement between the steady-state and short-duration facility results is good, but the corresponding agreement with the calculation is not as good as it was for the pressure surface. However, this surface is more difficult to calculate and in general the agreement is satisfactory. It was noted earlier that limited pressure data were taken on the NGV tip and hub endwall at the midendwall location and these results are presented in Fig. 9. The corresponding Garrett rig data were not available for comparison nor was the prediction. The most obvious feature of Fig. 9 is the strong acceleration on the hub endwall by comparison with the tip endwall. The feature of the pressure loading was anticipated from design considerations. Figure 10 presents the Denton code prediction for the blade meanline obtained for the experimental conditions as noted above. The lack of closure at the leading edge of the blade is somewhat greater than was shown for the vane and is again due to the cusp leading-edge approximation. However, for the purpose of obtaining a pressure loading that could be used to estimate the vane and blade Stanton number distributions for these experimental conditions, the calculation is adequate.

Figure 11 presents: (1) the Stanton number distribution obtained using equation (1) and the experimental data, and (2) the calculated flat-plate laminar and turbulent boundary-layer values for the LART NGV meanline. The Stanton numbers are presented as a percentage of wetted surface distance for both the suction and pressure surfaces. This NGV row contains vanes that have a contoured leading edge insert, a contoured strip insert on the pressure surface and a contoured strip insert on the suction surface (see Figs. 3, 4). The extent of both the leading edge insert and the contoured strips is noted on Fig. 11. The contoured strip inserts on the pressure and suction surfaces are installed so that a single passage is instrumented.

The solid lines presented on the pressure distribution plot of Fig. 8 were used to calculate the turbulent and laminar boundary layer flat-plate results using the equations given in [17] and these results are also shown on Fig. 11. In evaluating the heat-transfer coefficient necessary to calculate the local Stanton numbers, the values of T_0, T_w, $\dot{W}$, A, H_0, and H_w given in column 1 of Table 1 were used. The thermal conductivity and viscosity were evaluated at the reference temperature and the density was evaluated at the local pressure and the reference temperature. The local velocity is evaluated for the value of M_{crit} calculated at the local pressure ratio. The wetted distance is measured from the geometric stagnation point. In the computation of the flat-plate Stanton number for the NGV, the following values were used: $T_{ref} = 766$ R, $k = 2.0 \times 10^{-2}$ Btu/ft-hr-R, Pr = 0.696, and $\mu = 1.6 \times 10^{-5}$ lb_m/ft-s.

The peak in the measured Stanton number distribution occurred on the pressure surface at about 2 percent of wetted

distance. The Stanton number falls rapidly on the suction side until at 6 percent wetted distance a steep increase occurs. The gage that recorded this increase and the succeeding two gages were located on the insert. The insert was a highly polished surface made of Pyrex and has been carefully contoured to the leading edge profile. The pressure distribution given in Fig. 8 indicates that the flow over the suction surface is accelerating rapidly in this region. The behavior of the measured Stanton number distribution suggests that boundary-layer transition occurs in the vicinity of 6 percent wetted distance. The data obtained on the insert are shown to blend smoothly with those obtained on the contoured strip insert. Unfortunately, the gage at 15 percent wetted distance was damaged. The pressure distribution presented in Fig. 8 indicates that at about 37 percent wetted distance the local flow becomes sonic on the suction surface and the gradient in pressure begins to change from strongly negative to zero then becomes positive at approximately 60 percent wetted distance. The Stanton number distribution reflects this trend in that at about 30 percent the slope of the Stanton number distribution changes and approaches a nearly zero slope and remains so until about 60 percent wetted distance. At this 60 percent location, the standard deviation becomes relatively large and is followed by a significant decrease in Stanton number. A large standard deviation usually suggests that the flow in the local region is very sensitive to changes in the immediate vicinity. Note that the standard deviation for locations prior to 60 percent is relatively small and that beyond 60 percent the standard deviation falls within the symbol. The left-hand side of Fig. 11 presents the pressure surface Stanton number distribution as a function of wetted surface distance. On the pressure surface, the Stanton number falls by a factor of approximately two over the initial 11 percent of wetted distance, but then levels out and begins a slowly increasing trend toward the trailing edge. The relative locations of the leading-edge insert gages and the contoured strip insert are clearly noted on the figure. The trend of the data obtained using the separate inserts is to blend nicely together. The pressure-surface pressure distribution given on Fig. 8 suggests that the flow acceleration is very slow over the initial 50 percent of the vane pressure surface, but accelerates rapidly between 70 percent and 85 percent. This acceleration begins to slow noticeably beyond 85 percent. The Stanton number distribution reflects a similar trend after the initial decay within the first 11 percent wetted distance.

The Denton code-predicted pressure loadings presented in Fig. 8 were used to calculate the turbulent and laminar boundary layer flat-plate distributions shown on Fig. 11. This calculation is a local flat-plate calculation that is initiated at the geometric stagnation point with an initial zero boundary-layer thickness in the manner described in [17]. On the suction surface of the vane, the turbulent flat-plate calculation is a reasonable approximation to the experimental data over the first 10 percent of wetted surface. Between 10 percent and 60 percent, the prediction falls below the data by about 30 percent but comes significantly closer to the data from 65 percent wetted distance to the trailing edge. By comparison, the laminar boundary-layer prediction is far below the data, becoming worse as the distance from the leading edge increases. The turbulent boundary layer flat-plate prediction for the pressure side underpredicts the data over the entire suction surface. Over the initial 50 percent, the prediction is almost a factor of two below the experimental data and beyond 50 percent wetted distance it comes closer but is still well below the experimental data. The laminar boundary layer flat-plate prediction is almost an order of magnitude below the data over the entire surface, suggesting that the extent of the laminar boundary layer on the pressure surface is very limited.

Figures 12 and 13 present the Stanton number distributions for the NGV hub and tip endwalls, respectively. The data contained on these plots are for locations near the pressure surface, the midendwall region, and near the suction surface. The term "near the surface" means that the gage was on the endwall at a location generally on the order of 1.8×10^{-3} m (0.070 in.) from the intersection of the vane with the endwall. Over the initial 60 percent of wetted distance on both the hub and tip endwalls, the Stanton number was relatively uniform. At about 60 percent, the measured value near the pressure surface begins to increase reaching a peak value near 81 to 86 percent of wetted distance. The endwall predicted pressure loadings are not available to aid in interpretation of the heat transfer data and only a few measured pressures for the midendwall region (see Fig. 9) were available. However, the vane hub and tip pressure loadings calculated using [12, 13] were available for both the pressure and suction surface. The calculation predicted sign changes in the pressure gradient in the vicinity of where the peak in the Stanton number was observed.

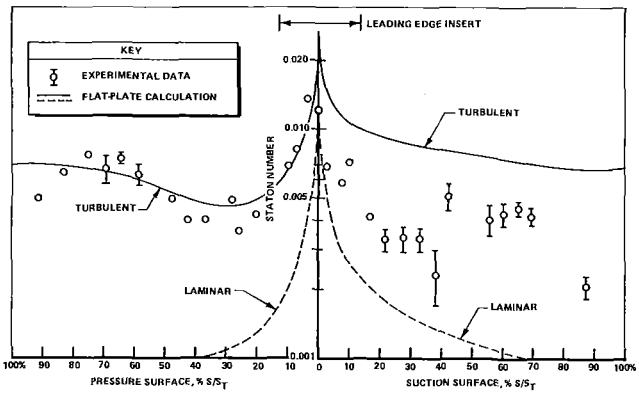

Fig. 14 Stanton number distribution for LART rotor midspan

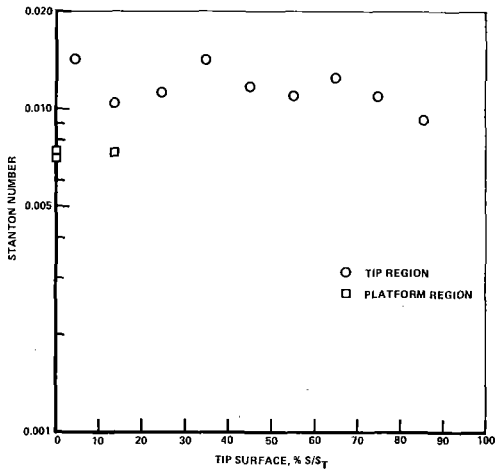

Fig. 15 Stanton number distribution for LART tip and platform regions

Heat-flux measurements were obtained on the LART IIA rotor. One of the blades had a contoured leading-edge insert as shown in the photograph of Fig. 5. The remainder of the heat-flux gages on the pressure surface, the suction surface, and the tip region of the blade were button-type gages. Except for the leading-edge region the small button gages were used on the blade because of the interest in time resolving local events taking place during wake and passage cutting. The extremely small dimensions of the thin-film on the button permit resolution of local events. Figure 14 presents the blade Stanton number distribution as a function of wetted surface distance and denotes the extent of the leading-edge insert. The calculated meanline blade pressure loading given in Fig. 10 is helpful in the discussion of the blade heat-transfer results. This pressure distribution in conjunction with the other output

of the code was used to calculate the local flat-plate laminar and turbulent boundary layer predictions that are also included on Fig. 14.

The peak Stanton number on the blade occurred at approximately 3.5 percent wetted distance on the pressure surface. As in the case of the vane, wetted distance is measured from the geometric stagnation point. It is not surprising that the peak occurred at this location because the LART IIA rotor is designed to have a +10 deg incidence angle at the midline and at the hub and 0 deg incidence at the tip. The suction surface Stanton number falls off rapidly until approximately 8 percent wetted distance, where a relatively sharp increase occurs followed by a correspondingly sharp decrease. Reference to the pressure loadings of Fig. 8 illustrates that in the region between 8 and 22 percent wetted distance, the pressure gradient changes from negative to zero, to positive, and back to negative. The behavior of the heat-transfer data appears to be related to the local flow situation. At about 30 percent wetted distance the local flow becomes sonic and a significant disruption in the Stanton number distribution is observed. The large standard deviation at this location is associated with a rapidly changing local flow environment and is felt to be indicative of boundary-layer transition. At about 70 percent wetted distance another rapid change in the sign of the pressure gradient occurs followed by a rapid change in the Stanton number distribution. Beyond 70 percent wetted distance, the blade becomes uncovered and strange events are known to occur. Further, the density of heat-flux gages beyond 70 percent decreased and detailed data were not available.

On the blade pressure surface, the Stanton number falls from a maximum at 3.5 percent wetted distance to a minimum at about 25 percent wetted distance. The calculated pressure loadings given in Fig. 8 indicate that the pressure-surface pressure gradient from the leading edge to about 20 percent is positive, becoming zero at about 25 percent and then becoming negative over the remainder of the surface. A noticeable increase and subsequent decrease in Stanton number occurs in this region of the pressure-gradient activity. The pressure gradient becomes noticeably more negative at about 70 percent wetted distance which also corresponds to a noticeable change in the Stanton number distribution. The pressure-surface flow does not become sonic until a location beyond the limit of the instrumentation coverage.

Also included in Fig. 14 are the turbulent and laminar boundary-layer local flat-plate predictions. The equations used to perform these calculations are described in [17]. The local flow parameters used in the heat-transfer calculation were taken from the results provided in [15]. The boundary layer is started at the geometric stagnation point with an initial thickness of zero. The rotor heat-transfer calculation utilized the calculated relative temperature in calculating $q(T_w)$ and in evaluating the local properties in calculating the heat-transfer coefficient from the equations given in [17]. The Stanton number was normalized by $H_0 - H_w(T_w)$ to be consistent with the data presentation.

On the suction surface, the turbulent boundary-layer prediction exceeds the data over the entire surface. The data suggest that boundary-layer transition occurs in the vicinity of 40 percent wetted distance. After transition, the prediction is closer to the data, but it is still high by a factor of almost two. By contrast, the laminar prediction is in reasonable agreement with the data up to about 5 percent wetted distance but it falls substantially below the data beyond 5 percent wetted distance. What appears to be a separation bubble occurring at about 8 percent wetted distance influences the agreement between the laminar prediction and the data. For the pressure surface of the blade, the turbulent boundary-layer prediction is fortuitously close to the experimental data over the entire surface. The same general calculation technique was used to obtain the comparison presented in Fig. 11 for the vane and in that case the predicted Stanton numbers were significantly below the data. However, it should be noted that a similarly good comparison for the blade was illustrated in [11] for the Garrett TFE 731-2 HP turbine. The laminar boundary-layer prediction is significantly below the experimental data suggesting that the blade pressure surface boundary layer was turbulent over most of the surface.

Button gages were placed at ten locations in the blade tip region and at three locations on the platform. Figure 15 presents the Stanton number distribution for both of these regions. The tip clearance for which these measurements were obtained was 1.0×10^{-3} m (0.039 in.). As anticipated on the basis of previous measurements using a different turbine [6], the tip region Stanton numbers were found to be larger than the platform values. The distribution of tip Stanton number was found to be reasonably uniform with a tendency to decrease toward the trailing edge. By comparison with the blade meanline data presented in Fig. 14, both the platform and the tip Stanton numbers are substantial, being comparable with the stagnation-region data.

Conclusions

Detailed heat-flux measurements have been obtained for the Garrett low-aspect-ratio turbine (LART) stage. These heat-flux values are used to calculate a Stanton number based on inlet flow conditions. Values of the inlet Stanton number are then presented for the meanline beginning at the leading edge of the NGV and continuing to near the trailing edge of the blade. The peak meanline value for the vane occurred at approximately 2 percent wetted distance on the pressure surface side. Boundary-layer transition occurs at 6 percent wetted distance on the suction surface side of the vane. The pressure surface boundary layer appears to be turbulent from near the leading edge all the way to the trailing edge. A turbulent boundary layer flat-plate prediction underestimates the data by a maximum of 30 percent on the suction side of the vane and underestimates the data for the early portion of the pressure surface by as much as 100 percent. The laminar boundary layer flat-plate prediction does not approximate the data on either surface of the vane except for very small wetted distances on the suction surface. For the blade, the peak Stanton number occurred at approximately 3.5 percent wetted distance on the pressure surface. The flat-plate prediction does a reasonably good job of correlating the data for the pressure surface of the blade, but it does not do nearly as well on the blade suction surface.

Acknowledgments

The author would like to thank G. Lukis, M. Urso, R. L. Orszulak, N. J. Kay, and S. J. Sweet of Calspan for their dedicated efforts during the course of this work.

The hardware utilized for this measurement program was the Garrett low-aspect-ratio turbine (LART) which was on loan to Calspan from the US Air Force (WPAFB) and the Garrett Turbine Engine Company. This work was supported by the Aero Propulsion Laboratory, Air Force Wright Aeronautical Laboratories, Air Force Systems Command, Wright-Patterson AFB, Ohio, and the Naval Air Propulsion Center, Trenton, New Jersey, under contract No. F33615-81-C-2017.

References

1 Dunn, M. G., and Stoddard, F. J., "Application of Shock-Tube Technology to the Measurement of Heat Transfer Rate to Gas Turbine Components," 11th International Symposium on Shock Tubes and Waves, July 1977.

2 Dunn, M. G., and Stoddard, F. J., "Measurement of Heat Transfer Rate to a Gas Turbine Stator," ASME JOURNAL OF ENGINEERING FOR POWER, Vol. 101, No. 2, Apr. 1979.

3 Dunn, M. G., and Hause, A., "Measurement of Heat Flux and Pressure

in a Turbine Stage,"ASME JOURNAL OF ENGINEERING FOR POWER, Vol. 104, No. 1, Jan. 1982.

4 Winstanley, D. K., Booth, T. C., and Dunn, M. G., "The Predictability of Turbine Vane Convection Heat Transfer," AIAA/SAE/ASME 17th Joint Propulsion Conference, July 27–30, 1981, Colorado Springs, CO, Paper No. AIAA-81-1435.

5 Dunn, M. G., and Holt, J. L., "Turbine Stage Heat Flux Measurements," AIAA/ASME 18th Joint Propulsion Conference, June 21–23, 1982, Cleveland, OH, Paper No. 82-1289.

6 Dunn, M. G., Rae, W. J., and Holt, J. L., "Measurement and Analysis of Heat-Flux Data in a Turbine Stage: Part I: Description of Experimental Apparatus and Data Analysis; Part II: Discussion of Results and Comparison With Predictions," ASME JOURNAL OF ENGINEERING FOR GAS TURBINES AND POWER, Vol. 106, Jan. 1984, pp. 229–240.

7 Dunn, M. G., "Turbine Heat Flux Measurements: Influence of Slot Injection on Vane Trailing Edge Heat Transfer and Influence of Rotor on Vane Heat Transfer," ASME Paper No. 84-GT-175.

8 Dunn, M. G., Lukis, G., Urso, M., Heimenz, R. J., Orszulak, R., and Kay, N. J., "Instrumentation for Gas Turbine Research in Short-Duration Facilities," Aerospace Congress and Exposition, Long Beach, CA, Oct. 15–18, Paper No. 841504.

9 Rivir, R. B., Elrod, W. C., and Dunn, M. G., "Feasibility of the Application of a Two-Spot Laser Velocimeter to Measure Velocity and Turbulence in a Shock-Tube Driven Turbine Stage," Propulsion and Energetics Panel 65th Symposium, AGARD, Bergen, Norway, May 6–10, 1985.

10 Dunn, M. G., "Heat-Flux Measurements and Analysis for a Rotating Turbine Stage," Propulsion and Energetics Panel, 65th Symposium, AGARD, Bergen, Norway, May 6–10, 1985.

11 Dunn, M. G., "Heat-Flux Measurements for the Rotor of a Full-Stage Turbine: Part I, Time-Averaged Results," ASME Paper No. 86-GT-77.

12 Denton, J. D., and Singh, U. K., "Time Marching Methods for Turbomachinery Flow Calculation. Part I – Basic Principles and 20 Applications and 11 Three Dimensional Flows," *Application of Numerical Methods to Flow Calculations in Turbomachinery*, VKI Lecture Series 1979-7, 1979.

13 Denton, J. D., "An Improved Time Marching Method for Turbomachinery Flow Calculations," ASME Paper No. 82-GT-239, Apr. 1982.

14 *Handbook of Supersonic Aerodynamics*, NAVORD Report 1488, Vol. 5, 1953.

15 Bush, D. B., and Booth, T. C., Garrett Turbine Engine Company, Private communication, Apr. 3, 1985.

16 "Low-Aspect-Ratio Turbine Technology Program Final Report for Phase II," AFAPL Report 75-211701(2), Mar. 1977.

17 Wysong, R. R., Prince, T. C., Lenahan, D. T., et al., "Turbine Design System," AFAPL TR-78-92, Nov. 1978.

Laminar and Transitional Boundary Layer Structures in Accelerating Flow With Heat Transfer

K. Rued[1]

S. Wittig

Lehrstuhl und Institut fuer
Thermische Stroemungsmaschinen,
Universitaet Karlsruhe,
Karlsruhe, West Germany

The accurate prediction of heat transfer coefficients on cooled gas turbine blades requires consideration of various influence parameters. The present study continues previous work with special efforts to determine the separate effects of each of several parameters important in turbine flow. Heat transfer and boundary layer measurements were performed along a cooled flat plate with various freestream turbulence levels ($Tu = 1.6$–11 *percent*), *pressure gradients* ($k = 0$–6×10^{-6}), *and cooling intensities* ($T_w/T_\infty = 1.0$–0.53). *Whereas the majority of previously available results were obtained from adiabatic or only slightly heated surfaces, the present study is directed mainly toward application on highly cooled surfaces as found in gas turbine engines.*

Introduction

The accurate prediction of heat transfer coefficients on the external surfaces of highly cooled gas turbine blades is a dominant factor for reliable blade-cooling design. Numerical calculation procedures for predicting airfoil boundary layers and heat transfer along blade surfaces must consider various influence parameters such as freestream turbulence, pressure gradients, wall-to-freestream temperature ratio, surface roughness, and surface curvature. The development and application of such numerical codes, commonly based on finite difference techniques and/or integral methods [1], requires extensive and reliable experimental data to illustrate and quantify effects of the influence parameters both on heat transfer and on boundary layer structures.

Previous analytical and experimental studies, aimed at separating the effects of influence parameters for gas turbine flow, have concentrated on idealized, nearly isothermal flat surface measurements to investigate the influence of freestream turbulence and pressure gradients (primarily acceleration) on boundary layer and heat transfer development [2–8]. These studies indicate that the primary effect of an increase in freestream turbulence is the upstream displacement of the onset of transition. Negative pressure gradients (i.e., acceleration) are shown to stabilize the laminar boundary layer and they tend to counteract the effect of freestream turbulence. Thus acceleration may, depending on its strength, result in a delay of transition onset and in an increase of transition length. In addition to the influence of pressure gradients on boundary layer transition, relatively strong effects of such gradients on local laminar and turbulent heat transfer rates have also been observed. With respect to the influence of freestream turbulence, the effects are more pronounced in turbulent boundary layer regions than in laminar boundary layers. Laminar flow is only affected when the boundary layer is additionally submitted to favorable pressure gradients. Under these conditions heat transfer rates are slightly increased by freestream turbulence [4]. The effects of freestream turbulence on turbulent boundary layer profiles lead to slightly fuller profiles and higher turbulence levels resulting in higher momentum thicknesses, smaller form parameters and increased heat transfer as well as skin friction coefficients [3, 5, 6]. The effects are more evident when turbulent boundary layers of the same momentum thickness Reynolds number are compared. With respect to the influence of turbulence intensity at the same streamwise location, the effects are partially offset by upstream displacement of transition.

A more recent work [9] has provided fundamental insights on boundary layer development and heat transfer characteristics for flows with wall cooling added to high freestream turbulence and intense negative pressure gradients. This study has shown experimentally that boundary layer transition process and freestream turbulence effects in turbulent boundary layers are not changed by even strong wall cooling intensities. However, wall cooling itself produces an increase in local heat transfer rates, which is different in laminar and turbulent boundary layer flows.

In continuing this previous study, the present work has been directed toward acquisition of more detailed information on the transitional boundary layer, including the combined influence of freestream turbulence, pressure gradients (i.e., acceleration), and wall cooling. Special emphasis is placed on the laminar-turbulent transition process. The experiments described in this paper were performed at freestream conditions similar to those found in gas turbine applications.

Freestream velocities up to 150 m/s, temperature ratios $0.53 < T_w/T_\infty < 1.0$ and freestream turbulence levels of $0.016 < Tu < 0.11$ were chosen. The maximum pressure gradient

[1] Present address: Arizona State University, Department of Mechanical and Aerospace Engineering, Tempe, AZ, USA

Contributed by the Gas Turbine Division of THE AMERICAN SOCIETY OF MECHANICAL ENGINEERS and presented at the 31st International Gas Turbine Conference and Exhibit, Düsseldorf, Federal Republic of Germany, June 8–12, 1986. Manuscript received at ASME Headquarters January 20, 1986. Paper No. 86-GT-97.

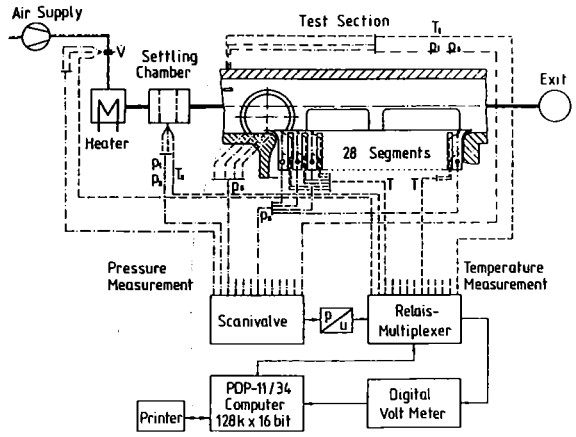

Fig. 1 Test section and instrumentation

(in terms of the parameter $k = \nu/u_\infty^2 \cdot du_\infty/dx$) used in the present work is $k = 6 \times 10^{-6}$.

Experimental Apparatus and Diagnostics

The test section used for the experimental analysis of the boundary layer and heat transfer characteristics is shown in Fig. 1. The test section itself consists of a 440 × 125 mm copper plate which is divided into 28 insulated segments. Each of the segments is cooled separately to ensure a constant plate surface temperature. The heat flux within the cooled segments is derived from one-dimensional heat condition analysis, i.e., from the temperature difference determined by thermocouple measurements in the segments. The results are supported by finite element heat conduction calculations and enthalpy balances within the boundary layer. The local Stanton number is readily obtained from the local heat flux. To ensure a laminar starting boundary layer, the leading edge, which is uncooled for the first 15 mm, has an elliptical profile, and suction of the entering boundary layer is applied. The two dimensionality and the laminar form of the starting boundary layer were confirmed by detailed profile measurements. Variation of the freestream turbulence is accomplished by calibrated turbulence grids located 170 mm upstream of the plate's leading edge [1].

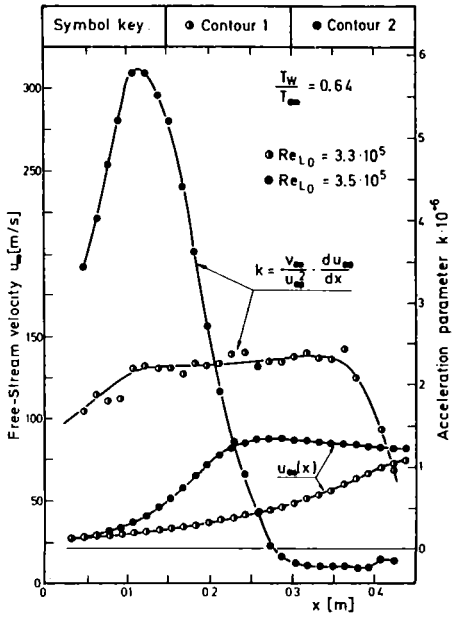

Fig. 2 Freestream velocity and acceleration parameter k (flow conditions 6 and 8, Table 1)

The freestream turbulence is determined by laser-Doppler anemometry as already described in detail in an earlier paper [10]. Pressure gradients along the plate are achieved by contoured upper channel walls. Two different acceleration parameter distributions of

$$k = \frac{\nu_\infty}{u_\infty^2} \cdot \frac{du_\infty}{dx} \tag{1}$$

were chosen as illustrated in Fig. 2. The strong variations of $k(x)$ with contour 2, which is the closer to actual gas turbine practice, are evident with k_{max} approximately 5.7×10^{-6}. Contour 1 produces smaller and more uniform acceleration parameters.

Nomenclature

c_f = skin friction coefficient = $2\tau_w/\rho_\infty \cdot u_\infty^2$
c_{f_0}, c'_{f_0} = skin friction coefficients without freestream turbulence
H_{12} = shape factor = δ_1/δ_2
L_e^u = dissipation length = $-(\overline{u'^2})^{3/2}/[u \cdot (d/dx)(\overline{u'^2})]$
k = acceleration parameter
k_{max} = characteristic value of k for contour 2
Pr = molecular Prandtl number
q = heat flux
Re_x = Reynolds number in $u_\infty \cdot x/\nu_\infty$
Re_2 = Reynolds number based on momentum thickness = $u_\infty \cdot \delta_2/\nu_\infty$
$Re_{L,0}$ = Reynolds number based on plate length and freestream conditions at the leading edge
St = Stanton number = $q_w/\rho_\infty \cdot U_\infty \cdot c_p \cdot (T_{t\infty} - T_w)$, based on local freestream conditions; c_p = specific heat
T = temperature
Tu = local freestream turbulence = $\sqrt{\frac{1}{3}(\overline{u'^2} + \overline{v'^2} + \overline{w'^2})}/u_\infty$
Tu_0 = freestream turbulence at the leading edge
u = velocity
u', v', w' = velocity fluctuations (u', v' = measured, $v' = w'$)
u_τ = skin friction velocity = $\sqrt{\tau_w/\rho_w}$
x = distance from the leading edge
y = distance from the wall
y^+ = normalized wall distance = $y \cdot u_\tau/\nu_w$
u^+ = u/u_τ
ρ = density
δ = boundary layer thickness
δ_2 = momentum thickness = $\int_0^\delta (\rho \cdot u)/(\rho_\infty \cdot u_\infty) \cdot (1 - u/u_\infty) dy$
δ_1 = displacement thickness = $\int_0^\delta (1 - (\rho \cdot u)/(\rho_\infty \cdot u_\infty)) dy$
$\delta_1^u, \delta_2^u, H_{12}^u$ = kinematic values of δ_1, δ_2, H_{12} (ρ = const)
ν = viscosity
ζ = uncooled starting length of plate

Subscripts

∞ = freestream
w = wall
t = total

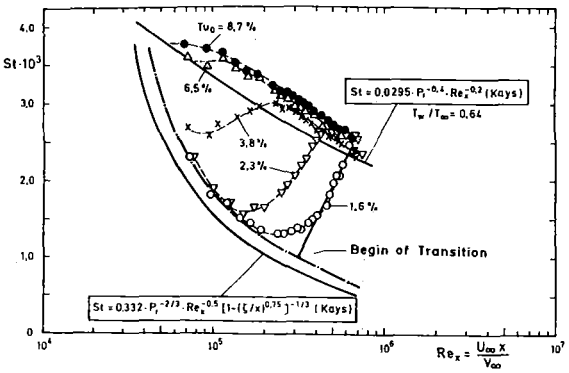

Fig. 3 Influence of freestream turbulence on heat transfer and boundary layer transition (flow condition 2-4, Table 1)

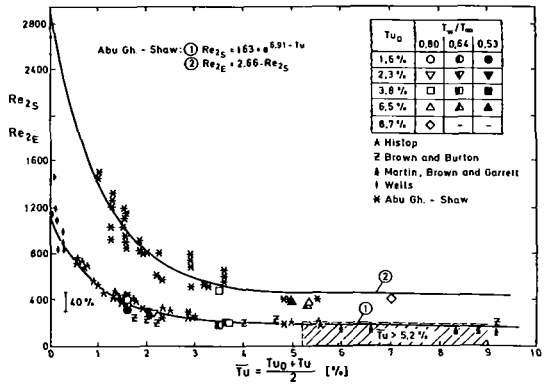

Fig. 4 Momentum thickness Reynolds numbers at the beginning and end of transition

Detailed boundary layer measurements were obtained in planes located 120, 220, 320, and 420 mm from the leading edge. Both pitot tube and total temperature measurements were made. The pitot tube total pressure profile was corrected following McMillan [11]. Turbulent skin friction was derived using the Preston technique [12] and additionally utilizing the law of the wall as shown in equation (2)

$$\frac{u}{u_\tau}=\frac{1}{0.41}\ln\left(\frac{y\cdot u_\tau}{\nu}\right)+5.1;\qquad u_\tau=\sqrt{\tau_w/\rho} \tag{2}$$

Only small discrepancies of less than 3 percent between the two techniques were observed. For the cooled plate in a hot gas flow, properties were calculated using the reference temperature scheme following Holmes and Luxton [13]. The application of the reference temperature for skin friction determination is confirmed by optical measurements of velocity profiles and turbulence structures in highly cooled turbulent boundary layers [14, 15].

Data acquisition is accomplished with the aid of a Scanivalve and Relay-multiplexer, both controlled by a minicomputer (PDP-11/34) as indicated in Fig. 1. More detailed information about the experimental setup and measurement techniques is available in [1].

Experimental Conditions

The experimental conditions imposed in the present study are summarized in Table 1. The wall temperature was kept nearly constant, and the freestream temperature was adjusted to vary the surface-to-freestream temperature ratio. Turbulence intensities were imposed on each of the freestream conditions by utilizing different turbulence grids with cylindrical bars. The resulting intensities Tu_0 varied from 1.6 to 11 percent at the leading edge of the plate. The turbulence decay behind the grids agreed fairly well with those observed by Baines and Peterson for constant freestream velocity flow [16], whereas in accelerating flow the decay was more intense. Detailed information about the present freestream turbulence structures including a check of turbulence isotropy has already been given [1, 9].

Results and Discussion

Heat Transfer and Boundary Layer Transition. The heat transfer measurements without pressure gradient reveal the influence of freestream turbulence and wall cooling on boundary layer transition and heat transfer rates. The results are shown in Figs. 3 and 4. Figure 3 shows the variation of transition onset induced by different freestream turbulence intensities for a highly cooled boundary layer ($T_w/T_\infty = 0.64$). The onset of transition is defined as indicated for $Tu_0 = 1.6$ percent. Increasing the turbulence level Tu_0 up to 8.7 percent leads to an upstream displacement of transition toward the leading edge. In the turbulent boundary layer regions tendencies toward higher Stanton numbers can also be observed, whereas in the unaccelerated laminar flow (see $Tu_0 = 1.6$ and 2.3 percent) turbulence effects seem to be negligible. In turbulent regions the effects at local streamwise position are partially offset by the upstream movement of transition. Because of this, information is best derived by comparing turbulent boundary layers at the same value of a boundary layer parameter, such as momentum thickness Reynolds number. Such comparison will be shown in Figs. 10–12 below.

For determining the additional effects of wall cooling on boundary layer transition, systematic comparisons were performed with transition data obtained by previous investigations in adiabatic flow (as summarized in [2]). In terms of the local Reynolds number Re_x, based on streamwise position and freestream viscosity, transition was observed to begin at the same value of Re_x in both cooled and uncooled boundary layers at corresponding values of freestream turbulence (compare [1]).

Figure 4 illustrates boundary layer transition data more generally by analyzing Reynolds numbers based on momentum thickness at both the beginnning and end of transition. The momentum thickness Reynolds numbers were derived from laminar boundary layer measurements as described in [1]. The new results, including wall cooling, show close agreement with available transition data for isothermal flows obtained by Hislop, Brown and Burton, Martin et al., Wells, and Abu-Ghannam and Shaw (compare [2]). As no additional delay of boundary layer transition induced by wall cooling can be observed, it can be concluded that freestream turbulence is dominant over the stabilizing effect of wall cooling. The stabilizing effect of cooling is postulated by boundary layer stability theory, at least in flows without freestream turbulence. At high turbulence intensities (above 5 percent), onset of transition occurs very close to the leading edge at very low Reynolds numbers. In contrast, the previous investigations included in Fig. 4 indicate existence of a minimum Reynolds number for the beginning of transition of about $Re_2 \approx 160$. It can be hypothesized that this different result in the present investigations is associated with the very thin leading edge of the present test plate (2 mm thick), providing the beginning laminar boundary layer with greater sensitivity to disturbances from freestream turbulence. The previous investigations, in contrast, were performed with thick leading edges, which tend to impose a stabilizing effect on the starting boundary layer through the superposed acceleration of the flow around the test plate nose. It should be noted that thin leading edges are very often a typical feature of actual gas turbine flow.

Influence of Wall Cooling. Figure 3 also compares the measured Stanton numbers at $T_w/T_\infty = 0.64$ with relations given by Kays [17] for laminar and turbulent heat transfer in

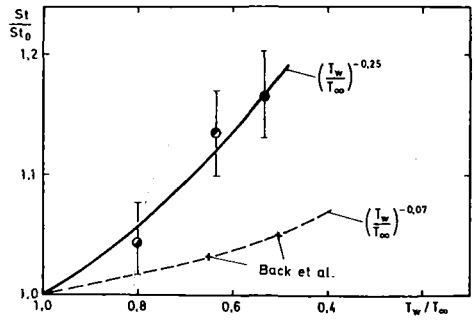

Fig. 5 Influence of wall cooling on laminar heat transfer

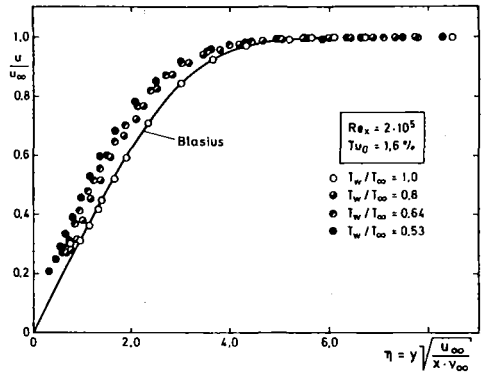

Fig. 6 Laminar boundary layer profiles for varying cooling intensities

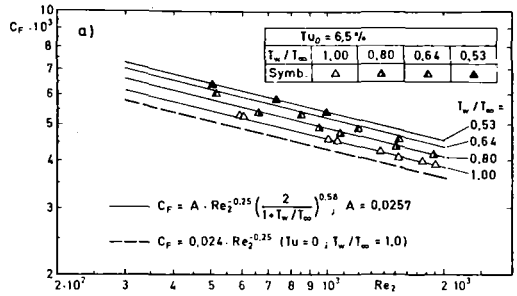

Fig. 7 The influence of wall cooling on turbulent skin friction coefficients

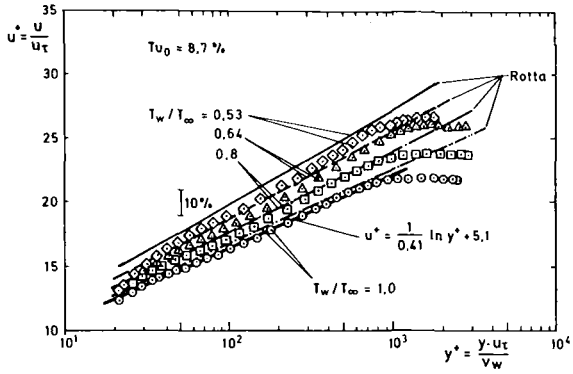

Fig. 8 The influence of wall cooling on the logarithmic law of the wall

nearly isothermal flow. For laminar boundary layers the measured Stanton numbers with wall cooling are higher by approximately 16 percent, a relatively large wall-cooling effect which is also confirmed at both higher and lower temperature ratios ($T_w/T_\infty = 0.8$ and 0.53, see also Fig. 5). This result is also supported by the measurements with pressure gradient [9]. In analyzing these effects by modifying Kays' relation (see also [9]) the temperature dependency of laminar heat transfer was derived as shown in Fig. 5. The results of the measurements agree fairly well with a cooling dependency described by the factor $(T_w/T_\infty)^{-0.25}$, whereas the information available from literature, e.g., [20], based exclusively on theoretical considerations, suggests a smaller dependency proportional to $(T_w/T_\infty)^{-0.07}$ as shown in Fig. 5. It should be noted that applying the Eckert reference temperature scheme on laminar heat transfer correlations leads to the same smaller temperature dependency and therefore also underpredicts the experimentally obtained wall cooling effect. The unexpected high laminar heat transfer increase due to wall cooling is likely caused by property variations producing modifications in the structure of the boundary layer profiles. Figure 6 illustrates such structural influences of the temperature ratio T_w/T_∞ on laminar velocity profiles. The data are plotted in normalized Blasius coordinates with temperature ratios varying from $T_w/T_\infty = 1.0$ to 0.53. As can be seen from Fig. 6, the velocity profiles are changed to a fuller shape by increased cooling intensity. This effect is accompanied by steeper wall gradients and a systematic decay of the kinematic profile shape parameter H_{12}^u from $H_{12}^u = 2.55$ for the isothermal flow to $H_{12}^u = 2.39$ for the case with the most intense wall cooling ($T_w/T_\infty = 0.53$). The steeper wall gradients are responsible for higher skin friction and heat transfer rates. It should be noted that applying the Levy transformation method [19], as described in [1], leads again to a full agreement with the isothermal Blasius solution for profiles at all different temperature ratios.

However, utilizing a mean viscosity to calculate the η coordinate (Fig. 6), as suggested by the Eckert reference temperature scheme, still reveals discrepancies between the profile measurements and the Blasius solution. This discrepancy is consistent with the observation of Fig. 5, where the Eckert reference temperature method yields too small increases in heat transfer rates.

Experimental results revealing the influence of wall cooling on turbulent boundary layers are presented in Figs. 7 and 8. Figure 7 quantifies the temperature influence on turbulent skin friction coefficients for flows with constant freestream turbulence. The data are plotted against momentum thickness Reynolds numbers. A steady increase of skin friction coefficients with decreasing T_w/T_∞ was observed, with a maximum measured increase of 18 percent when temperature ratio was reduced to $T_w/T_\infty = 0.53$. It should be noted that these cooling effects appear independent of the level of freestream turbulence, and this was confirmed by the measurements at lower and higher turbulence intensities. Utilizing the well-known relation for c_f in isothermal flow (where A is a factor dependent on turbulence intensity)

$$C_f = A \cdot \mathrm{Re}_2^{-0.25} \tag{3}$$

and applying a reference temperature scheme as suggested by Back and Cuffel [18] yields the following cooling dependency of skin friction coefficients

$$\frac{C_f}{C_{f(T_w/T_\infty = 1.0)}}\bigg|_{\mathrm{Re}_2 = \mathrm{const}} = \left(\frac{2}{1 + T_w/T_\infty}\right)^{0.58} \tag{4}$$

This theoretical result, presented in Fig. 7 by the solid lines, shows close agreement with the experimental results. Equation (4), therefore, provides a simple method for calculating cooling effects. In addition, it can also be used for predicting the influence of wall cooling on heat transfer rates, because the Reynolds-analogy factor, $2 \cdot \mathrm{St}/c_f$, was observed to be constant within a mean value of 1.1. The analogy factors, published in an earlier paper [9], are independent of both freestream turbulence and wall cooling intensity.

Boundary layer profiles corresponding to the skin friction coefficients of Fig. 7 are presented in Fig. 8. They describe the influence of varying wall cooling on the logarithmic law of the

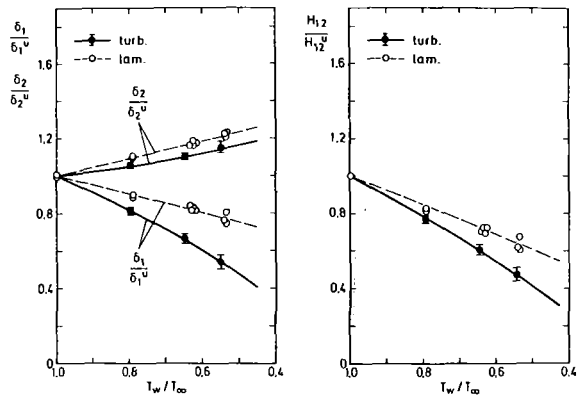

Fig. 9 Integral boundary layer parameters at varying cooling intensities

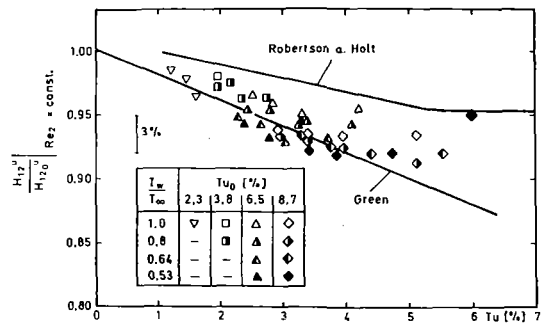

Fig. 10 Shape factors with relation to the influence of freestream turbulence and wall cooling

wall. The main effect of wall cooling is higher velocity values at the same normalized wall distance y^+.

Additionally, the logarithmic region seems to begin at greater distances from the wall and the profile gradients in the log law region are also slightly increased. In comparing these profiles with the analytical solution of Rotta [21] for the law of the wall, quite good agreement is observed as shown in the figure. Rotta's solution is based on the assumption that only the property variations across the boundary layer are of importance and therefore no changes in turbulence structure are responsible for the wall cooling effects. The good agreement with the present experimental results confirms this assumption.

Figure 9 provides a final survey on the influence of cooling on integral boundary layer profile parameters such as displacement thickness, momentum thickness, and shape factors. In Fig. 9 these parameters are normalized by their kinematic, i.e., incompressible, values. The data reveal a growth of the momentum thickness with reducing temperature ratio. In conjunction with this increase of momentum thickness, the displacement thickness decreases strongly, finally leading to a decay of the shape factor H_{12}/H_{12}^u. It should be mentioned that despite quite fundamental differences between laminar and turbulent boundary layer structures, the property influences due to wall cooling on the momentum thickness are quite similar in both cases (Fig. 9).

Influence of Freestream Turbulence. Detailed information on the influence of freestream turbulence on turbulent boundary layer characteristics was derived from careful boundary layer measurements as shown in Figs. 10–12.

The investigations were performed both in isothermal and nonisothermal flows in order to clarify the additional effect of superposed wall cooling. The initially measured boundary layer profiles revealed a more full shape at higher turbulence intensities, resulting in steeper profile gradients close to the

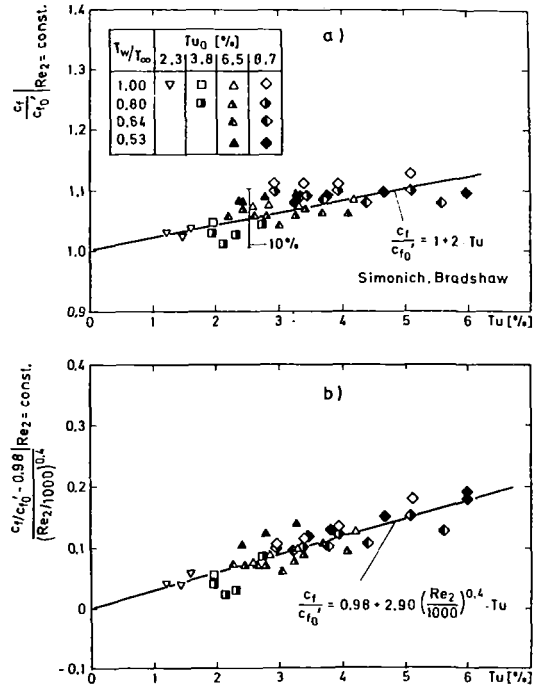

Fig. 11 Turbulent skin friction increase with freestream turbulence, considering Reynolds number effects ($Re_2 = 500$–2000)

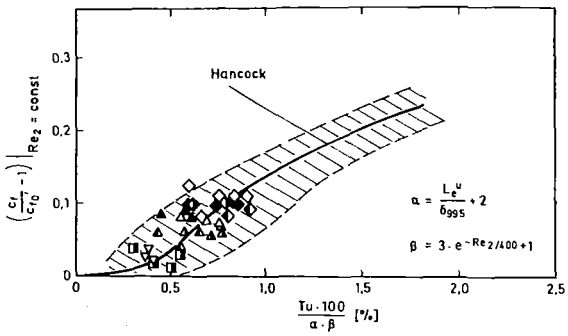

Fig. 12 The combined influence of freestream turbulence, length scale, and Reynolds number on turbulent skin friction coefficients

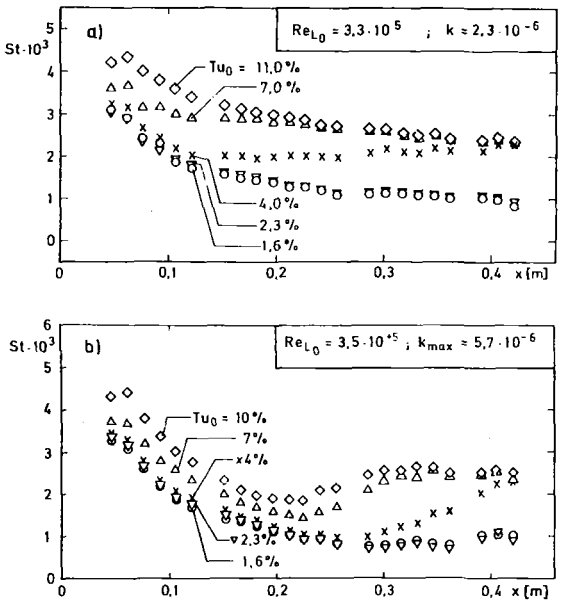

Fig. 13 Freestream turbulence effects in moderately and highly accelerating flows ($T_w/T_\infty = 0.64$; flow conditions 6 and 8, Table 1)

wall and in increased boundary layer thicknesses as well. In logarithmic u^+, y^+ coordinates, the logarithmic law of the wall is unaffected by freestream turbulence according to results of previous investigations for isothermal flows (see for instance [3, 5, 29]). The influence of freestream turbulence was restricted to a reduction of the size of the wake region at the outer edge of the boundary layer. This was observed in flows both with and without wall cooling and in both temperature and velocity profiles [1, 6].

The deformation of the turbulent velocity profile induced by freestream turbulence can be quantitatively expressed by normalizing the kinematic shape factors H_{12}^u with corresponding values for zero freestream turbulence flow, as shown in Fig. 10. The data in Fig. 10 include all the measured turbulence levels and temperature ratios in order to derive additional effects of wall cooling. The shape factors for the boundary layer without freestream turbulence were taken from the experimental results of Murlis [22]. The effects of freestream turbulence are reflected in a decrease of the shape factor, which is correlated by the analytical solution of Green [23] for local turbulence levels up to 4-5 percent. Above 4 percent turbulence the data show an asymptotic tendency toward a constant value of $H_{12}^u/H_{12,0}^u \approx 0.93$. This confirms the suggestion of Robertson and Holt [24], also shown in Fig. 10, and indicates that the end of the influence of freestream turbulence on profile deformation has been reached in the present experiments. It should be emphasized that the shape factors do not reflect an independent influence of wall cooling, which leads to the conclusion that freestream turbulence produces the same changes in profile shape with and without cooling.

In comparing turbulent skin friction for the boundary layer profiles with momentum thickness Reynolds numbers over the range 500–2000, typical for those encountered in gas turbine applications, the influence of freestream turbulence intensity as given by Simonich and Bradshaw [5] is largely confirmed, as shown in Fig. 11(*a*). C_{f_0} is the temperature-corrected skin friction using equation (4) combined with

$$C_{f_0} = 0.024 \cdot \mathrm{Re}_2^{-0.25} \tag{5}$$

C_{f_0} for turbulence free main flow was derived from averaging the nearly identical data of Murlis [22], Wieghard (see [22]), and Coles [25]. As our detailed LDF measurements [15] confirm the validity of the applied temperature correction for reference skin friction, no additional influence of wall cooling is evident (Fig. 11).

Following the analysis of McDonald and Kreskovsky [26] and the reasonings of Hancock and Bradshaw ([27, 28], compare also [3]) additional Reynolds number and length scale effects should be considered in determining the influence of freestream turbulence on turbulent boundary layers.

For low Reynolds numbers, $\mathrm{Re}_2 < 5000$ as for the present study, Reynolds number influences are expected to reduce turbulence effects. For taking such additional influences into account, a nonlinear Reynolds number dependent correction for the measured rates of skin friction increase, derived by Blair [3], was applied as shown in Fig. 11(*b*). In comparison with Fig. 11(*a*) the data scatter has been significantly reduced by incorporating the Re_2 dependency, which can be considered as a confirmation of the existence of Reynolds number effects.

To further explore the influence of freestream turbulence structure, characteristic dissipation length scales L_e^u were derived from the decay of the u component of freestream turbulence. Following Bradshaw [28], the impact of freestream turbulence should reach a maximum when L_e^u is in the order of the boundary layer thickness δ, whereas for higher ratios of L_e^u/δ the effects would be expected to diminish. The present data (compare also [1]) cover a range of $1.0 < L_e^u/\delta < 3.0$. Therefore, length scale influences might also be expected.

Hancock [27, 28] developed a correlation of these length scale effects on skin friction increase. Blair [29] improved the correlation by combining length scale and Reynolds number effects; the latter is used in Fig. 12 for depicting the skin friction coefficients of the present experiments. The agreement between the present results and Hancock's curve is quite acceptable.

The present results fit well within the scatter of all previous data, which are indicated by the shaded section around the correlation curve (compare [29]). The agreement was, however, primarily achieved by the included Reynolds number correction factor β. Neglecting this factor (i.e., $\beta = 1$ as for very high Reynolds numbers) the agreement was worse. This leads to the conclusion that for the present range of Reynolds numbers up to $\mathrm{Re}_2 = 2000$, Reynolds number effects dominate over length scale effects with respect to the influence of freestream turbulence. Therefore the analytical solution, derived in Fig. 11(*b*), provides a simpler yet adequate and therefore preferred method for describing freestream turbulence effects on skin friction coefficients in low Reynolds number flows with at least $\mathrm{Re}_2 < 2000$.

For turbulent heat transfer, the same turbulence effects including Reynolds number and length scale dependencies as shown for skin friction coefficients are to be expected. This conclusion is based on the Reynolds analogy, as previously mentioned. The analogy factors revealed a lack of dependency on both freestream turbulence and cooling intensity [9].

Pressure Gradient Effects. In analyzing the effects of strong negative pressure gradients, systematic comparisons of flow with different acceleration intensities were performed. From the results, which were already published earlier [9], it could be seen that flow acceleration leads to a delayed boundary transition and an increased transition length. Additionally laminar heat transfer rates are increased, whereas in turbulent boundary layers a decrease of the local Stanton numbers was observed. The reduced Stanton numbers in turbulent flow can be explained by the fact that acceleration has a damping effect on boundary layer turbulence intensity.

The results presented in this paper deal with special aspects of heat transfer and boundary layer development characteristics arising from the combination of varying freestream turbulence levels and very high acceleration intensities as found in the gas turbine application. To this purpose Fig. 13 shows heat transfer results for two different flows achieved by employing the two contoured upper walls as shown in Fig. 2. Stanton numbers are defined using local freestream conditions. Figure 13(*a*) is associated with contour 1 and represents a flow situation with moderate constant acceleration parameters, $k(x) \approx 2.3 \times 10^{-6} \approx \text{const}$. Figure 13(*b*) is associated with contour 2 and the highest acceleration intensities ($k_{\max} = 5.7 \times 10^{-6}$).

The inlet conditions at the leading edge of the plate are nearly the same in both flow situations ($\mathrm{Re}_{L,0} = 3.3 \times 10^5$ and 3.5×10^5). In comparing Fig. 13(*a*) and Fig. 13(*b*), substantial differences in heat transfer distributions and boundary layer development can be observed. Figure 13(*a*) confirms the well-known effects from previous studies with relatively weak acceleration. For example, the upstream displacement of boundary layer transition with increasing freestream turbulence (see, e.g., [4] and [7]) can be seen. Furthermore, the results of Fig. 13(*a*) confirm that freestream turbulence in accelerating flow also can produce, depending on the relative strength of turbulence and pressure gradient intensity, increases in laminar heat transfer rates. The results for $Tu_0 = 1.6$ and 4.0 percent at $x < 0.12$ m show an increase in Stanton numbers of 9 to 18 percent. Despite these moderately higher heat transfer rates the flow can still be classified as laminar. In contrast, totally different heat transfer and boundary layer characteristics were obtained for the highest acceleration as shown in Fig. 13(*b*). Even at high turbulence intensities, the transition is delayed. For lower turbulence levels up to 4 percent, transition is sup-

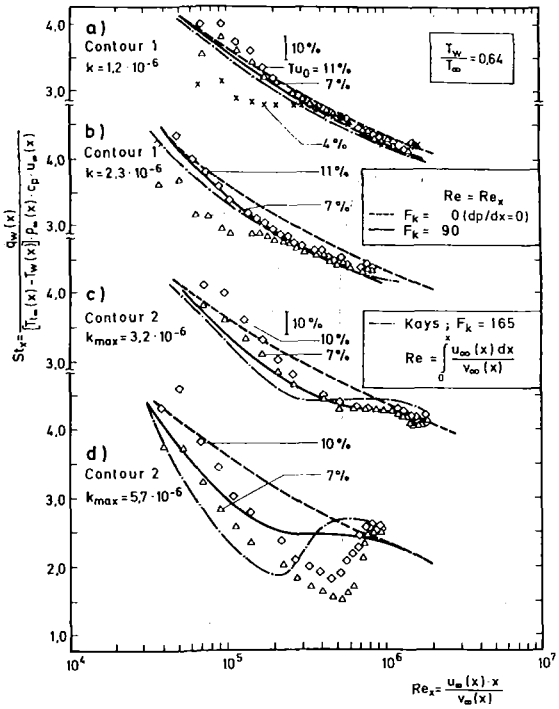

Fig. 14 Analytical correlations for predicting heat transfer in accelerated turbulent boundary layers

pressed altogether during acceleration ($x<0.27$ m) and laminar heat transfer is observed for $Tu_0=1.6$, 2.3, and 4 percent. Despite a significant increase in Stanton numbers with higher turbulence levels (up to 100 percent), the heat transfer even for $Tu_0=7$ and 10 percent shows similarities to laminar flow. However, as the boundary layer is strongly affected by freestream turbulence producing a definite transitional character, it cannot be classified, in our opinion, as laminar, despite its apparent overall behavior. Similar effects have been observed in cascade flows [30]; however, they were interpreted as a rise in laminar heat transfer. In analyzing this situation further, it is found that in addition to high freestream turbulence and acceleration intensities, the distribution of acceleration along the surface is very important in establishing the character of the boundary layer. The downstream increasing acceleration due to contour 2 prevents a continuously progressing transition process as was always observed in the zero pressure gradient or constant acceleration cases. It should be noted that these complex boundary layer situations lead to pronounced difficulties in applying numerical codes with existing turbulence models.

Turbulent Heat Transfer Correlations. The results of the present study provide the opportunity for testing and improving existing heat transfer correlations for turbulent boundary layers with pressure gradient. The correlation applied here is based on the analytically derived solution presented by Kays [17]

$$\mathrm{St}=0.0295\cdot\mathrm{Pr}^{-0.4}\cdot\mathrm{Re}^{-0.2}\cdot\left(1-F_k\cdot\frac{k(x)}{\mathrm{St}}\right)\cdot F_T \tag{6}$$

F_k determines the actual pressure gradient influence and F_T reflects the heat transfer increase due to wall cooling. Following Kays [17], an integral Reynolds number

$$\mathrm{Re}=\int_0^x\frac{u_\infty(x)dx}{\nu_\infty(x)} \tag{7}$$

and a value $F_k=165$ are applied and a comparison of this correlation with the present experimental data is shown in Fig. 14. The data were obtained with the two contours at different

Table 1 Flow conditions

No.	dp/dx	$T_{\infty,0}$ [K]	$T_w/T_{\infty,0}$ [−]	$u_{\infty,0}$ [m/s]	$\mathrm{Re}_{L,0}\times10^{-6}$ [−]
1	0.0	350	1.0	40	0.8
2	0.0	378	0.8	47	0.9
3	0.0	478	0.64	55	0.65
4	0.0	570	0.53	38	0.36
Contour 1 $k(x)=$const					
5	$k_{\max}=1.2\times10^{-6}$	466	0.64	49	0.64
6	2.3×10^{-6}	480	0.64	27	0.33
Contour 2 $k(x)=$const					
7	$k_{\max}=3.2\times10^{-6}$	463	0.64	48	0.65
8	5.7×10^{-6}	467	0.64	27	0.35

plate inlet Reynolds numbers for a constant cooling intensity with $T_w/T_\infty=0.64$ (flow conditions 5–8, Table 1). Corresponding to this temperature ratio, $F_T=1.08$ as derived from the zero pressure gradient flow in Fig. 3.

Even though developed for turbulent flow only, the correlation predicts the present results reasonably accurately over the entire length for the flows of contour 1, especially for the higher values of turbulence intensity (Figs. 14(a) and 14(b)). In Fig. 14(c), however, with contour 2, the correlation underpredicts heat transfer on the upstream portion of the surface even for the lower values of turbulence intensity. The underprediction is magnified considerably at the higher acceleration conditions with contour 2 (Fig. 4(d)). This tendency to overestimate the turbulence damping effects of high freestream acceleration is probably related to the fact that the correlation does not include any influence of freestream turbulence. Following this reasoning, a modification of the correlation could be achieved for the additional influence of freestream turbulence and for an easier handling of equation (6) by substituting the Reynolds number of equation (7) together with a new determination of the value of F_k. The Reynolds number is now defined by local values

$$\mathrm{Re}=\mathrm{Re}_x=\frac{u_\infty(x)\cdot x}{\nu_\infty(x)} \tag{8}$$

which can easily be calculated, and F_k was uniformly determined as $F_k=90$ (by the best-fit method) corresponding to the heat transfer data for the flows with high freestream turbulence and varying pressure gradient intensity. In general over the range of conditions shown in Fig. 14, this procedure results in improved agreement between the measurements and predictions, as shown by the solid lines. It is well to repeat that wall cooling proved to have no additional influence on the boundary layer development (compare [1, 9]). Therefore equation (6) provided the same accuracy as shown in Fig. 14 in predicting the heat transfer rates for the corresponding flow situations at higher and lower cooling intensities.

Acknowledgments

Thanks are due to Dr.-Ing. K.-H. Sill, Dipl.-Ing. S. Eriksen, and Dr.-Ing. G. Scheuerer for continuous discussions. Financial support was provided by the "Forschungsvereinigung fuer Verbrennungskraftmaschinen (FVV)." Dr.-Ing. D. Mukherjee was actively involved in initiating the program.

Thanks are also due to Prof. D. E. Metzger Ph.D. for his assistance in composing this paper.

References

1 Rued, K. P., "Transitionale Grenzchichten unter dem Einfluss hoher Freistromturbulenz, intensiver Wandkuehlung und starker Druckgradienten in Heissgasstroemungen," Dissertation, Universitaet Karlsruhe, 1985.

2 Abu-Ghannam, B. J., and Shaw, R., "Natural Transition of Boundary Layers—The Effects of Turbulence, Pressure Gradient and Flow History," TN, Turbomachinery Section, Department of Mechanical Engineering, University of Liverpool, Apr. 1979.

3 Blair, M. F., and Werle, M. J., "The Influence of Free-Stream Turbulence on the Zero Pressure Gradient Fully Turbulent Boundary Layer," United Technologies Research Center, East Hartford, CT, Rept. No. R80-914388-17, 1981.

4 Junkhan, G. H., and Serovy, G. K., "Effects of Free-Stream Turbulence and Pressure Gradient on Flat-Plate Boundary Layer Velocity Profiles and on Heat Transfer," ASME *Journal of Heat Transfer*, Vol. 89, May 1967.

5 Simonich, J. C., and Bradshaw, P., "Effect of Free-Stream Turbulence on Heat Transfer Through a Turbulent Boundary Layer," ASME *Journal of Heat Transfer*, Vol. 100, 1978, pp. 571–677.

6 Rued, K. P., Sill, K. H., and Wittig, S., "Einfluss der Freistromturbulenz auf den Waermeuebergang an stark gekuehlten Oberflaechen," *Thermische Stroemungsmaschinen '83*, VDI-Berichte No. 487, VDI-Verlag, 1983, pp. 171–180.

7 Blair, M. F., "Influence of Free-Stream Turbulence on Boundary Layer Transition in Favorable Pressure Gradients," ASME Paper No. 82-GT-4.

8 Turner, A. B., "Heat Transfer Measurements on a Gas Turbine Blade," *J. Mech. Eng. Sci.*, Vol. 13, No. 1, 1971.

9 Rued, K. P., and Wittig, S., "Free-Stream Turbulence and Pressure Gradient Effects on Heat Transfer and Boundary Layer Development on Highly Cooled Surfaces," ASME JOURNAL OF ENGINEERING FOR GAS TURBINES AND POWER, Vol. 107, Jan. 1984, pp. 54–59.

10 Eriksen, S., Wittig, S., Sakbani, K., and Rued, K., "Comparison of Laser-Doppler-, Laser-Dual-Focus- and Probe-Measurements in Laminar and Fully Turbulent Boundary Layers," *Proceedings of Int. Symposium on Application of Laser-Doppler Anemometry to Fluid Mechanics*, Lisbon, July 1982.

11 McMillan, F. A., "Experiments on Pitot Tubes in Shear Flow," Gt. Brit. ARC Rep. and Mem. 3028, London, 1959.

12 Patel, V. C., "Calibration of Preston-Tube and Limitations on Its Use in Pressure Gradients," *J. Fluid Mech.*, Vol. 23, Part 1, pp. 285–298.

13 Holmes, W. E., and Luxton, R. E., "Measurement of Turbulent Skin-Friction by a Preston Tube in the Presence of Heat Transfer," *J. Mech. Eng. Science*, Vol. 9, No. 3, 1967.

14 Eriksen, S., Wittig, S., and Dullenkopf, K., "The Application of LDA and LDF Anemometry to the Study of Boundary Layer Transport Properties Under Gas Turbine Conditions," presented at the Second Symposium on Application of Laser Anemometry to Fluid Mechanics, Lisbon, Portugal, July 1984.

15 Eriksen, S., Wittig, S., and Rued, K. P., "Optical Measurements of the Transport Properties in a Highly Cooled Turbulent Boundary Layer at Low Reynolds Number," *Proc. 4th Turbulent Shear Flow Conference*, Karlsruhe, W. G., 1983.

16 Baines, W. D., and Peterson, E. G., "An Investigation of Flow Through Screens," *Trans. ASME*, 1951, Paper No. 50-A-23.

17 Kays, W. M., *Convective Heat and Mass Transfer*, 1st ed., McGraw-Hill, New York, 1966.

18 Back, L. H., Cuffel, R. F., and Massier, P. F., "Effect of Wall Cooling on the Mean Structure of a Turbulent Boundary Layer in Low Speed Gas Flow," *Int. J. Heat Mass Transfer*, Vol. 13, 1970, pp. 1029–1047.

19 Levy, S., "Effect of Large Temperature Changes (Including Viscous Heating) Upon Laminar Boundary Layers With Variable Free-Stream Velocity," *Journal of the Aeronautical Sciences*, Vol. 21, No. 7, July 1954, pp. 459–472.

20 Back, L. H., Cuffel, R. F., and Massier, P. F., "Laminar, Transition, and Turbulent Boundary Layer Heat Transfer Measurement With Wall Cooling in Turbulent Air Flow Through a Tube," ASME *Journal of Heat Transfer*, 1969, pp. 477–487.

21 Rotta, J. C., "Ueber den Einfluss der Mach'schen Zahl und des Waermeuebergangs auf das Wandgesetz turbulenter Stroemung," *Zeitschrift der Flugwiss.*, Vol. 7, No. 9, 1959, pp. 264–274.

22 Murlis, B. J., "The Structure of a Turbulent Boundary Layer at Low Reynolds Number," Ph.D. thesis, Department of Aeronautics, Imperial College of Science and Technology, University of London, June 1975.

23 Green, J. E., "On the Influence of Free Stream Turbulence on a Turbulent Boundary Layer, as It Relates to Wind Tunnel Testing at Subsonic Speeds," AGARD Report 602, 1973.

24 Robertson, J. M., and Holt, C. F., "Stream Turbulence Effects on Turbulent Boundary Layers," ASCE *J. Hydraulics Div.*, Vol. 98, HY6, 1972.

25 Coles, D., "The Turbulent Boundary Layer in a Compressible Fluid," *The Physics of Fluid*, Vol. 7, No. 9, 1964.

26 McDonald, H., and Kreskovsky, J. P., "Effect of Free Stream Turbulence on the Turbulent Boundary Layer," *Int. J. Heat Mass Transfer*, Vol. 17, 1974, pp. 705–716.

27 Hancock, P. E., and Bradshaw, P., "The Effect of Free Stream Turbulence on Turbulent Boundary Layers," *J. Fluids Eng.*, Vol. 105, 1983, pp. 284–289.

28 Bradshaw, P., "Effects of Free-Stream Turbulence on Turbulent Shear Layers," Imperial College Aero Report 74-10, and ARC 35648, 1974.

29 Blair, M. F., "Influence of Free-Stream Turbulence on Turbulent Boundary Layer Heat Transfer and Mean Profile Development: Parts 1 and 2," ASME *Journal of Heat Transfer*, Vol. 105, Feb. 1983.

30 Krisnamoorthy, V., "Effect of Turbulence on Heat Transfer in a Laminar and Turbulent Boundary Layer Over a Gas Turbine Blade," ASME Paper No. 82-GT-146.

Systematic Study of Film Cooling With a Three-Dimensional Calculation Procedure

A. O. Demuren

W. Rodi

B. Schönung

Institute of Hydromechanics,
University of Karlsruhe,
Karlsruhe, Federal Republic of Germany

The present paper describes three-dimensional calculations of film cooling by injection from a single row of holes. A systematic study of the influence of different parameters on the cooling effectiveness has been carried out. Twenty-seven test cases have been calculated, varying the injection angle ($\alpha = 10/45/90$ deg), the relative spacing ($s/D = 1.5/3/5$) and the blowing rate ($M = 0.5/1/2$) for the same mainstream conditions. The governing three-dimensional equations are solved by a finite volume method. The turbulent stresses and heat fluxes are obtained from a k–ϵ model modified to account for nonisotropic eddy viscosities and diffusivities. Examples of predicted velocity and temperature distributions are presented and compared with available experimental data. For all the test cases, the laterally averaged cooling effectiveness is given. On the whole, the agreement with experiments is fairly good, even though there are discrepancies about details in some of the cases. The influence of the individual parameters on the film cooling effectiveness is predicted correctly in all cases. This influence is discussed in some detail and the parameter combination with the best overall cooling performance is identified.

Introduction

The continuing efforts to increase the efficiency of gas turbines has resulted in higher and higher temperatures at the inlet to the turbine section. Under such circumstances, a reasonable lifetime of the turbine blades can be ensured only when some means of protection is provided for them. Especially in the initial stages with particularly high temperatures of the gas stream, convection cooling is often not sufficient and the exposed blade surfaces can be kept below critical temperatures only by means of film cooling. In many film cooling applications, design considerations prevent the use of continuous slots for the introduction of the coolant. Discrete holes or slots with discontinuities are therefore used for injection. A typical film cooling configuration is shown in Fig. 1. The individual jets emerging from the discrete openings interact with the oncoming flow, which is basically two dimensional, generating thereby a strongly three-dimensional flow field near the injection. This field is fundamentally different from that resulting from a continuous slot injection. The film cooling effectiveness is now not only a function of the streamwise distance but also of the cross-stream location, and it is considerably smaller than for slot injections because hot ambient gas reaches the wall between the jets. The main parameters influencing the spreading of the injected jets and therefore also the film cooling effectiveness are the injection angle α, the relative hole spacing s/D, and the blowing rate $M = \rho_j Q_j / \rho_{in} U_{in}$. These parameters (which are defined in Fig. 1) need to be optimized in the design process of gas turbine blades. In addition, the film cooling effectiveness is also influenced by the longitudinal pressure gradient of the main stream, the density ratio of the cold jet and the hot main stream, the turbulence intensity of the main stream and the details of the hole geometry (see [1–4]).

As the interaction between the injected coolant and the main stream is dependent on all the parameters given above, systematic studies are necessary for the optimization of the film cooling design of gas turbine blades. Systematic experimental parameter investigations are always very expensive under realistic conditions, so that design engineers have a great need for prediction procedures. As the flow field is strongly three dimensional in the vicinity of the injection holes, a three-dimensional calculation is necessary for simulating realistically the flow and the associated heat transfer processes.

A calculation method which adequately accounts for three-dimensional effects has been presented by Patankar et al. [5]

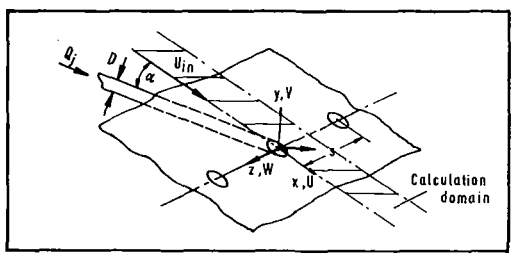

Fig. 1 Flow configuration and coordinate system

Contributed by the Gas Turbine Division and presented at the 1985 Beijing International Gas Turbine Symposium and Exposition, Beijing, People's Republic of China, September 1–7, 1985. Manuscript received at ASME Headquarters May 6, 1985. Paper No. 85-IGT-2.

for injection through discrete tangential slots. Patankar et al. [6] have analzyed the injection at high blowing rates from a single hole, normal to the main stream; similar cases for injection through a row of holes have been considered by Khan et al. [7] and Demuren [8]. Bergeles et al. [9] presented a calculation method based on simplified partially parabolic equations which cannot handle regions with reverse flow. Their method is therefore restricted to injections at very low blowing rates from a normal hole, or to medium rates from holes inclined at an angle to the main stream. These authors have also shown that, in the near-wall flow downstream of the injection hole, it was necessary to account for the anisotropy of the turbulent diffusion coefficients. They found the standard k–ϵ turbulence model, which assumes an isotropic eddy viscosity, to be inadequate and introduced a nonisotropic variant.

More recently, Demuren and Rodi [10] applied the locally elliptic procedure of Rodi and Srivatsa [11] to predict the flow and film cooling past a row of inclined jets. Because the elliptic equations are solved in the vicinity of the injection, there are no restrictions to low blowing rates or regions without reverse flow. Demuren and Rodi incorporated the modified k–ϵ model proposed by Bergeles et al. [9] in order to account for the anisotropy of the eddy viscosity and diffusivity. For one injection configuration ($\alpha = 35$ deg, $s/D = 3$) and for two blowing rates ($M = 0.35$, 1.5) they investigated the influence of different free-stream turbulence intensities and length scales and compared the results with the experimental data of Kadotani and Goldstein [4]. They obtained reasonable agreement with experiments for both blowing rates.

The present paper is an extension of the work of Demuren and Rodi [10] as it reports on an application of their prediction procedure for a wide range of different film cooling configurations. The aim of this study has been to examine systematically the influence of the injection angle α, the relative hole spacing s/D, and the blowing rate M on the film cooling effectiveness. Experimental investigations to this effect have been performed by Foster and Lampard [12] and by Kruse and Metzinger [13]. The three-dimensional partial differential equations governing the flow and temperature distribution are solved with the locally elliptic finite volume technique developed by Rodi and Srivatsa [11]. As was mentioned already, this method is applicable also to higher blowing rates and to situations with local regions of reverse flow. The turbulent stresses and heat fluxes are evaluated with the nonisotropic version of the k–ϵ model proposed by Bergeles et al. [9]. The present predictions are compared with the measurements of Kruse and Metzinger [13], and the downstream development of the laterally averaged cooling effectiveness is presented for all the test cases.

Mathematical Model

Mean-Flow Equations. The time-averaged partial differential equations governing the steady three-dimensional mean velocity, pressure, and temperature field may be written in Cartesian tensor notation as:

Continuity equation

$$\frac{\partial \rho U_i}{\partial x_i} = 0 \tag{1}$$

Momentum equations

$$\frac{\partial \rho U_i U_l}{\partial x_i} = -\frac{\partial P}{\partial x_l} - \frac{\partial \rho \overline{u_i u_l}}{\partial x_i} \tag{2}$$

Temperature equation

$$\frac{\partial \rho U_i T}{\partial x_i} = -\frac{\partial \rho \overline{u_i T'}}{\partial x_i} \tag{3}$$

In the above equations only the turbulent momentum and heat transport terms are included while their molecular counterparts have been neglected. The latter are important only in the viscous sublayer very near walls, and this layer is not resolved in the present calculation but bridged by wall functions as described in the section on boundary conditions. The temperature equation is a special form of the total enthalpy equation in which compressibility and kinetic heating effects have been neglected.

Turbulence Model. The turbulent stresses $-\rho\overline{u_i u_l}$ and heat fluxes $-\rho\overline{u_i T'}$ have to be determined with the aid of a turbulence model. According to the standard k–ϵ model (see [14]) the turbulent stresses may be expressed in tensor notation as

$$-\rho\overline{u_i u_l} = \mu_t \left(\frac{\partial U_i}{\partial x_l} + \frac{\partial U_l}{\partial x_i} \right) - \frac{2}{3} \rho k \delta_{il} \tag{4}$$

where $i, l = 1, 2, 3$, $(x_1, x_2, x_3) = (x, y, z)$ and $(U_1, U_2, U_3) = (U, V, W)$. μ_t is the scalar, isotropic eddy viscosity. The turbulent heat fluxes are similarly expressed as

$$-\rho\overline{u_i T'} = \frac{\mu_t}{\sigma_T} \frac{\partial T}{\partial x_i} \tag{5}$$

where $i = 1, 2, 3$, and σ_t is the turbulent Prandtl number. The eddy viscosity μ_t is related to the turbulent kinetic energy k and to its rate of dissipation ϵ by

$$\mu_t = \rho c_\mu k^2 / \epsilon \tag{6}$$

The distribution of k and ϵ over the flow field is determined from the following semi-empirical transport equations

$$\frac{\partial \rho U_i k}{\partial x_i} = \frac{\partial}{\partial x_i} \left(\frac{\mu_t}{\sigma_k} \frac{\partial k}{\partial x_i} \right) + \mu_t \left(\frac{\partial U_i}{\partial x_l} + \frac{\partial U_l}{\partial x_i} \right) \frac{\partial U_i}{\partial x_l} - \rho\epsilon \tag{7}$$

$$\frac{\partial \rho U_i \epsilon}{\partial x_i} = \frac{\partial}{\partial x_i} \left(\frac{\mu_t}{\sigma_\epsilon} \frac{\partial \epsilon}{\partial x_i} \right) + c_{1\epsilon} \frac{\epsilon}{k} \mu_t \left(\frac{\partial U_i}{\partial x_l} + \frac{\partial U_l}{\partial x_i} \right) \frac{\partial U_i}{\partial x_l} - c_{2\epsilon} \frac{\epsilon^2}{k} \tag{8}$$

The standard constants used in the k–ϵ model are as follows: $c_\mu = 0.09$, $\sigma_t = 0.9$, $\sigma_k = 1.0$, $\sigma_\epsilon = 1.3$, $c_{1\epsilon} = 1.44$, $c_{2\epsilon} = 1.92$.

Bergeles et al. [9] derived a nonisotropic eddy–viscosity relation by simplifying the Reynolds stress model proposed by

Nomenclature

D = diameter of the injection tube
k = turbulent kinetic energy
M = blowing rate
P = pressure
Q_j = jet velocity
s = hole spacing
T = temperature
T' = temperature fluctuation
U, V, W = velocity components
x, y, z = coordinates
α = injection angle
ϵ = dissipation rate
η = cooling effectiveness
μ_t = eddy viscosity
ρ = density
σ_ϕ = Prandtl/Schmidt number
θ = dimensionless temperature $= \dfrac{T_\infty - T}{T_\infty - T_j}$

Launder et al. [15] and the turbulent heat-flux model of Gibson and Launder [16]. By neglecting the transport terms in the modeled Reynolds stress and turbulent heat-flux equations as well as all the gradients of the lateral and vertical velocity components, they obtained for the film cooling situation as illustrated in Fig. 1

$$-\overline{\rho u w} = \mu_{t,z}\frac{\partial U}{\partial z} \qquad -\overline{\rho u v} = \mu_{t,y}\frac{\partial U}{\partial y} \tag{9}$$

$$-\overline{\rho w T'} = \frac{\mu_{t,z}}{\sigma_T}\frac{\partial T}{\partial z} \qquad -\overline{\rho v T'} = \frac{\mu_{t,y}}{\sigma_T}\frac{\partial T}{\partial y} \tag{10}$$

where

$$\mu_{t,y} = \mu_t = \rho c_\mu \frac{k^2}{\epsilon}$$

$$\mu_{t,z} = \begin{cases} \mu_t(1+3.5(1-y/\Delta)) & y \le \Delta \\ \mu_t & y > \Delta \end{cases} \tag{11}$$

and Δ is the local boundary-layer thickness. The form of the expression for $\mu_{t,z}$ was obtained from empirical data and represents a linear decay of the anisotropy from the wall to the edge of the boundary layer. According to relation (11), the eddy viscosity and diffusivity for the turbulent transport in the lateral (z) direction is increased over that in the normal (y) direction in the boundary-layer region. Hence, the nonisotropic eddy-viscosity relation causes a faster spreading of the injected jet in the lateral direction than the standard isotropic model.

Solution Procedure and Boundary Conditions. The partial differential equations given above were solved with the three-dimensional locally elliptic method of Rodi and Srivatsa [11]. This method is an extension of the partially parabolic procedure of Pratap and Spalding [17] and allows for an elliptic treatment of local regions with reverse flow, thereby saving computer storage over a fully elliptic method. The procedure employs a staggered Cartesian grid and the finite difference equations were derived by integrating the original differential equations over control volumes, making use of the hybrid central/upwind differencing scheme for the convective terms. The system of fully conservative difference equations is solved by an efficient tridiagonal matrix algorithm, and the solution employs a predictor corrector method for obtaining the velocity and pressure field.

Boundary conditions need to be prescribed at all of the six boundaries of the computation domain. As the flow is symmetric both with respect to the x–y plane through the center of the injection holes and to the x–y plane midway between two adjacent holes, only the domain between these two planes needs to be calculated as indicated in Fig. 1. The further boundaries are the inlet and the exit plane, the bottom wall including the injection holes and an upper plane where the free-stream conditions prevail. To simplify the description of the boundary conditions at this top plane and to simulate the presence of an opposite wall in wind tunnel experiments, wall boundary conditions have been used for the upper plane. As the distance between the top wall and the bottom wall from which the jets are ejected is about 25 times the boundary-layer thickness, the influence of the boundary-layer developing on the top wall on the free-stream velocity is negligible.

At the two side boundaries (symmetry planes) the normal velocity and normal gradients of all other variables are prescribed as zero. At the top and bottom walls, the wall-function approach described in Launder and Spalding [14] is adopted. This approach bridges the viscous sublayer by relating the velocity components at the first grid point outside this layer to the wall shear stress via the logarithmic law of the wall. The k and ϵ values at this point are also related to the wall shear stress via the assumption that the turbulence is in a state of local equilibrium. The inlet plane is placed 7.5 hole diameters upstream of the center of the injection hole. The inlet profiles for the velocity component U and for the turbulence quantities K and ϵ were generated by a two-dimensional boundary layer calculation to match the experimentally observed momentum thickness at $x=0$ in the absence of jet injections. The exit plane was positioned sufficiently far downstream of the injection (40 hole diameters) so that upstream influences from this boundary are transmitted only through pressure and exit conditions are required only for this quantity. The boundary condition imposed is to set the second streamwise derivative of the pressure to zero.

Uniform profiles were assumed for both the vertical and horizontal component of the jet exit velocity over the exit holes:

$$U_j = Q_j \cos\alpha \qquad V_j = Q_j \sin\alpha \tag{12}$$

Measurements have indicated a significant influence of the main stream on the jet exit profiles. Unfortunately, there is not sufficient experimental information available to cover the wide range of 10 deg $< \alpha <$ 90 deg and $0.5 < M < 2$ considered in this study. Hence, the most reasonable assumption appeared to be that of uniform profiles. The boundary conditions for k and ϵ were prescribed from jet data obtained in the absence of cross flow as

$$k_j = 0.005 V_j^2,\ \epsilon_j = k_j^{3/2}/0.5D \tag{13}$$

Test Cases

For the same mainstream conditions, taken from the experimental study of Kruse and Metzinger [13], 27 test cases have been calculated by varying the injection angle, the relative spacing and the blowing rate as follows:

injection angle	α	= 10/45/90 deg
spacing	s/D	= 1.5/3/5
blowing rate	M	= 0.5/1/2

This parameter variation has been chosen to cover most of the range used in practical film cooling applications. The predictions are compared with the experimental data of Kruse and Metzinger [13], and hence their main-stream conditions were specified for the calculations. These conditions are:

$$U_{in} = 65 \text{ m/s},\ \text{Tu} \cong 3 \text{ percent},\ \Delta \cong D (= 0.002 \text{ m})$$

The calculations were carried out with a $66 \times 41 \times 14$ grid in the (x, y, z)-directions. Because of the rectangular grid used, the edge of the exit hole had to be approximated by steps. Typically 15 × 7 grid points covered the hole in the (x, z)-directions. A typical calculation required 300 iterations for convergence and a core storage of 2048 kbytes and took about 90 minutes CPU time on a Siemens 7880 computer.

Results

Comparison With Experiments. Figures 2–4 compare the downstream development of predicted and measured laterally averaged film cooling effectiveness for different blowing rates, hole spacings and for two injection angles. The agreement is seen to be fairly good for the lower blowing rates $M=0.5$ and $M=1$. In particular, the influence of the spacing on the shape of the $\bar{\eta}(x/D)$ distribution is reproduced quite well (see, e.g., Fig. 2). For the case with the highest blowing rate ($M=2$, $\alpha=45$ deg) the agreement with measurements is not as good for the larger spacings. In all cases, the general trend of the $\bar{\eta}$ development is predicted correctly, including the influence of the spacing, but for the larger spacings the level of $\bar{\eta}$ is considerably lower than the measured one. In order to bring to light the reasons for this disagreement, the temperature field is examined. For the case of the largest

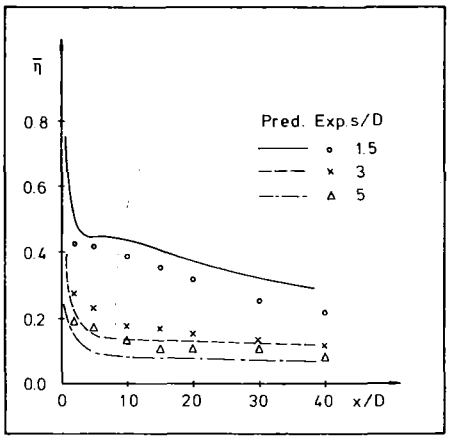

Fig. 2 Laterally averaged cooling effectiveness; comparison with experiments [13], $M = 0.5$, $\alpha = 45$ deg

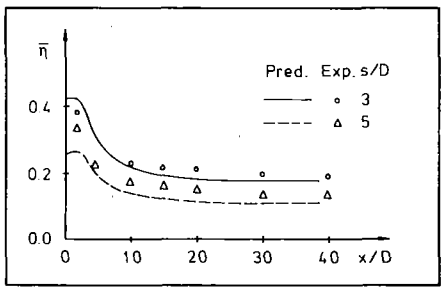

Fig. 3 Laterally averaged cooling effectiveness; comparison with experiments [13], $M = 1$, $\alpha = 10$ deg

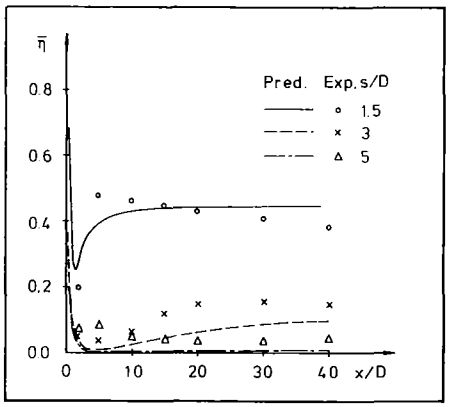

Fig. 4 Laterally averaged cooling effectiveness; comparison with experiments [13], $M = 2$, $\alpha = 45$ deg

spacing ($s/D = 5$), Figs. 5(*a*) and 5(*b*) compare, respectively, calculated and measured dimensionless temperature contours at the mid-x-y-plane through the injection holes ($z/D = 0$) and at the cross-sectional plane two hole diameters downstream from the injection. Considering the complexity of this flow with high blowing, the overall agreement is fairly good, even though the jet penetration into the outer stream appears to be somewhat overpredicted. What causes the disagreement in the cooling effectiveness are detailed differences near the wall. Here the measurements show higher dimensionless temperatures which would indicate higher mixing. However, the measurements of the small temperature differences prevailing in the near-wall region for this case are probably not very accurate. Further, some aspects of the measured temperature behavior are difficult to understand, for example the bending of the 0.05 contour and its constant distance to the wall. Hence, the disagreement about the cooling effectiveness is not very alarming. Yet, the calculations are probably also not

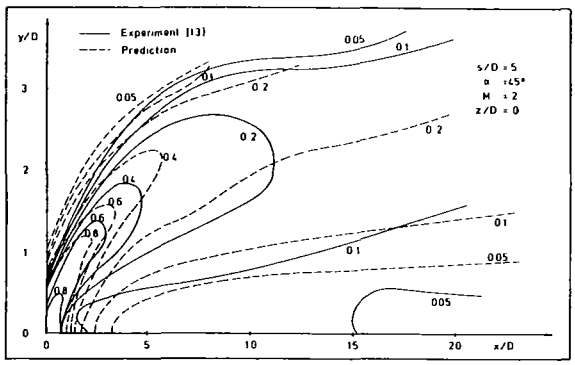

Fig. 5(*a*) Temperature distribution θ behind an injection hole for $M = 2$

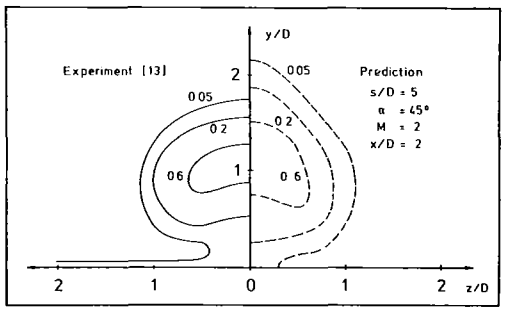

Fig. 5(*b*) Temperature distribution θ in a cross-stream plane for $M = 2$

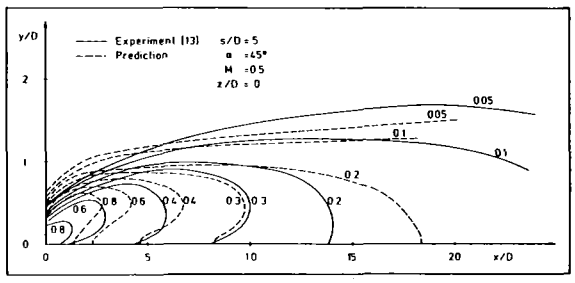

Fig. 6(*a*) Temperature distribution θ behind an injection hole for $M = 0.5$

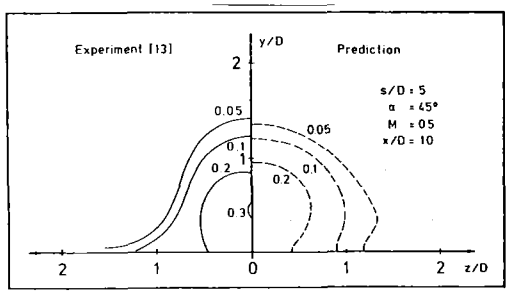

Fig. 6(*b*) Temperature distribution θ in a cross-stream plane for $M = 0.5$

very accurate for the following reasons. In this case with large spacing, the injected fluid behaves like individual jets in a cross flow for some distance downstream, and it has been observed experimentally by Andreopoulos and Rodi [18] that in such jets with high blowing rates the flow near the wall in the lee of the jet is indeed very complex. This region of the wake behind the jet, which may be influenced by periodic vortex shedding, and which interacts with the wall, has certainly not been resolved properly by the numerical grid employed. Further, the turbulent transport phenomena are so complex in this region that they can hardly be expected to be

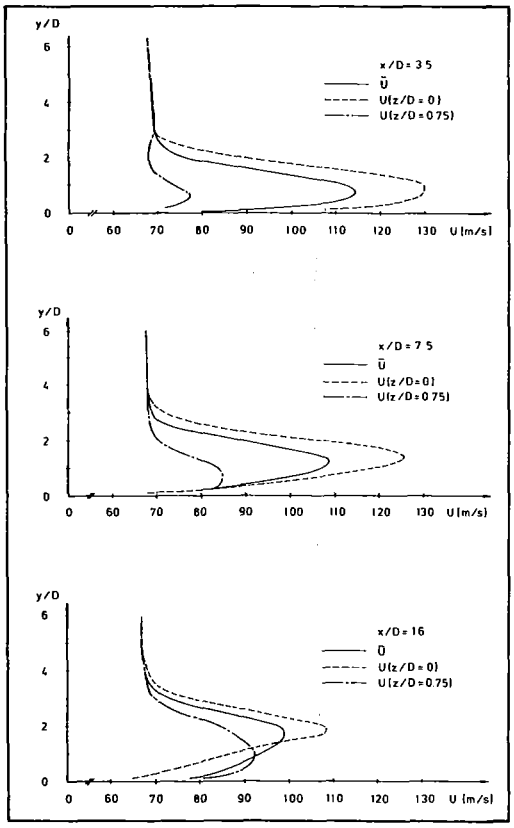

Fig. 7 *U* velocity profiles for the test case $\alpha = 10$ deg, $s/D = 1.5$, $M = 2$

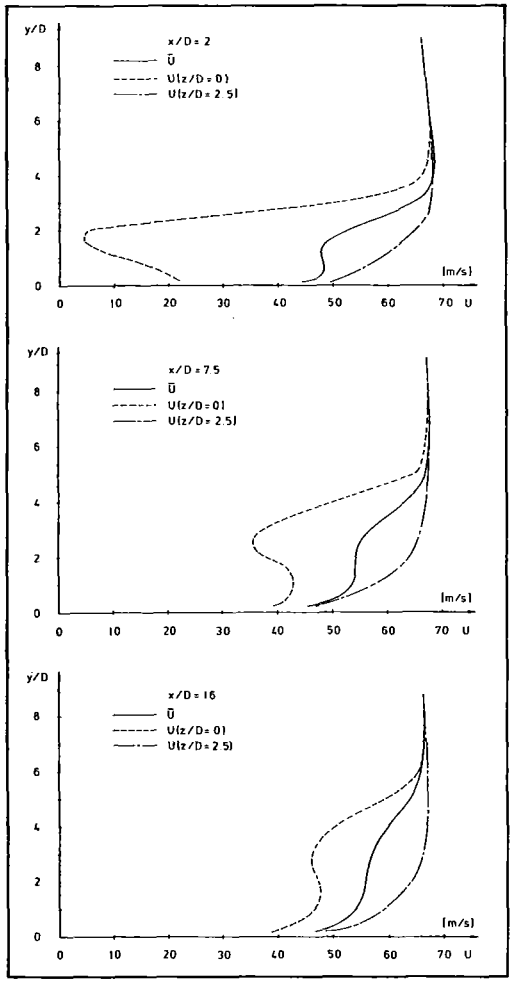

Fig. 8 *U* velocity profiles for the test case $\alpha = 90$ deg, $s/D = 5$, $M = 1$

well simulated by a turbulence model as simple as the eddy-viscosity model used in this study.

Figures 6(*a*) and 6(*b*) give the corresponding temperature contours for the case with the lower blowing rate $M = 0.5$ (the other parameters are the same). In this case, the jet bends over much more quickly and attaches to the wall. This attached wall flow is much less complex than the flow at a higher blowing rate where the jet penetrates into the outer stream. This conclusion was also reached by Andreopoulos and Rodi [18] in their detailed experimental study of single jets in a cross flow. The overall agreement between predicted and measured temperature contours seen in Fig. 6 is on the whole not necessarily much better than that in Fig. 5, but it is definitely better in the near-wall region. This is what leads to the relatively good agreement for the film cooling effectiveness at lower blowing rates. It may be concluded that the film cooling effectiveness is governed by the details in the near-wall region and that, in cases with large spacings where the jets retain their identity for some distance, these details are much more difficult to simulate for higher blowing rates than for lower ones. It should be remembered however that in these cases it is also more difficult to measure accurately the small temperature differences in the near-wall region.

Velocity Profiles. In order to illustrate the three dimensionality of the flow in the vicinity of the injection and the recovery to a two-dimensional flow, the U velocity profiles are presented at three downstream stations for the following two test cases:

$\alpha = 10$ deg, $s/D = 1.5$, $M = 2$, Fig. 7
$\alpha = 90$ deg, $s/D = 5$, $M = 1$, Fig. 8

These cases have been chosen to demonstrate that the injected jet can behave vastly differently for different parameter situations. The velocity profiles are given at two lateral positions (at the midplane of the injection holes, $z/D = 0$, and at the symmetry plane between the holes). Additionally, the laterally averaged $\bar{U}$ velocity distribution is also included. Figure 7 shows clearly the wall-jet behavior of the cooling jet in the case of the small injection angle. In this situation, the distance of the velocity maximum from the wall increases only slowly with x. Even for this case with a relatively small spacing, the flow is not yet two dimensional at the furthest downstream station considered ($x/D = 16$), and the fact that the velocity maximum occurs at different distances from the wall for $z/D = 0$ and $z/D = 0.75$ indicates that the bent-over jet is kidney shaped. This is in agreement with observations for jets in a cross flow [18]. Figure 8 presents the velocity profiles for the case with the highest injection angle and the largest spacing. In this case, the jet does not bend over and attaches to the wall immediately but penetrates the main stream, thereby acting like an obstacle behind which a wake is formed. This causes a momentum deficit behind the injection which can be seen clearly in Fig. 8. At this large spacing, the individual jets do not interfere with each other for some distance so that the velocity profile at the symmetry plane between the holes is hardly influenced by the injection and retains its typical boundary layer shape. As in the other case, the flow is not yet two dimensional at $x/d = 16$, and the velocity deficit behind the injection is still present at that station.

Laterally Averaged Film Cooling Effectiveness. The calculated influence of injection angle, spacing, and blowing rate on the downstream development of the laterally averaged cooling effectiveness is presented for all calculations in Fig. 9. One diagram always gives the distributions for a specific injection angle α and spacing s/D. For the test case $\alpha = 90$

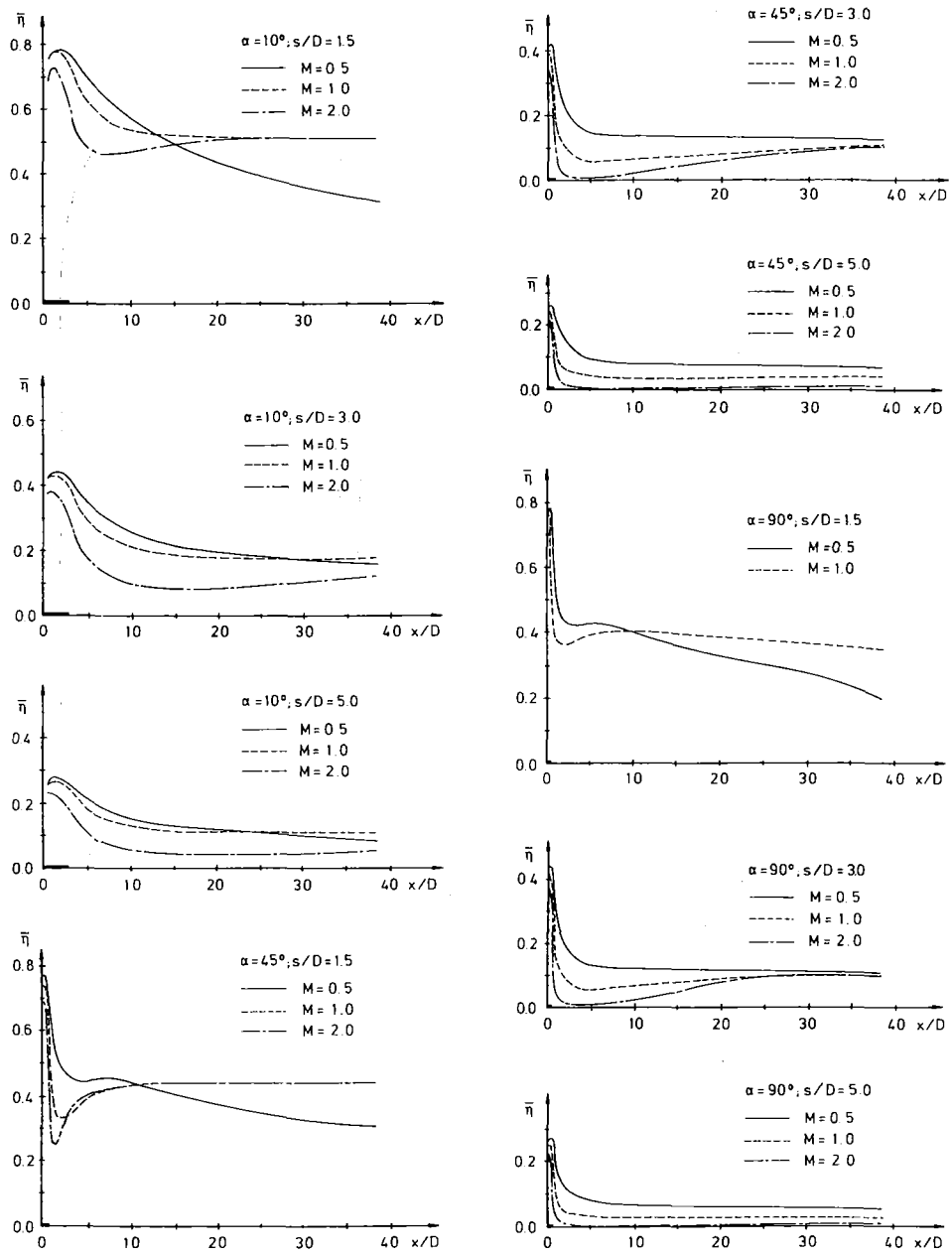

Fig. 9 Laterally averaged cooling effectiveness for all the test cases

deg, $s/D=1.5$, $M=2$, satisfactory results have not been obtained at the time of writing due to convergence problems. These are caused by the strong interaction between the individual injected jets on the one hand and the free stream on the other hand and can probably be overcome by choosing better initial conditions and imposing a stronger underrelaxation.

The influence of the different parameters on the laterally averaged film cooling effectiveness $\bar{\eta}$ can be summarized as follows:

1 For the lowest blowing rate ($M=0.5$), $\bar{\eta}$ decreases continuously with x past the injection hole (the extent of the hole is indicated in the figures). The reason for this is that, for low blowing, the cooling jet is bent over immediately after the injection and attaches to the wall. With increasing distance from the injection, hot gas is entrained into the wall jet which in turn causes a monotonic decrease of the cooling effectiveness.

2 For the highest blowing rate ($M=2$), $\bar{\eta}$ drops immediately after the injection to a minimum and increases again further downstream or remains constant. This behavior is due to the increased penetration of the cooling jets into the main stream because of which there is almost no cooling fluid present on the blade surface immediately after the injection. Some distance downstream, cooling fluid from the bent-over jet reaches the wall mainly due to turbulent diffusion so that the cooling effectiveness increases.

3 For the test cases with perpendicular injection ($\alpha=90$ deg), there is a sharp drop of $\bar{\eta}$ down to $x/D\cong 3$. In this case, the injected jet penetrates further into the main stream for all blowing rates than at smaller injection angles so that the same arguments hold as given under item 2.

4 When the spacing is increased, $\bar{\eta}$ decreases for all test cases, as the injection mass flow per unit width decreases.

5 The best cooling in the near field ($x/D<10$) is obtained with the lowest blowing rate, $M=0.5$. For this rate, the cooling jet attaches to the wall more or less immediately behind the injection hole so that there is optimal cooling in the near-hole region.

6 In the far field ($x/D>30$) an increase of the blowing rate

leads to higher values of $\bar{\eta}$ for the smallest spacing and to lower values of $\bar{\eta}$ for the largest spacing. The reason for this different behavior lies in the different flow interaction between the main and the injected fluid. For the smallest spacing, the individual jets of the row grow together fairly quickly after the injection and basically act like a two-dimensional slot injection, which results in the higher $\bar{\eta}$ values for higher blowing rates. For the largest spacing, however, the flow configuration is more like a single-jet injection. The jet penetrates further into the main stream at higher blowing rates and mixes more with the main-stream fluid so that the resulting cooling effectiveness is small in the far field.

7 For all blowing rates and all spacings, the best cooling in the far field is achieved with the smallest injection angle of $\alpha = 10$ deg as in this case the injected jet always attaches immediately to the wall. Assessing all the predicted test cases, the best overall cooling can be achieved with the configuration $\alpha = 10$ deg, $s/D = 1.5$, $M = 1$. For this case, the film cooling effectiveness is only slightly smaller in the near field than with $M = 0.5$, but is much better in the far field.

Conclusions

Three-dimensional calculations of film cooling by injection from a row of holes are presented. Altogether 27 test cases with the injection angle, the relative spacing and the blowing rate varying over the ranges of practical interest have been calculated. The predicted temperature fields agree in general fairly well with available measurements. The film cooling effectiveness, which represents the dimensionless wall temperature and is governed by the temperature behavior near the wall, is not in all cases in good quantitative agreement with the data. The agreement is satisfactory for the lower blowing rates up to 1 and for small spacings. For high blowing and large spacing only the general trends of the measurements are recovered but the predicted level of cooling effectiveness is lower than the observed one. In this case, the individual jets retain their identity for quite a distance and do not attach immediately to the wall but penetrate into the main stream. A very complex flow field is established behind the injection, with reverse flow and the wake behind the jet interacting with the wall. This region is certainly not properly resolved with the numerical grid used, and also the turbulent mixing processes are only very crudely simulated with the eddy-viscosity model. A more refined treatment of this region would be necessary to do justice to the complex phenomena occurring there. On the other hand, measurements of cooling effectiveness are probably also not very accurate for these cases. Further, the film cooling effectiveness is so low for these situations that they are not of practical interest anyway. In view of this, the calculations must be considered satisfactory on the whole; in any case, the influence of the individual parameters is always predicted correctly. Based on the calculation results, the influences of the individual parameters were discussed in detail. The best cooling effectiveness results for the smallest injection angle and the smallest spacing, and for the downstream distance considered the intermediate blowing rate of $M = 1$ provides the best overall cooling.

Acknowledgments

The research reported here was sponsored by the German Research Foundation and partly by the Forschungsvereinigung Verbrennungskraftmaschinen e.V. The calculations were carried out on the Siemens 7880 computer of the University of Karlsruhe, using a highly modified version of the FLAIR computer code of CHAM Ltd., London. The authors should like to thank Mrs. R. Zschernitz for the efficient typing of the manuscript.

References

1 Goldstein, R. J., Eckert, E. R. G., Eriksen, V. L., and Ramsey, J. W., "Film Cooling Following Injection Through Inclined Circular Tubes," *Israel J. Technology*, Vol. 8, 1970, pp. 145–154.

2 Goldstein, R. J., Eckert, E. R. G., and Burggraf, F., "Effects of Hole Geometry and Density on Three-Dimensional Film Cooling," *Int. J. Heat Mass Transfer*, Vol. 17, 1974, pp. 595–607.

3 Pedersen, D. R., Eckert, E. R. G., and Goldstein, R. J., "Film Cooling With Large Density Differences Between the Mainstream and the Secondary Fluid Measured by the Heat-Mass Transfer Analogy," ASME *J. Heat Transfer*, Vol. 99, 1977, pp. 620–627.

4 Kadotani, K., and Goldstein, R. J., "On the Nature of Jets Entering a Turbulent Flow, Part A and B," ASME JOURNAL OF ENGINEERING FOR POWER, Vol. 101, 1979, pp. 459–470.

5 Patankar, S. V., Rastogi, A. K., and Whitelaw, J. H., "The Effectiveness of Three-Dimensional Film-Cooling Slots—II Predictions," *Int. J. Heat Mass Transfer*, Vol. 16, 1973, pp. 1665–1681.

6 Patankar, S. V., Basu, D. K., and Alpay, S. A., "Prediction of Three-Dimensional Velocity Field of a Deflected Turbulent Jet," ASME *J. Fluids Engg.*, Vol. 15, 1977, pp. 758–762.

7 Khan, Z. A., McGuirk, J. J., and Whitelaw, J. H., "A Row of Jets in Cross Flow," AGARD CP 308, 1982.

8 Demuren, A. O., "Numerical Calculations of Steady Three-Dimensional Turbulent Jets in Cross Flow," *Comp. Meth. Appl. Mech. Engg.*, Vol. 37, 1983, pp. 309–328.

9 Bergeles, G., Gosman, A. D., and Launder, B. E., "The Turbulent Jet in a Cross-Stream at Low Injection Rates," *Numerical Heat Transfer*, Vol. 1, 1978, pp. 217–242.

10 Demuren, A. O., and Rodi, W., "Three-Dimensional Calculation of Film Cooling by a Row of Jets," *Proceedings of the Fifth GAMM-Conference on Numerical Methods in Fluid Mechanics*, Rome, Oct. 5–7, 1983, pp. 49–56.

11 Rodi, W., and Srivatsa, S. K., "A Locally Elliptic Calculation Procedure for Three-Dimensional Flows and Its Application to a Jet in Cross Flow," *Comp. Meth. Appl. Mech. Engg.*, Vol. 23, 1980, pp. 67–83.

12 Foster, N. E., and Lampard, "The Flow and Film Cooling Effectiveness Following Injection Through a Row of Holes," ASME JOURNAL OF ENGINEERING FOR POWER, Vol. 102, 1980, pp. 584–588.

13 Kruse, H., and Metzinger, H., "Der Einfluss der Belochungsgeometrie auf die Filmkühlwirkung einer Lochreihe," *Deutsche Forschungs- und Versuchsanstalt fur Luft- und Raumfahrt*, Köln, Interner Bericht IB 325-9-84, 1984.

14 Launder, B. E., and Spalding, D. B., "The Numerical Computation of Turbulent Flow," *Comp. Meth. in Appl. Mech. and Engg.*, Vol. 3, 1974, p. 269.

15 Launder, B. E., Reece, G. J., and Rodi, W., "Progress in the Development of a Reynolds-Stress Turbulence Closure," *J. Fluid Mech.*, Vol. 68, 1975, pp. 537–566.

16 Gibson, M. M., and Launder, B. E., "Ground Effects on Pressure Fluctuations in the Atmospheric Boundary Layer," *J. Fluid Mech.*, Vol. 86, 1978, pp. 491–511.

17 Pratap, V. S., and Spalding, D. B., "Fluid Flow and Heat Transfer in Three-Dimensional Duct Flows," *Int. J. Heat Mass Transfer*, Vol. 19, 1976.

18 Andreopoulos, J., and Rodi, W., "Experimental Investigation of Jets in a Cross Flow," *J. Fluid Mech.*, Vol. 138, 1984, pp. 93–127.

Heat Transfer Downstream of a Leading Edge Separation Bubble

W. J. Bellows[1]

R. E. Mayle

Department of Mechanical Engineering,
Rensselaer Polytechnic Institute,
Troy, NY 12180-3590

Experiments for flow about a two-dimensional blunt body with a circular leading edge are described. Measurements of the free-stream and boundary-layer velocity distributions are presented and indicate that a small separation "bubble" existed where the leading edge joined the body. In particular, it was found that the laminar leading edge boundary layer separated and reattached shortly downstream as a turbulent boundary layer with a low-momentum thickness Reynolds number. Heat transfer measurements around the body are also presented and show almost an order of magnitude increase across the bubble. Downstream of the bubble, however, the heat transfer could be correlated by a slightly modified turbulent flat plate equation using the separation point as the virtual origin of the heated turbulent boundary layer.

Introduction

Invariably, the design of a turbine airfoil involves a compromise between its aerodynamic and heat transfer performance. Since this compromise ultimately affects the engine's efficiency and durability, the designer must have the flexibility within his design system to accurately evaluate the effects of his trade-offs.

One area of concern is the airfoil's leading edge, which is required by aerodynamics to have a moderately small radius which blends smoothly into the rest of airfoil. On the other hand, present cooling schemes usually require a large leading edge radius which cannot be blended smoothly. As a result, a rapid change in surface curvature is found immediately downstream of the leading edge. The curvature actually changes sign on the pressure side of an airfoil. On either the pressure or suction side of the airfoil, however, this change in curvature can produce a localized "overspeed" region, accompanied by an adverse pressure gradient. For operation at off-design conditions, an overspeed region is almost always found on the surface opposite the direction of shift in angle of attack. Barring premature transition caused by large roughness, cooling flow injection, or high free-stream turbulence, the adverse pressure gradient almost always causes the normally laminar leading edge boundary layer to separate. If the boundary layer separates, questions which arise are: (*a*) Does the boundary layer reattach, (*b*) how large is the separated region, (*c*) does it reattach laminar or turbulent, and (*d*) what are the details of the reattached flow? An answer to the last is usually needed for many turbine heat transfer design systems to "restart" boundary-layer calculation programs. In general, for reasonably well-designed turbine airfoils operating at design conditions, a separating leading edge boundary layer does reattach, the separation region (bubble) is small compared to the leading edge radius, and the reattached boundary layer is turbulent, nonequilibrium, and has a low-momentum thickness Reynolds number. This situation is a challenge for any boundary layer program, particularly when one includes the effects of subsequent large favorable pressure gradients as exist on the suction surface and the high level of turbulence found in gas turbine core flows.

A survey of the literature provides many studies of boundary-layer separation and reattachment, which include reviews by Bradshaw [1] and Simpson [2], a summary of results collected by Chang [3], and a collection of papers published by AGARD [4]. Unlike the separation-reattachment problem found on turbine airfoils, however, most of the work concerns flows over backward and forward-facing steps, trips, and cylindrical bodies with wakes. Of these, even fewer provide heat transfer information relevant to the present study [5–12]. Of particular interest is the series of experiments conducted by Ota and Kon [9–12] who studied separated, reattached flow on parallel-sided blunt bodies. Although most of their work centered on flat, blunt leading edges, heat transfer for a body with an unheated circular leading edge is examined in [12]. Results are presented for the Reynolds number range of 5400–37,200 (based on leading edge diameter). In addition, two sets of velocity, temperature, and turbulence boundary-layer measurements (one immediately, and the other far downstream of reattachment) are presented. The results do show, however, that the heat transfer downstream of reattachment relaxes to the usual turbulent state, while the viscous boundary layer is still nonequilibrium 70 bubble lengths downstream.

The present investigation was initiated to examine separated, reattached leading edge flows at Reynolds numbers more appropriate to present high-pressure gas turbines and to provide more detailed information on pressure, velocity, and heat transfer distributions. For this, a test configuration similar to Ota and Kon's was used.

[1] Present address: Avco Lycoming Division, Stratford, CT 06497

Contributed by the Gas Turbine Division of THE AMERICAN SOCIETY OF MECHANICAL ENGINEERS and presented at the 31st International Gas Turbine Conference and Exhibit, Düsseldorf, Federal Republic of Germany, June 8–12, 1986. Manuscript received at ASME Headquarters January 10, 1986. Paper No. 86-GT-59.

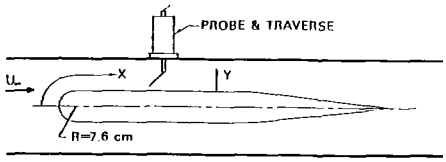

Fig. 1 Test section and test body

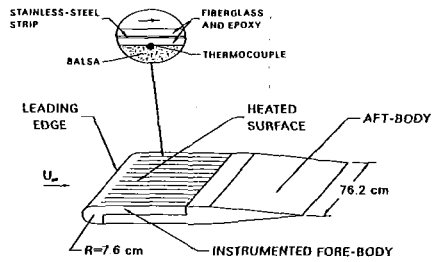

Fig. 2 Heat transfer test model

Experimental Apparatus

All of the tests were conducted in a low-speed, open-circuit wind tunnel consisting of a centrifugal fan, plenum chamber, nozzle, and a test section. The plenum contained a series of baffles, screens, and a section of honeycomb to provide a uniform and parallel flow entering the nozzle. A two-to-one contraction nozzle produced a uniform flow accurate to within one half of one percent across its exit except in the thin boundary layers near the walls. The flow could be varied by adjusting the fan's inlet guide vanes and was continually monitored by a pitot-static tube in the test section. Air leaving the tunnel entered the room, mixed with the surrounding air, and circulated back to the fan's inlet. An air conditioner in the room with its sensor placed in the tunnel automatically controlled the air temperature to within 1°C.

The test section, as shown in Fig. 1, was 46 cm high by 76 cm wide and contained the test body which spanned its entire width. Plexiglass sheets formed each side wall to facilitate flow visualization tests, while aluminum sheets were used for the top and bottom walls. Steel rods passing through the test body and each side wall were used to position and secure the body. In this regard, the body could be pivoted about its leading edge to fine tune the flow symmetry around the top and bottom of the model.

The test body was about 2.2 m long and had a cylindrical, semicircular leading edge with a radius $R=7.6$ cm which smoothly joined two parallel flat surfaces 1.1 m long. The surface, however, did have a step change in curvature at the joint which produced a local adverse pressure gradient and a laminar separation. The tapered trailing edge on the body was attached separately and merely served to diffuse the flow aft of the test region. Actually, two forebody models were constructed: one for aerodynamic measurements and the other for heat transfer. This was later found to be redundant after it was discovered that pressure taps could be placed in the heat transfer model without disturbing the heat transfer measurements. For the present series of tests, however, the aerodynamic measurements had already been obtained.

The aerodynamic model was fabricated from mahogany. Static pressure taps, formed from 0.8-mm brass tubing filed flush to the surface, were placed along the surface's centerline. Near the change in surface curvature, where rapid changes in pressure were anticipated, taps were clustered to each side. In addition, a second set having the same arrangement was placed one quarter of the distance across the surface to check for two dimensionality. All of the pressure tubing was led through a hole in the model's side. Finally, the whole body was painted with a polyurethane varnish, lightly sanded, and waxed to produce a smooth surface.

The heat transfer model is shown in Fig. 2. It was constructed mostly of wood and had the same overall dimensions as the aerodynamic model. The heated area extended across the body's width to within 5 cm of the side walls and from the lower edge of the cylindrical leading edge, around the front, and back about 60 cm along the top surface. The surface consisted of thirteen 0.025-mm-thick, 5.1-cm-wide stainless steel heater strips bonded side by side on a 13-mm-thick balsa wood substrate between two layers of fiberglass and epoxy resin. The metal strips were connected in series by copper bus bars buried in the surface, and the whole surface was heated by passing an electric current through the circuit. The surface temperature distribution was measured using 0.075-mm thermocouples, bonded between the strips and balsa substrate along the body's centerline, and at various locations to either side to check for two dimensionality. Their leads ran in opposite directions along the surface for a short distance to minimize heat loss, and then through the substrate. A number of thermocouples were also attached to the back of the balsa in order to determine the heat conducted through the substrate. In addition, a complete set of pressure taps was installed as on the aerodynamic model at roughly the one-quarter span position. All of the thermocouple leads, pressure tap tubing, and power leads were led out of the model's side. The internal cavity was filled with commercial fiberglass to reduce conduction losses and the surface was painted with a high emissivity black paint. A detailed account of the fabrication process is presented in DiElsi and Mayle [13].

Test Conditions and Procedures

The model was centrally located in the vertical direction within the test section. Surface pressure taps on the top and bottom of the model were used to align the model so that stagnation occurred on the leading edge along the model's

Nomenclature

C_f = skin friction coefficient
h = convective heat transfer coefficient
H = boundary layer shape factor
Pr = Prandtl number
q = convective heat flux
q_{cond} = heat loss by conduction
q_{gen} = heat generated by metal strips
q_{rad} = heat loss by radiation
R = leading edge radius
Re_D = Reynolds number based on the incident velocity and leading edge diameter
Re_X = Reynolds number based on the local velocity and distance along the surface
St = Stanton number based on the local velocity
T_M = measured surface temperature
T_∞ = free-stream temperature
u = velocity in the streamwise direction
U = local free-stream velocity
U_∞ = incident velocity
X = streamwise distance measured from stagnation
Y = distance measured normal to the surface
θ = momentum thickness
ν = kinematic viscosity
Π = Coles' wake strength parameter

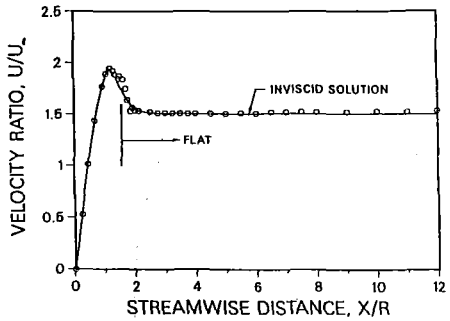

Fig. 3 Free-stream velocity distribution at $Re_D = 100{,}000$

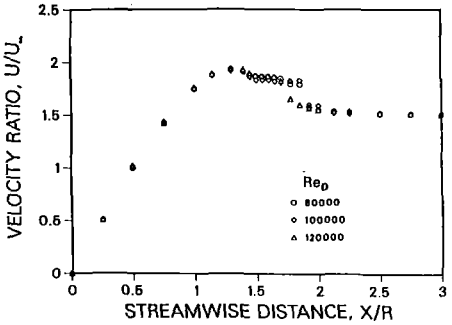

Fig. 4 Free-stream velocity distributions near separation

midplane. Tests were conducted at nominal Reynolds numbers based on the incident velocity and leading edge diameter Re_D of 80,000, 100,000, and 120,000 with an incident turbulence level of about 0.4 percent. Tests with a higher mainstream turbulence are planned in the future.

Mean velocity and turbulence measurements were made using a Thermo-Systems 1051 hot-wire anemometer system with a 1210T1.5 probe. To reduce probe interference, all boundary layer measurements were made using the hot-wire probe inclined 45 deg into the flow as suggested by Compte-Bellott et al. [14]. This was accomplished by plugging the probe into a 45 deg adapter attached to the vertical probe stem such that the wire was held parallel to the surface and perpendicular to the flow.

The free-stream temperature for all of the tests was nominally maintained at 20°C. For the heat transfer tests, the generated heat flux was about 670 w/m^2, which produced surface temperatures ranging from 32 to 50°C. A test conducted at a 25 percent higher heat flux produced results which agreed to within 3 percent of its counterpart. All tests were conducted under steady-state conditions. Although steady state for the heat transfer model was normally attained in about 3 hr, measurements were taken 6–8 hr after the experiment commenced.

The steady-state boundary condition on the heated surface was nominally that of constant heat flux. A slight modification of this, however, was caused by surface radiation, heat conduction through the substrate, and conduction in the metal strips parallel to the surface. In addition, the thermocouple junction and leads acted as a heat sink which resulted in measuring a lower surface temperature than would exist without the thermocouple. These effects, along with the local variations in strip resistance resulting from metal temperature variations, were included in the calculation of the heat transfer coefficients using

$$q = q_{\text{gen}} - q_{\text{rad}} - q_{\text{cond}}$$

and

$$h = q/(T_M - T_\infty - \Delta T)$$

where q is the convective heat flux, q with subscripts gen, rad, and cond refers to the heat flux generated, radiated, and conducted, respectively, h is the heat transfer coefficient, T_M is the measured surface temperature, T_∞ is the free-stream temperature, and ΔT is the surface temperature correction. The approximate magnitudes of the corrections are: radiation, 15 percent of the generated heat flux; heat loss through the substrate, 2 percent; heat conduction within the heater strips, less than one tenth of 1 percent; temperature correction, ΔT, about one half percent of the local wall, free-stream temperature difference. An uncertainty analysis was carried out after accounting for the above biased effects using the method of Kline and McClintock [15] and indicated that the reported heat transfer coefficients are certain to within 3.5 percent on 20-to-1 odds.

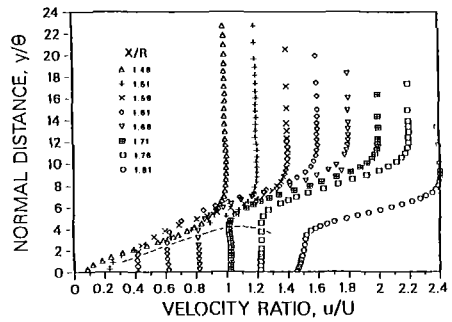

Fig. 5(a) Velocity profiles, separated region, $Re_D = 100{,}000$

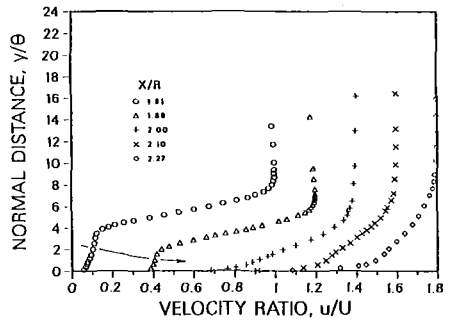

Fig. 5(b) Velocity profiles, turbulent-reattached region, $Re_D = 100{,}000$

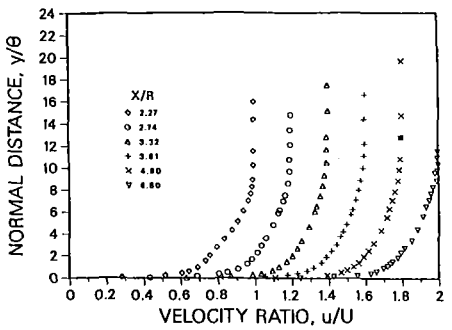

Fig. 5(c) Velocity profiles, turbulent region, $Re_D = 100{,}000$

Results

Surface flow visualization tests were carried out by using the china clay method. China clay (Kaolin) was sprayed over the whole forward surface of the test body. Patterns of low and high mass transfer were observed by swabbing the surface with oil of wintergreen and watching its rate of evaporation in the flow. Near the change of curvature on the body, these tests always displayed a region of low mass transfer immediately followed by a region of very high mass transfer. No uneven-

ness or change in length of the pattern could be detected across the body's span (except near the tunnel's sidewall) indicating that the flow in this region was two dimensional. This was further substantiated by both the pressure and heat transfer measurements.

Static pressures along the model's surface were measured for each Reynolds number. These pressures were used to determine the free-stream velocity distributions around the body using Bernoulli's equation. The results for an incident Reynolds number of 100,000 are plotted in Fig. 3 against a dimensionless streamwise distance measured along the body's surface from stagnation. The position $X/R = 1.57$ is where the surface changes from circular to flat. In addition, the figure contains the result of an inviscid, two-dimensional, incompressible flow calculation for the test configuration. On comparison, the data are seen to agree quite well with the calculation over most of the body, the notable exception being the region of diffusing flow near the $X/R = 1.57$ position where the flow visualization tests showed a large change in mass transfer. Here, the measured distribution is typical of that obtained by Crabtree [16] for a laminar separation bubble with turbulent reattachment. As will be seen, boundary layer measurements confirmed that a separation bubble existed at this location. The free-stream velocity distributions in the vicinity of the leading edge are plotted on an expanded scale in Fig. 4, where a region of constant velocity is followed by a rapid diffusion. The data for $Re_D = 100{,}000$ are identical to those presented in the previous figure. Comparing the distributions in Fig. 4 for different Reynolds numbers suggests that the bubble is shorter at higher Reynolds numbers. This is in agreement with the results of Crabtree who attributes the behavior to a shortening of the laminar-to-turbulent transition distance in the bubble's "free shear layer."

The velocity profiles within the boundary layer for $Re_D = 100{,}000$ are presented in Figs. $5(a-c)$, where the distance from the wall is normalized by the local momentum thickness. Consecutive profiles in each figure have been shifted to the right by 0.2 u/U. In addition, the velocity profiles have been grouped into three main categories: (1) separated, (2) turbulent–reattached, and (3) turbulent. As will be seen, all of the profiles in the last two categories can be classified as turbulent, nonequilibrium. The distinction between the profiles in these last categories is simply whether or not they possessed a recognizable logarithmic region. Profiles in the second category, which corresponded to traverses taken just downstream of reattachment, did not. Before continuing, it should be noted that measuring velocity profiles, with any reasonable degree of accuracy, in or near a small separation bubble using a hot-wire probe was of considerable concern. After preliminary tests with different probes and probe alignments, it was found that the probe arrangement used affected the flow the least. In particular, surface heat transfer measurements taken with the probe positioned in the separated region at various streamwise locations corresponded, within experimental accuracy, to that measured without the probe. The largest difference was observed with the probe positioned at "separation." In this case, it could be interpreted that the probe caused a streamwise shift in the separation position by no more than 0.05 R, which corresponds to about 10 percent of the observed bubble length.

The velocity profiles in the vicinity of the separation bubble are shown in Fig. 5(*a*). While the first profile of the series corresponds to that for laminar attached flow, the last profile corresponds to one called turbulent–reattached flow. Between these, all of the profiles indicate that a region of relatively stagnant flow existed near the wall (below the dashed line in the figure) characteristic of separation. Since a single hot wire cannot by itself sense the direction of the flow, the velocity data in this region were plotted simply as measured even though it is probably negative. From these measurements,

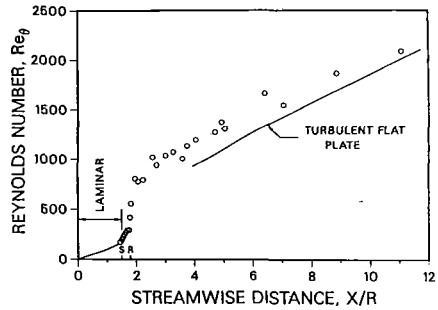

Fig. 6 Momentum thickness Reynolds number distribution, $Re_D = 100{,}000$

separation seems to have occurred around $X/R = 1.5$, while reattachment occurred about $X/R = 1.8$. With a lateral extent equal to the width of the body, the bubble's width-to-length ratio was about 30. In addition, the maximum height of the region is seen to be about 4–5 times the local momentum thickness or about 1 mm. This provides a separation bubble length-to-height ratio of about 20. Although these values are somewhat uncertain, they do provide insight to the order of magnitude of the separated region and indicate that an interactive boundary layer analysis such as Carter and Wornom's [17] may be used to predict the flow.

One of the most interesting features of the turbulent-reattaching profile data (Fig. 5*b*) is the extremely rapid acceleration near the wall directly after reattachment (indicated by the arrow drawn in the figure). A similar result was also noted by Ota and Itaska [18]. This acceleration occurs over a distance of about 30 bubble heights and appears to be associated with the establishment of new sub- and inner layers beneath an existing turbulent outer shear flow.

The streamwise distribution of momentum thickness Reynolds number $Re_\theta = U\theta/\nu$ is presented in Fig. 6. The separation and reattachment positions are noted in the figure by the letters S and R, respectively. Since velocity profile measurements were obtained mainly downstream of separation, the laminar solution using a finite difference program is shown for most of the leading edge region. It is noteworthy that the solution indicated laminar separation at $X/R = 1.6$. The measurements indicate that separation occurred near 1.5 with a momentum thickness Reynolds number of about 200. Also included in the figure is the flat plate turbulent boundary layer correlation using $X = 0$ for the virtual origin. Two important points to note are: (1) the nearly step change in momentum thickness across the separated, turbulent-reattached region, and (2) the low-momentum thickness Reynolds numbers for the reattached flow. For this case, the change in momentum thickness Reynolds number across the bubble is about 240, and the change across the turbulent-reattached region immediately following is about the same. This yields a total jump of about 580. Downstream of this region, where the pressure gradient is zero (Fig. 3), the momentum thickness Reynolds number begins to approach the flat plate correlation. Of interest, however, is that the maximum momentum thickness Reynolds number measured is only about 2000. The last measurement position has a Reynolds number based on streamwise distance $Re_X = 6(10)^5$ and corresponds to about 200 times the boundary layer thickness at reattachment.

The skin friction coefficient C_F, wake strength II, and boundary layer shape factor H (ratio of displacement to momentum thickness) results are all plotted against the momentum thickness Reynolds number so that they may be directly compared to those of Coles [19] for a turbulent boundary layer with zero pressure gradient. The comparison, however, is valid only for the present data in the reattached region where the pressure gradient is zero, i.e., for $X/R \geq 2$.

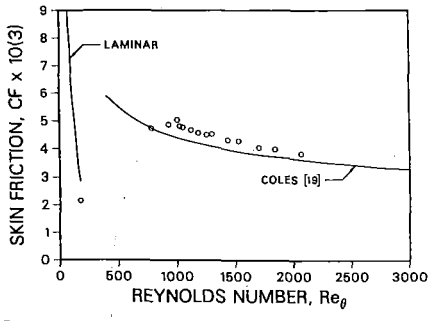

Fig. 7 Coles' skin friction plot, $Re_D = 100{,}000$

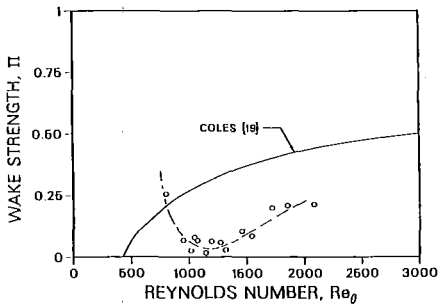

Fig. 8 Coles' wake strength plot, $Re_D = 100{,}000$

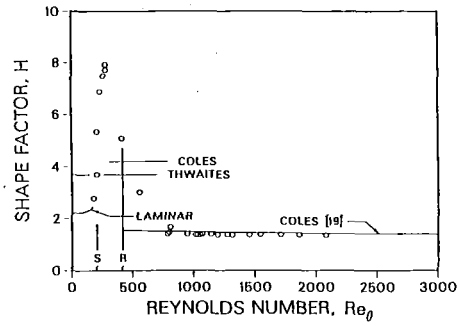

Fig. 9 Coles' shape factor plot, $Re_D = 100{,}000$

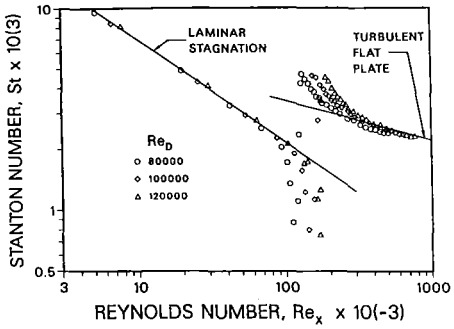

Fig. 10 Stanton number distribution

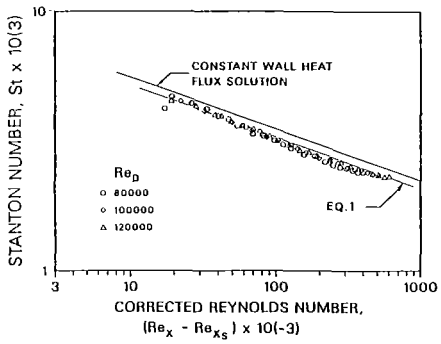

Fig. 11 Stanton number distribution modified for separation effects

Skin friction coefficients were not obtained in either the separated region where the flow is nearly stagnant, or the region immediately after reattachment where the profiles could not be fitted to the logarithmic law. In the separated region they should be negative and in the turbulent-reattached region they should rise rapidly from zero to the values plotted. For the laminar unseparated profile, the skin friction coefficient was obtained by using the slope of the velocity distribution near the wall, while for the turbulent profiles it was determined by fitting Coles' law of the wall using $K = 0.41$ and $B = 5.0$. The shape factor could be evaluated for all of the profiles.

The skin friction coefficient results are presented in Fig. 7, where the result of the laminar leading edge calculation and Coles' data are also shown. The corresponding plot for wake strength is provided in Fig. 8. A wake strength, of course, does not exist for the laminar or separated portion of the flow. As found by Coles for a large variety of "tripped" boundary layer flows, the skin friction downstream of reattachment overshoots his results for zero pressure gradient and then slowly approaches equilibrium from above, while the wake strength falls and approaches its equilibrium value from below. The present data exhibit the same trends. Of particular note is that even at the last measurement position, 200 boundary-layer thicknesses downstream of reattachment, an equilibrium turbulent boundary layer has not yet been attained. This is attributed to a slow relaxation of the turbulence in the outer layer of the reattached flow.

The shape factor distribution is presented in Fig. 9 where, again, the laminar solution and Coles' results are shown. In addition, lines giving Thwaite's criterion for separation, $H = 3.7$, and Coles' criterion for reattachment, $H = 4.2$, are provided. As expected, the shape factor first rises and then falls rapidly in the separated region. The maximum value attained is about 8. Although both Thwaite's and Coles' criteria appear to be met (reattachment seems to occur at a slightly higher value of about 5), the rapid changes make an exact evaluation difficult. Downstream of reattachment, however, the shape factor quickly attains a value close to its equilibrium value. In fact, if H was considered the only relevant profile shape parameter, one would conclude incorrectly that the boundary layer is completely relaxed when $Re_\theta = 750$, which corresponds to distance downstream of reattachment of about 10 boundary-layer thicknesses. Interestingly, turbulent boundary layers are usually considered to relax in a distance of about 20 boundary-layer thicknesses.

The heat transfer results are presented in Fig. 10 where Stanton number distributions for the three test Reynolds numbers are plotted against a Reynolds number based on X. Both numbers are based on the local free-stream velociy U as given in Figs. 3 and 4. Also included in the graph are the laminar solution for two-dimensional stagnation flow and the turbulent flat plate correlation for a constant heat flux surface, namely

$$St = 0.57\ Pr^{-0.6} Re_X^{-0.5} \text{ (laminar)}$$

and

$$St = 0.0307\ Pr^{-0.4} Re_X^{-0.2} \text{ (turbulent)}$$

respectively, where Pr is the Prandtl number.

The data on the leading edge agree quite well with the laminar stagnation solution, as they should, up to the point where the free-stream flow begins to deviate from that having the uniform acceleration associated with stagnation flow. At this point, the Stanton number rapidly falls to about half of its value and then rises just as rapidly to a value 50 percent higher

than that for turbulent flow. The position on the body at which this occurred corresponded exactly to the low and high mass transfer region observed in the china clay flow visualization tests. The distance between the points of lowest and highest Stanton numbers in the figure is seen to be about $Re_L = 1.9\,(10)^4$ for all three Reynolds numbers. If this distance is proportional to that between separation and reattachment, the bubble length is inversely proportional to the incident velocity. This is in agreement with the results from the free-stream velocity distributions in Fig. 4.

After reattachment, the Stanton number quickly decreases to what appears to be a final state lying slightly below the turbulent flat plate correlation. The same behavior is evident if the results are plotted against a Reynolds number based on enthalpy thickness. Since most of the resistance to heat transfer is found in the sublayers, the initial decrease in Stanton number can be attributed to their rapid readjustment as seen from the velocity measurements. The fact that the results farther downstream lie below the flat plate correlation can be attributed to an incomplete relaxation of the thermal profile in the outer wake region of the boundary layer. This process, as evidenced by the wake strength results, is much slower than had been initially thought.

If the data after reattachment are plotted using the distance measured from the position of lowest heat transfer, Fig. 11 is obtained. Again, the turbulent flat plate correlation is also shown. Apparently, all of the data downstream of reattachment can be simply correlated to within 10 percent by a slightly modified version of the turbulent flat plate correlation given above, namely

$$St = 0.0285\,Pr^{-0.4}(Re_X - Re_{XS})^{-0.2} \qquad (1)$$

Although the physics is known to be much more complicated, as a first approximation, the reattached thermal boundary layer can be considered to behave as a turbulent layer with a virtual origin at separation.

Conclusions

As found by Ota and Kon at low incident Reynolds numbers, the flow about a parallel-sided body having a circular leading edge with incident Reynolds numbers near 10^5 also separates, and reattaches shortly downstream as a turbulent boundary layer with a low-momentum Reynolds number. In particular, it was found that the length-to-height ratio of the separated region was about 20 and that a Reynolds number based on its length was about $1.9\,(10)^4$. Downstream of reattachment, the recovery of the viscous boundary layer is extemely slow. For the cases examined, the turbulent boundary layer had not yet reached equilibrium at 200 boundary-layer thicknesses downstream of reattachment.

Through the separation region, the surface heat transfer was found to change by almost an order of magnitude and near reattachment was about 50 percent higher than that predicted by the turbulent flat plate correlation. The results downstream of reattachment, however, could be correlated by a simple flat plate type of expression providing a shift is made to account for the separation; however, this disguises the actual physics which was found to be more complicated.

Acknowledgments

The work reported in the paper was sponsored by the Heat Transfer Research Group at Pratt & Whitney Aircraft, East Hartford, Connecticut.

References

1 Bradshaw, P., and Wong, F. Y. F., "The Reattachment of a Turbulent Shear Layer," *Journal of Fluid Mechanics*, Vol. 52, 1972, pp. 113–135.

2 Simpson, R. L., "Summary Report on the Colloquium on Flow Separation," Project Squid, Report SMU-3-PU, 1970.

3 Chang, P. K., *Separation of Flow*, Pergamon, New York, 1970.

4 "Flow Separation," *AGARD Conference Proceedings*, AGARD-CP-168, 1975.

5 Seban, R. A., "Heat Transfer to the Turbulent Separated Air Flow Downstream of a Step in the Surface of a Plate," ASME *Journal of Heat Transfer*, Vol. 86, 1964, pp. 259–264.

6 Krall, K. M., and Sparrow, E. M., "Turbulent Heat Transfer in the Separated, Reattached, and Redeveloped Regions of a Circular Tube," ASME *Journal of Heat Transfer*, Vol. 88, 1966, pp. 131–136.

7 Filetti, E. G., and Kays, W. M., "Heat Transfer in Separated, Reattached, and Redeveloped Regions Behind a Double Step at the Entrance to a Flat Duct," ASME *Journal of Heat Transfer*, Vol. 89, 1967, pp. 163–168.

8 Zemanick, P. P., and Dougall, R. S., "Local Heat Transfer Downstream of an Abrupt Circular Channel Expansion," ASME *Journal of Heat Transfer*, Vol. 92, 1970, pp. 53–60.

9 Ota, T., and Kon, N., "Heat Transfer in the Separated and Reattached Flow on a Blunt Flat Plate," ASME *Journal of Heat Transfer*, Vol. 96, 1974, pp. 459–462.

10 Ota, T., and Kon, N., "Heat Transfer in an Axisymmetric Separated and Reattached Flow Over a Longitudinal Blunt Circular Cylinder," ASME *Journal of Heat Transfer*, Vol. 99, 1977, pp. 155–157.

11 Ota, T., and Kon, N., "Turbulent Transfer of Momentum and Heat in a Separating and Reattaching Flow Over a Blunt Flat Plate," ASME *Journal of Heat Transfer*, Vol. 102, 1980, pp. 749–754.

12 Ota, T., and Kon, N., "Heat Transfer in the Separated and Reattached Flow Over Blunt Flat Plates – Effects of Nose Shape," *International Journal of Heat and Mass Transfer*, Vol. 22, 1981, pp. 197–206.

13 DiElsi, G., and Mayle, R. E., "A Composite Constant Heat Flux Test Surface," in: *Heat and Mass Transfer in Rotating Machinery*, D. E. Metzger and M. H. Afgan, eds., Hemisphere, Washington, DC, 1984, pp. 259–268.

14 Compte-Bellott, G., Strohl, A., and Alcaraz, E., "On Aerodynamic Disturbances Caused by Single Hot-Wire Probes," ASME *Journal of Applied Mechanics*, Vol. 38, 1971, pp. 767–774.

15 Kline, S. J., and McClintock, F. A., "Describing Uncertainties in Single Sample Experiments," *Mechanical Engineering*, 1953, pp. 3–8.

16 Crabtree, L. F., "The Formations of Regions of Separated Flow on Wing Surfaces," ARC R&M 3122, 1959.

17 Carter, J. E., and Wornom, S. F., "Solutions for Incompressible Separated Boundary Including Viscous-Inviscid Interaction," NASA SP-347, 1975, pp. 125–150.

18 Ota, T., and Itasaka, M., "A Separated and Reattached Flow on a Blunt Flat Plate," ASME *Journal of Fluids Engineering*, Vol. 98, 1976, pp. 79–86.

19 Coles, D. E., "The Turbulent Boundary Layer in a Compressible Fluid," RAND Corporation Report B-403-PR, 1962.

Flat-Plate Film Cooling With Steam Injection Through One Row and Two Rows of Inclined Holes

J. C. Han
Associate Professor.

A. B. Mehendale
Research Assistant.

Turbomachinery Laboratories,
Department of Mechanical Engineering,
Texas A&M University,
College Station, TX 77843

Experiments have been performed to investigate the film-cooling characteristics with steam injection through one row (7 tubes) and two rows (13 tubes) of holes, inclined at an angle of 35 deg, over a flat plate. The spacing between the holes as well as the distance between the rows is 2½ hole diameters. Data have been obtained for both steam and air film-cooling effectiveness at different axial and lateral locations downstream of the injection holes. The blowing rate M *varied from 0.2 to 1.5. In the case of one-row injection, the results show that the film-cooling effectiveness with steam injection is about 50 to 100 percent higher than that with air injection at downstream locations, depending upon the blowing rate; however, the increase in film-cooling effectiveness is reduced near the injection hole region at high blowing rates. In the case of two-row injection, the laterally averaged film cooling effectiveness* $\bar{\eta}$ *can be correlated with the two-dimensional film-cooling parameter* ξ. *The* $\bar{\eta}$ *with steam injection is about 80 to 100 percent higher than that with air injection at low blowing rates and/or at downstream locations* ($\xi \geq 15$). *However, the increase in* $\bar{\eta}$ *with steam injection is reduced near the injection hole region and/or at high blowing rates* ($\xi \leq 15$).

Introduction

Film cooling has been used for protecting turbine blades and vanes from the surrounding high-temperature gas stream. In aircraft gas turbine applications, the majority of the studies have used air as the cooling fluid. Very few studies have considered using other gases, such as helium, hydrogen, argon, or refrigerant-12 vapor, as the cooling fluid [1, 2]. In recent years, steam has been proposed for cooling gas turbine blades and vanes in a combined cycle for ground-base power generation [3, 4]. A theoretical study [5] has predicted that the film-cooling effectiveness of steam is about twice that of air under the same operating conditions due to its favorable thermal properties such as specific heat and Prandtl number. Conklin et al. [6] have studied the film-cooling effectiveness with steam injection through three staggered rows of holes, inclined at an angle of 60 deg over a symmetric aluminum airfoil with blowing rate varying from 0.3 to 1.8. They found that the film-cooling effectiveness using steam was from 50 to 150 percent higher than when air was used. However, the data were obtained for an uncommon injection geometry and over a highly conductive aluminum airfoil, making it difficult to compare these results with other investigators' air cooling data. Han et al. [7] have studied the heat transfer and film cooling with steam injection through a single hole inclined over a 0.0254-cm-thick, stainless steel flat plate. The results showed that the film-cooling effectiveness using steam was about 30 to 60 percent higher than that when air was used, while the heat transfer was about 10 to 15 percent higher for all test data. From an application point of view, both one row and two rows of inclined holes, instead of a single inclined hole, have been used for the turbine blade film-cooling design. Therefore, there is a need to obtain steam film-cooling data based on these common injection geometries.

After these preliminary studies in steam film cooling [5–7], some basic questions have been raised. The first question is whether the increased film-cooling effectiveness for steam cooling is simply due to the thermal properties' effect as described in [5] or due to some other factors. The data obtained in [6, 7] are not able to answer this question completely, because the test sections and the injection geometries in [6, 7] are not well defined. The other question is how to determine the film-cooling effectiveness with a steam/air mixture, e.g., injecting 10 to 30 percent steam or water into cooling air, for aircraft or industrial engines. Can the data obtained with 100 percent steam be extrapolated for those with 10 to 30 percent steam/air mixture? In order to seek solutions for these questions, there is a need to obtain reliable steam-cooling data based on a common injection geometry over a flat-plate test section, with a minimum heat conduction effect.

This study was intended to document a film-cooling data base with 100 percent steam injection through one row and two rows of holes inclined at 35 deg over a flat plate. The steam was maintained at saturated condition, while the mainstream air was heated to a temperature higher than that of the saturated steam. The injection hole spacing and the row spacing (for the case of two-row injection) were each 2½ hole diameters. The test section was made of a 0.635-cm-thick teflon flat plate. Both steam and air cooling data were ob-

Contributed by the Gas Turbine Division of THE AMERICAN SOCIETY OF MECHANICAL ENGINEERS and presented at the 31st International Gas Turbine Conference and Exhibit, Düsseldorf, Federal Republic of Germany, June 8–12, 1986. Manuscript received at ASME Headquarters January 20, 1986. Paper No. 86-GT-105.

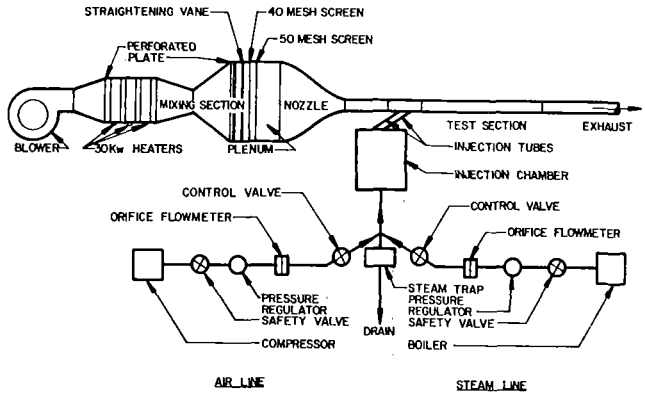

Fig. 1 Schematic of the test apparatus

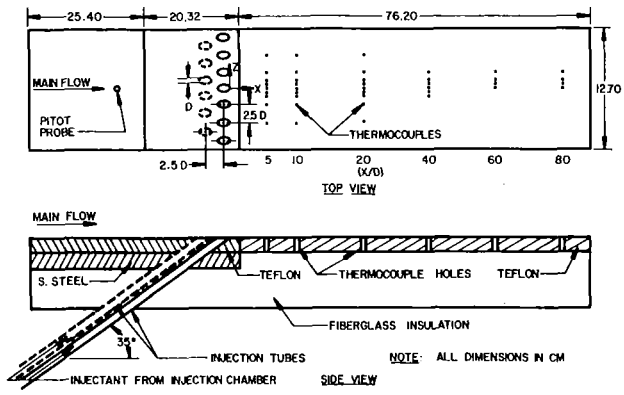

Fig. 2 Test section and injection tubes

tained at both axial and lateral locations downstream of the injection holes for blowing rates varying from 0.2 to 1.5. The density ratio for steam cooling was about 0.65 whereas that for air cooling was about 1.1. The air-cooling data were used for direct comparison with the steam-cooling data, based on the same test section, for the same blowing rate, and also with the air-cooling data existing in the open literature. The experiment will be described first, and then the results for steam and air cooling will be presented. Correlations between the laterally averaged film-cooling effectiveness $\bar{\eta}$ and the two-dimensional film-cooling parameter ξ for the case of two-row injection will be discussed.

Film-Cooling Test Rig

Wind Tunnel. A schematic diagram of the low-speed wind tunnel used for the previous studies [6, 7] is shown in Fig. 1. A 7-hp blower forced air at room temperature and pressure through 90 kW heaters and mixing sections into a plenum. A nozzle with a contraction ratio of 52:1 was used between the plenum and the test section to ensure that the air entering the test section had a uniform velocity and temperature distribution. From the end of the test section, the air was exhausted to the outside of the building. The maximum velocity of the heated air and its temperature, both at the inlet of the test section, were calibrated at about 49 m/s and about 155°C, respectively.

Injection Systems. For the air injection system, cooling air from a 17 m^3/min compressor passed through a pressure regulator (air pressure downstream of the regulator was about 2–3 psig), an orifice flow meter (the pressure drop was determined by Validyne transducer and demodulator), a control valve, and entered an injection chamber. The cooling air was then injected from the injection chamber through inclined injection tubes into the test section. The injection chamber was oriented in the vertical direction and had a cross section of 22.86 cm by 22.86 cm and a height of 50.8 cm. The injection tubes were either one row of seven tubes or two staggered rows of thirteen tubes at an angle of 35 deg to the direction of heated mainstream flow. The tubes had a 0.762-cm i.d. and were 45.72 cm long. The two sets of tubes, one on the injection chamber and the other on the test section, were connected by flexible tubes which were held in place by hose clamps. The

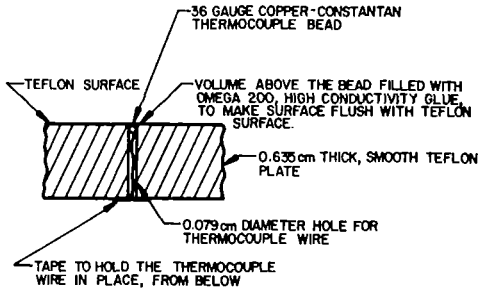

Fig. 3 A typical thermocouple mounting in the test plate

Nomenclature

C_p = specific heat
D = injection tube inside diameter
M = blowing rate = $\rho_2 U_2/\rho_\infty U_\infty$
$\dot{m}$ = mass flow rate
Re_D = mainstream Reynolds number based on hole diameter = $\rho_\infty U_\infty D/\mu_\infty$
Re_x = mainstream Reynolds number based on distance = $\rho_\infty U_\infty X/\mu_\infty$
Re_2 = injectant Reynolds number based on hole diameter = $\rho_2 U_2 D/\mu_2$
S = width of equivalent two-dimensional slot
T = temperature
T_{aw} = local adiabatic wall temperature with film cooling
T_w = local wall temperature with film cooling
T_{wo} = local wall temperature without film cooling
U = velocity
x = axial distance from the downstream edge of a downstream injection hole
Z = lateral distance from centerline of the center hole
α = injection angle
η = film cooling effectiveness; equations (1) and (2)
η_c = centerline film effectiveness
η_e = edgeline film effectiveness
$\bar{\eta}$ = laterally averaged film-cooling effectiveness; equations (4) and (5)
μ = viscosity
ξ = two-dimensional film-cooling parameter; equation (3)
ρ = density
$(\rho_2/\rho_\infty)_a$ = density ratio for air-to-air injection
$(\rho_2/\rho_\infty)_s$ = density ratio for steam-to-air injection

Subscripts

2 = coolant at outlet of injection hole
∞ = mainstream at inlet of test section
$2a$ = cooling air
$2s$ = cooling steam

Table 1 Test section and injection geometry

Test channel	12.7 cm by 12.7 cm in cross section, 121.92 cm long, and made of four teflon flat plates, each 0.635 cm thick
Test plate	12.7 cm wide, 76.2 cm long, and 0.635 cm thick teflon flat plate
One-row injection	7 tubes
Two-row injection	13 tubes
Injection tube inner diameter	D = 0.762 cm
Injection tube spacing	2.5 D
Injection row spacing	2.5 D
Injection tube angle	α = 35 deg

Table 2 Operating conditions

Mainstream heated air velocity at $X/D = -20$	$U_\infty = 49$ m/s
Mainstream air turbulence intensity at $X/D = -20$	$U'/U_\infty \leq 0.5\%$
Mainstream heated air temperature for air cooling at $X/D = -20$	$T_\infty = 76.7°C$
Mainstream heated air temperature for steam cooling at $X/D = -20$	$T_\infty = 154.4°C$
Mainstream heated air Reynolds number based on D at $X/D = -20$	$Re_D = 2 \times 10^4$
Mainstream heated air Reynolds number based on X at $X/D = -20$	$Re_x = 8 \times 10^5$
Cooling-air temperature	$T_2 = 21$–$27°C$
Cooling-steam temperature	$T_2 = 99$–$102°C$
Cooling-fluid Reynolds number	$Re_2 = 6 \times 10^3$–5×10^4
Density ratio with air cooling	$(\rho_2/\rho_\infty)_a = 1.1$
Density ratio with steam cooling	$(\rho_2/\rho_\infty)_s = 0.65$
Blowing rate	$M = 0.2$–1.5

lateral distance between the tubes and the axial distance between the rows (in the case of two-row injection) was 2½ diameters, respectively.

For the steam injection system, saturated steam from a 125 psig boiler passed through a piping line similar to that for air, except for a steam trap located at the bottom of the injection chamber to bleed off the condensate. The steam was passed through a throttling valve (regulator) to lower the steam pressure (steam pressure downstream of the regulator was about 3–5 psig) and temperature.

Thermocouples were placed inside the injection tubes (about 20 tube diameters downstream of the injection point), to measure the cooling air temperature (21–27°C) and cooling steam temperature (99–102°C). The blowing rate M was varied from 0.2 to 1.5 by controlling the coolant flow rate.

Test Section. The test channel was 12.7 cm by 12.7 cm in cross section and 121.92 cm long, and was made of teflon plates. The bottom plate of the test channel served as a flat-plate test section. The test section consisted of three segments as shown in Fig. 2. The first segment (25.4 cm long) of the test section contained a pitot tube probe with a thermocouple to determine the velocity and the temperature of the heated mainstream air at the upstream of injection holes, i.e., at the inlet of the test section. The second segment (20.32 cm long) contained one row (or two rows) of inclined injection tubes as described earlier. The third segment (76.2 cm long) of the test section contained the test plate. In order to minimize the heat conduction effect, the test plate was made of teflon with a smooth surface and was 0.635 cm thick. A total of 41, calibrated, 36-gauge copper-constantan thermocouples were placed at strategic locations on the test plate to measure the local surface temperature, as shown in Fig. 2. At these locations, 0.079-cm-dia holes were drilled and the thermocouples were inserted from below, bead first, until the top of the bead was level with the surface. The tiny cavity above the bead was filled with Omega 200 high thermal conductivity glue until the top surface of the hole was flush with the teflon test surface, so as not to disturb the flow conditions, as shown in Fig. 3. They were held in place, from below, by using a piece of aluminum tape. The entire test channel was covered by a

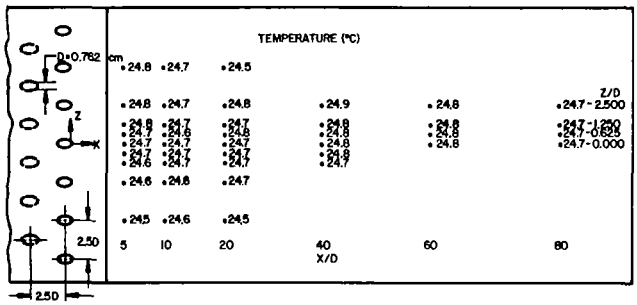

Fig. 4(a) Local wall temperature without film cooling (T_{wo}) at T_∞ = 25.8°C, U_∞ = 48.8 m/s

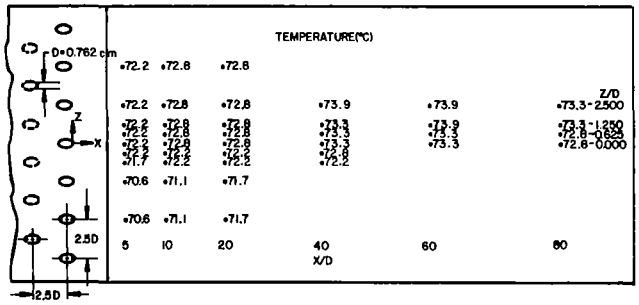

Fig. 4(b) Local wall temperature without film cooling (T_{wo}) at T_∞ = 76.7°C, U_∞ = 48.8 m/s

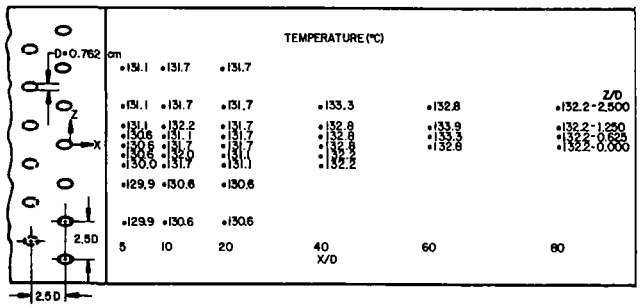

Fig. 4(c) Local wall temperature without film cooling (T_{wo}) at T_∞ = 154.4°C, U_∞ = 48.8 m/s

fiberglass insulation board, 10.16 cm thick, to reduce the heat losses to the environment. A Fluke 2280A Data Logger was used for the thermocouple instrumentation. Details of the test section and of the injection geometry are given in Table 1.

Test Conditions and Data Analysis

Test Conditions. Steady-state conditions were maintained during all tests. The mainstream air was kept at a constant temperature higher than the cooling steam to ensure that the steam would not condense on the test plate. The details of the operating conditions are presented in Table 2. Before beginning the film-cooling tests, experiments were conducted without injection, in order to check the mainstream flow conditions. The unheated velocity profile at a position 19.1 cm upstream of the leading edge of the leading row of injection holes, corresponding to $X/D = -20$, and at $Z/D = 0$, was measured by traveling a pitot tube probe across the boundary layer. At this location, the dimensionless velocity profile was fairly close to the 1/7th power velocity profile for a turbulent boundary layer as presented in [7]. The Reynolds numbers, Re_D and Re_x, were about 2×10^4 and 8×10^5, respectively. The corresponding mainstream turbulence intensity was measured to be less than 0.5 percent by using DISA 55 D 05 hot-wire anemometry. Therefore, the mainstream flow could

Table 3 Runs for adiabatic film-cooling effectiveness

Blowing rate	One row		Two rows	
	Cooling air	Cooling steam	Cooling air	Cooling steam
0.2	x	x	x	x
0.35	x	x	x	x
0.5	x	x	x	x
0.75	x	x	x	x
1.0	x	x	x	x
1.25			x	
1.5	x	x		

be assumed to have a turbulent boundary layer profile when approaching the injection holes.

Tests were performed without film cooling in order to check the thermocouple readings for different mainstream temperatures. The fairly uniform local wall temperature distribution for the unheated mainstream air is shown in Fig. 4(*a*), thus proving that the gluing technique used for the thermocouples is acceptable. Typical local wall temperature distributions for mainstream air temperatures of 76.7°C and 154.4°C are shown in Figs. 4(*b*) and 4(*c*), respectively. It can be seen that the local wall temperatures without film cooling T_{wo} are about 3.7°C to 21°C lower than the heated mainstream air, due to the heat loss through the test model.

Data Analysis. For a perfect adiabatic wall (without heat loss) the standard adiabatic film-cooling effectiveness is defined as

$$\eta = (T_\infty - T_{aw})/(T_\infty - T_2) \quad (1)$$

where T_∞ = mainstream air temperature, T_{aw} = local adiabatic wall temperature during film cooling, and T_2 = cooling-fluid temperature.

In order to justify the heat loss through the present teflon plate test section, the adiabatic film-cooling effectiveness in equation (1) may be rewritten as

$$\eta = (T_{wo} - T_w)/(T_{wo} - T_2) \quad (2)$$

where T_{wo} = local wall temperature without film cooling, T_w = local wall temperature with film cooling, and T_2 = cooling-fluid temperature.

For a perfectly adiabatic wall, equation (2) will reduce to equation (1), i.e., $T_{wo} = T_\infty$, and $T_w = T_{aw}$. Based on the present low-conductivity teflon plate and the heated mainstream temperature levels, the film-cooling effectiveness calculated from equation (1), without correction for heat loss, is higher than that from equation (2). In order to provide conservative (lower bound) adiabatic film-cooling data, equation (2) was chosen for the present investigation. The maximum uncertainty in the film-cooling effectiveness calculated from equation (2) was estimated to be 2 percent for both steam and air cooling. The details of the runs for the present study are given in Table 3. The detailed raw data of T_{wo} and T_w, and the calculated local η for all tests, are given in the contractor report prepared for AVCO-Lycoming [8].

It is worthwhile to note the theoretical one-dimensional model developed by Blair and Lander [9] to correct the film-cooling effectiveness due to heat losses through a urethane flat plate. They derived a relationship between the adiabatic effectiveness, the experimentally measured effectiveness, and the nonflow (without film cooling) effectiveness as presented in equation (A-7) [9]. By substituting the parameters of the experimentally measured effectiveness and the nonflow effectiveness defined in their paper into equation (A-7), the adiabatic effectiveness in equation (A-7) can be reduced to equation (2) of the present study. This further supports that equation (2) can be used, with confidence, to calculate the adiabatic film-cooling effectiveness when a finite (but small) heat loss through the test section is considered.

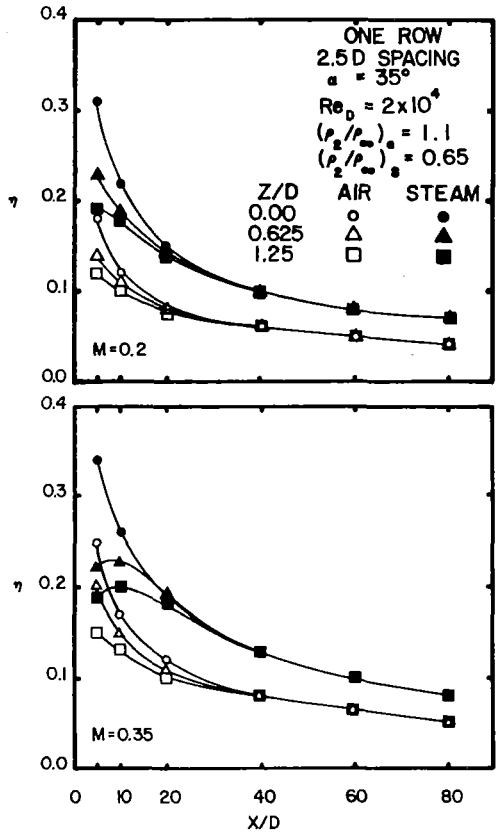

Fig. 5 Local film effectiveness versus axial distance for M = 0.2, 0.35

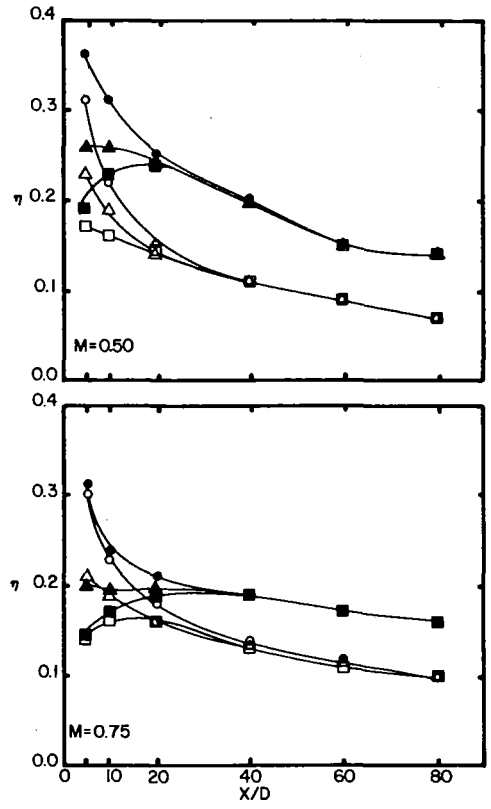

Fig. 6 Local film effectiveness versus axial distance for M = 0.5, 0.75

Results and Discussion

One Row. *Test results of film-cooling effectiveness with* air and steam injections through one row of tubes, inclined at

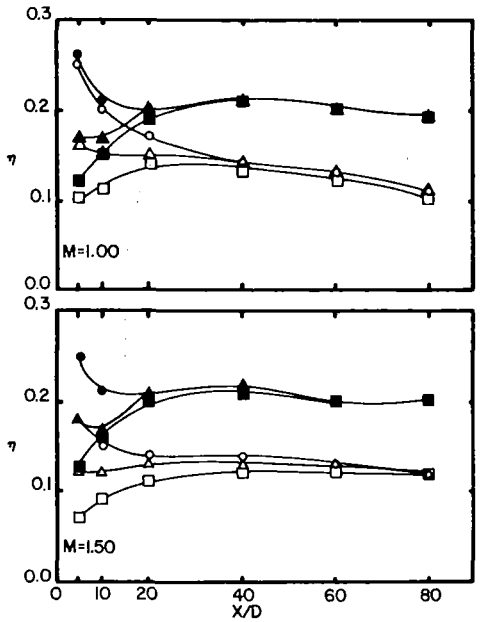

Fig. 7 Local film effectiveness versus axial distance for M = 1.0, 1.5

an angle of 35 deg, are shown in Figs. 5–7. It is expected that the centerline (Z/D = 0) cooling effectiveness decreases with increasing axial distance for all blowing rates for both steam and air injections. For air cooling, the edgeline effectiveness (Z/D = 1.25) decreases with increasing axial distance for low blowing rates ($M \leq 0.75$). For steam cooling, the edgeline effectiveness generally increases and then decreases with axial distance for low blowing rates ($M \leq 0.75$), whereas it increases and then reaches a plateau for high blowing rates ($M \geq 1.0$). The film-cooling effectiveness is fairly uniform in the lateral direction (z direction) at the farther downstream locations ($X/D \geq 20$). Significant variations in film-cooling effectiveness in the lateral direction appear near the injection hole region, caused by the fact that the cooling fluid penetrates into the mainstream boundary layer and creates the mixing between the coolant and mainstream along the edgelines of cooling holes (Z/D = 1.25). The effects are more pronounced for high blowing rates. These figures also indicate that steam injection provides a higher film-cooling effectiveness (50 to 100 percent higher) than that for air injection depending upon the blowing rate. This may be explained by the fact that steam has a higher specific heat (almost double) than air. It is interesting to note that the advantage of steam specific heat for film cooling is reduced near the injection hole region ($X/D \leq 10$), because of mixing, at high blowing rates.

The centerline (Z/D = 0) and edgeline (Z/D = 1.25) effectiveness versus blowing rate at different axial locations for steam and air injections is shown in Figs. 8 and 9, respectively. For one row injection, the centerline film-cooling effectiveness increases with increasing blowing rate and reaches a maximum value at a blowing rate of about 0.5–0.75 and then decreases with further increasing blowing rate for $X/D \leq 20$. However, the film cooling effectiveness gradually increases with blowing rate at the farther downstream locations ($X/D \geq 40$). It is noted that the effectiveness downstream is always lower than the effectiveness upstream at a given blowing rate. The edgeline effectiveness has the same trends as those of the centerline except that the edgeline effectiveness at the downstream ($X/D \geq 40$) is higher than that at the upstream for $M > 1.0$. These figures also show that the centerline effectiveness is always higher than the edgeline effectiveness, and the steam-cooling effectiveness is always higher than the air-cooling effectiveness for all blowing rates.

Two Rows. Test results of film-cooling effectivenesses for

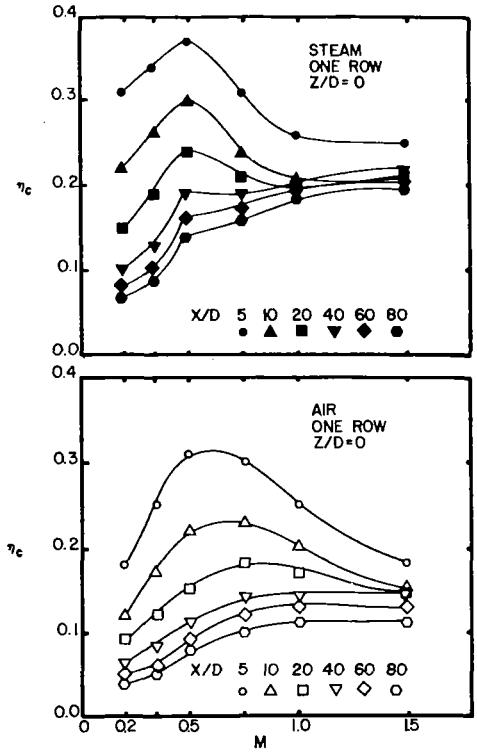

Fig. 8 Centerline film effectiveness versus blowing rate

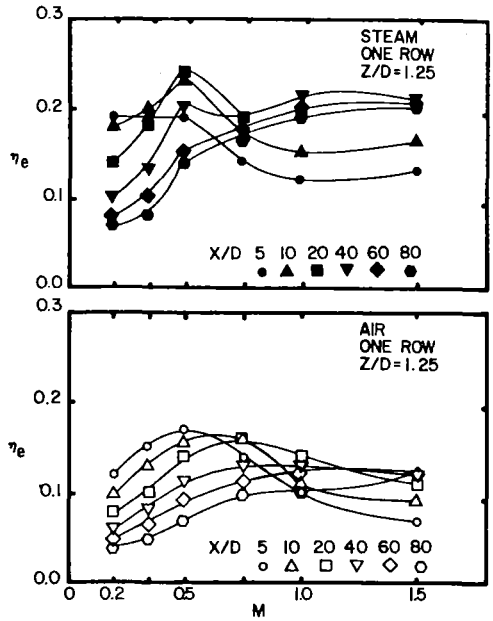

Fig. 9 Edgeline film effectiveness versus blowing rate

air and steam injections through two rows of tubes inclined at 35 deg are shown in Figs. 10 and 11. The centerline effectiveness is almost the same as the edgeline effectiveness, except that there is a very small difference near the injection hole region (X/D = 5) for both steam and air injections at all blowing rates. The effectiveness decreases with increasing axial distance, but the rate of decrease is smaller than that for the one-row injection. Again, the steam film-cooling effectiveness is about 80 to 100 percent higher than that for air. However, the increase in effectiveness is reduced near the injection hole region due to the mixing between the injection fluid and the mainstream flow.

The centerline effectiveness versus blowing rate at different

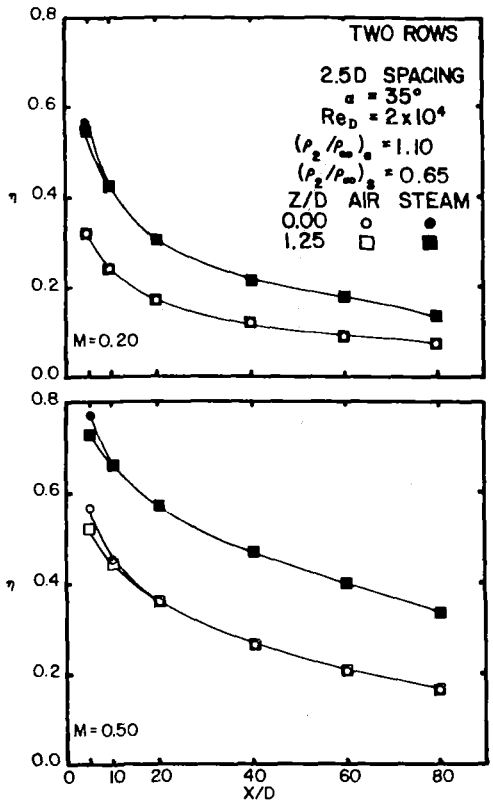

Fig. 10 Local film effectiveness versus axial distance for two rows at $M = 0.2, 0.5$

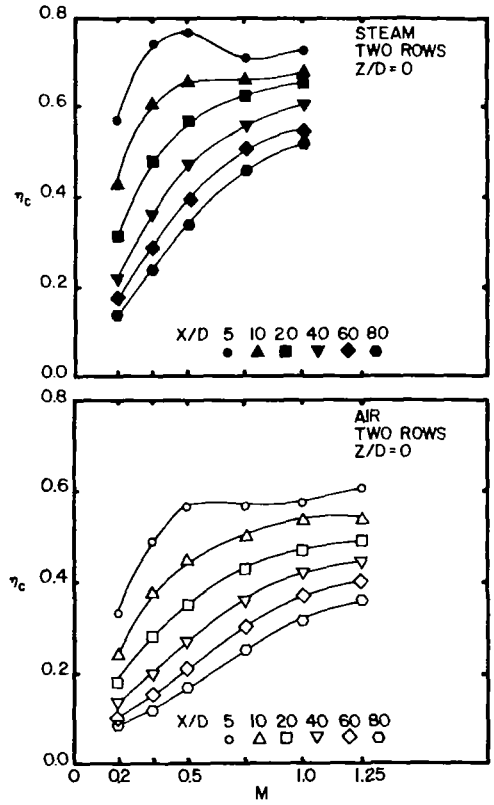

Fig. 12 Centerline film effectiveness versus blowing rate

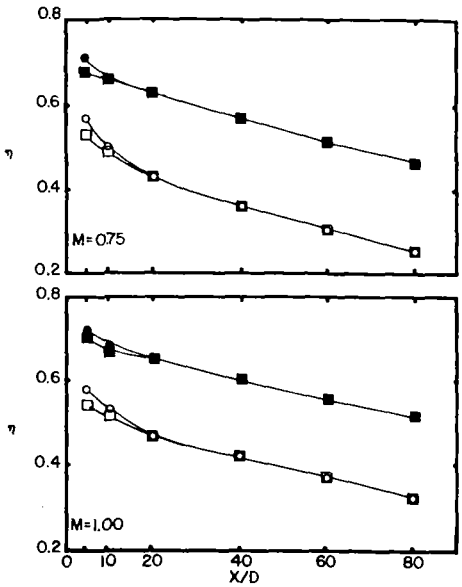

Fig. 11 Local film effectiveness versus axial distance for two rows at $M = 0.75, 1.0$

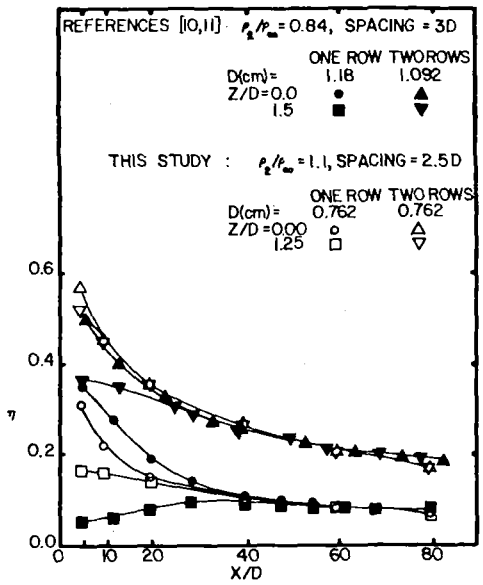

Fig. 13 Comparison of local film effectiveness for $M = 0.5$

axial distances is shown in Fig. 12. For two-row injection, the film-cooling effectiveness increases with blowing rate and then reaches a plateau at a blowing rate of about 1.0 for $X/D \leq 20$, but it increases continuously with blowing rate at the farther downstream locations, $X/D \geq 40$.

Comparison. Comparison of local film-cooling effectiveness for air injection, for both one and two rows, at a blowing rate of $M = 0.5$ with [10, 11] is shown in Fig. 13. For one-row injection, the spanwise variations of the film-cooling effectiveness for the present case are smaller than those for the Ericksen and Goldstein study [10], although the discrepancy decreases with increasing X/D ratio. This may be due to two factors: First, the injection tube diameter ($D = 1.17$ cm) and tube spacing ($3D$) in [10] are both larger than those for the present study ($D = 0.76$ cm, spacing $= 2.5D$); second, the density ratio ($\rho_2/\rho_\infty = 0.84$) in [10] is smaller than that for this study ($\rho_2/\rho_\infty = 1.1$). The larger hole diameter and spacing would provide a larger spanwise effectiveness variation, and the smaller density ratio will have a larger mixing between the coolant and mainstream flow, to provide a larger spanwise effectiveness variation; the effects are particularly severe near

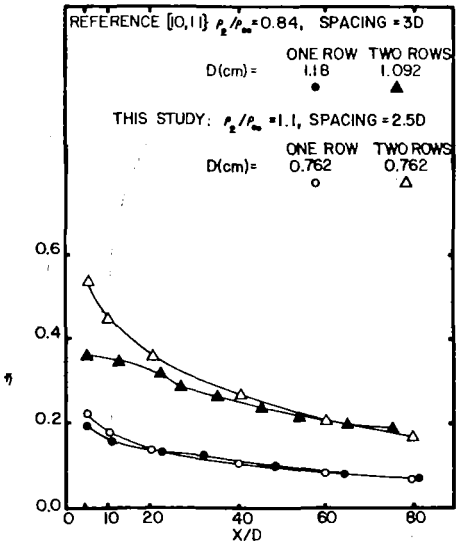

Fig. 14 Comparison of lateral average film effectiveness for $M = 0.5$

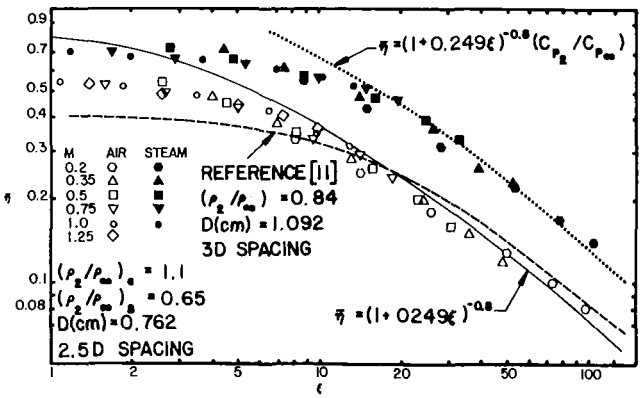

Fig. 15 Correlation of $\bar{\eta}$ versus ξ for two rows and comparison with two-dimensional film-cooling models

the injection hole region. However, the lateral (spanwise) average film-cooling effectiveness from the present data is very close to that in [10] as shown in Fig. 14.

For two-row injection, the data from Jabbari and Goldstein [11] show many more variations in spanwise direction near the injection hole region ($X/D \leq 20$) than this study, as shown in Fig. 13. This may be due to the larger hole spacing in both axial and lateral directions in [11]. However, the lateral average effectiveness of the present two-row data is higher than that from [11] as shown in Fig. 14, especially near the injection hole region ($X/D \leq 20$). This is because the present study has a relatively larger density ratio. The larger density ratio means that the injectant has a smaller momentum to penetrate through the mainstream flow and will provide a better film coverage over the surface; but the smaller density ratio in [11] will cause more mixing between the coolant and the main flow, the more mixing resulting in a larger spanwise effectiveness variation and the smaller lateral average effectiveness.

Correlation. For two-row injection, the laterally uniform effectiveness obtained for both air and steam injections suggests that these data may be correlated with two-dimensional film-cooling parameters as described earlier [11]. The correlations for both steam and air are shown in Fig. 15 in which the injection parameter ξ is defined by

$$\xi = [(x + 1.909D)/MS](\mathrm{Re}_2\mu_2/\mu_\infty)^{-0.25} \quad (3)$$

where $S = \pi D/5$, for the present study, is the width of an equivalent two-dimensional slot located midway between the two rows of holes in the flow direction. The two-row air-cooling data from [11], and one of the two-dimensional film-cooling predictions from [1], viz.

$$\bar{\eta} = (1 + 0.249\xi)^{-0.8} \quad (4)$$

are also shown in Fig. 15. For air cooling, the present data and the data from [11] are fairly close to equation (4) for $\xi \geq 10$. This implies that the two-dimensional film-cooling model is valid for low blowing rates and/or at the farther downstream locations. For high blowing rates and near the injection hole region ($\xi \leq 10$), the coolant fluid penetrates into the mainstream which results in a lower film-cooling effectiveness than that for the two-dimensional film-cooling model (slot injection). It is interesting to point out that the present $\bar{\eta}$ is higher than that in [11] for $\xi \leq 10$. As mentioned before, this is because the present study has a larger density ratio and a smaller hole spacing than that in [11]. In other words, the present data are closer to the two-dimensional character than [11] near the injection hole region and/or for high blowing rates.

For steam cooling too, the two-dimensional character will apply at the farther downstream locations and/or low blowing rates ($\xi \geq 15$). In this region, the laterally averaged effectiveness $\bar{\eta}$ can be approximately modified from equation (4) as

$$\bar{\eta} = (1 + 0.249\xi)^{-0.8}(C_{p2}/C_{p\infty}) \quad (5)$$

where the specific heat ratio $C_{p2}/C_{p\infty}$ of the present steam-cooling study is about 1.8. In the upstream region and/or at high blowing rates ($\xi \leq 15$), the jet departs from the two-dimensional behavior and results in a lower $\bar{\eta}$. Therefore, the advantage of the steam (higher specific heat) for cooling is somewhat reduced. The steam cooling behaves more like a three-dimensional character (the slope of $\bar{\eta}$ for steam is smaller than that for air at $\xi \leq 15$), as shown in Fig. 15, because in the present study, the density ratio for steam injection ($\rho_2/\rho_\infty = 0.65$) is lower than that for air injection ($\rho_2/\rho_\infty = 1.1$). As indicated earlier, the lower density ratio case will have a lower effectiveness (because of higher jet momentum and hence more mixing) [12]. Therefore, if the density ratio for steam injection were the same as the density ratio for air injection, the slope of $\bar{\eta}$ in Fig. 15 would be the same for both steam and air injection for $\xi \leq 15$, except that $\bar{\eta}$ for steam cooling would still be higher due to the effect of specific heat.

For the case of film cooling with a mixture injection (i.e., 10 to 30 percent steam mixed with air), the film effectiveness may be deduced from equation (5) or interpolated from Fig. 15. In this case, the coolant specific heat in equation (5) should be determined by the mass flow rate ratio of the mixture as

$$C_{p2} = (C_{p2s}\dot{m}_{2s} + C_{p2a}\dot{m}_{2a})/(\dot{m}_{2s} + \dot{m}_{2a}) \quad (6)$$

Conclusions

1 It is concluded that, in the two-dimensional film-cooling region (larger ξ, i.e., low blowing rates and/or farther downstream locations), the increased film-cooling effectiveness with steam cooling is simply due to the favorable specific heat as predicted in [5]. However, in the three-dimensional film-cooling region (small ξ, high blowing rates, and/or near injection hole region), the increase in film-cooling effectiveness is reduced because the advantage of higher specific heat is lessened due to the mixing between the injectant and the mainstream.

2 In this study, the density ratio for steam cooling is 0.65, while that for air cooling is 1.1. The film-cooling effectiveness for one-row steam injection is about 50 to 100 percent higher than that when air is used, at the downstream locations, depending upon the blowing rate; whereas the film-cooling effectiveness of two-row steam injection is about 80 to 100 percent higher at low blowing rates ($\xi \geq 15$). However, in

general, the increases in effectiveness is reduced near the injection hole region and/or at high blowing rates ($\xi \leq 15$).

3 The effect of density ratio on the film-cooling effectiveness is important near the injection hole region. The actual effectiveness augmentation for steam injection near the injection hole region should be higher than that presented in this paper. This is because in this study, the density ratio for steam injection is about 50 percent lower than that for air injection.

4 From the application point of view, the film-cooling effectiveness with two-row steam cooling can be determined from equation (5) for a given ξ and $C_{p2}/C_{p\infty}$ when $\xi \geq 15$. The film-cooling effectiveness for steam/air mixture cooling may be deduced from equations (5) and (6).

Acknowledgments

This work was sponsored by AVCO-LYCOMING DIVISION under contract N-832132-E and was monitored by Dr. H. F. Jen and Mr. E. O. Hartel. Their support is gratefully acknowledged. The assistance from Mr. H. W. Chen, Mr. E. Denk, and Dr. J. C. Bailey of the Turbomachinery Laboratories at Texas A&M University and Dr. P. E. Jenkins is also acknowledged.

References

1 Goldstein, R. J., "Film Cooling," *Advances in Heat Transfer*, Vol. 7, Academic Press, New York–London, 1971, pp. 321–379.

2 Goldstein, R. J., Rask, R. B., and Eckert, E. R. G., "Film Cooling With Helium Injection Into an Incompressible Air Flow," *Int. J. Heat Mass Transfer*, Vol. 9, 1966, p. 1341.

3 Rice, I. G., "Steam-Cooled Blading in a Combined Reheat Gas Turbine/Reheat Steam Turbine Cycle: Part I – Performance Evaluation," ASME Paper No. 79-JPGC-GT-2.

4 Rice, I. G., "Steam-Cooled Blading in a Combined Reheat Gas Turbine/Reheat Steam Turbine Cycle: Part II – Design Considerations," ASME Paper No. 79-JPGC-GT-2.

5 Han, J. C., and Jenkins, P. E., "Prediction of Film Cooling Effectiveness of Steam," ASME Paper No. 82-GT-100.

6 Conklin, G. E., Han, J. C., and Jenkins, P. E., "Film Cooling With Steam Injection Through Three Staggered Rows of Inclined Holes Over a Straight Airfoil," ASME Paper No. 83-GT-30.

7 Han, J. C., Chen, H. W., and Jenkins, P. E., "Heat Transfer and Film Cooling With Steam Injection Through an Inclined Hole Over a Flat Plate," ASME Paper No. 83-HT-9.

8 Han, J. C., and Mehendale, A. B., "Film Cooling and Heat Transfer With Steam Injection Through Inclined Circular Holes," Contract Report TEES 1600, Texas A&M University, under AVCO Lycoming Contract N-832132-E, May 1985.

9 Blair, M. F., and Lander, R. D., "New Techniques for Measuring Film Cooling Effectiveness," ASME *Journal of Heat Transfer*, Vol. 97, Nov. 1975, pp. 539–543.

10 Eriksen, V. L., and Goldstein, R. J., "Heat Transfer and Cooling Following Injection Through Inclined Circular Tubes," ASME *Journal of Heat Transfer*, Vol. 96, May 1974, pp. 239–245.

11 Jabbari, M. Y., and Goldstein, R. J., "Adiabatic Wall Temperature and Heat Transfer Downstream of Injection Through Two Rows of Holes," ASME JOURNAL OF ENGINEERING FOR POWER, Vol. 100, 1978, pp. 303–307.

12 Pedersen, D. R., Eckert, E. R. G., and Goldstein, R. J., "Film Cooling With Large Density Differences Between the Mainstream and the Secondary Fluid Measured by the Heat-Mass Transfer Analogy," ASME *Journal of Heat Transfer*, Vol. 99, Nov. 1977, pp. 620–627.

The Effect of Inlet Conditions on Heat Transfer in a Rotating Cavity With a Radial Outflow of Fluid

C. A. Long

J. M. Owen

Thermo-Fluid Mechanics Research Centre,
School of Engineering and Applied Sciences,
University of Sussex,
Brighton, Sussex, England

Flow visualization and heat transfer measurements have been made in the cavity between two corotating discs. The discs were 762 mm in diameter and could be rotated up to 2000 rpm. Air, at flow rates up to 0.1 kg/s, entered the cavity through either a central hole 76 mm in diameter or a porous inner shroud 380 mm in diameter; in both cases, the air left via holes in an outer shroud attached to the periphery of the discs. Flow visualization confirmed that Ekman-layer flow could occur: A source region, Ekman layers, sink layers, and interior core were observed. A simple theoretical model provided estimates of the size of the source region that were in satisfactory agreement with the observations. At sufficiently high rotational speeds, where Ekman layers form over much of the surface of each disc, measured Nusselt numbers were in reasonable agreement with values computed from the momentum- and energy-integral equations.

1 Introduction

The turbine discs in advanced gas turbine engines are often cooled by a radial outflow of air extracted from the compressor stages, and Fig. 1 shows a simplified arrangement of such cooling flows. The basic fluid dynamics and heat transfer can be more readily understood by the use of rotating disc systems (see [1]): The flow between a turbine disc and an adjacent stationary casing can be modeled by a rotor–stator system; the flow between corotating turbine discs can be modeled by a rotating cavity. In the latter case, which is shown in Fig. 2, the cavity comprises plane discs of radius b, separated by an axial gap s, and a peripheral shroud. Air enters the cavity at radius a, either through a hole in the center of one disc (which is referred to as the "upstream disc") or through a porous inner shroud; in both cases, the air leaves through discrete holes in the peripheral shroud.

The flow and heat transfer in a rotating cavity has been studied theoretically and experimentally by a number of research workers (see, for example, [2–13]). It is useful, however, to discuss the salient features of the flow structure for the radial-inlet and axial-inlet cases shown in Figs. 2(a) and 2(b), respectively. For the isothermal radial-inlet case, the source region distributes exactly half the flow into each of the Ekman layers,[1] and the sink layer distributes the flow from the Ekman layers into the holes in the peripheral shroud. In the interior core between the Ekman layers, viscous effects are negligible and there is a balance between Coriolis and pressure forces which cause the fluid to rotate (relative to a frame of reference rotating with the discs).

For the isothermal axial-inlet case, the incoming fluid can impinge on the downstream disc and flow outward as a wall jet, as shown in Fig. 2(b). Although this alters the structure and size of the source region compared with that for the radial-inlet case, the flow outside this region remains the same as that described above. This is true for both laminar and turbulent isothermal flow. However, if one disc of the cavity is heated (see [5, 7, 13]), buoyancy effects can result in the axial

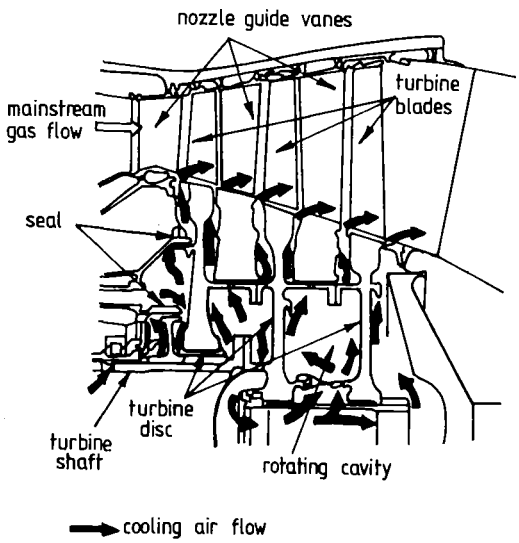

Fig. 1 An air-cooled gas turbine rotor

[1] The term "Ekman layer" is used here to refer to a boundary layer in which the nonlinear inertial forces are much smaller than the Coriolis forces. According to [12], transition from laminar to turbulent flow in such layers occurs at $Re_r = 180$, where Re_r is the radial Reynolds number defined in the Nomenclature.

Contributed by the Gas Turbine Division of THE AMERICAN SOCIETY OF MECHANICAL ENGINEERS and presented at the 31st International Gas Turbine Conference and Exhibit, Düsseldorf, Federal Republic of Germany, June 8–12, 1986. Manuscript received at ASME Headquarters January 20, 1986. Paper No. 86-GT-95.

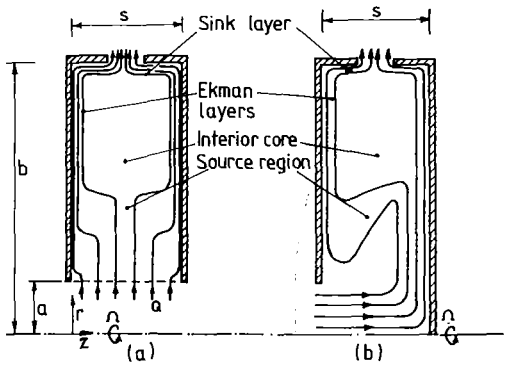

Fig. 2 Schematic diagram of the flow structure inside a rotating cavity with a radial outflow of coolant: (*a*) radial inlet; (*b*) axial inlet

transfer of fluid from one Ekman layer to the other. At sufficiently high rotational speeds, the fluid may reverse direction on the heated disc (flowing radially inward rather than outward) with subsequent transition from forced to free convection.

Heat transfer measurements in the studies referred to above were made under steady-state conditions and for one particular inlet configuration (the axial-inlet case with $a/b=0.1$). In the work described below, heat transfer was measured during thermal transients, and the results for two inlet configurations (the axial-inlet case with $a/b=0.1$ and the radial-inlet case with $a/b=0.5$) are compared. In Section 2, an outline of the experimental apparatus and data analysis is given. Section 3 provides a summary of the theoretical models that are used to calculate the size of the source region and the Nusselt numbers on the heated disc. Section 4 discusses the results of flow visualization and heat transfer measurements, and comparisons are made between the measurements and predictions for both inlet configurations tested.

2 Experimental Apparatus and Data Analysis

The apparatus and data analysis are described in detail in [9] so only the salient features are presented here.

2.1 Experimental Apparatus. The rig used for the rotating-cavity tests is shown in Figs. 3(*a*) and 3(*b*). The rotating cavity was formed from two steel discs, 762 mm in diameter and with an axial spacing of 102 mm, together with a

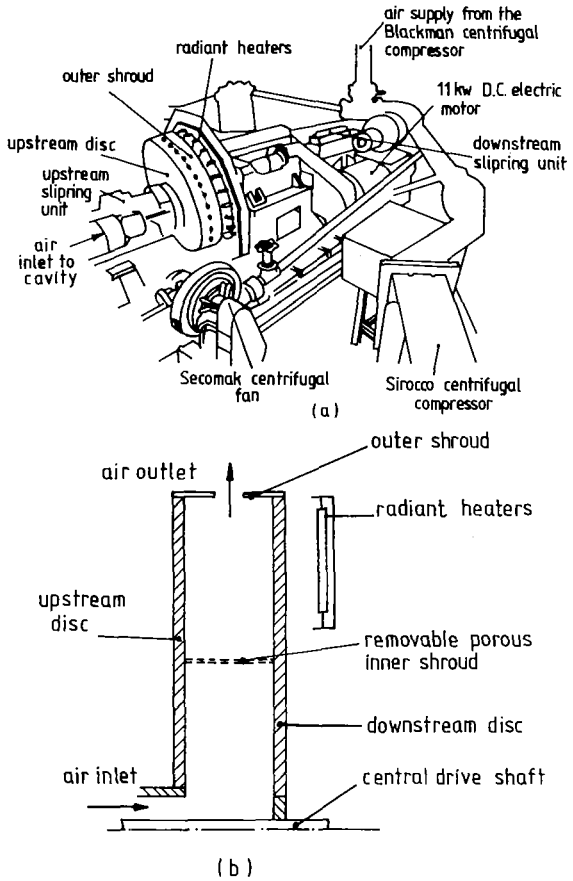

Fig. 3 The rotating-cavity rig: (*a*) schematic of the apparatus; (*b*) section through the cavity

peripheral outer shroud made from 1.5-mm-thick paxolin (a fiber-reinforced plastic material). The two discs were connected by a central drive shaft 25 mm in diameter, and cooling air was fed into the cavity through an annular hole, with inner and outer diameters of 25 mm and 76 mm, respectively, in the center of one of the discs (referred to as the "upstream disc"). The air left the cavity via holes in the outer shroud (30 holes 28.6 mm in diameter were arranged at 12-deg angular intervals in the midaxial plane of the shroud). For the radial-inlet configuration, a porous inner shroud with an outer diameter of

Nomenclature

A, B = constants in equations (3.7) and (3.8)
a = inner radius of cavity
b = outer radius of cavity
c = a/b = radius ratio
C_w = $Q/\nu b$ = flow rate coefficient
G = s/b = gap ratio
k = thermal conductivity
l = half-thickness of disc
N = number of finite-difference time steps
Nu = $qr/k(T_s-T_f)$ = local Nusselt number
Pr = ν/α = Prandtl number
q = heat flux
Q = volumetric flow rate of fluid entering the cavity
r = radial coordinate
r_i = inner radius of finite-difference grid
Re_r = $Q/2\pi\nu r$ = radial Reynolds number
Re_ϕ = $\Omega b^2/\nu$ = rotational Reynolds number
s = axial spacing between the rotating discs
t = time
T = temperature
$\bar{V}_\phi$ = tangential component of velocity, relative to a stationary frame, outside the Ekman layers
x = r/b = nondimensional radial coordinate
z = axial coordinate
α = thermal diffusivity
γ = $0.665 C_w^{-5/8}\mathrm{Re}_\phi^{1/2}$ = parameter in linear Ekman-layer theory
Δr = finite-difference radial step length
Δt = finite-difference time step length
Δz = finite-difference axial step length
θ = $(T_s-T_{\mathrm{ref}})/(T_{ss}-T_{\mathrm{ref}})$ = nondimensional disc temperature
ν = kinematic viscosity
Ω = angular speed of cavity

Subscripts

d = pertaining to disc
e = edge of source region
I = inlet to cavity
l = local value
ref = reference value
s = cavity-side surface of heated disc
ss = steady-state value

380 mm ($a/b=0.5$) was fitted in the cavity. This inner shroud was made from three-ply woven stainless-steel mesh of 1.5-mm thickness, and it was thermally insulated from the discs by means of neoprene rings of 5-mm axial width and 3-mm radial thickness.

A variety of centrifugal blowers was used, and the maximum flow rate for the tests discussed below was approximately 0.1 kg/s: The air was cooled to about 20°C before it entered the cavity. The flow rate was measured, to an accuracy of approximately 3 percent, by orifice plates or by other differential-pressure measuring devices. The cavity could be rotated up to 2000 rpm by a variable-speed electric motor, and the speed was controlled and measured to a precision of ±1 rpm.

The "downstream disc" of the cavity was heated by an equispaced array of thirty, 750-W, radiant "firebar" elements. Each element was arranged in a radial line extending from a radius of $r=230$ mm to $r=380$ mm, approximately equal to the outer radius of the cavity. The axial distance between the "back face" of the downstream disc and the outer surface of the elements was approximately 30 mm. Reflectors were used behind the elements to increase the useful radiative flux, and the back face of the disc was covered with "solar foil" to increase the absorptivity and to reduce the emissivity of the disc surface. The electrical input power, which was thyristor-controlled, was measured by a wattmeter.

Twelve chromel-constantan thermocouples, 0.13 mm in diameter, were embedded in each face of the heated downstream disc, and ten in each face of the unheated upstream disc. The surfaces of each disc were regarded as a number of imaginary rings of approximately equal area, and a thermocouple was placed at the edge of each ring. The signals from the thermocouples were brought out via two silver slip-ring assemblies (one for each disc). For each assembly, the temperature of the junctions between the silver and the thermocouple wires was measured using a semiconductor temperature sensor, which was calibrated to an accuracy of 0.1°C. These temperatures were used as the cold-junction reference temperatures for the upstream and downstream discs. The temperature of the cooling air was measured using a chromel-constantan thermocouple probe located in the stationary pipe immediately upstream of the cavity.

Signals from the thermocouples and temperature sensors, which were measured using a Solartron data logger controlled by a PDP11/34 minicomputer, could be scanned at a rate of 33 channels/s with a resolution of 1 μV (which corresponds to 0.015°C for chromel-constantan thermocouples), and the data were stored on magnetic discs and tapes for subsequent analysis. The overall accuracy of the measurement of the surface temperatures of the rotating disc depends on a number of factors, not least of which is the thermal-disturbance error of an embedded thermocouple (see [9]). However, for the tests reported in this paper, the temperatures are believed to be accurate to within ±0.5°C.

For the flow visualization, the paxolin shroud was replaced by one made from transparent polycarbonate, and a 4-W argon-ion laser was used to illuminate the r–z plane of the cavity. "Slit illumination" was produced using cylindrical and biconvex lenses which converted the laser beam into a sheet of light approximately 2 mm thick and 100 mm wide. Clouds of white smoke (consisting of micron-sized oil particles), produced by a Concept smoke generator, were injected into the inlet of the Secomak centrifugal fan and thence into the cavity. Video recordings of the flow were made using a Sony video camera and monitor, and a Sanyo video recorder. Photographs of the flow structure were taken with a Canon AE1 35-mm camera and Ilford ASA 400 film. A motor-drive unit allowed the photographs to be taken at five frames per second with a shutter speed of 1/90th second and an f2 aperture setting.

2.2 Data Analysis. The temperature inside the downstream disc was computed from the numerical solution of Fourier's heat conduction equation, which expressed in axisymmetric cylindrical polar coordinates is

$$\frac{\partial^2 T}{\partial r^2}+\frac{1}{r}\frac{\partial T}{\partial r}+\frac{\partial^2 T}{\partial z^2}=\frac{1}{\alpha_d}\frac{\partial T}{\partial t} \tag{2.1}$$

The measured surface temperatures were smoothed (in both time and radial distance) and used as boundary conditions for the sides $z=0$ (the cooled cavity-side face) and $z=2l$ (the heated face) of the disc, and one-dimensional heat transfer boundary conditions were assumed at the outer radius, $r=b$, and at the inner radius, $r=r_i$. For simplicity, the initial temperature at $t=0$ was obtained from linear, axial interpolation of the smoothed surface temperatures.

Equation (2.1) was solved by finite difference techniques, using the Crank–Nicolson method, with 21 radial nodes ($\Delta r=15$ mm), 7 axial nodes ($\Delta z=2.12$ mm), and 100 time steps. At each time step, the local heat fluxes at the surface nodes ($z=0$) were computed from second-order differences, and the convective flux q_s was found by subtracting the estimated radiant flux from the total flux. The local Nusselt number Nu was then calculated from

$$\mathrm{Nu}=q_s r/k(T_s-T_I) \tag{2.2}$$

3 A Simple Model of the Flow and Heat Transfer in a Rotating Cavity With a Radial Outflow of Fluid

3.1 The Isothermal Flow Structure. As stated in Section 1, the flow structure can be considered to comprise a source region, Ekman layers, a sink layer, and an interior core. Owen et al. [12] applied the momentum-integral equations to the flow over the discs in the cavity and obtained solutions for $\bar{V}_\phi$, the tangential component of velocity (referred to a stationary frame of reference) outside the boundary layers. They solved both the "linear equations," where nonlinear inertial forces (which are often small compared with Coriolis forces) are neglected, and the "nonlinear equations" (where inertial forces may be significant). For the radial outflow case considered here, although the solutions for $\bar{V}_\phi$ in the linear equations diverge from those for the nonlinear equations as $\bar{V}_\phi/\Omega r$ approaches zero, the linear solutions agree well with available experimental data for a wide range of flow rates and rotational speeds.

From the linear solutions given in [12] for the radial outflow case, Q_l, the *local* volumetric flow rate in *each* Ekman layer, is related to $\bar{V}_\phi$ by

$$\frac{Q_l}{\nu b}=\pi \mathrm{Re}_\phi^{1/2}\left(1-\frac{\bar{V}_\phi}{\Omega r}\right)x^2 \tag{3.1a}$$

for laminar flow, and

$$\frac{Q_l}{\nu b}=0.140\mathrm{Re}_\phi^{4/5}\left(1-\frac{\bar{V}_\phi}{\Omega r}\right)^{8/5}x^{13/5} \tag{3.1b}$$

for turbulent flow. In the source region, fluid is entrained into the Ekman layers until the total flow rate in *both* layers $2Q_l$ equals that supplied at the inlet Q. If all the available fluid is entrained at $r=r_e$, say, then for $r>r_e$ (outside the source region) the flow rate in each Ekman layer is invariant with r and $Q_l=Q/2$; equations (3.1) can then be used to calculate $\bar{V}_\phi$, the tangential component of velocity in the interior core. For $r<r_e$, in the source region itself, Q_l can be calculated from equations (3.1) providing $\bar{V}_\phi$ is known: A simple way of doing this is presented below.

When fluid enters the cavity, at $r=a$, via a porous inner shroud (as shown for the radial-inlet case in Fig. 3*b*), it is reasonable to assume that $\bar{V}_\phi=\Omega a$ at $r=a$ and that, outside the Ekman layers, the angular momentum of this fluid is conserved (that is, $r\bar{V}_\phi=\mathrm{const}$). Hence, for $a\le r\le r_e$ (or $c\le x\le x_e$, where $c=a/b$) it follows that

$$\bar{V}_\phi/\Omega r = c^2 x^{-2} \tag{3.2}$$

Using this expression in equations (3.1) gives

$$\frac{Q_I}{\nu b} = \pi \mathrm{Re}_\phi^{1/2}(x^2 - c^2) \tag{3.3}$$

for laminar flow, and

$$\frac{Q_I}{\nu b} = 0.140 \mathrm{Re}_\phi^{4/5}(1 - c^2 x^{-2})^{8/5} x^{13/5} \tag{3.4}$$

for turbulent flow. The radial extent of the source region can then be found from the condition that $x = x_e$ when $Q_I = \frac{1}{2}Q$, hence

$$x_e = \left[c^2 + \frac{1}{2\pi} C_w \mathrm{Re}_\phi^{-1/2}\right]^{1/2} \tag{3.5}$$

for laminar flow, and

$$x_e(1 - c^2 x_e^{-2})^{8/13} = 1.63 C_w^{5/13} \mathrm{Re}_\phi^{-4/13} \tag{3.6}$$

for turbulent flow.

This result differs from that derived by Owen et al. who assumed that the flow entered the cavity without swirl and that the entrainment in the source region was the same as that for a free disc. From their results

$$x_e = A C_w^{1/2} \mathrm{Re}_\phi^{-1/4} \tag{3.7}$$

for laminar flow, and

$$x_e = B C_w^{5/13} \mathrm{Re}_\phi^{-4/13} \tag{3.8}$$

for turbulent flow. For the radial-inlet case, $A = 0.424$ and $B = 1.37$. For the axial-inlet case, the above values of A and B are still appropriate if the incoming flow is distributed equally between the discs. If, however, the incoming flow impinges on the downstream disc, forming a wall jet, then the appropriate values are $A = 0.599$ and $B = 1.79$.

3.2 Heat Transfer. Northrop and Owen [14] obtained solutions of the energy-integral equation for turbulent Ekman-layer flow. They ignored the source region and sink layer, and assumed that Ekman layers extended over the entire surfaces of the discs. They also neglected buoyancy effects and assumed that the radial distribution of temperature was the same for each disc (the so-called "symmetrically heated cavity"). For the case where $(T_s - T_l) \propto x^{13/8}$ (which is an approximation of the disk temperatures used in the experimental work reported below), their solution for the local Nusselt number is

$$\mathrm{Nu} = 1.625 \frac{C_w \mathrm{Pr}}{4\pi x}(1 - \gamma^{13/8}) \tag{3.9}$$

where

$$\gamma = 0.665 C_w^{-5/8} \mathrm{Re}_\phi^{1/2} \tag{3.10}$$

Rogers [15] produced numerical solutions of the energy-integral equation used in conjunction with the nonlinear momentum-integral equations. Although the solutions are only strictly valid for the symmetrically heated cavity, they are more general than those of Northrop and Owen, and they cover the source region as well as the Ekman layers. Rogers' nonlinear solutions are compared with measured local Nusselt numbers in Section 4.

At high flow rates, the source region fills the entire cavity and Ekman-layer flow does not occur. Under these conditions, the heat transfer becomes independent of rotational

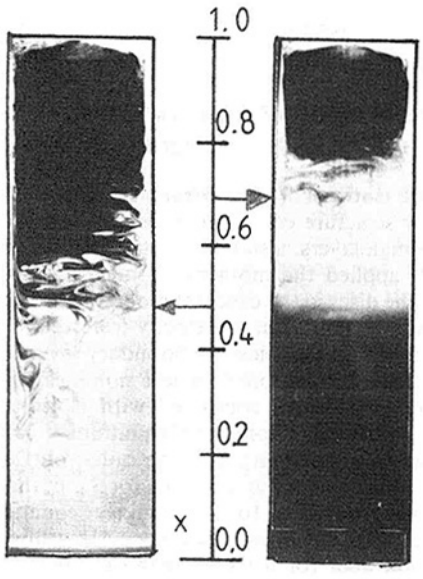

Fig. 4(a) $\mathrm{Re}_\phi = 10^5$

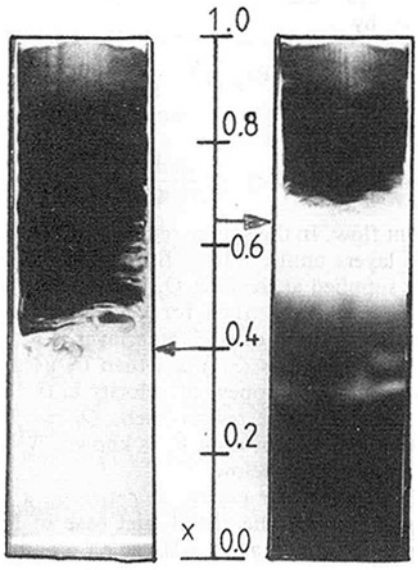

Fig. 4(b) $\mathrm{Re}_\phi = 2 \times 10^5$

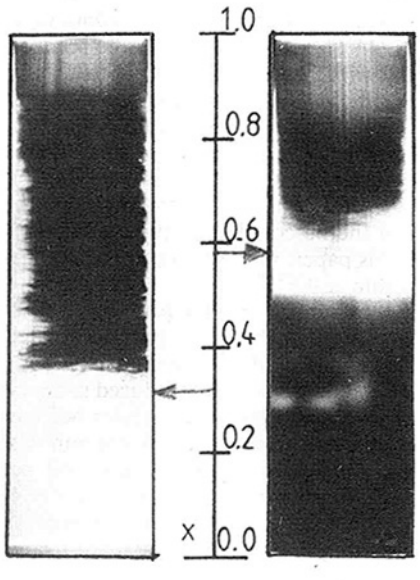

Fig. 4(c) $\mathrm{Re}_\phi = 6 \times 10^5$

Fig. 4 The flow structure in a rotating cavity with a laminar radial outflow of coolant, $C_w = 440$: (i) $a/b = 0.1$, and (ii) $a/b = 0.5$, – denotes edge of source region from equation (3.5)

speed, and Long [9] obtained the following approximate correlation for the 0.1 radius-ratio cavity with an axial inlet:

$$\mathrm{Nu} = 1.46 C_w^{2/3} G^{1/6} \tag{3.11}$$

4 Experimental Results

4.1 Flow Visualization. Figures 4 and 5 show the photographs that were taken using the flow visualization apparatus described in Section 2. The source region, Ekman layers, and sink layer (where smoke has penetrated) stand out in white in contrast to the black interior core. The air entered the cavity through the center of the upstream disc (at the bottom left-hand corner of the photographs); for the 0.5 radius-ratio cavity, the inner shroud prevented illumination for $x < 0.5$, and this region appears black in the photographs.

Figures 4(a, b, c) are for $C_w = 440$, for which value the flow in the Ekman layers is expected to be laminar (that is, $\mathrm{Re}_r < 180$) for $x > 0.39$. The value of x_e given by equation (3.5) can be seen to produce a reasonable estimate of the size of the source region for both values of a/b. Figures 5(a, b, c) are for $C_w = 1760$, for which value the flow in the Ekman layers is expected to be turbulent throughout the cavity, and equation (3.6) provides a reasonable approximation for the size of the source region. Careful inspection of Fig. 5 shows that for $a/b = 0.1$ the incoming flow impinges on the downstream disc forming a wall jet; for $a/b = 0.5$, where there is a radial inlet, the flow in the source region is more symmetric about the midaxial plane. By contrast, Fig. 4 shows little evidence of a wall jet, and the flow in the source region is reasonably symmetric for both $a/b = 0.1$ and 0.5.

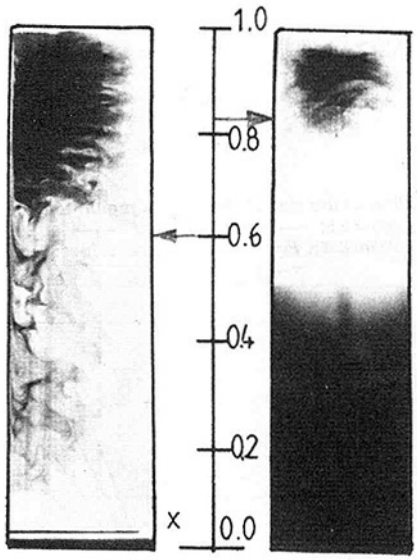

Fig. 5(a) $\mathrm{Re}_\phi = 3 \times 10^5$

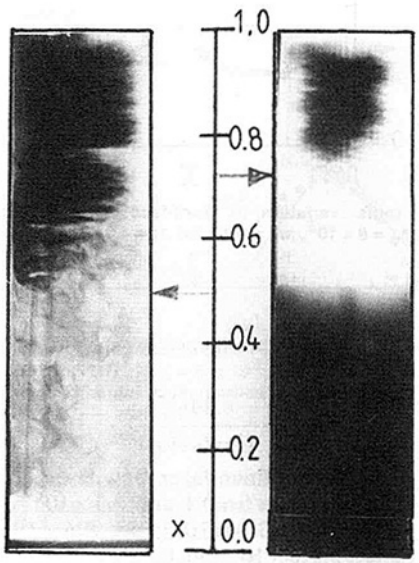

Fig. 5(b) $\mathrm{Re}_\phi = 6 \times 10^5$

A series of tests was conducted for $440 \le C_w \le 1760$ and $6 \times 10^4 \le \mathrm{Re}_\phi \le 1.2 \times 10^6$ where the size of the source region was measured (to within ± 10 mm) from video recordings. The results are presented in Figs. 6 and 7 for laminar and turbulent flow, respectively. From Fig. 6, it can be seen that equation (3.5) tends to underestimate the size of the source region at the larger values of $C_w^{1/2}\ \mathrm{Re}_\phi^{-1/4}$, particularly for $a/b = 0.1$. Similarly, Fig. 7 shows that equation (3.6) underestimates x_e for $a/b = 0.1$, but the agreement between the measured and theoretical values is good for $a/b = 0.5$.

Also shown in Figs. 6 and 7, for $a/b = 0.1$ are the values of x_e obtained from equations (3.7) and (3.8). The use of $A = 0.424$ (the radial-inlet value) in equation (3.7) and $B = 1.79$ (the "wall-jet" value) in equation (3.8) provides a good fit to the experimental data. The use of the radial-inlet value for laminar flow and the wall-jet value for turbulent flow is consistent with the photographic evidence presented in Figs. 4 and 5. It should be emphasized that, unlike equations (3.5) and (3.6), equations (3.7) and (3.8) are only appropriate for small values of a/b where the flow enters the cavity with little or no swirl.

4.2 Temperature Measurements. Most of the Nusselt numbers presented below were obtained during cooling tests. The downstream disc was heated to a maximum steady-state temperature T_{ss} of approximately 100°C; the heaters were then turned off and the disc allowed to cool.

Typical temperature profiles of the front (cavity-side) face of the heated disc are shown in Fig. 8 for $C_w = 3500$ and $\mathrm{Re}_\phi = 8 \times 10^5$ for the 0.1 radius-ratio cavity. The dimensionless front-face temperature θ is defined as

$$\theta = (T_s - T_{\mathrm{ref}})/(T_{ss} - T_{\mathrm{ref}}) \tag{4.1}$$

where T_s is the local surface temperature and T_{ref} is the temperature of the cooling air. For the results shown in Fig. 8, $T_{ss} = 97$°C and $T_{\mathrm{ref}} = 18$°C. The time can be calculated from

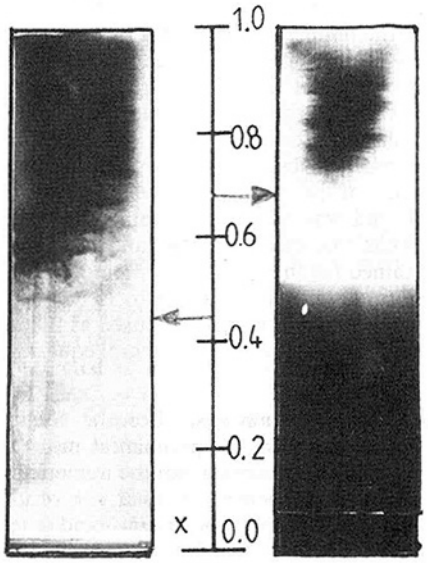

Fig. 5(c) $\mathrm{Re}_\phi = 8 \times 10^5$

Fig. 5 The flow structure in a rotating cavity with a turbulent radial outflow of coolant, $C_w = 1760$: (*i*) $a/b = 0.1$, and (*ii*) $a/b = 0.5$, – denotes edge of source region from equation (3.6)

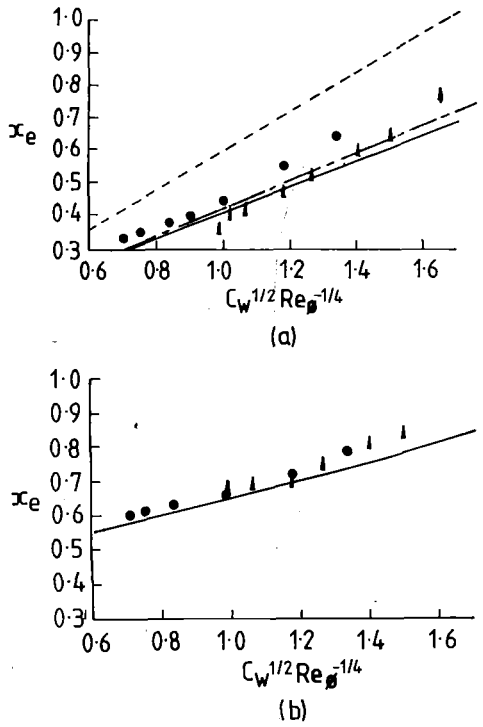

Fig. 6 Variation of the size of the source region for laminar flow: (*a*) *a/b* = 0.1, (*b*) *a/b* = 0.5; — equation (3.5); —·— equation (3.7), *A* = 0.424; ····· equation (3.7), *A* = 0.599; measured values: •, $C_w = 440$; ▲, $C_w = 880$

$$t = N\Delta t \tag{4.2}$$

where N is the number of time steps from the start of the computation and Δt is the finite-difference time step (4 s in this case) used in the solution of Fourier's equation, which was discussed in Section 2.

For the solution of the energy-integral equation, the time average of the measured disc surface temperatures was used as the boundary condition, and the measured cooling-air temperature was used to provide the initial condition. The cooling-air temperature was measured in the stationary pipe upstream of the cavity, and this provided a satisfactory measure of the inlet temperature for the 0.1 radius-ratio cavity. However, for the 0.5 radius-ratio cavity, allowance had to be made for the temperature rise that occurred up to $x = 0.5$. As there were no thermocouples fitted to the rig for measuring the air temperature at $x = 0.5$, separate measurements were made, after all heat transfer tests had been completed, with the outer shroud removed. This enabled a stationary temperature probe to be inserted between the two discs, and the temperature of the cooling air immediately downstream of the inner shroud was measured. From tests conducted at a number of rotational speeds and coolant flow rates, a correlation was obtained for the coolant inlet temperature at $x = 0.5$. This temperature, which could be up to 15°C higher than that measured in the stationary pipe, was used as the initial condition for the solution of the energy-integral equation for the 0.5 radius-ratio cavity.

4.3 Local Nusselt Numbers. For the Nusselt numbers discussed below, the term "experimental measurements" is used to signify values obtained from the numerical solution of Fourier's equation. "Theory" is used for results obtained from the solution of the momentum- and energy-integral equations using the method of Rogers [15].

Figures 9, 10, and 11 show the effect of Reynolds number on the radial variation of Nusselt number for $C_w = 3500$, 7000, and 14,000, respectively. For these three flow rates, the flow should be turbulent throughout the cavity, and the approximate size of the source region can be estimated from equation

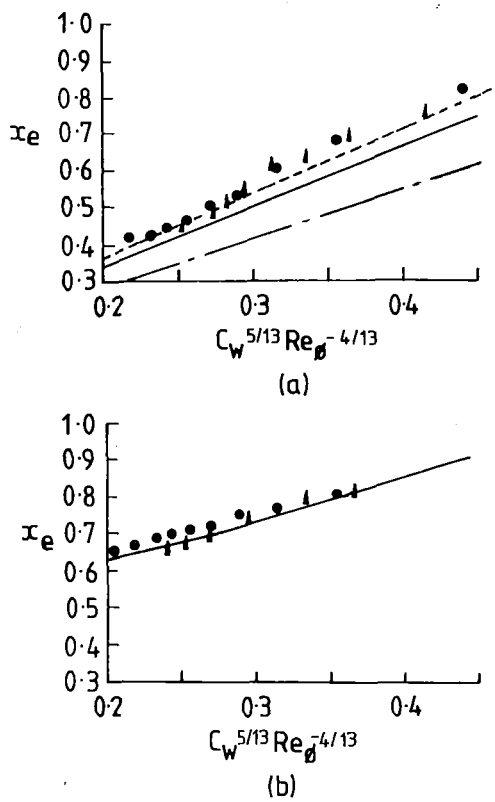

Fig. 7 Variation of the size of the source region for turbulent flow: (*a*) *a/b* = 0.1, (*b*) *a/b* = 0.5; — equation (3.6); —·— equation (3.8), *B* = 1.37; ····· equation (3.8), *B* = 1.79; measured values: •, $C_w = 1200$; ▲, $C_w = 1760$

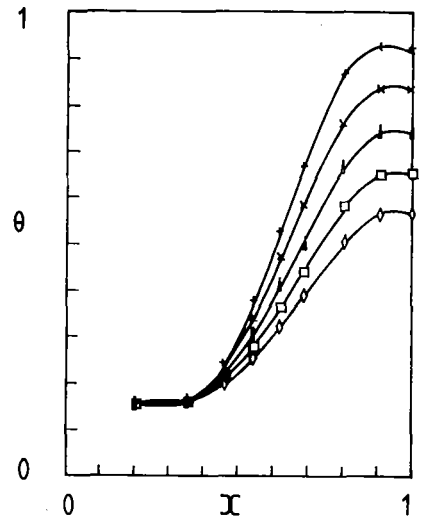

Fig. 8 The radial variation of front-face surface temperature for $C_w = 3500$: $Re_\phi = 8 \times 10^5$, *a/b* = 0.1, and Δt = 4.0 s

Symbol	+	×	△	□	◇
N, equation (4.2)	10	30	50	70	90

(3.6). It follows that Ekman-layer flow should only occur (that is, $x_e < 1$) if

$$Re_\phi > \frac{4.89 C_w^{5/4}}{(1-(a/b)^2)^2} \tag{4.3}$$

Thus, for $C_w = 3500$, Ekman-layer flow is expected to occur for $Re_\phi > 1.3 \times 10^5$ for $a/b = 0.1$ and 2.3×10^5 for $a/b = 0.5$; for $C_w = 7000$, $Re_\phi > 3.2 \times 10^5$ and 5.6×10^5; and for $C_w = 14{,}000$, $Re_\phi > 7.6 \times 10^5$ and 1.3×10^6.

Referring to Fig. 9, for $C_w = 3500$, both theory and experiment show that, for most cases, the local Nusselt numbers for

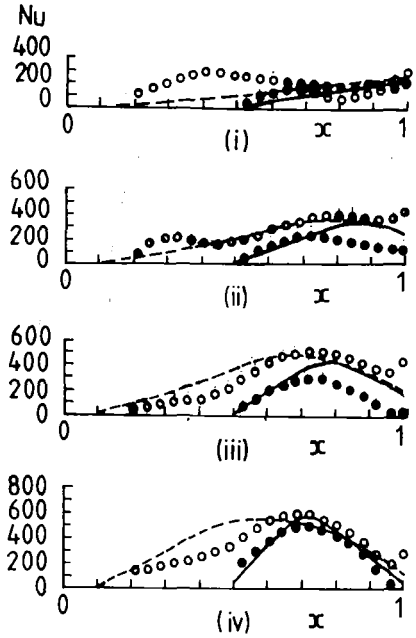

Fig. 9 The effect of Re_ϕ on the radial variation of Nu for $C_W \simeq 3500$: (*i*) $Re_\phi = 1.6 \times 10^5$; (*ii*) $Re_\phi = 4 \times 10^5$; (*iii*) $Re_\phi = 8 \times 10^5$; (*iv*) $Re_\phi = 1.6 \times 10^6$; experimental measurements: ○, $a/b = 0.1$; ●, $a/b = 0.5$; theory: ····· $a/b = 0.1$; —— $a/b = 0.5$

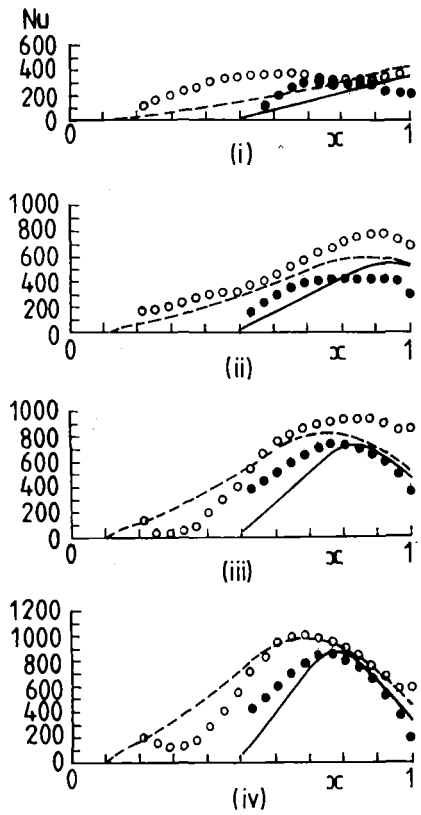

Fig. 10 The effect of Re_ϕ on the radial variation of Nu for $C_W \simeq 7000$: (*i*) $Re_\phi = 2.5 \times 10^5$; (*ii*) $Re_\phi = 6 \times 10^5$; (*iii*) $Re_\phi = 1.2 \times 10^6$; (*iv*) $Re_\phi = 2 \times 10^6$; experimental measurements: ○, $a/b = 0.1$; ●, $a/b = 0.5$; theory: ····· $a/b = 0.1$; —— $a/b = 0.5$

the 0.5 radius ratio cavity are smaller than those for the 0.1 radius ratio. It can also be seen that the agreement between the experimental results and the theoretical values improves with increasing Re_ϕ. The turning point in the theoretical curves marks the approximate limit of the source region: For smaller values of x, where the Ekman layers entrain fluid, Nu increases with increasing x; for larger values of x, where nonentraining Ekman layers form, Nu decreases with increasing x. The latter effect is associated with "thermal saturation": The temperature of the fluid in the Ekman layer progressively approaches that of the disc surface. Under certain conditions, particularly where the disc temperature decreases with increasing x, the temperature of the fluid in the Ekman layer can exceed that of the disc, and negative Nusselt numbers (not shown here) have been predicted and measured.

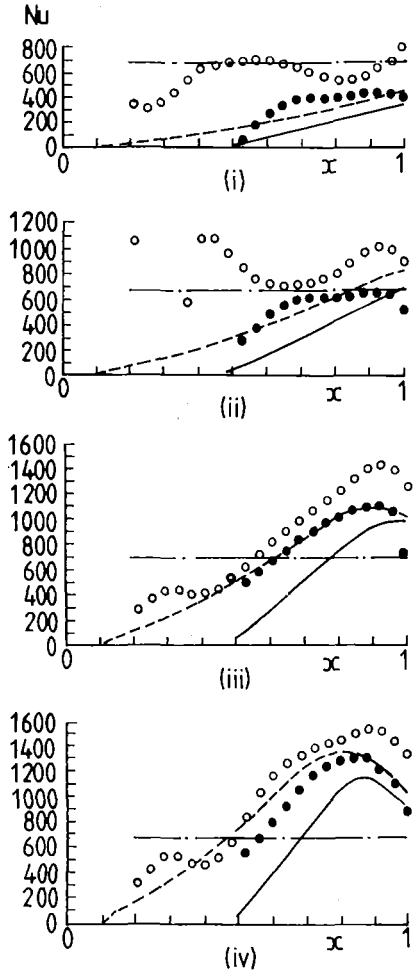

Fig. 11 The effect of Re_ϕ on the radial variation of Nu for $C_W \simeq 14{,}000$: (*i*) $Re_\phi = 2.5 \times 10^5$; (*ii*) $Re_\phi = 6 \times 10^5$; (*iii*) $Re_\phi = 1.2 \times 10^6$; (*iv*) $Re_\phi = 2 \times 10^6$; experimental measurements: ○, $a/b = 0.1$; ●, $a/b = 0.5$; theory: ····· $a/b = 0.1$; _____ $a/b = 0.5$; wall-jet correlation, equation (3.11): —·—

The results in Fig. 10, for $C_w = 7000$, show similar trends to those for Fig. 9. The theoretical and experimental Nusselt numbers for the 0.1 radius ratio are, in the main, larger than those for the 0.5 radius ratio. Also, the agreement between the theoretical curves and the experimental data improves with increasing Re_ϕ, and the radial position of the maximum Nusselt number is predicted accurately in most cases.

In Fig. 11, for $C_w = 14{,}000$, the agreement between theory and experiment is not so good. However, it should be remembered that, at this flow rate, Ekman-layer flow is only expected to occur for $Re_\phi > 7.6 \times 10^5$ for $a/b = 0.1$ and $Re_\phi > 1.3 \times 10^6$ for $a/b = 0.5$. For Reynolds numbers less than this, the experimental data tend to be significantly higher than the theoretical curves, particularly for $a/b = 0.1$. For these conditions the impinging flow has a significant effect on the heat transfer from the downstream disc. This is illustrated in Fig. 11 where, for the lower values of Re_ϕ, the experimental measurements for $a/b = 0.1$ are closer to the "wall-jet correlation" (equation (3.11)) than they are to the theoretical curves.

As shown in [11], the transient temperature on a rotating disc can be predicted with reasonable accuracy even when there are significant errors in the convective boundary conditions. It was also shown in [16] that simple convective correlations obtained for plane discs can give reasonable temperature predictions on actual compressor discs. It is therefore tentatively suggested that, if Ekman-layer flow occurs (according to the criterion given in equation (4.3)), the Nusselt numbers produced by the solution of the momentum- and energy-integral equations should be adequate for design purposes. For higher flow rates, empirical correlations such as equation (3.11) may be acceptable.

5 Conclusions

Experiments have been conducted to determine the effect of inlet conditions on the flow and heat transfer in a rotating cavity with a radial outflow of air. The rig comprised two steel discs 762 mm in diameter, separated by an axial gap of 102 mm, and a peripheral shroud, all of which could be rotated up to 2000 rpm. Air, at flow rates up to 0.1 kg/s, was admitted to the cavity either through a central hole 76 mm in diameter in one disc (the upstream disc) or through a porous inner shroud 380 mm in diameter. These are referred to as the 0.1 and 0.5 radius-ratio cavities, respectively, and for both cases air left the cavity via discrete holes in the peripheral shroud.

Flow visualization was used to study the isothermal flow structure, and, at sufficiently high rotational speeds, Ekman-layer flow was observed. Under these conditions, the flow structure comprised a source region, Ekman layers on each disc, a sink layer, and an interior core. A simple theoretical model was used to estimate the size of the source region for laminar and turbulent flow, and the agreement between measured and predicted values was reasonable for both the 0.1 and 0.5 radius-ratio cavities.

Heat transfer measurements were made by heating the downstream disc up to approximately 100°C and allowing it to cool. Using the transient temperature measurements as boundary conditions, the local heat fluxes (and hence the Nusselt numbers) were determined from the numerical solution of Fourier's conduction equation. These experimentally determined local Nusselt numbers were compared with values obtained from the solution of the turbulent momentum- and energy-integral equations. Providing that the rotational speed was high enough to ensure that Ekman-layer flow occurred, the agreement between the experimental and theoretical local Nusselt numbers was, in the main, reasonable for both the 0.1 and 0.5 radius-ratio cavities. Under these conditions, the local Nusselt numbers exhibited a maximum value at a radial location corresponding to the approximate edge of the source region, and the magnitude of the Nusselt number increased with increasing rotational speed and increasing coolant flow rate. If the flow rate were too high for Ekman layers to form, the measured Nusselt numbers tended to be significantly higher than the theoretical values. This was attributed to the formation of a wall jet on the heated disc, and the resulting heat transfer was virtually independent of rotational speed.

Acknowledgments

The authors wish to thank Motoren- und Turbinen-Union, Rolls-Royce Limited, and the Science and Engineering Research Council for supporting the research reported in this paper. They also wish to thank Dr. J. R. Pincombe for his assistance with the flow visualization and Dr. R. H. Rogers for the use of her program for solving the momentum- and energy-integral equations.

References

1 Owen, J. M., "Fluid Flow and Heat Transfer in Rotating Disc Systems," in: *Heat and Mass Transfer in Rotating Machinery*, D. E. Metzger and N. H. Afgan, eds., Hemisphere, Washington, 1984, p. 81.

2 Hide, R., "On Source-Sink Flows in a Rotating Fluid," *J. Fluid Mech.*, Vol. 32, 1968, p. 737.

3 Bennetts, D. A., and Hocking, L. M., "On Nonlinear Ekman and Stewartson Layers in a Rotating Fluid," *Proc. R. Soc. Lond.*, Vol. A333, 1973, p. 469.

4 Bennetts, D. A., and Jackson, W. D. N., "Source-Sink Flow in a Rotating Annulus: A Combined Laboratory and Numerical Study," *J. Fluid Mech.*, Vol. 66, 1974, p. 689.

5 Owen, J. M., and Bilimoria, E. D., "Heat Transfer in Rotating Cylindrical Cavities," *J. Mech. Engng. Sci.*, Vol. 19, 1977, p. 175.

6 Owen, J. M., and Pincombe, J. R., "Velocity Measurements Inside a Rotating Cylindrical Cavity With a Radial Outflow of Fluid," *J. Fluid Mech.*, Vol. 99, 1980, p. 111.

7 Owen, J. M., and Onur, H. S., "Convective Heat Transfer in a Rotating Cylindrical Cavity," ASME JOURNAL OF ENGINEERING FOR POWER, Vol. 105, 1983, p. 265.

8 Chew, J. W., Owen, J. M., and Pincombe, J. R., "Numerical Predictions for Laminar Source-Sink Flow in a Rotating Cylindrical Cavity," *J. Fluid Mech.*, Vol. 143, 1984, p. 451.

9 Long, C. A., "Transient Heat Transfer in a Rotating Cylindrical Cavity," D. Phil. thesis, University of Sussex, England, 1984.

10 Chew, J. W., "Computation of Convective Laminar Flow in Rotating Cavities," *J. Fluid Mech.*, Vol. 153, 1985, p. 339.

11 Long, C. A., and Owen, J. M., "Prediction of Transient Temperatures for an Air-Cooled Rotating Disc," AGARD CP 390, 1985, p. 21-1.

12 Owen, J. M., Pincombe, J. R., and Rogers, R. H., "Source-Sink Flow Inside a Rotating Cylindrical Cavity," *J. Fluid Mech.*, Vol. 155, 1985, p. 233.

13 Firouzian, M., Owen, J. M., Pincombe, J. R., and Rogers, R. H., "Flow and Heat Transfer in a Rotating Cylindrical Cavity With a Radial Inflow of Fluid," *Int. J. Heat Fluid Flow*; Part 1: "The Flow Structure," Vol. 6, 1985, p. 228; Part 2: "Velocity, Pressure and Heat Transfer Measurements," Vol. 7, 1986, p. 21.

14 Northrop, A., and Owen, J. M., "Heat Transfer Measurements in the Mark II Rotating Cavity Rig," Report No. 83/TFMRC/59, Thermo-Fluid Mechanics Research Centre, University of Sussex, England, 1983.

15 Rogers, R. H., "Computation of Heat Transfer in a Rotating Cavity With a Radial Outflow of Fluid. Part 1: The symmetrically-heated cavity," Report No. 85/TFMRC/71, Thermo-Fluid Mechanics Research Centre, University of Sussex, England, 1985.

16 Reile, E., Radons, U., and Hennecke, D. K., "Transient Thermal Behaviour of a Compressor Rotor With Ventilation—Test Results Under Simulated Conditions," AGARD CP 390, 1985, p. 36-1.

J. E. Doorly

M. L. G. Oldfield

Department of Engineering Science,
Oxford University,
Oxford, England

New Heat Transfer Gages for Use on Multilayered Substrates

The paper describes a technique which enables measurements of the surface heat transfer rate to be made using thin-film gages deposited on a vitreous enamel-coated metal model. It is intended that this will have particular application in rotating turbine test rigs, where it offers considerable advantages over present techniques. These include ease of manufacture, instrumentation, durability, and lack of interference with the basic flow. The procedures for gage calibration and measurement processing are outlined, and the results of wind tunnel tests which confirm that the method is both practical and accurate are described.

Introduction

For many years, experimental research into aspects of the flow through gas turbine engine components has relied upon two-dimensional stationary models of the components mounted in wind tunnels, simulating an essentially "steady" flow. Although steady-flow cascade simulations have contributed greatly to the understanding of engine flows and are still required for many tasks, they do not entirely represent the rotational and unsteady nature of the engine flow. The considerable effect which flow unsteadiness may produce has been clearly demonstrated in studies of the boundary layer behavior of compressor blades by [1, 2], and in low-speed turbine studies by [3, 4].

In heat transfer research, in particular, there is a major gap between the information provided by conventional cascade tests (which suffer from poor flow modeling), and the high-temperature fully rotating systems used in development trials, where the limitations on instrumentation severely restrict the quality and quantity of the measurements which may be made.

1 Current Heat Transfer Techniques

Many methods for the measurement of heat transfer rate rely on transient techniques, often in conjunction with short-duration wind tunnels. The use of short-duration wind tunnels is very attractive, since the energy requirements are much lower than for equivalent continuous facilities.

The model to be tested may be initially at room temperature, and the flow duration is so short that the temperature rises in the working section and the model are small.

The I.L.P.T. (Isentropic Light Piston Tunnel) is a transient facility at Oxford [5] for testing fixed two-dimensional cascades at full-scale engine Reynolds and Mach numbers. Machinable glass model turbine blades are used, instrumented with thin-film surface resistance thermometers, which are applied either by vacuum deposition, or by hand painting followed by firing, to the blade surface [6]. The range of simulation of such cascades may be extended by generating a time-varying inlet flow to the cascade, where the parameters of the flow are chosen to simulate the major component of unsteadiness (i.e., that produced by the wakes shed by the blades in an upstream blade row) [7]. Although the measurements reported in [7] clearly demonstrated the major heat transfer effects of flow unsteadiness and identified much of the unsteady boundary layer behavior, it is not possible for such simulations to reproduce all the complex phenomena (including, for example, the unsteady secondary flow behavior) which occur in the engine.

To obtain measurements of the heat transfer rate to the blades under conditions which more nearly simulate the engine flow, rotation of the rotor blades is required. The purpose of this paper is to describe a new procedure for application to rotating test rigs, whereby it is hoped that detailed measurements similar to those of [7], although in a more exact simulation of the engine flow, may be obtained. Mechanical strength limitations prevent the use of machinable glass for rotating turbine blades and thus a system of instrumenting metal turbine blades with heat transfer gages is essential. Dunn [8] uses thin-film gages deposited on miniature quartz plugs inserted in metal blades, in a fully rotating turbine stage. This approach suffers from surface discontinuities in temperature, and possibly also height, and is effectively limited to "spot" measurements. Epstein et al. [9] have recently described the use of heat transfer gages consisting of thin-film resistance thermometers sputtered onto both sides of a flat 25-μm-thick polyamide sheet. It would be possible to use these gages in the manner described in this paper.

2 Thin-Film Gages on Multilayered Substrates: Governing Equations

This work proposes the use of metal turbine blades which are completely coated with an electrically insulating layer, and which may subsequently be instrumented with thin-film resistance gages. The conventional procedure (using a single-layer substrate) is first outlined, since many of the techniques

Contributed by the Gas Turbine Division of THE AMERICAN SOCIETY OF MECHANICAL ENGINEERS and presented at the 31st International Gas Turbine Conference and Exhibit, Düsseldorf, Federal Republic of Germany, June 8-12, 1986. Manuscript received at ASME Headquarters January 20, 1986. Paper No. 86-GT-96.

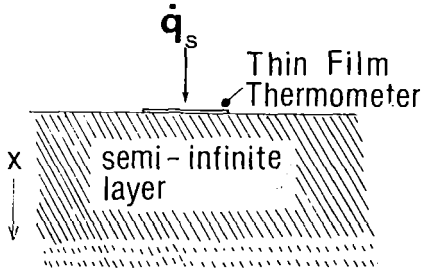

Fig. 1 Thin-film gage on single layer semi-infinite substrate

developed for this case may successfully be extended to multilayered substrates. The ensuing discussion will be brief; the details are described in [10] and more fully in [11].

2.1 Gage on Single-Layer Substrate. The conventional technique employs gages on a single-layer "semi-infinite" (within the timescale of the experiment) electrically insulating substrate (Fig. 1). For short times, and neglecting the thermal capacity of the film itself, it may be assumed that the one-dimensional heat conduction equation governs the heat flow in the substrate, i.e.

$$\frac{\partial^2 T}{\partial x^2} = \frac{1}{\alpha}\frac{\partial T}{\partial t} \tag{1}$$

with the boundary conditions

$$-k\frac{\partial T}{\partial x} = \dot{q}_s \qquad \text{at } x=0 \tag{2}$$

$$T = 0 \qquad \text{at } x=\infty \tag{3}$$

and the initial condition

$$T = 0 \qquad \text{at } t=0 \tag{4}$$

By taking the Laplace transform of equation (1), it may be shown [12] that

$$\bar{\dot{q}}_s(s) = (\rho c k s)^{1/2}\bar{T}_s \tag{5}$$

where $\bar{}$ denotes Laplace transform and s is the Laplace transform variable.

The change in resistance of the thin film is directly proportional to the change in surface temperature. Thus the surface heat transfer rate $\dot{q}_s$ may be calculated from equation (5) either by a numerical calculation applied to a digital recording of the surface temperature signal [12], or by using an analogue [13, 14] to transform the temperature signal into the equivalent surface heat transfer rate.

2.2 Gage on a Two-Layered Substrate. The thin-film gage on a two-layered substrate is shown schematically in Figs. 2 and 3, where the second layer may be considered "finite" or "semi-infinite." The discussion of the use of such gages will be restricted here to the semi-infinite case. The governing one-dimensional equations to be solved are

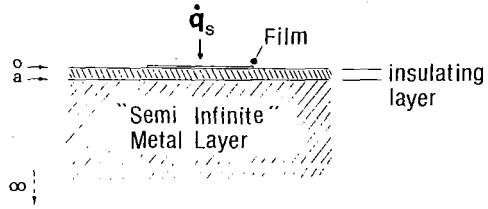

Fig. 2 Thin-film gage on two-layered substrate with semi-infinite metal layer

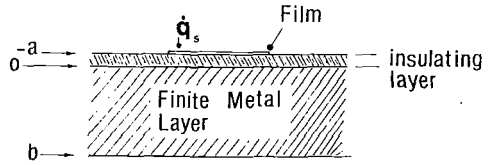

Fig. 3 Thin-film gage on two-layered substrate with finite metal layer

$$\frac{\partial^2 T_1}{\partial x^2} = \frac{1}{\alpha_1}\frac{\partial T_1}{\partial t} \qquad 0 \le x \le a \tag{6}$$

$$\frac{\partial^2 T_2}{\partial x^2} = \frac{1}{\alpha_2}\frac{\partial T_2}{\partial t} \qquad a \le x \le \infty \tag{7}$$

with the boundary conditions

$$\dot{q}_s = -k\frac{\partial T}{\partial x} \qquad x=0 \tag{8}$$

$$T_1 = T_2 \qquad x=a \tag{9}$$

$$k_1\frac{\partial T_1}{\partial x} = k_2\frac{\partial T_2}{\partial x} \qquad x=a \tag{10}$$

$$T_2 = 0 \qquad x=\infty \tag{11}$$

As shown in [11], the equations can be solved to obtain

$$\bar{\dot{q}}_s(s) = (\rho c k s)^{1/2}\frac{(1 - A\exp\{-2a(s/\alpha_1)^{1/2}\})\bar{T}_s}{(1 + A\exp\{-2a(s/\alpha_1)^{1/2}\})} \tag{12}$$

where $A = [\sqrt{(\rho_1 c_1 k_1)} - \sqrt{(\rho_2 c_2 k_2)}]/[\sqrt{(\rho_1 c_1 k_1)} + \sqrt{(\rho_2 c_2 k_2)}]$.

For constant heat transfer rate, $\bar{\dot{q}}_s = Q/s$, the surface temperature $T_s(t)$ is given by

Nomenclature

A = $\dfrac{\sqrt{(\rho_1 c_1 k_1)} - \sqrt{(\rho_2 c_2 k_2)}}{\sqrt{(\rho_1 c_1 k_1)} + \sqrt{(\rho_2 c_2 k_2)}}$
A/D = analogue to digital
c = specific heat capacity
c = distributed capacitance/unit length
erfc = complimentary error function
h = heat transfer coefficient
$h(t)$ = gage step calibration function
$H(s)$ = Laplace transformed step calibration function
i = current
k = thermal conductivity
K_a = analogue calibration constant
mgc = machinable glass ceramic
Nu = Nusselt number
$\dot{q}_s$ = surface heat transfer rate
Q = constant heat transfer rate
r = resistance/unit length
Re = Reynolds number
s = Laplace transform variable
T = temperature rise during experiment
t = time
Tu = overall turbulence intensity, percent
$U(t)$ = unit step function
V = voltage
V_a = analogue output voltage
V_0 = film set voltage
x = vertical coordinate
α = thermal diffusivity
α_R = temperature coefficient of resistance
ρ = density
σ = $\left[\dfrac{\rho_2 c_2 k_2}{\rho_1 c_1 k_1}\right]^{1/2}$

Subscripts and Superscripts

0 = stagnation
1 = insulating layer
2 = second layer
s = surface
$-$ = Laplace transform

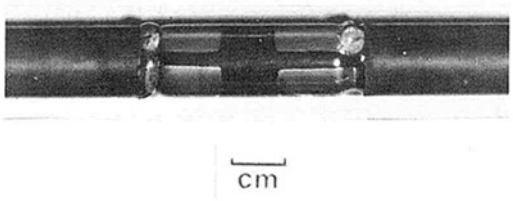

Fig. 4 Central enameled section of mild steel cylinder, with painted film and tags

$$T_s(t)=\frac{2Q}{\sqrt{(\rho_1 c_1 k_1)}}\left[(t/\pi)^{1/2}+2\sum_{n=1}^{n=\infty}A^n\left\{(t/\pi)^{1/2}\exp\left[\frac{-n^2a^2}{\alpha_1 t}\right]-\frac{na}{\sqrt{\alpha_1}}\text{erfc}(na/(\alpha_1 t)^{1/2})\right\}\right] \quad (13)$$

For this case, again, numerical computation may be used to establish the surface heat flux from the temperature signal. Alternatively, an electrical analogue may again be used, though in this case an analytic correction must be made to the analogue output signal (since the analogue only models case (*a*) exactly).

3 Construction and Calibration of Multilayered Models

3.1 Construction

(*a*) *Requirements of the Coating.* The coating was required to

(*i*) provide an electrically insulating layer
(*ii*) adhere well to the base metal
(*iii*) provide a smooth or polishable surface for ease of instrumentation

An alternative to instrumenting a coated blade is to use a thin polyamide film (Kapton) as used in [9], instrumented with films by vacuum deposition, which may subsequently be attached to the blade surface. This approach was fully tested (as reported in [11]), but found to suffer from several limitations, namely:

(*i*) the problems of satisfactory vacuum deposition of the films
(*ii*) the problems of successfully wrapping the instrumented film around the highly curved blade surfaces, without introducing discontinuities or damaging the films
(*iii*) the restriction to comparatively low flow temperatures

The preferred method for thin-film instrumentation was by hand painting followed by firing, directly on a coated blade. For this process, it is necessary for the coating to withstand temperatures of approximately 650°C used in firing the platinum paint, and secondly for the coating to remain impervious to the paint, before and during the firing.

(*b*) *Recommended Coating.* A coating of vitreous enamel fired onto mild steel (EN1A) was found to satisfy the above requirements [11]. Cylinder models machined from mild steel were constructed, followed by enameling and instrumentation (Fig. 4) to test the technique.

3.2 Calibration

(*a*) *Temperature Coefficient* α_R. α_R relates the fluctuating voltage across the film to the surface temperature T_s. The calibration of the gage is commonly done by immersing the model in a deionized water bath, since the operating range is 20°–90°C.

For a single-layer substrate, from equation (5), all that remains to be determined is the thermal product $\sqrt{(\rho ck)}$ of the substrate material. For the two-layered substrate, from equation (12), $\sqrt{(\rho_2 c_2 k_2)}$ of the base metal as well as $\sqrt{(\rho_1 c_1 k_1)}$ of the coating is required. In addition, the ratio $a/\sqrt{\alpha_1}$ or a/k_1 (since $\sqrt{(\rho_1 c_1 k_1)}$ must be known) must be determined.

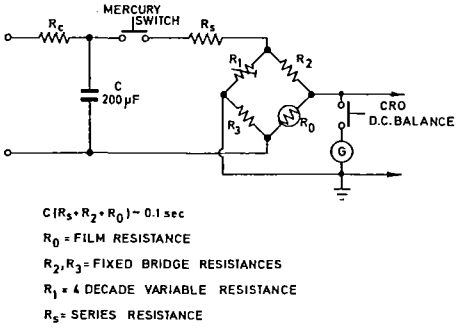

Fig. 5 Simple circuit for measurement of $\sqrt{(\rho ck)}$ from [12]

(*b*) *Thermal Product* $\sqrt{(\rho_1 c_1 k_1)}$. To determine $\sqrt{(\rho_1 c_1 k_1)}$ of the top layer, electrical discharge methods [12] and/or radiant heating methods may be used. The electrical discharge method has proved more useful for this work, but the use of a radiant method for calibration will be described in section 5.1, and is fully described in [11].

For the discharge calibration technique, the temperature response of the substrate to a step in surface heat transfer is monitored by suddenly applying a constant current through the film (producing ohmic heating) and monitoring the change in film resistance (hence temperature). A simplified bridge circuit from [12], which applies a current step to the film, is shown in Fig. 5.

The test is first conducted in vacuum or still air, where the heat loss to the surroundings is negligible in comparison with the heat transferred by conduction to the substrate, and the change in film voltage $\Delta V_1(t)$ is recorded.

Repeating the test, with the film surface covered in a liquid of known thermal properties such as glycerine, and again recording the change in film voltage $\Delta V_2(t)$, it may be shown [15] that

$$\sqrt{(\rho_1 c_1 k_1)}_{\text{substrate}}=\frac{\sqrt{(\rho ck)}_{\text{glycerine}}}{\dfrac{\Delta V_1/\sqrt{t}}{\Delta V_2/\sqrt{t}}-1} \quad (14)$$

The test must be conducted within a sufficiently short time, which depends upon the film dimensions, for the process to remain one dimensional.

The determination of the extra constants $\sqrt{(\rho_2 c_2 k_2)}$ and a/k_1, required for the use of multilayered gages, will now be considered.

3.3 Determination of a/k_1, $\sqrt{(\rho_2 c_2 k_2)}$. Explicit determinations of local values of a/k_1 at each instrumented point on a model cannot satisfactorily be performed from separate measurements of a and k_1, as the properties of deposited layers differ markedly from the bulk properties of the material, so that k_1 cannot be assumed known. A technique has been devised in this study, to allow the electrical discharge calibration technique to be extended to determine both a/k_1 and $\sqrt{(\rho_2 c_2 k_2)}$.

For a step in heat transfer rate applied to the surface, from equation (13),

$$T_s(t)=\frac{2Q}{\sqrt{(\rho_1 c_1 k_1)}}\left[(t/\pi)^{1/2}+2\sum_{n=1}^{n=\infty}A^n\left\{(t/\pi)^{1/2}\exp\left[\frac{-n^2a^2}{\alpha_1 t}\right]-\frac{na}{\sqrt{\alpha_1}}\text{erfc}(na/(\alpha_1 t)^{1/2})\right\}\right]$$

As shown in [11], for large t

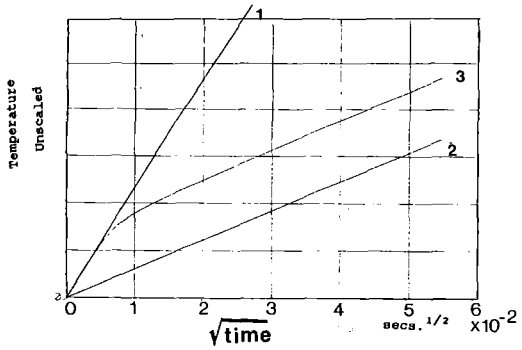

Fig. 6 Predicted surface temperature signals for step in heat transfer rate: (1) insulator alone; (2) metal alone; (3) insulator coated metal

$$T_s \to 2Q\left[\frac{t}{\pi\rho_2 c_2 k_2}\right]^{1/2} + a\frac{Q}{k_1}\left[1-\frac{\rho_1 c_1 k_1}{\rho_2 c_2 k_2}\right] \tag{15}$$

which is effectively the temperature which would be recorded from a gage on metal alone, with an offset to account for the presence of the insulator.

For short times

$$T_s(t) = 2Q\left[\frac{t}{\pi\rho_1 c_1 k_1}\right]^{1/2} \tag{16}$$

Figure 6 shows the predicted surface temperatures for metal alone, insulator alone, and insulator-coated metal. The time corresponding to the intersection of equations (15) and (16), which both describe straight lines in $\sqrt{\text{time}}$, is given by

$$\sqrt{t} = \left[\frac{\pi}{2}\right]^{1/2}\frac{a}{k}\left[\frac{\rho_2 c_2 k_2}{\rho_1 c_1 k_1}\right]^{1/2}\{(\rho_1 c_1 k_1)^{1/2} + (\rho_2 c_2 k_2)^{1/2}\} \tag{17}$$

and is referred to as the "switch" point. $\sqrt{(\rho_1 c_1 k_1)}$ for the insulator is known from the standard air–glycerine test. The ratio of the slope of the line obtained in plotting $T_s(t)$ against $\sqrt{t}$, in equation (15), to that from equation (16), is

$$\frac{(\rho_2 c_2 k_2)^{1/2}}{(\rho_1 c_1 k_1)^{1/2}}$$

thus $\sqrt{(\rho_2 c_2 k_2)}$ can be determined, and hence a/k_1 obtained from equation (17).

4 Determination of Surface Heat Transfer Rate Using Gage on Multilayered Substrate

As mentioned in section 2, the surface heat transfer rate may be evaluated from the temperature response of the film, either by purely numerical means, or by using an electrical analogue, together with an analytic correction. For the purely numerical calculation, equations (6) and (7) are solved with the boundary condition

$$T_1 = T_s(t) \text{ at } x = 0 \tag{18}$$

where $T_s(t)$ is the temperature measured by the film, together with boundary conditions (9), (10), and (11) and an initial condition (4). A large number of standard numerical procedures may be used, such as a simple finite-difference scheme [11].

The purely numerical computation of the surface heat flux from a digitally recorded heat flux signal introduces undesirable noise, however. It may be shown that noise, whether interference, or due to digital conversion present in the temperature signal, is greatly magnified in the numerical computation of $\dot{q}_s$ from T_s. In principle, such effects may be minimized by using high-precision A/D converters and low-noise temperature amplifiers. The approach preferred for this work, however, involved the use of electrical analogue circuits, which, as mentioned, exactly model the one-layer case, together with an analytic correction to accommodate the second layer. It has been shown [12–14] that an ideal RC transmission line analogue circuit is analogous to the semi-infinite heat transfer case where $\dot{q}_s$ is analogous to i and T to V. A typical analogue circuit (from [5]) is shown in Fig. 7. The constant current source is adjusted so that, for $T=0$, the film voltage is V_0. The change in voltage when the film is at a temperature T is given by

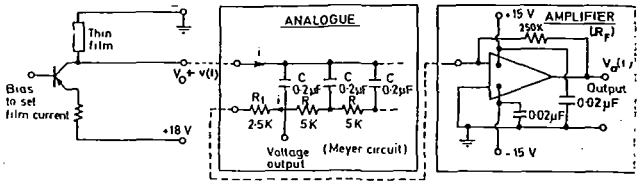

Fig. 7 Typical electrical analogue circuit for thin film use; from [5]

$$V = \alpha_R V_0 T \tag{19}$$

The current

$$\bar{i} = s^{1/2}\left[\frac{c}{r}\right]^{1/2}\alpha_R V_0 \bar{T} \tag{20}$$

It may be shown [12], that for this single-layer case

$$\bar{\dot{q}}_s = \frac{(\rho c k)^{1/2}}{\alpha_R V_0}\left[\frac{r}{c}\right]^{1/2}\bar{i} \tag{21}$$

Hence the surface heat transfer rate is directly proportional to the analogue current.

The general relationship between the surface heat transfer rate and the surface temperature T_s for any thin-film gage on a multilayer substrate may be expressed as

$$\bar{\dot{q}}_s(s) = F(s)\bar{T}_s \tag{22}$$

From (19), (20), and (21), the analogue voltage output is given by

$$\bar{V}_a = \frac{s^{1/2}\bar{V}}{K_a} = \frac{V_0}{K_a}s^{1/2}\alpha\bar{T}_s \tag{23}$$

where K_a = analogue calibration constant. Thus,

$$\bar{\dot{q}}_s = \frac{K_a F(s)\bar{V}_a}{V_0\alpha\sqrt{s}} \tag{24}$$

If we define, for the gage, a step calibration function $h(t)$ with Laplace transform

$$H(s) = \frac{F(s)}{(\rho_1 c_1 k_1)^{1/2}s^{3/2}} \tag{25}$$

then (23) may be expressed as

$$\bar{\dot{q}}_s(s) = \frac{K_a}{\alpha V_0}H(s)(\rho_1 c_1 k_1)^{1/2} \tag{26}$$

Then inverting equation (26) gives

$$\dot{q}_s(t) = \frac{K_a}{\alpha V_0}h(t)(\rho_1 c_1 k_1)^{1/2} \tag{27}$$

The digitally sampled analogue output signal (23) can be considered to be a series of step functions such that

$$V_a(n\tau) = \sum_{n=1}^{N} a_n U(N\tau - n\tau) \tag{28}$$

where $U(t-\tau)$ is the unit step function.

The Laplace transform of equation (28) is

$$\bar{V}_a(s) = \sum_{n=1}^{N} a_n\frac{e^{-st}n}{s} \tag{29}$$

where $t_n = n\tau$ and $a_n = V_a(n\tau) - V_a(n-1)\tau$. Then

$$\bar{\dot{q}}_s(s) = \frac{1}{\alpha V_0}H(s)(\rho_1 c_1 k_1)^{1/2}\bar{V}_a(s) \tag{30}$$

so

$$\dot{q}_s(t) = \frac{K_a}{\alpha V_0}(\rho_1 c_1 k_1)^{1/2}\Sigma h(N-n)\tau(V_a(n\tau) - V_a(n-1))\tau \tag{31}$$

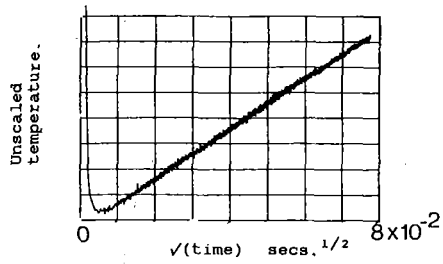

Fig. 8 Temperature response from film on enamel/steel cylinder in air

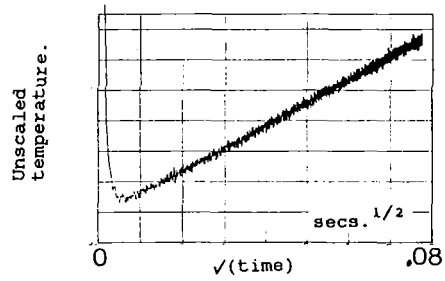

Fig. 9 Temperature response from film on enamel/steel cylinder in glycerine

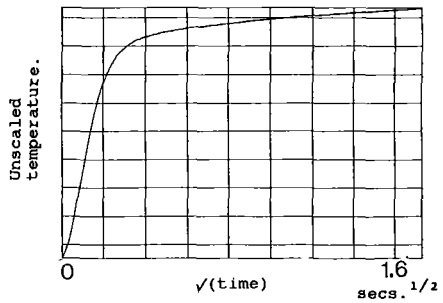

Fig. 10 Measured surface temperature response for enamel/steel cylinder in air

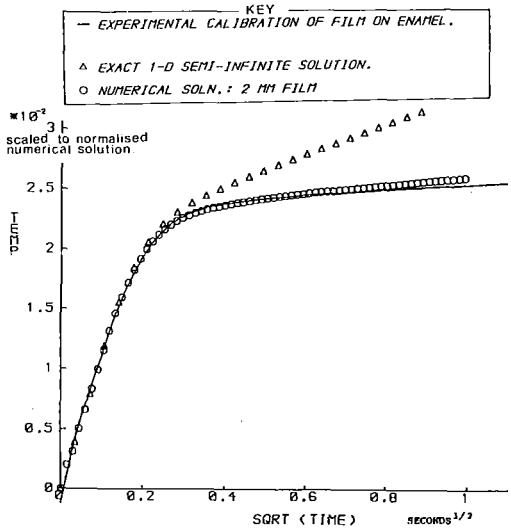

Fig. 11 Comparison of experimental calibration of film on enamel/steel cylinder with exact one-dimensional semi-infinite solution and two-dimensional numerical solution

Thus for a gage on any multilayered substrate, only $h(t)$ is needed to determine the heat transfer rate from the analogue output.

For the single-layer, semi-infinite gage, $h(t) = u(t)$, the unit step. For the two-layered, semi-infinite gage considered here, from (12),

$$h(t) = 1 + 2\sum_{m=1}^{\infty} (-1)^m A^m \operatorname{erfc}\frac{ma}{\sqrt{(\alpha_1 t)}}$$

Table 1 Thermal products

Material	$\sqrt{(\rho ck)}$, $Jm^{-2}s^{-1/2}K^{-1}$	Source
Glycerine	925	[12]
Macor machinable glass	1808	calibration
ENIA mild steel	14186	TPRC data series
Vitreous enamel	1468	calibration
Kapton	560	calibration

Thus, as stated in section (3), the heat transfer rate for a gage on a two-layered composite with semi-infinite metal layer can be determined from equation (31) if $\sqrt{(\rho_1 c_1 k_1)}$, $\sqrt{(\rho_2 c_2 k_2)}$, and $a/\sqrt{\alpha_1} = (a/k_1)\sqrt{(\rho_1 c_1 k_1)}$ are known.

5 Experimental Results

Testing of the electrical discharge calibration technique and result processing method was carried out using circular cylinder models approximately 13 mm in diameter, machined from mild steel with the central span coated with vitreous enamel of thickness approximately 200 μm (Fig. 4). After calibration, the models were used to measure the stagnation point heat transfer for a cylinder in cross flow, using the Isentropic Light Piston Tunnel at Oxford. The results obtained using the new two-layer technique were compared with those from testing a single-layer machinable glass ceramic cylinder and processing using the existing one-layer technique, and independently, with an accepted correlation [15], for stagnation point circular cylinder heat transfer.

5.1 Model Calibration. The air–glycerine calibration technique [16] was used to obtain $\sqrt{(\rho_1 c_1 k_1)}$ of the enamel, and the typical temperature versus $\sqrt{\text{time}}$ traces are shown in Figs. 8 and 9, giving a value of 1468 J $m^{-2}s^{-1/2}K^{-1}$ for $\sqrt{(\rho_1 c_1 k_1)}$ of the enamel layer.

The temperature–$\sqrt{\text{time}}$ trace for a test of longer duration, 2.6 s, is shown in Fig. 10, clearly exhibiting the form of Fig. 6. The analysis of sections 3 and 4 assumed that the one-dimensional heat conduction equation was valid throughout the test, or equivalently, that the whole surface of the substrate is heated. Since the film itself is the surface heat source, the heat produced by ohmic dissipation is applied to a narrow strip of the width of the film (maximum width typically 2 mm). Further analysis and numerical methods [11], combined with practical calibrations, illustrated that two-dimensional conduction within the substrate may become significant at a time depending on coating properties, thickness, and base properties. The effect of two-dimensional conduction results in a lowering of the second part of the curve from the ideal one-dimensional two-layer semi-infinite solution. This is illustrated in Fig. 11, where the trace from the calibration using a film of width 2 mm is plotted with the exact one-dimensional solution, and with the solution from a two-dimensional numerical scheme. As can be seen, the one-dimensional assumption is valid up to the switch point. A modified procedure of calibration was thus adopted, since the slope of the second part of the curve is grossly affected by lateral conduction. A line of best fit is drawn to the first section of the curve, and its slope calculated. For models where the thermal properties of the second layer are known to a good degree of precision, as is certainly the case for mild steel, the second line can be fitted to the second section of the curve, so that it is tangential to the curve in the region where the switch point is expected to occur, and such that its slope is in the ratio

$$\frac{\text{slope 1}}{\text{slope 2}} = \frac{\dfrac{1}{\sqrt{(\rho_1 c_1 k_1)}}}{\dfrac{1}{\sqrt{(\rho_2 c_2 k_2)}}}$$

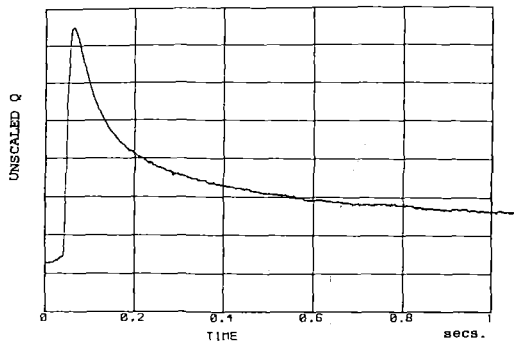

Fig. 12(*a*) Analogue output from radiant test for film on enamel/steel cylinder

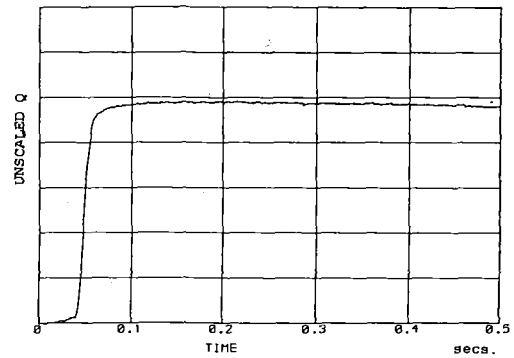

Fig. 12(*b*) Reconstructed heat transfer rate for enamel/steel cylinder

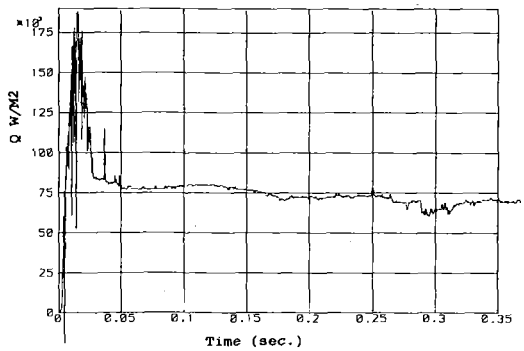

Fig. 13 Stagnation point heat transfer rate for machinable glass cylinder, sampled by transient recorder

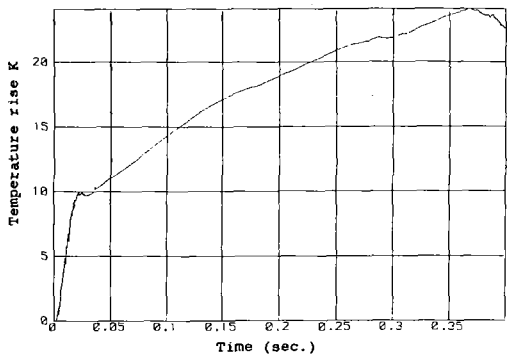

Fig. 14 Reconstructed surface temperature for machinable glass cylinder

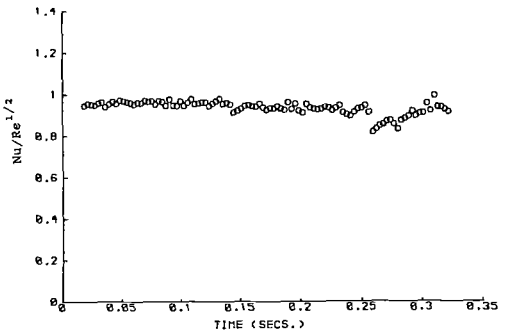

Fig. 15 Plot of $Nu/Re^{1/2}$ for machinable glass cylinder

where $\sqrt{(\rho_1 c_1 k_1)}$ has been determined from an air–glycerine test and $\sqrt{(\rho_2 c_2 k_2)}$ is known. This contrasts with the procedure outlined in sections 3 and 4, where the second line is drawn as a least-squares fit to the second part of the curve.

For the trace shown in Fig. 10 the "switch point" or point of intersection was found to occur at 0.20 $(s)^{1/2}$, which resulted in a value of 1.39×10^{-4} for the constant a/k_1.

In view of the difficulties associated with lateral conduction in the electrical discharge calibration, a simple system of radiative heating [11] was used in conjunction with the electrical discharge technique, with an element from a car cigarette lighter powered by a 12-V battery being used as the heat source. A camera shutter was used to apply a step in heat flux to the surface of the model, over an area much larger than the gage. The surface temperature response can thus be obtained from the film output voltage. For the purpose of these tests, however, the use of the radiant testing was restricted to checking the accuracy of the calibration constants obtained from the electrical discharge tests. A battery-powered electrical analogue was used to apply 1 V across the film, and a thin coating of matte black paint was sprayed across the whole surface. Heat was provided to the surface for a finite length of time and the analogue output was recorded on a DATALAB Transient recorder. The calibrations obtained in this study are summarized in Table 1.

From equation (31), it was shown that if the analogue output $V_a(t)$ is represented as a series of steps, then if the parameters $\sqrt{(\rho_1 c_1 k_1)}$ and a/k_1 have been correctly obtained, the reconstructed $\dot{q}_s$ for the radiant test will be a step.

A sampled analogue output and the reconstructed heat transfer rate using the calibrated values are shown in Figs. 12(*a*) and 12(*b*) for a gage on a two-layer model. It can be seen that the reconstructed $\dot{q}_s$ is a step function.

5.2 Wind Tunnel Testing. Separate tests were performed in which one of two enamel/steel circular cylinder models or a machinable glass cylinder model was placed in the working section of the Isentropic Light Piston Tunnel at Oxford, in front of a cascade of turbine blades. The I.L. P.T. provides a constant property flow of warm (432 K) air for about 0.4 s. Two independent data acquisition systems were used to record the output signals from the heat transfer analogue circuits, namely a PDP 11/34A computer at a sampling rate of 330 Hz and a "stand-alone" transient recorder (Datalab model DL2800) at a sampling rate of 5 kHz.

During the course of a run, the heat transfer from the warm air to the model surface may produce an appreciable rise in surface temperature. In order to correct for the consequent drop in heat flux caused by the drop in the driving temperature potential the surface temperature rise must also be known. As discussed by [5], however, the temperature signal can easily be reconstructed from the surface heat transfer rate to an excellent degree of accuracy. This optimizes the amount of data available per tunnel run and avoids the need for separate recordings of the temperature.

Single Layer Substrate. The measured heat transfer rate trace using the conventional technique is shown in Fig. 13, and the corresponding reconstructed surface temperature rise in

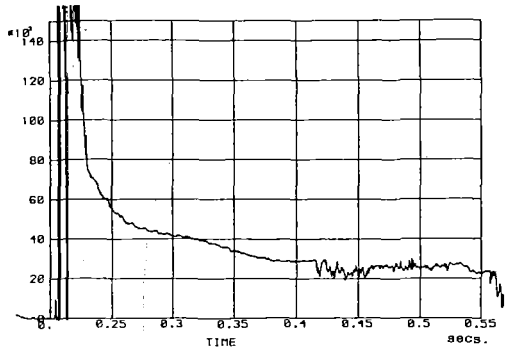

Fig. 16 Analogue output for enamel/steel cylinder

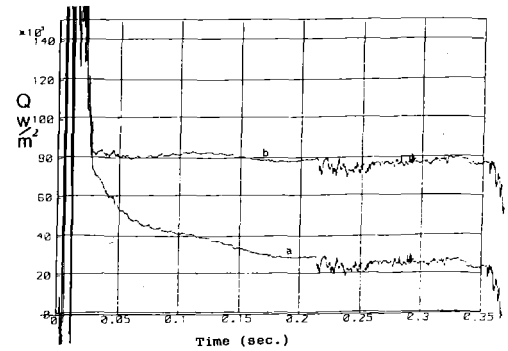

Fig. 17 Uncorrected analogue output (a) and corrected heat transfer rate (b) for enamel/steel cylinder

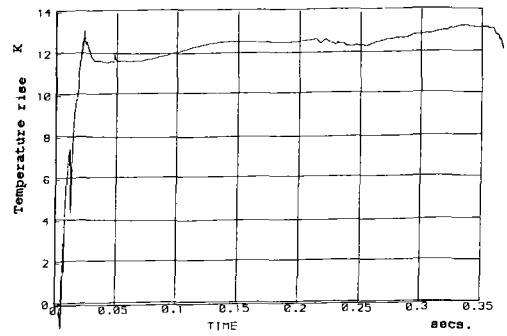

Fig. 18 Reconstructed surface temperature rise for enamel/steel cylinder

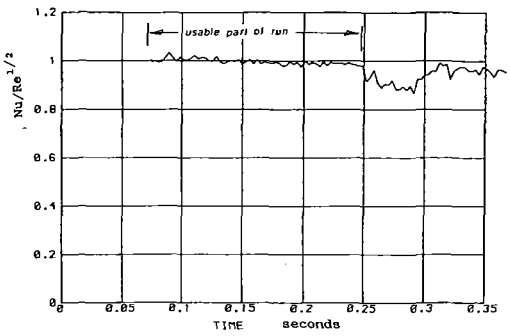

Fig. 19 Plot of $Nu/Re^{1/2}$ for enamel/steel cylinder

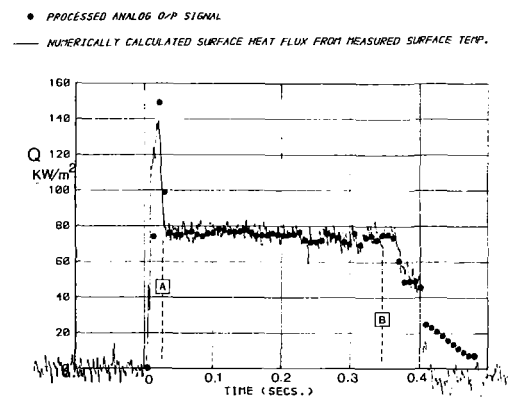

Fig. 20 Comparison of heat flux obtained from corrected analogue output with that from numerical computation using surface temperature

Fig. 14. The heat transfer rate is obtained directly from the calibrated sampled analogue output voltage. The measured values of the heat transfer rate at the cylinder stagnation point were compared with the correlation of Lowery and Vachon [15]. For Tu = 0, $Nu/Re^{1/2} = 1.01$.

The Nusselt number $Nu = hl/k$, where l is a characteristic body length (= diameter for a cylinder), k is the local thermal conductivity of the freestream and $h = \dot{q}_s/(T_0 - T_s)$ is the heat transfer coefficient, with T_0 the stagnation and T_s the surface temperature.

A plot of $Nu/Re^{1/2}$ against time, which removes effects caused by slight oscillations in flow conditions and the change of T_s with time is shown in Fig. 15 for the machinable glass cylinder. This shows excellent agreement with Lowery and Vachon's correlation. Point-by-point comparisons of the measured $\dot{q}_s$ with $\dot{q}_s$ predicted from [15] give agreement to within 3 percent.

Two-Layered Substrate. The sampled analogue output voltage is shown in Fig. 16. This is no longer the actual heat transfer rate, as in the single-layer output, but must be corrected, from equation (31). The corrected, actual heat transfer rate and the raw analogue output are superimposed in Fig. 17, showing the magnitude of the correction. A plot of the reconstructed surface temperature rise is shown in Fig. 18, and it can be seen that it is much less than for the insulating model and approaches steady-state conditions. The plot of $Nu/Re^{1/2}$ against time is shown in Fig. 19, and illustrates that the overall accuracy is very good. Point-by-point comparison of $\dot{q}_s$ measured with $\dot{q}_s$ predicted gives agreement to within 4 percent.

A comparison between the stagnation point heat transfer rate using an electrical analogue, and that computed directly from a recorded temperature signal is shown in Fig. 20. The agreement is very good, but shows that the trace computed purely numerically is far noisier than that obtained using an analogue. Numerical filtering of the temperature signal would reduce this noise. The use of the analogue together with the correction is, however, very advantageous.

6 Conclusions

A new, accurate and computationally efficient method for determining the surface heat flux to a multilayered model turbine blade has been developed. Development tests indicate that vitreous enameling was the preferred method for producing a tough insulating coating. New procedures have been described to enable the relevant properties of such coatings to be established. Analytic processing procedures have been found which allow electronic circuitry, or numerical methods to measure the surface heat flux on a model instrumented with thin-film gages. The gage system described here is now in use on steel NGV blades under test in the short-duration annular cascade tunnel [17] at RAE Pyestock.

Acknowledgments

The authors are grateful to the Science and Engineering

Research Council and to M.O.D.P.E. (RAE Pyestock) for their support of this work. They also wish to acknowledge the valuable technical assistance given to them by Mr. J. L. Allen of Oxford University, and members of the enameling industry in the U.K.

References

1 Walker, G. J., "The Unsteady Nature of Boundary Layer Transition on an Axial Flow Compressor Blade," ASME Paper No. 74-GT-135.

2 Evans, R. L., "Boundary Layer Transition and Separation on a Compressor Rotor Airfoil," ASME JOURNAL OF ENGINEERING FOR POWER, Vol. 104, Jan. 1982, pp. 251–253.

3 Dring, R. P., Joslyn, H. D., Hardin, L. W., and Wagner, J. H., "Turbine Rotor-Stator Interaction," ASME JOURNAL OF ENGINEERING FOR POWER, Vol. 104, 1982, pp. 729–742.

4 Hodson, H. P., "Boundary Layer and Loss Measurements on the Rotor of an Axial Flow Turbine," ASME JOURNAL OF ENGINEERING FOR GAS TURBINES AND POWER, Vol. 106, 1984, pp. 391–399.

5 Jones, T. V., Schultz, D. L., Oldfield, M. L. G., and Daniels, L. C., "A New Transient Facility for the Measurement of Heat Transfer Rates," AGARD CP-229, *High Temperature Problems in Gas Turbine Engines*, Ankara, 1979.

6 Oldfield, M. L. G., Jones, T. V., and Schultz, D. L., "On-Line Computer for Transient Turbine Cascade Instrumentation," *IEEE Transactions on Aerospace and Electronic Systems*, Vol. AES-14, No. 5, Sept. 1978, pp. 738–749.

7 Doorly, D. J., and Oldfield, M. L. G., "Simulation of the Effects of Shock Wave Passing on a Turbine Rotor Blade," ASME JOURNAL OF ENGINEERING FOR GAS TURBINES AND POWER, Vol. 107, 1985, pp. 998–1006.

8 Dunn, M. G., "Measurement of Heat Flux and Pressure in a Turbine Stage," ASME JOURNAL OF ENGINEERING FOR GAS TURBINES AND POWER, Vol. 107, 1985, pp. 76–83.

9 Epstein, A. H., Guenette, G. R., Norton, R. J. G., and Cao Yuzhang, "High Frequency Response Heat Flux Gauges for Metal Blading," AGARD-CPP-390, Gergen, Norway, 1985.

10 Doorly, J. E., and Oldfield, M. L. G., "The Theory of Advanced Thin Film Heat Transfer Gauges," to be published.

11 Doorly, J. E., D. Phil. Thesis, Oxford University, Mar. 1985.

12 Schultz, D. L., and Jones, T. V., "Heat Transfer Measurements in Short Duration Hypersonic Facilities," AGARD, AG-165, 1973.

13 Meyer, R. F., "A Heat Flux Meter for Use With Thin Film Surface Thermometers," NRC Canada, Aero. Rep. LR-279, 1960.

14 Oldfield, M. L. G., Burd, H. J., and Doe, N. G., "Design of Wide-Bandwidth Analogue Circuits for Heat Transfer Instrumentation," *Proc. 14th ICHMT Symposium on Heat and Mass Transfer in Rotating Machinery*, Dubrovnik, 1982.

15 Lowery, G. W., and Vachon, R. I., "The Effect of Turbulence on Heat Transfer From Heated Cylinders." *Int. J. Heat Mass Transfer*, Vol. 18, 1975, pp. 1229–1242.

16 Maulard, J., "Calibration Method Used at ONERA for Hotshot and Shock Tube Heat Transfer Transducers," *Proc. 3rd Int. Congr. Instr. Aerosp. Simul. Facilities*, IEEE G-AES, May, 1969, p. 96.

17 Brooks, A. J., Colbourne, D. E., Wedlake, E. T., et al., "The Isentropic Light Piston Annular Cascade Facility at RAE Pyestock," AGARD-CPP-390, Bergen, Norway, 1985.